DEVELOPMENT OF AN ELECTROMAGNETIC INDUCTION METHOD FOR NON-INVASIVE BLOOD FLOW MEASUREMENT

Maythem Ali

BEng

A thesis submitted to the University of Huddersfield in partial fulfilment of the requirements for the degree of Doctor of Philosophy

ABSTRACT

Blood flow is an important measurement in the diagnosis of cardiovascular diseases – the main cause of death globally. Cardiovascular diseases are often associated with atherosclerosis, which is a condition that causes the narrowing of arteries due to a build-up of lipids on the wall of the arterial vessels. Atherosclerosis occurring in the upper or lower limbs (referred to as peripheral arterial diseases) may lead to heart attack, stroke or severe health complications. Early detection of peripheral arterial diseases will enable primary prevention, and thus a reduction in morbidity, mortality and associated resources and financial costs.

Limitations and drawbacks in the current methods for peripheral arterial blood flow measurement were primary factors in directing this research, which focuses on developing a reliable, easy-to-use and low-cost, non-invasive blood flow metering method that can replace or be an alternative option to current methods. This thesis describes the design and development of a novel electromagnetic induction method that can be used for peripheral arterial blood flow measurement non-invasively. In general terms, an electromagnetic induction flow metering technique is desirable because it is linear and insensitive to viscosity, temperature, conductivity and pressure loss. Additionally, and unlike previous non-invasive electromagnetic blood flow meters, the proposed method can be calibrated offline and is insensitive to velocity profile. The latter is important in obtaining measurements with high accuracy as blood flow in mammals is asymmetric.

A mathematical model was developed for the proposed electromagnetic induction method based on the theory of "weight functions" by Shercliff and the "virtual current" theory by Bevir. This model demonstrated that, for multiple flow channels within a cross-sectional area bounded by a multi-electrode array and across which a uniform

magnetic field is applied, flow induced potentials, due to the flow interaction with the magnetic field, can be predicted. From these flow induced potentials, the total volumetric flow rate can be found, irrespective of the number, size and location of the flow channels within the area bounded by the electrode array using a technique based on the Discrete Fourier Transform method. This proposed method allows the venous and arterial blood flow in a limb to be found.

Next, a finite element model was developed in COMSOL Multiphysics software to validate the theoretical work. This was achieved by modelling multiple flow channels within a cylindrical region and obtaining flow induced potentials, which were compared with the theoretical values. From these induced potentials, the volumetric flow rate was found, using the DFT method, and confirmed.

Finally, a practical model was designed and built which consisted of a physical pipework model (simulating a human limb), an electromagnet and signal conditioning and processing systems. Flow induced potential difference measurements were made using this model and compared with the predicted theoretical values. Overall, a good agreement was found between the theoretical results, computer simulations and practical results. Based on this work and additional work that is suggested in this research, a medical prototype non-invasive electromagnetic blood flow meter device can be developed for clinical trials.

ACKNOWLEDGEMENTS

This research work would not have been possible to complete without the guidance and support of several people. First, I would like to express my gratitude to my supervisor, Prof. Gary Lucas, for his valuable support, contribution, patience and encouragement throughout my research journey. I have enjoyed working with him very much and learned a lot from his great research experience.

I would also like to give special thanks to Dr. Laszlo Kollar, for his contribution to my research work, and my fellow colleagues Dr. Sanjin Berberkic, Tim Amsdon, Ogheneochuko Obie, Raymond Webilor and Michael Agolom for the numerous interesting conversations we had.

I would also like to thank the School of Computing and Engineering for the tuition fee-waiver and providing me with the facilities to conduct my research.

Last but not least, I would like to thank my beloved family for their continued support during all my studying years at the University of Huddersfield.

DECLARATION

No portion of the work referred to in this thesis has been submitted to support an application for another degree or qualification at this or any other university or other institute of learning.

TABLE OF CONTENT

LIST OF FIGURES

LIST OF TABLES

Chapter 1

Introduction: The Importance of Blood Flow Measurement

Contents

1.1 Introduction

This thesis describes the research and development that has been undertaken in order to develop a method based on electromagnetic (EM) induction for application in blood flow rate measurement. The method allows the maximum blood flow rate in the major arteries of a human (lower or upper) limb to be measured non-invasively, irrespective of the number of blood vessels at the site of measurement. It is known that over one cardiac cycle the net blood flow rate in a limb is zero because the arterial and venous blood flow rates are equal and opposite. However, the maximum arterial blood flow rate can be found by taking blood flow rate measurements at different times over the cardiac cycle and this will be discussed later in this chapter. A non-invasive method, built around this idea, allows for a device to be applied to the living skin to perform the blood flow measurement and does not require any surgical intervention. The method is based on the application of Faraday's law of induction, which states that an electromotive force (emf) is induced in a conductor moving in a magnetic field.

EM induction was utilised invasively and non-invasively by several researchers, starting with Kolin, in the application of blood flow measurement [1]. However, the method described in this thesis aims to overcome the limitations of previous attempts and to improve the accuracy of the measurement of blood flow rate. This method was developed theoretically and then tested using Finite Element Analysis (FEA) modelling software. Afterwards, a prototype device was built to demonstrate and test the method experimentally in an artificial environment. A clinical device, built on this method, will be of great importance in the study of cardiovascular diseases (CVD), particularly in the diagnosis of peripheral arterial disease (PAD).

In this chapter, **Section 1.2** presents an overview of the human circulatory system. It is essential in understanding the physiology of blood and how it is transported via blood vessels to the organs and tissues of the human body. The subject of the human circulatory system is vast. Accordingly, only the relevant information, that is important to this research, is stated and explained. Following this, in **Section 1.3**, the importance of blood flow measurement in medical applications is discussed and particularly in the areas of cardiovascular and renal diseases. Lastly, the aims and objectives of this research and the thesis structure will be presented in **Section 1.4** and **Section 1.5**, respectively.

1.2 Overview of the Circulatory System

The circulatory system (also known as the cardiovascular system) is one of the major systems in the human body alongside other systems such as the muscular, nervous, respiratory, digestive systems and so forth. It comprises three main parts: the heart – which pumps the blood to all organs and tissues in the human body; the blood vessels – which deliver blood from the heart to all organs and vice versa and the blood – which is the travelling medium which carries O_2, nutrients and other elements [2-4]. Figure 1.1 illustrates the circulatory system of the human body. The primary functions of the system are performed via the blood (the carrier). These functions are:

- Transportation of O_2, nutrition (glucose, vitamins and minerals) and hormones to targeted cells
- CO_2, waste and by-product removal by carrying them to specific organs for excretion
- Defensive and protective tasks, e.g. disease elimination by white-blood cells and blood clotting to repair damaged vessels and stop bleeding
- Regulation of body temperature and pH balance, i.e. homeostasis

1.2.1 The Heart and Cardiac Output

The heart is a muscle that pumps blood through the blood vessels in the human body [2, 3]. It is located between the lungs, slightly to the left of the body's midline. The size of the heart is approximately equal to the fist of the person. It weighs 250-300 g for women and 300-350 g for men. Like skeletal muscles, the heart (cardiac muscle) can be noticeably larger in athletes due to exercise. Exercise enlarges the cells in the heart without any increase in their number. Moreover, the heart of athletes is trained for efficient pumping of blood throughout the body. The heart has four chambers: two receiving chambers – located in the upper part of the heart – called the left atrium and the right atrium and two pumping chambers – located in the lower part of the heart – known as the left and right ventricles.

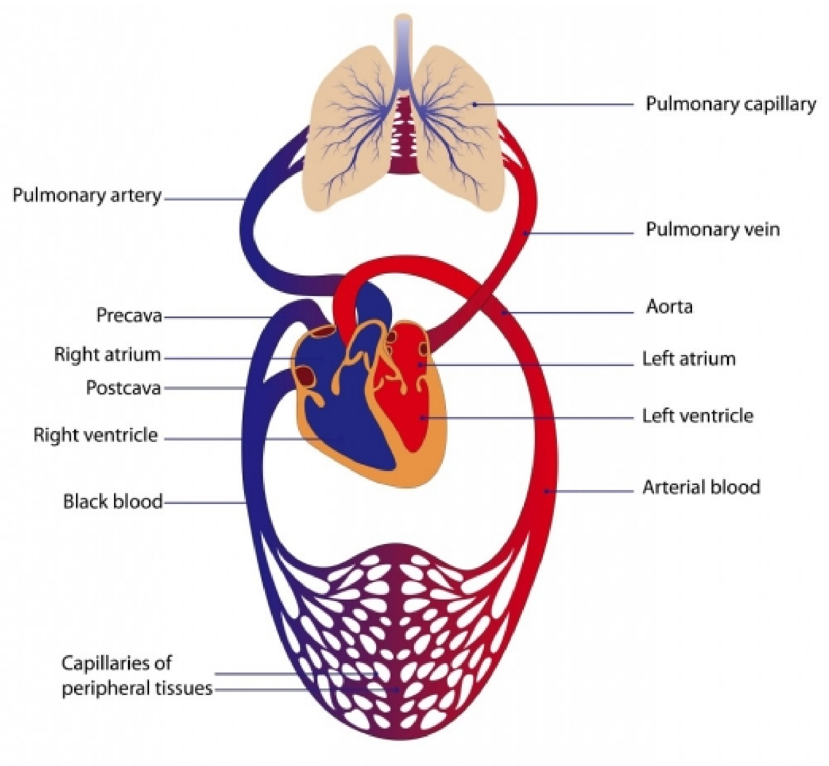

Figure 1.1: The human circulatory system[5]

The right atrium receives deoxygenated blood from organs and body tissues. Then, this blood is sent to the right ventricle, which pumps the deoxygenated blood into the pulmonary circuit, which transports blood between the heart and the lungs. This blood moves via the pulmonary artery branches to the lungs. At the pulmonary capillaries, exchange of gas occurs, i.e. O_2 enters the blood and CO_2 leaves the blood. The oxygenated blood that returns to the left atrium is then sent to the left ventricle. The latter pumps the blood to the systemic circuit which distributes the blood between the heart and all other organs and tissues. At the systemic capillaries, another exchange occurs, in which O_2 and nutrients leave the blood and CO_2 and waste enter. This blood is then sent back to the right ventricle and the whole process is repeated. The pulmonary and systemic systems are presented in Figure 1.2.

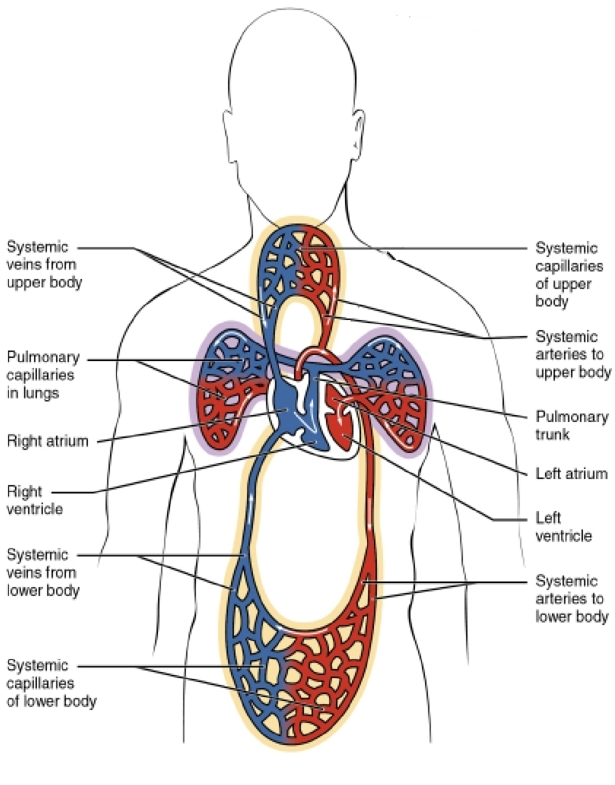

Figure 1.2: The pulmonary and systemic systems [6]

The contraction of the heart starts at the atria (atrial systole), which results in a pressure rise. This pressure causes the blood in the atria to be pumped to corresponding ventricles via the atrioventricular valves, i.e. the mitral and tricuspid valves as shown in Figure 1.3. The atrial systole lasts approximately 100 ms. By the end of the atrial systole, the blood volume (known as end diastolic volume (EDV)) in each ventricle is about 130 mL. As the contraction of the atria is completed, the right and left ventricles contract (ventricular systole). The ventricular systole takes place in two stages. During the first stage, known as isovolumetric contraction, no blood is ejected. However, the pressure in the ventricles rises until the atrioventricular valves are closed. In the second phase, known as ventricular ejection, the pressure in the ventricles is higher than the pressure in the pulmonary artery and the aorta. Therefore, both right and left ventricles pump equal amounts of blood (via the pulmonary semilunar and aortic semilunar valves) to the pulmonary and systemic systems, respectively. The total blood volume ejected by each ventricle is known as stroke volume and it is in the range of 70-80 mL in the normal human condition. This leaves a blood volume – known as end systolic volume (ESV) – of about 50-60 mL in the ventricles. The ventricular systole lasts a period of about 270 ms. The phase of the ventricular contraction is known as systole.

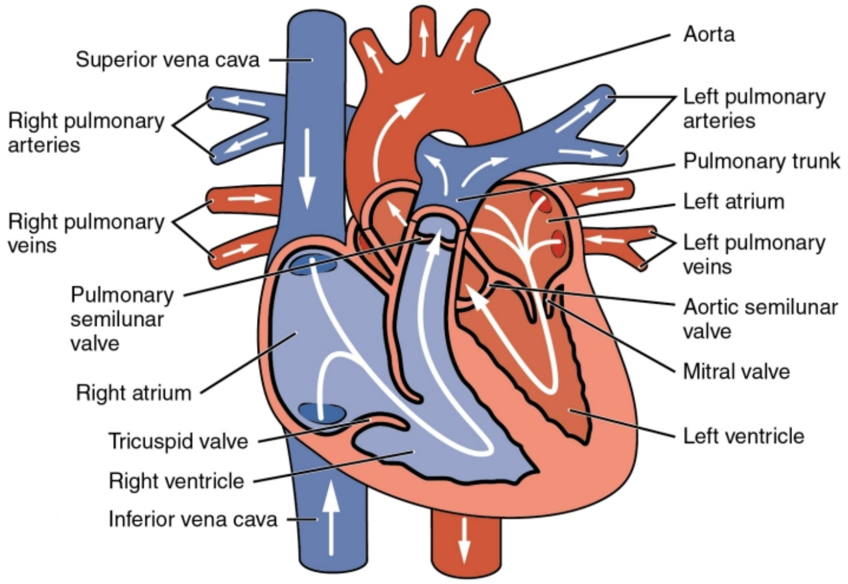

Figure 1.3: Human heart [6]

When the ventricular systole starts, the atria enter a resting phase known as atrial diastole in which they are filled with blood as shown in Figure 1.4. Once the phase of the ventricular systole is completed, the ventricles enter also a relaxation phase known as ventricular diastole which lasts 430 ms. The ventricles, during this time, are filled with blood. Near the end of the relaxation period of the ventricles, the atrial contraction starts and the atria systole starts again. The phase in which the ventricles are in relaxation is known as diastole. One complete cycle of systole and diastole is known as the cardiac cycle. The cardiac cycle lasts about 0.8 s for a resting heart (75 beats per minute on average). The cardiac cycle can be correlated with the compound electrical signal of the heart, i.e. the electrocardiograph (ECG) signal as shown in Figure 1.4. The atrial systole and ventricular systole are represented by the P and QRS waves of the ECG, respectively. The ventricular diastole is represented by the end of T wave of the ECG signal.

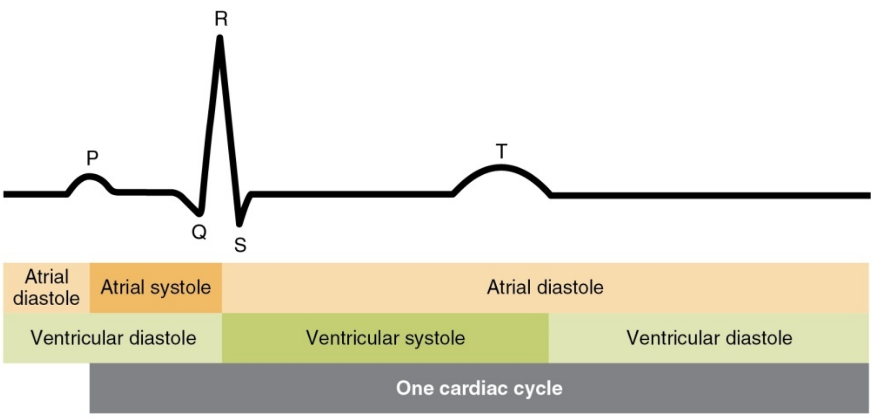

Figure 1.4: Relationship between cardiac cycle and ECG (x-axis is time in s and y-axis is amplitude in V) [7]

Figure 1.5 illustrates the correlation between the ECG signal and the cardiac cycle events, particularly for the left ventricle (LV) which pumps blood to the systemic system. It can be seen that during the period QRS of the ECG signal, the pressure in the left ventricle (LVP) rises until it reaches a point at which its level is higher than the aortic pressure (AP). At this point, a rapid ejection of blood occurs from the left ventricle to the systemic system via the aorta, and the arterial blood flow rises substantially (Phase 3 in Figure 1.5). The point marked in blue in Figure 1.5 corresponds to the point at which the maximum arterial blood flow rate in the aorta is reached. Figure 1.6 shows typical pressure and volume waveforms in human arteries. It can be seen that the maximum flow rate is reached slightly before the maximum pressure point.

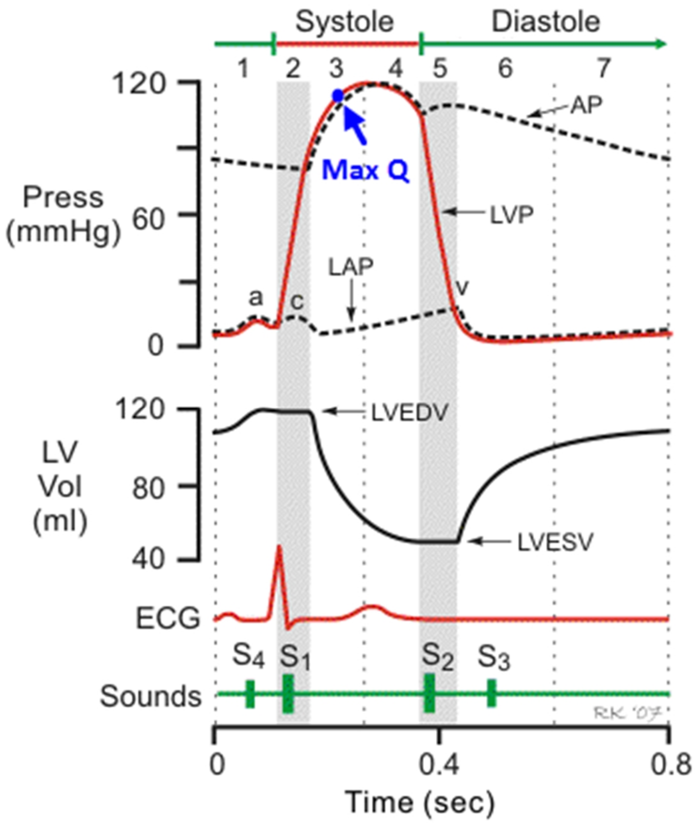

Figure 1.5: The cardiac cycle showing the aortic pressure (AP), the left ventricle pressure (LVP), the left atrium pressure (LAP), end and start left ventricle blood volume (LVEDV and LVESV) and the ECG signal [8]

One of the most important measurements for the assessment of the heart is the cardiac output (CO). It is given by the stroke volume multiplied by the heart rate (HR). The stroke volume is the amount of blood ejected by one ventricle and the heart rate is the number of heart beats per minute (bpm). Stroke volume is the difference between the

EDV and ESV. Each can be measured by echocardiogram [2]. Normal stroke volume for an adult at rest, who weighs 70 kg, is approximately 70 mL. However, this value may change depending on the condition of the person. The heart rate for a resting person is in the range of 60-100 bpm and, on average, it is about 75 bpm. Based on these values, the range of the cardiac output can be between 4-8 L/m with an average value of 5.25 L/m. In healthy athletes, the values of stroke volume and HR can increase to 130 mL and 150 bpm, respectively. This means that the cardiac output can reach 19.5 L/m.

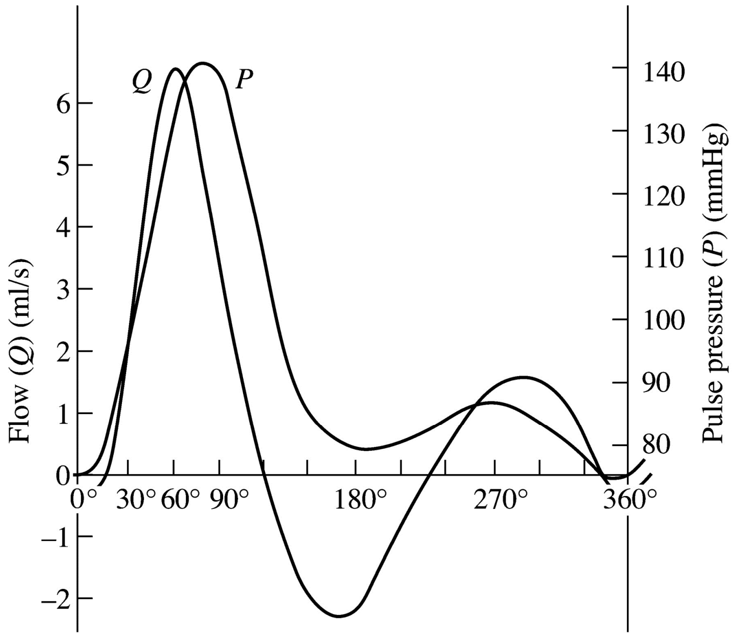

Figure 1.6: Typical blood flow rate and pressure waveforms in human arteries [9]

1.2.2 The Blood Composition and Characteristics

All the functions of the circulatory system are performed via the blood. The blood consists of the formed elements and the plasma. The formed elements are red blood cells (RBC), white blood cells (WBC) and platelets [2]. The red blood cells – clinically known as erythrocytes – transport oxygen. The percentage of RBC in a blood sample is referred to as haematocrit. Normally, the mean haematocrit value in the blood ranges between 42-52% (mean value 47%) for men and 37-47% (mean value 41%) for women. The number of WBC (leukocytes) and platelets (thrombocytes) is very small (< 1%) compared with the haematocrit level. WBCs protect the body from infection and platelets help in blood clotting. The remaining percentage accounts for the plasma level, i.e. 53% for men and 59% for women. The plasma is about 93% water and the remaining percentage accounts for the other substances, i.e. proteins (mostly), nutrients, lipids and hormones. Figure 1.7 shows the percentage levels of blood components in normal and ill conditions (anaemia and polycythaemia). Note that the term "buffy coat" refers to the white layer between the red blood cells (haematocrit) and the plasma in a blood sample. This white layer contains white blood cells and platelets [10].

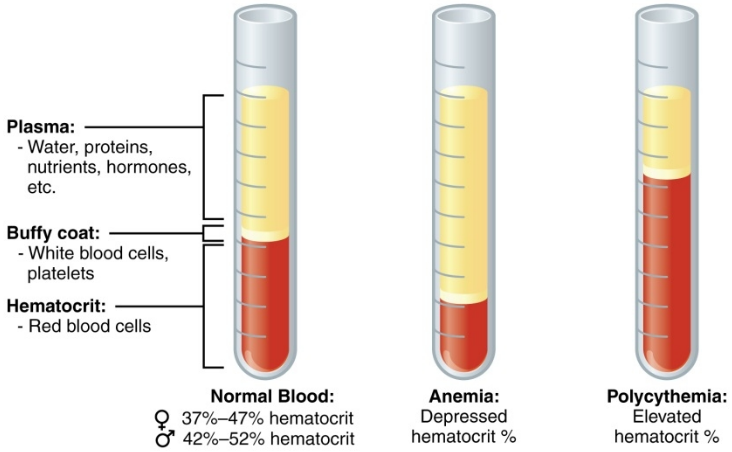

Figure 1.7: Composition of blood [11]

The blood distribution in the human body, at any instant in time, is as follows: 84% of blood is in the systemic circuit, 9% in the pulmonary circuit and 8% in the heart [12, 13]. The distribution of blood in the systemic circuit alone is as follows: 64% of the blood is in the veins and venules; 13% in the arteries and arterioles and 7% in the capillaries. It can be seen that at any instant, there is about 5 times more blood in the veins than the arteries. In normal conditions, the weight of an individual's blood accounts for about 8% of the total, and the amount of blood in an average-size adult is 5-6 L for males and 4-5 L for females.

Other important properties of blood are its viscosity, temperature and pH. Blood has a viscosity about 5 times that of water (8.94×10^{-4} Pa.s) and, hence, it is considered to be viscous. The temperature of the blood is normally 38^{o} C, which is slightly higher than the temperature of the body. Lastly, the pH of blood ranges between 7.35 and 7.45 (7.4 mean value) in a healthy person which means the blood is basic.

1.2.3 The Blood Vessels

The blood vessels in the human body are classified into three categories: arteries, veins and capillaries [2]. Blood is transported in the pulmonary and systemic circuits by arteries and veins. Arteries carry oxygenated blood away from the heart to the body tissues. They branch into smaller vessels called arterioles. Arterioles branch into the capillaries for exchange of gas, nutrients and wastes. Blood low in oxygen is returned back to the heart along the other side of the capillaries, the venules and veins. Blood vessels have a lumen through which blood flows. The cross-section of arterial lumen is nearly circular, whereas in veins, the shape of the cross section is irregular as illustrated in Figure 1.8c. Arteries and arterioles have thick walls to withstand the high pressure of blood coming from the ventricles. Their lumen is smaller than that of the vein to maintain the pressure of blood flow. In contrast, veins and venules have thinner walls as the blood returned to the heart is low in pressure. They also have larger lumen allowing more blood to flow. Note that, during surgery, all blood vessels mentioned can be seen apart from the capillaries as they are microscopic.

The velocity of blood in the veins is lower than the velocity of blood in the arteries. The total arterial and venous flow rate is equal but opposite within the cross sectional area of a limb. The velocity in the arteries is higher but since they have a smaller diameter, therefore, the net blood flow rate is zero. Nevertheless, the blood flow velocity in veins is constant throughout the cardiac cycle – whereas the velocity in the major arteries varies considerably (at maximum shortly after QRS event in Figure 1.4, and lower during the rest of the cardiac cycle). The maximum arterial blood flow can be found by taking two blood flow measurements over the cardiac cycle. One of the measurements is obtained when the arterial blood flow is at minimum (between P and Q in Figure 1.4) and the other measurement is taken when the arterial blood flow is at maximum. The difference between those two measurements is equivalent to the maximum arterial blood flow rate. This method is described mathematically in Section 3.6. Typical velocities of blood in major arteries are given in Section 1.2.4.

Arteries and veins have three layers (tunics): the inner layer – tunica intima; the intermediate layer – tunica media and the outer layer – tunica externa (Figure 1.8a&b). These layers differ in structure, depending on the type of blood vessel and its location within the human body. The tunica intima of arteries nearer to the heart has more elastic fibres to allow arteries (referred to as elastic arteries) to expand and maintain pressure gradient.

Arteries that are larger than 10 mm in diameter are usually elastic to withstand the high pressure of blood and are located close to the heart. Arteries that are distant from the heart have fewer elastic fibres in the tunica intima and more smooth muscles (decreasing resistance to flow) in the tunica media. These arteries are called muscular arteries and their diameter ranges between 0.1-10 mm. Muscular arteries can contract to reduce blood flow during a haemorrhage (bleeding), also known as vasoconstriction. The opposite can happen too, relaxing to let more blood flow which is known as vasodilation. The tunica externa helps in holding the blood vessels in place. Arterioles have lumen with a diameter of 30 μm or less. They can contract (vasoconstriction) or relax (vasodilation) depending on the amount of blood flow required. This process is controlled via neural or chemical means. Figure 1.9 depicts the types of arteries and arterioles.

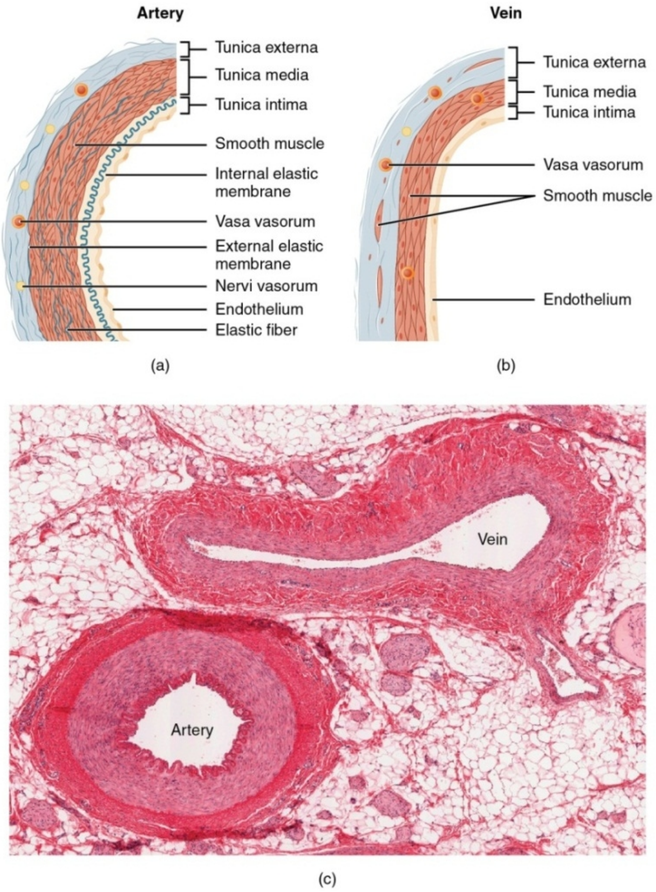

Figure 1.8: Structure of blood vessels [14]

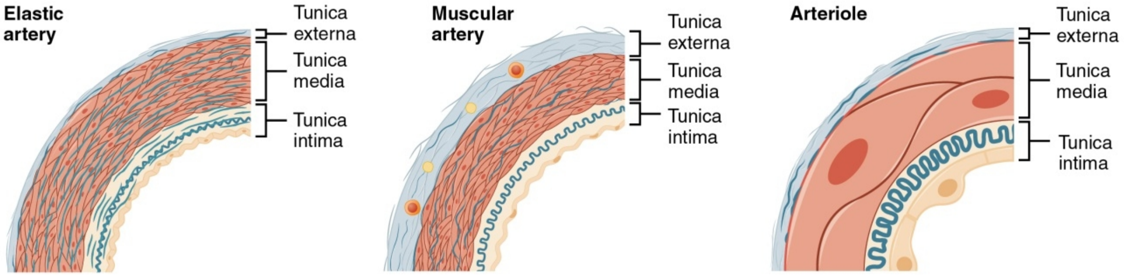

Figure 1.9: Types of arteries and arterioles [15]

Veins have thick tunica externa, especially the superficial veins, to hold them in place. The pressure of blood in veins is low and therefore, veins have valves to prevent back flow by ensuring that blood flow is unidirectional. The diameter size of the veins ranges between 0.05-3 cm. The size of post-capillary venules (connected to the other end of the capillaries) is between 50-200 μm, which pass the blood, low in O_2, to the muscular venules. The muscular venules can contract or relax in a similar way to the muscular arteries to control the blood flow. Then, the blood is passed to the veins to return to the heart. Figure 1.10 illustrates the shape and structure of the veins and venules.

The oxygenated blood is pumped into the systemic arteries – starting from the aorta – during the contraction of the left ventricle. The systemic arteries deliver the oxygenated blood to all body organs and tissues. All major systemic arteries are illustrated in Figure 1.11. The axillary and the subsequent arteries supply blood high in O_2 to the upper limbs, i.e. the arms. The blood which is delivered to the lower limbs, i.e. the legs, begins in the external iliac artery. The arteries in the upper and lower limbs are depicted in Figure 1.12 and Figure 1.13. The normal diameters of the external iliac and femoral arteries are 8-10 mm and 7-9 mm, respectively.

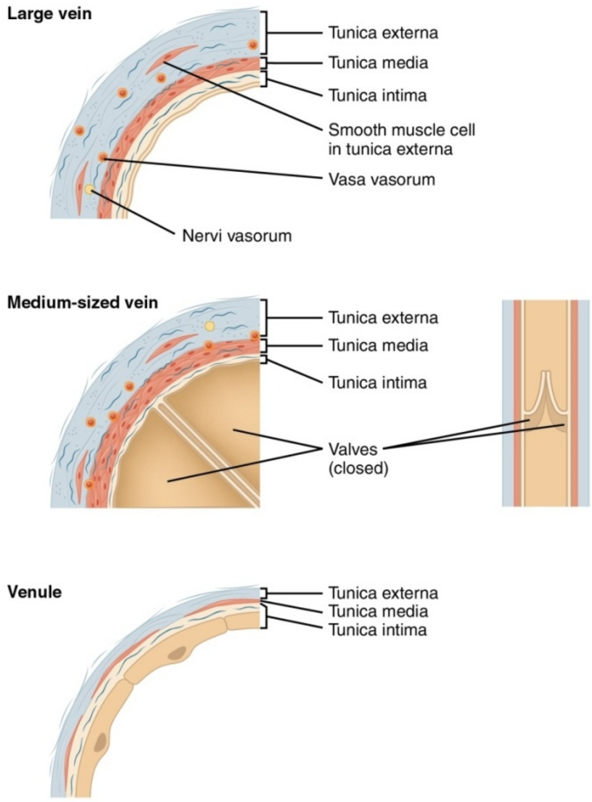

Figure 1.10: Veins and venules [16]

Blood low in O_2 (venous blood) returns from the organs and tissues to the right atrium in the heart via the systemic veins (Figure 1.14). In the upper limbs (refer to Figure 1.15), blood enters the thorax through the subclavian veins – starting from the digital veins in the fingers. It can be noted from Figure 1.15 that veins can be either superficial, such as the brachial vein, or deep, such as the median cubital. In the lower limbs (Figure 1.16), blood from the legs enters the abdominal region through the common iliac – starting from the digital veins in the toes. The study of arteries and veins in the upper and lower limbs is of great importance in the field of cardiovascular disease. Arteries and veins in the upper or lower limbs can be infected by PAD and DVT, respectively. These diseases are discussed greater detail in Section 1.3.

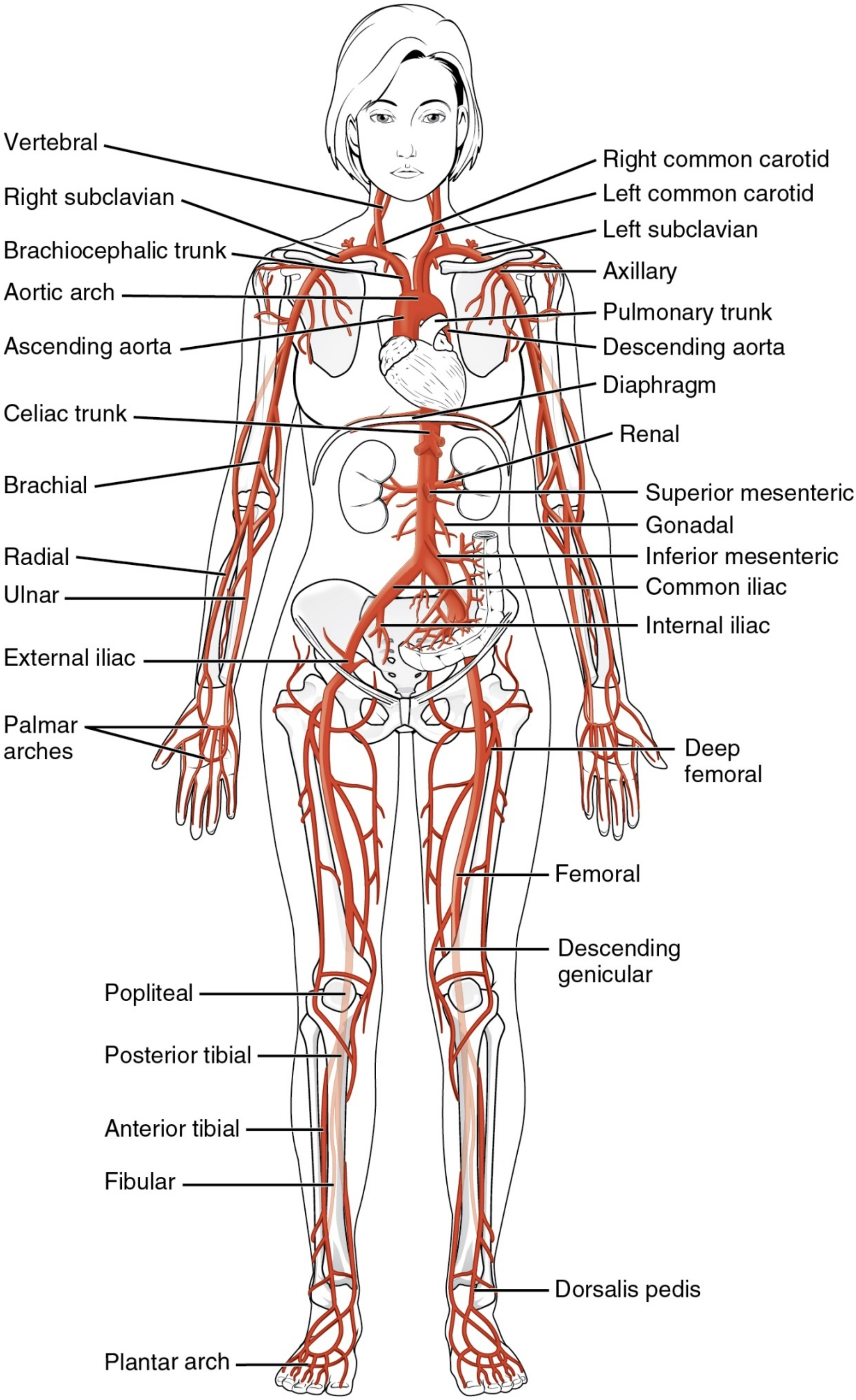

Figure 1.11: Systemic arteries [17]

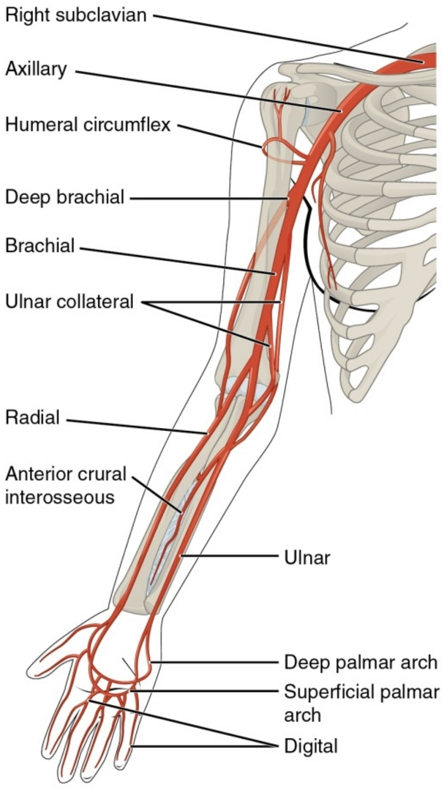

Figure 1.12: Systemic arteries of upper limb [18]

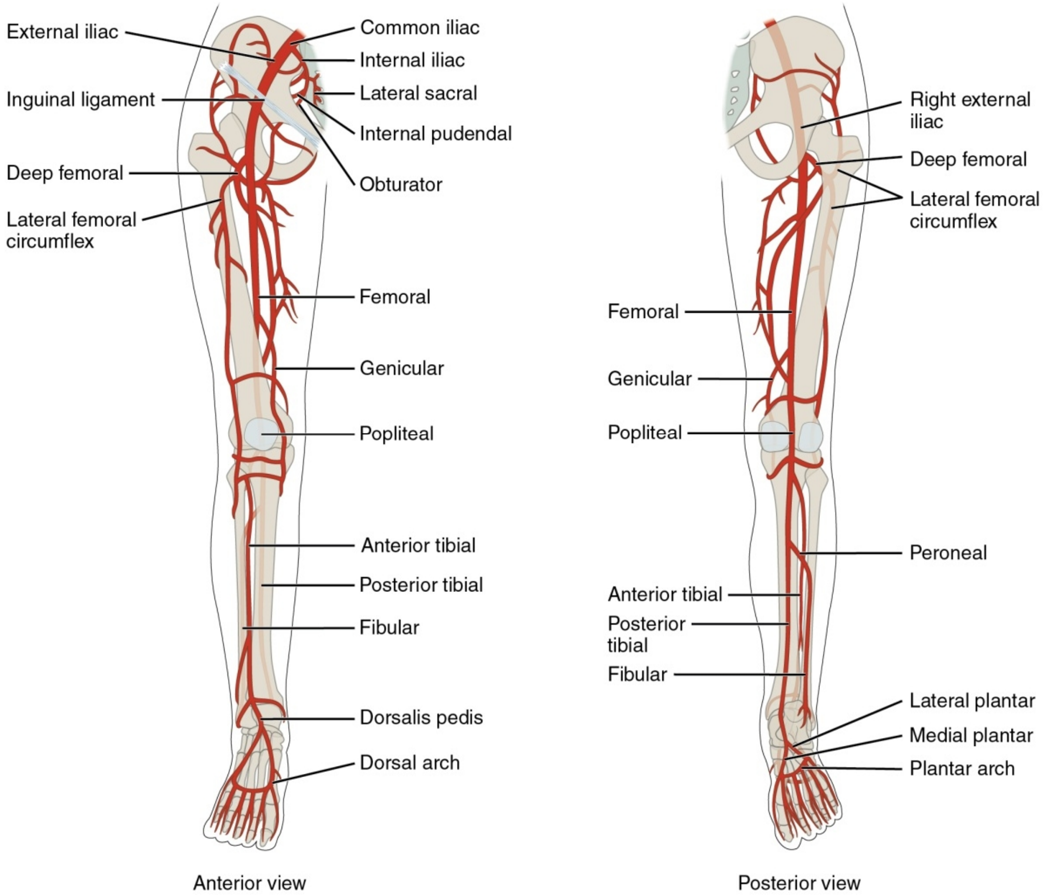

Figure 1.13: Systemic arteries of lower limbs [19]

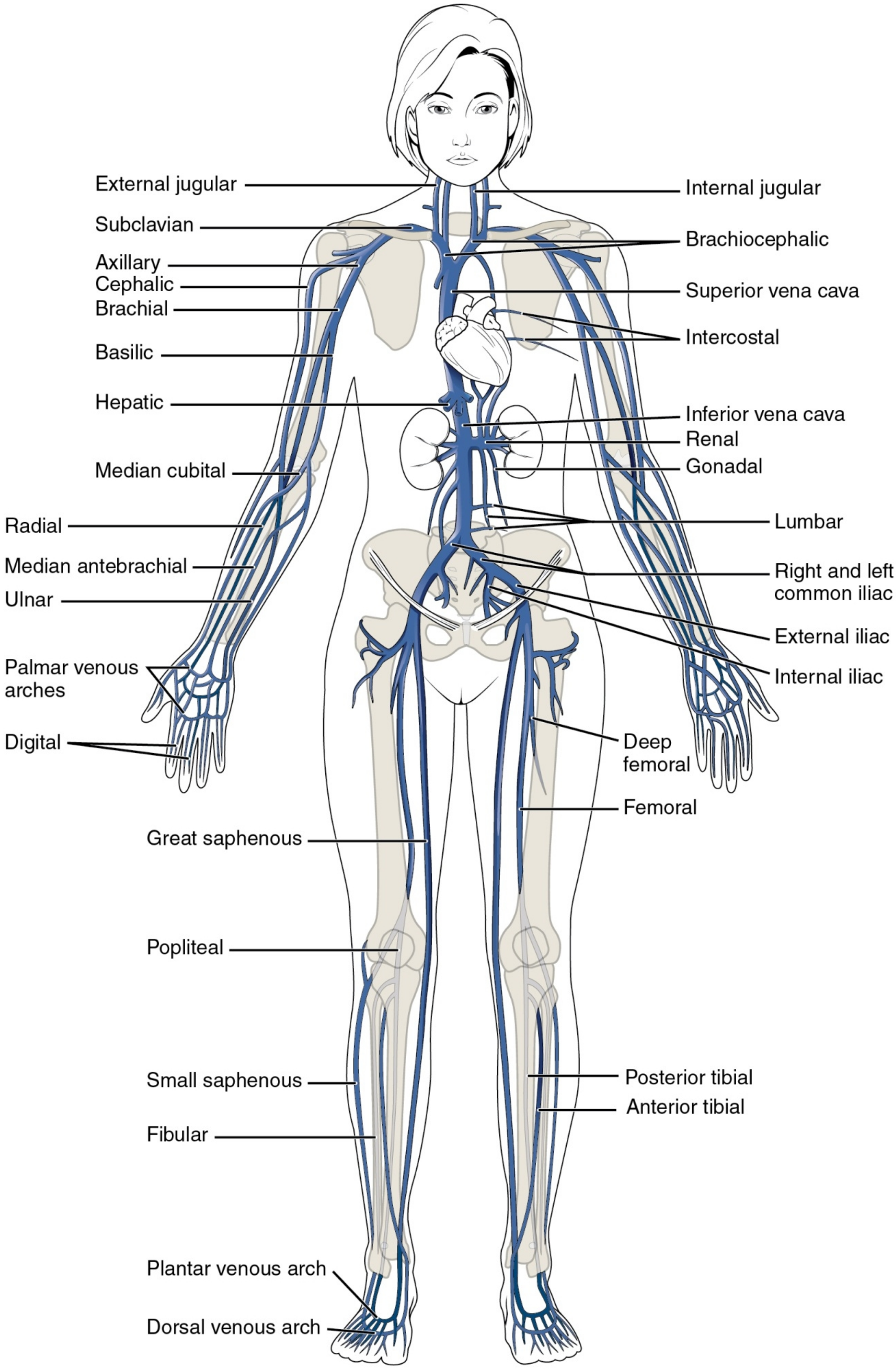

Figure 1.14: Systemic veins [20]

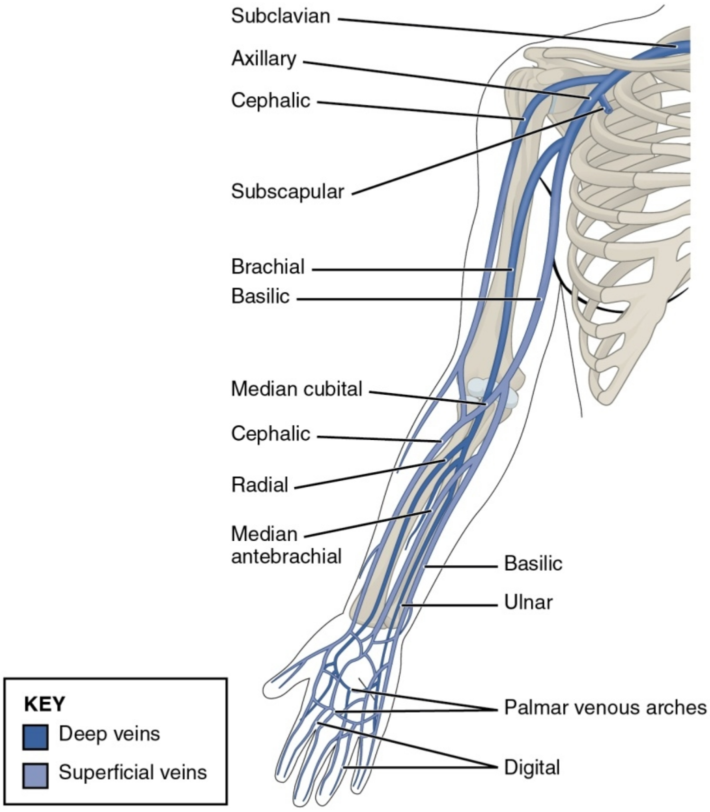

Figure 1.15: Veins of the upper limb[21]

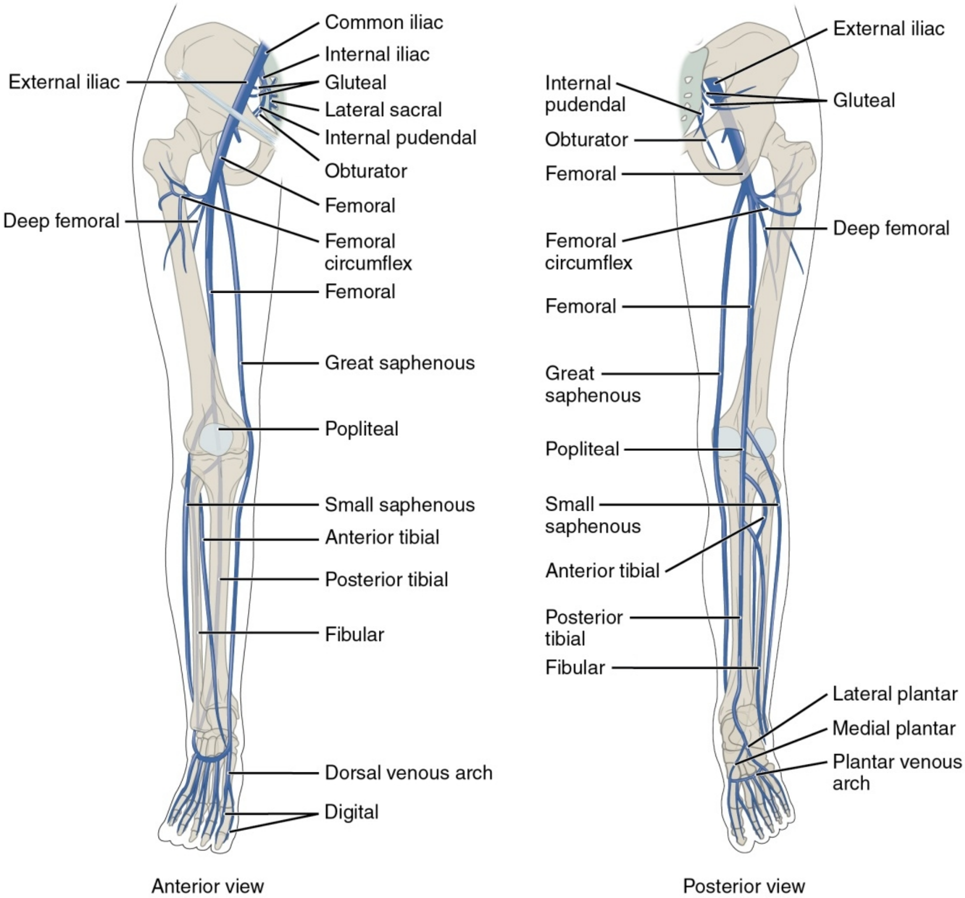

Figure 1.16: Veins of the lower limb [22]

1.2.4 Blood Flow and Pressure

Blood flow rate refers to the amount of blood (volume) per unit time. The SI unit of blood flow rate is m^3/s. Blood pressure is hydrostatic and it is defined as the force exerted at a point on the wall of the blood vessels. The measurement of blood pressure is typically taken from the blood pressure in the systemic circuit. It is often measured using the brachial artery of the arm and its SI unit is the Pascal (N/m^2). However, in medicine, the standard unit is millimetre of mercury (mmHg). Millimetre of mercury is defined as the pressure exerted by a column of mercury one millimetre high at 0° C under the acceleration of gravity and it is equal to about 133.3 Pa. The blood pressure measurement is expressed as a ratio between the systolic and diastolic pressures. Systolic and diastolic pressures are the pressure of blood during arterial systole and diastole (ventricular contraction and relaxation), respectively. For an adult, blood pressure is normally 120/80 mmHg. Note that blood flow and pressure in arteries are pulsatile. Normal blood pressure for different blood vessels is depicted in Figure 1.17.

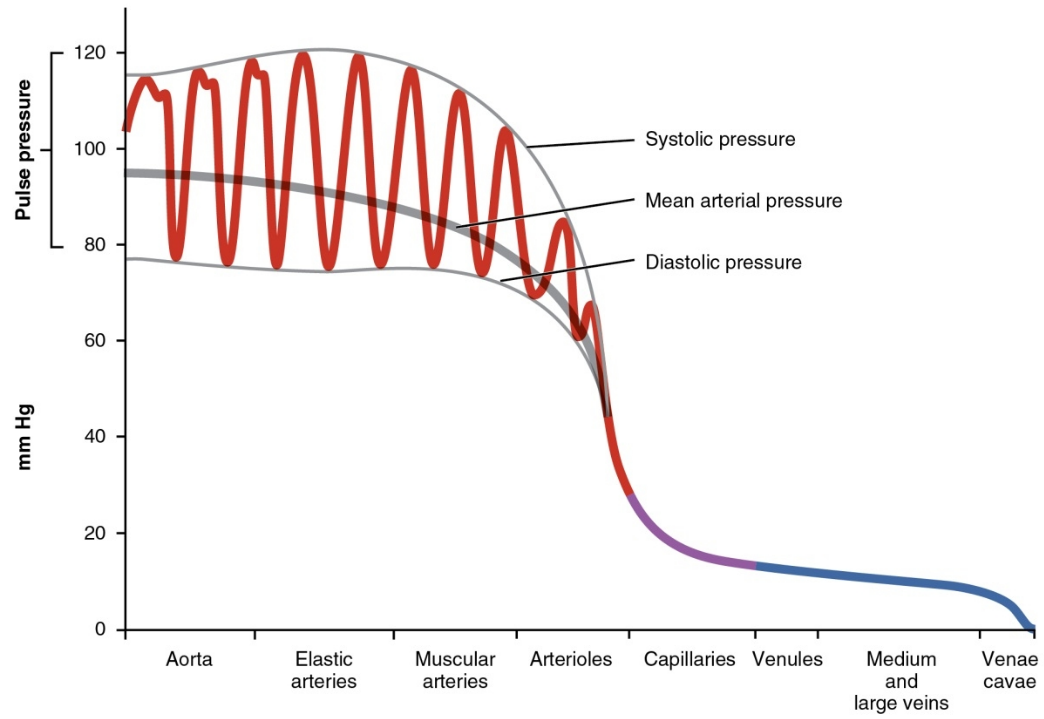

Figure 1.17: Normal pressure value of different blood vessels [23]

The difference between the systolic and diastolic pressures is called the pulse pressure. For a healthy adult, the pulse pressure should be 30-40 mmHg (120 minus 80). Any long-lasting pulse pressure value at or above 100 mmHg is an indication of high resistance to blood flow which can be caused by various conditions including arteriosclerosis – the narrowing of arteries due to a build-up known as plaque.

The blood flow rate and pressure can be affected by the following factors: (1) cardiac output, (2) compliance, (3) volume of blood, (4) viscosity of blood and (5) blood vessel length and diameter. The cardiac output is the product of the stroke volume and the heart rate as explained in Section 1.2.1. Compliance determines how elastic the artery or vein is in order to withstand an increased amount of blood. Low compliance leads to high resistance to flow. This results in lower flow and higher blood pressure, which can be an indication of vascular disease.

Flow of blood is caused by a pressure difference (gradient). The relationship between the blood flow rate Q and the pressure difference ΔP, i.e. $P_2 - P_1$ is given by

$$Q = \frac{\Delta P}{R} \qquad \text{Eq. 1-1}$$

where R is the vascular resistance to flow (unit: $Pa.s/m^3$). The vascular resistance R increases with an increase in the length of the blood vessel l and blood viscosity η (unit: Pa.s), and decreases with the radius of the vessel r [24]. The resistance to flow is expressed mathematically by

$$R = \frac{8\eta l}{\pi r^4} \qquad \text{Eq. 1-2}$$

Eq. 1-2 is called Poiseuille's law for resistance. Note that the radius r is raised to the fourth power in Eq. 1-2. This means that any small change in radius will have a significant effect on the resistance to flow. Combining Eq. 1-1 and Eq. 1-2 gives

$$Q = \frac{\pi \Delta P r^4}{\pi 8 \eta l} \qquad \text{Eq. 1-3}$$

Eq. 1-3 is called Poiseuille's law for laminar flow. It can be observed that the flow rate is directly proportional to pressure difference ΔP and 4^{th} order of the radius of the blood vessel r and is inversely proportional to the length of the vessel l and blood viscosity η. The blood viscosity and vessel length vary gradually in the body. The radius of the blood vessels can change substantially during vasoconstriction and vasodilation. Figure 1.18 shows graphs of the diameter, cross-sectional area, blood pressure and mean velocity (over cardiac cycle) of the different blood vessels in the human body.

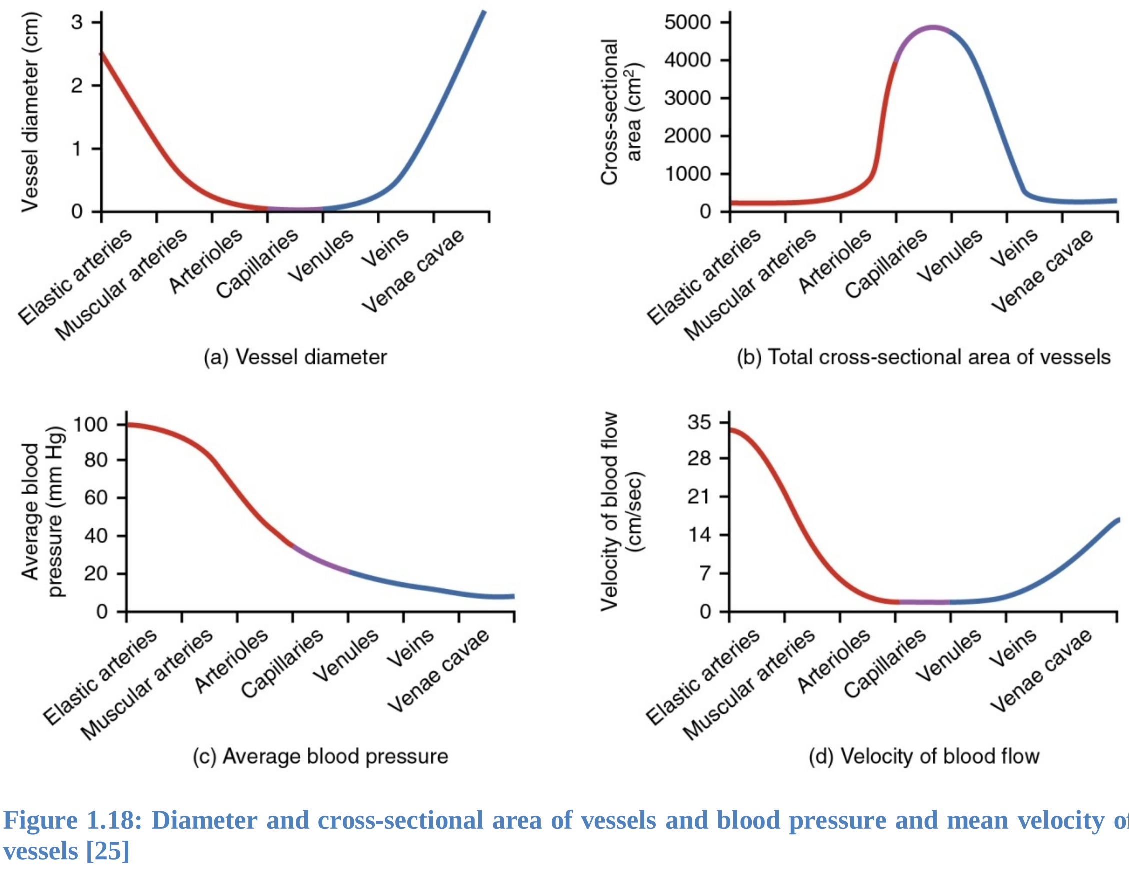

Figure 1.18: Diameter and cross-sectional area of vessels and blood pressure and mean velocity of vessels [25]

Table 1-1 shows typical values for the diameter of, and the peak velocity of blood in, arteries in adults such as the aorta, the carotid, the brachial, the femoral and the popliteal arteries [9, 26-32]. The proposed EM method for blood flow rate measurement in this research aims to measure the blood flow rate in the peripheral arteries such as the brachial artery in the upper limbs and the common femoral artery in the lower limbs.

Artery Name	Diameter (mm)	Peak velocity (m/s)
Aorta	30	1.1
Carotid	5.5-7.5	0.9
Brachial	4-5	0.6
Femoral	8-10	1.1
Popliteal	5-5.3	0.7

Table 1-1: Diameter of, and peak of blood velocity in, the aorta, carotid, brachial, femoral and popliteal artieres

1.3 Importance of Blood Flow Measurement

1.3.1 Cardiovascular Diseases

Blood flow measurement is a method that correlates directly with the measurement of O_2 and nutrients supplied to organs or tissues in the human body. Blood pressure can give an indication of abnormal pressure levels in a human limb. Abnormal pressure levels indicate irregular blood flow. However, pressure methods do not provide quantitative information on the amount of blood being delivered to an organ or tissue. Measurement of blood flow rate is of significant importance in the study of the circulatory system and cardio-vascular diseases. Measurement of the blood flow rate in individual blood vessels can lead to detection of arterial stenosis, the narrowing of arteries causing a reduction of blood flow to tissue as shown in Figure 1.19 [33, 34]. Arterial stenosis caused by atherosclerosis is primarily a disease of large- and medium-size arteries, and is characterised by a build-up of lipids forming plaques which narrow and eventually block the blood vessels causing damage to organs or tissues. Atherosclerosis is associated with cardiovascular diseases – the main cause of death globally.

CVDs affect the circulatory system, i.e. heart and blood vessels. Strokes and transient ischemic attacks are caused by the blockage of arteries that supply blood to the brain. Heart attack and angina are caused by the blockage of blood vessels in the heart. Peripheral arterial diseases, which include pain during walking or exercising (claudication), deficiency in wound healing and/or leg ulcers (limb ischemia), are caused by blocked arteries in human limbs – mainly in the legs as shown in Figure 1.20 [35]. According to the World Health Organisation, 17 million people died in 2008 from cardiovascular diseases [36].

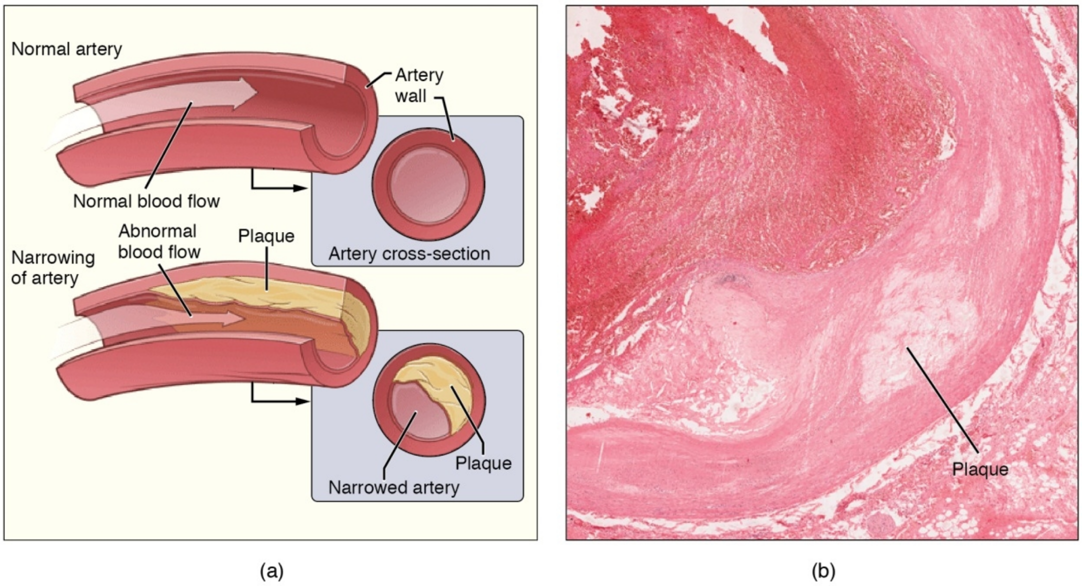

Figure 1.19: Atherosclerosis: (a) build-up of calcified deposits and fat and (b) build-up of tissue (another form of plaque) at the arterial wall [37]

Cardiovascular diseases are mainly caused by an unhealthy diet, lack of exercise, smoking, high blood pressure and advanced age. Patients with both type I and II diabetes also suffer from poor blood circulation which can lead to PADs [38]. High blood glucose levels cause damage to blood vessels in the long term and this may lead to an accumulation of plaque which obstructs the blood flow to organs and tissues. Severe PADs can cause lower limb amputation due to gangrene and secondary infection. Hence, blood flow rate is an important measurement in the fields of diabetes and obesity research.

Peripheral Arterial Disease

The diagnosis of PADs is very important for the elderly, smokers and obese individuals as they are at higher risk than young, healthy individuals. Patients who have PADs can also be at increased risk of other CVDs such as stroke and heart attack [39]. In 2010, an international research team reported that about 202 million people suffer from PADs worldwide [40]. Nationwide, 1 in 5 men and 1 in 8 women aged between 50 and 75 suffer from PADs.

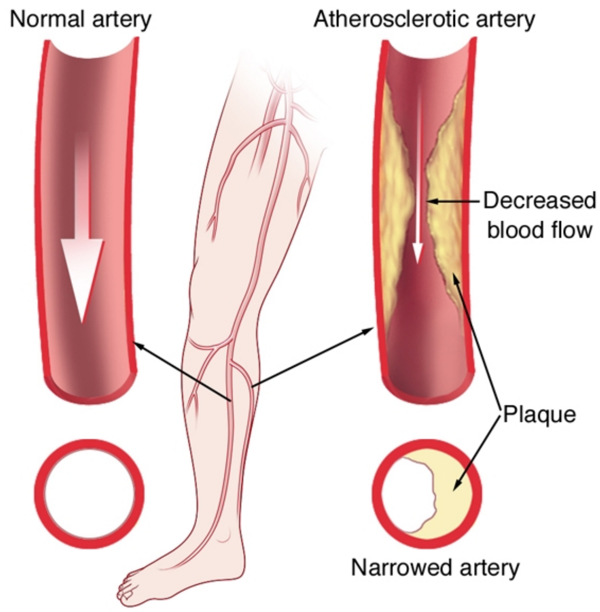

Figure 1.20: Peripheral arterial disease (PAD) [41]

PADs usually affect the lower limbs; nevertheless, patients can have PAD in the upper limbs. Severe PAD can lead to limb ischemia as stated earlier. In the UK, limb ischemia costs the health service over £200 million per year. In many cases, for patients with PADs, symptoms do not appear, as they depend on the severity of the PAD. Physical examination is required by a doctor to verify the presence of PAD. In the case of PAD in the upper limbs, a large pressure difference could be detected between the left and right arms [42]. For the lower limbs, the diagnosis is performed by using the Ankle-Brachial index (ABI) pressure test.

ABI is a test in which the pressure difference is taken between the arm and ankle using a Doppler ultrasound probe in conjunction with a sphygmomanometer (cuff inflator). The test is performed by first placing the sphygmomanometer in close proximity to where the pressure measurement is to be taken by the ultrasound probe [43]. For the brachial artery, the cuff is placed around the elbow (antecubital fossa) and for the posterior tibial or dorsalis pedis arteries (located at the ankle), the cuff is placed slightly above the ankle area as illustrated in Figure 1.21. The ultrasound probe is placed on the artery (satisfactory pulse signal) and ideally at an angle of 45^{o} to the blood vessel of interest for optimum frequency shift and signal amplitude. Then, the cuff is inflated until the pulse of the artery disappears. Afterwards, the cuff is gradually deflated while the probe is placed on the artery. Once the pulse is detected by the probe, this reading correlates with the systolic pressure. This procedure is applied to both arms and legs. The ABI index is the ratio between the systolic pressure values of the posterior tibial or dorsalis pedis and the brachial arteries. Normally, this index value should be higher than 1 for patients with no sign of PAD. Any ABI value between 0.6 and 0.8 is an indication of claudication and any value below 0.5 is a sign of severe PAD.

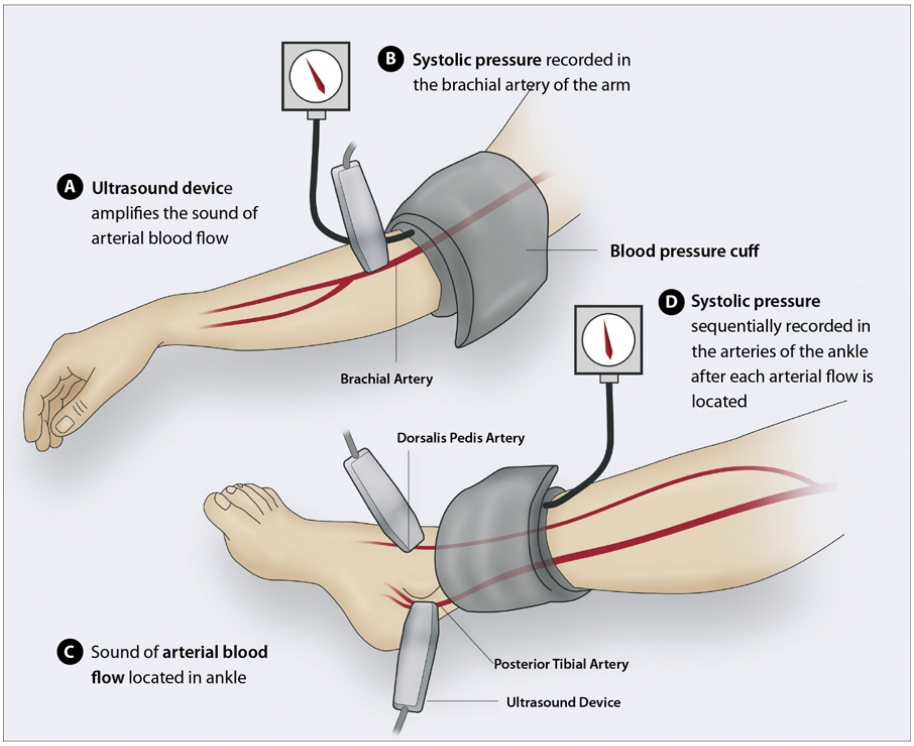

Figure 1.21: ABI test [44]

ABI is normally a reliable and useful test for determining PAD. Multiple blood pressure measurements on each leg might also be needed using 3-4 pressure cuffs. However, in elderly and diabetic patients, the sensitivity of ABI is significantly low [45]. Such patients are required to have other tests such as duplex ultrasound, computed tomography (CT) or magnetic resonance imaging (MRI). These tests can create an image of the blood vessels and the infected blood vessels can then be identified. Moreover, the operator of the ultrasound must be experienced in using a Doppler ultrasound probe to avoid false diagnosis. Additionally, the ABI test is lengthy and this is one of the barriers limiting its use in primary care settings due to a shortage of staff [46].

Blood flow is also an important measurement in dermatology research. Lack of blood flow to a limb can cause damage to skin tissues. Blood flow to the skin is commonly measured using laser Doppler ultrasound or laser speckle contrast imaging (LSCI) [47]. Moreover, the measurement of forearm blood flow is widely used in the study of the response of drugs and mediators on the arterial blood flow [48].

Deep Vein Thrombosis

Deep vein thrombosis – also known as venous thrombosis – is blood clotting (or blockage) in a deep vein as illustrated in Figure 1.22. It usually occurs in the deep veins that are located between the muscles of the calf and thigh. DVT causes pain, paleness, tenderness and swelling in the leg [49]. It may also lead to fatality when this blood clot travels from the leg to the blood vessels in the lungs causing what is known as pulmonary embolism, i.e. when blood is prevented from reaching the lungs [50]. In the UK, 1 in 1000 people have DVT and in the US, statistics show that the number of people affected by DVT is between 300,000 and 600,000 every year [50, 51].

There are several causes of DVT [52]:

- Immobility due to a surgical operation, paralysis, illness or a long journey during which the person is mostly sitting still. In a normal healthy human, blood moves continuously in the veins by muscle action during movements. When a patient is under anaesthetic or paralysed, muscles do not move as normal; this will slow the blood flow and DVT may occur;

- Injury to a vein due to fractures, muscle injury or after major surgery;
- Increase in the oestrogen hormone caused by birth control pills or during pregnancy;
- Patients with chronic diseases such as heart or lung diseases or cancer are also at high risk of DVT;
- Other factors are advanced age, obesity and a family history of DVT.

There are several methods used to diagnose DVT such as duplex ultrasound, venography, impedance plethysmography, MRI and CT scan [53]. All these methods rely on the visualisation and measurement of blood flow to identify DVT. These techniques are described in Chapter 2.

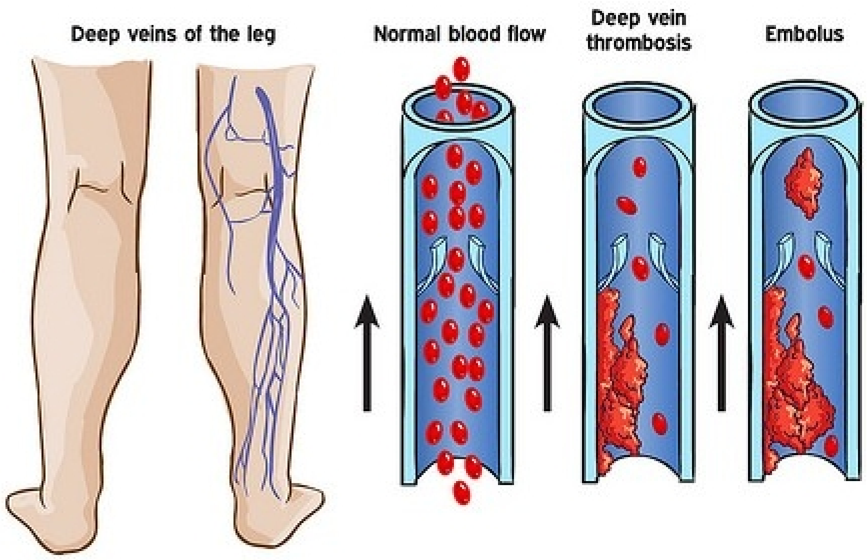

Figure 1.22: Deep vein thrombosis [54]

1.3.2 Renal Disease

Renal disease is partial or full malfunction of the kidneys in the human body. There are two types of renal disease: acute and chronic. Acute failure refers to the sudden malfunction of the kidneys whereas, in chronic failure, the kidneys fail to work after a long-term period. End-stage renal disease (ESRD) is when the kidneys are no longer in operation [55]. Patients with acute, chronic or end-stage renal disease require a routine common process known haemodialysis. Haemodialysis – which replaces the function of the kidneys - is the filtration of wastes and fluid from the blood by a dialysis machine (dialyser) outside the body. In the UK, over 40,000 patients have renal disease and over half of them require dialysis [56].

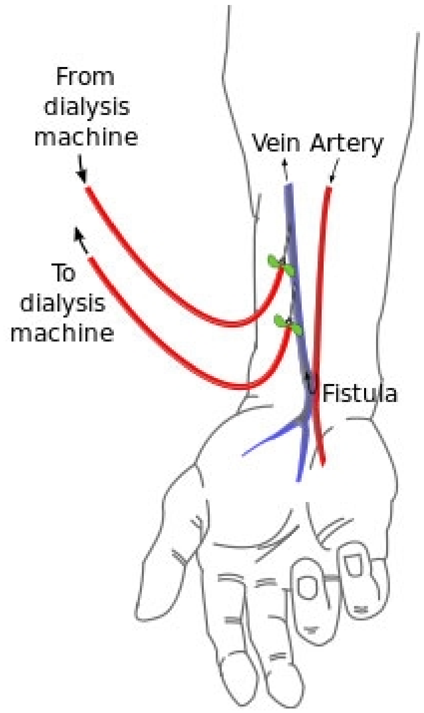

Figure 1.23: Vascular access fistula [57]

Haemodialysis requires an operation known as vascular access (VA) to improve delivery of blood to the body. There are several methods used to perform vascular access but the most common method is the arteriovenous fistula [58]. In this method, surgery is carried out to connect an artery to a vein – usually the radial or brachial artery to the cephalic or basilica veins in the arm as shown in Figure 1.23 [59]. This allows the vein lumen to expand in size and the vessel wall to thicken. This enables the vein to endure repeated puncture with large needles and to handle large amounts of blood flow, between 0.6 and 0.8 L/min. The vein usually takes 3-4 months to be ready (mature) for haemodialysis.

Patients with renal disease and receiving haemodialysis are at very high risk of cardiovascular disease. In fact, there is a 63% probability of death from cardiovascular disease in the first 5 years [58]. This probability increases to 71% for diabetic patients. The vascular access must also be maintained and checked regularly for any stenosis or thrombosis as it is one of the frequent causes of morbidity and mortality [60]. Early diagnosis of stenosis or thrombosis allows the VA to be repaired before starting haemodialysis. In a recent study, it was shown that this can be done non-invasively by using Doppler ultrasound to examine the brachial artery [61]. Abnormal blood flow in the brachial artery is an indication that the VA requires repair. The Doppler ultrasound method and limitations are explained in detail in Chapter 2. However, it is important to note that the Doppler method may suffer from significant errors due to operator, machine or patient-related mistakes. Blood vessels in dialysis patients are at more risk of accumulating calcium build-up or calcified plaque which blocks ultrasound beams resulting in velocity measurement error. Moreover, blood vessels in lower limbs such as femoral arteries may also suffer from calcification preventing a non-invasive Doppler ultrasound device from obtaining an accurate measurement of blood velocity [62].

1.4 Aims and Objectives

The broad aim and objective of this thesis is to investigate current methods of blood flow measurement, particularly non-invasive methods used in the diagnosis of peripheral cardiovascular diseases. These methods will be addressed in terms of their operation and clinical applications. Furthermore, their limitations and associated drawbacks will also be highlighted. Based on this initial study, methodologies will be proposed to develop and validate an alternative method for non-invasive blood flow rate measurement which offers advantages such as portability, low cost, accuracy and ease of use.

1.5 Structure of Thesis

The thesis is structured as follows. **Chapter 2** surveys the literature for current methods for mainly non-invasive blood flow measurement. It covers four methods: tomography such as X-ray and magnetic resonance imaging, plethysmography, ultrasound and EM induction. Each method is described in terms of its operation, design, clinical application and any drawbacks or limitations. Notable theoretical work and mathematical tools of some methods are also reviewed. These mathematical tools are found to be useful for the current research. Lastly, the research aim and methodology are stated based on literature findings.

Chapter 3 details the mathematical modelling of the proposed EM induction technique for non-invasive blood flow measurement. This mathematical model is an extension of "virtual current" theory introduced by Bevir. Firstly, a mathematical model is provided to obtain flow induced potentials at the boundary of a cross-sectional area which contains one flow channel only. Subsequently, the theory is extended to obtain flow induced potentials due to multiple flow channels in a cross-sectional area bounded by multiple electrodes. Lastly, the relationship between the DFT obtained from the flow induced potentials, the total volumetric flow rate due to multiple flow channels and the applied magnetic field is explained.

Chapter 4 describes the finite element (FE) modelling work performed in COMSOL Multiphysics software to verify the mathematical model developed in Chapter 3. A 3D computer model of a cross section with multiple flow channels simulating a limb and blood vessels (simulated vascular system or 'SVS') is presented. The design of an electromagnet for generating the applied magnetic field is described. Then, the flow induced potentials obtained from the FE model are compared with the theoretical model in different test settings.

Chapters 5, 6 and **7** describe the practical model that was designed, built and tested to implement the proposed EM induction technique described in Chapter 3. The aim was to validate the mathematical model by comparing the results obtained from the theoretical and practical models. The first part of **Chapter 5** describes the mechanical design of a physical simulated vascular system (SVS), its built-in electrode array and the electromagnet. The dimensions and materials used to design the physical SVS are presented. Detailed design of the electromagnet is provided including the physical size, electrical power requirements and the number of turns for its coil to generate the desired magnetic flux density. The second part of **Chapter 5** describes the design of the power supply of the electromagnet. Then, the AC signal conditioning system, used to filter and amplify the flow signals before digitisation for further processing, is presented and analysed. Lastly, the data acquisition device (DAQ), used to digitise and store the flow induced potentials, and the associated MATLAB program written to control the DAQ device are presented.

The first part of **Chapter 6** presents the last design element of the practical model which is the signal processing system. The theory of phase sensitive detection (PSD) technique and common methods for its implementation are first introduced. Then, the implementation of PSD using a DFT method in MATLAB is provided, and finally, an example of the implementation of PSD is described. The second part of **Chapter 6** presents the practical test results of bench testing the electromagnet and its AC power supply and the AC signal conditioning system. This includes the test setups and equipment used. Discussion of the results is also provided.

Chapter 7 describes and discusses the flow induced potential difference measurements obtained from the practical model for varying numbers of flow channels and different flow channel positions within a circular cross-sectional area bounded by an electrode array. Comparison between the practical and theoretical results is also provided. Lastly, the relationship between the DFT obtained from the flow induced potential distribution, measured at the electrode array, and the total volumetric flow rate of blood flowing in multiple channels is discussed and related to the theoretical work presented in Chapter 3.

Chapter 8 concludes the research work and summarises the original work that contributed to knowledge of EM blood flow rate measurement techniques. Recommendations for further work are also proposed.

1.6 Summary

An overview of the human circulatory system was provided in Section 1.2. This included basic physical and biological descriptions of the heart, blood vessels and the blood. The heart is responsible for pumping blood into the pulmonary and systemic systems. Blood travelling away from the heart through arteries carries oxygen and nutrients to body tissues and organs. Blood travelling towards the heart through veins is deoxygenated. This blood is then delivered via the heart to the pulmonary circuit to be supplied with oxygen, and then sent back to the heart to be pumped to the systemic system. Figures on cardiac output, blood flow and pressure as well as the diameter of blood vessels for normal healthy adults were also provided in Section 1.2.4.

The importance of blood flow measurement in the diagnosis of CVD was discussed, noting that CVDs are the main cause of death globally. In 2008, 17 million people died from CVDs worldwide. CVDs are mainly associated with atherosclerosis – the narrowing of arteries due to a build-up of lipids on the arterial wall of the arteries. Common CVDs are peripheral arterial disease and deep venous thrombosis. PAD is the narrowing of arteries in the upper and lower limbs due to atherosclerosis. Patients with diabetes, renal failure or obesity are at high risk of PAD. Severe PAD can lead to limb ischemia and possibly heart attack or stroke. The common, routine diagnosis for PAD is through the ABI test during which the pressure of the ankle is compared with the pressure of the arm. However, this test may lead to false diagnosis in the elderly and diabetic patients and is not an ideal method due to staff shortages since it is a time-consuming process. Alternative methods for PAD diagnosis are duplex ultrasound, MRI and arteriography.

DVT is a blood clot that forms on the wall of veins – usually in the leg. DVT can be a life-threatening disease as the blood clot can break off and travel to the lungs causing pulmonary embolism. DVT also causes pain, paleness, tenderness and swelling in the leg. In the UK, 1 in 1000 people suffer from DVT and US statistics show that between 300,000 and 600,000 people are diagnosed with DVT yearly. Common methods used for the diagnosis of DVT are impedance plethysmography and duplex ultrasound. Advanced screening techniques for DVT include MRI and venography.

Based on the above statistics and figures, it can be concluded that the study of peripheral blood flow measurement is of great importance in clinical applications. The availability of easy and reliable methods for early detection of, for example, stenosis in the femoral and iliac arteries (i.e. PAD), will enable aggressive primary prevention and thus, a reduction in incidences of associated morbidity and mortality with a consequent reduction in the resources required to deal with the aftermath of health damage. Additionally, methods that can obtain an accurate diagnosis quickly will encourage their use in regular health check-ups by health centres and doctors for global health (DGH).

Finally, the structure of the thesis has been presented in the previous section, describing the content of each chapter, starting from Chapter 2 which is the literature review and finishing with Chapter 8 which is the conclusions and further work.

Chapter 2
Methods of Blood Flow Measurement

Contents

2.1 Introduction

There are several methods for blood flow rate measurement that are in use today. The methods are either based on tomography, plethysmography, ultrasound or EM induction. The choice of method depends on the region of the body, where the blood flow must be monitored, and whether an invasive or non-invasive method is required. Generally non-invasive methods are preferred over invasive techniques as they do not require surgical intervention. Hence, complications such as blood contamination can be avoided. Current methods can be used for measuring:

- Cerebral blood flow rate
- Cardiac output and nearby blood vessels in the thorax and abdomen
- Peripheral blood flow rate

The primary focus here will be on the non-invasive technologies that are commonly used for peripheral blood flow measurement. However, invasive methods based on ultrasound and EM induction will also be studied.

Firstly, methods based on tomography are reviewed in **Section 2.2**, including conventional X-ray, computerised tomography and magnetic resonance imaging. The operation of these methods is described, followed by their clinical applications which include blood flow measurement and lastly, their drawbacks. In a similar approach, **Section 2.3** reviews the principle of operation of blood flow measurements based on plethysmography and particularly, electrical impedance plethysmographic devices. **Section 2.4** discusses ultrasound-based techniques used in blood flow measurement, namely transit (invasive method) and Doppler (invasive and non-invasive). This section also describes how imaging and flow rate measurement techniques are combined in a duplex ultrasound device to view blood vessels and measure their corresponding blood flow rate. Common artefacts and errors are then reviewed.

Lastly, **Section 2.5** is a review of the invasive and non-invasive methods of blood flow measurement using EM induction. Firstly, the theory behind the EM induction flow meter is discussed including Faraday's law of induction, the "weight function" approach developed by Shercliff and the "virtual current" theory developed by Bevir. Moreover, general analysis of the detected potential signals from the electrodes of EM flow meters is discussed. This includes the signal conditioning and processing requirements. After the literature review on the work that has been achieved in the area of blood flow measurement, the research aims and methodologies are specified.

2.2 Tomography

Tomography (imaging) techniques such as X-ray radiography, MRI, computed tomography and nuclear medicine scans such as positron-emission tomography (PET) have a range of applications including diagnosis of cancer, broken bones and cerebrovascular and cardiovascular diseases [63]. They can provide information on blood flow rate in any part of the human body. These techniques have different principles of operation as will be shown in the following sections.

2.2.1 X-ray Radiography

An X-ray beam is an EM wave generated in an X-ray tube. When a target is exposed to directed X-ray beams (photons), the X-ray photons are passed through, scattered or absorbed by the target, depending on the target density [64]. Bone is the densest among soft tissues, fat and air and they all appear on an X-ray image (radiograph) as shades of black, white or grey. Higher density materials absorb X-ray beams more efficiently. Figure 2.1 shows types of tissues with different densities and how they would appear on an X-ray radiograph [65]. X-ray radiography is often used to identify the state of bone structures, i.e. fractured or broken bones. In a traditional X-ray device, one X-ray projection is performed. The patient is placed between the emitter (tube) and the detector of the X-ray machine. The patient can be either in a sitting, standing or lying position. Medical X-ray detectors distinguish between absorbed and passed X-ray photons which then form an image. Targets that absorb X-ray photons appear on the image with higher contrast.

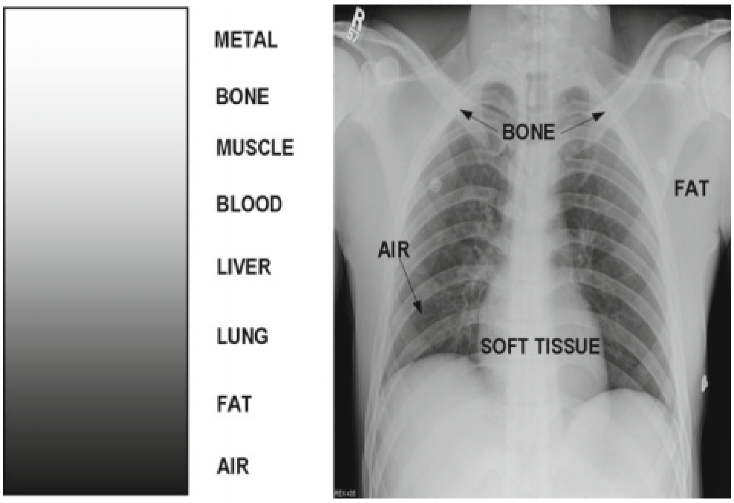

Figure 2.1: Visibility of different types of tissues on a radiographic image [65]

X-ray radiography can also be used to visualise blood flow in the circulatory system. This is referred to as X-ray angiography. For visualisation of blood flow, a special dye (contrast agent) is injected in either the arterial (arteriography) or venous (venography) system to view blood – causing the blood in arteries or veins to be more absorptive of X-ray photons than other soft tissues. Any blockage in arteries or veins would appear in different contrast as shown in Figure 2.2. In Figure 2.2(a) the arrow points at a blockage in the coronary artery, and in Figure 2.2(b), the blockage has been removed.

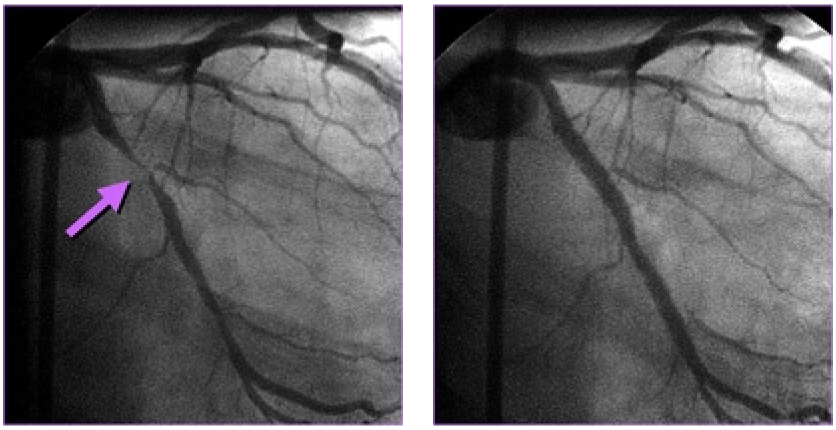

(a) (b)

Figure 2.2: (a) Stenosed coronary artery (b) Same artery after stenosis is removed [66]

Arteriography and venography can be used to diagnose PAD and DVT. Traditional X-ray methods only visualise blood flow. However, when combined with computer technology, i.e. CT scan, measurement of blood flow rate and velocity can be obtained.

2.2.2 Computerised Tomography

CT is a more advanced radiographic system that combines X-ray and computer technologies to produce detailed images of the target area as shown in Figure 2.3. CT generates ionising radiation, i.e. photons with sufficient energy to ionise tissues through which they pass. This allows the CT system to visualise, in greater depth, the different types of tissues; it can differentiate between types of soft tissues (better contrast), unlike traditional X-ray techniques [65]. CT systems perform multiple small projections in an axial plane across the body, creating cross-sectional images, or “slices”, of the body. These images are then combined by the computer to create very detailed 2D or 3D images. CT is often used to diagnose bone structures, cancerous tumours, cardiovascular (heart related) and cerebrovascular diseases. CT is not a common procedure for PAD or DVT; however, it is used in certain cases if advanced diagnostic testing is required. Similarly to traditional X-ray techniques, dye injection is also required in CT for blood visualisation.

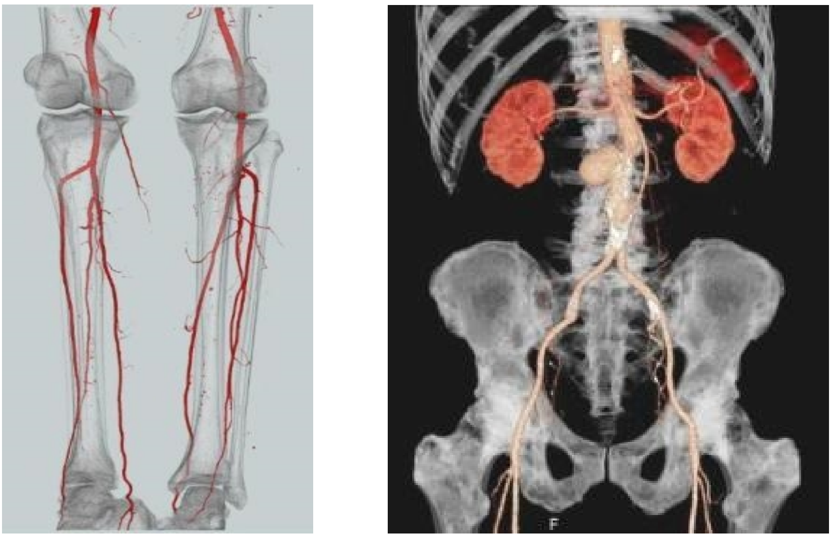

Figure 2.3: (a) CT scan of lower limb arteries. (b) CT scan of kidney and arteries at the pelvis

2.2.3 Magnetic Resonance Imaging

In an MRI system, the patient is exposed to a strong magnetic field. This magnetic field arranges the hydrogen nuclei within the patient's body in a certain direction [65]. The magnetic flux density for the medical MRI system is usually between 0.2-2 T. A radio-frequency (RF) pulse is then emitted at a section (axial slice) of the patient's body. This RF pulse excites the hydrogen nuclei and alters their alignment in the presence of the external magnetic field. Thus, it changes the energy state of the nuclei from a low to a high energy state. The RF frequency at which the nucleus changes its state from low to high is known as Larmor frequency (resonant frequency) [67]. When the RF pulse is stopped, the nuclei return to their original alignment and release the high-state RF energy to revert to the initial low-energy state. This energy (signal) is picked up by RF receiving coils and processed by computer software to determine what the examined section is. Several signals are required for each body section in order to reconstruct an image. The above procedure is then repeated for another section of the patient's body.

MRI is ideally used to examine soft tissues, i.e. to diagnose multiple sclerosis, brain tumours, spinal infections, torn ligaments and strokes in their earliest stages [67]. For blood flow measurement using MRI (also called MR angiography or MRA), a modified process known as phase contrast MRI (PC-MRI) is applied to visualise moving fluids. This process differentiates between the nuclear spins of the moving blood and spins of surrounding stationary tissues [68]. PC-MRI is often used for cerebrovascular, heart, aorta and pulmonary arteries. A contrast dye injection is also used in MRI for better image quality [69]. Functional block diagrams of aforementioned imaging devices and the type of electronics used are illustrated in this reference [70].

2.2.4 Disadvantages and Challenges

X-ray, CT and MRI devices are not used for routine check-ups and are often used for advanced diagnostic tests, i.e. heart, brain, bones or cancer diagnosis. They require a large space for installation and are expensive to buy and run; therefore, they are beyond the means of most local health centres and doctors for global health [67]. Moreover, the contrast dye injected for X-ray-based and MRI devices may have side effects on patients such as diarrhoea, increased heart rate (which can be fatal), urticaria (itchy rash), angioedema (swelling of deep layers of the skin), bronchospasm (constriction of muscles in the wall of bronchioles), cardiovascular collapse (failure of the system to maintain the supply of oxygen and nutrients to organs and tissues) and many other side effects [69, 71]. Hospitals are usually prepared to deal with potentially fatal side effects; however, such effects can put the patient’s life at risk in the future. In addition, for X-ray-based systems, patients with partial or full renal disease are at high risk of further damaging the kidney function when using contrast dyes [72]. It is often recommended that X-ray-based devices be avoided with patients who show severe reactions or have advanced renal disease or diabetes.

Furthermore, concerns about exposure to medical radiation have been raised [73]. CT devices expose patients to relatively large amounts of radiation in comparison with conventional X-ray techniques. Radiation has risks associated with cancer. During the screening of asymptomatic patients more CT scans are obtained and this means that the patient is exposed to larger amounts of radiation [74]. During MRI scans, measurements take a long time to be obtained while the patient is inside the device which might cause discomfort or claustrophobia. Finally, each one of these method suffer from “artefacts” that affect either the accuracy or quality of the reconstructed images [75, 76].

2.3 Plethysmography

2.3.1 Principle of Operation

Plethysmography is the measurement of a change in volume ΔV. It can be used to monitor blood flow rate Q by observing the change in the volume of a body part over time, i.e.

$$Q = \frac{\Delta V}{\Delta t} \qquad \text{Eq. 2-1}$$

It was used to measure blood flow in the human arm for the first time over 100 years ago [77]. Since then, it has been used in a variety of applications including the measurement of cardiac output, peripheral blood flow, cerebral blood flow and intrathoracic fluid volume [78]. Nowadays, it is mainly used in peripheral blood flow rate measurement – referred to as venous occlusion plethysmography – for cardiovascular research as other technologies such as tomographic methods superseded plethysmography in the areas of cardiac output and cerebral blood flow. It is also commonly used during intra-arterial drug administration in the forearms. For example, it is used for the assessment of drugs and hormones on blood vessels such as the brachial artery [79]. Another application for plethysmography is the diagnosis of deep venous thrombosis [80].

Figure 2.4 shows one of the early types of plethysmographic devices – known as chamber plethysmography – to measure peripheral blood flow rate [80]. The chamber section in Figure 2.4 senses the volume change of the leg using air- or water-filled calibrated volumes which are attached to the chamber. Any change in the volume of the leg will affect the air or water volume. The venous occlusion cuff stops venous blood from leaving the leg. However, it does not stop arterial blood flow. The cuff is usually inflated to 50 mmHg (6.7 Kpa). Hence, the increase of volume in the leg corresponds only to the arterial blood flow. If arterial blood flow is required to be measured in a particular segment of the leg, then an arterial occlusion cuff is also placed, and usually inflated to 180 mmHg (24 kPa). Figure 2.5 shows the graph obtained from this process. The marker ‘on’ is when the venous occlusion cuff is inflated and the ‘off’ marker indicates when the cuff is deflated. The interval between the ‘on’ and ‘off’ markers is related to the arterial blood flow. When the cuff is released, venous flow leaves the leg and the volume returns to normal as shown in A in Figure 2.5. If there is a blood clot in the veins (venous thrombosis), the volume will take longer to return to normal as shown in B in Figure 2.5.

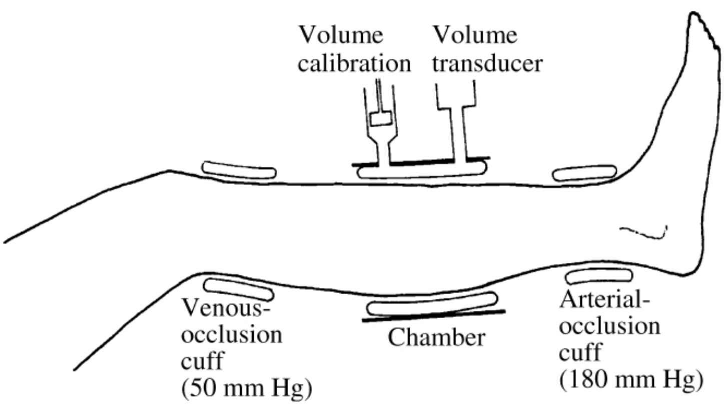

Figure 2.4: Chamber-type plethysmography [80]

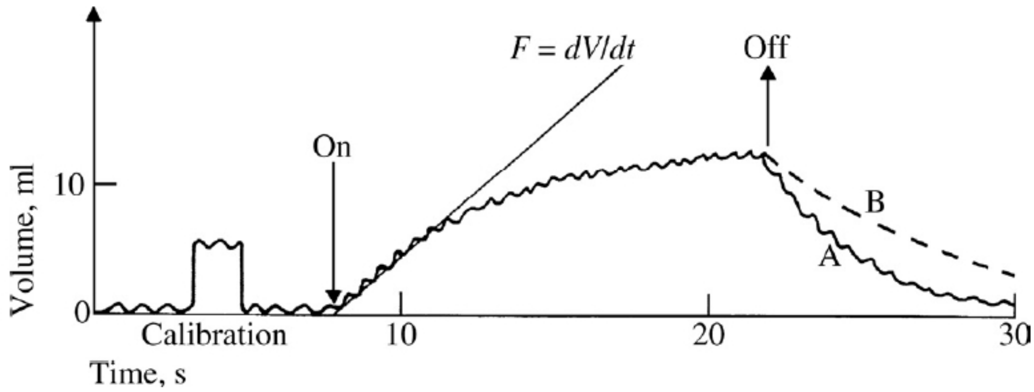

Figure 2.5: Typical graph obtained from plethysmography. F is the blood flow rate, dV the rate of change of volume and dt is the time derivative [80]

2.3.2 Impedance Plethysmography

Modern plethysmographic devices measure the change in electrical impedance of the limb, resulting from additional blood volume entering the limb during the cardiac cycle. A change in blood volume alters the resistivity of the limb and causes a change in the measured impedance. This impedance change is then correlated to volume change and thus, the flow rate can be found. Impedance plethysmographic (IPG) devices are more desirable in comparison with chamber-type devices as they are simpler, more accurate and easier to automate. IPG is an attractive method because it is non-invasive, safe and relatively simple to use for monitoring blood flow [81]. Assuming a cylindrical limb segment, the change of volume ΔV is given by

$$\Delta V = \rho_b \left(\frac{L^2}{Z^2}\right) \Delta Z \qquad \text{Eq. 2-2}$$

where ρ_b is the resistivity of blood (assumed to be 1.5 Ωm), L is the shortest distance between sensing electrodes (2-electrode or 4-electrode systems can be used), Z is the initial impedance and $\Delta Z = (Z_1 - Z)$ is the change in impedance, i.e. the initial value Z subtracted from the new value Z_1 [82]. A typical IPG device comprises two or four electrodes and an electronic measurement system which obtains the impedances Z and ΔZ. In the two-electrode system, both electrodes are used for driving in current and also sensing the potential difference which is proportional to impedance. However, this method is inaccurate due to several problems. These problems are solved in the four-electrode system, illustrated in Figure 2.6, in which current I_1 flows through the outer electrode to the body and back to the device, i.e. I_2, and the other inner electrodes sense the potentials V_1 and V_2.

The electronic measurement system then obtains the initial impedance Z and the impedance change ΔZ. The electronic measurement system consists mainly of an amplifier, a phase-sensitive detector and a voltage balancing circuit. Amplification is required as the voltages sensed are very small. Phase-sensitive detection (PSD) is a method in which the target voltage signal is detected in the presence of other noise sources. The target signal has a unique frequency as the driving electrodes are excited by an AC current source. This method can be implemented using analogue or digital electronic solutions. In this research, PSD was used for measuring low-level voltages and is further discussed, in detail, in Chapter 6. The voltage balancing circuit allows the initial voltage, related to the initial impedance, and the voltage change, associated with the change in impedance, to be distinguished and measured.

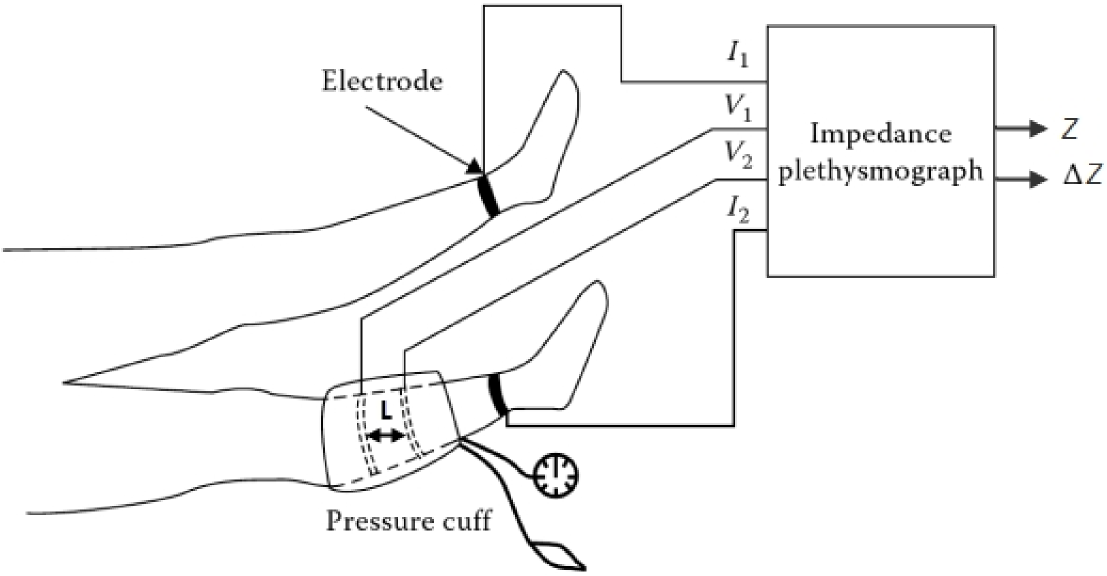

Figure 2.6: Four-electrode electrical impedance plethysmography [82]

2.3.3 Drawbacks

There are several drawbacks related to IPG that might cause poor accuracy of measurement. Firstly, it is assumed that arteries expand uniformly and this is not a valid assumption in the case of diseased arteries. It is also assumed that the blood resistivity ρ_b is constant. However, it has been shown that resistivity of blood decreases as velocity increases [80]. Another problem is that elevated venous pressure can lead to false diagnosis of DVT [71]. The reliability of IPG has been shown to vary from one clinical study to another. In one study, the sensitivity of IPG to DVT – i.e. the ability to identify patients with the disease – was found to be about 77% and the specificity – i.e. the ability to identify patients without the disease – was 93% [83]. Another study tested IPG on patients with acute DVT [84]. It was reported that the sensitivity and specificity were 75% and 45%, respectively with an overall accuracy of 57%, which is significantly low. In both studies, Doppler ultrasound achieved significantly more accurate measurements in comparison with IPG.

2.4 Ultrasound

2.4.1 Physics of Ultrasound

Ultrasound waves are mechanical vibrations – which may be generated by a piezoelectric transducer - that have frequencies above the human hearing range, i.e. above 20 kHz. The piezoelectric transducer is a device that converts electrical energy into mechanical energy and vice versa [85]. These vibrations create high and low pressure areas which travel in a forward direction as sound. The material used in making the transducer depends mainly on two factors: sensitivity and bandwidth. Sensitivity defines the response of the transducer to a reflected signal (echo). Transducers with high sensitivity generate higher signal strength (amplitude) from echoes [86]. Bandwidth is the operating frequency range of the transducer. Imaging transducers require wide bandwidth to attain high spatial resolution. Transducers used for fluid velocity measurement require narrow bandwidth to increase selectivity of the desired frequencies [87]. Common materials used are crystal quartz, polymers and ceramics. Crystal quartz is characterised by high sensitivity and narrow bandwidth whereas polymers have low sensitivity and high bandwidth. Ceramic transducers fall between quartz and polymers in terms of sensitivity and bandwidth and are often used in medical applications.

The frequency range often used in medical applications is between 500 kHz and 100 MHz. When ultrasound waves (acoustic signals) travel into the tissues of the body, these waves will be absorbed, refracted, scattered or reflected. This is due to the difference of acoustic impedance between the tissues. Acoustic impedance depends on several factors such as density, speed of sound, absorption coefficient and homogeneity of the tissues. When the acoustic impedance changes at the interface between two tissues, some of the sound waves are either reflected or refracted. Reflected signals are received by the piezoelectric transducer and interpreted to an image. The strength of the reflected signals depends on the difference between the acoustic impedance of the tissues. Signals of large amplitude are reflected when the difference between the acoustic impedance of the tissues is significant. The refracted signals might also reach another tissue interface, and some of them will be reflected and so on until they are totally attenuated as they reach deeper tissues.

The choice of ultrasound frequency range is dependent on the level of depth (penetration through tissues) and the spatial resolution required. Low-frequency signals have a longer wavelength than high-frequency signals. Low-frequency signals can penetrate tissues further; however, constructed images will have low spatial resolution. In contrast, high-frequency signals have a short range of penetration; however, they provide higher spatial resolution. A trade-off must be made between depth and resolution in order to obtain satisfactory images of the scanned area of the body. Usually, for non-invasive imaging and flow rate measurement, a lower frequency range is used, i.e. 1 to 5 MHz; for invasive and intravascular (within the vessel) imaging, a frequency range of 5 to 50 MHz is used and for cuff-type probes (mounted around blood vessels), a frequency range of 45 kHz and 20 MHz is utilised [85].

2.4.2 Principle of Operation

The principle of ultrasound operation is that the time t taken for the transmitted ultrasound wave (pulse mode) to be sent and reflected off an object is given by

$$t = 2d/c \tag{Eq. 2-3}$$

where d is the distance between the transducer and the reflector, i.e. body tissue and c is the speed of sound in the tissues of the body [85]. The speed of sound in the tissues of the body (blood, water, muscle, etc) is approximately 1500 ± 100 m/s. If the transmitted signal is a tone burst (burst mode) with a frequency f_0, the phase of the received signal ϕ, measured with respect to the transmitted signal, can also be used to measure the distance d between the transducer and the reflector as shown in the expression below [85].

$$\frac{\phi}{2\pi} = \frac{2d}{\lambda} = 2df_0/c \qquad \text{Eq. 2-4}$$

where λ is the wavelength. Eq. 2-3 or Eq. 2-4 is used to determine the distance (1D) between the transducer and the tissue. Measuring several locations simultaneously can create a 2D image of the tissue. This will be explained in detail in Section 2.4.4.

If the object (blood) is moving with respect to the transducer, the velocity of the object V can be measured in pulse mode or burst mode. In pulse mode, a single-cycle pulse is transmitted followed by an 'off' period, whereas in burst mode, multiple-cycles are sent successively and then followed by an 'off' period. The governing equation for velocity measurement in the pulse mode is given below [85].

$$\frac{\Delta t}{t_{avg}} = 2\left(\frac{V}{c}\right) \qquad \text{Eq. 2-5}$$

Δt is the difference in arrival times between two transducers placed on either side of the blood vessel (refer to Figure 2.8). In other words, it is the time difference between the time taken for a pulse to be sent from transducer 1 to 2 (t_1) and the time taken for the pulse to be sent from transducer 2 to 1 (t_2) as illustrated in Figure 2.7. Both transducers alternate in sending and receiving ultrasound waves. t_{avg} is the average arrival time, i.e. $(t_2 + t_1)/2$.

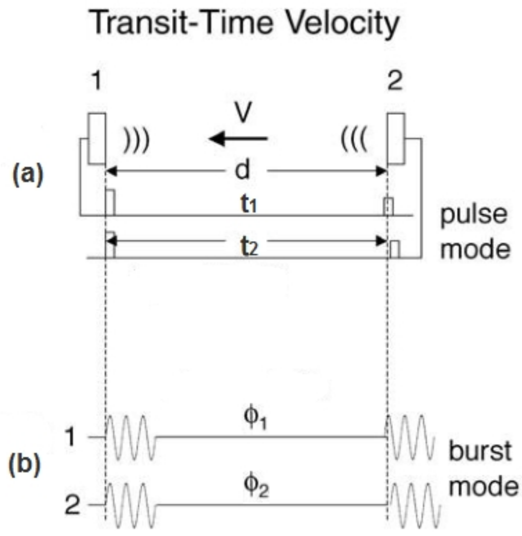

Figure 2.7(a) Pulse mode: difference in arrival time Δt. (b) Burst mode: difference in phase $\Delta\phi$ [85]

In burst mode, the phase difference $\Delta\phi$ between the transmitted and received signals (transducer 1 to 2 and transducer 2 to 1) is related to the velocity of the flow stream V as shown below [85].

$$\frac{\Delta\phi}{2\pi} = 2\left(\frac{dV}{\lambda c}\right)\cos\theta \qquad \text{Eq. 2-6}$$

where d is the distance between both transducers, λ is the wavelength of the ultrasonic frequency and θ is the angle between the flow direction and the ultrasound beam which is known as the angle of insonation as shown in Figure 2.8. Eq. 2-5 and Eq. 2-6 are known as the transit-time mode equations for velocity measurement. The transit-time method is illustrated in Figure 2.8. This mode is only used in invasive blood flow measurement as it requires two transducers placed at opposite side of the conduit (vessel) of the moving fluid (blood). Note that for flow rate measurement, the ultrasound beam must entirely cross the blood vessel.

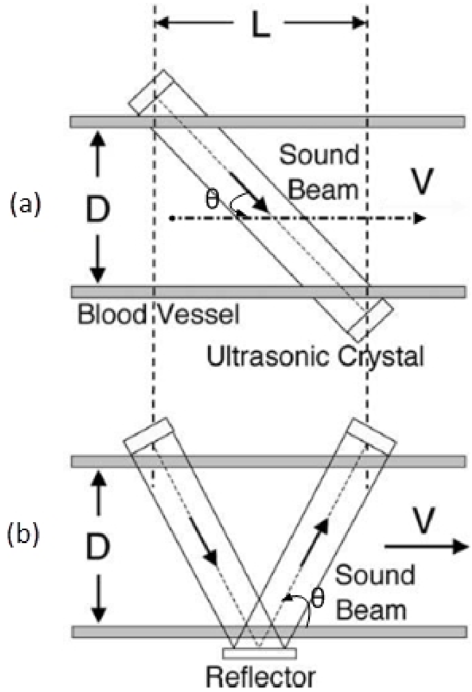

Figure 2.8: Transit-mode ultrasound (two methods): (a) transducers are on opposite sides (b) transducers are on the same side [88]

2.4.3 Doppler Mode

Alternatively, the Doppler Effect can be utilised to determine the velocity of flow. The Doppler Effect is the difference in frequency for an observer with respect to the source. This means, when a transmitted tone burst is emitted at a given frequency f_0, the red blood cells in motion will reflect this burst at a different frequency [89]. This difference or shift in frequency is proportional to the velocity of the red blood cells, i.e. the blood. Stationary tissues will reflect the ultrasound signal at the same frequency as the transmitted signal. The mathematical equation of Doppler mode is given by [85]

$$\frac{\Delta f}{f_0} = 2(V/c)\cos\theta \qquad \text{Eq. 2-8}$$

Δf is the difference in frequency between the original transmitted signal f_0 and the frequency of the reflected signal f'. The angle θ is the angle of insonation as depicted in Figure 2.9. Eq. 2-8 is often referred to as Doppler mode for velocity measurement. Similarly to the transit-mode ultrasound, the Doppler mode is sensitive to the angle of insonation θ. Ideally, the angle should be zero; however, this is not possible. It is usually recommended that the angle should be between 45^{o} and 60^{o} to achieve accurate velocity measurements [90]. The effect of the angle of insonation on the velocity measurement is discussed in Section 2.4.6.

There are two methods of operation for Doppler mode: continuous-wave (CW) Doppler and pulsed Doppler [85]. In CW Doppler, two transducers are used; one continuously transmits ultrasound signals and the other one receives the reflected signals. Note that both transducers can be placed on the same or opposite sides of the scanned area. The sample volume (SV) is defined by the size, shape, angle and focus of the beam. These settings are controlled by the technologist operating the Doppler device. Both modes are illustrated in Figure 2.10. The smaller the SV, the more accurate the measurement of velocity will be. In CW Doppler, the control of the SV area is limited and therefore, the accuracy is poor compared to pulsed Doppler.

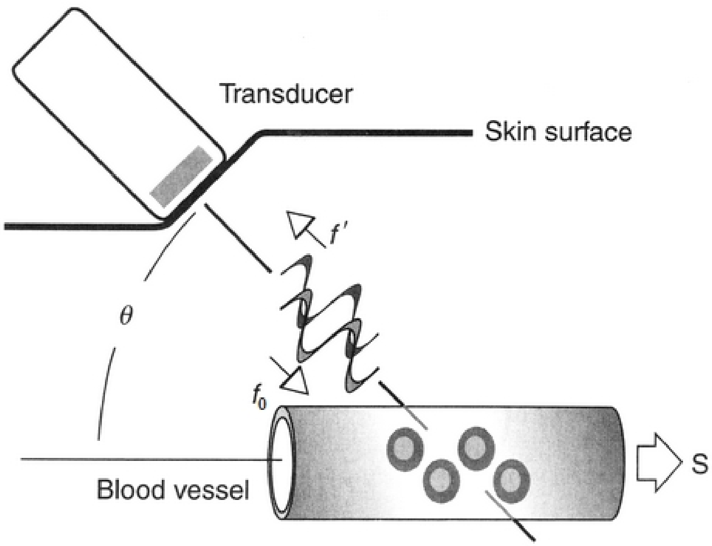

Figure 2.9: Doppler principle for blood velocity measurement [91]

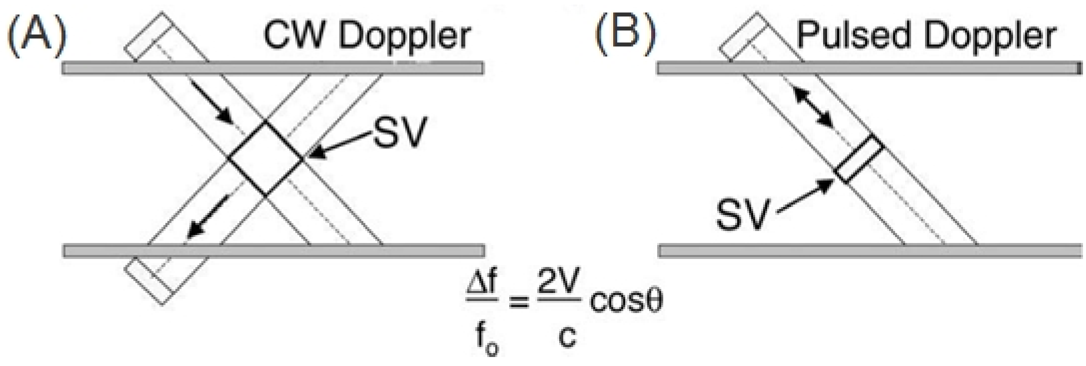

Figure 2.10: Doppler-mode ultrasound. (A) Continuous-wave Doppler and (B) Pulse Doppler [88]

In pulsed Doppler, one transducer transmits and receives the ultrasound waves. The SV is further controlled in pulsed Doppler by modifying the size ('on' time) of the pulses and also the time between sending and receiving the signals. For flow rate measurement, it is often better to use transit-time mode (refer to Section 2.4.2) as the SV covers the whole cross section of the vessel. Doppler mode is more accurate in measuring the velocity of the blood at a given point.

2.4.4 Ultrasound Imaging

Ultrasound imaging has numerous applications in medical research and clinical practice. It is often used, for example in diagnostics related to the pelvis, cardiovascular examination, ophthalmology and orthopaedics [92]. Ultrasound methods can be categorised into two groups: non-invasive and invasive. Non-invasive ultrasound methods are more desirable as they do not require surgery, and are safe to apply to the skin of the patient. Current non-invasive medical ultrasound devices can perform either imaging, flow measurement or both. Images created by ultrasound are referred to as sonograms. The part of the ultrasound device which contains the piezoelectric transducers is called the probe. Probes vary in size, shape and number of transducers depending on the type of ultrasound device and the modes of operation (Figure 2.11).

Figure 2.11: Different types of Doppler probe [93]

Notably, there are four modes for ultrasound imaging: A-mode, B-mode, M-mode and Doppler mode [92]. A-mode (amplitude mode) ultrasound is a one-dimensional mode and is used to determine the depth of tissue or organ. It can be used, for example, to measure the depth of the eyeball. When acoustic signals are transmitted, a straight tracing line is displayed on the screen. Once the signals arrive at a tissue interface, the transducer receives the reflected signals and displays them as amplitude, as illustrated in Figure 2.12.

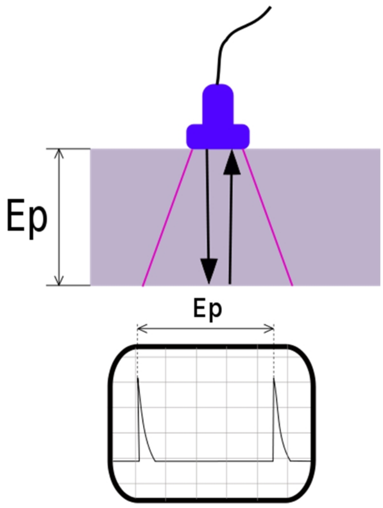

Figure 2.12: A-mode Doppler ultrasound. Ep is the distance between the transmitter and the surface from which the signal was reflected [94]

B-mode (Brightness mode) is a method which uses an array of transducers in the probe. The transducers are excited in sequence. The strength of the reflected signal is displayed as a pixel with a brightness level on the screen. A large number of transducers increase the number of spatial pixels and, therefore, the resolution of the image is improved. B-mode creates a 2D image of the scanned area, and it is often the standard mode in most medical ultrasound devices. In modern devices, B-mode images are often refreshed on the screen at a frame rate of at least 20 frames per second to create real time imaging of the scanned area.

Figure 2.13 shows a B-mode image of a carotid artery with atherosclerosis (see small arrows on Figure 2.13). Tissues with high reflectivity are presented in white (inner layer of the arterial wall of the carotid); low-reflective tissues are in grey, i.e. muscles, and non-reflective tissues are in black (fluids). In the diagnosis of arterial stenosis in the upper and lower limbs, a B-mode image can provide information on anatomy (course, variants), vessel contour (stenosis), wall structure (calcification, plaque) and perivascular structures (hematoma, abscess, muscles).

The M-mode also creates a 2D image of the scanned area; however, it also displays the movement of structure such as heart valves as a waveform (a dynamic view is created if the frame rate is high). Figure 2.14 illustrates the M-mode of mitral valve of the heart.

Figure 2.13: B-mode image of stenosed carotid artery [95]

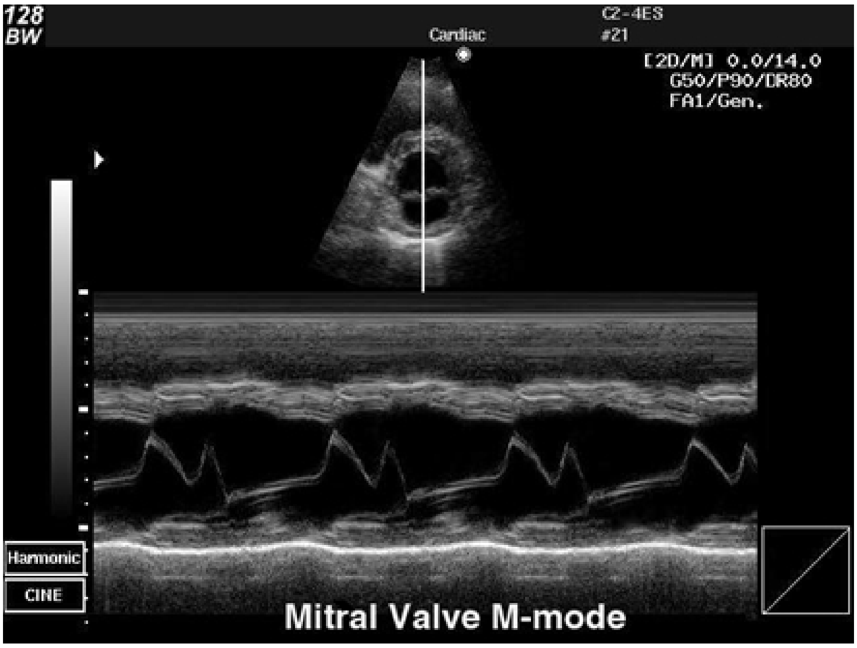

Figure 2.14: M-mode image of mitral valve [96]

Doppler mode allows the flow of blood to be measured and/or visualised. The principle of operation is as described earlier in Section 2.4.3. Pulsed Doppler mode is often combined with B-mode to show an image of the blood vessels and the blood flow velocity. This combined mode of operation is known as duplex ultrasound [97]. Continuous-wave Doppler is not suitable for duplex ultrasound as it continually transmits ultrasound signals. A time interval between transmitted pulses is required in order to determine at which depth the echoes originated.

In modern types of duplex ultrasound, the blood flow velocity is also viewed in colour on the display screen. This mode of operation is known as colour Doppler. In colour Doppler, the reflected ultrasound, due to blood flow velocity, is represented in colour, and is overlaid on the B-mode image. The Doppler method can only determine the velocity of the flow and not the flow rate. However, when it is combined with B-mode, the diameter of the vessel can be found. Therefore, the cross-sectional area can be determined and the flow rate can be calculated [89].

In Figure 2.15, a duplex scan of the femoral artery is shown. The red colour indicates where the flow is moving away from the transducer; and the blue colour indicates where the blood flows towards the transducer. The lower section of Figure 2.15 represents the velocity waveform of the pulsatile arterial blood flow, i.e. velocity (cm/s) vs time (s). This is known as spectral Doppler. Note that, spectral Doppler only devices are available and they only show results of the velocity of the blood in the blood vessel as shown in the lower part of Figure 2.15. Duplex Doppler can be used to assess a variety of medical conditions such as carotid occlusive disease, deep vein thrombosis and varicose (swollen and enlarged) veins. Additionally, Doppler ultrasound or duplex Doppler is used to diagnose patients who are suspected to have stenosis such as coronary heart disease (CHD) and PAD. It is an alternative (or additional) method to CT scans and MRI which both require dye methods [98, 99].

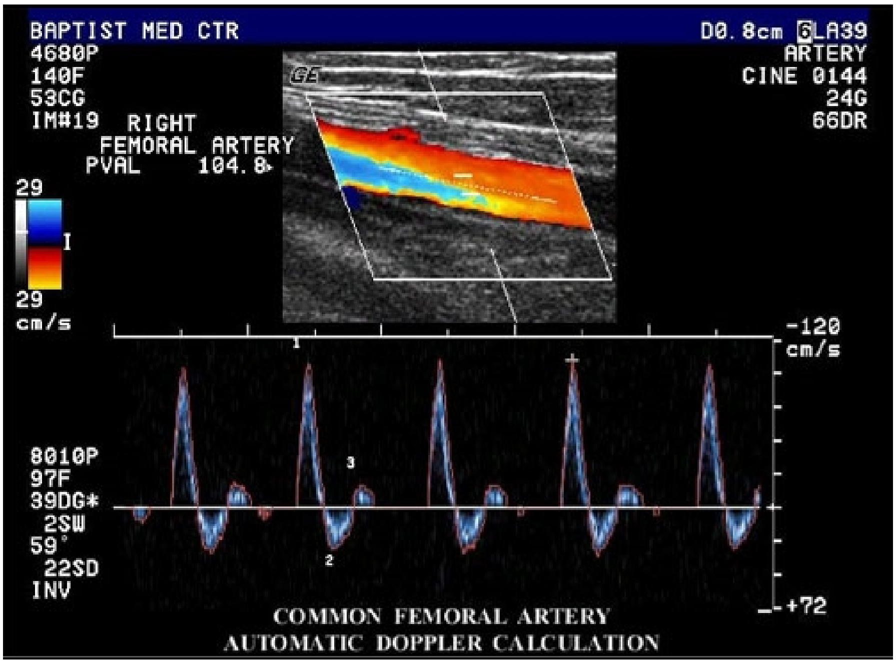

Figure 2.15: Duplex image of femoral artery[100]

Much information can be obtained from a duplex scan that can help with diagnosing stenosis:

- B-mode image
- Spectral Doppler which shows peak velocity of blood flow
- Broadening of Doppler spectrum
- Colour map produced by Doppler

Commonly, the measurement of peak velocity is the determining factor in assessing the severity of stenosis [101]. Spectral broadening refers to the presence of high-frequency spikes on the spectral Doppler which are due to turbulent or disturbed flow due to stenosis. In Figure 2.16(a) spectral Doppler is shown for a healthy femoral artery. It can be observed that the outline of the waveform is smooth. On the other hand, Figure 2.16(b) shows the spectral Doppler for a femoral artery affected by stenosis. A range of high-frequency spikes are superimposed on the waveform. However, spectral broadening can also be caused by incorrect sample volume, determined by the setting of the ultrasound device. It can also be due to the presence of several velocities within the sample volume [89]. Technologists operating either Doppler mode only or a duplex ultrasound device must carefully configure the parameters/settings to avoid artefacts which can lead to incorrect diagnosis of stenosis. Doppler artefacts and sources of error are discussed later.

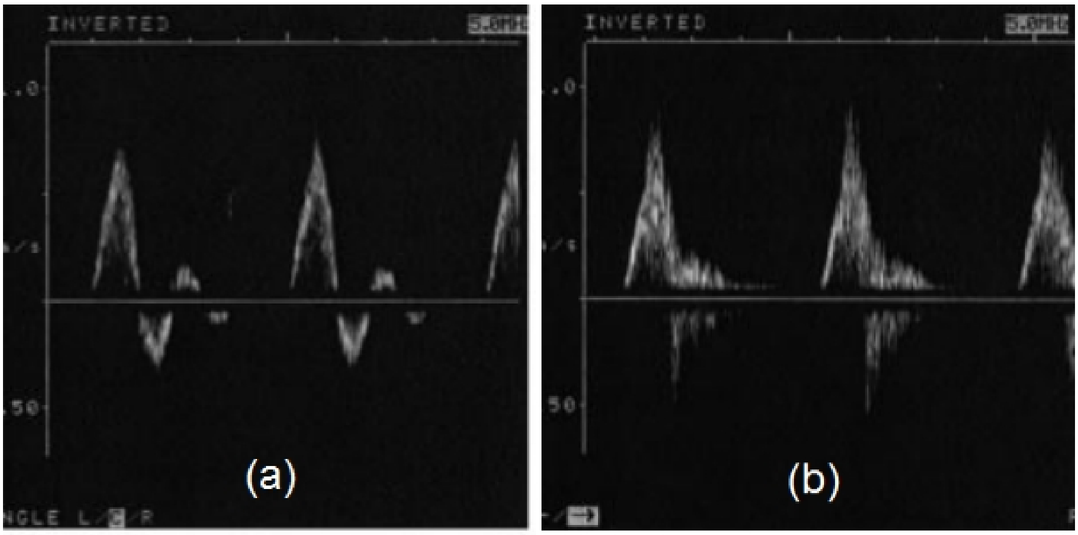

Figure 2.16: (a) Spectral Doppler of healthy artery and (b) spectral Doppler of stenosed artery[89]

2.4.5 Invasive Ultrasound

Invasive methods mean that surgical intervention is required to expose the blood vessel of interest. A cuff-type (or clamp-type) ultrasound flow meter is placed around the blood vessel. Alternatively, a catheter-type probe can be inserted into blood vessels via a skin incision. The probe can then be moved to enter larger blood vessels. For blood flow rate measurement, it is more desirable to use transit-time mode than Doppler mode as the sample volume of the probe covers the entire flow cross section, unlike for the Doppler method in which the sample volume is limited. However, for a local velocity measurement, Doppler mode is often used as the sample volume can be controlled to provide higher accuracy of velocity measurement at a given point. It is possible to use Doppler to perform flow rate measurements; this would require careful shaping, focusing and angling of the ultrasound beam to cover the cross section of the flow. Figure 2.17 shows two types of ultrasound invasive probes: (A) pulsed Doppler and (B) transit-time.

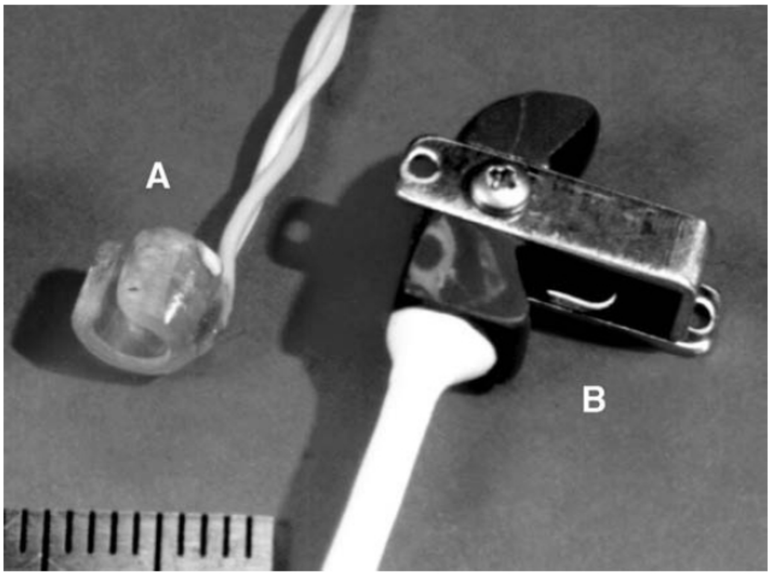

Figure 2.17: (A) cuff-type Doppler probe and (B) transit-time probe [88]

2.4.6 Artefacts and Drawbacks

Despite the fact that Doppler mode and duplex ultrasound are intensively used in medical diagnosis and are accepted by health practitioners, there are several sources of error associated with Doppler mode in ultrasound imaging and velocity measurement devices. These errors can lead to false diagnosis of arterial stenosis. Errors can either be caused by the technologist, Doppler device or the patient [101]. Errors made by the technologist due to improper configuration of the Doppler device can add significant error to the peak velocity measurement. As stated earlier, the peak velocity measurement is often relied on for the diagnosis of the severity of stenosis. The device parameters such as Doppler angle of insonation, placement and size of sample volume, the pulse repetition frequency and gain setting play an important role in the accuracy of the velocity measurement [90, 101, 102].

Angle of Insonation

The uncertainty of the angle of insonation between the ultrasound beam and the reflector can lead to a significant error in velocity measurement. According to Eq. 2-8, the frequency change Δf is proportional to the cosine of the angle of insonation θ. It is recommended that the probe is angled at 60^{o} or less to minimise the error. Angles above 60^{o}, will introduce significant error in the velocity measurement [90]. Figure 2.18 shows a measurement of systolic blood peak velocity of the same blood vessel but at two different angles of insonation: 42^{o} and 70^{o}. The velocity measurement for the angles 42^{o} and 70^{o} were 80 cm/s and 176 cm/s, respectively. It should be noted that the predicted velocity has more than doubled in the second reading. Moreover, even if the probe is angled at 60^{o} or less, it is assumed that the velocity vectors of blood are parallel to the wall of the blood vessel, but this is not necessarily correct. Red blood cells, which are the main reflectors in the blood, can be in different positions, and also they do not all always travel at the same velocity. Moreover, the assumption that the velocity vector of the red blood cells is parallel to the vessel wall becomes invalid when the vessel is stenosed because it has been shown by Hoskin that the difference between the measured angle of insonation θ and the actual angle for a stenosed vessel can be up to 25° [103]. This angle difference can significantly affect the accuracy of the velocity measurement in the stenosed vessel. Other factors that can invalidate this assumption are (1) vessel branching, tortuosity and curvature and (2) blood flow pulsatility and turbulence [88].

Furthermore, the direction of blood flow has a significant impact on the received Doppler signals as shown in Figure 2.19 [102]. In case A, the beam is more aligned to the direction of flow than the beam in case B. Therefore, the amplitude of the Doppler signal obtained from case A is higher. The amplitude of the signal is a direct representation of the velocity of the blood flow. Hence, for the same blood vessel, two blood velocities can be measured depending on the alignment between the Doppler beam and the direction of blood flow. In case C, the beam is almost at 90° with respect to blood flow. The cosine of 90° is zero and according to Eq. 2-8, the difference in frequency is zero. Hence, in case C, the Doppler signal shows that the velocity is very low. Lastly in case D, the flow direction is away from the beam and hence, the representation of the received Doppler signal shows a negative velocity.

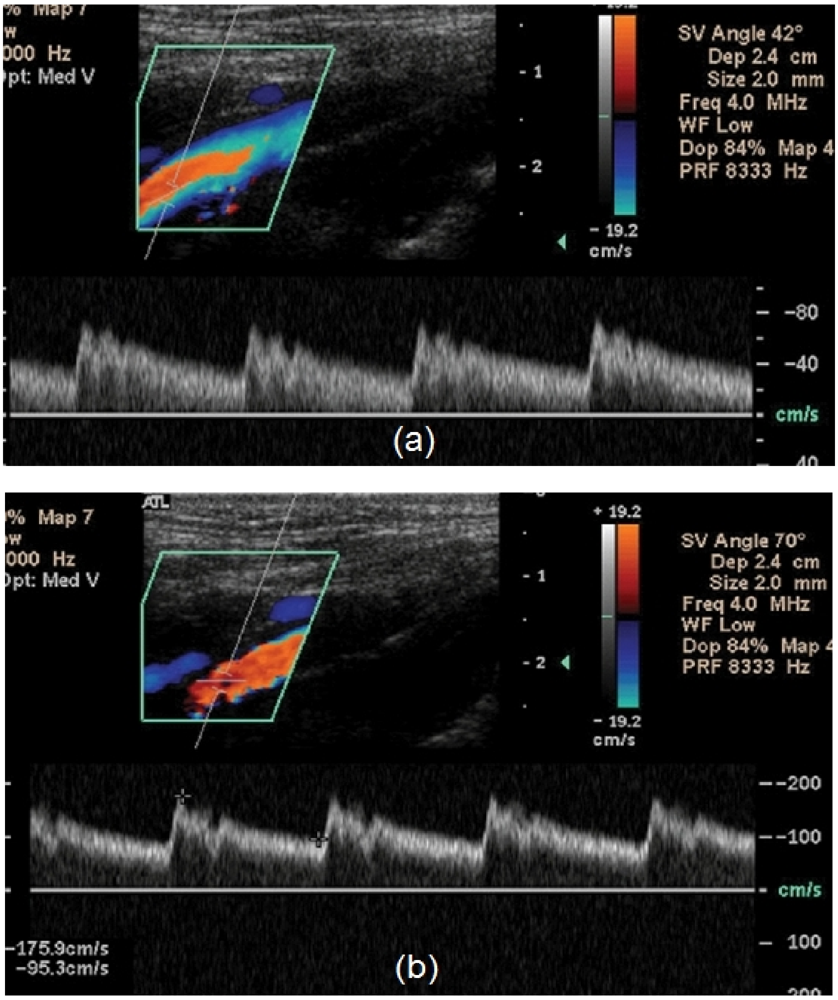

Figure 2.18: Impact of angle of insonation on duplex image: (a) θ = 42° and measured velocity = 80 cm/s and (b) θ = 70° and measured velocity = 176 cm/s (by Teodorescu [90])

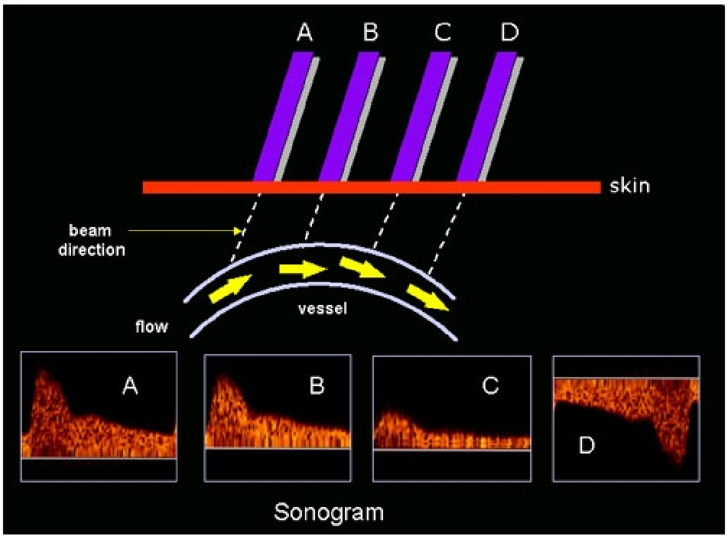

Figure 2.19: Effect of direction of the ultrasound beam with respect to blood flow (by Deane [104])

Placement and size of the sample volume

The placement of the sample volume within the vessel under examination is a crucial factor [101]. The technologist must ensure that the sample volume size is configured suitably in order to be placed in the centre of the vessel. The sample volume must also be placed as close as possible to the site of maximum stenosis to obtain a high-accuracy velocity measurement. The error due to the placement of the sample volume depends highly on the experience of the technologist. Insufficient training or lack of experience can increase this error in the velocity measurement.

Pulse repetition frequency and gain settings

The maximum frequency, resulting from the combination of flow velocity and beam angle, that can be measured by a Doppler device must be at least half the pulse repetition frequency to avoid aliasing [102]. In signal processing, aliasing causes the ultrasound system to measure a frequency that is different from the actual flow frequency. The pulse repetition is determined by the depth of penetration and the sample volume required. It must also be ensured that there is sufficient time between transmitted pulses to allow the transducer to discriminate between the associated reflected signals to eliminate any range ambiguity, i.e. the tissue by which the signal has been reflected. Hence, for scanning deep tissues, the pulse repetition must be reduced to give sufficient time for the reflected signal to be detected. At the same time, the Doppler frequency, resulting from the flow and angle of insonation, must not be higher than half of the pulse repetition frequency. This puts a constraint on the maximum blood velocity that can be measured at a given depth.

In duplex ultrasound, simultaneous modes of operation work together, i.e. B-mode, Doppler mode and colour mode [102]. These operations use the same set of transducers, but utilise different types of information. This affects the frame rate of the B-mode image, the colour resolution of the flow and the pulse repetition frequency. Improper device settings may lead to poor resolution or incorrect velocity measurement. Figure 2.20 shows a velocity waveform (spectral Doppler) of arterial blood flow obtained using Doppler ultrasound. In Figure 2.20(a), aliasing occurred due to the incorrect setting of the pulse repetition frequency. It can be seen that negative velocities appeared. In Figure 2.20(b), the aliasing was corrected by adjusting the pulse repetition frequency.

The gain setting of the amplifier of the ultrasound system must be correctly selected to ensure accuracy. Very low gain may cause the system to misread low-flow velocities whereas high gain can generate random noise which can appear as spectral broadening which is a sign of the presence of stenosis. Figure 2.21 illustrates the effect of high and low gain setting of the Doppler device. The left-hand side of the spectral Doppler is as a result of low gain setting and, on the right-hand side, the gain setting was increased. It can be noted that, at high gain setting, the random noise significantly increased.

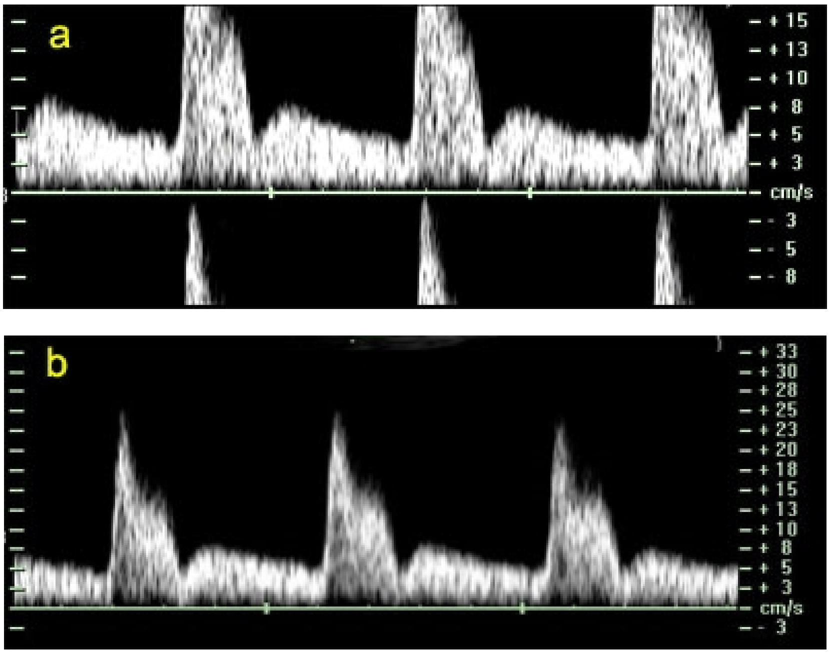

Figure 2.20: (a) Aliasing occurring in Doppler ultrasound due to improper setting of the pulse repetition frequency and (b) the same velocity waveform after correction of the aliasing (by Deane [104])

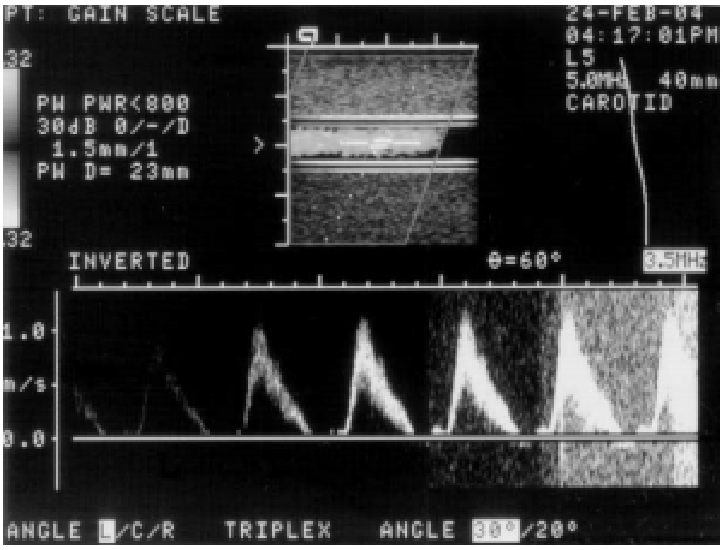

Figure 2.21: Effect of low and high gain settings on spectral Doppler (by Lui [101])

Interobserver variability

The last significant error due to "human factors" is the difference in interpretation and gathering of results among technologists and it is referred to as interobserver variability. The error resulting from interobserver variability can be significant even if other sources of error such as angle of insonation, placement of sample volume and gain are fixed. In one study [101], the impact of four factors on the velocity measurement were investigated. They were:

- Interobserver variability
- Angle of insonation
- Placement of the sample volume
- Signal gain setting

In these tests, one parameter was tested at time and the others were fixed. Four experienced technologist (14-20 years of experience) participated in this study. The tests were carried out in an artificial environment. The flow model was comprised of two tubes (vessels): one was stenosed and one was not. These two tubes were inserted into tissue-like material made of agar. The true peak velocity values were known during all tests. In the interobserver variability test, the probe was fixed using a holder at angle of insonation of 60°, the sample volume was placed in the centre of the blood vessel and the gain was set to an ideal value. The four technologists used only the screen cursors on the device display to obtain velocity measurements. The velocities measured for the stenosed and unstenosed tubes from this test were between 9% and 14% higher than the true velocity values. In the second test, the effect of the angling and positioning of the sample volume was examined. The four technologists manually adjusted the angle and position of the sample volume. For the unstenosed tube, the velocity measured was 7% to 16% higher, whereas for the stenosed tube, the measurement was 7% to 28% higher than the true velocity value. Finally, for the gain setting, three options were available: low, high and ideal. The error percentage was similar for all technologists. For the high, low and ideal gain values, the error in measurement was 19%, 12% and -10%, respectively. This study shows how significant the error can be due to one source of error. It is likely that the error will be more significant if it is due to two or more sources.

Device and Patients Errors

In addition to human error, Doppler or duplex Doppler devices result in errors associated with sample volume shape, aperture size, beam steering, beam refraction, system noise and the assumption of sound in blood and tissues [101]. Errors arising from using a single speed value in all tissues, assumption of the speed of sound in blood and the angle measurement of refraction can introduce an error of up to 8% [105].

Lastly, the errors associated with patients are: vessel morphology, patient motion and most importantly, plaque calcification [101]. Plaque calcification is the build-up of calcium on the walls of blood vessels. It is formed from calcium deposits between the wall and the atheromatous plaques. Calcified plaque blocks ultrasound signals and prevents the measurement of blood flow velocity [106]. Calcified plaque is common in the femoral arteries of dialysis patients [62]. Such problems can prevent the use of ultrasound to perform a velocity measurement or obtain an accurate measurement of the blood velocity [90].

2.5 Electromagnetic Induction

2.5.1 History of Electromagnetic Flow Metering

When a conducting object (solid or fluid) moves in a magnetic field, it experiences a magnetic force. As a result, an electromotive force is induced in the conductor which is directly proportional to the velocity of the object. This experiment was one of the first that Faraday conducted in 1831 to demonstrate his law, which is known as *Faraday's Law of Induction*. There are many applications based on Faraday's law of induction, including electrical motors, generators, transformers, inductors and EM induction flow meters. EM flow metering falls within the area of *Magnetohydrodynamics* – the study of fluid dynamics and electromagnetism.

In 1832, Faraday attempted to measure the velocity of the River Thames by placing two gigantic electrodes on opposite sides of the river and using the Earth's magnetic field. This experiment was not successful due to spurious voltages arising from electrochemical and thermoelectric effects. Many years later (1917), oceanographers used this principle to measure the speed of ships by measuring the induced emf between two electrodes due to the presence of magnetic fields emanating from the ships [107].

Williams [108] was the first to apply the principle described above to a closed conduit, creating the first conventional EM flow meter. The measuring tube of the flow meter was made of non-conducting material, to avoid a short circuit between the tube and the conducting fluid. Two electrodes were placed normal to the direction of the magnetic field (y-axis) and perpendicular to the direction of the flow (z-axis). The electrodes were made of non-corrosive material and were in contact with the fluid through the tube wall as shown in Figure 2.22. The magnetic field generated was uniform i.e. the magnitude and direction of the magnetic field were the same throughout the cross-section of the tube.

Williams concluded that for a uniform magnetic flux density B, the potential difference U measured between the two electrodes is directly proportional to the flow rate of the conductive fluid Q. He also realised that the induced potential distribution would not be uniform (refer to Figure 2.23a) due to the fact that the pipe is circular and the velocity of the moving liquid in the centre of the pipe is higher than at the pipe wall. Thus, the induced emf in the centre of the pipe is greater than the induced emf at the pipe wall. Therefore, circulating currents are created in the pipe cross section (Figure 2.23b).

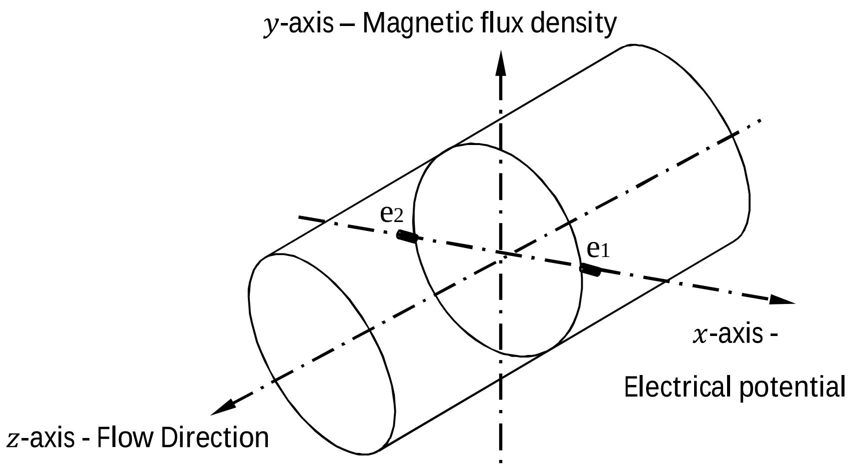

Figure 2.22: Conventional EM flow meter

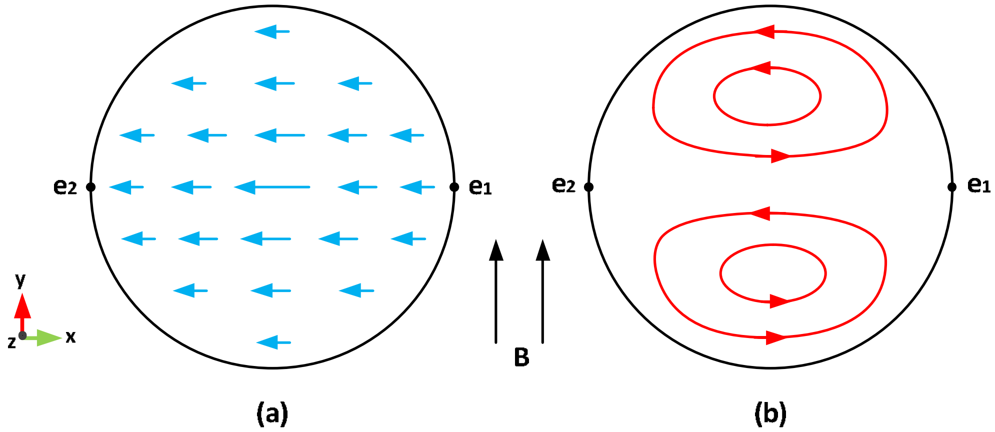

Figure 2.23: (a) Non-uniform induced potential in the flow cross section; (b) circulating currents due to non-uniform induced potential distribution [107]

This would mean that the actual induced emf along the imaginary line connecting the electrodes e_1 and e_2 is reduced by voltage drop due to ohmic resistance. Therefore, the induced voltage is affected by the velocity distribution. However, Thürlemann proved that for an axisymmetric velocity profile, i.e. one which has rotational symmetry about the tube axis, the induced emf is proportional to the mean velocity of the conducting liquid, as if it were travelling in a uniform manner in the cross-section of the pipe [109]. From Williams's experiment, it was concluded that for an axisymmetric velocity profile and uniform magnetic field, the induced emf is directly proportional to the mean velocity of the fluid, regardless of the velocity distribution and conductivity of the fluid.

Mathematically, this is given by

$$\Delta U = B \cdot d \cdot \bar{v} \qquad \text{Eq. 2-9}$$

where B is the magnetic flux density, d is the distance between the electrodes (the diameter of the pipe) and $\bar{v}$ is the mean velocity of the conducting liquid. The relationship between the volumetric flow rate Q and velocity of a fluid in a cylindrical conduit (assuming axisymmetric flow) is expressed as follows

$$Q = \bar{v} \cdot A \qquad \text{Eq. 2-10}$$

where Q is the flow rate, v is the velocity and A is the cross-sectional area of the conduit. The area of the circle is $\pi d^2/4$ (d is the diameter of the cross-sectional area). Hence, the flow rate of the fluid can be given by

$$Q = \Delta U \cdot \frac{\pi d}{4B} \qquad \text{Eq. 2-11}$$

In 1932, Fabre was the first physiologist to propose the use of an EM flow meter for non-invasive blood flow measurement. A few years later, an EM flow meter for blood flow measurement was successfully implemented invasively for clinical use independently by Kolin and Wetterer [110]. The EM flow probe consisted of an electromagnet, sensing electrodes and input (power source) and output (voltmeter or measuring equipment) as shown in Figure 2.24.

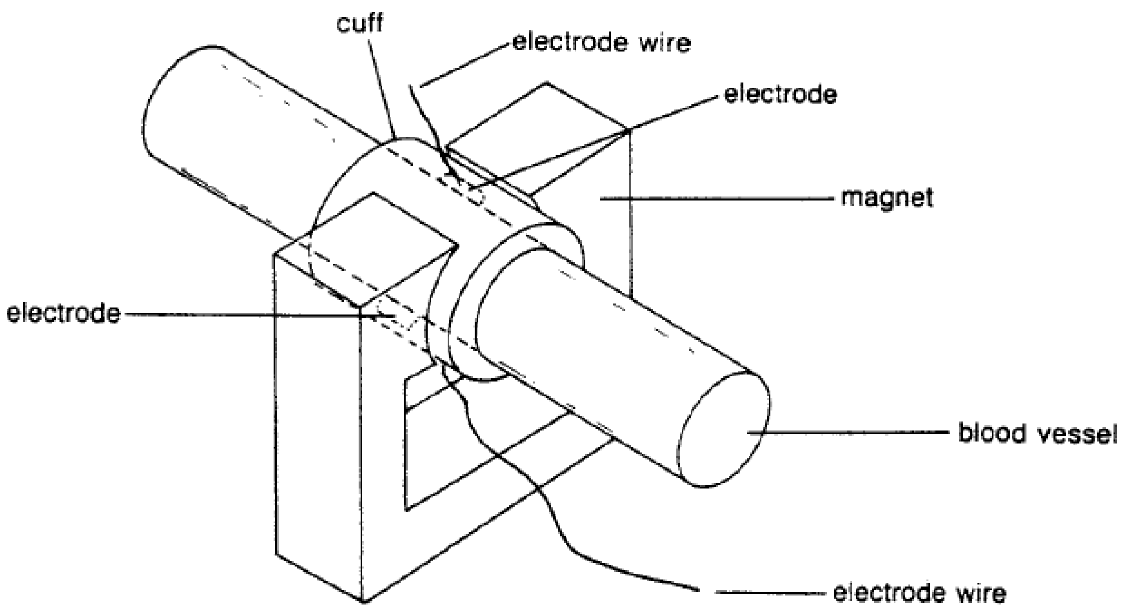

Figure 2.24: Invasive EM blood flow probe (Kolin's method) [111]

Shercliff [107] presented a comprehensive theoretical foundation of EM flow metering and soon after, the development of blood EM flow meters for invasive and non-invasive use increased substantially. Mostly, the EM flow metering technique is attractive because [112]:

- It is a linear device, i.e. $\Delta U \propto Q$
- It can detect forward or backward flow direction
- It is insensitive to viscosity, density, temperature, conductivity and pressure loss
- It is unaffected by velocity profile, provided the velocity profile is axisymmetric

2.5.2 Faraday's Law of Induction

When a straight conducting bar moves through a uniform and static magnetic field with a velocity $\boldsymbol{v}$ as shown in Figure 2.25, the charged particles of the conductor experience a force called the Lorentz force [113] which is mathematically given by

$$\boldsymbol{F} = q\boldsymbol{v} \times \boldsymbol{B} \qquad \text{Eq. 2-12}$$

where $\boldsymbol{F}$ is the Lorentz force, q is the electrical charge of the particle under the influence of the force, and $\boldsymbol{B}$ is the magnetic flux density. Note that the velocity $\boldsymbol{v}$ and the magnetic flux density $\boldsymbol{B}$ are vectors with vector components of $\widehat{\boldsymbol{x}}$, $\widehat{\boldsymbol{y}}$ and $\widehat{\boldsymbol{z}}$ and $\times$ is the cross product. The Lorentz force acts at right angles to the velocity of the conducting bar $\boldsymbol{v}$ and the magnetic flux density $\boldsymbol{B}$. This force causes a charge separation between the positively and negatively charged particles (polarisation) of the conductor. As a result, an electric field $\boldsymbol{E_L}$ is produced within the conductor and the Lorentz forces $q\boldsymbol{E_L}$ on positive charges are in the negative y-direction $(-\widehat{\boldsymbol{y}})$.

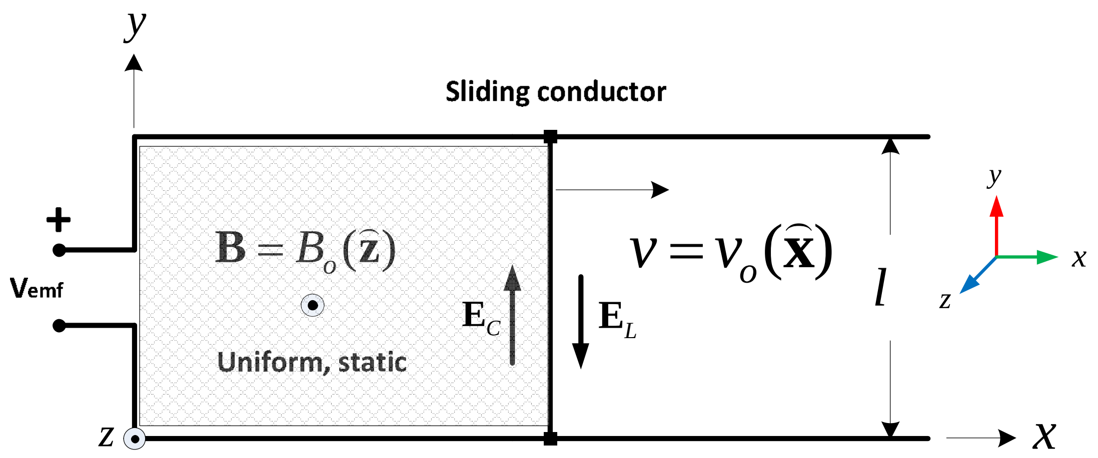

Figure 2.25: Sliding conductor moving in a uniform and static magnetic field [114]

The charge separation continues until equilibrium is reached between the Lorentz force $q\boldsymbol{E_L}$ and the electric force due to free charges $q\boldsymbol{E_C}$, that is

$$q\boldsymbol{E_C} = q(\boldsymbol{v} \times \boldsymbol{B}) \quad \text{or} \quad \boldsymbol{E_C} = (\boldsymbol{v} \times \boldsymbol{B}) \qquad \text{Eq. 2-13}$$

From Figure 2.25, the electric field due to free charges $\boldsymbol{E_C}$ can be found as follows

$$\boldsymbol{E_C} = \boldsymbol{v} \times \boldsymbol{B} = [v_o\widehat{\boldsymbol{x}}] \times [B_o(\widehat{\boldsymbol{z}})] = v_oB_o\widehat{\boldsymbol{y}} \qquad \text{Eq. 2-14}$$

where v_o and B_o are the values of the velocity $\boldsymbol{v}$ and the magnetic flux density $\boldsymbol{B}$. Due to the electrostatic field $\boldsymbol{E_C}$, an electromotive force is generated V_{emf}. This electromotive force is equal to the integral of the electric field $\boldsymbol{E_C}$ around the path of the conductor, and it is an application of Faraday's law of induction [115], i.e.

$$V_{emf} = \int \boldsymbol{E_C} \cdot dl = \int (\boldsymbol{v} \times \boldsymbol{B}) \cdot dl \qquad \text{Eq. 2-15}$$

where dl is an incremental segment of the distance (path) between the positively and negatively charged particles, and it is equal to

$$dl = dy\hat{\boldsymbol{y}} \qquad \text{Eq. 2-16}$$

Substituting Eq. 2-14 and Eq. 2-16 into Eq. 2-15 gives

$$V_{emf} = \int_0^l (v_o B_o \hat{\boldsymbol{y}}) \cdot (dy\hat{\boldsymbol{y}}) = v_o B_o \int_0^l dy = v_o B_o l \qquad \text{Eq. 2-17}$$

where l is the length of the conductor. This emf is known as 'motional' emf which occurs due to the motion of the conductor in the static EM field of flux density $\boldsymbol{B}$. It can be observed that Eq. 2-9 and Eq. 2-17 are similar.

For varying magnetic flux density in the positive z-axis direction, that is (refer to Figure 2.25; however the magnetic field is now time-varying)

$$\boldsymbol{B} = B_o \cos \omega t \, (\hat{\boldsymbol{z}}) \qquad \text{Eq. 2-18}$$

The total emf generated is the sum of the 'motional' emf V_m, which is given in Eq. 2-15, and also, 'transformer' emf V_t due to the time-varying (AC) magnetic field. Using Faraday's law of induction [114], the total emf V_{emf} can be represented mathematically as

$$V_{emf} = V_t + V_m = -\iint \frac{\partial \boldsymbol{B}}{\partial t} \cdot ds + \int \boldsymbol{E_C} \cdot dl \qquad \text{Eq. 2-19}$$

where $\frac{\partial \boldsymbol{B}}{\partial t}$ is the rate of change of the magnetic field with time and ds is an incremental segment of the surface (area) bounded by the conductor and is given by

$$ds = dxdy\hat{\boldsymbol{z}} \qquad \text{Eq. 2-20}$$

The minus sign in the first right-hand side term of Eq. 2-19 is a consequence of Lenz's law. From Eq. 2-19, the rate of change of the magnetic field with time $\frac{\partial \boldsymbol{B}}{\partial t}$ is given by

$$\frac{\partial \boldsymbol{B}}{\partial t} = -\omega B_o \sin \omega t \, (\hat{\boldsymbol{z}}) = -\omega B_o \sin \omega t \, \hat{\boldsymbol{z}} \qquad \text{Eq. 2-21}$$

The electric field due to charge separation $\boldsymbol{E_C}$ is found as follows

$$\boldsymbol{E_C} = \boldsymbol{v} \times \boldsymbol{B} = [v_o\hat{\boldsymbol{x}}] \times [B_o \cos \omega t \, (\hat{\boldsymbol{z}})] = v_o B_o \cos \omega t \, \hat{\boldsymbol{y}} \qquad \text{Eq. 2-22}$$

Substituting Eq. 2-21 and Eq. 2-22 into Eq. 2-19, gives

$$\begin{aligned} V_{emf} &= -\iint_{0,0}^{x,l} (-\omega B_o \sin \omega t \hat{\boldsymbol{z}}) \cdot (dxdy\hat{\boldsymbol{z}}) + \int_0^l (v_o B_o \cos \omega t \, \hat{\boldsymbol{y}}) \cdot dy\hat{\boldsymbol{y}} \\ &= \omega B_o \sin \omega t \iint_{0,0}^{x,l} (dxdy) + v_o B_o \cos \omega t \int_0^l dy \\ &= \omega x l B_o \sin \omega t + v_o l B_o \cos \omega t \end{aligned} \qquad \text{Eq. 2-23}$$

where xl is the shaded area enclosed by the sliding conductor (refer to Figure 2.25) as the sliding conductor moves at distance x, and it can be denoted as A. Hence, the total emf V_{emf} due to the movement of the conductor in the time-varying magnetic field is given by

$$V_{emf} = v_o l B_o \cos \omega t + \omega A B_o \sin \omega t \qquad \text{Eq. 2-24}$$

Eq. 2-24 shows that for an applied time-varying (AC) magnetic flux density $\boldsymbol{B}$, the total induced voltage in the conductor V_{emf} is the algebraic sum of two different emf components V_m and V_t. Only the motional emf V_m is related to the velocity of the conductor. The transformer emf is 90° out of phase with the motional emf, and it is proportional to the frequency of the supply voltage. From Eq. 2-18 and Eq. 2-24, it can be seen that the motional emf V_m is in phase with the magnetic flux density $\boldsymbol{B}$.

2.5.3 The Mathematical Model of a Conventional EM Induction Flow Meter

For a conventional EM induction flow meter as described in Figure 2.22, the electric current density $\boldsymbol{j}$ in the conducting fluid, in the presence of electric and magnetic fields, is given by Ohm's law [107]

$$\boldsymbol{j} = \sigma(\boldsymbol{E} + \boldsymbol{v} \times \boldsymbol{B}) \qquad \text{Eq. 2-25}$$

where σ is the local fluid electrical conductivity. The electric field $\boldsymbol{E}$ is the result of free charge distribution (electrostatic) and $\boldsymbol{v} \times \boldsymbol{B}$ arises from forces on the charged particles due to their motion in a magnetic field as explained in Section 2.5.2. From the theory of electrostatics [116], the integral of the electric field around a path is zero, i.e.

$$\oint \boldsymbol{E} \cdot dl = 0 \qquad \text{Eq. 2-26}$$

Applying Stokes' theorem [116] gives

$$\nabla \times \boldsymbol{E} = 0 \qquad \text{Eq. 2-27}$$

Hence, the curl of the electric field is zero and as a result, the electric field $\boldsymbol{E}$ is given by the gradient of the electric potential U. Mathematically, it is given by [116],

$$\boldsymbol{E} = -\nabla U \qquad \text{Eq. 2-28}$$

For a stationary magnetic field, the rate of change of charge density is zero, i.e. $\partial\rho/\partial t = 0$. As a result, the *continuity equation* for local current density becomes [116]

$$\nabla \cdot \boldsymbol{j} = 0 \qquad \text{Eq. 2-29}$$

Eq. 2-29 can be re-written using Eq. 2-25 and Eq. 2-28, as [117]

$$\nabla \cdot \boldsymbol{j} = \sigma(-\nabla \cdot \nabla U) + \sigma\nabla \cdot (\boldsymbol{v} \times \boldsymbol{B})$$
$$\sigma(\nabla^2 U) = \sigma\nabla \cdot (\boldsymbol{v} \times \boldsymbol{B}) \qquad \text{Eq. 2-30}$$

Assuming the conductivity σ in the flow cross-section is constant, then Eq. 2-30 can be simplified to

$$\nabla^2 U = \nabla \cdot (\boldsymbol{v} \times \boldsymbol{B}) \qquad \text{Eq. 2-31}$$

Eq. 2-31 is the general partial differential equation (Laplacian equation) of the conventional EM induction flow meter presented by Shercliff [107] for uniform fluid conductivity. Solving this equation, by the application of the appropriate boundary conditions, gives the electrical potential distribution U due to the motion of the fluid $\boldsymbol{v}$ in the uniform magnetic field $\boldsymbol{B}$.

2.5.4 Shercliff's Weight Function

In conventional EM induction flow meters, it is assumed that the velocity profile is axisymmetric with a mean velocity $\bar{v}$ as used in Eq. 2-9. Eq. 2-9 does not hold true for asymmetric velocity profiles and significant errors can result if Eq. 2-9 is used in such flows. Shercliff [107] introduced the weight function W which shows the contribution of each point in the flow cross-section to the output signal measured between the two electrodes for rectilinear asymmetric velocity profiles.

Figure 2.26 illustrates the weight function (given in Eq. 2-38) distribution plot. It can be seen that the flow near the electrodes contributes more (value of 2) towards the flow induced potential difference between the electrodes than flow at the tube wall (value of 0.5). Hence, if the flow is asymmetric, the induced emf can indicate an incorrect flow rate. The weight function distribution is dependent entirely on the magnetic field flux density, shape of electrodes and tube geometry. It is used to calculate the contribution of flow at different points in the pipe cross-section towards the flow induced potential difference between the electrodes. Note that the weight function can also be used with axisymmetric velocity profiles. However, it would be simplified to a constant value of 2π (for a circular cross-sectional area) and when applied to Eq. 2-40, Eq. 2-9 will be obtained as will be shown later in this section.

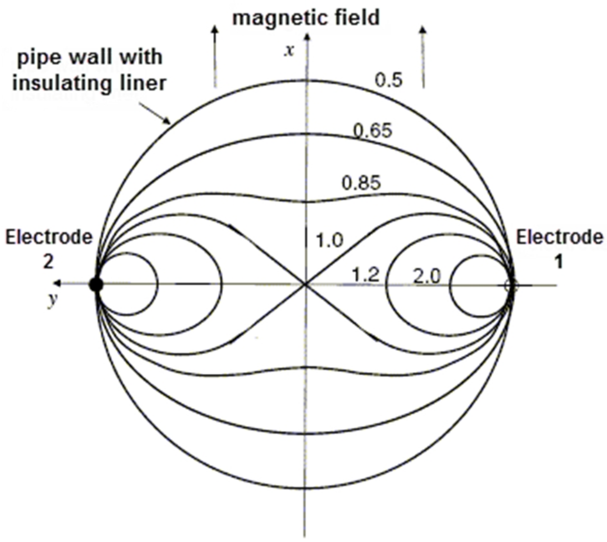

Figure 2.26: Weight function plot for uniform magnetic flux density [107]

The flow cross section from Figure 2.22 is only redrawn in Figure 2.27. Electrodes e_1 and e_2 are point-like galvanic contacts in the x-direction placed normal to the direction of the magnetic field which is in the y-direction and perpendicular to the direction of flow which is in the z-direction.

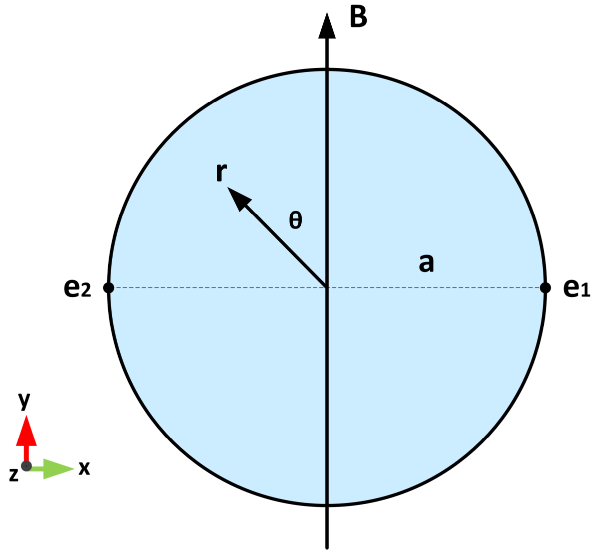

Figure 2.27: Flow cross-sectional area with two electrodes (Flow is out of the page)

For velocity $\boldsymbol{v}$ and magnetic flux density $\boldsymbol{B}$ given by

$$\boldsymbol{v} = v_x\boldsymbol{i} + v_y\boldsymbol{j} + v_z\boldsymbol{k} \quad \text{Eq. 2-32}$$

$$\boldsymbol{B} = B_x\boldsymbol{i} + B_y\boldsymbol{j} + B_z\boldsymbol{k} \quad \text{Eq. 2-33}$$

and assuming that the magnetic flux density $\boldsymbol{B}$ and the mean velocity of the fluid $\bar{v}$ are constant in the flow cross section, Eq 2-31 can be expressed as [107]

$$\nabla^2 U = \frac{\partial(B_y v_z - B_z v_y)}{\partial x} + \frac{\partial(B_z v_x - B_x v_z)}{\partial y} + \frac{\partial(B_x v_y - B_y v_x)}{\partial z} \quad \text{Eq. 2-34}$$

The magnetic flux density components B_x and B_z are assumed to be zero. Only the magnetic field component B_y is considered in the flow cross-section. The flow is also assumed to be rectilinear, i.e. $\boldsymbol{v} = [0,0,v_z]$ and perpendicular to the magnetic field component B_y.

As a result, Eq. 2-34 can be simplified to

$$\nabla^2 U = B\frac{\partial v}{\partial x} \qquad \text{Eq. 2-35}$$

where the velocity component $v_z = v$ and the magnetic flux density component $B_y = B$. Note that the magnetic flux density is assumed to be constant. Eq. 2-35 is now a two-dimensional equation where, on the boundary (pipe wall) $v = 0$ and $\partial U/\partial r = 0$ at the pipe wall ($r = a$ which is the radius of the flow cross section).

Shercliff introduced the concept of weight function W to analyse the effects of velocity profile (non-symmetrical flow) on the potential difference ΔU. In other words, the weight function determines the contribution of flow at any point in the flow cross-section to the total electric potential difference signal between the electrodes ΔU. According to Shercliff [107], for a circular pipe, the solution to Eq. 2-35 to find the electrical potential difference between electrodes e_1 and e_2 is given by

$$\Delta U = \frac{2B}{\pi a}\iint v(x,y)W(x,y)dxdy \qquad \text{Eq. 2-36}$$

where a is the radius of the pipe, $W(x,y)$ is the contribution of the velocity component $v(x,y)$ at a point (x,y) in the flow cross section to the potential difference signal ΔU between the electrodes. In polar coordinates [118], Eq. 2-36 can be written as

$$\Delta U = \frac{2B}{\pi a}\iint_{0,0}^{2\pi,a} v(r,\theta)\, W(r,\theta) r\, dr\, d\theta \qquad \text{Eq. 2-37}$$

The weight function in Cartesian $W(x,y)$ and polar $W(r,\theta)$ forms is given by

$$W(x,y) = \frac{a^2 + a^2(y^2 - x^2)}{a^4 + (y^2 + x^2)^2 + 2a^2(y^2 - x^2)} \qquad \text{(a)} \quad \text{Eq. 2-38}$$

$$W(r,\theta) = \frac{a^2 + a^2r^2\cos 2\theta}{a^4 + r^4 + 2a^2r^2\cos 2\theta} \qquad \text{(b)}$$

where r and θ are the radial and angular coordinates, respectively. The weight function $W(r,\theta)$ is the contribution of the velocity component $\boldsymbol{v}(r,\theta)$ at a point (r,θ) in the flow cross section to the potential difference signal ΔU between the electrodes. Note that the angular coordinate θ is zero in the direction of the magnetic field (refer to Figure 2.27). For an asymmetric flow, if the velocity profile $v(x,y)$ is fully known then Eq. 2-36 and Eq. 2-38(a) could be used to predict the potential difference ΔU. The graphical representation of Eq. 2-38 is Shercliff's weight function plot (Figure 2.26).

For an axisymmetric flow, i.e. $v(r,\theta) = v(r)$, the weight function $W(r,\theta) = W(r)$ which is given by

$$W(r) = \int_0^{2\pi} W(r,\theta)d\theta = 2\pi \qquad \text{Eq. 2-39}$$

Substituting Eq. 2-39 into Eq. 2-37, gives

$$\Delta U = \frac{2B}{\pi a} \cdot 2\pi \int_0^{a} v(r)r\,dr = 2a \cdot v \cdot B \qquad \text{Eq. 2-40}$$

The induced voltage due to the motion of the conductive fluid in the magnetic flux density in Eq. 2-40 is identical to Eq. 2-9 for an axisymmetric flow.

This analysis is for a conventional EM flow meter with two electrodes. However, it has been extended successfully by several authors by adding additional electrodes to improve the accuracy of mean velocity and volumetric flow rate measurements and to reduce sensitivity to asymmetric velocity profiles [119, 120]. In the design of an EM flow meter by Leeungculsatien and Lucas, the number of electrodes was increased to 16 to reconstruct the axial velocity profile in multiphase flow [121]. This was performed by finding the local axial velocity distribution using a tomographic approach based on an extension of Shercliff's weight function method. This is discussed in Section 2.5.6.

2.5.5 Virtual Current Theory

From Shercliff's work, intensive research has been carried out to develop an EM induction flow meter that is insensitive to velocity profiles for clinical and industrial use. Bevir [122] extended the work of Shercliff to a 3D model, and introduced the weight vector $\boldsymbol{W}$ using the concept of virtual current density $\boldsymbol{j_v}$. Bevir showed that for a conductive fluid flow (with a velocity distribution) moving in a magnetic field, the induced emf between the two electrodes e_1 and e_2 (refer to Figure 2.27) is given by

$$\Delta U = \int_{\tau} \boldsymbol{v} \cdot \boldsymbol{W} \, d\tau \qquad \text{Eq. 2-41}$$

where $\boldsymbol{v}$ is the velocity vector, i.e. $\boldsymbol{v} = [v_x, v_y, v_z]$, $\boldsymbol{W}$ is the weight vector and τ is the volume of the moving fluid. The weight vector $\boldsymbol{W}$ is similar to the weight function, i.e. it measures the contribution of each point in the flow cross-section towards the measured induced potential difference ΔU and is given by

$$\boldsymbol{W} = \boldsymbol{B} \times \boldsymbol{j_v} \qquad \text{Eq. 2-42}$$

where $\boldsymbol{B}$ is the magnetic flux density and $\boldsymbol{j_v}$ is the virtual current density. The virtual current density is the result of an imaginary unit current entering one electrode and leaving another in the absence of the magnetic field and flow, i.e.

$$\nabla \cdot \boldsymbol{j_v} = 0 \qquad \text{Eq. 2-43}$$

From Ohm's law and assuming uniform conductivity σ,

$$\boldsymbol{j_v} = \nabla\phi \qquad \text{Eq. 2-44}$$

where $\nabla\phi$ is the virtual potential gradient. Combining Eq. 2-43 and Eq. 2-44 gives the equation for the virtual potential which is Laplace's equation,

$$\nabla^2\phi = 0 \qquad \text{Eq. 2-45}$$

Once Eq. 2-45 is solved by applying the appropriate boundary conditions and the virtual potential $\phi = \phi(r, \theta)$ is obtained, the virtual current density $\boldsymbol{j_v}$ can be found using Eq. 2-44 as follows:

$$\boldsymbol{j_v} = \begin{bmatrix} j_r \\ j_\theta \end{bmatrix} = \begin{bmatrix} \dfrac{\partial\phi}{\partial r} \\ \dfrac{1}{r}\dfrac{\partial\phi}{\partial\theta} \end{bmatrix} \qquad \text{Eq. 2-46}$$

The virtual current does not exist in practice, and it is affected only by the following factors:

- The conductivity, isotropy and homogeneity of the flowing medium if not uniform
- The shape, size and position of the electrodes within the flow cross section
- The geometry of the flow cross-section

The weight vector can also be considered as the medium interaction model, which is the third element required in any tomographic technique in addition to excitation source and external measurements [123]. Bevir indicated that if the magnetic field is uniform and point-like electrodes are in use, then the flow near the electrodes has greater weight (contributes more towards the output signal) than the flow in the other parts of the flow cross-section; this observation is similar to Shercliff's conclusion. Therefore, the flow induced emf will be sensitive to the velocity profile. This was also confirmed by Wyatt [124] when he imposed a water flow in various parts of the flow cross-section of a flow meter, and some results showed up to 100% error in the measured induced emf.

When a rectilinear flow, i.e. $\boldsymbol{v} = [0, 0, v_z]$, and uniform and transverse magnetic flux density in the negative y-direction, i.e. $\boldsymbol{B} = [0, -B_o, 0]$ are assumed, the only non-zero component of the weight vector is W_z [125] ($j_z = 0$) and it is given by

$$W_z = B_o j_r \cos\theta - B_o j_\theta \sin\theta \qquad \text{Eq. 2-47}$$

Hence, Eq. 2-41 can be simplified from a 3D to a 2D problem and can be expressed as:

$$\Delta U = \iint_{0,0}^{2\pi,a} W(r,\theta) v(r,\theta)\, r\, dr\, d\theta \qquad \text{Eq. 2-48}$$

where $W(r,\theta) = W_z$ and $v(r,\theta) = v_z$. When the flow has an axisymmetric distribution, i.e. $(r,\theta) = v(r)$, Eq. 2-48 can be written as

$$\Delta U = 2\pi \int_0^a W'(r) v(r)\, r\, dr \qquad \text{Eq. 2-49}$$

where $W'(r)$ is known as the axisymmetric weight function [125] and it is given by

$$W'(r) = \frac{1}{2\pi} \int_0^{2\pi} W(r,\theta)\, d\theta \qquad \text{Eq. 2-50}$$

Eq. 2-48 is applicable to any geometry of flow cross-section and electrodes and Eq. 2-49 is the condition of the weight vector $\boldsymbol{W}$ for axisymmetric rectilinear flow so that the flow signal is directly proportional to flow rate [125]. Bevir stated that the solution to Eq. 2-50 is constant for any axisymmetric velocity profile. For point-like electrodes and circular cross-section as depicted in Figure 2.27, the axisymmetric weight function $W'(r)$ is given by

$$W'(r) = \frac{2B}{\pi a} \qquad \text{Eq. 2-51}$$

Combining Eq. 2-49 and Eq. 2-51 yields the exact equation, Eq. 2-40, suggested by Shercliff. This shows that weight function and virtual current theory lead to the same conclusion. The weight vector method is a powerful technique which enables the prediction of flow contribution to the output signal even for point-like electrodes as long as the flow is rectilinear [126]. It has also been successfully used with asymmetric velocity profiles when large electrodes are used (assuming rectilinear flow) [126]. Such prediction analysis is known as ‘dry calibration’, and it is very useful in relating the flow induced potential to the flow rate even if the flow is not axisymmetric.

The uniformity of the weight vector, i.e. insensitive to velocity profile, can be improved in a number of ways [127]:

- Modification of the magnetic field distribution and optimisation of the coil design [128]
- Use of relatively large electrodes as Bevir suggested [126]
- Use of a multi-electrode system instead of a single pair [129]

2.5.6 Multi-electrode Electromagnetic Flow Meters

One of the methods considered as a design for an EM flow meter that is insensitive to velocity profile distribution was a model using multiple electrode pairs. In industrial conventional EM flow meters (two electrodes), it is strongly recommended that a straight pipe of a length 5-10 times its diameter be installed upstream from the flow meter to ensure that the flow has an axisymmetric velocity profile. In other words, the straight pipe keeps the flow meter away from pipe bends or valves which can distort the velocity profile. Otherwise, significant error can occur in the measurement readings [129]. Engl [130] showed mathematically that for a flow $\boldsymbol{v_z}$ (rectilinear) along the z-axis in the pipe cross-section and a uniform magnetic field in the negative y-direction, the mean velocity of the flow $\overline{v_z}$ in the cross section is found by integrating the flow induced potential distribution at the boundary of the cross-section (circular surface) of the non-conducting pipe wall as follows

$$\bar{v_z} = \frac{1}{\pi}\int_0^{2\pi} \frac{1}{B} U(\varphi) \cos\varphi \, d\varphi \qquad \text{Eq. 2-52}$$

where $U(\varphi)$ is the potential at the boundary of the flow cross-section at angle φ. Horner utilised this equation and developed a mathematical model using Fourier series to estimate the mean velocity using an N-electrode sensor array [119]. He also used two magnetic field projections to improve the measured data. His results showed that for 2-electrode and 4-electrode systems, the relative error in the mean velocity of the flow in the cross-section was large. However, when 8-electrode and 16-electrode systems were used, the error was significantly reduced and the latter system had a relative error in the velocity for distorted velocity profiles of less than 10%.

From Horner's multi-electrode system design, Xu [120] developed a chord measurement method and used a rotating magnetic field. The induced potentials from different magnetic field projections were fused (data fusion) to estimate the mean velocity in the flow cross-section for asymmetric velocity profiles. Horner and Xu used the multi-electrode system only to improve the accuracy of the mean velocity measurement in a single phase measurement. The major drawback of their devices is that they cannot determine the local axial velocity profile which is essential in identifying the flow rate of a particular phase in multiphase measurements where the local volume of fraction distribution of that phase is also known [131].

This drawback was one of the main thrusts of recent research work in the Systems Engineering group[1] of the University of Huddersfield. Significant progress has been

[1] The author is a member of this research group and was led by Prof. Gary Lucas at the time of this research

made by the research group in the development of techniques (combining EM induction flow metering and tomographic techniques) to determine the local axial velocity profile of the conducting phase in both single phase and multiphase pipe flow. Flow meters have been constructed, each comprising an array of 16 electrodes equally spaced around the internal pipe diameter. A magnetic field was applied across the electrode array normal to the axial flow direction and N independent flow induced potential difference measurements were made between pairs of electrodes. By the use of a matrix inversion technique [131], it was found possible to determine the local axial flow velocity, to an accuracy of better than $\pm 5\%$, in each of N sub-regions (pixels) into which the region bounded by the electrodes was divided. In one particular flow meter design [132], the flow cross section was divided into 7 sub-regions (i is the sub-region index) as shown in Figure 2.28. Seven potential difference measurements were made between electrode pairs e_6-e_4, e_7-e_3, e_8-e_2, e_9-e_1, e_{10}-e_{16}, e_{11}-e_{15} and e_{12}-e_{14}. For a single phase flow of conducting liquid, the local volumetric flow rate in the i^{th} sub-region was given by $Q_i = v_i A_i$ where v_i and A_i respectively represent the relevant sub-region velocity and cross-sectional area. For multiphase flow, the measured sub-region velocity was the mean velocity of the conducting continuous phase in that sub-region. For such multiphase flows, accurate sub-region velocity measurements were made, even when the local mixture conductivity varied by as much as 5 to 1 in the flow cross section.

The knowledge, experience and results obtained from the industrial research work, described above, were a major inspiration to the work presented in this thesis. It encouraged the author to investigate the possibility of using a multi-electrode EM method for the application of non-invasive blood flow measurement. Many of the techniques developed in the industrial research work can also potentially be applied to the blood flow measurement method developed in this thesis, and this is discussed in detail in the Further Work (Section 8.3.1)

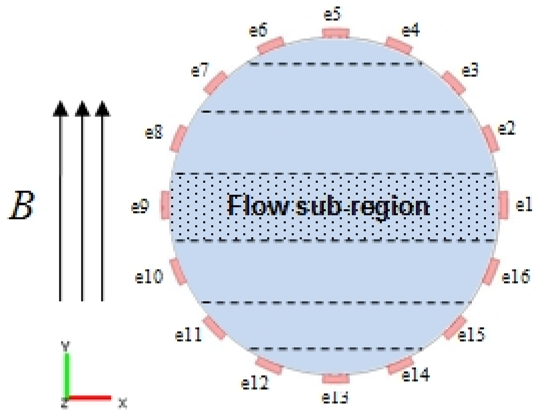

Figure 2.28: Flow cross-section divided into regions and bounded by 16 electrodes [132]

2.5.7 Invasive Electromagnetic Blood Flow Meters

Invasive EM blood flow meters must be inserted into the human body, and this can be achieved by using one of three methods [127]. The first method – and least desirable – is by cutting the blood vessel and inserting a cannula flow meter. This requires surgical intervention and may lead to complications such as blood contamination. The second method is by using Kolin's [1] approach, in which the flow probe is attached around the blood vessel. This is more favourable than the first method; however, it is usually performed in surgery. The last method involves the use of a catheter-type flow meter, which is inserted first into the skin by incision into small blood vessels, and then into the major ones. The catheter-type flow meter is also named after the inventor Mills – Mills' catheter-tip velometer – who was the first to utilise a catheter with EM flow meters [133]. Kolin's EM induction and Doppler ultrasound probes are the most common techniques used for blood flow rate measurement invasively [134].

Cannula Flow Meters

A cannula flow meter consists of a non-conducting insulated tube, electromagnet and two point-like electrodes attached at the opposite sides of the flow cross section of the non-conducting tube. Figure 2.29 shows a medical cannula flow meter device which can be inserted between two ends of a blood vessel that has been cut out as illustrated in Figure 2.30. Cannula flow meters come in different sizes depending on the diameter of the blood vessel under examination. As stated earlier in Section 2.5.5, for an axisymmetric velocity profile and uniform magnetic field, the blood flow rate is proportional to the flow induced potential difference measured between the electrodes. Designs of cannula flow meter have achieved a measurement accuracy of $\pm 1\%$ of the true flow rate when a uniform magnetic field was applied and the velocity profile was axisymmetric.

However, the velocity profile in the circulatory system of mammals is known to be non-axisymmetric [135]. The point-like electrodes are sensitive to velocity profile as demonstrated by Shercliff and discussed in Section 2.5.4. Moreover, short-end flow meters, such as cannula flow meters, cannot ensure that the velocity profile is axisymmetric as observed by Bevir [126]. Larger electrodes were successfully used in an attempt to reduce the flow meter sensitivity to velocity profile. This would, however increase the impedance of electrode/electrolyte interface and therefore, it would require a signal conditioning system with large input impedance to avoid any attenuation in the measured flow induced potential difference signal.

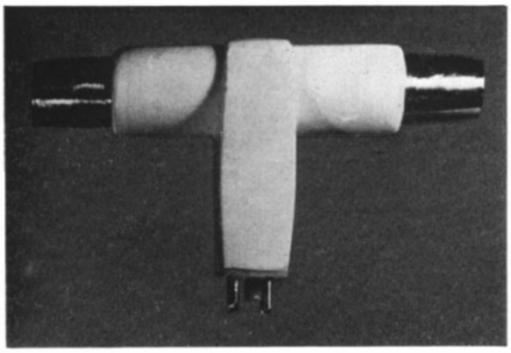

Figure 2.29: Cannula blood flow meter by Nycotron [112]

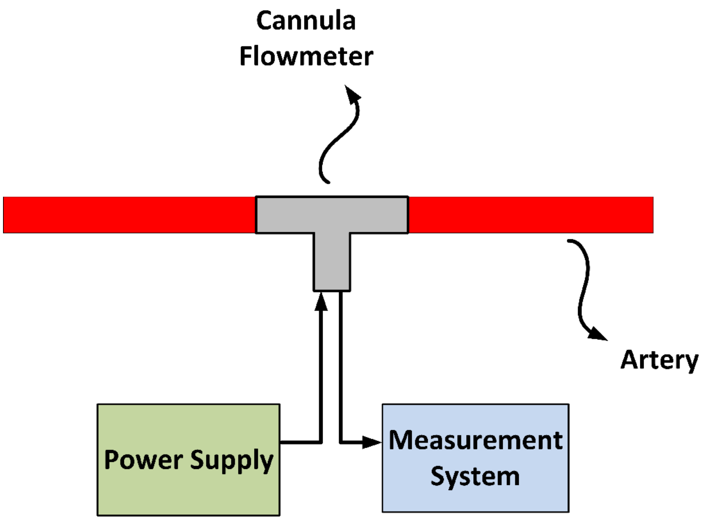

Figure 2.30: Cannula flow meter inserted between two ends of an artery that has been cut out

It was noted by Wyatt [127] that haematocrit level – the percentage of red blood cells in a blood sample – can affect the sensitivity of invasive EM blood flow meters to velocity profiles. Wyatt found that for haematocrit level change from 0-66%, the blood flow rate value of cannula flow meters which were tested altered by 4% for a laminar flow. However, this percentage change was much increased when the flow was turbulent. He concluded that the haematocrit level can affect invasive flow meters in a number of ways:

- It can change the source impedance of the flow meter. It must be ensured that the input impedance of the measurement system is high enough in comparison with the source impedance to avoid any signal loss. This can be achieved by a careful design of the interfacing measurement circuit.

- It can make the blood anisotropic. However, it was found that the blood isotropy has minimal effect on the flow meter sensitivity to velocity profile.
- It can change the blood viscosity and that changes the velocity profile. The sensitivity to velocity profile due to viscosity can be overcome by reducing the sensitivity of the flow meter to asymmetric velocity profiles by using one of the methods described in Section 2.5.5.
- It can affect the conductivity relationship between the vessel wall and the blood. The effect from this conductivity relationship is more related to perivascular flow metering probes which are discussed in the next section.

Perivascular Flow Meters

Perivascular flow meters are based on Kolin's blood flow meter design [110]. The flow meter probe comprises an electromagnet and two electrodes, attached at the outer surface of the probe, in addition to its signal conditioning and power systems. Perivascular probes come in different shapes and sizes depending on the blood vessels which with they are to be used. There are several types of probe such as cuff-type, 'clothespin' type and clip-type as illustrated in Figure 2.31. The placement of the probe around the blood vessel is critical as it should be placed so that the blood flow is perpendicular to the magnetic field. Some cuff-type probes have a slot closure which improves the uniformity of the magnetic field distribution across the blood vessel. The non-uniformity of the magnetic field can cause the flow meter to be sensitive even to axisymmetric velocity profiles. In some other probe designs, the magnetic field near the electrodes is modified (shaped) using pieces of permalloy in an attempt to make the magnetic field as uniform as possible [127].

Perivascular probes are also sensitive to asymmetric velocity profiles. Asymmetric blood flow can occur near the heart valves and large arterial branches. It can also be caused by diseased blood vessels, i.e. partially blocked by plaque. They are also affected by several factors even if the magnetic field is uniform and the flow profile is axisymmetric and these factors include [125, 136, 137]:

- The ratio between the conductivity of the blood σ_1 and the vessel σ_2
- The ratio between the inner and outer radii, r_1 and r_2 of the vessel

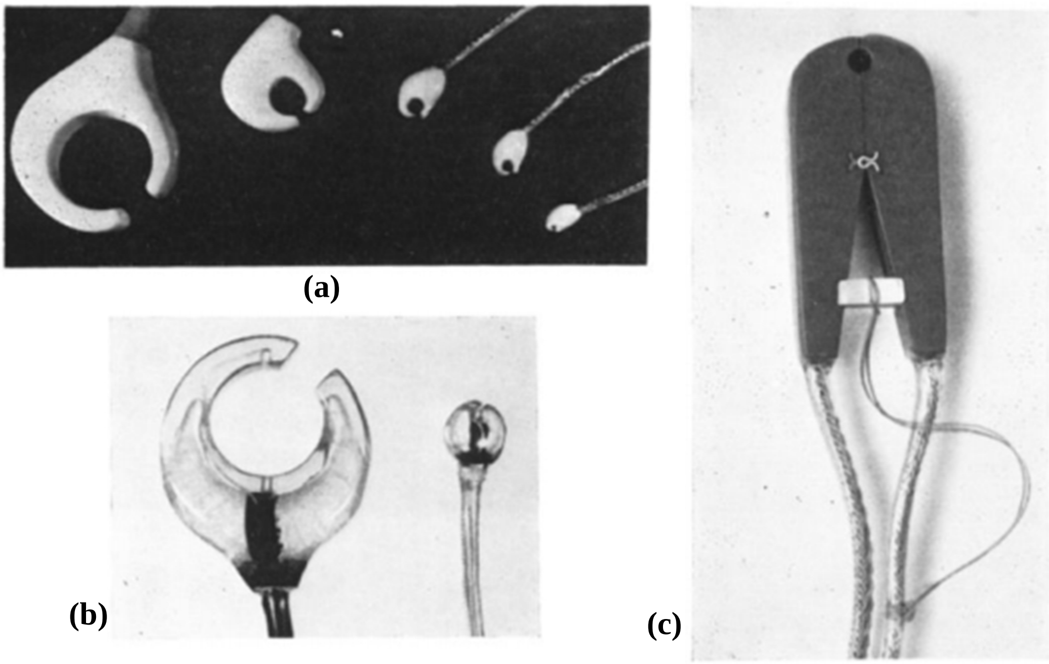

(a) (b) (c)

Figure 2.31: (a) & (b) cuff-type flow meters. (c) 'clothespin' probe

If the conductivity of the blood vessel and blood is similar, the velocity profile is axisymmetric (which is unlikely) and the weight function is uniform, i.e. $W'(r)$ = constant, then the flow signal is independent of the velocity profile, i.e. insensitive to the velocity profile. However, if the conductivity of the vessel is higher or lower than the blood, then the flow meter will give either a lower or higher flow reading than the actual measurement, correspondingly. However, it was found that the majority of errors arise from the inner and outer diameter of the blood vessel. It was experimentally found that ratios between inner and outer diameters, of $d_1/d_2 = 0.8$ and $d_1/d_2 = 0.9$ can cause an error of 9% and 5%, respectively [136]. The effects of the vessel wall can be reduced by ensuring that the vessel is clean (adventitia removed), uniform and that the probe is well-fitted around the vessel.

Nevertheless, perivascular EM flow probes are considered the 'gold standard' to measure the blood flow rate and cardiac output [9]. Wyatt stated that in *in vivo*[2] acute experiments, he found that the difference between the induced flow signal measured by a cannula flow meter and properly installed cuff-type flow meter is no more than 5% [127]. They have been successfully applied to arteries such as the aorta, carotid, femoral, coronary, renal, splenic and hepatic [9]. A flow induced potential of 144 μV was measured in a human aorta which corresponded to a mean velocity of 0.16 m/s over the cardiac cycle. The probe used for this experiment had a coil that generated a magnetic flux density of 30 mT [110]. Both cannula flow meters and perivascular probes can be 'dry' calibrated using a weight vector approach, and also *in vivo* by injecting blood from an external source.

Mills' Catheter-tip Velometer

The last type of invasive method for blood flow measurement is Mills' catheter-tip velometer [133]. Catheters have been used long before the implementation of EM flow metering methods for blood flow measurement. Examples for the use of catheters include [138]:

- Administration of drugs, gases and fluids into the human body
- Chest fluid and urine drainage
- Measurement of blood pressure in a particular vein or artery

[2] In vivo: inside the body of a living organism.

Catheters are inserted through the skin into small veins or arteries, and then into the main designated ones. Mills' catheter-tipped velometer is illustrated in Figure 2.32. Mills' probe is made of nylon and has a diameter of 3 mm. The length of the coil is 4 times the diameter and the electrodes are placed at the surface of the catheter, approximately at the mid-point of the length of the coil. The probe also has a tube used for pressure measurement. The distance between the tip and the electrodes improves the flow profile [127]. The blood flows alongside the surface of the probe rather than through it.

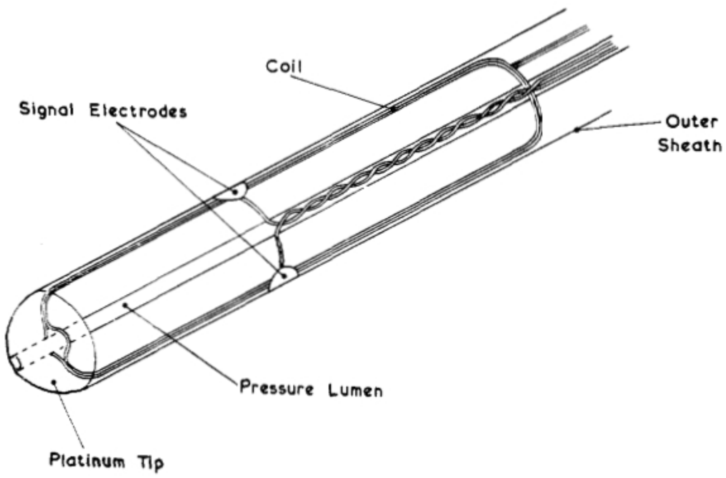

Figure 2.32: Mill's Catheter-tip Velometer [112]

The flow induced potential difference resulting from the flow passing through the magnetic field near the electrodes is directly proportional to the mean velocity of the blood, assuming an axisymmetric velocity profile. For this assumption to be acceptable, usually Mills' probes are used in large arteries or veins. The main difference between Mills' probe and the other flow meters is that it provides information about the blood mean velocity even if the vessel diameter is unknown. However if the diameter of the vessel is known, obtained by means of radiography, or if several velocity measurements are taken across the vessel, then the flow rate can be determined.

Unlike, Kolin's-type probes, the Mills' probe is insensitive to the vessel wall; nevertheless, it can be affected by the haematocrit level in the blood as this changes the blood conductivity, viscosity or source impedance as discussed earlier. Catheter-type probes have been used in the study of cardiovascular haemodynamics and for other clinical purposes [127].

Perivascular and catheter-type probes must be carefully designed with minimum heat dissipation in order to avoid any thermal risks. For this reason, there are other designs of probe which do not contain an invasive electromagnet which is the only source of power dissipation. In such designs, the magnetic field is applied externally by an electromagnet placed outside the body. However, other problems associated with the direction of the magnetic field with respect to blood flow and the sensing electrodes are introduced by these designs. These problems may lead to significant error in the measured flow induced potential difference signal [127].

2.5.8 Non-invasive Electromagnetic Blood Flow Meters

Installation of a cannula flow meter between two ends of a cut blood vessel or perivascular EM flow meter around the blood vessel is a complex surgical procedure. Hence, such flow meters can only be used by surgeons. Similarly, catheter-type probes can only be used by qualified physicians. Moreover, these flow meters can only be applied to one artery at a time, and therefore, the total blood flow in a limb cannot be found. The total arterial blood flow in the limb is an important diagnostic measurement for detecting PAD [139].

Non-invasive EM flow metering is a method whereby the total blood flow in a region, or to a peripheral (arm or leg), is monitored without any surgical intervention. Fabre proposed the idea of non-invasive blood flow measurement using the principle of EM induction. However, the first non-invasive blood flow measurement using EM induction was achieved by Togawa et al. [140]. They demonstrated the principle by placing an entire rabbit in 1 T of magnetic flux density and observing induced potentials due to the blood flow. A few years later, they performed an experiment *in vitro*[3] in which a rectangular block made of starch gel (carbohydrate) was placed in the air gap of a 35 mm of an electromagnet. The magnetic flux density in the air gap was 0.1 T. The centre of the block had a tube through which liquid was pumped. Electrodes were placed at the opposite sides of the block to sense flow induced potentials.

Following this experiment, they carried out *in vivo* tests on living dogs to measure the blood flow in the femoral artery (in the thighs). Needle electrodes were inserted in the hypodermis (lowermost layer of the skin) and at the opposite sides of the femoral artery. It was observed that the potential difference detected by the electrodes was due to the arterial flow. Furthermore, the blood flow in the veins had a negligible effect on the measured signal. The measured signal from the non-invasive method was compared to the signal measured from an invasive EM cuff-type flow meter applied to the same artery. A linear relationship was observed from both signals. However, this device was not a true non-invasive method as needles were inserted in the skin.

Another significant step towards developing a non-invasive blood flow monitor was made by Boccalon et al. [141]. A theoretical model of a limb (calf) was developed using Maxwell's equations to relate flow induced potentials to blood flow. This model was used to calibrate the blood flow meter (dry calibration). It allowed the contribution towards the total flow signal of each artery (anterior tibial, posterior tibial, peroneal) within the calf to be found. Boccalon et al. also stated that his model did not account for the bones (fibula and tibia) within the calf. When it was tested and compared to a

[3] In vitro means performed outside the living body (artificial environment).

physical model without the bones' influence, the difference between both models was less than 3%. When the physical model was modified to include the effects of the bones, the flow voltage measured across the model increased by a factor of 35.

Reasons for this voltage increase are not clear, especially given that it has been noted that the conductivity of bones is negligible when compared to muscles and fat. It is possible that this change in the flow induced signal was due to an asymmetric velocity profile and the effect of point-like electrodes as described by Shercliff and Bevir (Sections 2.5.4 and 2.5.5). The effect of flow in different parts of the cross section was not demonstrated. Nevertheless, a calibration factor was obtained for the measurement site (calf). This was used to correct the results of flow induced potential differences obtained from *in vivo* tests.

Boccalon performed extensive *in vitro* and *in vivo* tests to assess the effects of the following factors on the measured flow induced signal:

- Blood chemical composition
- Haematocrit level change
- Venous blood flow

The blood electrolyte composition (Na^+ and K^+) was modified *in vitro* so that its effect on the flow induced potential difference signal could be observed. The effects of different concentrations of Na^+ and K^+ were negligible. Variation in the haematocrit level altered the amplitude of the flow potential signal. When the haematocrit level changed from 45% to 29%, the flow induced potential signal increased. Several factors can be changed simultaneously due to the haematocrit level in the blood as explained in Section 2.5.7. Conductivity was the only factor claimed as a reason for the flow potential difference percentage change. However, two-electrode measurements can be sensitive to a distorted velocity profile which can be caused by the haematocrit level change [127]. Furthermore, if the input impedance of the electronic measurement system is low, the flow induced potential signal would be affected as a change in the haematocrit level alters the source impedance. When this flow induced potential difference was compared to the flow induced potential difference obtained from the invasive method (Kolin's method), a correction factor of up to 10% was required.

Lastly, the impact of venous blood flow in the measurement site (calf) was investigated. The effect can be removed from the flow signal by averaging or by using a pressure cuff to convert the pulsatile flow (due to aspiration of the right ventricle of the heart) to continuous flow. Boccalon used his instrument clinically on 1200 patients to identify peripheral arterial disease of the lower limbs. The instrument consisted of a horseshoe permanent magnet, amplifier, computer processor and chart recorder. It was used to provide information about the pulsatile arterial blood flow rate. This information was analysed alongside data from Doppler velocity measurements, arterial blood pressure and treadmill tests to diagnose the patient.

Kanai et al. developed a non-invasive blood flow meter to be applied to arteries close to the surface of the skin (transcutaneous) [142]. The electrodes are applied on one side of an artery as shown in Figure 2.33. This device was tested on cubital arteries at the elbow joint. The theoretical model, given in Eq. 2-53, was developed for the device based on the assumptions that the magnetic field is uniform over the cross section of the blood vessel and the blood flow is an axisymmetric laminar flow.

$$U_{AB} = \frac{4B_x}{\pi} Q_s \left(\frac{\sigma_1}{(\sigma_1 + \sigma_2)(d^2 + s^2)} \right) \qquad \text{Eq. 2-53}$$

where U_{AB} is the potential difference between electrodes A and B, σ_1 and σ_2 are the conductivities of the blood and tissues, respectively, s is half the distance between the electrodes and d is the distance between the centre of the vessel and the skin (depth of the vessel). From Eq. 2-53, it can be noted that the flow induced potential difference is affected by the depth of the vessel d. The depth of the vessel varies from one patient to another depending on the body weight and size. The flow meter was used *in vivo* to measure the blood flow rate of 10 mL/s in cubital arteries at a depth of 3 cm.

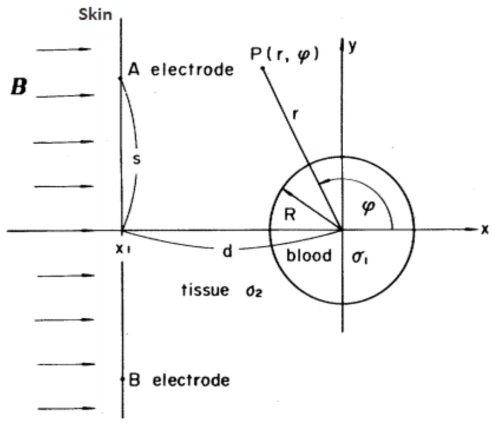

Figure 2.33: Analytical model by Kanai et al. for a non-invasive blood flow measurement [142]

There are several drawbacks which arise out of the work of Boccalon et al. and Kanai et al. Boccalon et al. stated that an analytical model is required for each region of the human body to obtain its calibration factor. This seems to be impractical as the size of an arm or leg differs from one person to another. A poor calibration factor leads to significant errors when the flow induced potential differences are translated to flow rate. Hence, a mathematical model must be developed independently of the measurement site. Moreover, a two-electrode measurement is sensitive to velocity profile which can lead to significant error in the flow rate measurement as discussed before. The use of a multi-electrode system will reduce the sensitivity of the flow meter to velocity profile and the accuracy of flow rate reading will be improved noticeably as Horner demonstrated in his work (Section 2.5.6).

Moreover, based on the recent work carried out by the University of Huddersfield Systems Engineering research group [143], with a 16-electrode measurement system, it is possible to reconstruct the velocity profile in the flow cross-section. This would enable the location of the arteries within the flow cross section to be determined. In addition, the flow rate in each artery could also be found. Modelling of a multi-electrode EM flow metering method for a flow cross section with multiple flow channels using the virtual current theory does not exist in literature. The flow meter developed by Kanai can only measure the blood flow in the cubital arteries. If the d parameter is unknown, the measurement of the flow signal will be highly affected by errors. The development of an EM blood flow monitor that can be applied to the upper or lower limbs to aid in the diagnosis of PADs is one of the main aims of this research. Such a device should require minimal calibration and should be relatively insensitive to, or independent of, the velocity profile resulting from the distribution of blood velocity in the vessels within the measurement region, i.e. the cross section of a limb.

2.5.9 Electronics Requirements for Signal Conditioning and Processing

All industrial and medical EM flow meters operate on the principle of EM induction. The fundamental design structure of such devices is similar. Any EM flow meter consists of an electromagnet, transducers (electrodes), input and output systems. The input system is the power supply unit of the electromagnet, which can be either DC or AC. The output system conditions the measured total voltage signal from the electrodes, processes the signal and then stores or displays the results. It mainly consists of signal conditioning and signal processing sub-systems. The signal conditioning sub-system performs the following functions: (1) impedance transformation, (2) amplification and (3) filtering of unwanted signals. The signal processing sub-system discriminates the flow signal from unwanted signals, if they have the same frequency, by methods that will be described later in this section.

Early designs of EM flow meters used permanent magnets or DC-powered electromagnets for the generation of a uniform magnetic field. This meant that the flow signal was in the form of a DC potential difference. However, polarisation normally occurs at the surface of the electrodes due to electrochemical effects between the electrodes and the conductive fluid, blood vessel wall or skin surface [9]. Polarisation also creates a DC potential which is hard to differentiate from the DC flow potential difference. Moreover, the DC flow induced signal is typically very small and requires significant amplification by a direct-coupled amplifier. The amplitude of the DC offset due to polarisation is usually much larger than the flow induced voltage signal and therefore, it causes the amplifier to saturate (exceeds its dynamic operating range).

For these reasons, DC-powered electromagnets (or permanent magnets) are not desirable. Alternating current (AC) methods overcome this problem as the detected flow induced signal becomes an AC potential difference and any DC offsets can be minimised considerably by using an AC-coupled amplifier [127]. The AC-coupled amplifier combines a high-pass filter and an amplifier. The alternating current can be sinusoidal, square-wave or trapezoidal. Each one of these excitation source methods has certain advantages over the others as will be described below.

Normally, the physiological potential difference signal ΔU measured by a two-electrode or multi-electrode AC flow metering system is mathematically given by

$$\Delta U = k_1 B v + k_2 \frac{dB}{dt} + \sum \varepsilon_{(t)} + \sum e_{(t)} + e_n \qquad \text{Eq. 2-54}$$

The first term of the right-hand side of Eq. 2-54 is the flow induced potential. k_1 is the calibration factor of the device which is related to the geometry of the flow cross section, and the size and shape of electrodes. B and v are the mean values of magnetic flux density and the conductive liquid velocity, respectively.

From Faraday's law of induction, a transformer emf is induced in any conducting loop in the presence of a time-varying magnetic field as was shown in Section 2.5.2. The conductive liquid (blood), the electrodes and the connecting cables form a conductive loop. Therefore, this transformer emf superimposes on the flow induced voltage signal, and it is given by the term $k_2\, dB/dt$. For a sinusoidal AC magnetic field, the transformer emf has a similar frequency ω and waveform to the flow induced signal. It is also proportional to the excitation frequency of the electromagnet, unlike the flow induced signal. The transformer emf can be minimised by careful design of the electrodes and the cabling. The cables connecting the electrodes should always be positioned in parallel with the plane of the magnetic field. However, in practical devices, this is hard to achieve and therefore, there will always be some magnetic flux cutting the cabling loops. Additionally, twisted-pair cables reduce the transformer emf as this minimises the area of the cable loops that the magnetic flux can get into and there is also a cancelling effect as induced potentials are in opposite directions.

Yet, the transformer emf is not usually fully eliminated using the methods suggested above and other methods must be utilised to ensure the transformer emf does not interfere with the flow induced signal measurement. One method for removing the transformer emf from the measured signal is by sensing it at the electrodes using a "pickup" coil [124]. Then, the signal from the "pickup" coil is used to subtract the transformer emf from the total signal at the input of the amplifier.

Alternatively (or additionally), a PSD method can be utilised to distinguish the induced emf from the transformer emf for a sinusoidal AC excitation as they are out of phase by 90° from each other as seen in Eq. 2-24. In other words, if the excitation current is a cosine wave, then the waveform of the magnetic field will also be a cosine wave. The flow induced signal is in phase with the magnetic field, and consequently it will have the same phase as the current [127, 144, 145]. However, the transformer emf will be a sine wave. Note that sine and cosine waves are sinusoids of different phases. The PSD allows the flow induced signal to be separated from the transformer emf. This is a method whereby the measured signal is multiplied by a reference signal. The reference signal is in phase with the flow induced signal. Then, the resultant output is averaged over time. As a result, the output is a DC value which corresponds to the root mean square (RMS) value of the AC flow induced signal. This method has been implemented in EM flow metering using analogue and digital electronics [146-149].

In this research, a PSD method was utilised to discriminate the flow induced signal from the transformer emf. There are two schemes that are available in the literature to perform PSD. The first scheme is as briefly described above and the other scheme relates to the use of Discrete Fourier Transform (DFT) [150]. This method has not been implemented before in the application of EM blood flow metering. It requires a high-speed data acquisition device to sample the total measured signal and the reference signal. The reference signal can be the coil current as it is in phase with the magnetic field. The DFT is applied to both signals to obtain their magnitude and phase. Subsequently, the in-phase component, i.e. the flow induced voltage signal, can be determined. This method is described in greater detail in Chapter 6.

There is another method used to discriminate between the sinusoidal flow signal and the transformer emf, which involves sampling using gating electronics [151]. This method also relies on the fact that the transformer emf is 90° out of phase with the flow signal. When the transformer emf is at zero-crossing point, the flow induced signal is at maximum (negative or positive). If a portion of the total measured signal is sampled at the zero-crossing point of the transformer emf, this portion of the signal is only related to the liquid flow. This method can be implemented using an amplifier that is controlled by a timing circuit. In the literature such an amplifier is called a 'gated' amplifier and is controlled by a control circuit which uses the excitation signal of the electromagnet as a reference signal to generate the timing sequence for sampling [151, 152]. Note that this method can also be achieved by using microcontrollers or DAQ devices and a numerical software such as MATLAB. Both methods, i.e. the PSD and sampling rely on phase integrity from the input of the measuring system to its output to ensure accurate extraction of the flow induced voltage signals.

The transformer emf is sinusoidal if the electromagnet excitation signal is a sine wave. However, if the power source of the electromagnet is a square waveform, the transformer emf appears as a voltage spike (transient) with a time constant $\tau = L/R$ (where L is the inductance of the electromagnet and R is the DC resistance of the electromagnet coil) as illustrated in Figure 2.34. Such a flow meter is referred to as a square-wave EM flow meter. This voltage spike appears when the polarity of the excitation signal changes ($L\frac{di}{dt}$). Thus, the flow induced voltage signal is measured after the voltage spike transient has died away. This can be achieved by a time-delay insertion during the sampling of the flow induced voltage signal. This requires the 'on' period of the magnetic field to be long enough to allow the transient to pass and then, the flow induced signal is recorded. However, this means that the excitation frequency has to be low. The advantages of the square-wave excitation are (1) the process of discrimination of the flow signal from the transformer emf is simple in comparison with the sinusoidal excitation and (2) the inductive impedance is also much lower (function of frequency) which means that more current can be supplied to the electromagnet for the same voltage source, and this results in the generation of a stronger magnetic field. However, low frequency signals are more sensitive to RF and mains interferences and usually have a poor signal to noise (SNR) ratio. Furthermore, low frequency excitation means that the electronics in the signal conditioning sub-system have a slower transient response and therefore, take significant amount of time to reach a steady-state value.

In terms of power efficiency, the square-wave excitation is more efficient than the sine-wave excitation. In the square-wave flow meter, the electromagnet is seen as a resistive (DC) load and therefore, the total power consumed is due to copper losses (I^2R), i.e. active power. However, in the sine-wave flow meters, the electromagnet is seen as inductive load, and therefore the power consumed is the vector sum of the active power (copper loss) and reactive power due to the reactance of the electromagnet, which is mainly inductance in the case of an electromagnet. Nevertheless, this reactive power can be reduced significantly using a technique known as Power Factor Correction (PFC).

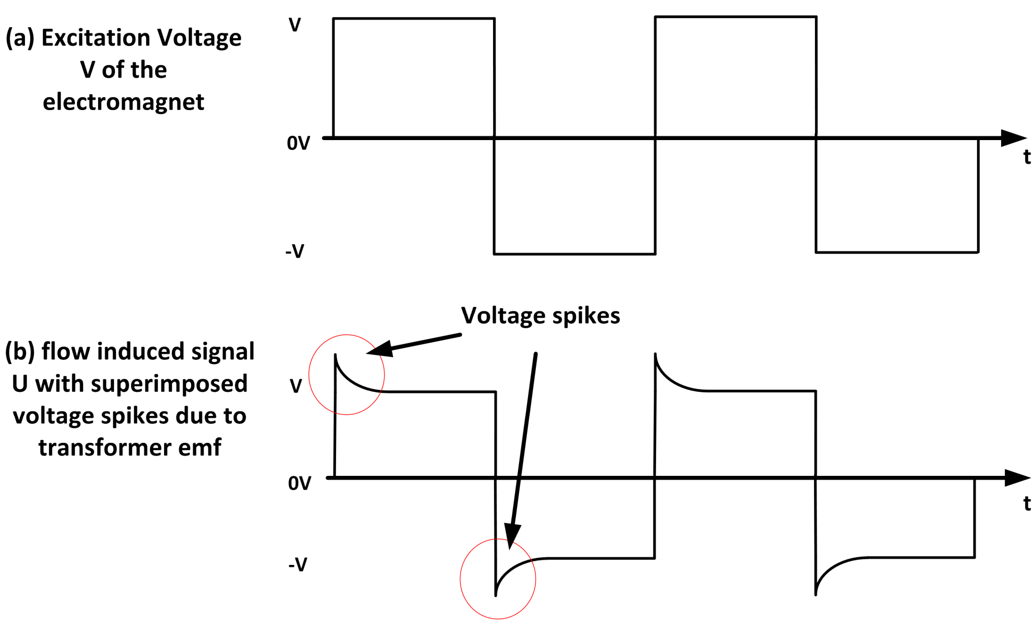

Figure 2.34: (a) Excitation voltage of the electromagnet (b) Measured voltage signal containing the flow induced potential difference and the transformer emf.

PFC refers to a method that can be used to reduce the reactive power withdrawn from the power supply [153]. This is achieved by placing a capacitor in parallel with the inductive load. The value of the capacitor is determined by setting the reactance of the electromagnet (X_L) equal to the reactance of the capacitor (X_C), i.e. $X_L = X_C$. It is found to be a useful technique as it lowers the current requirement for the power source of the electromagnet.

The term $\sum \varepsilon_{(t)}$ in Eq. 2-54 accounts for the sum of transformer emfs that are of the same waveform as the flow induced signal; however, they are not 90^{o} out of phase as will be explained below. The sources of these emfs can be from:

- The coupling between the electromagnet coil and the electrode leads
- Magnetic flux getting into tissues, the interface between the electrode and the electrolyte or/and the input measurement system.

The impedance elements in those sources, i.e. tissues, electrode/electrolyte interface and the input measurement system will alter the phase relationship between the transformer and motional emfs, so that it is no longer 90° out of phase. This means that some of the transformer emfs generated by those sources will be in phase with the flow induced signal and therefore, they cannot be fully distinguished from the flow induced voltage signal using PSD. However, with proper magnetic and electrostatic shielding methods [154, 155], the use of cavity electrodes [127] and transformer emf nulling (calibrating the device when there is no flow) [127], these sources of error can be reduced to a minimum. Note that these emfs are not significant for square-wave flow meters as they will appear as voltage spikes (refer to Figure 2.34) and will elapse after a time period of about 5τ approximately where $\tau = L/R$.

The next error term, $\sum e_{(t)}$, is due to mains interference, DC offset and biopotentials. Mains interference refers to the 50 Hz frequency component and its harmonics, i.e. 100 Hz and 150 Hz [156]. Polarisation occurs at the interface between the electrode and skin, vessel wall or conductive liquid. As a result, a DC offset is generated which can be in the range of a few hundreds of millivolts. Biopotentials include electrocardiogram (ECG) signals, i.e. heart potential (0.01 Hz to 3.5 Hz) and electromyogram (EMG) signals, i.e. muscle potentials (2 Hz to 500 Hz) [157]. All these error components, if not minimised, can reduce the SNR and make the flow induced signal difficult to measure. Moreover, the amplifier of the measurement system has a very large gain because the flow induced signals are usually in the microvolt range. If these error signals are not minimised, they will be amplified and can cause the amplifier to exceed its dynamic operating range (saturation).

Normally, these error signals appear at the input of the measurement system as common mode. Hence, it is necessary that the input of the amplifier of the measurement system should have a high common mode rejection ratio (CMRR) to reject these potentials efficiently. These potentials can also become differential due to the imbalance of the impedance of the electrodes and associated cables. Unwanted differential potential can be eliminated by the use of differential RC filters. The polarisation offset is a potential at DC, i.e. 0 Hz, and can be eliminated by using high-pass filters. Using the sine-wave excitation for the electromagnet allows a specific frequency to be selected, avoiding mains frequency and its harmonics. This frequency can be discriminated from all other unwanted signals by the PSD method described above. Hence, the SNR of the flow induced voltage signals will be high. This is an advantage of the sine-wave excitation over the square-wave method.

The last term, e_n, in Eq. 2-54 is associated with the internal 'intrinsic' noise of the electronics. All electronic components such as resistors, reactances, amplifiers and transistors generate noise. The noise source can either be modelled as voltage or current noise. There are 4 main types of noise: (1) thermal (Johnson noise), (2) shot noise, (3) flicker noise and (4) Burst 'popcorn' noise [158]. Thermal noise is associated with the thermal movement of charge carriers. It is normally considered to be white noise, i.e. its power spectral density is constant throughout the frequency spectrum. The shot, flicker and burst noises are associated with amplifiers, i.e. transistors, PN junctions and the fabrication process. Datasheets of amplifiers usually state the value of two parameters, i.e. the input-referred voltage and current to model the total noise generated in the amplifier. These noise levels vary at different frequencies and bandwidths.

Noise analysis can be simplified if the dominant noise sources are determined. The total voltage noise of a circuit is the square root of the sum of all noises. This total noise can be critical in high-gain and/or high-frequency analogue circuits. It is important to be aware of this error to ensure that the flow induced potential signals have good SNR. Careful design and selection of components reduces the effect of the noise associated with electronic components.

2.6 Research Aims and Methodology

The aim of this research is to design and develop a non-invasive, EM induction technique that can be used for measuring the total blood flow rate in blood vessels within a cross-sectional area of an upper or lower limb. The limb is to be inserted into a circular multi-electrode array across which a uniform magnetic field is applied. Flow induced potentials measured by the electrodes are then related to the total volumetric flow rate due to the blood flow in a single blood vessel or in multiple blood vessels. The technique is intended to overcome the previously encountered problems noted in the literature for EM flow meters such as sensitivity to asymmetric velocity profiles at the measurement site and the need for frequent calibration. The development of a robust mathematical model for this method will also allow the device, built using this method, to be calibrated offline (‘dry’ calibration).

This device should also be low cost due to its simple design and thus, it could be available in health centres and clinics to be used by General Practitioners, nurses, physiotherapists and podiatrists in various applications including the diagnosis of PAD and DVT. The methodologies that will be used to achieve the objectives are listed below.

1. To develop a mathematical model using the “virtual current” theory for a cross-sectional area with multiple flow channels (multiple blood vessels) bounded by a multi-electrode system and across which a uniform magnetic field is applied. This model will allow the measurement of the total instantaneous volumetric blood flow rate in all major blood vessels at the position of the electrode array. This total flow rate measurement will be independent of the size and location of the flow channels within the cross-sectional area bounded by the electrode array.
2. To develop a finite element (FE) model to simulate a cross-sectional area with multiple flow channels. The FE model will consist of an electromagnet to generate a uniform magnetic field across a geometric model which will consist of one or multiple tubes, simulating blood vessels. From the FE model, flow induced potential differences will be obtained. These potential differences will be compared with the those obtained from the mathematical model developed in 1. The aim of this work is to validate the developed mathematical model.

3. To design a practical experiment in order to validate the mathematical model developed in 1. This work comprises the design of a physical pipe model (mechanical system) that has multiple flow channel and an electromagnet – with its power supply – to generate a uniform magnetic field. Signal conditioning and processing systems will be designed to allow measurement of low level and noisy flow induced potential differences.
4. To perform flow tests on the practical SVS model and obtain flow induced potential differences related to water flow imposed in the channels within the SVS. The flow rate will be varied in the channels and their location will be changed with respect to the magnetic field direction. The flow induced potential differences obtained from the practical experiment will be quantitatively compared with the flow potential differences obtained from the mathematical model developed in 1 above.

2.7 Summary

MRI and X-ray devices were discussed in terms of their operation, clinical applications and drawbacks. MRI and X-ray-based devices are advanced screening instruments that are usually used for advanced diagnostic tests and not for routine check-ups. They are not available in many health centres and hospitals as they require a large space for installation, they are expensive to buy and operate, and must be operated by experienced radiologists for accurate diagnosis. The injected dye in MRI and X-ray devices may cause bad reactions in patients. Additionally, MRI may cause discomfort for patients as it is performed in an enclosed space. Impedance plethysmography has been used in the past for cardiac output and peripheral blood flow measurements. However, currently it has more limited application due to its poor accuracy compared with other medical devices such as duplex ultrasound and nowadays it is often only used for DVT diagnosis. Clinical studies described in Section 2.3.3 showed that IPG can have an accuracy of 58% which is significantly poor and may lead to false diagnosis.

Currently for the diagnosis of PAD and DVT diseases, the most common device used is the duplex ultrasound. Ultrasound waves are any vibrations generated with a frequency above the human hearing range, i.e. 20 kHz. The Doppler method is used for image reconstruction of targets and also measurement of blood velocity if required. Despite its acceptance by health practitioners for use in clinical applications, the duplex ultrasound has its drawbacks and limitations. From a duplex ultrasound scan, the peak velocity measurement is the most relied upon for estimating the severity of stenosis. This measurement can be affected by errors that are caused by the technologist operating the Doppler device, the device itself or the patient. Errors arising from the technologist can be due to the angle of insonation, improper placement and size of sample volume, pulse repetition frequency, gain setting and interobserver variability. In a stenosed artery, it was found that an error of up to 28% can be caused by the technologist. Errors from the Doppler device itself, including the sample volume shape, the system noise and the assumption that the sound velocity is constant in all tissues, can cause an error of up to 8%. Hence, all the error sources noted above can limit the accuracy of duplex ultrasound and may lead to false diagnosis. Moreover, dialysis patients are more likely to suffer from plaque calcification. Such a condition prevents ultrasound beams from penetrating the wall of the blood vessel to allow the velocity measurement to be taken. Thus, the duplex ultrasound device is not the ideal device for PAD or DVT diagnosis in dialysis patients.

EM flow meters were successfully used invasively for blood flow measurements in different blood vessels. The EM flow metering method is attractive because it is a linear technique, insensitive to viscosity, density, temperature and pressure loss, and is unaffected by the velocity profile given that the velocity distribution is axisymmetric. There are three types of invasive EM blood flow meters; cannula flow meters, perivascular and intravascular probes. Cannula flow meters are inserted between two ends of a blood vessel that has been cut out, and it is the least favourable method as it may cause health complications in patients. Perivascular probes are cuff- or clip-type probes that are mounted around a blood vessel and are considered the ‘gold standard’ for invasive blood flow rate measurement. Intravascular devices are catheter-type probes that are inserted via the skin, and then into the desired blood vessel.

A review of previous and current methods in the use of invasive EM blood flow meters provided an insight into the problems encountered during the design and operation of EM flow meters for blood flow rate measurement. It was found that, in all designs of blood flow meters noted in the literature, a conventional-type EM flow metering method was implemented, i.e. using two point-like electrodes. EM flow meters with point-like electrodes are sensitive to asymmetric velocity profiles. Such sensitivity can lead to an error of 100% in the measured flow induced emf. Thus, it is important to design EM flow meters that are independent of velocity profile.

It was found that the velocity profile in the circulatory system of mammals is non-axisymmetric. Moreover, cannula flow meters are short-end devices, and Bevir observed that in such structures, the velocity profile cannot be ensured to be axisymmetric. The haematocrit level in the blood was also found to affect EM flow meters in a number of ways. A higher level of haematocrit level increases the source impedance and therefore, the front-end of the measurement system must have high input impedance to avoid any signal loss. Moreover, an increase in haematocrit level increases the viscosity, and that distorts the velocity profile and, as a result, will affect the accuracy of the conventional-type EM flow meter. Other problems were noted in perivascular and catheter-tipped probes including heat dissipation and improper placement of the probe around or in the vessel. Nevertheless, perivascular and catheter-tip probes were used intensively by several authors in clinical applications, and a high accuracy of measurement was achieved.

The most notable attempt to develop a non-invasive EM flow meter for peripheral blood flow measurement was by Boccalon et al. However, there are several issues associated with the flow meter method that was designed. Firstly, the design was based on a conventional-type EM flow meter which has been found to be sensitive to asymmetric velocity profile resulting from blood velocity in vessels positioned in different locations in the measurement region and also due to the asymmetry of blood flow in the blood vessels themselves. Moreover, an analytical model was required for each region of the human body to obtain its calibration factor which seems to be cumbersome and impractical. There was no example in the literature of a non-invasive EM flow meter that is insensitive to velocity profile.

According to the literature, there are three methods that can significantly reduce the effect of velocity profile: (1) use of relatively larger electrodes, (2) optimisation of the magnetic field distribution by enhancing coil design, and (3) use of a multi-electrode system. Based on the work by Engl, Horner developed multi-electrode EM flow meters and showed that, for a 16-electrode system, the error in the velocity measurement for distorted (asymmetric) velocity profile was less than 10%. Recent research work in the Systems Engineering group of the University of Huddersfield achieved a tomographic EM flow metering technique to determine the axial velocity within a flow cross-sectional area bounded by 16 electrodes. It is possible to adapt this research progress to develop an EM flow metering method that can be used for non-invasive blood flow rate measurements. Additionally, the mathematical modelling techniques developed by Shercliff and Bevir, i.e. the weight vector and virtual current density, are powerful techniques that can be used to model, calibrate and predict flow contribution in various regions within the flow cross-section to the output signal in EM flow meters.

Following the literature review, the research aims and methodology have been described and are given in the previous section. The research work started with developing the mathematical model for the non-invasive EM flow metering method (Chapter 3). This mathematical model was then validated using computer simulation and this is described in Chapter 4. The remaining chapters cover the design and execution of the practical experiment which aimed at validating the mathematical model in practice. The practical experiment also identified the main subsystems that are required to build a medical device based on the proposed EM induction method.

Chapter 3
Theory of the Novel Non-invasive Electromagnetic Induction Blood Flow Measurement

Contents

3.1 Introduction

This chapter presents a mathematical model of the proposed EM induction method. For a given location of single or multiple flow channels (blood vessels) within a region (a limb), the flow rate in the channels and the magnetic flux density generated across, the mathematical model calculates the flow induced potentials at the boundary of the cross-sectional area of the region. From these flow induced potentials, the total volumetric flow rate for all the flow channels can be found irrespective of the number, location and size of the flow channels. This mathematical model is an extension of the virtual current theory introduced by Bevir (refer to Section 2.5.5). This chapter also discusses a method that can be used to determine the contribution of the arterial and venous blood flow to the total flow rate measurement.

Firstly, the virtual current theory is applied to find the weight function distribution for a full circular and conductive flow cross section, and this is presented in **Section 3.2**. Then, in **Section 3.3**, this weight function is modified for a conductive cross-sectional area with a single flow channel. Afterwards, in **Section 3.4**, the potential difference equation is determined for two electrodes, and then extended for a multi-electrode array. A single flow channel model describes a simple case of a human limb cross-section with a single blood vessel. In **Section 3.5**, the flow induced potential equation is extended for multiple flow channels, and a method is shown to find the total volumetric flow rate for flow channels located within a cross-sectional area bounded by the multi-electrode array. This total volumetric flow rate measurement is independent of the number, size and location of the flow channels. In **Section 3.6** a method is described to enable the measurement of the arterial and venous blood flow independently over a cardiac cycle.

3.2 Weight Function Distribution for a Full Circular Pipe

Consider a full circular conductive cross sectional area with radius R as illustrated in Figure 3.1. Assume the magnetic field is in the negative y-direction, i.e. $B = -B_o\hat{\boldsymbol{y}}$, and that a unit current I_{in} is injected at an angle of ψ_{in} and the unit current I_{out} leaves the circumference of the pipe at an angle of ψ_{out}.

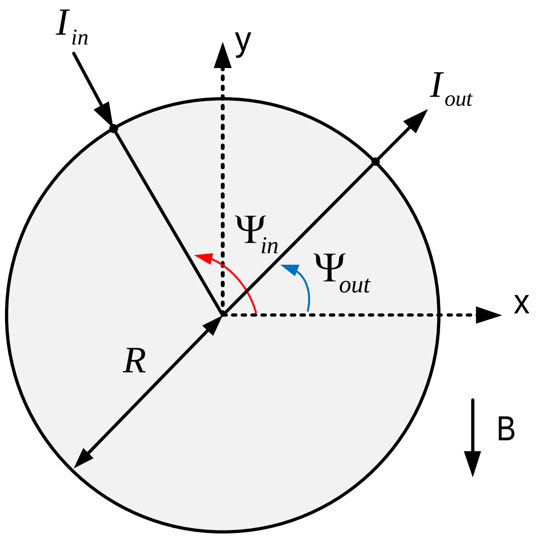

Figure 3.1: Flow in a full circular pipe with radius *R*

In the absence of the magnetic field and flow, the virtual current density $\boldsymbol{j_v}$ is given by [122]

$$\nabla \cdot \boldsymbol{j_v} = 0 \qquad \text{Eq. 3-1}$$

Assuming uniform conductivity σ, the virtual current density is related to the virtual potential gradient $\nabla\phi$ by the following equation

$$\boldsymbol{j_v} = \nabla\phi \qquad \text{Eq. 3-2}$$

Substituting Eq. 3-2 into Eq. 3-1 gives the equation for the virtual potential ϕ which is Laplace's equation, i.e.

$$\nabla^2\phi = 0 \qquad \text{Eq. 3-3}$$

The equations stated above were previously discussed in Section 2.5.5 and stated here for convenience. Laplace's equation in Eq. 3-3 is a classic problem encountered in many fields of engineering. It can be used to describe the steady-state of temperature, potential, stress or flow distributions [159]. The general solution is obtained using the method of separation of variables and is provided in the literature [160, 161]. The general solution for the virtual potential ϕ in polar coordinates (r, θ) takes the form

$$\phi(r,\theta) = C_0 + \sum_{n=1}^{\infty} r^n \left(A_n \cos n\theta + B_n \sin n\theta\right) \qquad \text{Eq. 3-4}$$

where C_0 is an arbitrary constant, and A_n and B_n are found by applying appropriate boundary conditions.

3.2.1 Boundary Condition Assuming Dirac 1D Delta Function

The boundary condition applied was the Neumann boundary condition using Dirac delta function[4] [162]. Referring to Figure 3.1, the Neumann boundary condition ($\left.\frac{\partial\phi}{\partial r}\right|_{r=R}$) at the circumference in polar coordinates using Dirac function δ and for a unit radius, i.e. $R = 1$ (using polar coordinates), can be written as follows

$$\boldsymbol{j_v} \cdot \boldsymbol{n}|_{r=R} = \left.\frac{\partial\phi}{\partial r}\right|_{r=R} = \delta(\theta - \psi_{out}) - \delta(\theta - \psi_{in}) \qquad \text{Eq. 3-5}$$

where $\boldsymbol{n}$ is a unit vector of the circumferential surface, and δ is the delta function (impulse response) which is applied to express a unit current entering a surface at an angle ψ_{in} and leaving at an angle of ψ_{out}. The angles of ψ_{in} and ψ_{out}, in practice, refer to the locations of the electrodes across which the potential difference is measured.

[4] I am grateful to Dr. Laszlo Kollar and Prof. Gary Lucas for their work in the mathematical modelling of the EM Induction blood flow meter system using the virtual current theory.

To include the effect of the radius R, consider two circular pipes with different radii, R_1 and R_2 as shown in Figure 3.2. Assume a pipe with a unit length so that the problem can be simplified to a two-dimensional one. Referring to Figure 3.2, the unit current I_x passing through the length d_1 inside the section of the pipe with radius R_1 is the same as the unit current passing through the length d_2 inside the pipe section with radius R_2, if the ratio of d_1/R_1 is equal to the ratio d_2/R_2. Mathematically, this can be written as

$$\frac{d_1}{R_1} = \frac{d_2}{R_2} \quad \rightarrow \quad \frac{d_1}{d_2} = \frac{R_1}{R_2} \qquad \text{Eq. 3-6}$$

Hence, the current I_x in both cross sections is given by

$$I_x = j_1 d_1 = j_2 d_2 \qquad \text{Eq. 3-7}$$

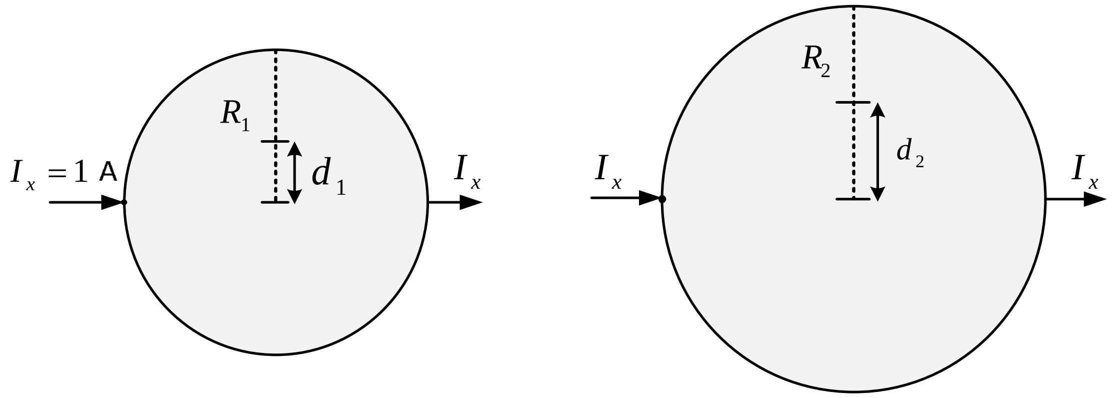

Figure 3.2: Two circular cross sections with different radii *R*

From Eq. 3-6 and Eq. 3-7, the ratio of the virtual current densities j_1 and j_2, in the two pipes can be expressed as

$$\frac{j_2}{j_1} = \frac{d_1}{d_2} = \frac{R_1}{R_2} \qquad \text{Eq. 3-8}$$

According to Eq. 3-8, it can be noted that the virtual current density is proportional to $1/R$. Hence, the boundary condition in Eq. 3-5 at the circumference, where the electrode is placed on a surface with curvature $1/R$, is modified as follows

$$\boldsymbol{j_v} \cdot \boldsymbol{n}|_{r=R} = \left.\frac{\partial \phi}{\partial r}\right|_{r=R} = \frac{1}{R}(\delta(\theta - \psi_{out}) - \delta(\theta - \psi_{in})) \qquad \text{Eq. 3-9}$$

Eq. 3-9 is the boundary condition that will be applied to find the solution to Laplace's equation given in Eq. 3-3 to find the virtual potential $\phi(r, \theta)$. Note that for a given size pipe and uniform conductivity, the virtual current density distribution will be the same regardless of the actual fluid conductivity. Therefore, for this analysis which follows, it is satisfactory to assume that $\sigma = 1$.

3.2.2 Solution to Laplace's Equation to Obtain the Virtual Potential

Applying the boundary condition in Eq. 3-9 to the general solution of Laplace's equation, i.e. Eq. 3-4 gives the following

$$\left.\frac{\partial \phi}{\partial \mathrm{r}}\right|_{r=R} = \sum_{n=1}^{\infty} nR^{n-1}\,(A_n \cos n\theta + B_n \sin n\theta) = \frac{1}{R}(\delta(\theta - \psi_{out}) - \delta(\theta - \psi_{in})) \qquad \text{Eq. 3-10}$$

Multiplying both sides in Eq. 3-10 by $\cos m\theta$ and integrating with respect to θ from 0 to 2π gives

$$\sum_{n=1}^{\infty} nR^{n-1}\left(\underbrace{\int_0^{2\pi} A_n \cos m\theta \cos n\theta \mathrm{d}\theta}_{\begin{smallmatrix}\pi A_n & m=n \\ 0 & m\neq n\end{smallmatrix}} + \underbrace{\int_0^{2\pi} B_n \cos m\theta \sin n\theta \mathrm{d}\theta}_{0}\right) = \qquad \text{Eq. 3-11}$$

$$= \frac{1}{R}\int_0^{2\pi} \cos m\theta\, \delta(\theta - \psi_{out}) \mathrm{d}\theta - \int_0^{2\pi} \cos m\theta\, \delta(\theta - \psi_{in}) \mathrm{d}\theta$$

From the orthogonality of trigonometric functions, i.e.

$$\int_0^{2\pi} \cos mx \cos nx \mathrm{d}x = \pi\delta_{mn} = \begin{cases} \pi & m = n \\ 0 & m \neq n \end{cases} \qquad m, n \geq 1 \qquad \text{Eq. 3-12}$$

$$\int_0^{2\pi} \cos mx \sin nx \mathrm{d}x = 0 \qquad \text{Eq. 3-13}$$

Equation 3-11 can be simplified to

$$nR^{n-1}\pi A_n = \frac{1}{R}(\cos n\psi_{out} - \cos n\psi_{in}) \qquad \text{Eq. 3-14}$$

By rearranging Eq. 3-14, the value for A_n is given by

$$A_n = \frac{\cos n\psi_{out} - \cos n\psi_{in}}{nR^n\pi} \qquad \text{Eq. 3-15}$$

Similarly, multiplying both sides in Eq. 3-10 by $\sin m\theta$ and integrating with respect to θ from 0 to 2π gives

$$\sum_{n=1}^{\infty} nR^{n-1}\left(\underbrace{\int_0^{2\pi} A_n \sin m\theta \cos n\theta \mathrm{d}\theta}_{0} + \underbrace{\int_0^{2\pi} B_n \sin m\theta \sin n\theta \mathrm{d}\theta}_{\begin{matrix}\pi B_n & m=n \\ 0 & m\neq n\end{matrix}} \right) = \qquad \text{Eq. 3-16}$$

$$= \frac{1}{R}\int_0^{2\pi} \sin m\theta \delta(\theta - \psi_{out})\mathrm{d}\theta - \int_0^{2\pi} \sin m\theta \delta(\theta - \psi_{in})\mathrm{d}\theta$$

From the orthogonality of trigonometric functions, i.e.

$$\int_0^{2\pi} \sin mx \sin nx \mathrm{d}x = \pi\delta_{mn} = \begin{cases}\pi & m = n \\ 0 & m \neq n\end{cases} \qquad m,n \geq 1 \qquad \text{Eq. 3-17}$$

and also Eq. 3-13, Eq. 3-16 can be simplified to

$$nR^{n-1}\pi B_n = \frac{1}{R}(\sin n\psi_{out} - \sin n\psi_{in}) \qquad \text{Eq. 3-18}$$

By rearranging Eq. 3-18, the value for B_n is given by

$$B_n = \frac{\sin n\psi_{out} - \sin n\psi_{in}}{nR^n\pi} \qquad \text{Eq. 3-19}$$

Since C_0 is an arbitrary constant and the virtual current density $\boldsymbol{j_v}$ is the derivative of the virtual potential ϕ thus, the C_0 term will not appear, i.e. $C_0 = 0$ in Eq. 3-4.

Next, substituting Eq. 3-15 and Eq. 3-19 into Eq. 3-4, the solution to the Neumann boundary value problem is obtained as follows

$$\phi(r,\theta) = \sum_{n=1}^{\infty} \frac{1}{n\pi}\left(\frac{r}{R}\right)^n (\cos n\psi_{out} \cos n\theta - \cos n\psi_{in} \cos n\theta + \sin n\psi_{out} \sin n\theta - \sin n\psi_{in} \sin n\theta) \quad \text{Eq. 3-20}$$

Using trigonometric identities, Eq. 3-20 can be simplified to

$$\phi(r,\theta) = \frac{1}{\pi}\sum_{n=1}^{\infty} \frac{1}{n}\left(\frac{r}{R}\right)^n (\cos n(\psi_{out} - \theta) - \cos n(\psi_{in} - \theta)) \quad \text{Eq. 3-21}$$

3.2.3 Virtual Current Density and Weight Function

The solution to the virtual current density $\boldsymbol{j_v}$ is obtained from the virtual potential equation given in Eq. 3-21 thus; the virtual current density $\boldsymbol{j_v}$ can be found from calculating the derivatives of the virtual potential ϕ as follows

$$\boldsymbol{j_v} = \begin{bmatrix} j_r \\ j_\theta \end{bmatrix} = \begin{bmatrix} \frac{\partial \phi}{\partial r} \\ \frac{1}{r}\frac{\partial \phi}{\partial \theta} \end{bmatrix}$$

$$= \begin{bmatrix} \frac{1}{R\pi}\sum_{n=1}^{\infty}\left(\frac{r}{R}\right)^{n-1} (\cos n(\psi_{out} - \theta) - \cos n(\psi_{in} - \theta)) \\ \frac{1}{R\pi}\sum_{n=1}^{\infty}\left(\frac{r}{R}\right)^{n-1} (\sin n(\psi_{out} - \theta) - \sin n(\psi_{in} - \theta)) \end{bmatrix} \quad \text{Eq. 3-22}$$

The local weight function $\boldsymbol{W}$ is defined as [122]

$$\boldsymbol{W} = \boldsymbol{B} \times \boldsymbol{j_v} \quad \text{Eq. 3-23}$$

Assuming a uniform and transverse magnetic flux density in the negative y-direction, i.e. $\boldsymbol{B} = [0, -B_o, 0]$, the weight vector simplifies to a 2D problem and since $j_z = 0$, the only non-zero component is W_z (Bevir's conclusion [125]) which is given by

$$W_z = B_o j_r \cos\theta - B_o j_\theta \sin\theta \qquad \text{Eq. 3-24}$$

Substituting the virtual current density $\boldsymbol{j_v}$ (Eq. 3-22) into the weight function expression in Eq. 3-24 gives the following

$$W_z = \frac{B_0}{R\pi}\sum_{n=1}^{\infty}\left(\frac{r}{R}\right)^{n-1}[\cos n(\psi_{out}-\theta)\cos\theta - \cos n(\psi_{in}-\theta)\cos\theta - (\sin n(\psi_{out}-\theta)\sin\theta - \sin n(\psi_{in}-\theta)\sin\theta)] \qquad \text{Eq. 3-25}$$

Simplifying Eq. 3-25 using trigonometric identities gives the following local weight function distribution for a circular pipe full of conductive fluid.

$$W_z = \frac{B_0}{R\pi}\sum_{n=1}^{\infty}\left(\frac{r}{R}\right)^{n-1}[(\cos(n\psi_{out}-(n-1)\theta) - \cos(n\psi_{in}-(n-1)\theta)] \qquad \text{Eq. 3-26}$$

The angles of ψ_{in} and ψ_{out} in practice correspond to the angular position of the electrodes across which the potential difference is measured as will be shown below.

3.3 Weight Function for a Region with a Single Flow Channel

Consider a full circular conductive medium with radius R including a small flow channel (tube) with a unit depth as shown in Figure 3.3. The flow channel has a radius of h, its centre is located at polar coordinates (r_g, θ_g), and a conductive fluid with the same conductivity as the conductive medium flows inside it. This models a simple cross-section of a human limb that includes one blood vessel. Assume a uniform magnetic field in the negative y-direction, and that a unit current is injected at an angle of ψ_{in} and that unit current leaves the circumference of the medium at an angle of ψ_{out}. The weight function distribution obtained in Eq. 3-26 can be modified by setting the angle at which the current leaves to zero, i.e. $\psi_{out} = 0$ (which can be considered to be the reference point), the radial coordinate r to the radial coordinate of the channel r_g, i.e. $r = r_g$, and the angular coordinate θ to the angular coordinate of the channel θ_g, i.e. $\theta = \theta_g$. As a result, Eq. 3-26 can be written as

$$W_z(r_g, \theta_g) = \frac{B_0}{R\pi} \sum_{n=1}^{\infty} \left(\frac{r_g}{R}\right)^{n-1} \left[\cos((n-1)\theta_g)) - \cos(n\psi_{in} - (n-1)\theta_g)\right] \quad \text{Eq. 3-27}$$

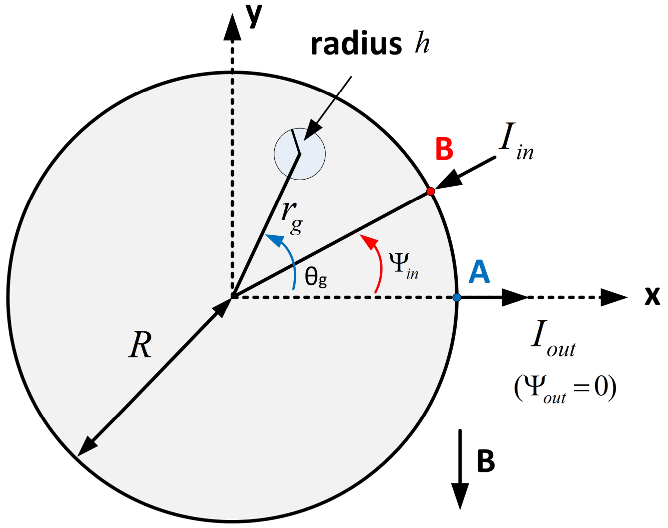

Figure 3.3: Flow in a small channel within a medium cross section

3.4 The Flow Induced Potential for a Single Flow Channel

Referring to Figure 3.3, assuming a rectilinear flow and uniform magnetic field (to simplify Bevir's equation Eq. 2-43 from a 3D to a 2D problem) , the potential difference between two points where a current enters at point B (at angle of ψ_{in}) and leaves the medium at A (at angle of $\psi_{out} = 0$) is given by

$$\Delta U_{AB} = \int_{\Omega} \boldsymbol{W} \cdot \boldsymbol{v} \, d\Omega \quad \text{Eq. 3-28}$$

where Ω is the volume of the flowing medium. For a small channel, $\int_{\Omega} \boldsymbol{W} \cdot \boldsymbol{v} \, d\Omega$ approximates to $\boldsymbol{W} \cdot \boldsymbol{v}$ multiplied by the cross-sectional area of the flow channel (assuming a unit depth), i.e. πh^2 (where h is the radius of the flow channel), at the position of the channel since the velocity is zero everywhere else. Assuming that the flow velocity (or mean velocity) in the channel is constant and its direction is perpendicular to the xy-plane, i.e. $\boldsymbol{v} = v_g \hat{\boldsymbol{z}}$, and assuming also a unit depth, then Eq. 3-28 can be written in the form

$$\Delta U_{AB} = W_z v_g \pi h^2 = W_z Q_g \qquad \text{Eq. 3-29}$$

where Q_g (equal to $v_g \pi h^2$) is the volumetric flow rate of the fluid flowing in the channel. Substituting the weight function $W_z(r_g, \theta_g)$ given in Eq. 3-27 into Eq. 3-29 leads to the following equation

$$\Delta U_{AB} = \frac{Q_g B_0}{R\pi} \sum_{n=1}^{\infty} \left(\frac{r_g}{R}\right)^{n-1} \left[\left(\cos(n-1)\theta_g\right) - \cos(n\psi_{in} - (n-1)\theta_g)\right] \qquad \text{Eq. 3-30}$$

Using trigonometric identities, Eq. 3-30 can be written as

$$\Delta U_{AB} = -\frac{Q_g B_0}{R\pi} \sum_{n=1}^{\infty} \left(\frac{r_g}{R}\right)^{n-1} \cos\left((n-1)\theta_g\right)$$
$$+ \frac{Q_g B_0}{R\pi} \sum_{n=1}^{\infty} \left(\frac{r_g}{R}\right)^{n-1} \left[\cos(n\psi_{in}) \cos\left((n-1)\theta_g\right) + \sin(n\psi_{in}) \sin\left((n-1)\theta_g\right)\right] \qquad \text{Eq. 3-31}$$

It can be noted that the first term on the r.h.s of Eq. 3-31 is independent of ψ_{in}. This term is, in fact, a DC offset U_{off} as was also seen in the practical experimentation. For multiple electrodes, as shown in Figure 3.4 (different injection angle of current ψ_{in} for each j^{th} electrode), Eq. 3-31 can take the form of the following equation

$$U_j = U_{off} + 2k_1 Q_g B_0 \sum_{n=1}^{\infty} \left(\frac{r_g}{R}\right)^{n-1} \left[\cos(n\psi_j) \cos\left((n-1)\theta_g\right)\right.$$
$$\left. + \sin(n\psi_j) \sin\left((n-1)\theta_g\right)\right] \qquad \text{Eq. 3-32}$$

where:

$$k_1 = \frac{1}{2R\pi} \qquad \text{Eq. 3-33}$$

The index j refers to the j^{th} electrode in which the current is injected (Figure 3.4). The angle ψ_j in Eq. 3-32 corresponds to ψ_{in}, and it is the angle at which the current is injected. The potential difference U_j is between the j^{th} electrode (where current enters) and electrode e_5 where current leaves the cross-section of the medium.

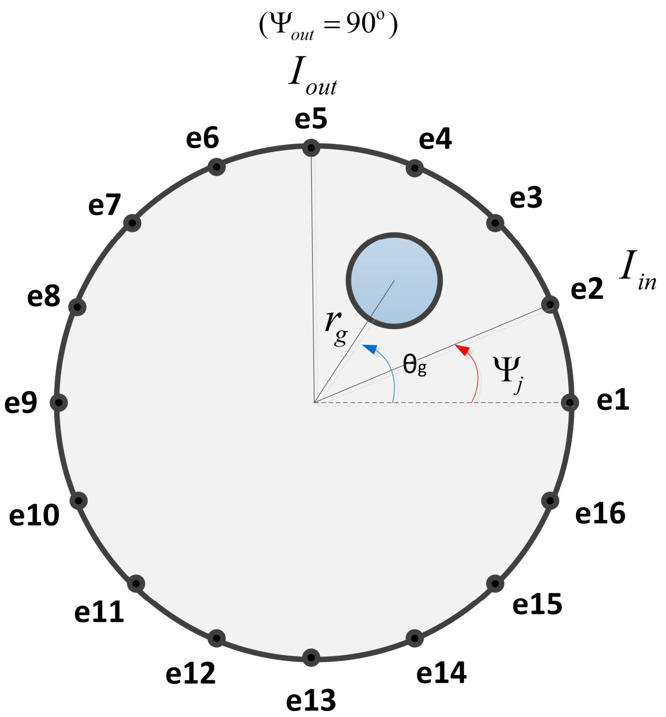

Figure 3.4: Cross-sectional area with 16 electrodes

In the theory developed in this chapter, the reference electrode that was considered is at angular position ψ_{out} = 0° (see Figure 3.3). However, any of the sixteen electrode positions e_1 to e_{16} (Figure 3.4) can be selected as the reference electrode and the distribution of the electrical potential is still defined by Eq. 3-32 and Eq. 3-33. The choice of the reference electrode only affects the value of U_{off} in Eq. 3-32. In the computer simulations and practical work, described later in the thesis, electrode e_5 was actually chosen as the reference electrode. As will be seen in Section 3.5, the value of U_{off} is not important in the modelling work undertaken in this research.

As a final point, the potential differences defined by Eq. 3-32 and Eq. 3-33 are between the reference electrode (point A) and the j^{th} electrode (point B), i.e. ΔU_{AB}. For the computer model and the practical work, the relevant "sense" of the potential difference measurement was not ΔU_{AB} but ΔU_{BA} where $\Delta U_{BA} = -\Delta U_{AB}$. The sign of the value k_1 depends on the direction of the magnetic flux density B_0, the direction of the fluid flow Q_g and the relevant "sense" of the potential difference measurement, ΔU_{AB} or ΔU_{BA} as shown in Table 3-1.

Condition	k_1 Value	Notes
$\boldsymbol{B}$ +y, $\boldsymbol{\Delta U_{AB}}$ and $\boldsymbol{Q_g}$ +z	negative	
$\boldsymbol{B}$ +y, $\boldsymbol{\Delta U_{AB}}$ and $\boldsymbol{Q_g}$ −z	positive	
$\boldsymbol{B}$ +y, $\boldsymbol{\Delta U_{BA}}$ and $\boldsymbol{Q_g}$ +z	positive	Used in the FE model
$\boldsymbol{B}$ +y, $\boldsymbol{\Delta U_{BA}}$ and $\boldsymbol{Q_g}$ −z	negative	
$\boldsymbol{B}$ −y, $\boldsymbol{\Delta U_{AB}}$ and $\boldsymbol{Q_g}$ +z	positive	Used in the theoretical model
$\boldsymbol{B}$ −y, $\boldsymbol{\Delta U_{AB}}$ and $\boldsymbol{Q_g}$ −z	negative	
$\boldsymbol{B}$ −y, $\boldsymbol{\Delta U_{BA}}$ and $\boldsymbol{Q_g}$ +z	negative	
$\boldsymbol{B}$ −y, $\boldsymbol{\Delta U_{BA}}$ and $\boldsymbol{Q_g}$ −z	positive	Used in the practical model

Table 3-1: The value of k_1 depending on the direction of the magnetic field density B_0, the fluid flow Q_g and the relevant "sense" of the potential difference ΔU_{AB} or ΔU_{BA}

3.5 The Total Volumetric Flow Rate for Multiple Channels

For multiple channels in a circular region in which a conductive fluid is flowing in each channel, the potential distribution for 16 electrodes placed 22.5° apart (Figure 3.4) U_j ($j = 1$ to 16), based on the principle of superposition [113], is given by

$$U_j = U_{off} + \sum_{g=1}^{G} 2k_1 Q_g B_0 \sum_{n=1}^{\infty} \left(\frac{r_g}{R}\right)^{n-1} \left[\cos(n\psi_j)\cos\left((n-1)\theta_g\right) + \sin(n\psi_j)\sin\left((n-1)\theta_g\right)\right] \quad \text{Eq. 3-35}$$

where U_j is the potential at the j^{th} electrode and G is the number of flow channels. Note that U_j is dependent upon the volumetric flow rate Q_g in each channel. If the DFT of the potential distribution U_j is taken[5], the m^{th} term (m = 1, 2, 3 …) of the DFT series, i.e. $X(m)$ is given by

$$X(m) = \sum_{g=1}^{G} k_1 B_0 Q_g \left(\frac{r_g}{R}\right)^{m-1} \left[\cos(m-1)\theta_g - j\sin(m-1)\theta_g\right] \quad \text{Eq. 3-36}$$

For $m = 1$, i.e. the DFT term corresponds to the fundamental frequency $X(1)$ of the series U_j. By finding the modulus $|X(1)|$ of the DFT component $X(1)$, the expression in Eq. 3-36 can be simplified to the following

$$|X(1)| = \sum_{g=1}^{G} k_1 B_0 Q_g \quad \text{Eq. 3-37}$$

$|X(1)|$ is the modulus of the fundamental DFT component $X(1)$. The values of k_1 and B_0 are constant. Hence, Eq. 3-37 can be arranged to have the form

[5] In the following chapters the electric potentials U_j obtained from multiple electrodes are referred to as "flow induced potentials" and also "boundary potentials".

$$\sum_{g=1}^{G} Q_g = \frac{|X(1)|}{k_1 B_0} \quad \text{Eq. 3-38}$$

where the left hand side of Eq. 3-38 represents the total volumetric flow rate Q_T. Therefore, it is clear that the total volumetric flow rate can be obtained in practice from the modulus $|X(1)|$ of the DFT component $X(1)$ of the measured flow induced boundary potential distribution. This result can also be inferred from the literature [119, 130]. From Eq. 3-38, it can be shown that

$$|X(1)| = k_1 Q_T B_0 \quad \text{Eq. 3-39}$$

Hence, the modulus $|X(1)|$ of the DFT component $X(1)$ of the flow induced boundary potential distribution is directly proportional to the total volumetric flow rate Q_T and the magnetic flux density B_0. From Eq. 3-39, the unit of the constant factor k_1 can be derived and it is m^{-1} (see Appendix A for unit derivation). The equation of the boundary flow potential distribution U_j (Eq. 3-35) and the total volumetric flow rate Q_T (Eq. 3-38) were validated in simulation using Finite Element Analysis (FEA) modelling (described in Chapter 4) and, in practice, by building a physical model of pipework which included small flow channels and a 16-electrode array (described in Chapters 5, 6 and 7).

3.6 Arterial and Venous Blood Flow over a Cardiac Cycle

At a cross-sectional area of a real human limb, blood flows towards the end of the limb through arteries with a total volumetric flow $Q_{T,A}$ and away from the end via the veins with a total volumetric flow rate $Q_{T,V}$. However, $Q_{T,V}$ remains essentially constant over the cardiac cycle whilst $Q_{T,A}$ varies greatly as described in Chapter 1. Hence, the total blood flow rate over a cardiac cycle is zero. Figure 3.5 shows quantitatively the venous, arterial and total blood rates over a cardiac cycle. The total arterial blood flow rate $Q_{T,A}$ can be measured as follows:

- Firstly by measuring the total volumetric flow rate during the cardiac cycle when no arterial blood flows, i.e. at time t_1 as shown in Figure 3.5, the total flow rate in the veins $Q_{T,V}$ at the relevant limb section is measured. Note that $Q_{T,V}$ is numerically negative because it is in the opposite direction to the arterial blood flow.
- Next take another measurement at time t_2 which is during the part of the cardiac cycle when the peak arterial blood flow rate occurs. This flow rate corresponds to $\tilde{Q}_{T,A,max}$ in Figure 3.5.
- Assuming $Q_{T,V}$ is constant throughout the cardiac cycle, the total maximum arterial blood flow $Q_{T,A,max}$ is given by

$$Q_{T,A,max} = \tilde{Q}_{T,A,max} - Q_{T,V} \qquad \text{Eq. 3-40}$$

Using Eq. 3-40, the maximum arterial blood flow in a human limb can be determined.

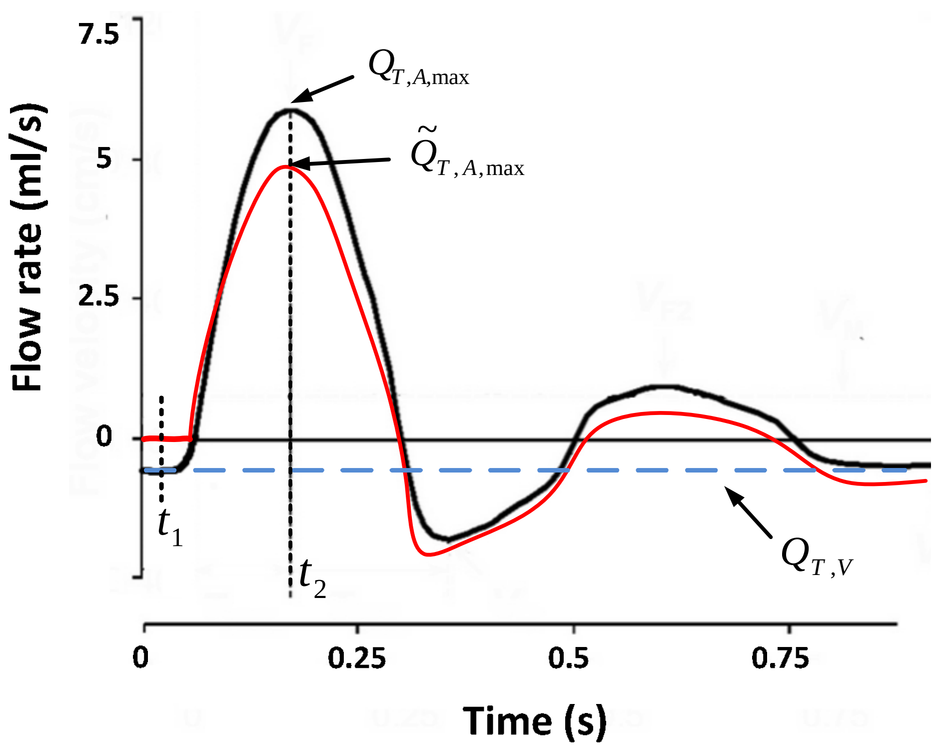

Figure 3.5: Peak arterial blood flow rate $\tilde{Q}_{T,A}$, maximum total arterial blood flow rate $Q_{T,A}$ and the venous blood flow rate $Q_{T,V}$

3.7 Summary

Virtual current theory was applied to a circular cross-section and that resulted in the virtual potential ϕ equation, which is a Laplace's equation (Eq. 3-3). This equation was solved by using the appropriate boundary condition which was given in Eq. 3-9. The solution of the virtual current density $\boldsymbol{j_v}$, i.e. Eq. 3-2, was found by calculating the derivatives of the virtual potential ϕ equation given in Eq. 3-21, and it was expressed in Eq. 3-22. Assuming a uniform and transverse magnetic flux density in the negative y-direction, i.e. $\boldsymbol{B} = [0, -B_o, 0]$, the weight vector $\boldsymbol{W}$ was simplified to 2D, and the only non-zero component was W_z. The solution of the virtual current density $\boldsymbol{j_v}$ was then used to find the weight function W_z which was presented in Eq. 3-26. This weight function was then modified and extended for a circular medium with a single channel.

Assuming the velocity in the flow channel within the medium is constant, the flow potential difference equation between two electrodes at the boundary of a medium including a single channel was derived, and it was given in Eq. 3-31. This equation was then extended for 16 electrodes placed at the boundary of the medium and 22.5^o apart from each other as shown in Eq. 3-32 and Eq. 3-33. Then, for multiple channels in the medium bounded by 16 electrodes, the flow induced potential difference for each electrode could be found using Eq. 3-35. Hence, for a number of flow channels of different sizes and in different locations within the medium, the flow induced potentials at the boundary could be predicted given that the radial and angular coordinates (r_g and θ_g) of, and the flow rate Q_g in, the flow channels are known. It was also shown that by applying the DFT on Eq. 3-35, the DFT components of the boundary potential distribution U_j are given by Eq. 3-36. The modulus $|X(1)|$ of the DFT component $X(1)$ was found to be directly proportional to the total volumetric flow rate Q_T of all flow channels and the magnetic flux density B_o, irrespective of the number, size and location of the flow channels within the medium as shown in Eq. 3-37.

In the next chapter, an FE model was created to verify the mathematical relationship given in Eq. 3-35. The simulation work involved FE modelling of a conductive cylinder which contained two tubes in which a conductive fluid was flowing in either one or both of them. The location of the tubes was varied within the cross-section of the cylinder. A uniform magnetic field was generated across the flow cross-section and the flow induced potentials were collected at the location of the electrodes at the boundary of the cross-section as shown in Figure 3.4. The flow induced potential differences were compared to the mathematical model in Eq. 3-35 for a given total volumetric flow rate Q_T and magnetic flux density B_o. Then, the relationship between the term $|X(1)|$, obtained from the DFT of the boundary potential distribution, and the total flow rate Q_T was investigated. The FEA simulation is discussed in detail in Chapter 4.

Chapter 4
Finite Element Modelling of the Non-invasive Electromagnetic Induction Method

Contents

4.1 Introduction

This chapter describes the computer modelling of the proposed EM method (described in Sections 3.4 and 3.5) which could be used to obtain the total flow rate Q_T of one flow channel or more (several blood vessels) within a cross-section (upper or lower human limb) across which a uniform magnetic field B_0 is applied. The computer modelling was performed using the Finite Element (FE) method. The simulated model consisted of a conductive cylindrical region that had one or two flow channels and a Helmholtz coil to generate a uniform magnetic field across the flow channels. Water flow (conductive fluid) was imposed in either one or both flow channels. Water was used instead of blood so that the FE model would agree with the practical experiment described in Chapter 7. Note that typical blood conductivity is 0.7 S/m whereas the conductivity of water in Northern England is around 0.013 S/m [163]. This cylindrical region was given the name Simulated Vascular System (SVS).

For each test setup of the FE model, i.e. different number and location of, and the water flow rate in, the flow channels, 16 electrical potentials U_j, generated by the interaction of water flowing (z-component of the velocity vector $\boldsymbol{v}$) in the flow channels and the magnetic field (y-component of $\boldsymbol{B}$), were collected at the boundary of the cross-sectional area of the cylindrical region where the electrodes are located as shown in Figure 3.4. The reference potential was chosen to be the potential at electrode e_5 and the potential differences were determined with respect to this electrode, i.e. $U_j - U_5$ (j = 1 to 16). Note that the reference electrode can be arbitrarily set as discussed in Section 3.4. The flow potential differences obtained from the FE model were compared with the flow potential differences obtained from the mathematical model given in Eq. 3-35 for the same value of the magnetic field, the flow rate and the number, size and location of the flow channels.

The DFT was then applied to the flow potential differences obtained from the FE and theoretical models for each test. Afterwards, the modulus $|X(1)|$ of the DFT component $X(1)$, corresponding to the fundamental frequency of the boundary potential distribution, was found for both models. Then, the constant factor k_1 in Eq. 3-33 was calculated for both models and compared.

The overall system of the FE model had two coupled EM phenomena that required modelling: (1) the magnetic field generated due to the current flowing through the Helmholtz coil and (2) the electrical potentials generated by the interaction of water and the magnetic field. The governing equations for both phenomena are a set of partial differential equations (PDEs) based on Maxwell's equations [164]. These PDEs are described in Section 4.4 and were solved using the FE method. The FE method was applied using COMSOL Multiphysics 3.5a software. The purpose of the simulation was to validate the relationship between the total volumetric flow rate Q_T and the modulus of the DFT component $|X(1)|$ as described in Section 3.5. Moreover, the effect of the number, size and location of the flow channels on the flow induced boundary potential distribution was investigated.

The layout of this chapter is as follows: an overview of COMSOL Multiphysics software is given in **Section 4.2**. Afterwards, the design of the SVS model and the Helmholtz coil are presented in **Section 4.3**. The governing equations of the model built in COMSOL Multiphysics and the modelling settings are defined in **Section 4.4** and **Section 4.5**, respectively. The results of the magnetic field density distribution across the SVS model, obtained from solving the overall model in COMSOL, are given in **Section 4.6**. Then, in **Section 4.7**, the flow induced potential differences obtained from the SVS FE model are compared with the mathematical model given in Eq. 3-35 for the same flow configuration. Finally, the DFT analysis of the flow induced potential differences is described and analysed in **Section 4.8**.

4.2 COMSOL Multiphysics Software

COMSOL Multiphysics software is designed to solve multiple physics problems simultaneously, in either 2D or 3D [165]. It has a wide range of application areas such as acoustics, bioscience, electromagnetics and fluid dynamics. It also offers specific add-on modules which include methods to solve particular science and engineering problems. The modules include AC/DC, heat transfer and RF. The AC/DC module (known as the AC/DC interface) can solve EM problems including electrostatics, magnetostatics, DC and AC current flow and AC electromagnetics [166]. All these problems are solved in COMSOL using the differential form of Maxwell's equations. COMSOL Multiphysics utilises the FE method to solve these equations with the appropriate boundary conditions being set by the user. The types of studies that the module can perform are stationary analysis, frequency domain, time domain and small signal analysis.

COMSOL Multiphysics works as follows: (1) the AC/DC interface is selected, then (2) a 2D or 3D model is created, (3) the materials of the model and sources (currents, voltages) are set, (4) the meshing procedure is applied to the model, (5) an appropriate solver is selected and executed (usually COMSOL automatically selects the solver type, depending on the AC/DC interface) and (6) the results are displayed.

4.3 Model Geometry

4.3.1 Simulated Vascular System

The Simulated Vascular System (SVS) COMSOL model consisted of a conductive cylindrical region of 40 mm in diameter and 20 mm in length. This region crudely simulated a lump of muscle and fat tissues in a human limb. The cross sectional dimensions of the SVS COMSOL model were chosen to be the same as the practical SVS system which is discussed in Chapter 5. The COMSOL SVS cylindrical region was also surrounded by a 5 mm annulus (also 20 mm long) which represented a layer of static water as illustrated in Figure 4.1(b). This annulus modelled wet, conductive skin (skin with applied electrolyte gel). Hence, the overall diameter of the SVS COMSOL model was 50 mm. Note that the length of the SVS COMSOL model was chosen to be 20 mm, unlike the length of the SVS practical model which was 200 mm as will be shown in Chapter 5, in order to reduce simulation time. When the model is smaller, COMSOL will take less computational time to work out the solution to the PDEs. This length factor did not affect the results of the flow induced potential differences obtained as the only area of interest was the cross sectional area, where the imposed water flow in the tubes intersects with the magnetic field.

At the boundary of the area where the water flow intersected with the applied magnetic field, 16 electric potentials were collected starting from electrode e_1 (at 0°) and at rotational intervals of 22.5° up to electrode e_{16}, as shown in Figure 4.1(a). In the practical experiment, these measurement points were electrodes that are in contact with the static layer of water. The SVS COMSOL model had two tubes ‘a’ and ‘b’ of 10 mm in diameter and 20 mm in length. Both tubes were offset from the centre by $\pm$10 mm. Water flow was either imposed in tube ‘a’ only, ‘b’ only or both. Moreover, each tube could be positioned at different angles with respect to e_1. In Figure 4.1(a), tubes 'a' and 'b' are at 0° and 180° with respect to electrode e_1, respectively. The other tube positions will be described in detail in Section 4.7. Figure 4.1(b) shows the COMSOL 3D model of the SVS.

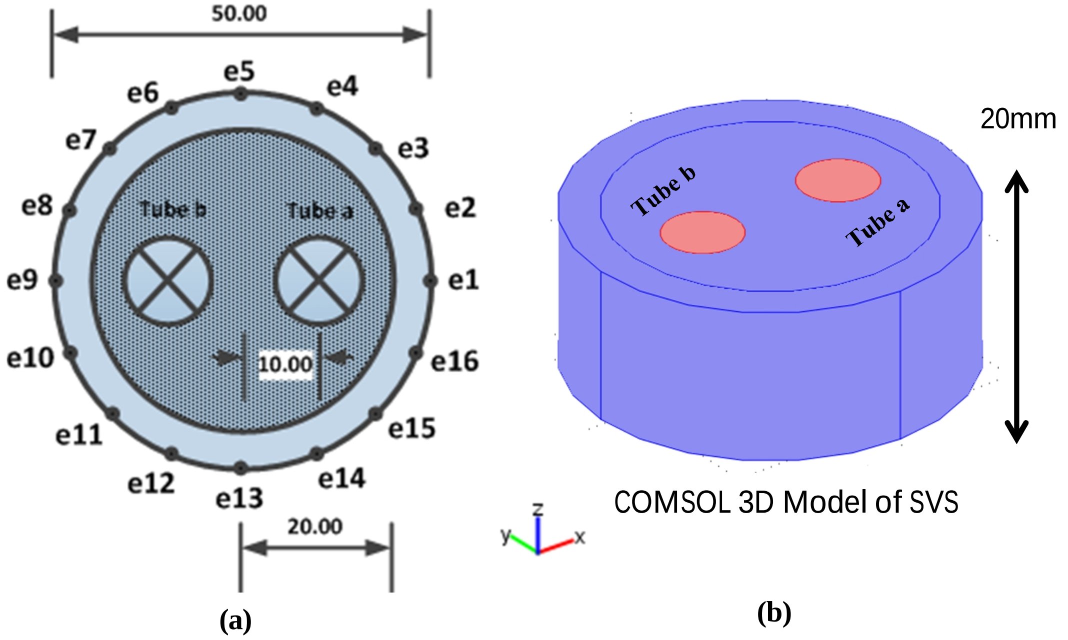

Figure 4.1: (a) SVS dimensions and electrode locations at which the electric potential measurements are taken (b) COMSOL 3D model

4.3.2 Helmholtz Coil

A Helmholtz coil is a pair of two identical solenoid electromagnets separated by a distance equal to their radius as shown in Figure 4.2. When the coil is excited, the magnetic field generated in the region bounded by the two solenoids is near uniform. This magnetic field is directly proportional to the number of turns of the coils and the applied current. A Helmholtz coil is used in a wide range of applications due to its simple design and the fact that it can easily be mathematically modelled to determine its magnetic flux density [167, 168]. The applications include magnetic sensor calibration, electromagnetic compatibility (EMC) testing, EM flow metering and bio-magnetic studies. The magnetic field generated can be static or time-varying, depending on the excitation source, i.e. DC or AC.

Both coils in the Helmholtz coil were designed to have a radius of 80 mm and a square cross-section of 20 mm as illustrated in Figure 4.3. The design and modelling of the Helmholtz coil is provided in the 'COMSOL AC/DC Module Model Library Handbook Version 3.5a' [169]. Note that, in the practical experiment described in Chapter 5, a C-shaped silicon-steel core electromagnet was built with an air-gap of 80 mm into which the SVS pipe was inserted. The reason for this was that an electromagnet with a metal core (higher permeability μ) generates stronger magnetic flux density than an air-core electromagnet ($B = \mu H$). Both the steel-core electromagnet in the practical experiment and the Helmholtz coil in the COMSOL simulation give a near-uniform magnetic field (in the y-direction) across the electrode array of the SVS. In COMSOL, it was easier to generate a uniform magnetic field using the Helmholtz coil by specifying the current density flowing in the coils at a given point in time. Figure 4.3 and Figure 4.4 show the SVS inserted between the coils.

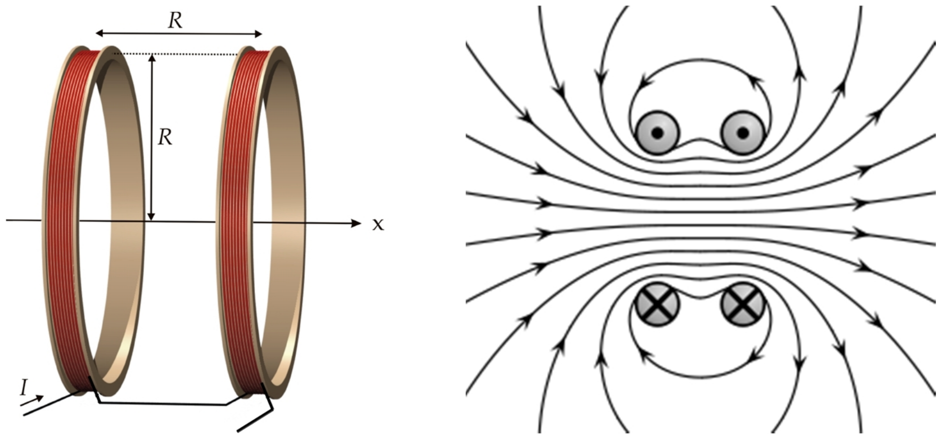

(a) **(b)**

Figure 4.2: (a) Helmholtz coil (b) uniform magnetic field in the region bound by both solenoids [170]

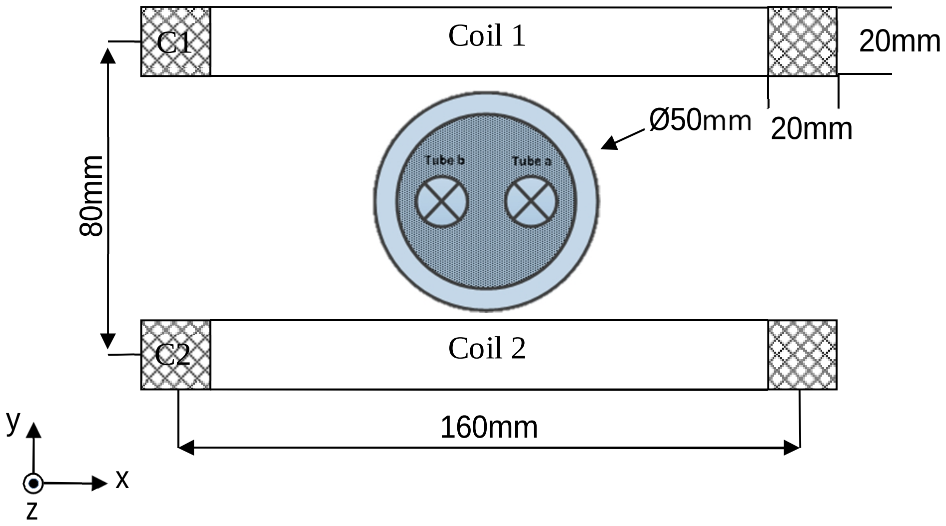

Figure 4.3: Helmholtz coil dimensions

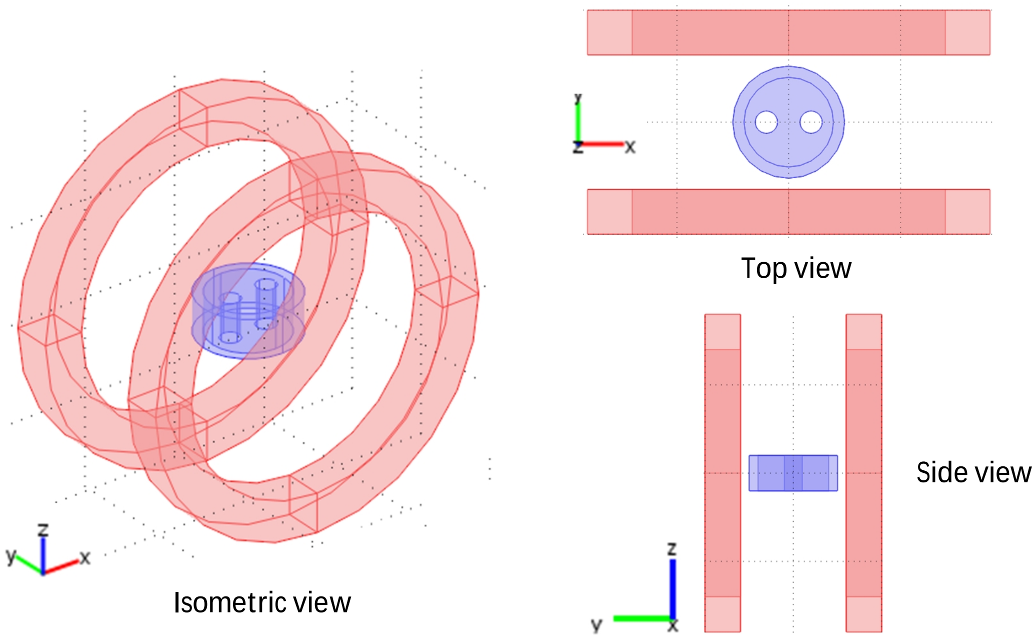

Figure 4.4: COMSOL 3D model of the Helmholtz coil and the SVS

Finally, the whole FE model was enclosed by a spherical computing domain of radius 0.15 m as shown in Figure 4.5. The computing domain is the exterior computing boundary domain where the conditions correspond to zero magnetic flux density. The magnetic boundary of the domain was set to magnetic insulation and its electric boundary was set to ground. Note that the magnetic field density B_0 direction in the model was set to be in the positive y-direction whereas, in Eq. 3-35, the magnetic field is in the negative y-direction. The effect of changing the direction of the magnetic field is explained in Section 3.4.

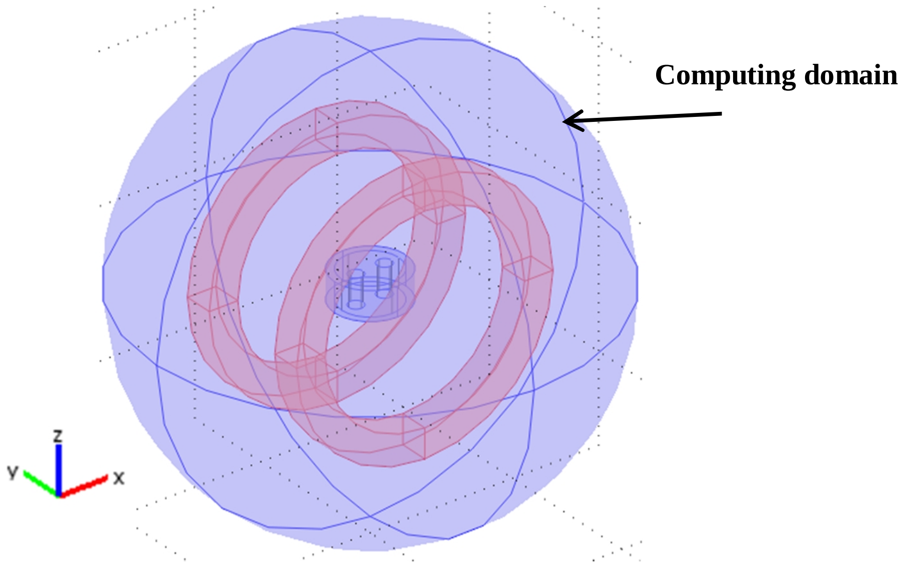

Figure 4.5: The Helmholtz coil and the SVS enclosed by a spherical computing domain

4.4 Governing Equations of the COMSOL FE Model

The local current density $\boldsymbol{j}$ (unit: A/m^2) for a conductive fluid in the presence of an EM field in a state of equilibrium, as described in Chapter 3, is given by

$$\boldsymbol{j} = \sigma(\boldsymbol{E} + \boldsymbol{v} \times \boldsymbol{B}) \qquad \text{Eq. 4-1}$$

where σ is the local fluid conductivity, $\boldsymbol{E}$ is the local electric field due to the force that charges exerted on one another and $\boldsymbol{v} \times \boldsymbol{B}$ is the local electric field generated by the moving charges through the magnetic field. For fluids with constant conductivity, Eq. 4-1 is simplified so that the distribution of the potential U in the flow cross-section can be obtained by solving the following partial differential equation

$$\nabla^2 U = \nabla \cdot (\boldsymbol{v} \times \boldsymbol{B}) \qquad \text{Eq. 4-2}$$

In conjunction with Eq. 4-1 and Eq. 4-2, COMSOL uses the magnetostatics form of Maxwell's equations to add modelling constraints (stationary magnetic field, i.e. steady current) which are [165, 169]

$$\nabla \cdot \boldsymbol{B} = 0 \qquad \text{Eq. 4-3}$$

$$\nabla \cdot \boldsymbol{j} = 0 \qquad \text{Eq. 4-4}$$

Eq. 4-3 states that the magnetic field lines have no sources or sinks and Eq. 4-4 indicates that the net charge density ρ is constant, i.e. steady current ($\partial\rho/\partial t = 0$). The Helmholtz coil represents another case in magnetostatics where the current applied to the coils is steady (steady flow of charge). Hence, the equations governing the magnetic field generation in the Helmholtz coil are also Eq. 4-3 and Eq. 4-4 as well as the equation stated below

$$\nabla \times \boldsymbol{B} = \mu_0 \boldsymbol{j_f} \qquad \text{Eq. 4-5}$$

where μ_0 is the permeability of vacuum and $\boldsymbol{j_f}$ is the total current density due to free charges. Alternatively, the governing Maxwell's equation in terms of the magnetic field intensity is

$$\nabla \times \boldsymbol{H} = \boldsymbol{j_f} \qquad \text{Eq. 4-6}$$

where $\boldsymbol{j_f}$ is the free current density. Eq. 4-5 can be written as the curl of the magnetic vector potential $\boldsymbol{A}$, [171] as follows

$$\boldsymbol{B} = \nabla \times \boldsymbol{A} \qquad \text{Eq. 4-7}$$

The ratio between the magnetic flux density $\boldsymbol{B}$ and the magnetic field intensity $\boldsymbol{H}$ is the permeability of vacuum μ_0 (for a Helmholtz coil). Thus,

$$\boldsymbol{H} = {\mu_0}^{-1} \boldsymbol{B} \qquad \text{Eq. 4-8}$$

From Eq. 4-6 to Eq. 4-8, and assuming static currents and fields,

$$\nabla \times ({\mu_0}^{-1} \nabla \times \boldsymbol{A}) = \boldsymbol{j_f} \qquad \text{Eq. 4-9}$$

Eq. 4-9 is the domain equation that COMSOL Multiphysics uses to solve this magnetostatic problem [171]. The current density $\boldsymbol{j_f}$ is known as the external applied current density $\boldsymbol{j^e}$ in COMSOL Multiphysics and is defined by the user. Note that the current density in the coil is given by

$$j = \frac{NI}{A} \qquad \text{Eq. 4-10}$$

where j is the current density, N is the number of turns, I is the current and A is the cross-sectional area of the coil (m^2).

4.5 Physics Settings of the Model, Mesh Generation and Solver Type

There were several parameters that it was necessary to set for the SVS model and the Helmholtz coil in COMSOL Multiphysics. These parameters included, the conductivity of the water and Helmholtz coil, the relative permeability of the materials, the external current density (j^e) applied to the Helmholtz coil and the velocity of water in the flow channels. These parameters were configured from “Sub-domain Settings” in the “Physics” drop-down menu in the main toolbar of COMSOL Multiphysics software.

The COMSOL SVS model was set to the conductivity of water which is 0.013 S/m (typical conductivity value in Northern England). The material of the Helmholtz coil was set to copper which has a conductivity of 5.998×10^7 S/m. The relative permeability of the SVS and Helmholtz coil was set to 1. The external applied current density (j^e) of the Helmholtz coil was set to -3.3389×10^6 A/m^2. For this value, COMSOL generated a magnetic flux density in the y direction of approximately 1 mT (10 gauss) across the SVS model. The negative sign sets the magnetic field direction in the positive y-direction. The water flow velocity was set to 50 m/s. This value is artificially high in comparison to the peak velocity of blood flow in arteries which is around 1 m/s as shown in Section 1.2.4. However, in the practical SVS system described in Chapter 5, the magnetic flux density value was 42.5 mT and the flow induced electric potentials are directly proportional to the product of the flow velocity v and the magnetic flux density B. Hence, the magnitude of the flow induced potentials obtained from the FE will be approximately similar in magnitude to the flow induced potentials which are obtained from the practical experiment.

Once all the parameters were set, the meshing process was applied to the model. The aim was to predefine the mesh settings to achieve a good balance between accuracy and required CPU time. The finer the mesh, the more accurate the results would be. However, a finer mesh requires more CPU time. In the region of the SVS, including the flow channels and the static layer of water, the mesh settings were entered manually. There were two settings which had to be predefined: "Maximum element size" and "Element growth rate[6]", and they were set to 0.08 and 1.2, respectively. The mesh settings for the Helmholtz coil and the computing domain were set to "Coarse" which is a predefined mesh size that is automatically set by COMSOL Multiphysics.

The mesh of the SVS region was finer than the mesh of the Helmholtz coil and the computing domain as it was the region of interest. These settings showed a good balance between CPU time and spatial resolution. Figure 4.6 shows the mesh of the complete model. The solver selected was the SPOOLES direct solver which is one of the linear system solvers provided by COMSOL Multiphysics. This solver supports multithreading and error checking. The results obtained from solving the model in COMSOL are the magnetic flux density generated across, and the flow induced electric potentials at the boundary of, the SVS cross-section. The magnetic flux density was expected to be uniform and in the order of 1 mT.

[6] Element growth rate determines how fast the elements should grow from small to large over a domain (COMSOL User's Guide Manual 2013).

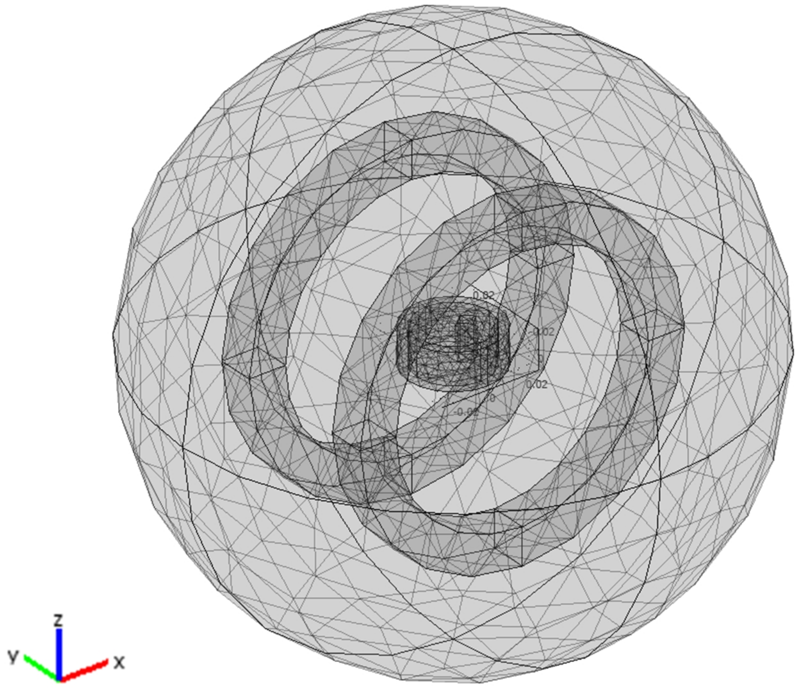

Figure 4.6: The mesh of the 3D COMSOL FE model.

4.6 Magnetic Flux Density Distribution of the Helmholtz coil

The magnetic flux density plot of the Helmholtz coil model is shown in Figure 4.7 and Figure 4.8. The colour bar indicates the magnetic flux density value and the red arrows indicate the direction of the magnetic field. It can be seen that the magnetic flux density across the SVS is uniform (straight red arrows where the SVS is). The magnetic flux density was approximately 1 mT (10 gauss) in the region of the SVS. The y-component of the magnetic flux density is the component that is perpendicular to the flow direction (z-component). Figure 4.9 show the magnetic flux density in the cross section of the SVS in x-y plane where z = 0. It can be seen from Figure 4.10 that the variation in the magnetic flux density within the cross section of the SVS, i.e. between −0.02 to 0.02 m is very small. In fact the variation in that area is between 0.9891 and 1.006 mT which is only 0.4%. Hence, it is clear that the magnetic field is approximately uniform across the SVS model.

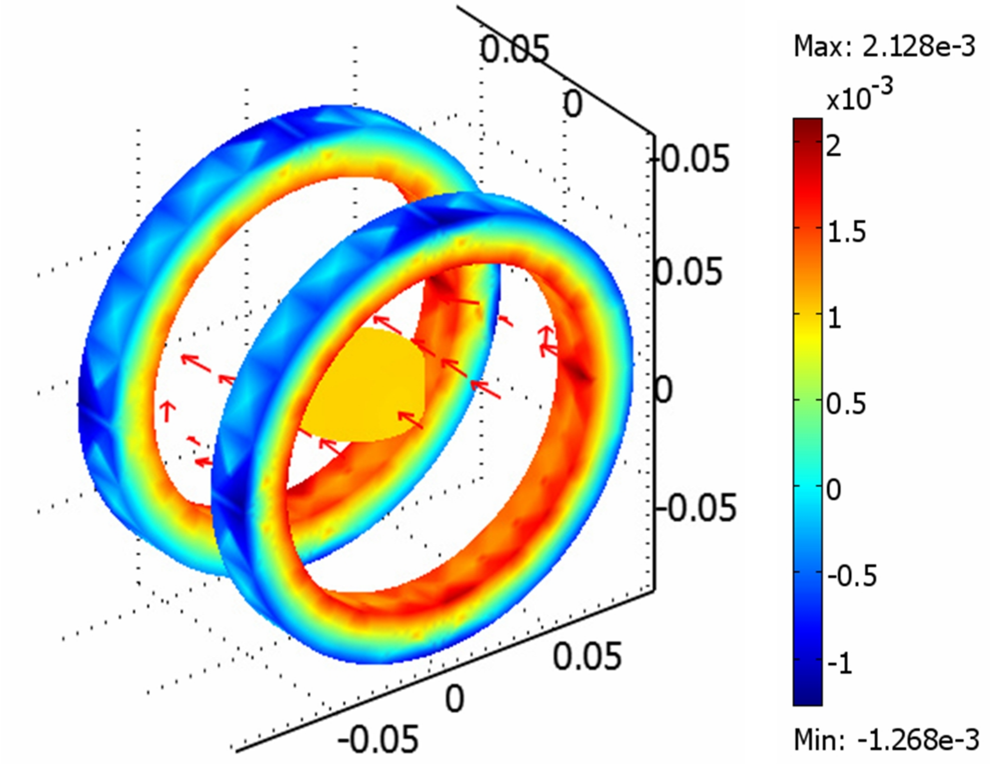

Figure 4.7: Subdomain: colour scale magnetic flux density, y component (T). Arrow: magnetic field direction. Note that x, y and z axes are in metres.

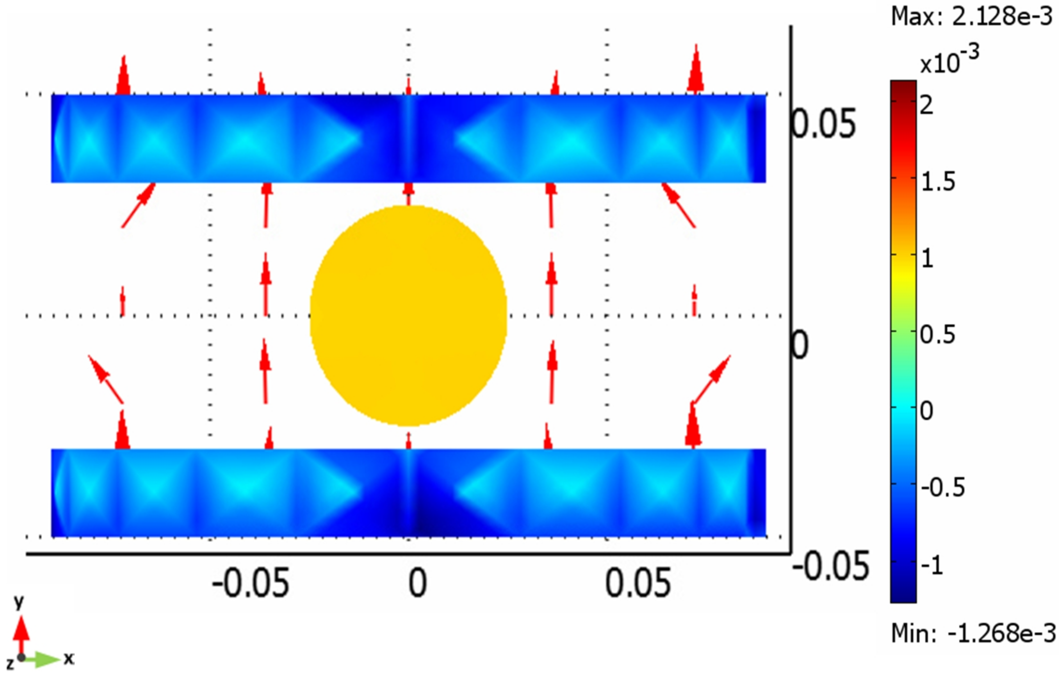

Figure 4.8: Subdomain: colour scale magnetic flux density, y component (T). Arrow: magnetic field direction. Note that x, y and z axes are in metres.

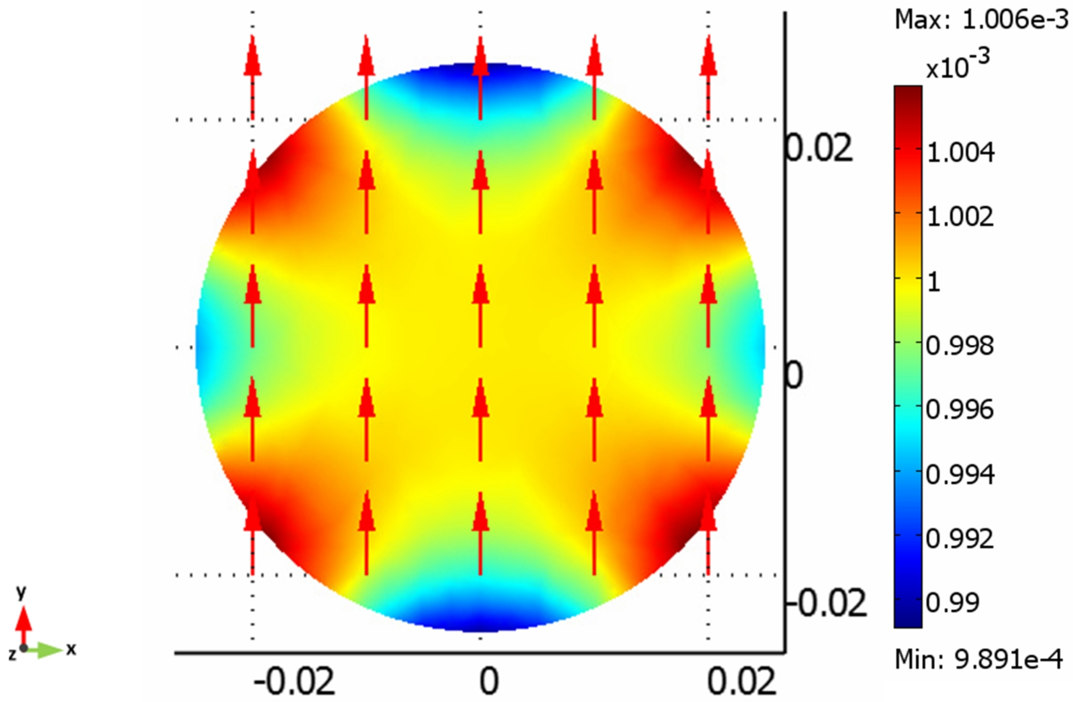

Figure 4.9: Subdomain: colour scale magnetic flux density, y component (T). Arrow: magnetic field direction. Note that x, y and z axes are in metres.

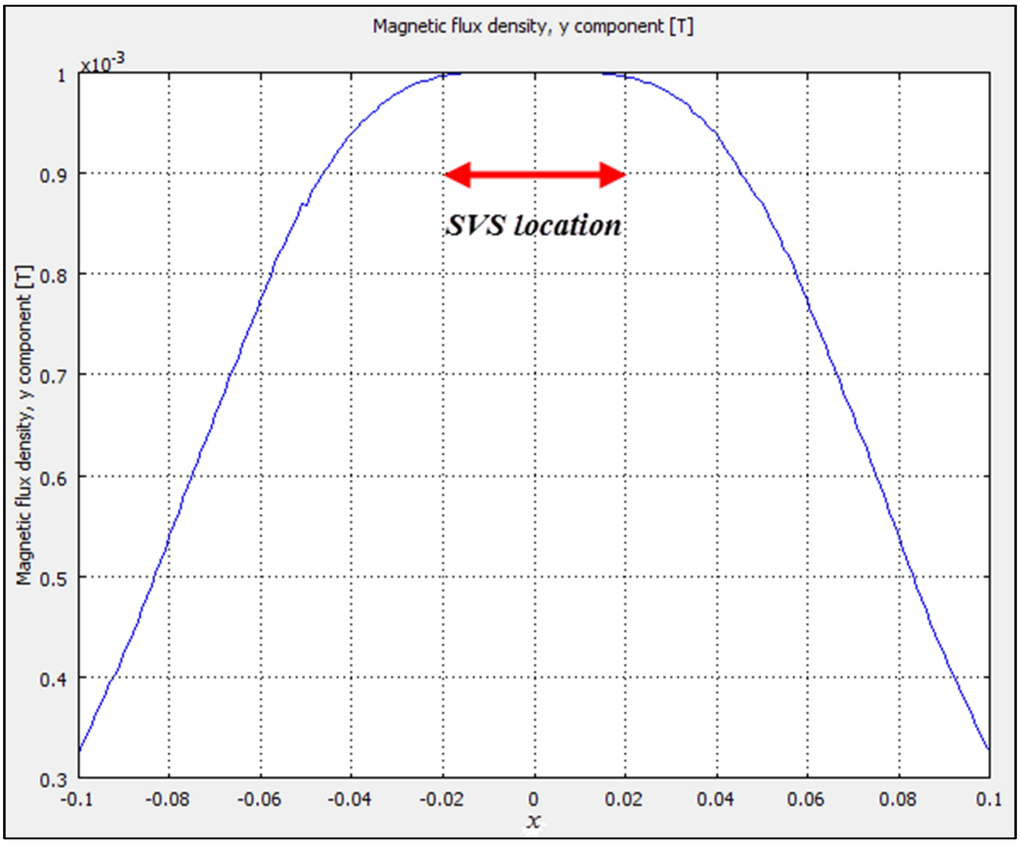

Figure 4.10: Magnetic flux density, y component (T) across the SVS model. Note that x axis is in metres.

4.7 SVS Flow Induced Potential Difference Measurement Results

4.7.1 Test Setups

The flow induced potentials U_j were collected at the boundary of the SVS region, where the electrode points are, as shown in Figure 4.1(a). Three main tests were performed:

1. Water flow imposed through tube ‘a’ only
2. Water flow imposed through tube ‘b’ only
3. Water flow imposed through tubes ‘a’ and ‘b’ simultaneously

For each test, tube ‘a’ or ‘b’ (or both) was rotated by steps of 22.5° clockwise with respect to electrode point e_1. For example, tube ‘a’ was first at 0° with respect to electrode point e_1 and the model was solved and the flow induced potentials were collected. Then, it was rotated by another 22.5° and so on. Tube ‘a’ was rotated until it was at 135° with respect to electrode e_1. Figure 4.11 shows tube ‘a’ at different positions with respect to electrode e_1.

For every new position for tube ‘a’, 16 flow induced potential differences were obtained, i.e. e_1-e_5, e_2-e_5, e_3-e_5 … e_{16}-e_5. Moreover, two flow velocities v were used for each tube position, $v = 25$ m/s and $v = 50$ m/s. Tube ‘a’ is 10 mm in diameter and hence, for these two velocities, the corresponding flow rate in tube ‘a’ would be $Q_T = 1.96\times10^{-3}$ m^3/s and $Q_T = 3.93\times10^{-3}$ m^3/s. Similarly, tube ‘b’ was positioned firstly at 180° with respect to e_1 and it was rotated by steps of 22.5° until it was at 292.5° with respect to e_1. At each position, the flow induced potentials were collected for the same flow rates in the tube ‘a’ test. Figure 4.12 shows the positions of tube ‘b’ with respect to electrode e_1.

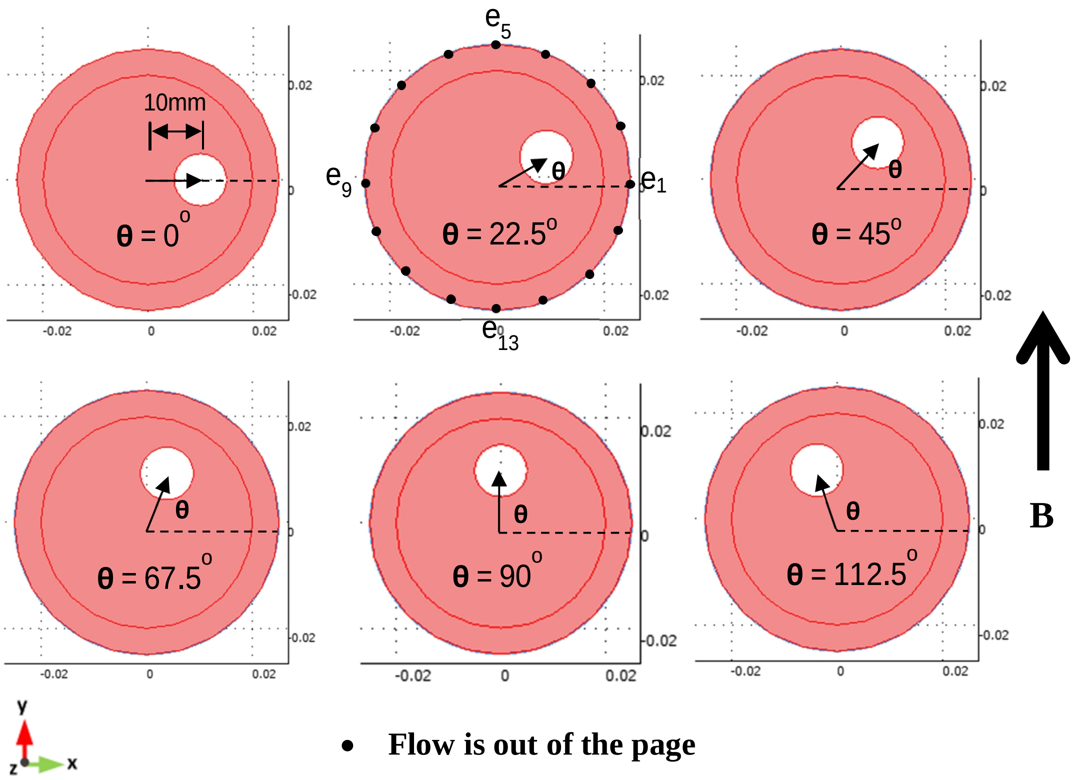

Figure 4.11: Tube 'a' at different positions with respect to electrode e_1

Lastly, water flow was imposed through both tubes ‘a’ and ‘b’, starting with tubes ‘a’ and ‘b’ positioned at 0° and 180° with respect to electrode e_1, respectively. Then, both tubes were rotated in steps of 22.5°. The water flow velocity was 12.5 m/s in each tube for a total flow rate of 1.96×10^{-3} m^3/s, and 25 m/s for a total flow rate of 3.93×10^{-3} m^3/s (maintaining the same total volumetric flow rate as in the other two tests). Figure 4.13 shows all positions of both tubes ‘a’ and ‘b’ with respect to electrode e_1. Note that the magnetic flux density in all the tests was the same – approximately 1 mT.

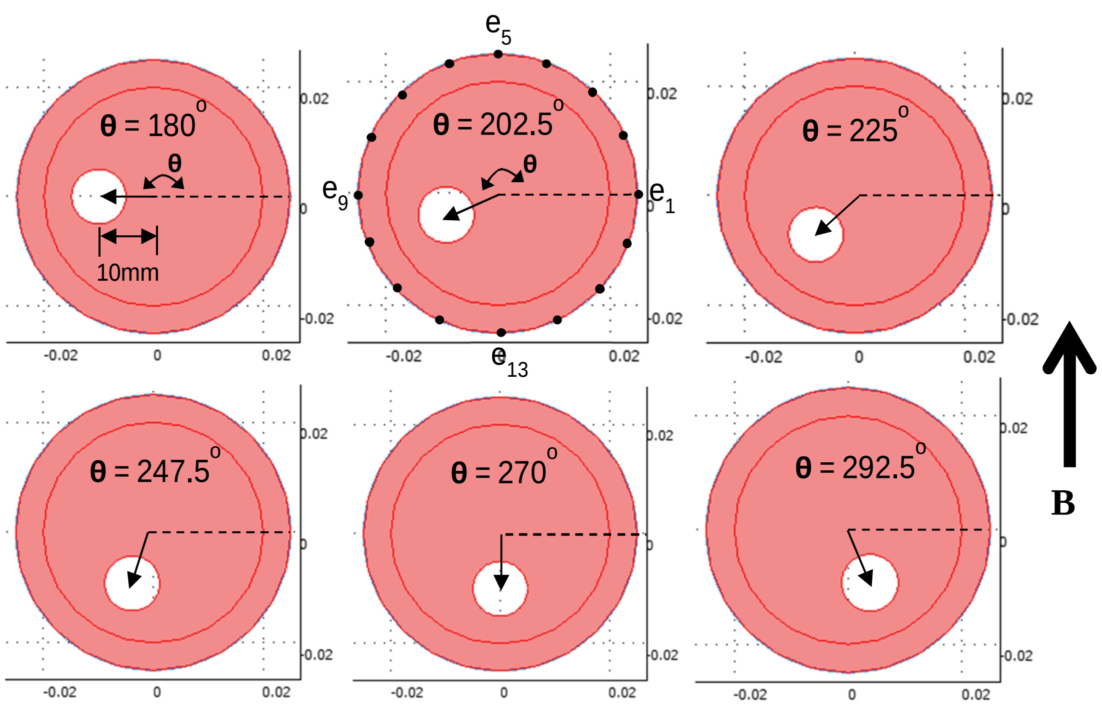

- **Flow is out of the page**

Figure 4.12: Tube 'b' at different positions with respect to electrode e_1

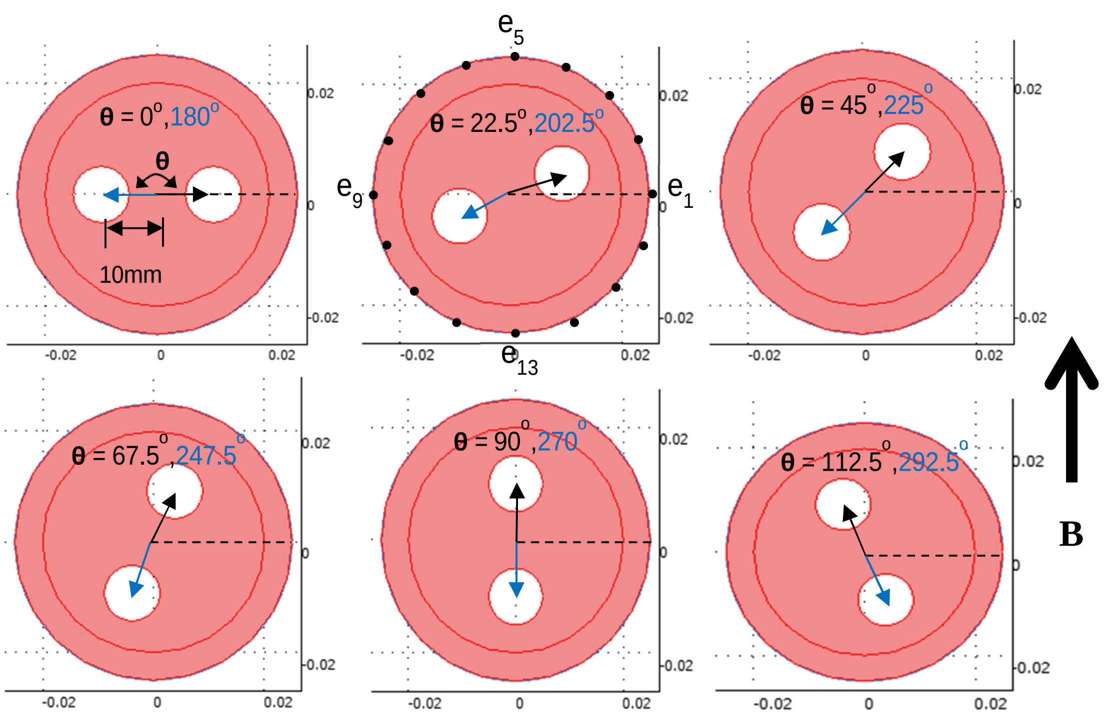

- **Flow is out of the page**

Figure 4.13: Tubes 'a' and 'b' at different positions with respect to electrode e_1

4.7.2 Flow Induced Potential Difference Measurement Results

The flow induced potential measurements U_j at the boundary of the SVS were collected for each tube/s location and flow rate, as described in Section 4.7.1. These flow induced potentials were referenced to the potential at electrode e_5 (reference electrode), i.e. $U_j - U_5$ to obtain flow induced potential differences. Then these potential differences were compared with the flow induced potential differences obtained from the mathematical model given in Eq. 3-32 and Eq. 3-33 in Chapter 3. The same flow rate and magnetic flux density values were used in the FE and the mathematical models. For example, to obtain the flow induced potential differences using Eq. 3-32 and Eq. 3-33 for tube 'a' only located at 0^o with respect to electrode e_1 as shown in Figure 4.11, the steps are as follow:

- Setting the values of r_g = 10 mm, θ_g = 0° (polar coordinates of tube 'a' with respect to electrode e_1)
- Setting the magnetic flux density B_o = 1 mT, the flow rate in the channel Q_g = 1.96×10^{-3} m^3/s and $k_1 = \frac{1}{2\pi R}$ where R = 25 mm
- Then, finding the value of U_j where j = 1 to 16 (the number of electrodes) by changing the angle value of ψ_{in} from 0° to 337.5° in steps of 22.5°, i.e. for electrode e_1, ψ_{in} = 0°, for electrode e_2, ψ_{in} =22.5° and so on.
- Lastly, referencing all 16 potentials U_j to the potential U_5, i.e. $U_j - U_5$

Test 1: Water Flow Imposed in Tube ‘a’

Figure 4.14 depicts the contour plot of the electrical potential distribution for tube ‘a’, positioned at 0° with respect to electrode e_1 for two different flow rates, i.e. 1.96×10^{-3} m^3/s and 3.93×10^{-3} m^3/s. Contour plots were only performed in the COMSOL FE model. The magnetic flux density B_o was in the positive y-direction and the water flow was in the positive z-direction (out of the page). Hence, the Lorentz force $\boldsymbol{v} \times \boldsymbol{B}$ was in the negative x-direction, represented by the blue arrows in Figure 4.14 (Fleming’s right-hand rule). If the magnetic field is changed to be in the negative y-direction or the flow is changed to be in the negative z-direction, the Lorentz force will then to be in the positive x-direction (mutually perpendicular vectors). For all the other tests, the direction of the Lorentz force was the same as the direction of the magnetic field and the water flow was not changed.

The flow induced potential differences U_j (j = 1 to 16) for tube ‘a’ located at 0° with respect to electrode e_1 obtained from the FE and theoretical models are plotted in Figure 4.15. It can be noted that there is very good agreement between the flow induced potential difference distribution of the FE model and the theoretical model. However, there was a slight difference between the results for both models due to numerical errors in the COMSOL FE model which is dependent on the FE solver type and mesh size. However, the results were very similar and satisfactory.

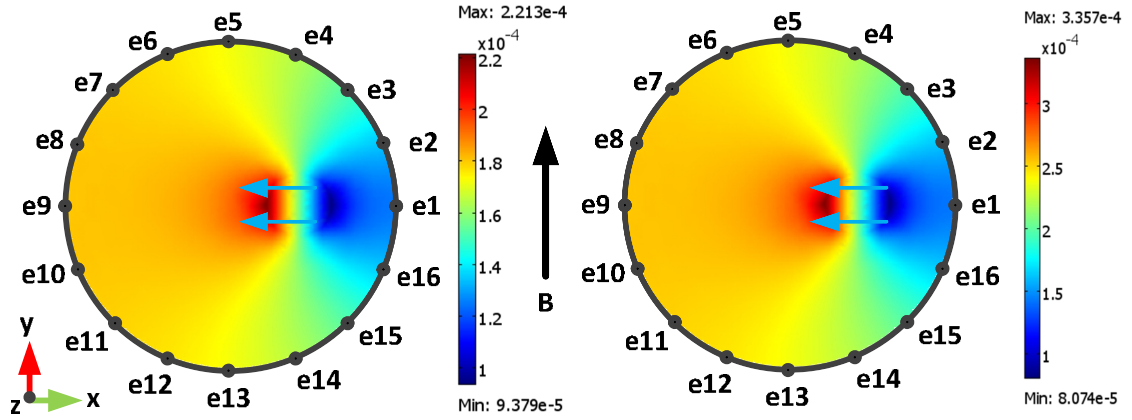

Figure 4.14: Electrical potential distribution for tube 'a' positioned at 0° with respect to e_1 for flow rates of 1.96×10^{-3} m^3/s (left) and 3.93×10^{-3} m^3/s (right). The blue arrows indicate the direction of Lorentz force.

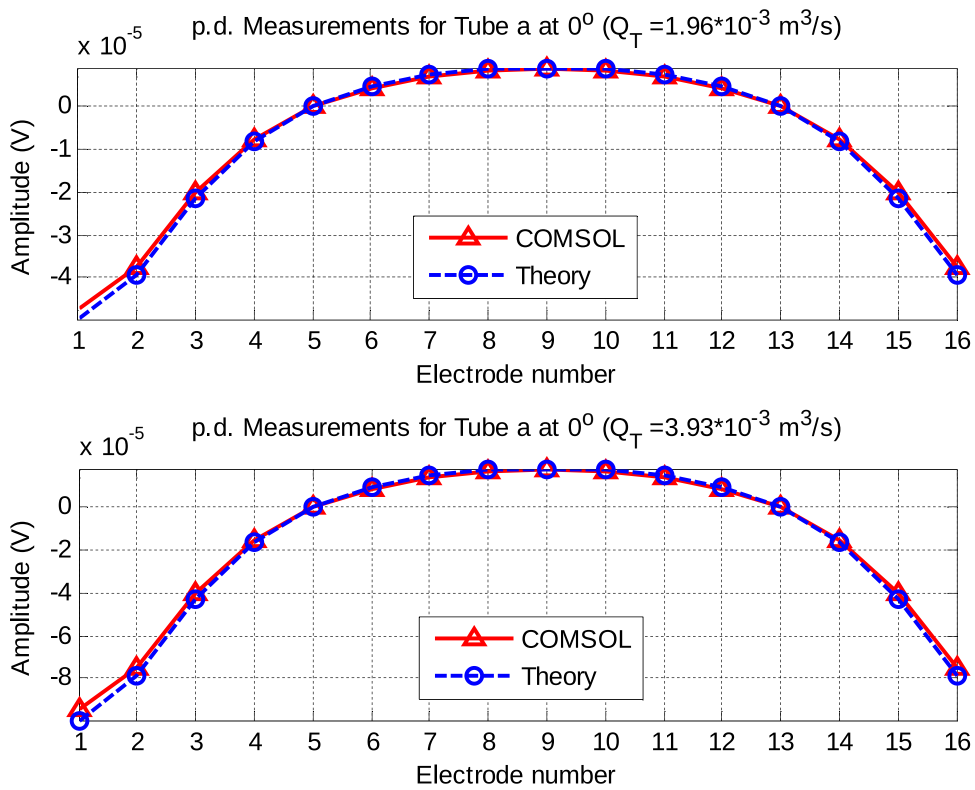

Figure 4.15: Induced potential difference measurements for tube 'a' positioned at 0° with respect to e_1 for flow rate values of 1.96×10^{-3} m^3/s and 3.93×10^{-3} m^3/s

Tube 'a' was then rotated by 22.5° with respect to electrode e_1. Figure 4.16 shows the contour plot of the electrical potentials for the low and high flow rates. The flow induced potential differences obtained from the FE and theoretical models for this test are presented in Figure 4.17.

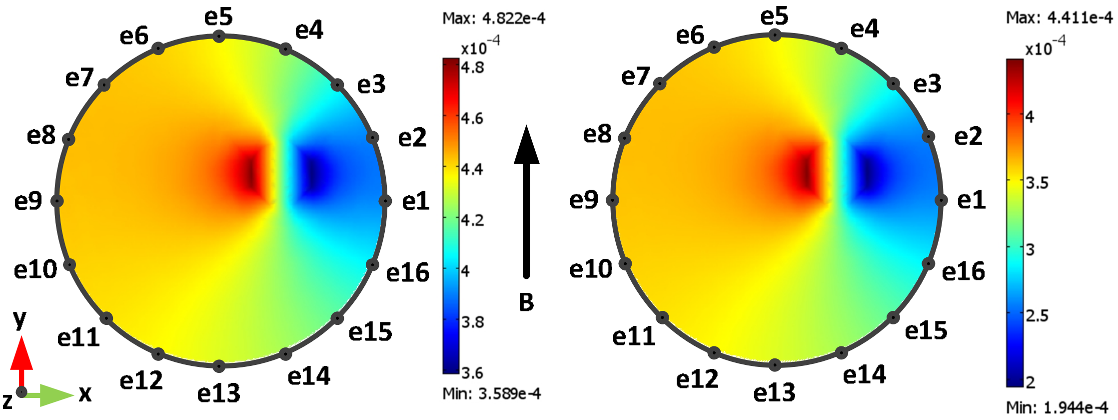

Figure 4.16: Electrical potential distribution for tube 'a' positioned at 22.5° with respect to e_1 for flow rates of 1.96×10^{-3} m^3/s (left) and 3.93×10^{-3} m^3/s (right) (COMOSL model only)

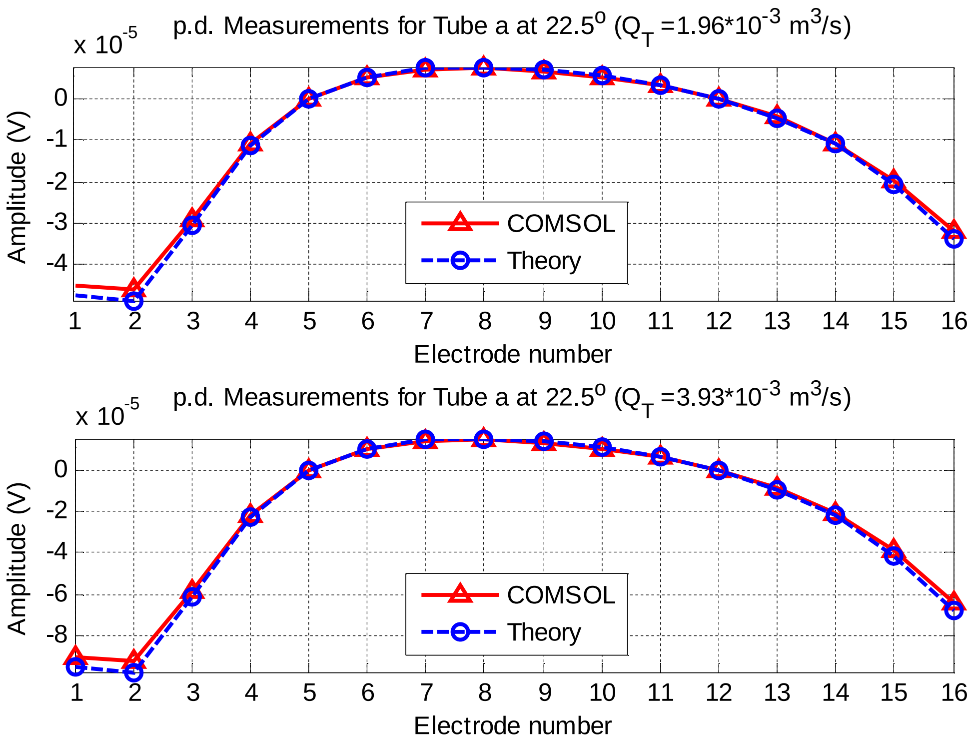

Figure 4.17: Induced potential difference measurements for tube 'a' positioned at 22.5° with respect to e_1 for flow rate values of 1.96×10^{-3} m^3/s and 3.93×10^{-3} m^3/s

It can be noted from Figure 4.17 that for the same tube position, the profile of the flow induced potential difference distribution for both flow rates was identical. However, the amplitude of the flow induced potential differences for the high flow rate was greater (double the value) than the amplitude of the flow induced potential differences for the low flow rate. This was expected as the flow induced potentials are directly proportional to the flow rate and the high flow rate is twice greater than the low flow rate. Moreover, the tube position within the cross section of the SVS had an effect on the profile of the flow induced potential difference distribution when comparing Figure 4.17 with Figure 4.15.

Overall, Figure 4.17 shows that there is good agreement between the COMSOL and theoretical models for tube ‘a’ located at 22.5° with respect to e_1 for the given flow rate and magnetic flux density. The following plots show the remaining contour plots and flow induced potential difference distribution for the other positions of tube ‘a’ within the cross section of the SVS. Similar observations can be made in terms of the effects of the flow rate on the amplitude of the flow induced potential differences and the location of the tube on the profile of the flow induced potential difference distribution. The results obtained from the FE and theoretical models for tube ‘a’ for different flow rate and location within the cross-sectional area of the SVS showed very good agreement which validate the mathematical expression proposed in Eq. 3-32 and Eq. 3-33.

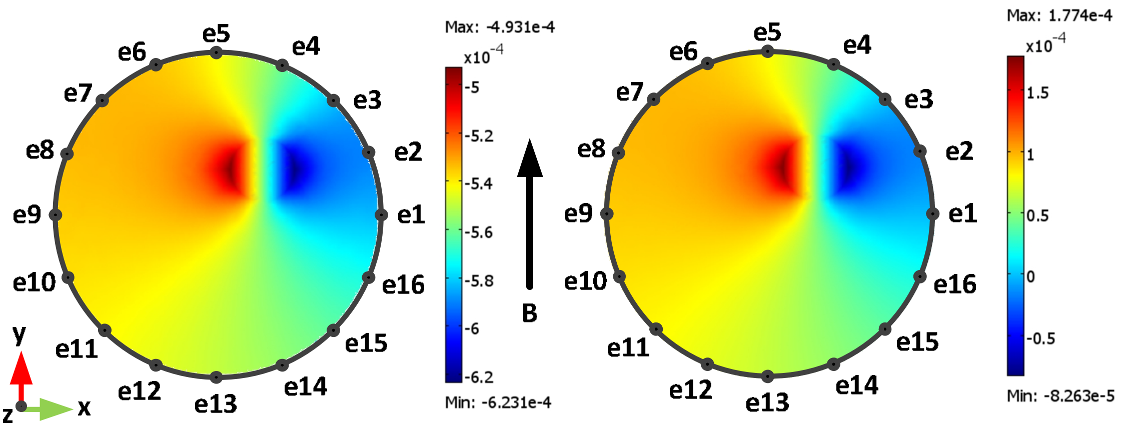

Figure 4.18: Electrical potential distribution for tube 'a' positioned at 45° with respect to e_1 for flow rates of 1.96×10^{-3} m^3/s (left) and 3.93×10^{-3} m^3/s (right) (COMOSL model only)

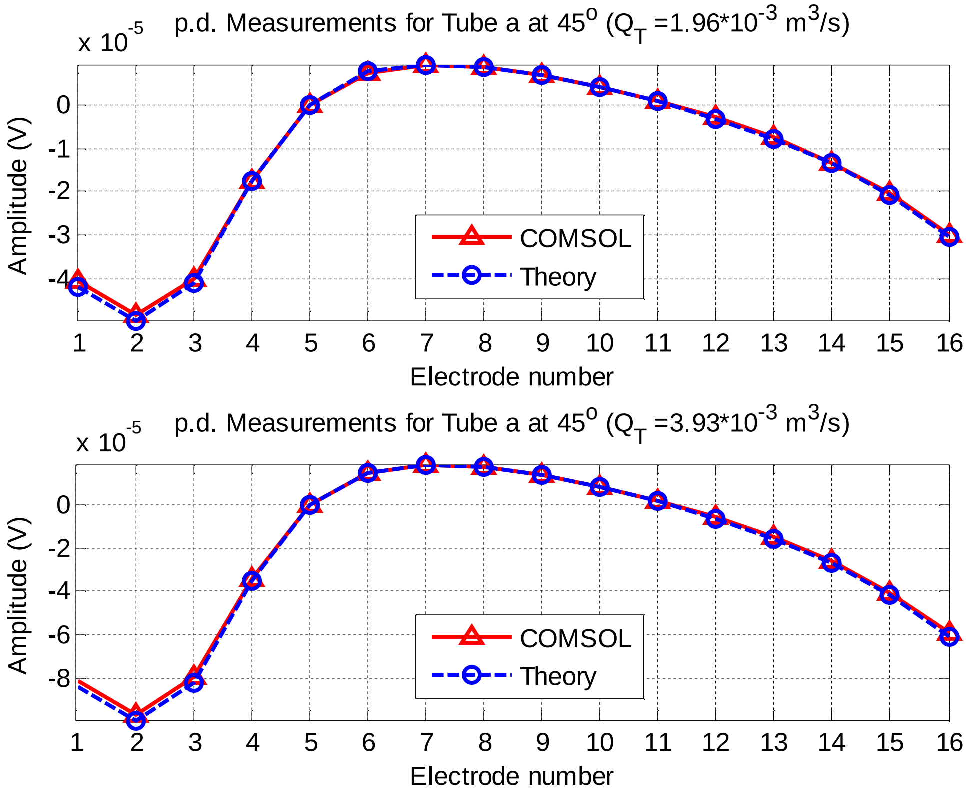

Figure 4.19: Induced potential difference measurements for tube 'a' positioned at 45° with respect to e_1 for flow rate values of 1.96×10^{-3} m^3/s and 3.93×10^{-3} m^3/s

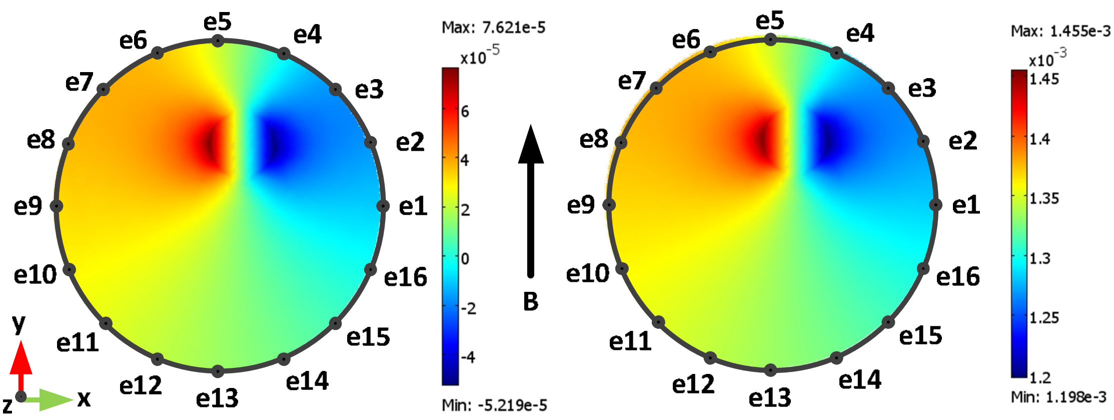

Figure 4.20: Electrical potential distribution for tube 'a' positioned at 67.5° with respect to e_1 for flow rates of 1.96×10^{-3} m^3/s (left) and 3.93×10^{-3} m^3/s (right) (COMOSL model only)

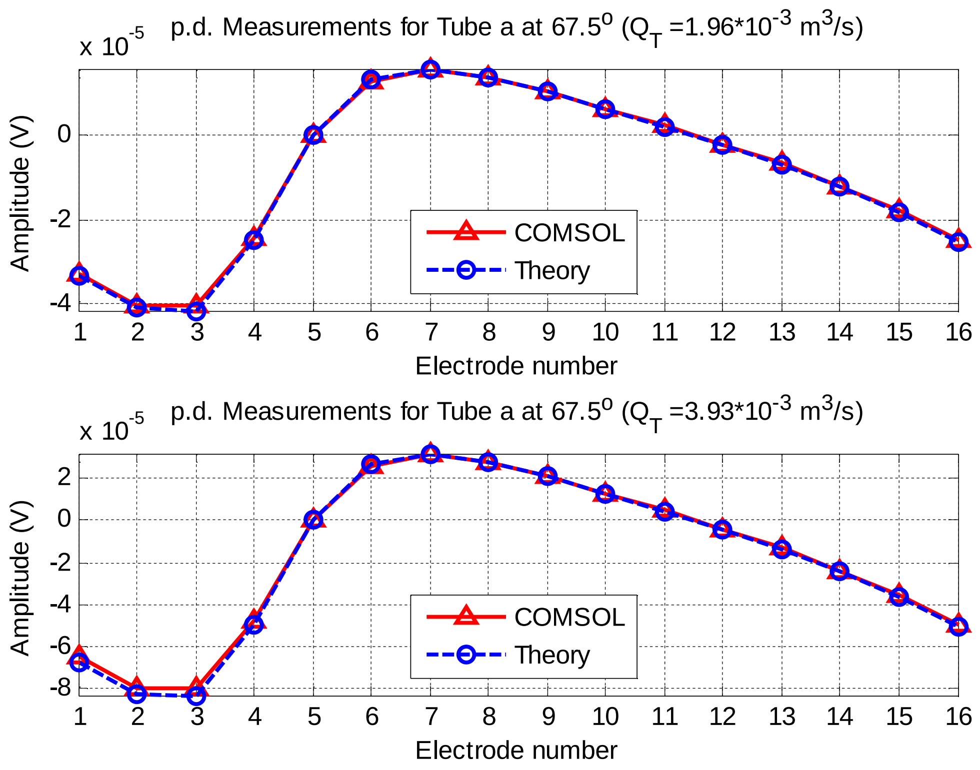

Figure 4.21: Induced potential difference measurements for tube 'a' positioned at 67.5° with respect to e_1 for flow rate values of 1.96×10^{-3} m^3/s and 3.93×10^{-3} m^3/s

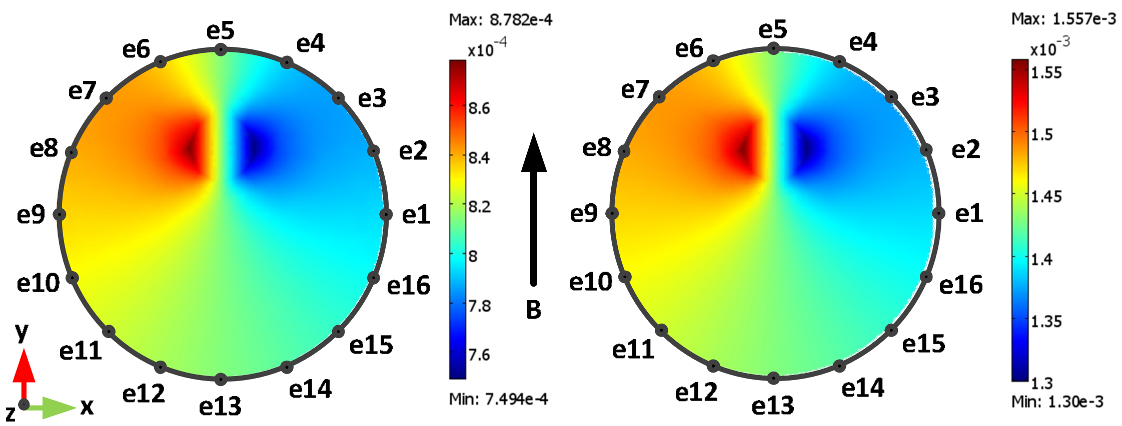

Figure 4.22: Electrical potential distribution for tube 'a' positioned at 90° with respect to e_1 for flow rates of 1.96×10^{-3} m^3/s (left) and 3.93×10^{-3} m^3/s (right) (COMOSL model only)

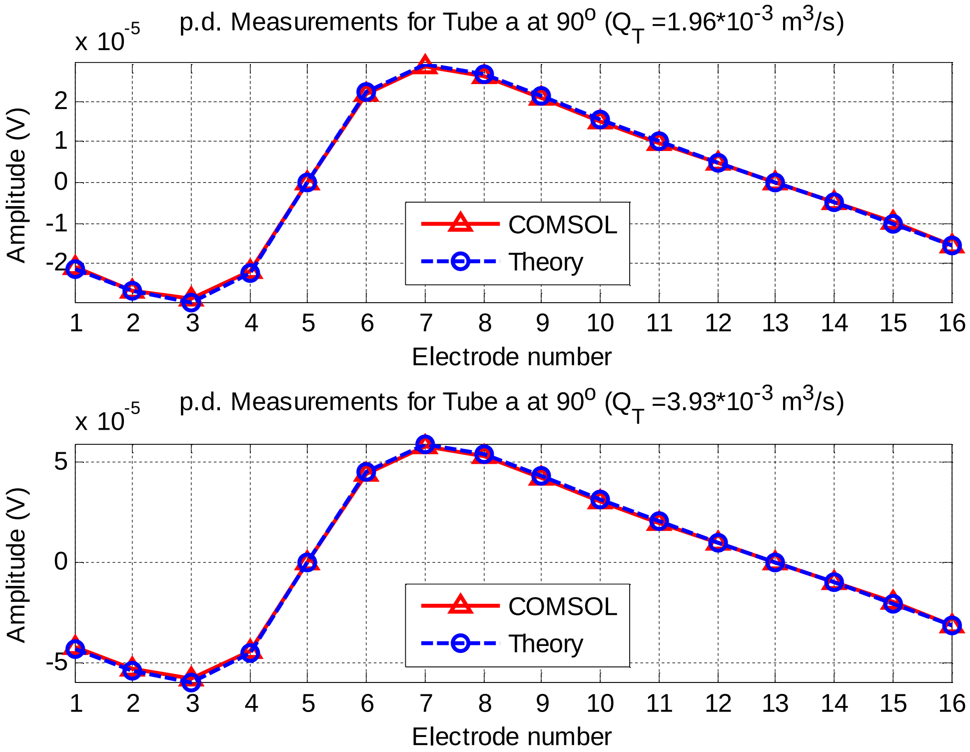

Figure 4.23: Induced potential difference measurements for tube 'a' positioned at 90° with respect to e_1 for flow rate values of 1.96×10^{-3} m^3/s and 3.93×10^{-3} m^3/s

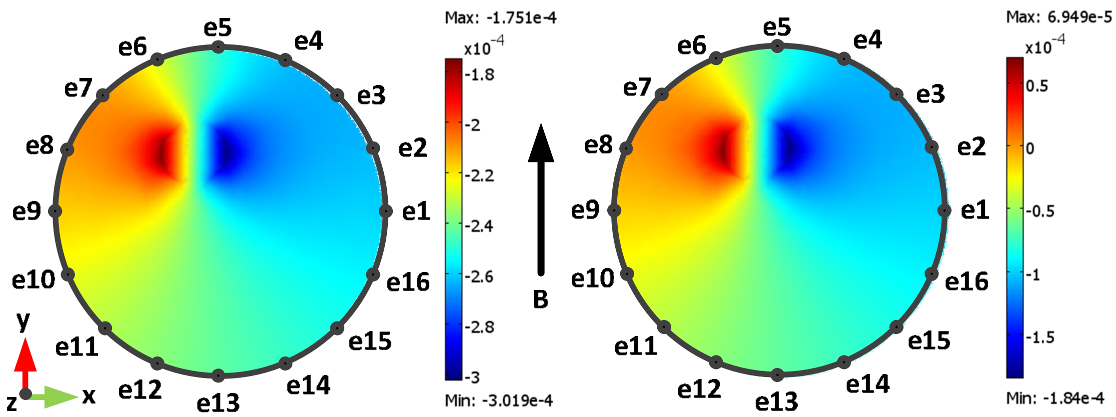

Figure 4.24: Electrical potential distribution for tube 'a' positioned at 112.5° with respect to e_1 for flow rates of 1.96×10^{-3} m^3/s (left) and 3.93×10^{-3} m^3/s (right) (COMOSL model only)

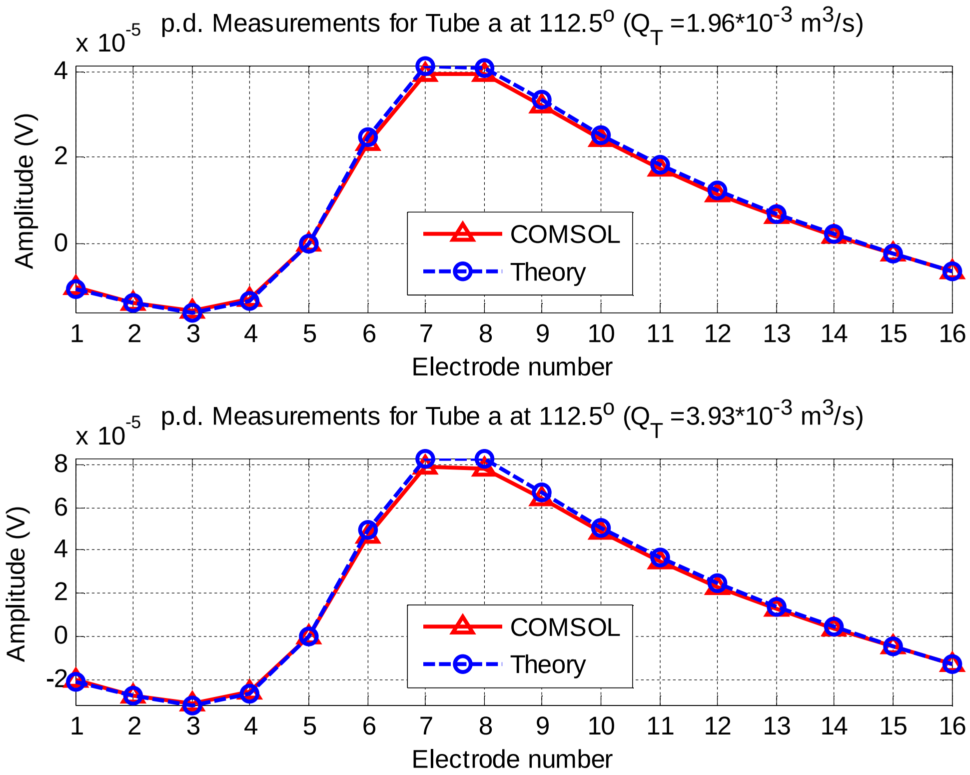

Figure 4.25: Induced PD measurements for tube 'a' positioned at 112.5° with respect to e_1 for flow rate values of 1.96×10^{-3} m^3/s and 3.93×10^{-3} m^3/s

Test 2: Water Flow Imposed in Tube ‘b’

In the following results, the contour plots of the electrical potential obtained from the FE model for tube ‘b’ at different locations within the cross section of the SVS for two flow rates, 1.96×10^{-3} m^3/s and 3.93×10^{-3} m^3/s, are presented. The flow induced potential differences $(U_j - U_5)$ obtained from the FE model were also compared with the flow induced potential difference measurements obtained from the theoretical model for the same flow rate values.

Similar observations to the ones noted from the tube ‘a’ tests can be made. Firstly, for a given tube location, the profile of the induced potential difference distribution was similar for the low and high flow rates in both FE and theoretical models as shown in Figure 4.27. It can also be seen from the same figure that the total flow rate was directly proportional to the amplitude of the flow induced potential difference (relative to e_5) at a given electrode. Hence, the amplitude of the flow induced potential differences obtained from the high flow rate test was greater (double the value) than the amplitude of the flow induced potential differences obtained from the low flow rate test. Lastly, the profile of the induced potential difference distribution was dependent on the location of the tube within the cross section bounded by the electrodes. It can be observed that the flow induced potential difference distribution for tube 'b' located at 180° with respect to electrode e_1 (Figure 4.27) is different from the flow induced potential distribution for the tube when it was located at 202.5° with respect to electrode e_1 (Figure 4.29) for the same flow rate value.

The following plots of the flow induced potential distribution for tube 'b' show that there is good agreement between the COMOSL FE model and the theoretical model given in Eq. 3-32 and Eq. 3-33, and this validates the proposed mathematical model.

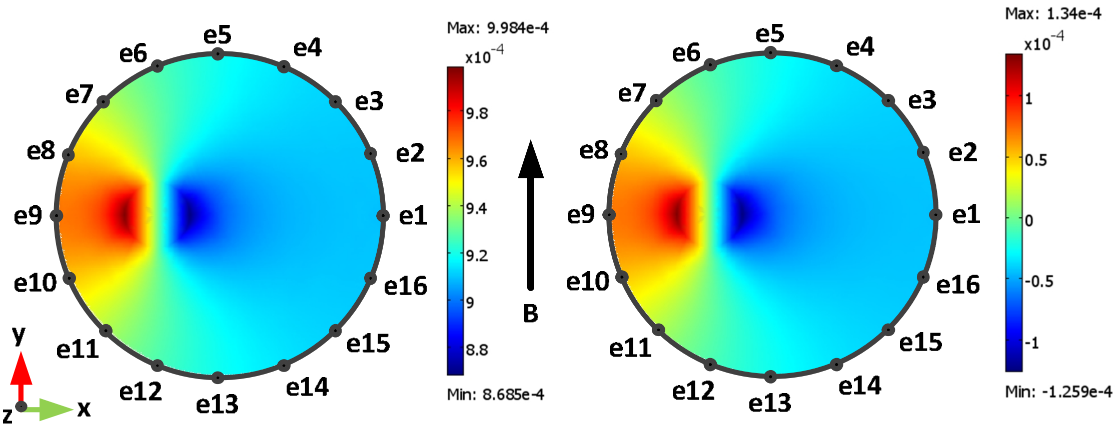

Figure 4.26: Electrical potential distribution for tube 'b' positioned at 180° with respect to e_1 for flow rates of 1.96×10^{-3} m^3/s (left) and 3.93×10^{-3} m^3/s (right) (COMOSL model only)

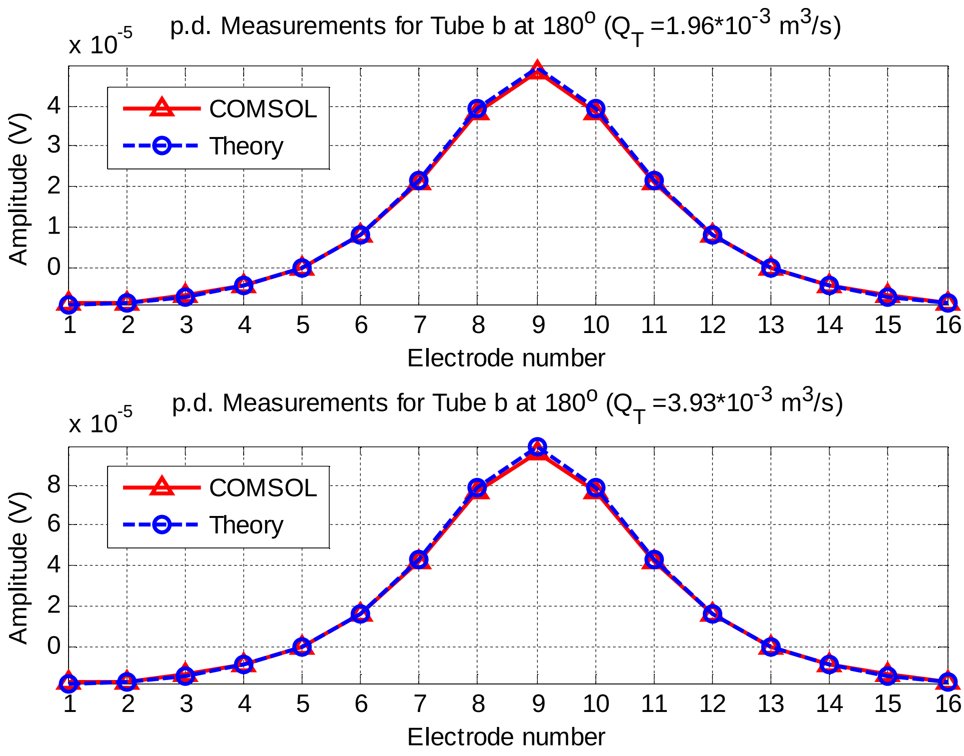

Figure 4.27: Induced potential difference measurements for tube 'b' positioned at 180° with respect to e_1 for flow rate values of 1.96×10^{-3} m^3/s and 3.93×10^{-3} m^3/s

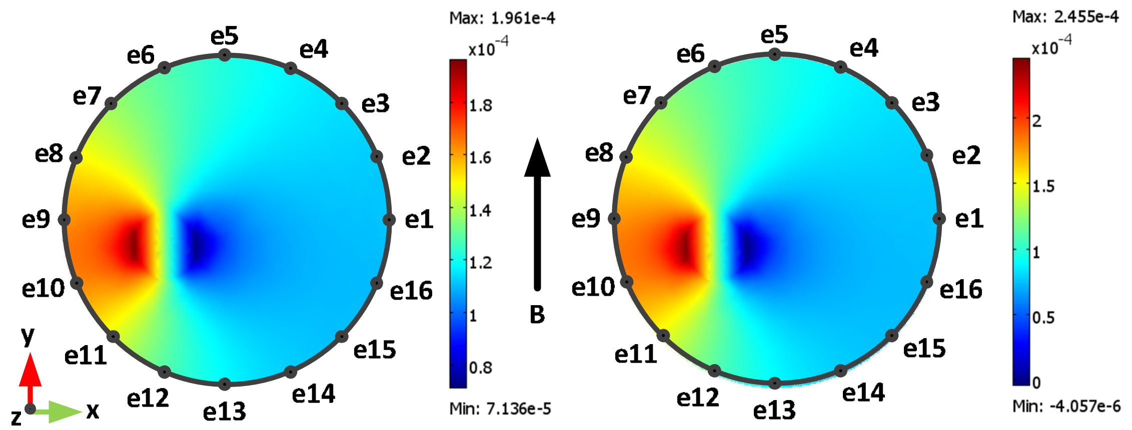

Figure 4.28: Electrical potential distribution for tube 'b' positioned at 202.5° with respect to e_1 for flow rates of 1.96×10^{-3} m^3/s (left) and 3.93×10^{-3} m^3/s (right) (COMOSL model only)

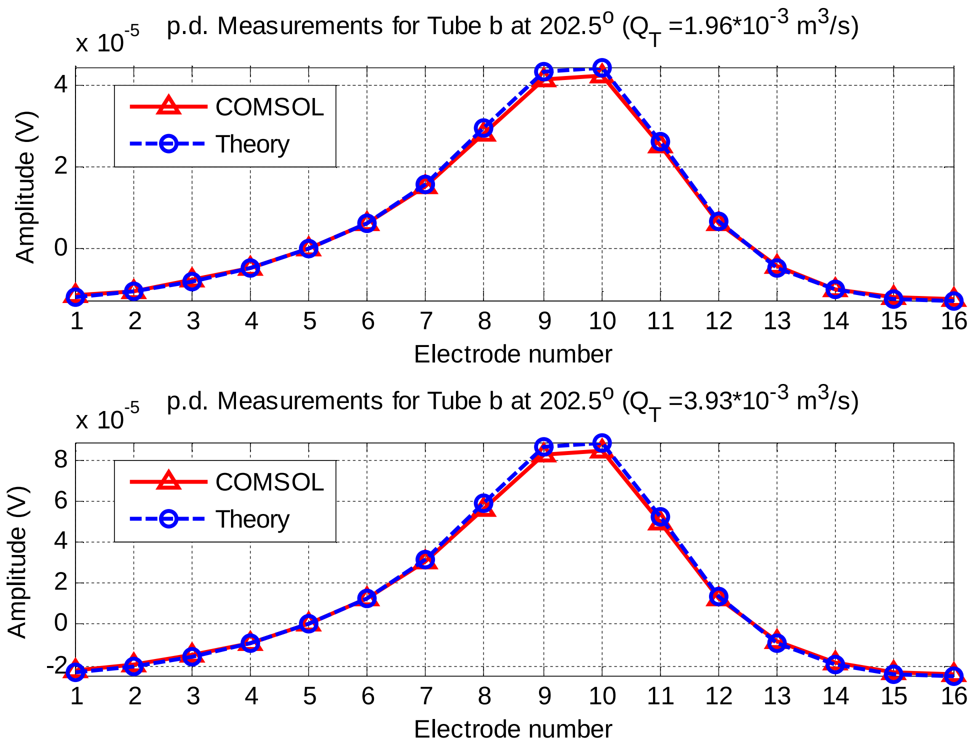

Figure 4.29: Induced potential difference measurements for tube 'b' positioned at 202.5° with respect to e_1 for flow rate values of 1.96×10^{-3} m^3/s and 3.93×10^{-3} m^3/s

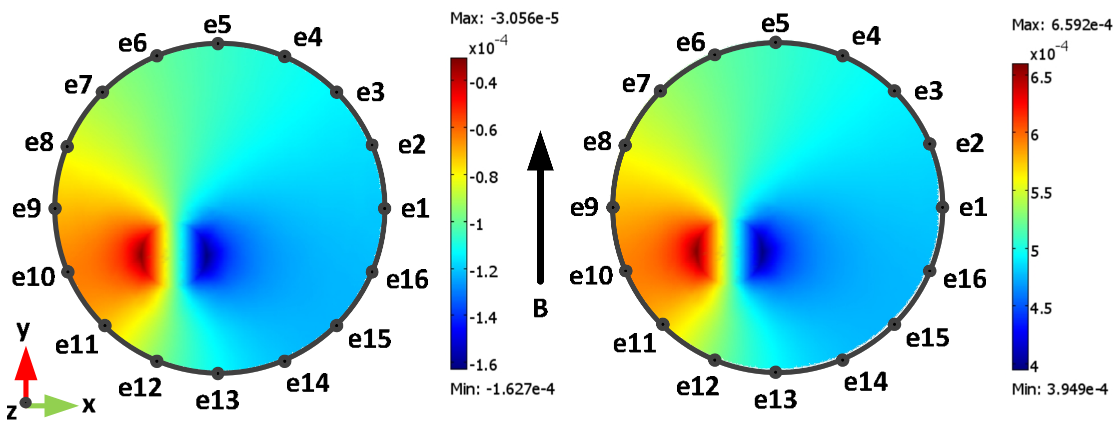

Figure 4.30: Electrical potential distribution for tube 'b' positioned at 225° with respect to e_1 for flow rates of 1.96×10^{-3} m^3/s (left) and 3.93×10^{-3} m^3/s (right) (COMOSL model only)

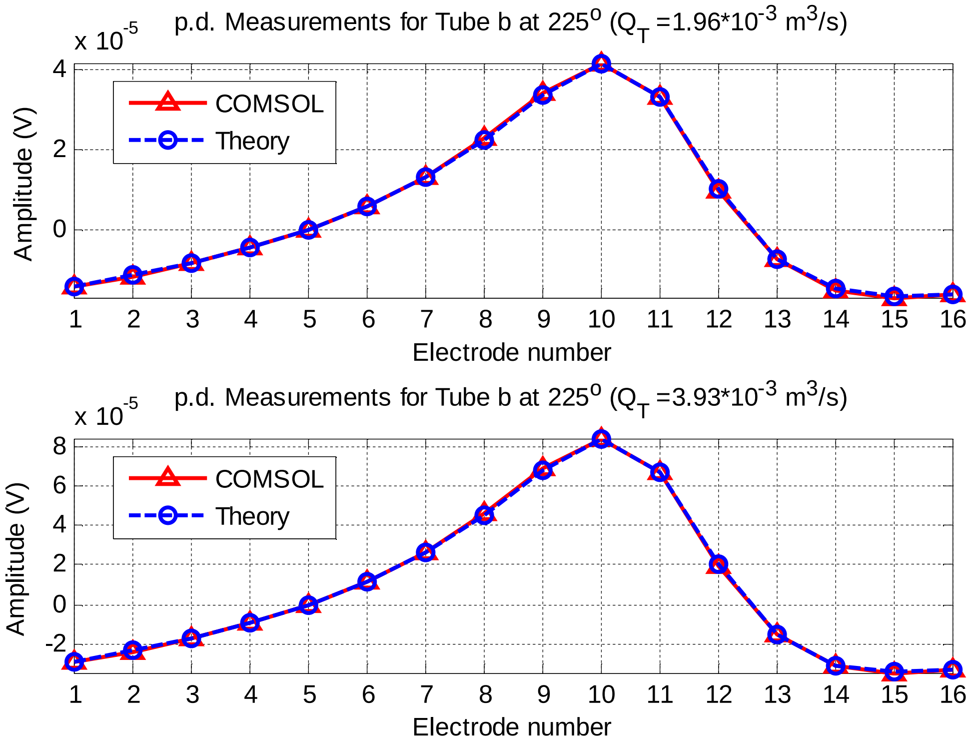

Figure 4.31: Induced potential difference measurements for tube 'b' positioned at 225° with respect to e_1 for flow rate values of 1.96×10^{-3} m^3/s and 3.93×10^{-3} m^3/s

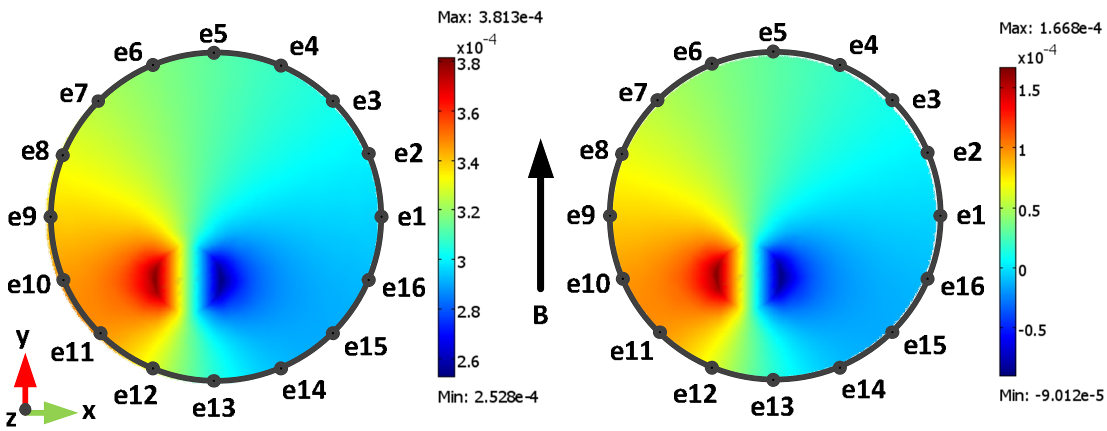

Figure 4.32: Electrical potential distribution for tube 'b' positioned at 247.5° with respect to e_1 for flow rates of 1.96×10^{-3} m^3/s (left) and 3.93×10^{-3} m^3/s (right) (COMOSL model only)

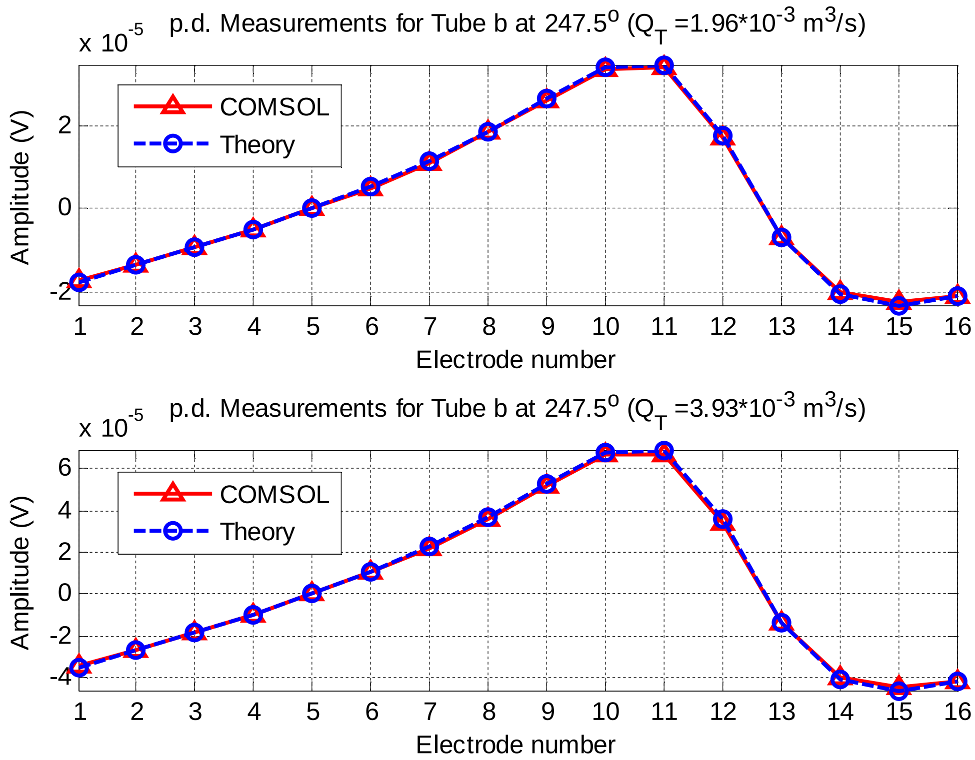

Figure 4.33: Induced potential difference measurements for tube 'b' positioned at 247.5° with respect to e_1 for flow rate values of 1.96×10^{-3} m^3/s and 3.93×10^{-3} m^3/s

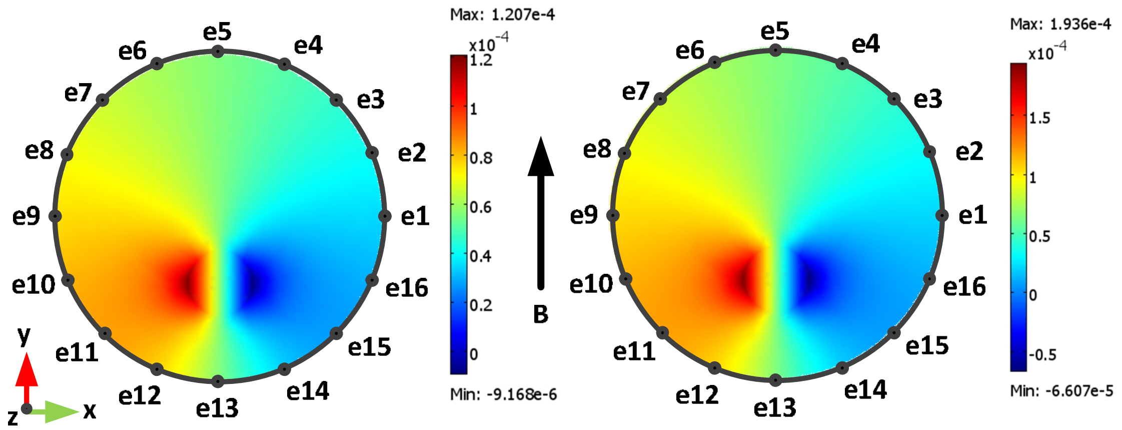

Figure 4.34: Electrical potential distribution for tube 'b' positioned at 270° with respect to e_1 for flow rates of 1.96×10^{-3} m^3/s (left) and 3.93×10^{-3} m^3/s (right) (COMOSL model only)

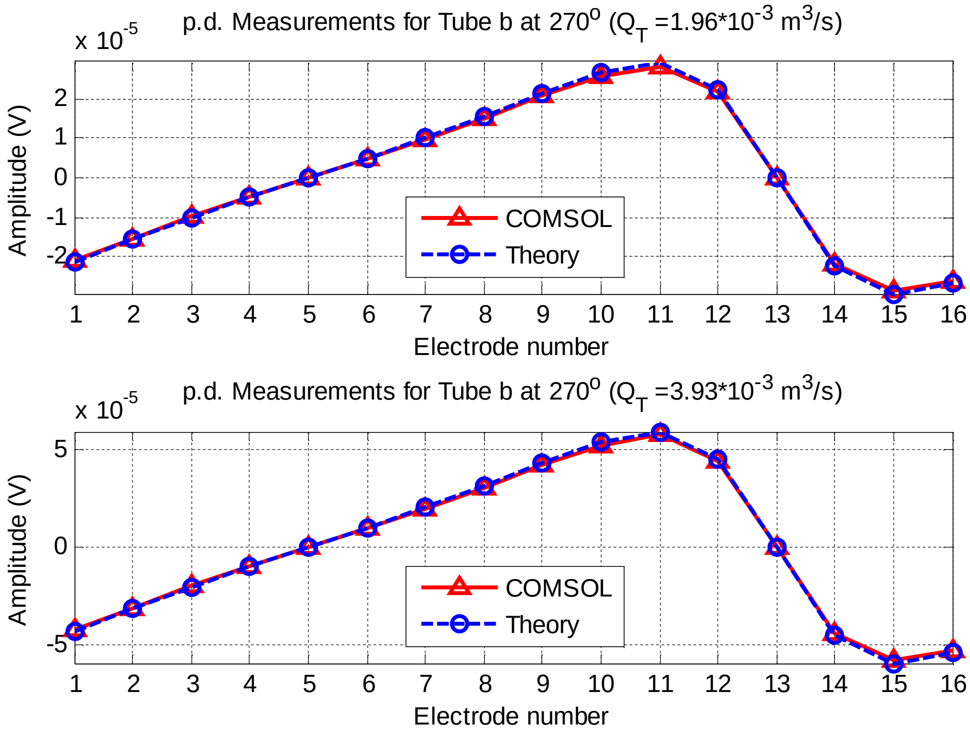

Figure 4.35: Induced potential difference measurements for tube 'b' positioned at 270° with respect to e_1 for flow rate values of 1.96×10^{-3} m^3/s and 3.93×10^{-3} m^3/s

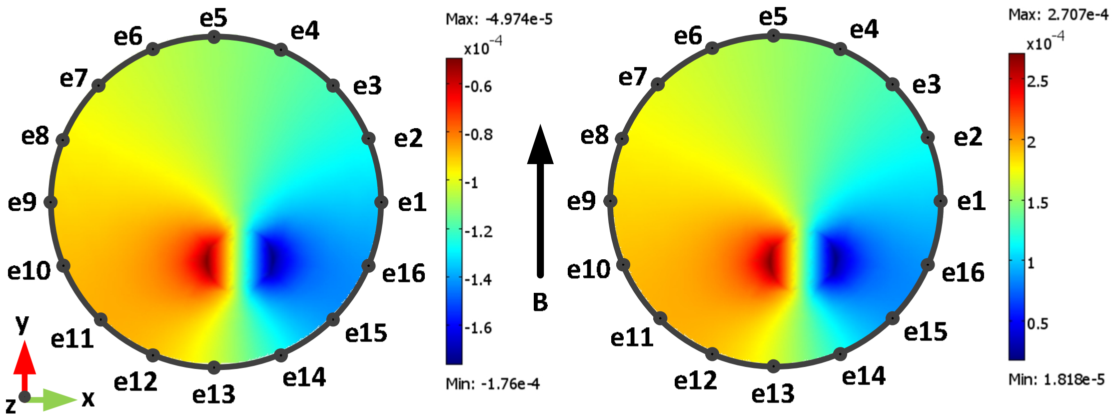

Figure 4.36: Electrical potential distribution for tube 'b' positioned at 292.5° with respect to e_1 for flow rates of 1.96×10^{-3} m^3/s (left) and 3.93×10^{-3} m^3/s (right) (COMOSL model only)

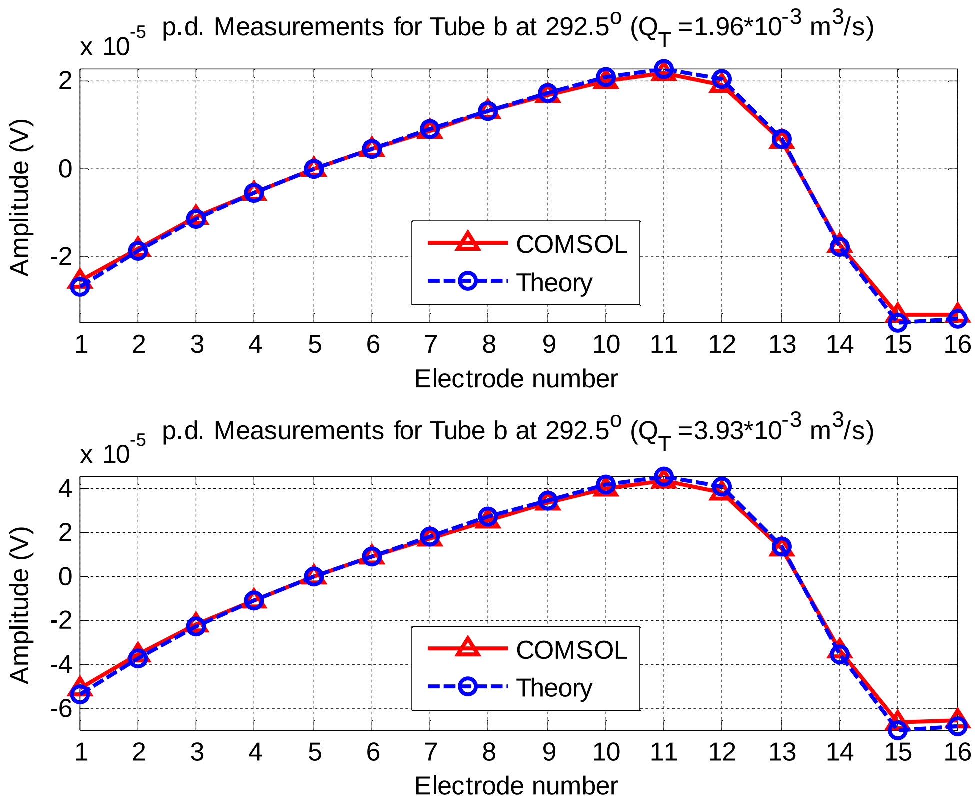

Figure 4.37: Induced potential difference measurements for tube 'b' positioned at 292.5° with respect to e_1 for flow rate values of 1.96×10^{-3} m^3/s and 3.93×10^{-3} m^3/s

Test 3: Water Flow Imposed in Tubes ‘a’ and ‘b’

Lastly, water flow was imposed in both tubes ‘a’ and ‘b’ simultaneously. For the low flow rate tests, the flow rate in each tube was 0.98×10^{-3} m^3/s and therefore, the total flow rate value was 1.96×10^{-3} m^3/s which is the same value used for the low flow rate tests in single tubes explained above. For the high flow rate tests, the flow rate in each tube was 1.965×10^{-3} m^3/s, and this resulted in a total flow of 3.93×10^{-3} m^3/s.

In Figure 4.38, tubes ‘a’ and ‘b’ were at 0° and 180° with respect to electrode e_1, respectively. The flow induced potential differences $(U_j - U_5)$ obtained from the FE model for this setup are presented in Figure 4.39. For the theoretical model, the flow induced potential differences were calculated by finding the flow induced potential differences due to water flow in tubes ‘a’ and ‘b’ independently using Eq. 3-32 and Eq. 3-33 and then, the induced potential differences from both tubes were added together. For example, the flow induced potential difference $U_1 - U_5$ at electrode e_1 due to the water flow in both tubes ‘a’ and ‘b’ is the sum of the flow induced potential difference $U_{1a} - U_5$ (flow in tube ‘a’ only) and $U_{1b} - U_5$ (flow in tube ‘b’ only). The theoretical flow induced potential differences, presented in Figure 4.39, are due to flow in both tubes ‘a’ and ‘b’. It can be seen, in Figure 4.39, that there is very good agreement between the flow induced potential differences from the FE and the theoretical models. This demonstrates an important point, that the overall flow induced potential distribution for multiple flow sources, such as the system being investigated here, is obtained by summing the flow induced potentials from the individual flow sources.

Similarly to the previous tests, when the location of the tubes was altered, as shown in Figure 4.40, the profile of the flow induced potential distribution was changed (comparing Figure 4.39 with Figure 4.41) leading to the conclusion that the profile of the flow induced potential distribution is dependent on the location of the tubes within the cross section bounded by the electrodes. Moreover, a higher or lower flow rate would only increase or decrease the amplitude of the flow induced potentials given that the location of the tubes remains the same.

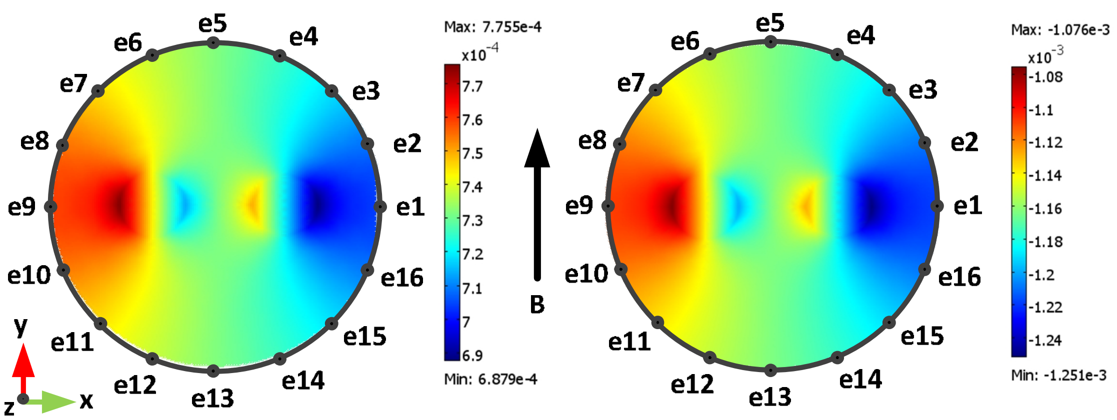

Figure 4.38: Electrical potential distribution for tubes ‘a’ and 'b' positioned at 0° and 180° with respect to e_1 for flow rates of 1.96×10^{-3} m^3/s (left) and 3.93×10^{-3} m^3/s (right) (COMOSL model only)

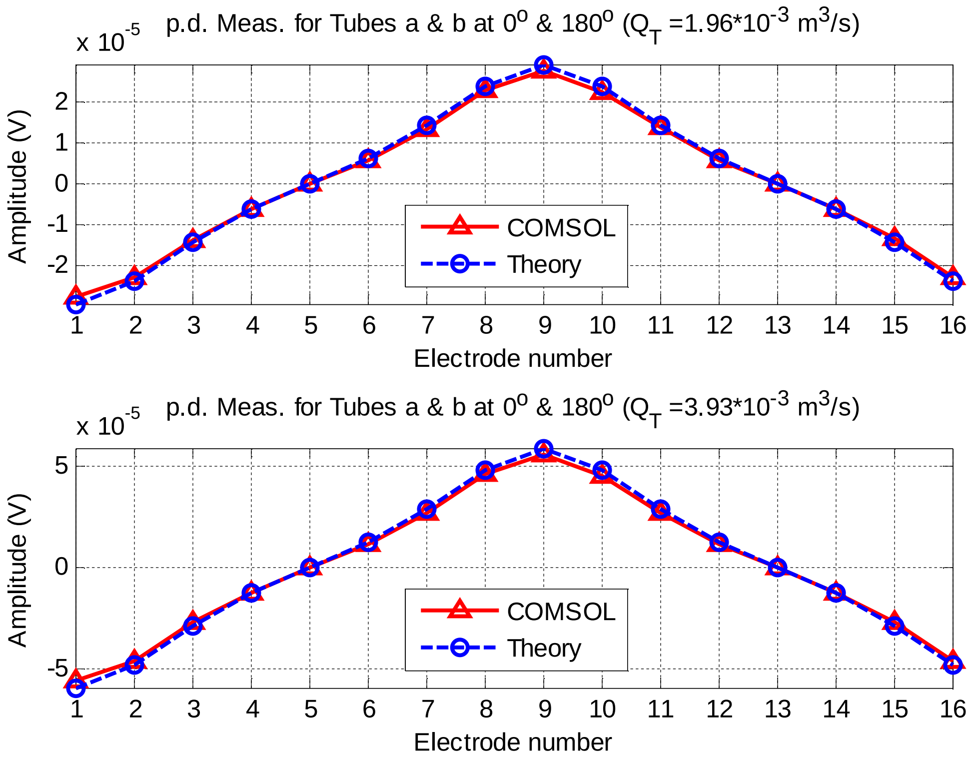

Figure 4.39: Induced potential difference measurements for tubes 'a' and 'b' positioned at 0° and 180° with respect to e_1 for flow rate values of 1.96×10^{-3} m^3/s and 3.93×10^{-3} m^3/s

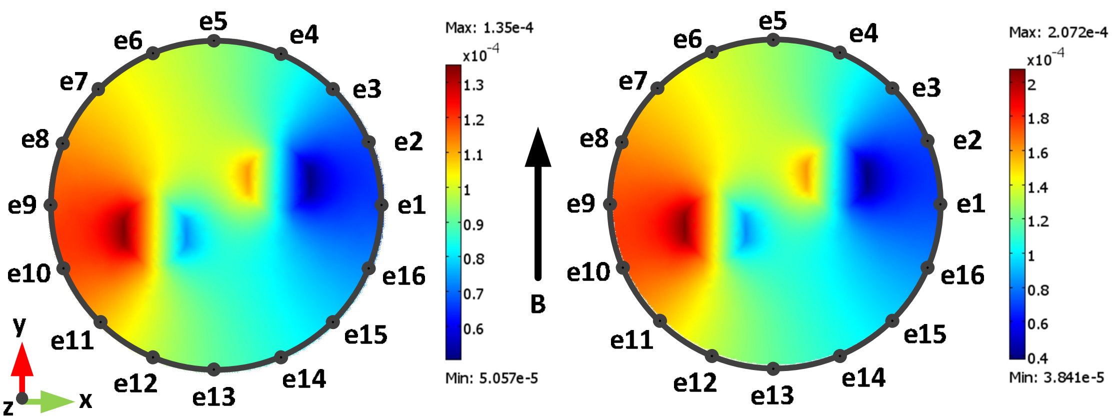

Figure 4.40: Electrical potential distribution for tubes 'a' and 'b' positioned at 22.5° and 202.5° with respect to e_1 for flow rates of 1.96×10^{-3} m^3/s (left) and 3.93×10^{-3} m^3/s (right) (COMOSL model only)

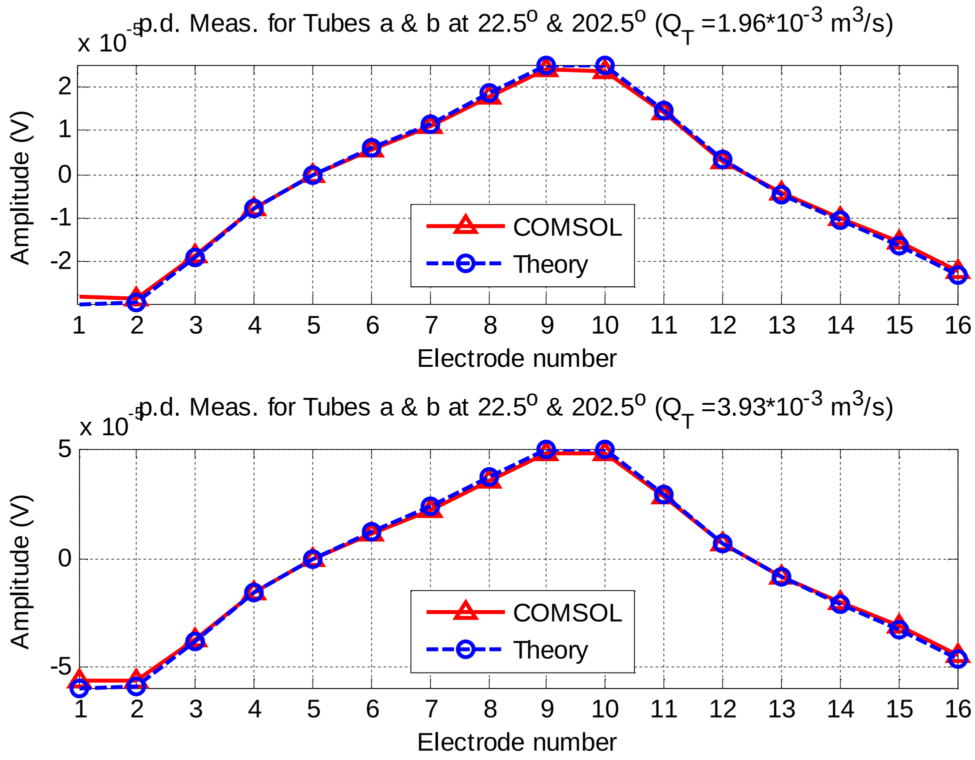

Figure 4.41: Induced potential difference measurements for tubes ‘a’ and 'b' positioned at 22.5° and 202.5° with respect to e_1 for flow rate values of 1.96×10^{-3} m^3/s and 3.93×10^{-3} m^3/s

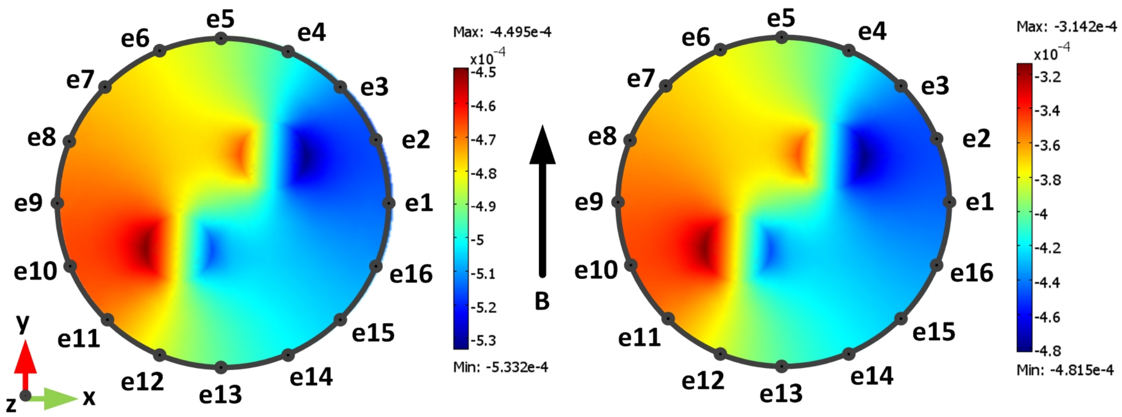

Figure 4.42: Electrical potential distribution for tubes ‘a’ and 'b' positioned at 45° and 225° with respect to e_1 for flow rates of 1.96×10^{-3} m^3/s (left) and 3.93×10^{-3} m^3/s (right) (COMOSL model only)

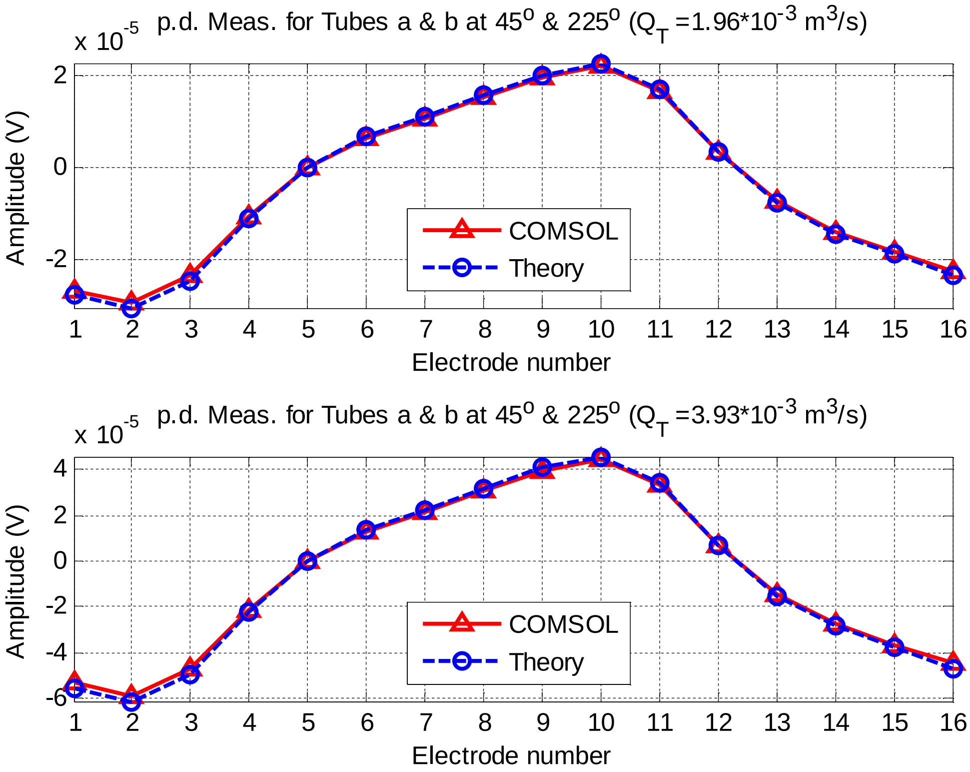

Figure 4.43: Induced potential difference measurements for tubes ‘a’ and 'b' positioned at 45° and 225° with respect to e_1 for flow rate values of 1.96×10^{-3} m^3/s and 3.93×10^{-3} m^3/s

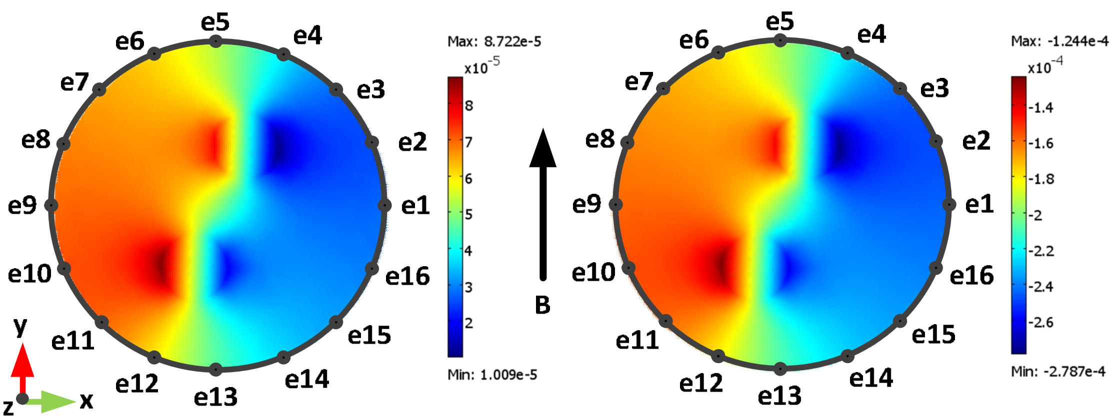

Figure 4.44: Electrical potential distribution for tubes ‘a’ and 'b' positioned at 67.5° and 247.5° with respect to e_1 for flow rates of 1.96×10^{-3} m^3/s (left) and 3.93×10^{-3} m^3/s (right) (COMOSL model only)

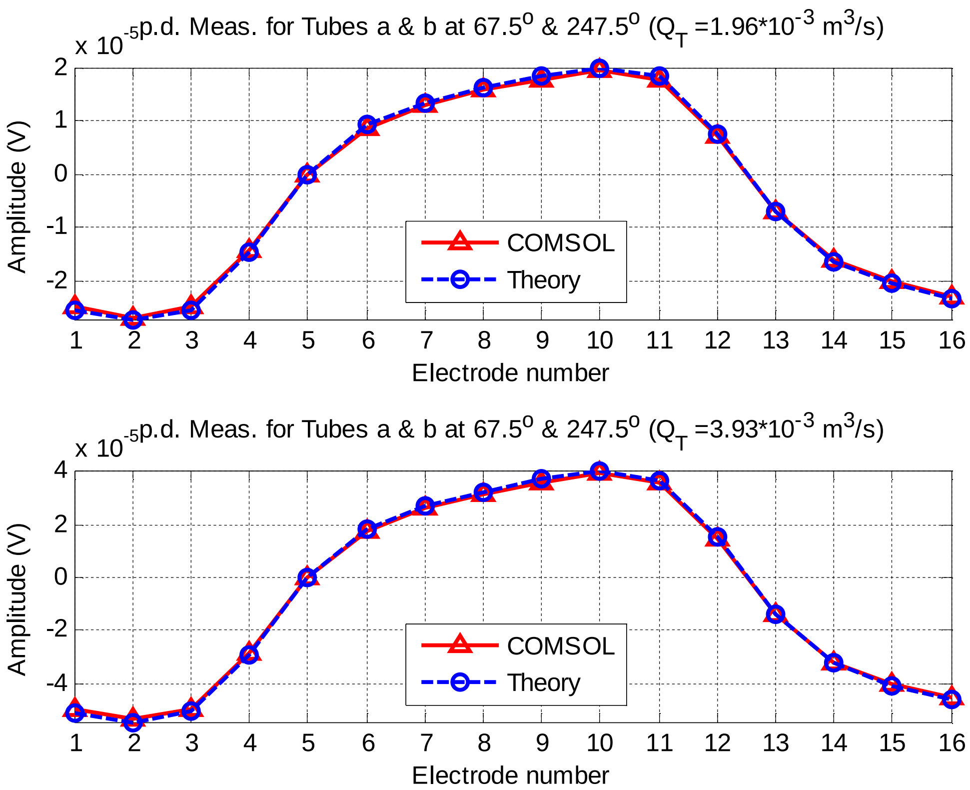

Figure 4.45: Induced potential difference measurements for tubes ‘a’ and 'b' positioned at 67.5° and 247.5° with respect to e_1 for flow rate values of 1.96×10^{-3} m^3/s and 3.93×10^{-3} m^3/s

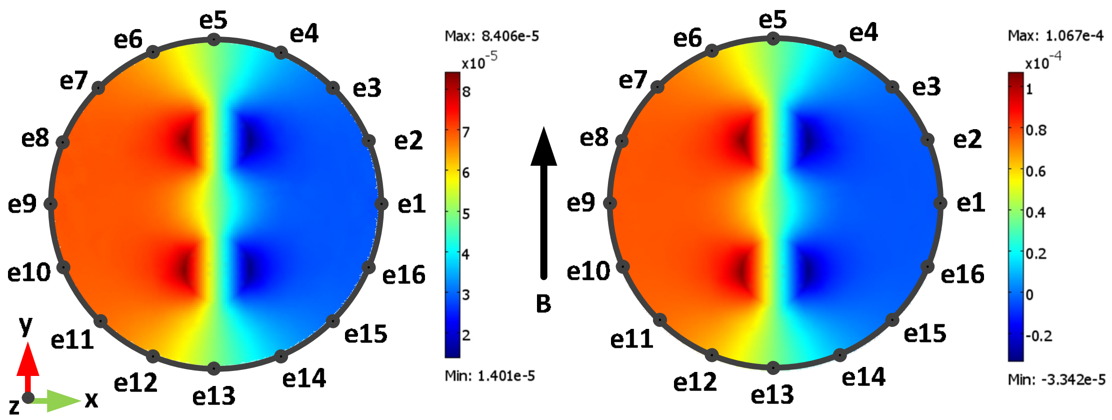

Figure 4.46: Electrical potential distribution for tubes ‘a’ and 'b' positioned at 90° and 270° with respect to e_1 for flow rates of 1.96×10^{-3} m^3/s (left) and 3.93×10^{-3} m^3/s (right) (COMOSL model only)

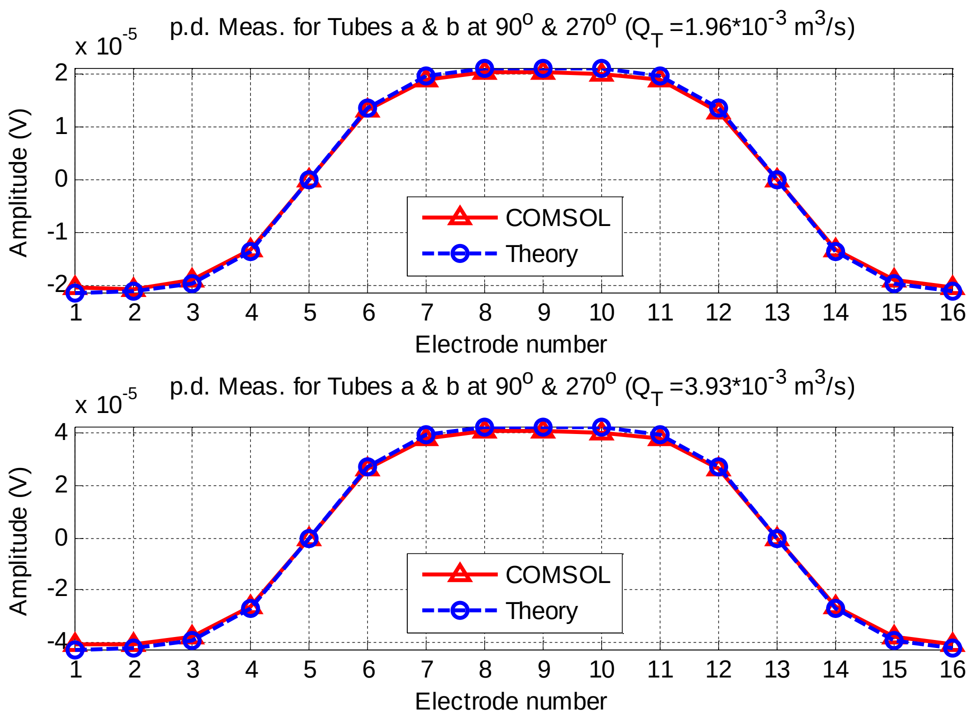

Figure 4.47: Induced potential difference measurements for tubes ‘a’ and 'b' positioned at 90° and 270° with respect to e_1 for flow rate values of $1.96{\times}10^{-3}$ m^3/s and $3.93{\times}10^{-3}$ m^3/s

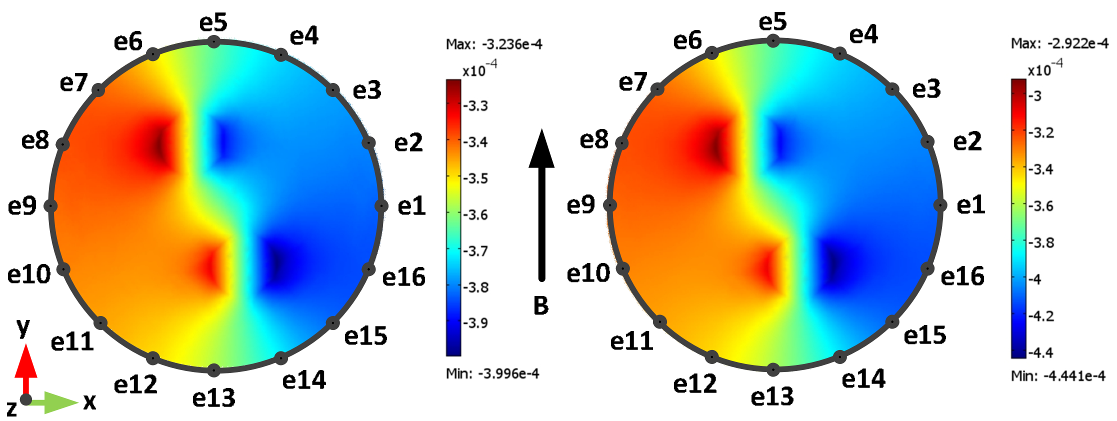

Figure 4.48: Electrical potential distribution for tubes ‘a’ and 'b' positioned at 112.5° and 292.5° with respect to e_1 for flow rates of $1.96{\times}10^{-3}$ m^3/s (left) and $3.93{\times}10^{-3}$ m^3/s (right) (COMOSL model only)

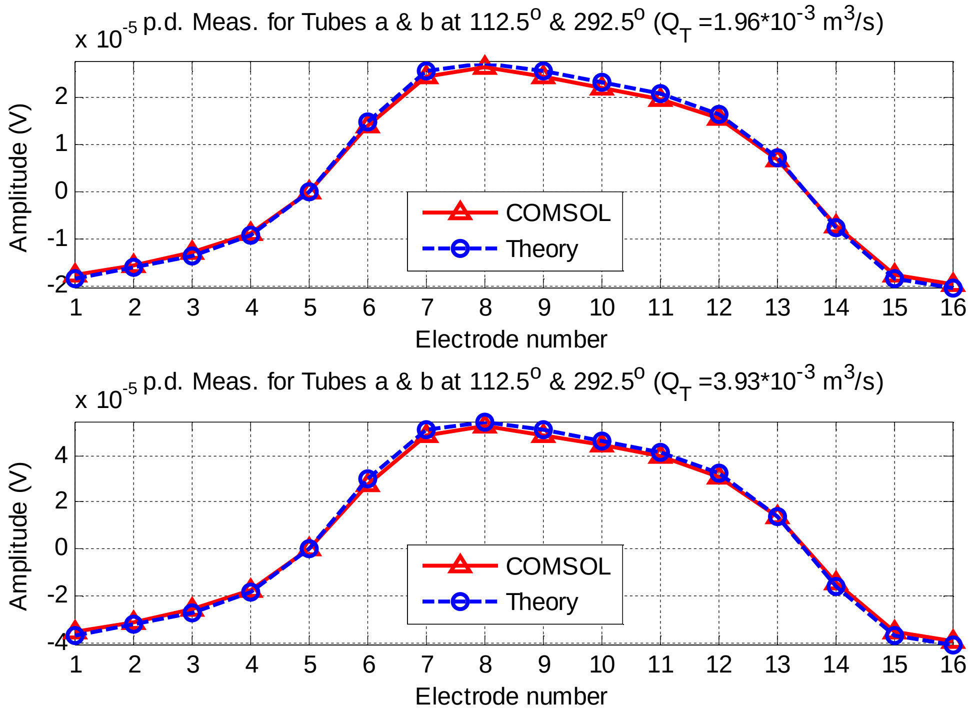

Figure 4.49: Induced potential difference measurements for tubes ‘a’ and 'b' positioned at 112.5° and 292.5° with respect to e_1 for flow rate values of 1.96×10^{-3} m^3/s and 3.93×10^{-3} m^3/s

4.8 Discrete Fourier Transform of the Flow Induced Potential Differences

The DFT was applied to the 16 flow induced potential difference measurements $U_j - U_5$ obtained from the COMSOL FE and theoretical models for each test described above. Then, the modulus $|X(1)|$ of the DFT component $X(1)$ was calculated. The modulus $|X(1)|$ is proportional to the total volumetric flow rate Q_T and the peak magnetic flux density B_0 within the boundary of the cylinder, where the electrical potentials were measured, as demonstrated mathematically in Eq. 3-39 (Section 3.5). For convenience, the relationship between the modulus $|X(1)|$, the total flow rate Q_T and the peak magnetic flux density B_0 is stated here, being given by

$$|X(1)| = k_1 Q_T B_0 \qquad \text{Eq. 4-11}$$

where k_1 is a calibration factor. Note that from the theoretical model, the calibration value k_1 can be also calculated using Eq. 3-33, i.e.

$$k_1 = \frac{1}{2R\pi} \qquad \text{Eq. 4-12}$$

where R is the radius of the cross section bounded by the electrodes and it is 25 mm for the current model under investigation. Hence, the calibration factor $k_1 = 6.37$ m^{-1}. This value can also be obtained if $|X(1)|$ and the total flow rate Q_T are known for a given magnetic flux density B_0. Hence, from the flow induced potential differences obtained from the COMSOL FE, the calibration value k_1 will be calculated. The calibration factor k_1 should be a constant value regardless of the number of, the position of and the flow rates in, the flow channels. Table 4-1 and Table 4-2 present the $|X(1)|$ value calculated from the potential difference distribution obtained from the FE and theoretical models for the total flow rates 1.96×10^{-3} m^3/s and 3.93×10^{-3} m^3/s, respectively. The peak magnetic flux density B_0 was 1 mT.

#Test	**Position of tubes ‘a’ and ‘b’**	**COMSOL Model**		**Theoretical Model (Eq. 3-39)**	
		Q_T = 1.96×10^{-3} m^3/s, B_0 = 1 mT			
		$\lvert X(1)\rvert$ (μV)	**k_1 (m^{-1})**	**$\lvert X(1)\rvert$ (μV)**	**k_1 (m^{-1})**
1	‘a’ at 0^o	11.81	6.02	12.48	6.37
2	‘a’ at 22.5^o	11.78	6.00	12.48	6.37
3	‘a’ at 45^o	12.15	6.19	12.48	6.37
4	‘a’ at 67.5^o	12.10	6.16	12.48	6.37
5	‘a’ at 90^o	12.11	6.17	12.48	6.37
6	‘a’ at 112.5^o	11.90	6.06	12.48	6.37
7	‘b’ at 180^o	12.11	6.17	12.48	6.37
8	‘b’ at 202.5^o	11.87	6.05	12.48	6.37
9	‘b’ at 225^o	12.50	6.36	12.48	6.37
10	‘b’ at 247.5^o	12.12	6.17	12.48	6.37
11	‘b’ at 270^o	12.05	6.14	12.48	6.37
12	‘b’ at 292.5^o	11.85	6.04	12.48	6.37
13	‘a’ and b’ at 0^o and 180^o	11.77	6.00	12.48	6.37
14	‘a’ and b’ at 22.5^o and 202.5^o	11.84	6.03	12.48	6.37
15	‘a’ and b’ at 45^o and 225^o	11.95	6.09	12.48	6.37
16	‘a’ and b’ at 67.5^o and 247.5^o	12.09	6.16	12.48	6.37
17	‘a’ and b’ at 90^o and 270^o	11.92	6.07	12.48	6.37
18	‘a’ and b’ at 112.5^o and 292.5^o	11.83	6.03	12.48	6.37
Avg		12.00	6.14	12.48	6.37

Table 4-1: $\lvert X(1)\rvert$ and k_1 values obtained from the FE and theoretical models for the low flow rate tests, i.e. Q_T = 1.96×10^{-3} m^3/s

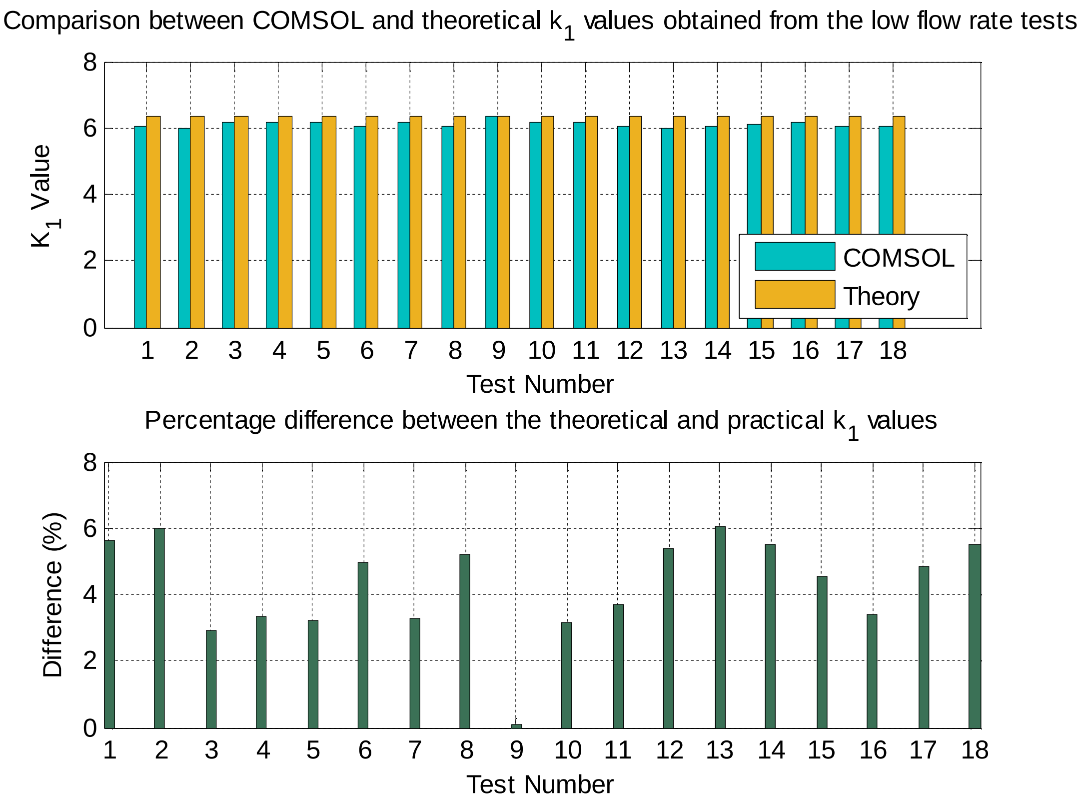

Figure 4.50: Comparison of k_1 values obtained from the FE and theoretical models for the low flow rate tests, i.e. Q_T = 1.96×10^{-3} m^3/s

#Test	Position of tubes a and b	COMSOL Model		Theoretical Model (Eq. 3-39)	
		Q_T = 3.93×10^{-3} m^3/s, B_0 = 1 mT			
		$\lvert X(1)\rvert$ (μV)	k_1 (m^{-1})	$\lvert X(1)\rvert$ (μV)	k_1 (m^{-1})
1	‘a’ at 0^o	23.57	6.00	25.03	6.37
2	‘a’ at 22.5^o	23.55	6.00	25.03	6.37
3	‘a’ at 45^o	24.25	6.17	25.03	6.37
4	‘a’ at 67.5^o	24.19	6.16	25.03	6.37
5	‘a’ at 90^o	24.19	6.16	25.03	6.37
6	‘a’ at 112.5^o	23.79	6.06	25.03	6.37
7	‘b’ at 180^o	24.20	6.16	25.03	6.37
8	‘b’ at 202.5^o	23.71	6.04	25.03	6.37
9	‘b’ at 225^o	24.97	6.36	25.03	6.37
10	‘b’ at 247.5^o	24.21	6.17	25.03	6.37
11	‘b’ at 270^o	24.10	6.14	25.03	6.37
12	‘b’ at 292.5^o	23.65	6.02	25.03	6.37
13	‘a’ and b’ at 0^o and 180^o	23.50	5.99	25.03	6.37
14	‘a’ and b’ at 22.5^o and 202.5^o	23.67	6.03	25.03	6.37
15	‘a’ and b’ at 45^o and 225^o	23.87	6.08	25.03	6.37
16	‘a’ and b’ at 67.5^o and 247.5^o	24.16	6.15	25.03	6.37
17	‘a’ and b’ at 90^o and 270^o	23.83	6.07	25.03	6.37
18	‘a’ and b’ at 112.5^o and 292.5^o	23.68	6.03	25.03	6.37
Avg		24.00	6.10	25.03	6.37

Table 4-2: $\lvert X(1)\rvert$ and k_1 values obtained from the FE and theoretical models for the high flow rate tests, i.e. Q_T = 3.93×10^{-3} m^3/s

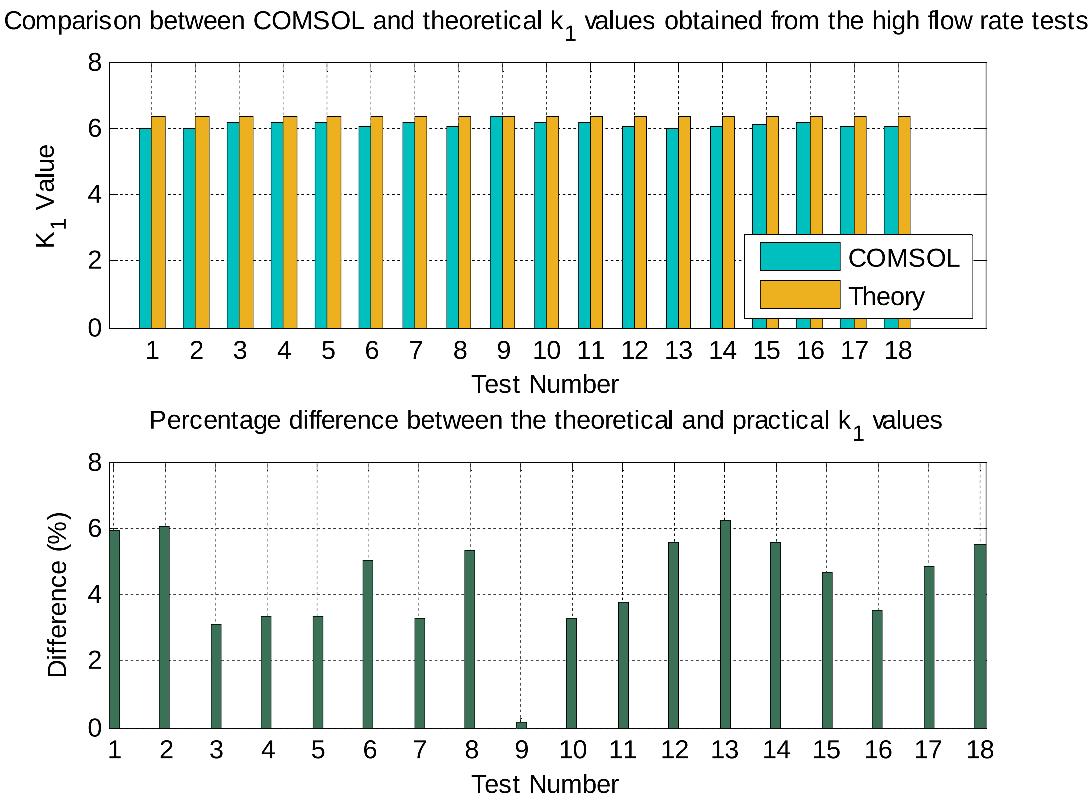

Figure 4.51: Comparison of k_1 values obtained from the FE and theoretical models for the high flow rate tests, i.e. Q_T = 3.93×10^{-3} m^3/s

4.9 Discussion

The flow induced potential differences obtained from the COMSOL FE and theoretical models showed good agreement. It can be concluded that the theoretical model (given in Eq. 3-32 and Eq. 3.33) – used to obtain the induced potential differences due to flow in a number of channels – has been verified and validated using COMSOL Multiphysics software. The results showed that the amplitude of the flow induced potential difference measurements are directly proportional to the total volumetric flow rate Q_T in the flow channels. Moreover, the profile of the induced potential difference distribution is dependent on the number and location of the flow channels within the cross-sectional area bounded by the electrodes.

Tables 4-1 and 4-2 show the modulus $|X(1)|$ of the DFT component $X(1)$ and the calibration factor k_1 values obtained from the FE and theoretical models for all low and high flow rate tests described in Section 4.7, i.e. Q_T = 1.96×10^{-3} m^3/s and Q_T = 3.93×10^{-3} m^3/s. The magnetic flux density value used was 1 mT in all tests. From Table 4-2, it can be seen that the mean value of the modulus $|X(1)|$ for the FE and theoretical models is 25 μV for Q_T = 3.93×10^{-3} m^3/s which is twice the mean value of $|X(1)|$, in Table 4.1, for Q_T = 1.96×10^{-3} m^3/s, i.e. 12.5 μV. This confirms the linear relationship between $|X(1)|$ and Q_T for a given value of the magnetic flux density B_0.

It can be seen from Tables 4-1 and 4-2 that the k_1 value obtained from the FE model for the low and high flow rates varied from one test to another. This variation caused a difference between the theoretical and FE k_1 values as shown in Figure 4.50 and Figure 4.51. The percentage difference between the FE and theoretical k_1 values for the low flow rate tests was 4.26% on average with a standard deviation of 1.46%. For the high flow rate tests, the percentage difference between the FE and theoretical k_1 values was

4.36% on average with a standard deviation of 1.48%. The cause of the variation in the FE k_1 values was due to numerical errors in the COMSOL modelling. For a few test cases, when the mesh size was reduced to investigate if the mesh size has an effect on the accuracy of the results (i.e. the number of mesh element was increased), the agreement of the flow induced potential measurements with the theoretical model was improved. However, it was decided not to reduce the mesh size in the FE modelling for the majority of the conditions considered since the results were satisfactory as they stood and also, reducing mesh size would increase the computational time required to solve the FE model. Nevertheless, both percentages, i.e. 4.26% and 4.36%, are small and give a solid indication that there is good agreement between the FE and theoretical models.

Henceforward, the total flow rate for any imposed flow criteria in the SVS cross-section can be determined, once the flow induced potential difference measurements U_j are collected for a known magnetic flux density, using the calibration factor k_1. The calibration factor value can be either the value obtained from the theoretical model or FE model as the percentage difference is small and will not affect the accuracy of the total flow rate measurement significantly. For example, another test was performed in COMSOL in which water flow was imposed in tube ‘a’ only. Tube ‘a’ was located at 45^o with respect to electrode e_1 and the water velocity was set in COMSOL to 35 m/s instead of 25 m/s or 50 m/s. Hence, the reference volumetric flow rate is 2.75 $\times 10^{-3}$ m^3/s, given that the diameter of tube ‘a’ is 10 mm. When the DFT was applied to the 16 flow induced potential difference measurements, obtained from this test, the modulus $|X(1)|$ of the DFT component $X(1)$ was 17 μV. For the same magnetic flux density $B_0 = 1$ mT and by using the theoretical calibration factor $k_1 = 6.37$ m^{-1}, the total volumetric flow rate Q_T is given by

$$Q_T = \frac{|X(1)|}{k_1 B_0} = \frac{17\ \mu\mathrm{V}}{(6.37\ \mathrm{m}^{-1})(1\ \mathrm{mT})} = 2.67 \times 10^{-3}\ \mathrm{m}^3/\mathrm{s}$$

It can be seen that the error between the actual flow rate value (2.75 $\times 10^{-3}$ m^3/s) and the predicted value is 2.9%. In the practical experiment (Chapter 7), the SVS model had similar dimensions to the COMOSL model. Hence, the calibration factor k_1 obtained practically would be very close to the values, obtained from the FE and theoretical models, stated above. In fact, the value of k_1 obtained from the physical SVS model was 6.25 m^{-1} (Section 7.4) compared with k_1 = 6.10 m^{-1}, obtained from the FE model, and k_1 = 6.37 m^{-1}, obtained from the theoretical model, which were given in Table 4-2. It can be seen that there is better agreement between the practical and theoretical k_1 values, i.e. 6.25 m^{-1} and 6.37 m^{-1} than the practical and the FE k_1 values, which is expected as the practical model is not subjected to FE modelling error. However, the practical value of k_1 was also affected by noise as will be discussed in Chapter 7.

In the practical experiment, the flow induced potential difference measurements were measured via the signal conditioning system, and then, signal processing techniques were applied, i.e. PSD and DFT, to obtain the modulus $|X(1)|$ of the DFT component $X(1)$. The calibration factor k_1 value was found by imposing a known water flow rate through the practical SVS model. The mechanical design of the SVS and the necessary signal conditioning and processing systems are explained in the following chapters.

The COMSOL model has informed some design decisions for the practical experiment. Firstly, the dimensions of the physical model were similar to the COMSOL model, i.e. the diameter of the cross-sectional area and the flow channels were 50 mm and 10 mm, respectively. Moreover, in the simulation work, for a water velocity of 50 m/s and magnetic field density of 1 mT, the flow induced potential differences were in the range of 10 to 100 μV. For the practical experiment, it was decided to use very low water velocity of around 1 m/s as this is in the same range as the blood flow velocity in the human body (Refer to Section 1.2.4). Therefore, the magnetic field density was aimed to be increased to 50 mT, in order to obtain similar values for the flow induced potential differences. Such values can be measured by the analogue front-end circuitry. The magnetic field in the COMSOL model was generated using a HelmHoltz coil, but it was more practical to use an electromagnet that has a ferromagnetic core in order to generate a stronger magnetic field.

4.10 Summary

The FE model was created in COMSOL Multiphysics 3.5 and used to verify the theoretical work provided in Chapter 3. According to Eq. 3-32 and Eq. 3-33, the flow induced potentials due to flow in multiple channels can be predicted for given radial and angular coordinates of, and the flow rate in, the flow channels. Moreover, Eq. 3-37 indicates that the term $|X(1)|$, obtained by applying the DFT to the flow induced potential differences, is directly proportional to the total volumetric flow rate Q_T of all flow channels and the peak magnetic flux density B_0, regardless of the number and location of the flow channels within the cross-sectional area of the medium. The aim from the FE model was to verify the theoretical model of the proposed multi-electrode EM induction flow measurement method.

The FE model consisted of a conductive cylindrical region that had multiple flow channels (one and two flow channels) and a Helmholtz coil to generate a uniform magnetic field across the flow channels. This simulated a basic model of a human limb including two blood vessels. Water flow was imposed in these flow channels with conductivity similar to the conductivity of water in North England which is 0.013 S/m.

This is approximately 54 times lower than the conductivity of blood, and this value was used, in particular, because water was used for the practical experiments (to be described in Chapter 7) which had similar conductivity, as will be explained in the next chapter.

Flow induced potential differences were obtained from the FE model for different test setups, i.e. different numbers and locations of, and the total flow rates in, the flow channels. Then, these induced potential differences were compared with the flow induced potential difference measurements which were obtained from the mathematical model given in Eq. 3-32 and Eq. 3-33 for flow channels of the same geometry and flow rates and magnetic flux density of the same value. Good agreement was found between the results of both models as discussed in Section 4.7. Subsequently, the DFT was applied to the flow induced potential difference measurements obtained from both models, and it was confirmed that the modulus $|X(1)|$ of the fundamental DFT component $X(1)$ is directly proportional to the total volumetric flow rate Q_T in all of the flow channels, irrespective of their number, location and flow rate value. The value of the calibration factor k_1 obtained from the theoretical model was 6.37 m^{-1}, and from the FE model, it was 6.14 m^{-1} for a total flow rate of Q_T = 1.96×10^{-3} m^3/s. The percentage difference between the theoretical and FE values for k_1 was only 3.67%. For a total flow rate of Q_T = 3.93×10^{-3} m^3/s, the value k_1 obtained from the FE model, it was 6.10 m^{-1}, resulting in a percentage difference of 4.33%. Both percentages are small, indicating that the theoretical model agrees to a high degree of accuracy with the FE model. This validates the proposed EM method described in Eq. 3-32, Eq. 3-33 and Eq. 3-39.

In the next chapters, the physical SVS model, built in the laboratory, is explained. The objective was to validate the theoretical model in practice, which is a very important step. The practical work will also help in understanding the hardware and software requirements to build a medical device based on this EM method.

Chapter 5

Design and Construction of the Practical Simulated Vascular System, the Electromagnet and its Power Supply and the Signal Conditioning System

Contents

5.1 Introduction

The first part of this chapter addresses the mechanical design of the SVS and AC-excited electromagnet. The mechanical design of the SVS, previously described in the FE modelling, is presented in **Section 5.2**. It had similar physical dimensions to the FE model in terms of the diameter of the cross-sectional area of the medium and the number and size of the flow channels included. It is a pipe model designed to simulate two blood vessels and a lump of muscle and fat tissues. An array of 16 electrodes was embedded within the SVS to measure the flow induced potentials due to the interaction between flowing water (simulating blood) through the SVS and a uniform magnetic field generated by an electromagnet. The design of the electromagnet is discussed in **Section 5.3** which includes the selection of the core material, the number of turns of the coil and the required coil current to generate a uniform magnetic field of sufficient magnetic flux density to be applied across the physical SVS. **Section 5.4** discusses the decision behind running the AC-excited electromagnet at frequency 30 Hz instead of 50 Hz which was used initially. This is followed by a discussion of the design of the flow test rig, in **Section 5.5**, which was used to conduct the experimental tests.

The second part of this chapter focuses on the design of the power supply of the AC-excited electromagnet and the AC signal conditioning system. The AC electromagnet – referred to in Section 5.3 – required a sophisticated power supply design in order to be supplied with the required coil current to generate the desired magnetic flux density at 50 Hz or 30 Hz. The electromagnet is an inductive load, similar to an AC motor, which cannot be connected directly to an AC voltage supply due to its inrush current. Inductive loads can draw current several times more than the steady-state current when they are first turned on. This can be a serious issue which may lead to power surge or fire risk as the coil of the electromagnet is rated at a peak current of 10 A, and the excessive heat due to the high inrush current can burn out the insulation between the coil windings, causing a short circuit. In **Section 5.6**, the design of the 50 Hz supply is discussed first in **Section 5.6.1** as it was initially used in an attempt to measure flow induced potential differences at the electrode array of the SVS due to water flow. Then, the design of the 30 Hz power supply, which replaced the 50 Hz power supply and was used for all the flow induced potential difference measurement tests described in Chapter 7, is explained in **Section 5.6.2**.

The design of the AC signal conditioning system is described in **Section 5.7**. During the flow induced potential difference measurement tests, the flow induced potential differences detected by the electrodes were in the range of 10-185 μV. These voltage signals were too small for direct analogue to digital (AD) conversion and hence, they required voltage amplification. They also had a large DC offset due to electrode polarisation and were affected by electromagnetic interference (EMI), i.e. mains and radio-frequency. Thus, the implementation of filters was necessary. Moreover, the electrodes were high-impedance sources and therefore, impedance transformation was essential to avoid loading the electrodes [172]. Loading occurs when the output of the first circuit (electrode) has higher impedance than the input of the second circuit (measuring circuit). As a result, a current is drawn from the first circuit causing the actual voltage amplitude to drop. For these reasons, an AC signal conditioning circuit was designed to overcome the above issues.

There are 16 electrodes embedded within the SVS and each electrode reading was measured with respect to the reference electrode e_5 (electrode e_5 was chosen as the reference electrode). Each measurement required signal conditioning to be suitable for the AD conversion. It was more practical to design an analogue multiplexer circuit, so that only one signal conditioning circuit is needed. The analogue multiplexer which was used had 16 analogue switches which were all connected to one single output. It also had a 4-bit binary control input which can be set digitally to select the electrode that is required to be measured as will be shown in **Section 5.8**. The analogue multiplexing is usually implemented in systems in which many electrodes (transducers) are used such as electrical impedance tomographic (EIT) systems [173, 174].

MATLAB software was used to perform the signal analysis and processing on the flow induced potential difference measurements. The signal conditioning circuit was interfaced with the PC via a National Instruments (NI) PCI-6254 data acquisition device which is presented in **Section 5.9**. The NI PCI-6254 is an optimised DAQ device for accurate voltage measurement at fast sampling rates [175]. A program code was written in MATLAB for the PCI-6254 DAQ to control the switching of the analogue multiplexer and to sample the output of the signal conditioning circuit every time the selection switch of the multiplexer was changed and this is discussed in **Section 5.10**.

5.2 The Simulated Vascular System

The physical SVS was designed and built to model a simplified human limb that has two blood vessels. Porous ceramic was used to model the human tissue, muscles and fat because, when it is saturated in water, it has significant electrical conductivity. This is important as it allows the flow induced potentials to be measured at the boundary of the SVS system. The blood vessels were simulated by holes drilled into the porous ceramic. In addition to its porosity, ceramic material was chosen due to its high resistance to corrosion, good rigidity and dimensional stability [176].

The porous ceramic used was 40 mm in diameter, 200 mm in length. It had two holes of 10 mm in diameter drilled along its length and offset from its axis as shown in Figure 5.1, Figure 5.2 and Figure 5.3.

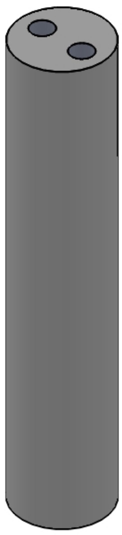

Figure 5.1: SVS ceramic cylinder

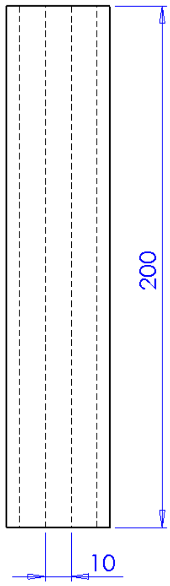

Figure 5.2: Ceramic cylinder dimensions in mm.

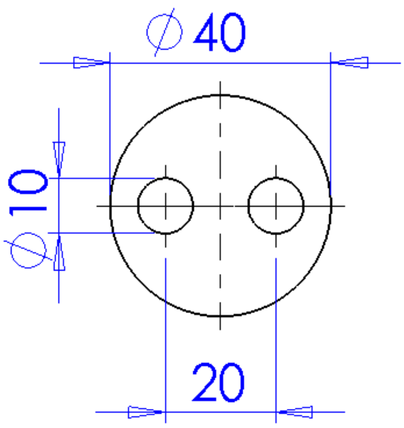

Figure 5.3: Ceramic cylinder dimensions in mm.

The ceramic cylinder is fragile because it is highly brittle and therefore, it was contained within a plastic housing (Figure 5.4) which was machined from Delrin material. Delrin is a non-conducting, non-magnetic material with a relative permeability of 1. The housing had a length of 240 mm and external and internal diameters of 75 mm and 50 mm, respectively (refer to Figure 5.5). The top part of the housing can be unscrewed to place the ceramic cylinder inside as illustrated in Figure 5.6.

The diameter of the porous ceramic is 40 mm and the inner diameter of the Delrin housing is 50 mm; thus, when the porous ceramic was placed inside, there was a gap of 5 mm as shown in Figure 5.6. This gap is filled with water when water is flowing through the SVS, and it simulates wet skin (electrolyte applied to a skin). The electrodes of the SVS are in contact with this layer of water.

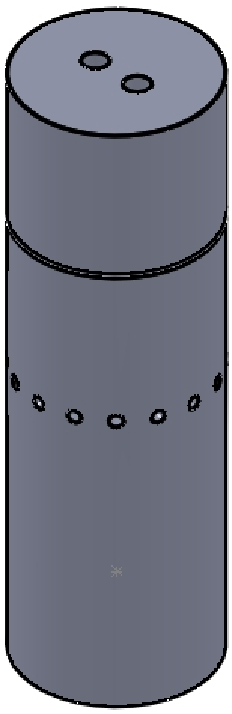

Figure 5.4: The Delrin housing and the electrode array

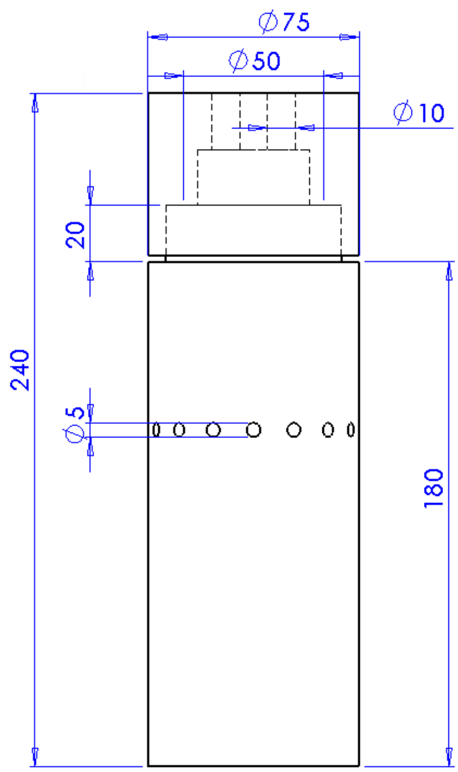

Figure 5.5: Delrin housing dimensions in mm

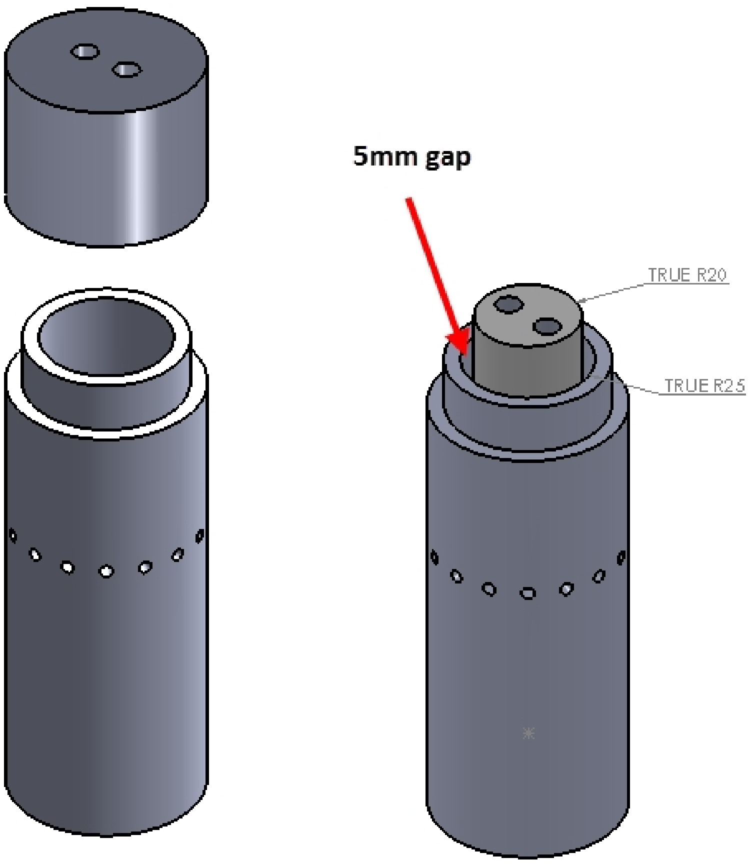

Figure 5.6: Porous ceramic inserted into the Delrin housing

The Delrin housing had 16 electrode housings which were machined at angular intervals of 22.5° and each housing had a diameter of 5 mm. The electrodes used were 316L stainless steel M5 10mm-long bolts. 316L stainless steel has a very low relative permeability, i.e. it is non-magnetic. Non-magnetic electrodes are used in the SVS in order to avoid any localised fluctuations in the magnetic field. If magnetic electrodes were used, then this would affect the local magnetic flux density distribution and hence, its overall uniformity. This would invalidate the mathematical modelling as it is assumed throughout that the magnetic flux density B is uniform. 316L stainless steel also has a high resistance to corrosion when immersed in water due to its low carbon property. The head of each electrode bolt was tapped in order to attach an M3 screw to it. This allowed wires to be connected to the electrodes via solder tags as illustrated in Figure 5.7.

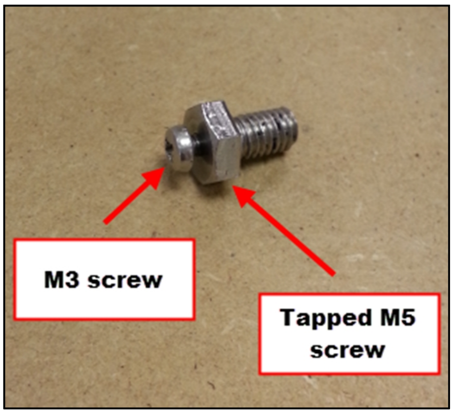

(a)

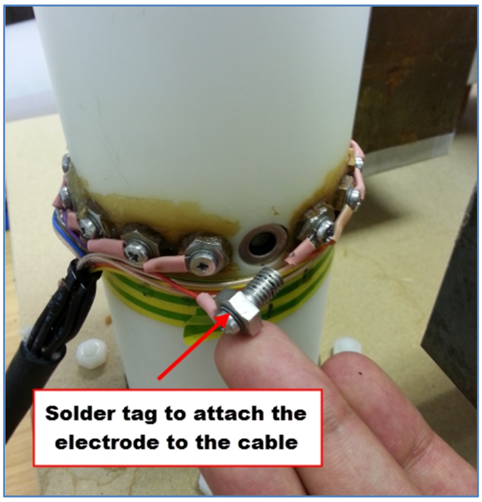

(b)

Figure 5.7: (a) Tapped M5 and M3 screws; (b) solder tag attached to the electrode.

Other external parts were machined from Delrin (Figure 5.8) in order to fix the ceramic cylinder firmly inside the Delrin housing and connect the water supply to the SVS. Two of the parts presented in Figure 5.8(a) were made, to be placed at the top and bottom of the Delrin housing, and 4 of the parts shown in Figure 5.8(b) were made to be placed in the top and bottom holes which were used to connect the water supply to the SVS via reinforced PVC hoses.

The complete system is shown in Figure 5.9 which shows the Delrin housing, the porous ceramic and the external fittings, which were placed at the top and bottom of the SVS. Figure 5.10 shows the SVS system and the electrode cable. Two metal 'T' connector hose fittings were also used; one was to connect the water supply (water tap) to both tubes at the top of the SVS and the other was to connect the ends of the tubes of the SVS to the water drain as illustrated in Figure 5.11. Therefore, the water was flowing in the same direction in both tubes from the top to bottom of the SVS. Figure 5.11 illustrates the SVS system, the hosing and necessary connectors. In the setup shown, the water flows through both tubes 'a' and 'b' normally. However, to impose water in one of the tubes only, the other tube was sealed temporarily using a cork.

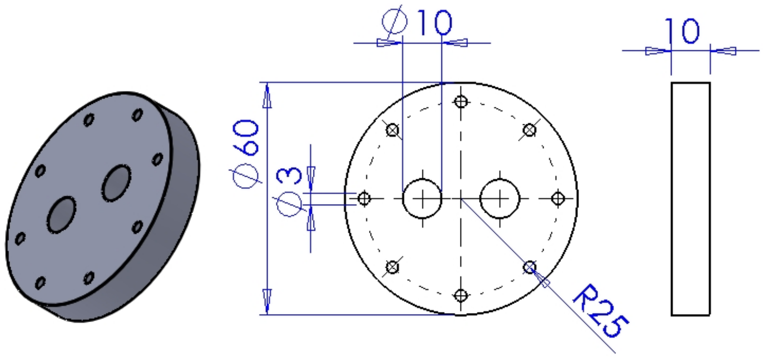

(a)

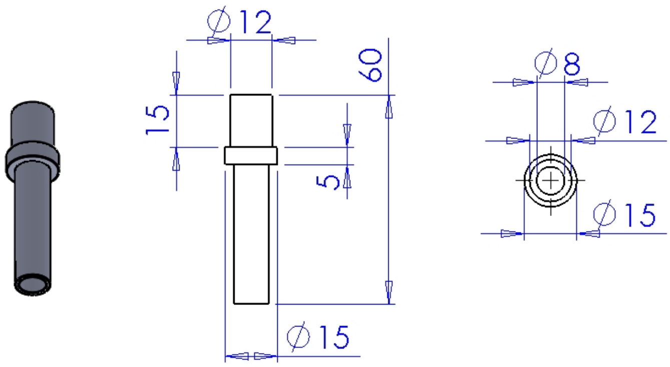

(b)

Figure 5.8: (a) Delrin disc placed at the top and bottom of the Delrin housing; (b) fittings used to connect the water supply to the SVS via PVC hoses

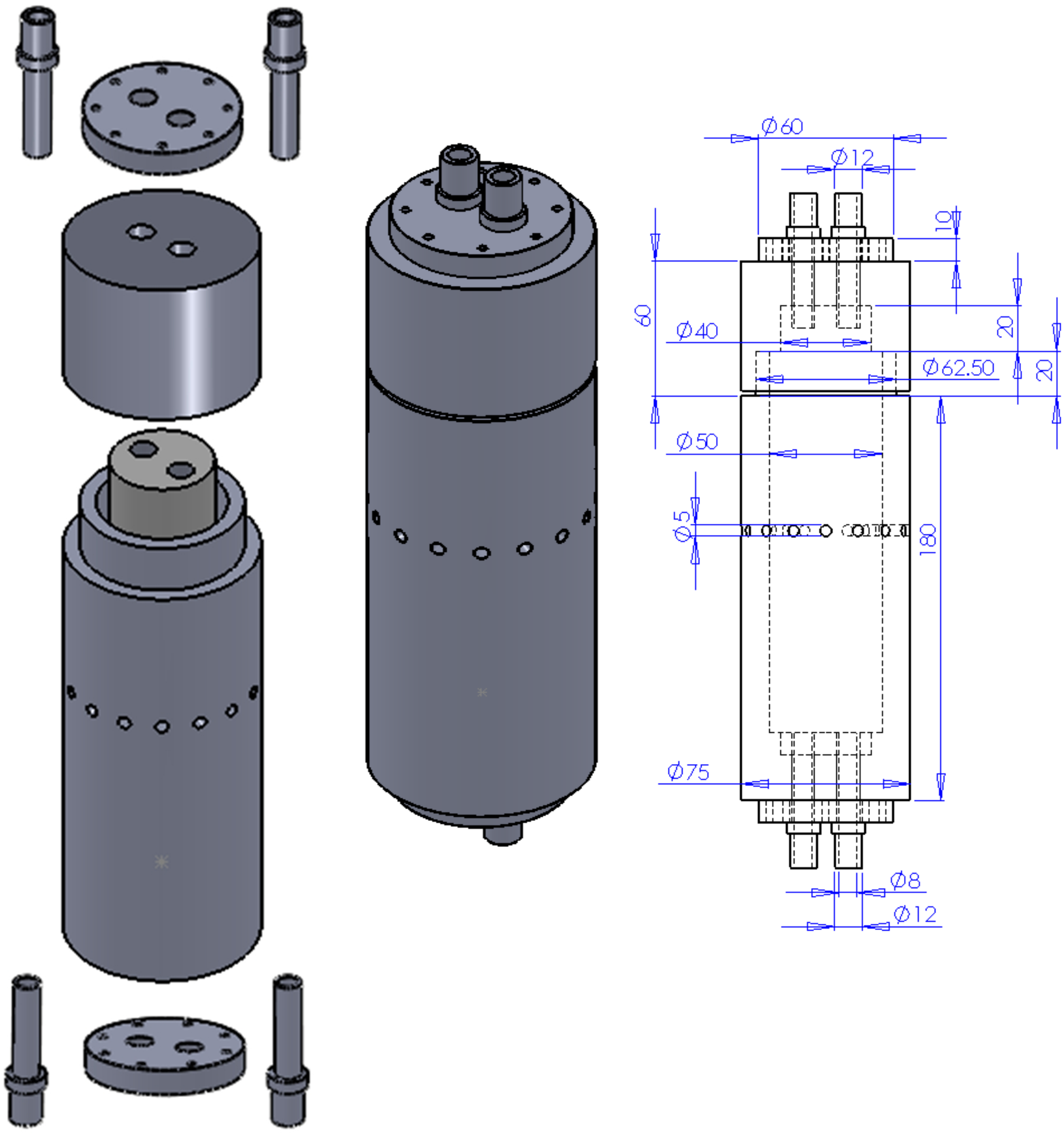

Figure 5.9: Complete SVS designed in SolidWorks (dimensions in mm)

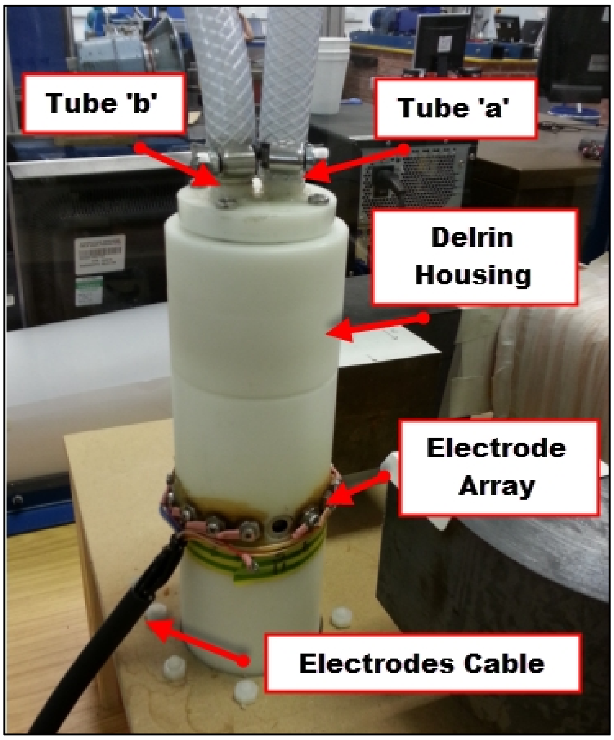

Figure 5.10: SVS system and the electrode array and its cable

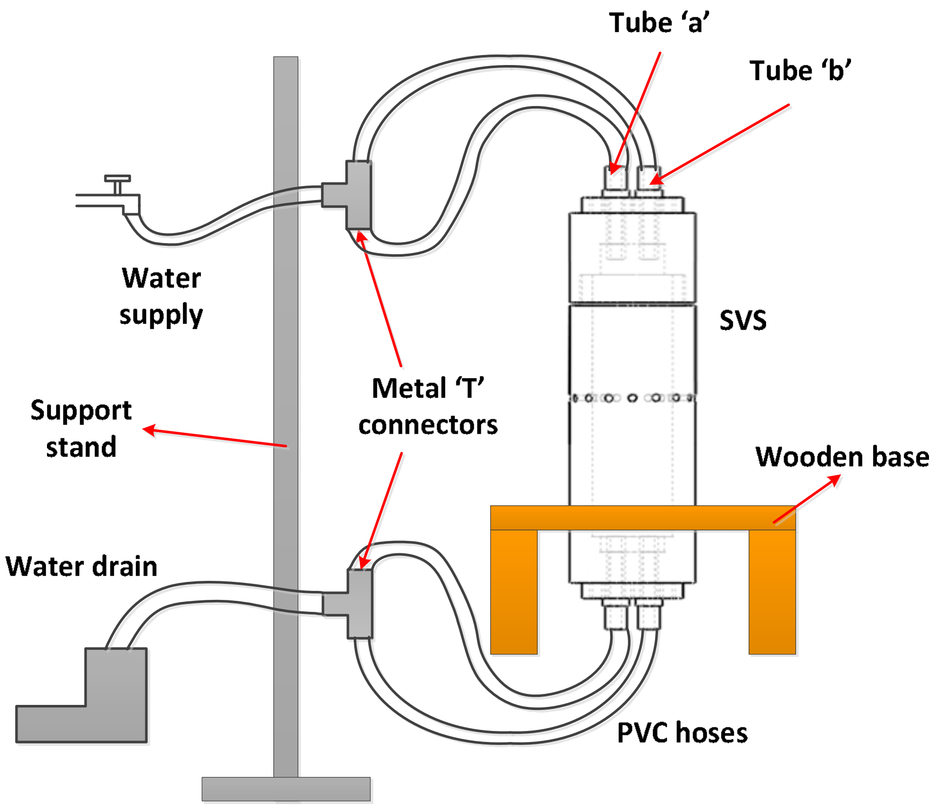

Figure 5.11: Flow test rig setup (without the electromagnet)

5.3 The AC-powered Electromagnet

It was necessary to generate a uniform magnetic field across the electrode array of the SVS pipe model. An electromagnet was chosen for this application as it was more suitable in practical terms in comparison to the Helmholtz coil because it is able to generate a stronger magnetic field for the same amount of current due to its ferromagnetic core. The electromagnet design consisted of two parts: (1) the ferromagnetic core and (2) the coil. The ferromagnetic core had a high permeability to increase the strength of the magnetic field and the number of turns of the coil windings depended on the required magnetic flux density B_0 value.

5.3.1 The Electromagnetic Core Design

The SVS had an external diameter of 75 mm (outer diameter of the Delrin housing) and the protrusion of the electrodes was about 3 mm. Therefore, a C-shaped ferromagnetic core was manufactured to have an air gap of 80 mm × 80 mm. The ferromagnetic core was manufactured from laminated silicon steel sheets of 0.3 mm in thickness (M4 lamination grade) to minimise power losses due to eddy currents. This type of silicon steel has relative permeability μ_r of around 40,000. The mean length of the core was 0.8 m and its cross-sectional area was 6400 mm^2. The density of silicon steel is around 7670 kgm^{-3}[177] and therefore, the mass (mass=density×area×length) of the core was 39 kg approximately. Figure 5.12 depicts the 3D model of the silicon steel core designed in SolidWorks and Figure 5.13 shows the practical build. It is important to note that the silicon steel which was used has a magnetic saturation point of 1.5 T, which means that, after this point, any increase in the coil current I_0 or the number of turns N will not result in an increase in the magnetic flux density B_0. The operating temperature range of this core is between $-55°$ C and 300° C.

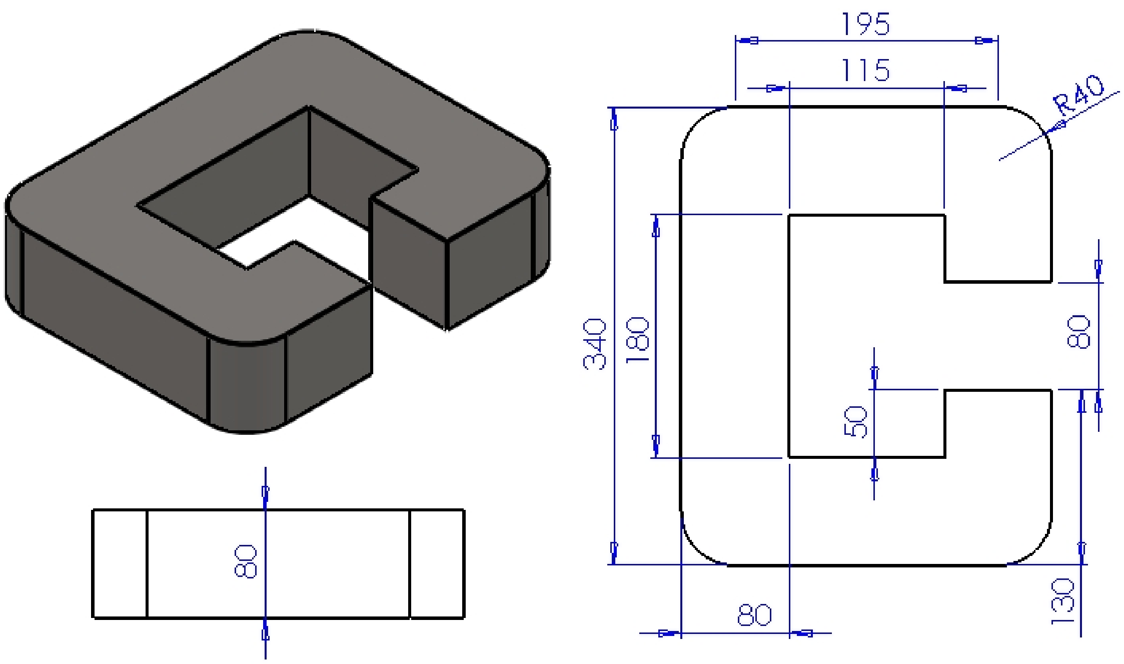

Figure 5.12: Dimensions of the silicon steel core

Figure 5.13: The practical build of the silicon steel core

5.3.2 The Electromagnet Coil Design

Based on the computer FE modelling work (Chapter 4), a magnetic flux density B of 50 mT (500 gauss) generated in the air gap of the electromagnet is sufficient to induce a potential difference of 260 μV between electrodes e_1 and e_9 for a flow rate of 118×10^{-6} m^3/s. Voltages down to 10 μV are detectable using a carefully designed signal conditioning system which is explained in depth in **Section 5.7**. To achieve a peak magnetic flux B_0 of 50 mT, the number of coil turns N, the peak supply voltage V_0 and peak coil current I_0 were calculated using the magnetic circuit theory [153].

The peak magnetic flux density B_0 in the air gap of the electromagnet can be described in terms of the peak supply voltage V_0, the peak current I_0, the reluctance of the air gap $\mathcal{R}_g$ (the reluctance of the core is negligible), the area of the air gap A_g and the frequency of the supply voltage f as shown below

$$B_0 = \frac{1}{A_g}\sqrt{\frac{V_0 I_0}{2\pi f \mathcal{R}_g}} \qquad \text{Eq. 5-1}$$

The derivation of Eq. 5-1 is provided in Appendix B. Another important equation is the relationship between the inductance of the electromagnet L, the number of turns of the coil N and the reluctance of the air gap $\mathcal{R}_g$ (reluctance of the core is negligible) [153] which is given by

$$L = \frac{N^2}{\mathcal{R}_g} \qquad \text{Eq. 5-2}$$

Practical electromagnets suffer from leakage and fringing fluxes (at the air gap) unlike an ideal electromagnet (refer to Figure 5.14). This means that the magnetic flux density B_0 in the air gap of the core would be less than that predicted theoretically. The total magnetic flux produced by the electromagnet is the sum of the magnetic useful, fringing and leakage fluxes. For this electromagnet, the total magnetic flux is produced at the centre of the coil and the useful magnetic flux is generated in the air gap of the core. This useful magnetic field is near uniform as will be seen in Section 6.8.

The leakage and fringing fluxes can be modelled as reluctance $\mathcal{R}_L$ in parallel with the air gap reluctance $\mathcal{R}_g$ as shown in Figure 5.15. They can be accounted for by introducing a factor k in Eq. 5-1 and Eq. 5-2; hence, these equations can be written as,

$$B_0 = \frac{1}{A_g}\sqrt{\frac{V_0 I_0}{2\pi f \mathcal{R}_g k}} \qquad \text{Eq. 5-3}$$

$$L = \frac{N^2 k}{\mathcal{R}_g} \qquad \text{Eq. 5-4}$$

where k is the ratio between the calculated air gap reluctance $\mathcal{R}_g$ and the actual air gap reluctance $\mathcal{R}_A$. This means that the actual reluctance of the air gap $\mathcal{R}_A$ is less than the calculated reluctance $\mathcal{R}_g$ by a factor of k. In other words, the actual inductance of the electromagnet is higher than the calculated inductance by the factor k as the inductance L of the magnetic circuit is inversely proportional to the reluctance of the air gap of the core (reluctance of the core is negligible) as shown in Eq. 5-2.

The factor k can be found experimentally (or using FE tools) by finding the inductance L for a given number of turns N and then calculating the actual and the theoretical air gap reluctances $\mathcal{R}_A$ and $\mathcal{R}_g$, respectively, using Eq. 5-2. For this electromagnet k was measured to be 10.7. The calculations that were performed to determine the number of turns N and the current required for the coil to generate a peak magnetic flux B_p of 0.05 T in the core air gap are shown below.

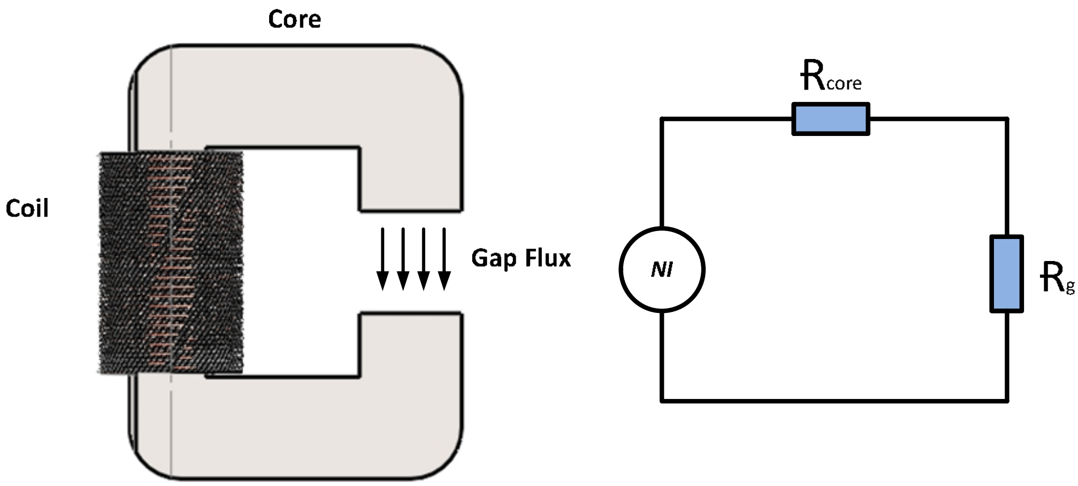

Figure 5.14: The ideal electromagnet

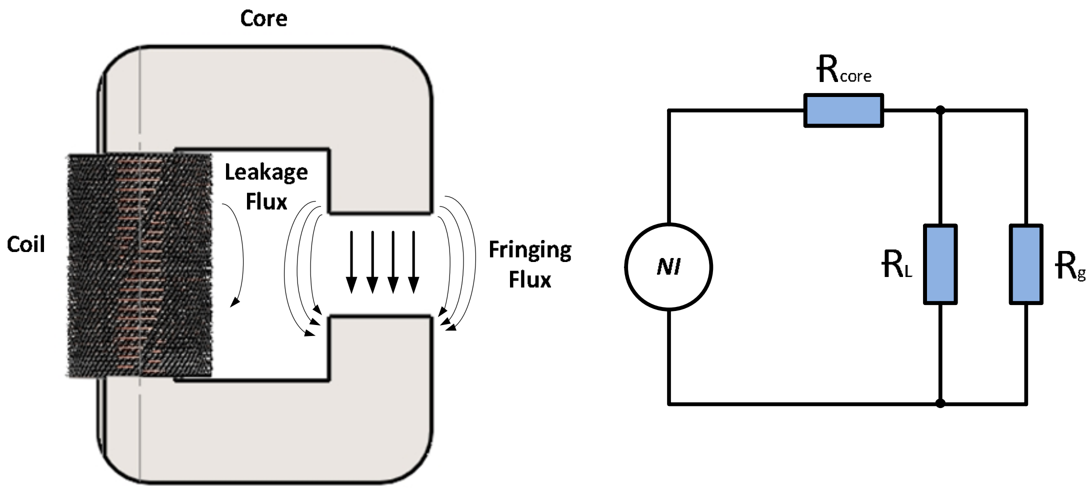

Figure 5.15: The practical electromagnet

The reluctance of the core air gap $\mathcal{R}_g$ was determined to be equal to 9.95 M At/Wb. The area of the core air gap was 6400 mm^2. For a peak supply voltage V_0 of 340 V (240 V$_{rms}$) and a frequency f of 50 Hz, the required peak current I_0 can be determined using Eq. 5-3 as follows,

$$I_0 = \frac{(2\pi k f)B_0^2 A_g^2 \mathcal{R}_g}{V_0} = \frac{2\pi(10.7)(50)(0.05)^2(6.4 \times 10^{-3})^2(9.95 \times 10^6)}{340} \approx 10\ A$$

The reactance of the electromagnet X_L was calculated as follows

$$X_L = \frac{V_0}{I_0} = \frac{340}{10} \approx 34\Omega$$

The inductance L was found from

$$L = \frac{X_L}{2\pi f} = \frac{34}{2\pi(50)} \approx 110\text{mH}$$

Finally, the number of turns of the coil N was calculated using Eq. 5-4 as follows

$$N = \sqrt{\frac{L\mathcal{R}_g}{k}} = \sqrt{\frac{(110 \times 10^{-3})(9.95 \times 10^{6})}{k}} \approx 320 \text{ turns}$$

The coil was wound on the side of the core and opposite the core air gap.

The wire selected for the coil was multi-stranded (170 strands) enamelled copper wire. Multi-stranded wire had to be used in order for the wire to be flexible enough to be wound around the core. Each strand had a diameter of 0.14 mm and the 170 strands in total created a cross sectional area of 2.62 mm^2 (diameter of 1.83 mm) which is the same cross-sectional area as 15 SWG wire gauge (13 AWG). The 15 SWG wire gauge is rated at a peak current of 10 A (7 A_{rms}). For 320 turns, the total length and weight of the wire used were approximately 102 m and 2.2 kg, respectively. The coil windings were wound on the core in 6 layers and each layer was insulated with high-temperature silicone polyimide tape to hold the windings in place. Figure 5.16 and Figure 5.17 show the electromagnet under construction and the finished unit.

Figure 5.16: The AC electromagnet under construction.

Figure 5.17: The complete AC electromagnet

5.4 Operating Frequency of the Electromagnet

Initially, the electromagnet was built to operate at mains supply voltage and frequency (240 V and 50 Hz); however, it was found at a later stage that this operating frequency would not be ideal for the operation of the practical system due to 50 Hz mains interference. The flow induced potential differences, resulting from the interaction between the uniform magnetic field generated by the electromagnet and water flow at the electrode array of the SVS, also had the same frequency and it was difficult to distinguish the flow potentials from the mains noise.

Fluorescent lights, motors or power cables induce and/or radiate noise at mains frequency which can enter an electric/electrical system in number of ways including capacitive and inductive coupling [154]. This noise was coupling to the voltage measurement electronics of the signal conditioning system. It was also detected by the electrodes embedded within the SVS. Using electrostatic shielding (Faraday's cage) would have reduced this noise, but this method would not work if the noise was magnetically induced [155]. Magnetic shielding would be required to reduce the magnetically induced noise.

The alternative solution was to operate the electromagnet at 30 Hz which meant that the flow induced potential differences had a unique frequency. This enabled the signal conditioning and processing systems to detect these potential differences accurately. The peak magnetic flux density B_0 would be the same for V_0 = 340 V at 50 Hz as the peak for V_0 = 200 V at 30 Hz since both settings give a peak coil current I_0 = 10 A. Moreover, the inductive impedance is directly proportional to the frequency of the voltage supply, i.e. $X_L = 2\pi f L$. Hence, lowering the frequency of the supply voltage decreases the impedance X_L allowing more current to flow, but when the voltage is also reduced, the current can be maintained in the circuit. This is explained in depth in Section 5.6.

5.5 The Complete SVS Test Rig

The SVS pipe model was inserted into the core air gap of the electromagnet and it was ensured that the embedded electrode array was at the centre of the air gap as illustrated in Figure 5.18. The electromagnet was placed flat down on a wooden stand. The stand was also drilled so that the SVS could be fitted in and held firmly. The water supply was connected to the SVS via the reinforced PVC hoses, and some additional pipe fittings were used as explained earlier in Section 5.2.

The total flow rate of a fluid in a circular pipe section Q is given by

$$Q = \frac{\pi}{4} v \cdot d^2 \qquad \text{Eq. 5-5}$$

where v is the fluid flow velocity and d is the diameter of the circular pipe. The total water flow rate Q_w through both SVS tubes was measured to be around 210×10^{-6} m^3/s (12.44 L/min). Using Eq. 5-5, the water flow velocity through each tube v_w was calculated as follows (each tube has a diameter of 10 mm),

$$v_w = \frac{1}{2} \times \frac{4Q_w}{\pi d^2} = \frac{2(210 \times 10^{-6})}{\pi (10 \times 10^{-3})^2} = 1.34 \text{ m/s}$$

The SVS was connected directly to a water tap and since there was no water flow stabiliser the flow rate could vary slightly from one test to another. However, a reference measurement was taken immediately before the start of each test. This measurement was performed by finding the time it took for the water flow through the SVS to fill a 2 L calibrated bucket. Then, the flow rate was found by dividing the volume of water in the bucket by the total time. The PVC hose connecting the bottom of the SVS to the water drain was easy to insert in the calibrated bucket.

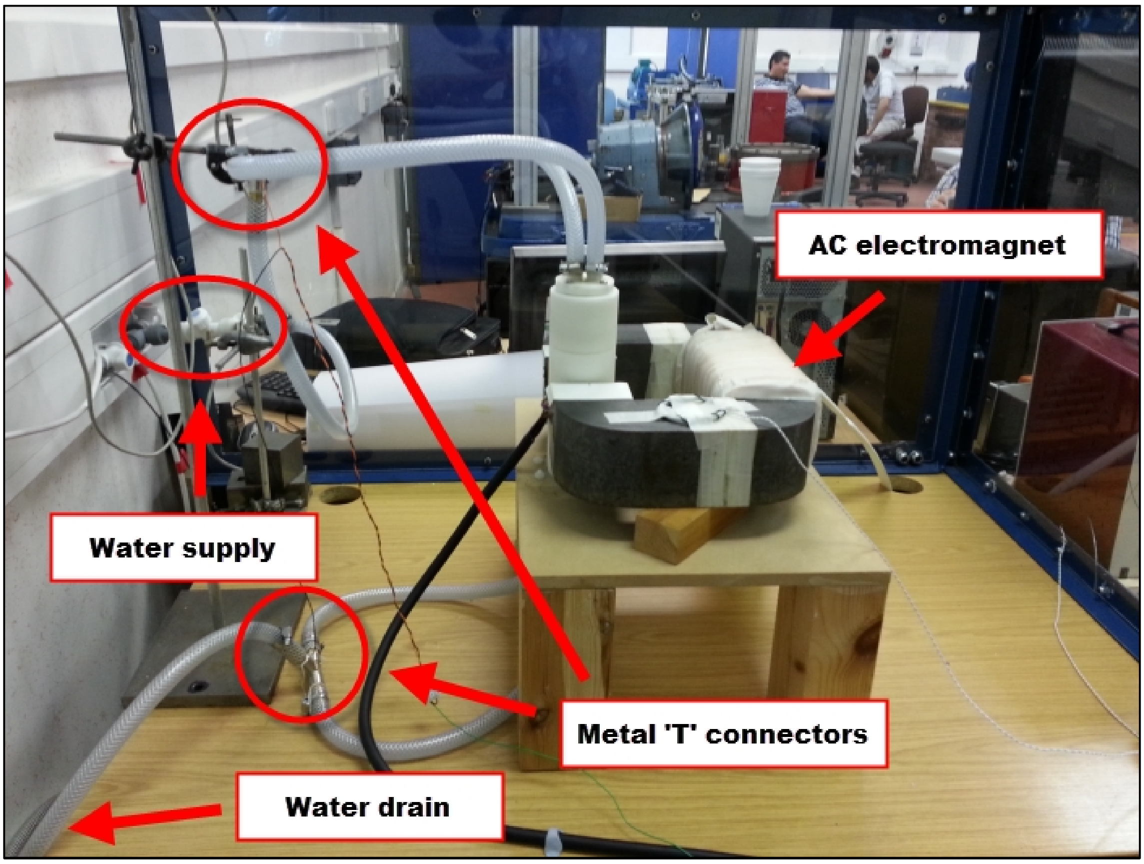

Figure 5.18: The flow test rig, the SVS and AC electromagnet

5.6 Electromagnet Power Supply Design

5.6.1 Operating the Electromagnet at 50 Hz

The electromagnet was initially powered by mains power supply in an attempt to measure the flow induced potentials detected by the electrode array before switching to the 30 Hz power supply. The electromagnet was connected to the mains power supply via a variable AC transformer (variac). This allowed the voltage across the electromagnet to be increased gradually to avoid inrush current associated with inductive loads as explained in Section 5.1. The setup of the electromagnet and the power supply is shown in Figure 5.19. A power analyser (PA) was used to monitor the voltage, current and the active and reactive powers supplied to the electromagnet.

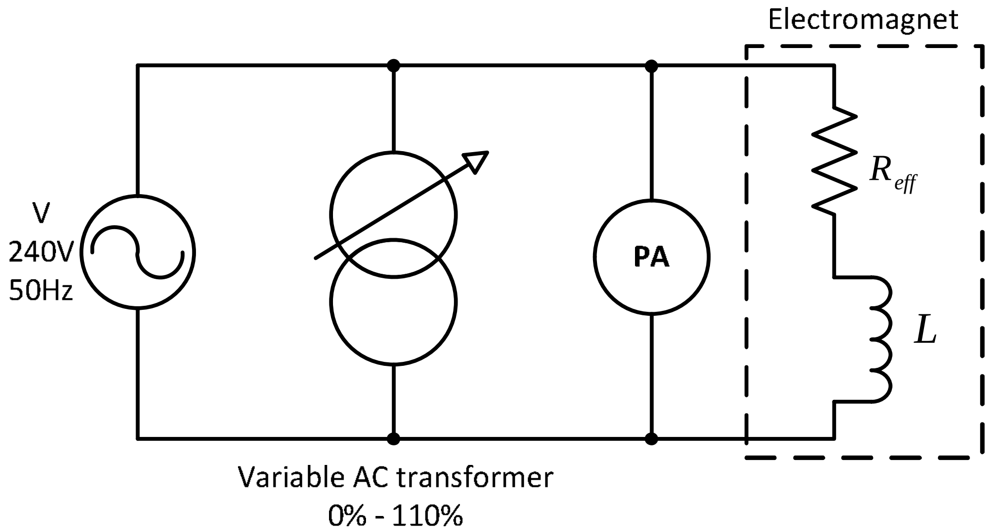

Figure 5.19: Electromagnet setup for 50 Hz operation

Power in AC Circuits

The electromagnet is an inductive load which has a very small resistance. The total current I_T drawn from the mains supply to the electromagnet is a complex number, i.e.

$$I_T = I_R - jI_L \qquad \text{Eq. 5-6}$$

The real part of the current I_R (load current) is drawn due to the effective resistance R_{eff} in the electromagnet. The effective resistance is different from the DC resistance due to effects related to time-varying voltage and current, in other words, radiation losses, eddy currents and hysteresis losses [153]. The imaginary part of the current jI_L (magnetising current) is the current necessary for the electromagnet to generate the required magnetic flux density in the air gap of the electromagnet. The total power delivered from the mains supply to the electromagnet is known as the apparent power S (unit: VA), and is given by the magnitude product of the voltage supply V and the total current I_T as shown in the following equation [153]

$$S = VI_T \qquad \text{Eq. 5-7}$$

For a pure inductive load, the total current lags the voltage by 90°. However, the electromagnet has a very small resistance and therefore, the total current I_T would lag the voltage by an angle that is slightly less than 90°. The power consumed due to the effective resistance R_{eff} is called the real (or active) power P (unit: watt) and it is expressed mathematically as

$$P = VI_T \cos\theta \qquad \text{Eq. 5-8}$$

where θ is the angle at which the total current I_T lags the supply voltage V and $\cos\theta$ is called the power factor (PF) of the electric circuit. From Eq. 5-7 and Eq. 5-8, the PF is the ratio between the real power P and the apparent power S, i.e.

$$\mathrm{PF} = \frac{P}{S} \qquad \text{Eq. 5-9}$$

When the PF is 1, the load is purely resistive and when it is 0, the load is purely inductive. This gives an indication of how resistive or inductive the load is. For most loads the PF is usually between 0 and 1. The real power P is also given in terms of the total current I_T and effective resistance R_{eff} as follows

$$P = {I_T}^2 R_{eff} \qquad \text{Eq. 5-10}$$

The power associated with the inductive (reactive) element of the electromagnet is called the reactive power Q_L (unit: VAr) and is calculated as follows

$$Q_L = S\sin\theta \qquad \text{Eq. 5-11}$$

or

$$Q_L = {I_T}^2 X_L \qquad \text{Eq. 5-12}$$

where X_L is the reactance of the inductor. This reactive power is drawn during the positive AC half cycle and returned to the power supply during the negative AC half cycle, and therefore, the net flow of power is zero. In other words, the reactive power is not dissipated at the load (electromagnet) and it only travels back and forth between the power supply and the load. Capacitors are also reactive elements and therefore, they draw reactive power Q_C from, and return it to, the power supply. Eq. 5-11 and Eq. 5-12 also apply to capacitors. However, the reactance of the capacitor X_C is given by

$$X_C = \frac{1}{2\pi f C} \qquad \text{Eq. 5-13}$$

where f is the frequency of the supply voltage and C is the capacitance. The difference between a capacitor and inductor is that the current leads the voltage by 90° in the capacitor, whereas in the inductor the current lags the voltage by 90°.

All three powers are related by the Pythagorean Theorem [153] (Figure 5.20), that is,

$$S^2 = P^2 + Q^2 \qquad \text{Eq. 5-14}$$

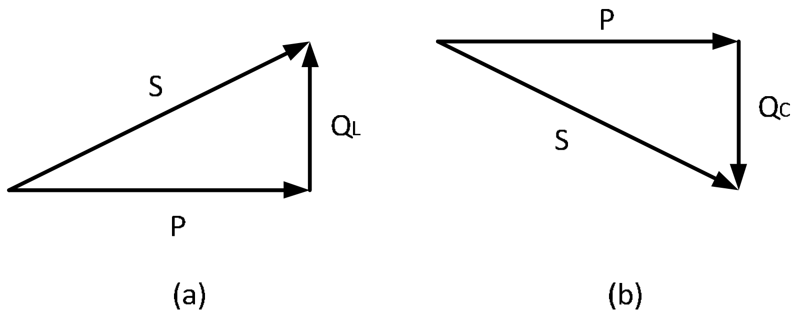

Figure 5.20: (a) Power diagram for inductive loads
(b) Power diagram for capacitive loads

Power Factor Correction

PFC refers to a method by which a capacitor is placed in parallel (refer to Figure 5.21) with the inductive load in order to bring the PF to unity. This has the advantage of reducing the total current I_T drawn from the power supply. The implication of having the total current I_T reduced is that the power requirements for the power supply and the variable transformer can be minimal and this is beneficial in terms of the physical size and cost of equipment.

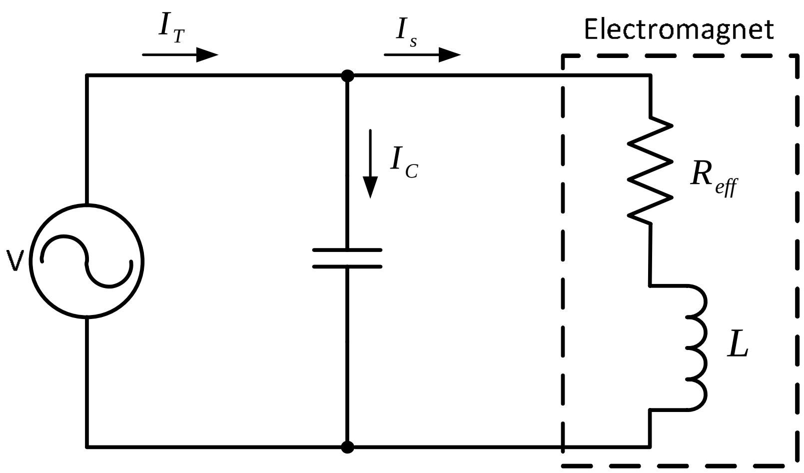

Figure 5.21: Placing a capacitor in parallel with the electromagnet for PFC

In Figure 5.21, the total current I_T is the algebraic sum of the current flowing through the capacitor I_C and the current following through the inductive load $I_s = I_R - jI_L$ (Kirchhoff's current law).

Thus,

$$I_T = jI_C + I_R - jI_L = I_R + j(I_C - I_L) \qquad \text{Eq. 5-15}$$

If $I_C = I_L$ then,

$$I_T = I_R + j(0) = I_R < 0° \qquad \text{Eq. 5-16}$$

It can be seen that the total current I_T is now in phase with the supply voltage, and as far as the power supply is concerned the load looks 'resistive'. All the power supplied to the load is absorbed, achieving maximum efficiency. By setting $X_C = X_L$ (to get $I_C = I_L$), the capacitor and the inductive part of the load are at resonance. The resonance frequency ω_0 is given by

$$\omega_0 = \frac{1}{\sqrt{LC}} \quad \text{or} \quad f_0 = \frac{1}{2\pi\sqrt{LC}} \qquad \text{Eq. 5-17}$$

A parallel LC circuit, at resonance, theoretically has an infinite impedance looking at its input terminals. The total impedance of the parallel LC network , i.e. Z_T, is presented in the following equation

$$Z_T = \frac{Z_C Z_L}{Z_C + Z_L} \qquad \text{Eq. 5-18}$$

where $Z_C = -jX_C$ and $Z_L = jX_L$. Hence, Eq. 5-18 can be written as

$$Z_T = \frac{-j\omega L}{\omega^2 LC - 1} \qquad \text{Eq. 5-19}$$

when the frequency of the power supply ω (or $2\pi f$) is equal to the resonant frequency ω_0, i.e. $\omega^2 LC = 1$, the total impedance is infinity.

Note that the peak current I_0 flowing between the capacitor and the electromagnet coil is not at minimum and is given by

$$I_0 = \frac{V_0}{X_L} \qquad \text{Eq. 5-20}$$

Calculation of the PFC Capacitor

The reactance of the electromagnet X_L was calculated previously in Section 5.3.2 to be 34 Ω at 50 Hz. The capacitance value C should be selected so that the reactance of the capacitor X_C is equal to the reactance of the electromagnet X_L, i.e. $X_C = X_L$, at the same operating frequency to implement the PFC. The value of the capacitance C is calculated as follows:

$$X_C = \frac{1}{2\pi f C} = 34\ \Omega$$

For a frequency f of 50 Hz,

$$C = \frac{1}{2\pi f X_C} = \frac{1}{2\pi(50)(34)} \approx 94\ \mu\text{F}$$

When the electromagnet was tested in the laboratory using the same setup as shown in Figure 5.19, the voltage supply was 242 V, and for a current of 7.07 A (10 A_{pk}), the reactance of the electromagnet was

$$X_L = \frac{V}{I} = \frac{242}{7.07} = 34.23\ \Omega$$

Therefore, the capacitance value was slightly less as shown below:

$$C = \frac{1}{2\pi f X_C} = \frac{1}{2\pi(50)(34.23)} \approx 93\ \mu\text{F}$$

when the capacitor (rated at 13 A) was placed in parallel with the electromagnet, the total current I_T drawn from the mains supply was 629 mA which means that the total required current was reduced by 91%. The PF was also increased to 0.5 from 0.05. When the capacitor was not placed in parallel with the electromagnet, the AC variable transformer had to be rated at 8 A (rms value) at least, whereas with the capacitor inserted, the AC variable transformer was replaced with another transformer rated at 1 A.

5.6.2 Operating the Electromagnet at 30 Hz

It was discussed in Section 5.4 how the electromagnet was operated at 30 Hz for the practical setup to avoid mains interference affecting the flow rate measurement experiments (see Section 5.4 for details). The electromagnet was operated previously at 50 Hz, which is the frequency of the mains supply, and for a 30 Hz operation, a new design of power supply was required. The reactance of the electromagnet at 30 Hz would change as it is dependent on the frequency. The new reactance was

$$X_L = 2\pi f L = 2\pi(30)(110 \times 10^{-3}) \approx 20.7\Omega$$

For a peak current of 10 A (to maintain the desired magnetic flux density B), the voltage across the electromagnet should be,

$$V_0 = I_0 X_L = (10)(20.7) = 207\ \mathrm{V}$$

For the PFC, the capacitance value C was also changed to

$$C = \frac{1}{2\pi f X_L} = \frac{1}{2\pi(30)(20.7)} \approx 260\ \mu\mathrm{F}$$

The new power supply was comprised of a Topward 8105 function generator, an LPA05A power amplifier and a $1:5$ custom-made step-up transformer. Figure 5.22 shows the new power supply, the PFC capacitor and the electromagnet RL model.

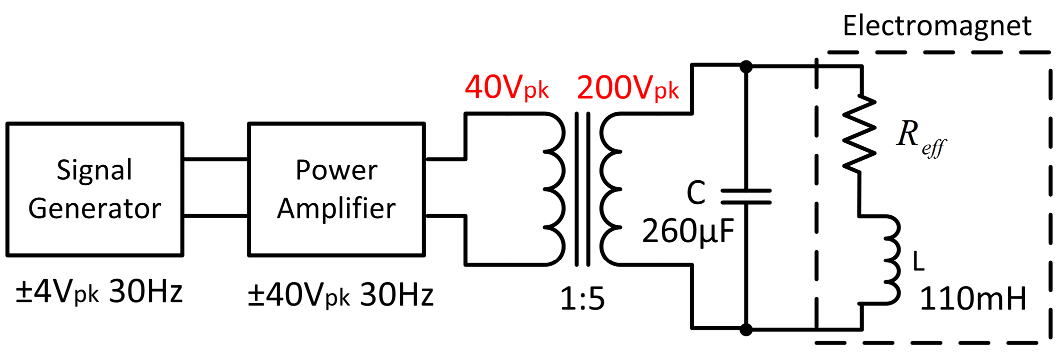

Figure 5.22: Electromagnet setup for 30 Hz operation

The function generator has a frequency range of 0.1 Hz to 2 MHz, an AC peak output voltage of 2.5 V to 10 V and an AC output peak current of 1.4 A [178]. The power amplifier has an AC peak input voltage of ±4 V, an AC output voltage of ±40 V and a maximum AC output peak current of 5 A [179]. The ratio of the step-up transformer was selected by finding the ratio between the peak voltage required across the electromagnet V_0, which is 207 V, and the peak voltage of the power amplifier, which is 40 V. The result is 5.2; however, experimentally, it was found that a voltage of about 200 V was required to achieve a peak current of 10 A in the coil of the electromagnet. The peak current rating of the primary of the transformer is the same as the current rating of the power amplifier which is 5 A. The calculations for the peak current rating of the secondary of the transformer are detailed below.

From the transformer theory [153] and referring to Figure 5.23,

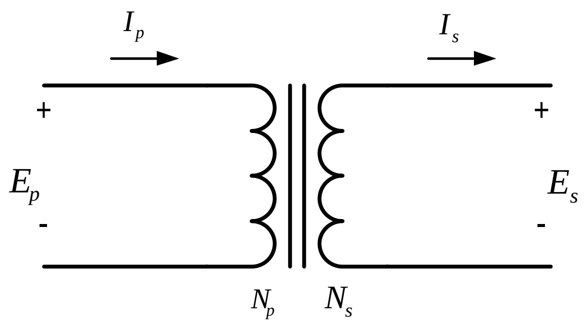

Figure 5.23: Iron-core transformer

The ratio between the magnitude of the induced voltages of the primary E_p and the secondary E_s is equal to the ratio between the number of turns of the primary N_p and the number of turns of the secondary N_s and is given by

$$\frac{E_p}{E_s} = \frac{N_p}{N_s} \qquad \text{Eq. 5-21}$$

Moreover, the ratio between the primary and the secondary currents of the transformer is the ratio between the number of turns of the secondary and the number of turns of the primary i.e.

$$\frac{I_p}{I_s} = \frac{N_s}{N_p} \qquad \text{Eq. 5-22}$$

From Eq. 5-21 and Eq. 5-22, the following relationship can be deduced, i.e.

$$\frac{E_p}{E_s} = \frac{I_s}{I_p} \qquad \text{Eq. 5-23}$$

From Eq. 5-23, it can be seen that if the primary voltage is amplified by a factor, the maximum output current of the secondary would be reduced by the same factor. Hence, for a voltage ratio of 1:5, the current ratio would be 5:1. The primary peak current was 5 A and therefore, the secondary peak current was 1 A, and this is the maximum current that can be drawn from the power supply – avoiding the risk of damaging the power amplifier.

5.7 AC Signal Conditioning System Design

The flow induced voltage signal detected between each electrode and electrode e_5 consisted of 4 components: (1) a small flow induced potential difference (2) a transformer induced voltage (3) a large DC offset due to electrode polarisation and (4) radio-frequency and mains interference. The small flow induced potential differences required amplification for suitable AD conversion. The transformer induced voltage arises from the electrode loop which is formed by the electrode, the cable and the conductive fluid, in the presence of a changing magnetic field [180].

The flow induced potential differences are proportional to the magnetic field strength, whereas the transformer voltages are proportional to the time derivative of the magnetic field as shown in Eq. 2-19 in Section 2.5.2. The separation between the flow induced potential differences and the transformer induced voltage was achieved by using a phase sensitive detection method [181] which is explained in detail in Chapter 6. This was necessary as the transformer induced voltage was the largest (dominant) of the total voltage signal components (typically a few mV) measured by the electrodes, and it was not possible to determine the flow induced potential differences without using this method. However, the transformer induced voltages were initially attenuated by using twisted-pair cables and aligning the electrode cables at the electrode array in such a way that they were parallel to the magnetic field in the electromagnet air gap. This meant that any electrode loop was not cut by the time-varying magnetic field by a large angle. The advantage of minimising the transformer voltages lay in avoiding a compromise of the gain value of the signal conditioning system in order to ensure that the system did not exceed its operational dynamic range.

Polarisation occurs due to ion-electron exchange between electrodes and water, which is a weak electrolyte. The result of polarisation is the presence of a large DC offset in the voltage signals picked up by the electrodes. Large DC offsets would limit the gain that can be set in the amplifier circuit to amplify the very small flow induced potential differences. High gain amplification is essential for accurate flow rate measurements as the flow induced potential difference signals were in the μV range. Radio-frequency and mains interference often exist in any environment where fluorescent lighting, electronic equipment and electrical machines are present and should preferably be attenuated to ensure a high signal to noise ratio. Each of these components (apart from the transformer induced voltages) was addressed by the AC signal conditioning circuit described below. Note that these issues are often encountered in electrode-based systems such as the medical instrumentation developed for Electrocardiography and Electroencephalography. Following detailed analysis of previous literature and application notes for such medical devices as well as datasheets supplied by semiconductor manufacturers [111, 157, 182-185], the following novel AC signal conditioning circuit was designed.

5.7.1 Description of the AC Signal Conditioning Circuit

The schematic diagram of the AC signal conditioning circuit is illustrated in Figure 5.24. It is comprised of the radio frequency interference (RFI) suppression filter, the 1st-stage AC-coupled instrumentation amplifier, the 2nd-stage inverting amplifier and the "right-leg" drive amplifier. Each part of the signal conditioning system is explained independently in the following sections. Note that all amplifiers were powered by a ± 15 V dual DC power supply.

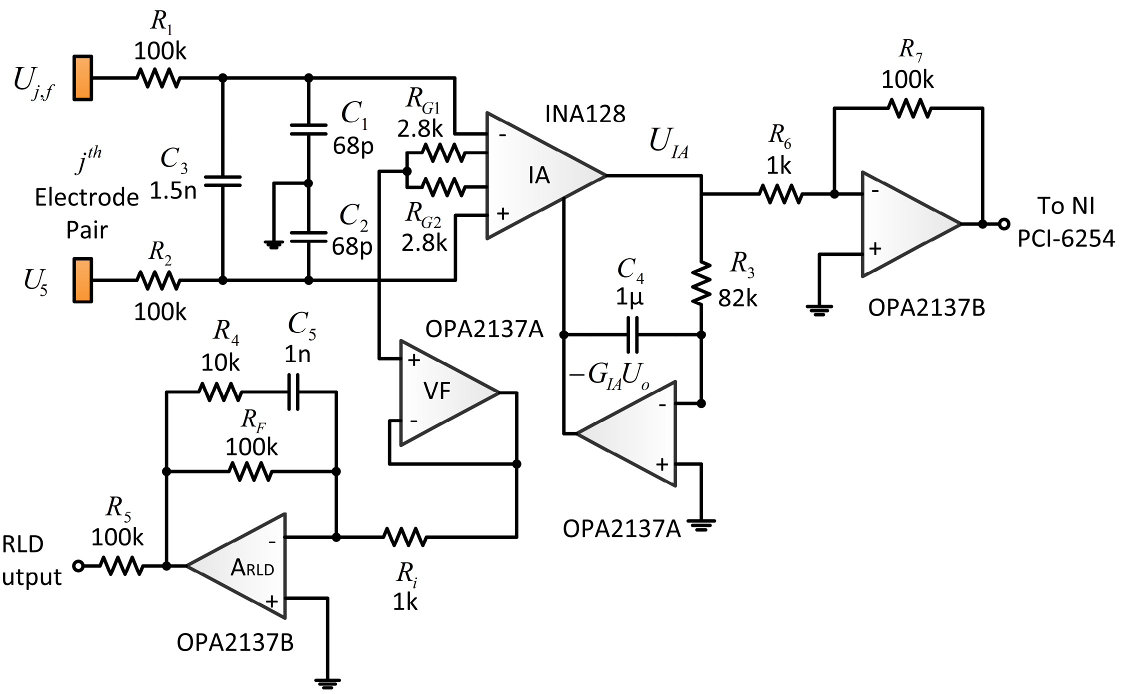

Figure 5.24: AC signal conditioning circuit

5.7.2 RFI Suppression Filter

The RFI filter is a low-pass filter (Figure 5.25) that attenuates common and differential RF signals which may be superimposed on the voltage signals detected by the electrodes. These RF signals normally range from 535 kHz (AM radio) to 2-3 GHz (mobile phones and WIFI). The purpose of the RFI filter is to attenuate any strong RF signals that could be detected by the electrodes. The INA128 instrumentation amplifier

(IA), which is used in this circuit design and other modern instrumentation amplifiers are very efficient at attenuating common-mode frequencies from dc to 100 Hz; hence, they are attractive to be used for low frequency measurements as they can reject 50/60 Hz – the common source of noise in low frequency measurements. However, their performance starts to degrade significantly for higher frequencies. Moreover, they cannot reject RF signals that are not common to their inputs. The absence of the RFI filter at the instrumentation amplifier input may cause the amplifier to rectify the RF signals (become DC voltage), and this leads to a DC offset error at the output of the amplifier [186, 187].

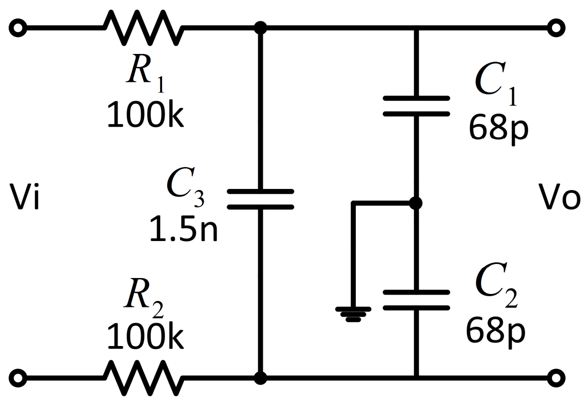

Figure 5.25: RFI differential filter

The RFI filter shown in Figure 5.25 has differential (differential signal applied) and common-mode (common signal applied) bandwidths. The passive networks R_1C_1 and R_2C_2 provide AC common-mode rejection and the capacitor C_3 adds a differential signal rejection capability. The -3 dB common-mode bandwidth is shown in the following equation,

$$f_{com} = \frac{1}{2\pi RC} \qquad \text{Eq. 5-24}$$

where R is the value of R_1 and R_2 and C is the value of C_1 and C_2. The -3 dB differential bandwidth f_{diff} is given by

$$f_{diff} = \frac{1}{2\pi R(2C_3 + C)} \qquad \text{Eq. 5-25}$$

The R_1C_1 and R_2C_2 networks should be as closely matched as possible since any mismatch reduces the high common-mode rejection ratio of the IA. However, the capacitor $C_{3,}$ shown in Figure 5.25, reduces any AC common-mode rejection errors (common-mode signal becomes differential) from C_1 and C_2 mismatching. As a design guideline, it is recommended that C_3 is set to be 10 times larger than C_1 and C_2 as this would reduce the AC common-mode error arising from C_1 and C_2 mismatch [187].

The component values used for the RFI filter were as follow; the resistors R_1 and R_2 were set to 100 kΩ, the capacitors C_1 and C_2 were set to 68 pF and C_3 was set to 1.5 nF. Using Eq. 5-24 and Eq. 5-25, the -3 dB common-mode and differential cut-off frequencies are 23.4 kHz and 517 Hz, respectively. These two -3 dB frequencies are confirmed in simulation as shown in Figure 5.26 and Figure 5.27. All circuit simulation work, performed in this research, is performed using TI-TINA 9 SPICE software [188].

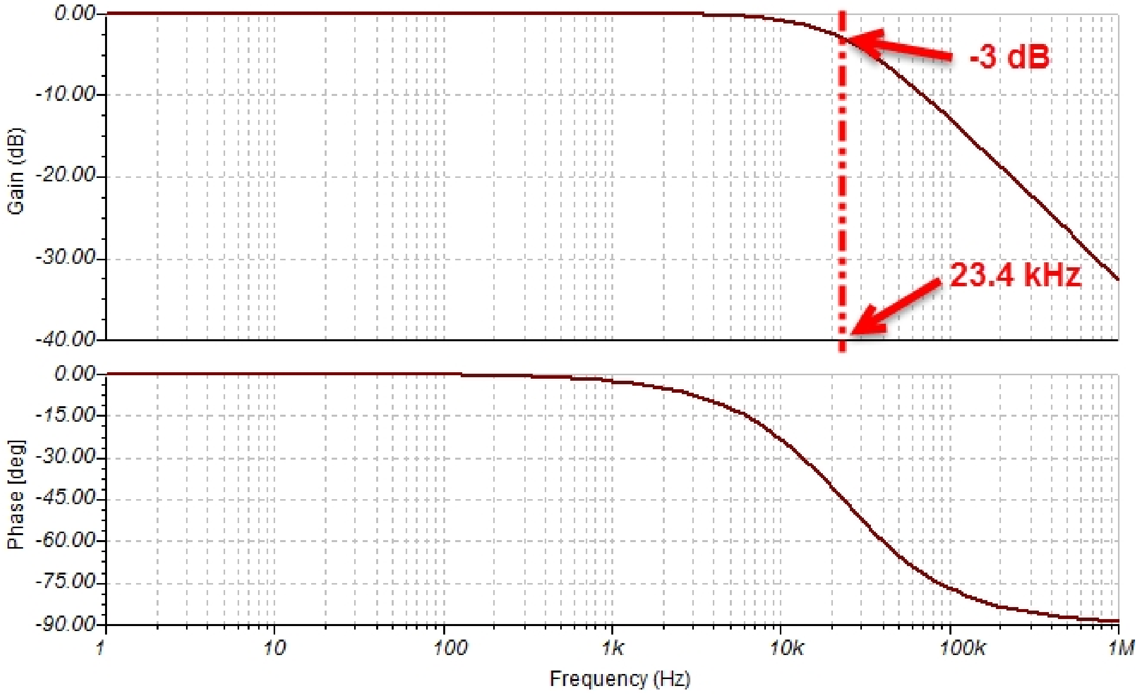

Figure 5.26: Frequency response of the RFI filter for a common--mode signal at the inputs

It can be seen in Figure 5.26 that the RFI filter attenuates considerably RF common-mode signals and that is important for the proper operation of the IA as explained above. Figure 5.27 shows the frequency response of the RFI filter for a differential signal in simulation. If a differential RF signal above 517 Hz is present at either one of the electrodes connected to the signal conditioning, it will be attenuated significantly by the RFI filter.

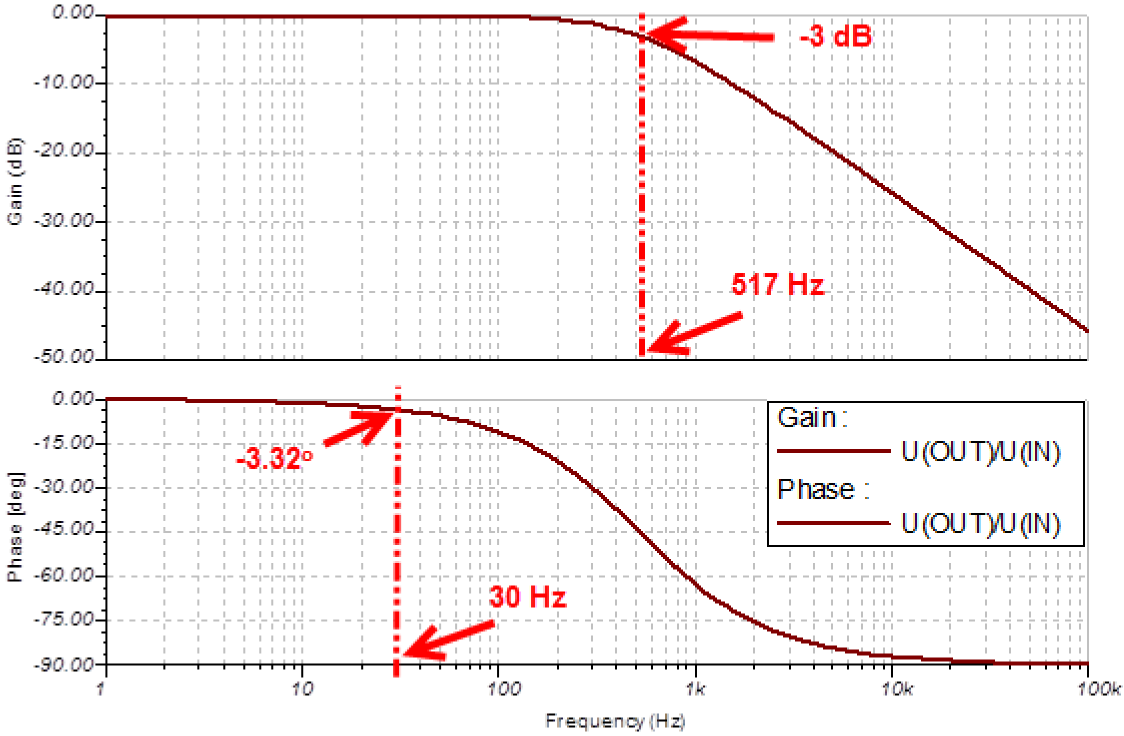

Figure 5.27: Frequency response of the RFI filter for a differential signal at the inputs

Note that Figure 5.27 shows that at 30 Hz, there is a phase lag of 3.32^o between the output and the input of the filter. This is a critical point as the flow induced potential difference at each electrode (with respect to e_5) is at 30 Hz (differential signal), and in order to effectively distinguish it from the transformer induced voltage using the PSD technique (explained in Chapter 6), the AC signal conditioning circuit should not introduce any phase lead or lag from its input to output otherwise, error in the flow induced potential difference measurements will occur. Nevertheless, the overall phase lead or lag from input to output of the signal conditioning circuit was measured and then, compensated for in the PSD software which is explained in the next chapter.

5.7.3 1st-stage AC-coupled Instrumentation Amplifier

There are two important advantages of using an IA: (1) it has very high input impedance (≈1GΩ) and (2) it has very high CMRR (≈100 dB) at low frequencies, i.e. dc to

100 Hz. The INA128 instrumentation amplifier that was used for this circuit has a very low offset voltage (50 μV) and low temperature drift (0.5 μV/C°) [189]. The gain of IA, G_{IA}, was limited to 10 due to the high DC offset U_0 which can be several orders of magnitude higher than the amplitude of the AC signal measured by the electrodes (flow and transformer induced voltages and EMI). Once the DC offset is removed via the AC-coupling technique (DC rejection, see below) of the IA, the voltage signal $U_{j,f}$ is amplified by a gain of 100 provided by the 2nd-stage inverting amplifier to achieve an overall gain of 1000. The gain of the IA (INA128) was set by the gain resistors R_{G1} and R_{G2} (Figure 5.28).

The value of each resistor was 2.8 kΩ with a tolerance of 1%. The total resistance was therefore, 5.6 kΩ. According to the IA datasheet [189], the gain equation is given by

$$G_{IA} = 1 + \frac{50\ \mathrm{k\Omega}}{R_{G1} + R_{G2}} \qquad \text{Eq. 5-26}$$

Thus, for the given resistor values, the total gain of the IA was 9.93. The reason for splitting the gain resistor R_G into two equal resistors R_{G1} and R_{G2} was to obtain the common-mode signal at the inputs of the IA, which is necessary for the implementation of the “right-leg” drive amplifier circuit.

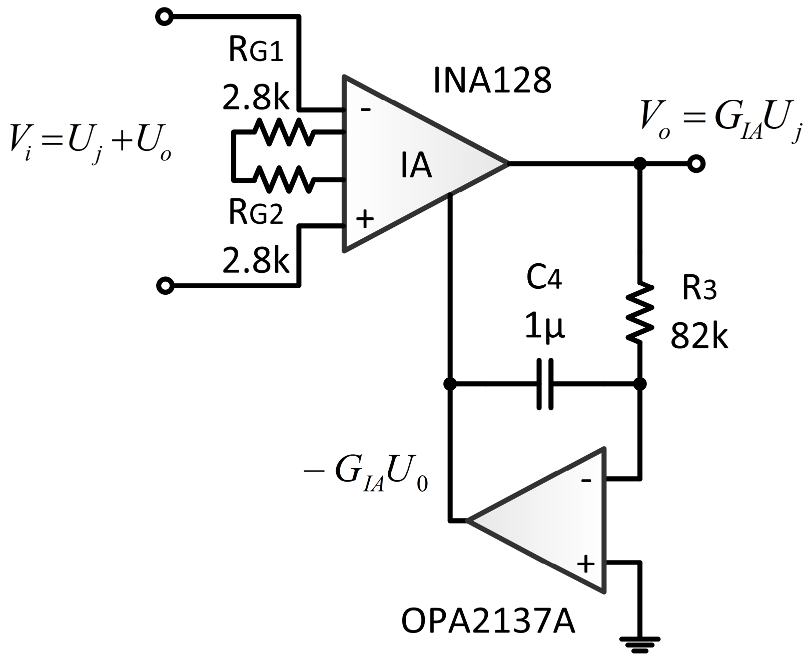

Figure 5.28: AC-coupled instrumentation amplifier

The AC-coupling was implemented by introducing an active low-pass filter in the feedback to the reference pin of the IA. The low-pass filter consisted of an RC low-pass network R_3C_4 and FET-input op-amp OPA2137A. The OPA2137A is a dual op-amp that is suitable for applications such as active filters [190]. The other op-amp was used for the final gain stage (x100) of the signal conditioning circuit. The –3 dB frequency of the low pass filter is given by

$$f_{LP} = \frac{1}{2\pi R_3 C_4} \qquad \text{Eq. 5-27}$$

For the resistor value R_3 of 82 kΩ and the capacitor value C_4 of 1 μF, the -3 dB frequency is 1.94 Hz. The low-pass filter removes the higher frequencies from the output of the IA and passes and inverts the amplified DC offset $G_{IA}U_0$. The AC-coupled IA, in principle, is a high-pass filter with a -3 dB frequency given in Eq. 5-27. The transfer function of the low-pass filter is given in Eq. 5-28.

$$LP(s) = \frac{1}{\tau_1 s} \qquad \text{Eq. 5-28}$$

where τ_1 is the time constant and is equal to R_3C_4. The closed loop transfer function of IA with the feedback low-pass filter is [191]

$$HP(s) = \frac{G_{IA}}{1 + G_{IA}LP(s)} \qquad \text{Eq. 5-29}$$

Substituting Eq. 5-28 into Eq. 5-29 gives

$$HP(s) = \frac{G_{IA}\tau_1 s}{1 + G_{IA}\tau_1 s} \qquad \text{Eq. 5-30}$$

Eq. 5-30 represents a high pass transfer function with a gain of G_{IA} and -3 dB frequency that is given in Eq. 5-27. The frequency response of the transfer function in Eq. 5-30, in simulation, is shown in Figure 5.29. Referring to Figure 5.29, the -3 dB frequency of the IA filter is 1.94 Hz which appears as 17 dB due to the gain G_{IA} of 20 dB (gain of 10). The phase shift between the input and the output of the AC-coupled instrumentation amplifier (1st stage) at 30 Hz is $-177.08°$. However, the AC-coupled instrumentation amplifier (Figure 5.28) is followed by an inverting amplifier (Figure 5.31), so the overall effect of the 1st-stage amplifier and the 2nd-stage amplifier is a phase lead of 2.92° ($-177.08° + 180°$).

The AC-coupling could be implemented by placing two RC high-pass networks at the inputs of the IA. However, this would lower the input impedance and degrade the CMRR of the IA due to impedance imbalance caused by mismatched components. A 1% mismatch for two 1 MΩ resistors can already create a -60 dB loss in the CMRR [192].

Both the RFI suppression filter (low-pass filter) and the overall 2-stage amplifier (high-pass filter) form a band-pass filter as shown in the simulation of the frequency response in Figure 5.30. The lower −3 dB frequency is 1.94 Hz and the higher −3 dB frequency is 517 Hz. The phase integrity between the inputs of the AC signal conditioning circuit and the output is critical for the PSD technique (Chapter 6) to work effectively. However, phase lag and lead are introduced by the low-pass and the high-pass filters, respectively. In simulation, the RFI filter caused a phase lag of 3.32^{o} (refer to Figure 5.27) and the 2-stage amplifier caused a phase lead of 2.92^{o} (refer to Figure 5.29). Thus, the net effect of the phase lag of the RFI filter (−3.32°, see Section 5.7.2) and the phase lead of 2-stage amplifier (2.92°) is a phase lag of 0.4° between the input of the RFI circuit and the output of 2-stage amplifier when they are connected in series.

In the practical circuit (refer to Section 6.9), this phase shift was measured as 2.4° (leading) due to component tolerances; however, it was compensated for in the PSD software as explained in Section 6.6. Note that Figure 5.30 shows the frequency response between the input and output of the RFI and 1st-stage AC-coupled amplifier circuits only, thus; the phase of the output of IA is −180.4^{o} at 30 Hz. When it is inverted by 180^{o} due to the 2nd-stage inverting amplifier, the phase becomes −0.4^{o}.

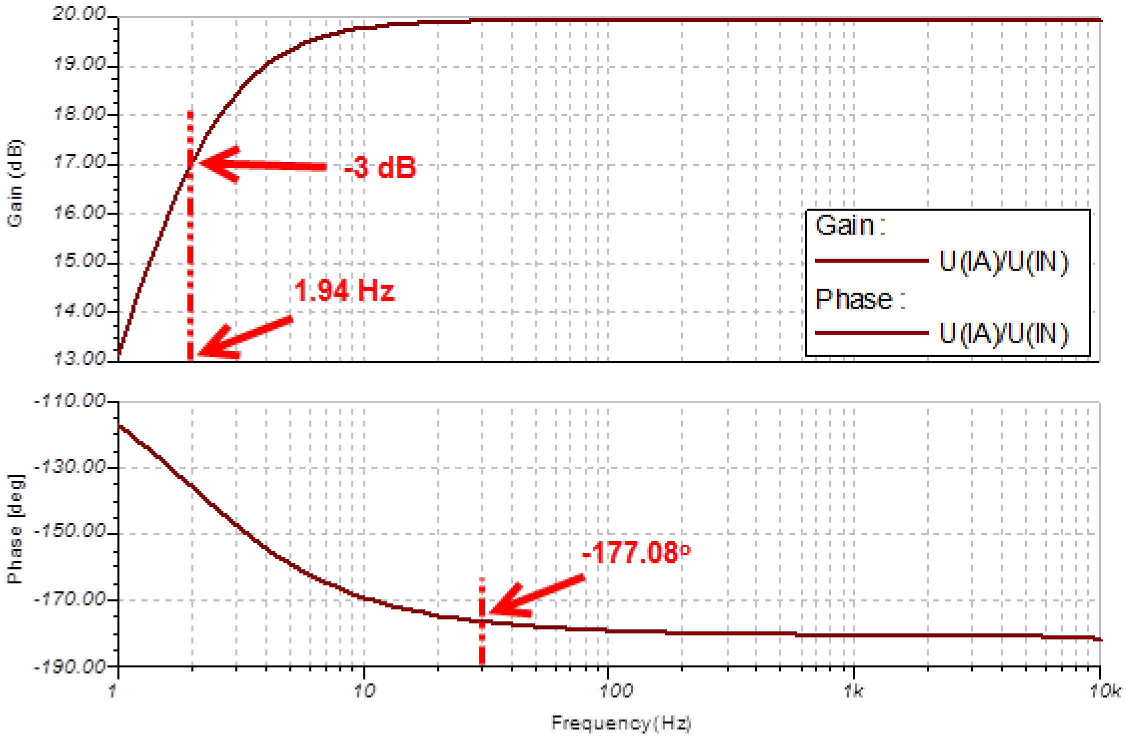

Figure 5.29: Frequency response of the 1st-stage AC-coupled instrumentation amplifier

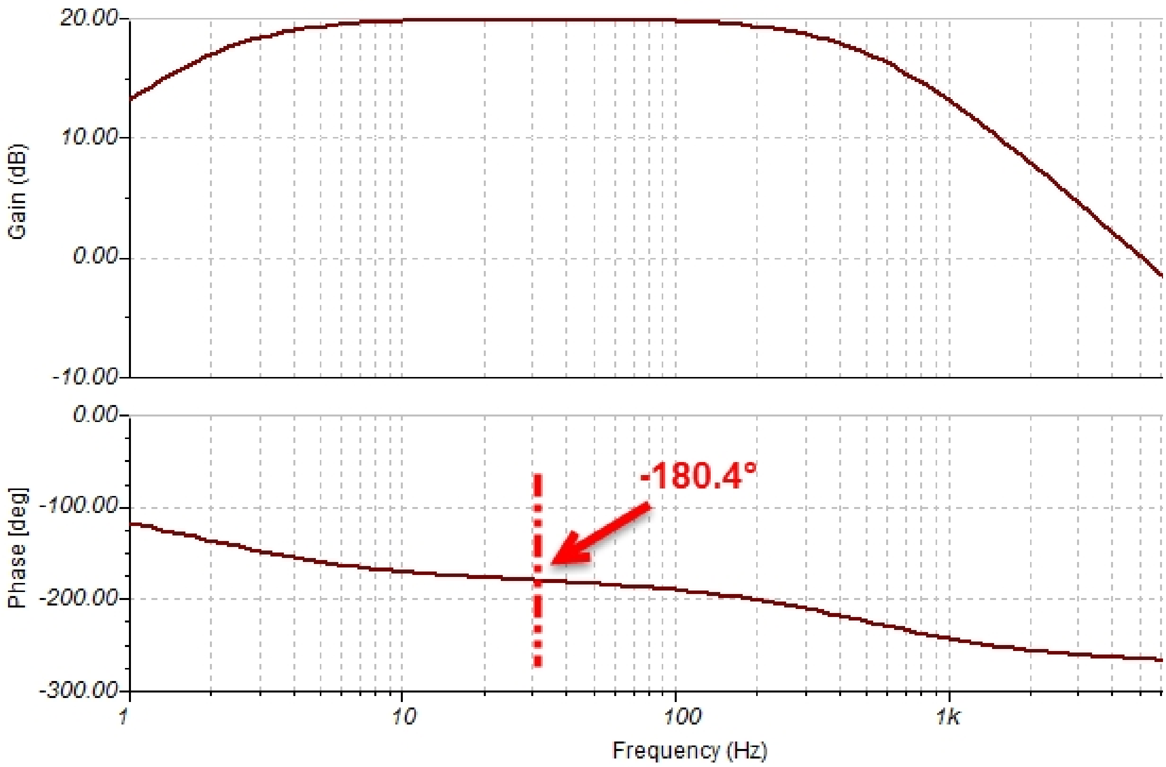

Figure 5.30: Frequency response of the RFI filter and the 1st-stage amplifier

5.7.4 2nd-stage Gain Inverting Amplifier

In Figure 5.24, the 2nd-stage gain inverting amplifier (also shown in Figure 5.31) boosts the measured signal by a factor of 100. The gain is set by R_6 = 1 kΩ and R_7 = 100 kΩ. Hence, the overall gain of the signal conditioning circuit, including both 1st-stage and 2nd-stage amplifiers, was about 1000 approximately.

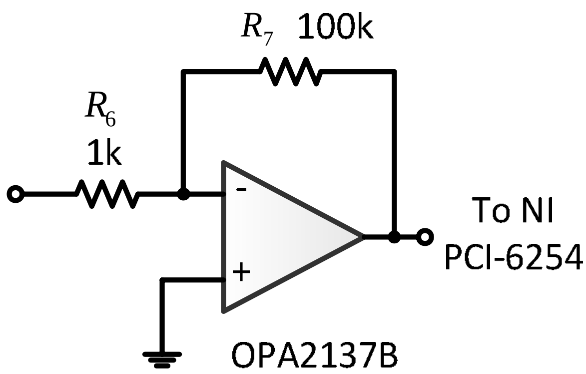

Figure 5.31: 2nd-stage inverting amplifier

5.7.5 "Right-leg Drive" Inverting Amplifier

The CMRR of the signal conditioning circuit is a measurement that shows how the AC-coupled instrumentation amplifier (or any differential amplifier) effectively rejects a signal that is common to both its inputs. It is defined as the ratio of the differential-mode gain A_d to the common-mode gain A_{cm} and is often expressed in dB as shown in Eq. 5-31.

$$CMRR = 20\log_{10}\frac{A_d}{|A_{cm}|} \qquad \text{Eq. 5-31}$$

All the CMRR tests in this section were performed in simulation using TINA-TI 9 software (Refer to Appendix C) by applying 50 Hz at both inputs (common-mode) of the AC-coupled instrumentation amplifier to simulate mains interference – the main source of noise at low frequency measurements. The flow induced potential differences are not affected by the CMRR of the AC-coupled amplifier as they are differential signals. Referring to Figure 5.24, assuming that the impedances of the j^{th} electrode Z_j and the reference electrode Z_5 are matched, and the RC networks of the RFI filter are also identical, the CMRR of the circuit would be around 106 dB at 50 Hz as shown in Figure 5.32. Note that on the Gain vs Frequency plot in Figure 5.32, the -86 dB gain measurement at 50 Hz, at the output of the IA, is after 20 dB gain (gain of 10); thus the input referred CMRR is 86 dB plus 20 dB which gives 106 dB. The CMRR value was also confirmed by comparing it to the INA128 datasheet [189].

For unbalanced source impedances Z_j (impedance of the j^{th} electrode) and Z_5 (impedance of electrode e_5), the output of the AC-coupled instrumentation amplifier, U_{IA}, with a finite CMRR, gain of G_{IA} and input impedance Z_{in}, is given by [111]

$$U_{IA} = G_{IA}U_{j,f} + \frac{G_{IA}U_{com}}{CMRR} + G_{IA}U_{com}\left(1 - \frac{Z_{in}}{Z_{in} + Z_j - Z_5}\right) \qquad \text{Eq. 5-32}$$

where U_{com} is the common-mode voltage, i.e. RF and mains interference. Unbalanced source impedances in the range of 5 kΩ to 10 kΩ are common in electrode-based systems [111]. For a 1% mismatch between the RC networks of the RFI filter alone, the CMRR drops to 94 dB (74 dB on graph) at 50 Hz, as shown in Figure 5.33. In practice, there is always a mismatch in electrode impedances, cable impedances and the RC networks, which are connected to the inputs of the AC-coupled instrumentation amplifier. This results in a significant impedance imbalance which leads to common-mode to differential-mode signal conversion. Therefore, in practice, the CMRR will be much lower than 94 dB. In medical instrumentation design, the Emergency Care Research Institute (ECRI) recommends that CMRR should be 100 dB and higher at 50

Hz and the input impedance of the measuring circuit should be higher than 100 MΩ for accurate low measurement systems [111, 193].

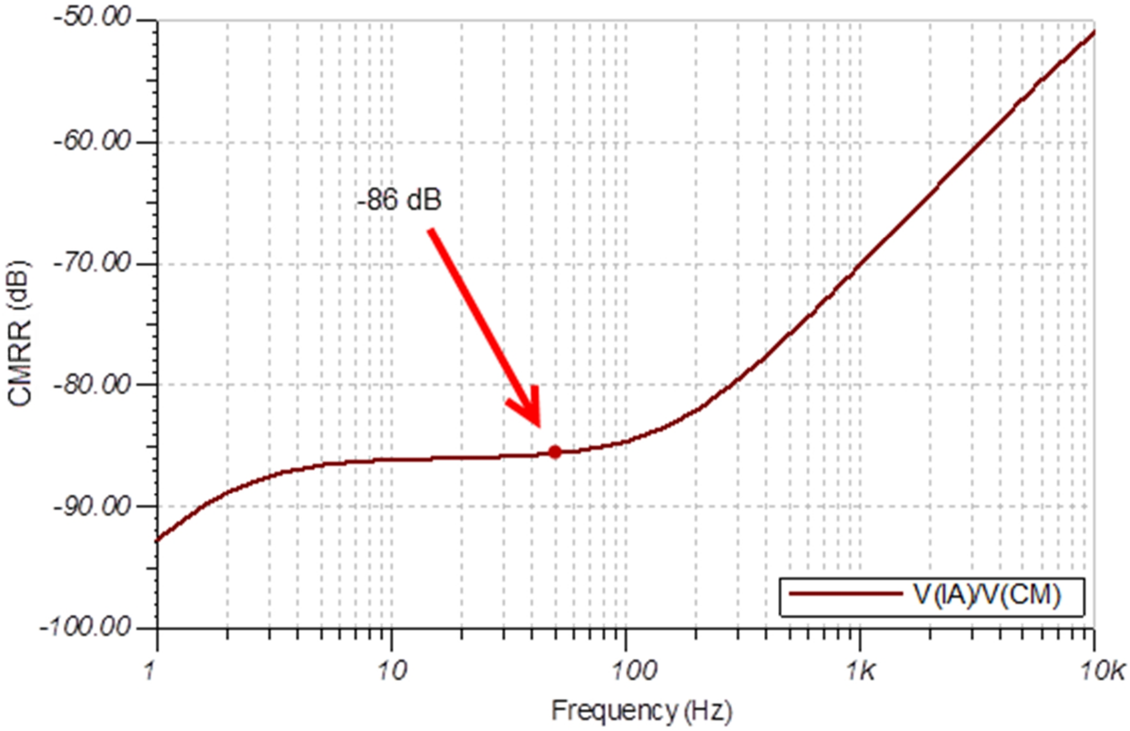

Figure 5.32: CMRR vs frequency of INA128 for matched source impedances (Z_j and Z_5)

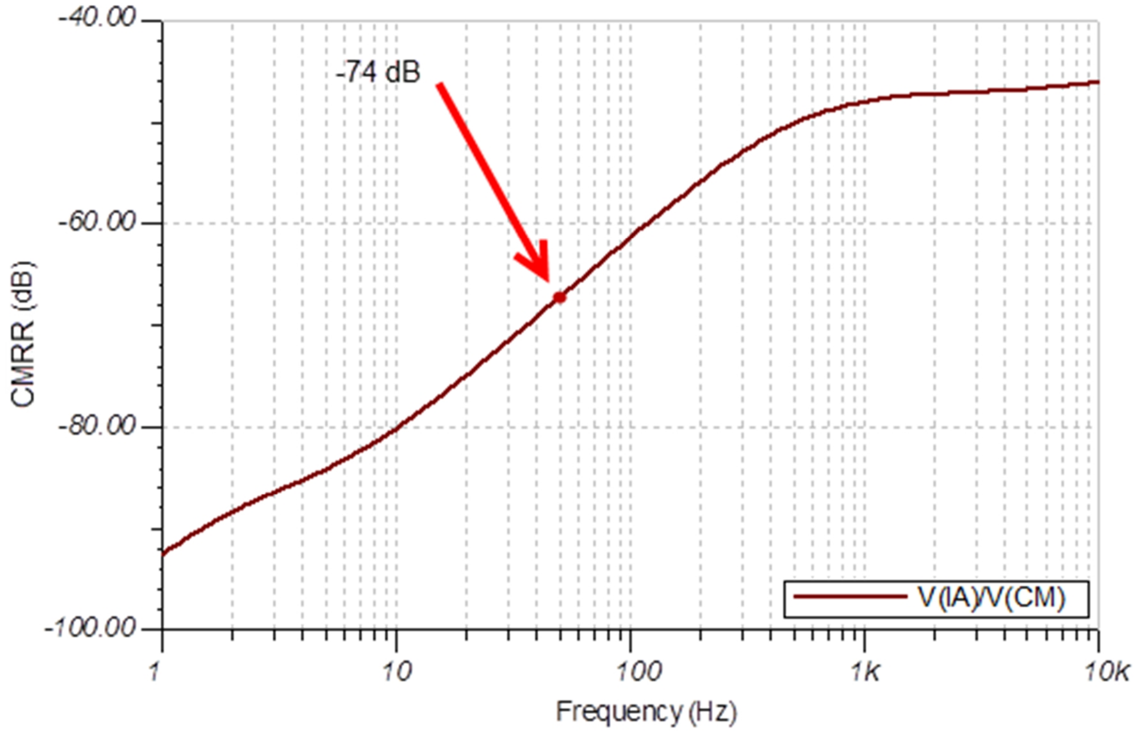

Figure 5.33: CMRR vs frequency of INA128 when there is a 1% mismatch between the RC networks of the RFI filter

There are several ways to improve the CMRR of the system: (1) precision RC components, (2) Faraday shielding and (3) noise cancellation using the "Right-Leg Drive" (RLD) inverting amplifier [194]. RLD is a technique by which the common-mode voltage is sensed, phase inverted and amplified by an inverting amplifier (A_{RLD} in Figure 5.34). Then, the inverted signal is fed back to the source to reduce the common-mode interference. The higher the gain of the amplifier A_{RLD}, the higher the CMRR. However, a very high gain can result in instability issues in the overall circuit [195]. The RLD method is used in ECG medical devices in which the output of the RLD amplifier is connected to the right leg of the patient under examination, and hence its name [85].

In some other medical literature, this method is referred to as body potential driver (BPD). This method, in principle, is similar to the active noise cancellation technique implemented in high quality audio headphones using Digital Signal Processing (DSP) [196]. The noise in the surroundings is sensed by a built-in microphone in the headset. This noise is then phase inverted and added to the combined noise and audio signals to attenuate the noise signal only. Note that this active noise cancellation method can also be implemented in industrial EM flow meters for EM interference reduction. A common technique used in the installation of EM flow meters in industry is to add grounding rings near the EM flow meter to minimise noise and ensure that the fluid and sensors are at the same potential [197]. Grounding the fluid is sometimes not sufficient in minimising noise, especially mains interference, as was experimentally observed by the author. It was also found that grounding the reference electrode should not be done as the voltage measurement of each electrode should be made differentially with respect to the reference electrode to eliminate common-mode noise interference effectively.

The schematic diagram of the RLD amplifier is shown in Figure 5.34. The midpoint of the averaging gain resistors R_{G1} and R_{G2} (refer to Figure 5.24) is the common-mode voltage. This midpoint is connected to a voltage follower VF to avoid any loading effects which may affect the gain of the AC-coupled instrumentation amplifier. The output of the VF is connected to the inverting amplifier A_{RLD}.

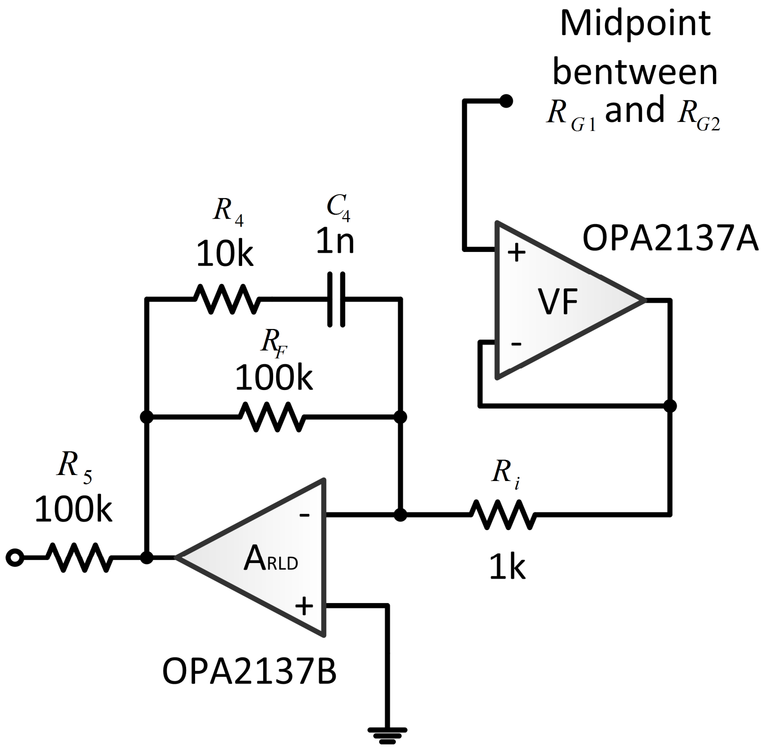

Figure 5.34: Right-leg drive inverting amplifier

The gain of A_{RLD} was set by the resistors R_F = 100 kΩ and R_i = 1 kΩ, using the gain equation of the inverting amplifier which is

$$G_{A_{RLD}} = -\frac{R_F}{R_i} \qquad \text{Eq. 5-33}$$

Hence, the gain is 100. For a balanced impedance at the inputs of the IA, the CMRR of the IA at 50 Hz (frequency of the common-mode signal) in simulation, with the amplifier A_{RLD} set to a gain of 100, is 146 dB (126 dB on graph) as shown in Figure 5.35. The CMRR is also shown for different A_{RLD} gains, i.e. 1, 10, 100 and 1000. The CMRR simulation test setup for the AC-coupled IA, with and without the RLD amplifier, is shown in Appendix C.

Figure 5.36 shows the CMRR for different A_{RLD} gains for imbalanced impedance of 10% at the input of the IA (one input of the IA has 10% impedance higher than the other). The CMRR of the IA at 50 Hz, with A_{RLD} gain set to 100, is 108 dB (88 dB in Figure 5.36). In the practical system, the input resistors at the IA are accurate to 1%; however, this test showed that even if the imbalance in impedance is 10% – accounting for impedance imbalance in source impedance, electrodes and cables – the CMRR of the IA remained above 100 dB. Note that, in the practical experiments (in Section 7.3), the output of the “right-leg drive” inverting amplifier was connected to the metal ‘T’ connectors shown in Figure 5.18. These connectors are electrically conductive, in contact with the water and near the electrode array where the measurements were taken. Figure 5.37 shows the complete practical AC signal conditioning circuit, built using stripboard.

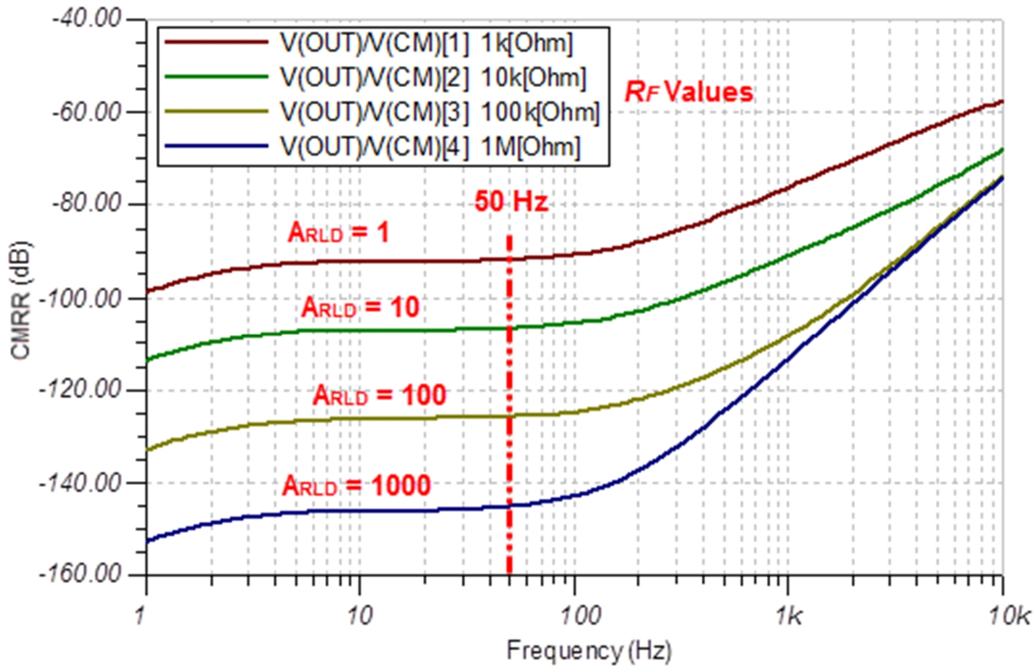

Figure 5.35: CMRR vs frequency of INA128 for different gains A_{RLD} without any impedance imbalance

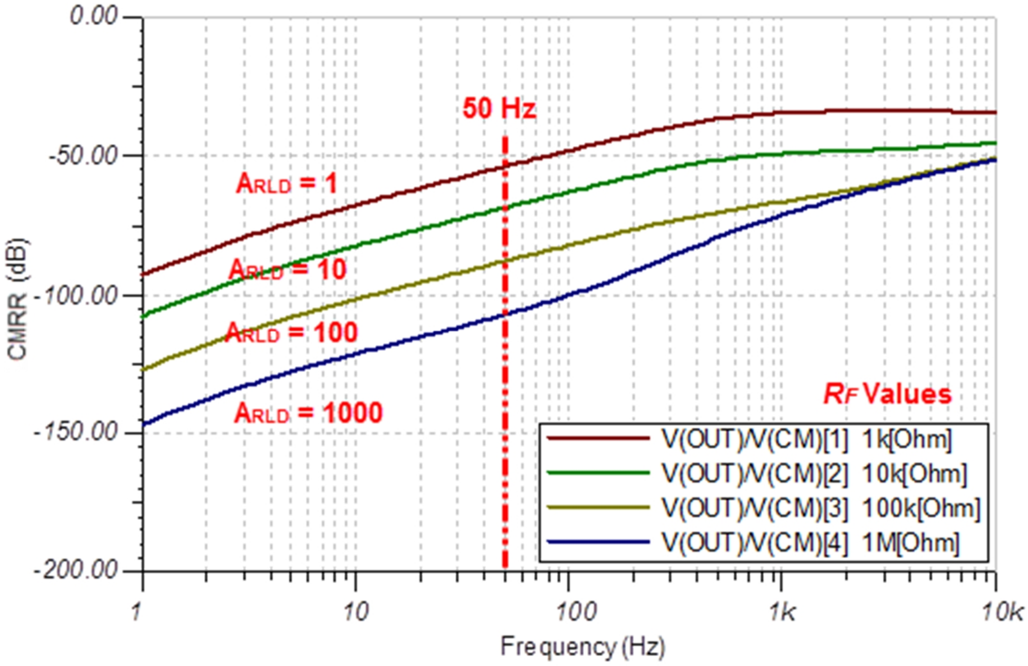

Figure 5.36: CMRR vs frequency of INA128 at different gains A_{RLD} for imbalanced source impedance

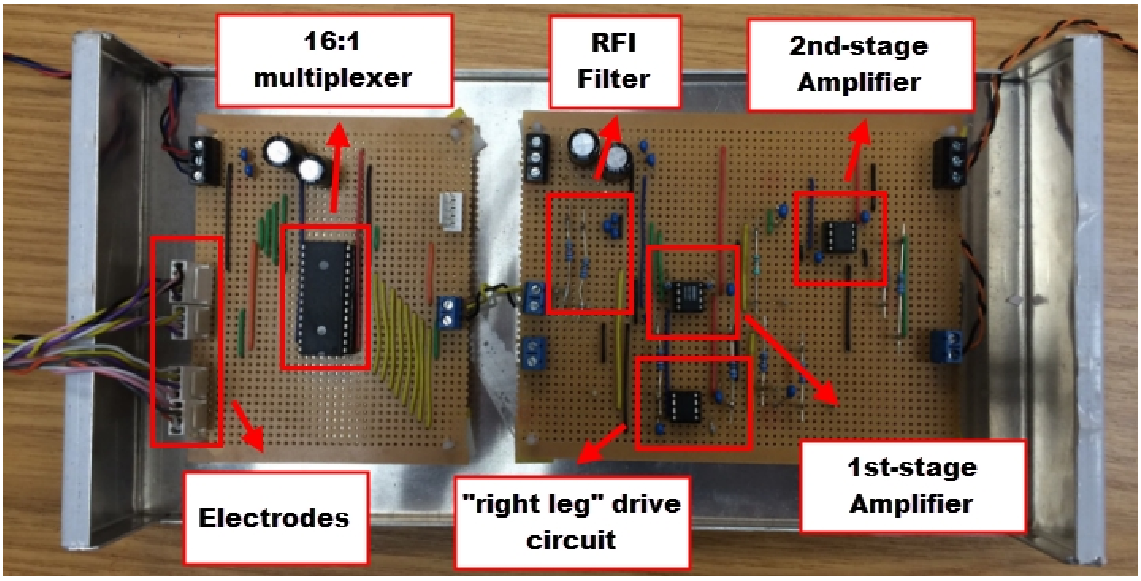

Figure 5.37: The practical AC signal conditioning system

5.7.6 Simulation Tests for the AC Signal Conditioning Circuit

The AC signal conditioning circuit was tested for its frequency, transient and normal responses in TINA-TI 9 software [188]. All schematic diagrams for the test setups are provided in Appendix C. Figure 5.38 shows the frequency response of the overall circuit in simulation. At 30 Hz (operating frequency of the electromagnet), the gain of the overall circuit was 59.89 dB (≈987) and the output led the input by 0.4°.

For the transient response, a step input of 200 mV was applied to the circuit. This test was useful in determining the delay time required for the circuit before sampling its output via the ADC. This test simulated the switching of the electrodes via the 16:1 multiplexer circuit. When the switch is changed, there will be some DC offset applied to the input of the signal conditioning circuit, which is due to electrode polarisation, in addition to the flow induced voltage. It can be seen in Figure 5.39 that for 200 mV DC offset, the circuit takes about 0.5 s to reach its steady-state value. It was experimentally found that the maximum DC offset on the electrodes was about 150 mV.

Finally, the circuit was tested for its normal operation, i.e. after the transient response has elapsed. The test simulated a flow-induced peak voltage of 100 μV at a frequency of 30 Hz at electrode e_j with a DC offset of 250 mV and a flow induced voltage of 50 μV peak at electrode e_5 at the same frequency, but with DC offset of 100 mV as shown in Figure 5.40. Moreover, a common-mode noise of 50 mV at 50 Hz (500 times greater than the flow induced potential difference which is 50 μV) was added to both electrodes (see Appendix C: Normal Test Operation Circuit). Hence, the dominant voltage signal at electrodes e_j and e_5 was the 50 Hz noise signal as shown in Figure 5.41.

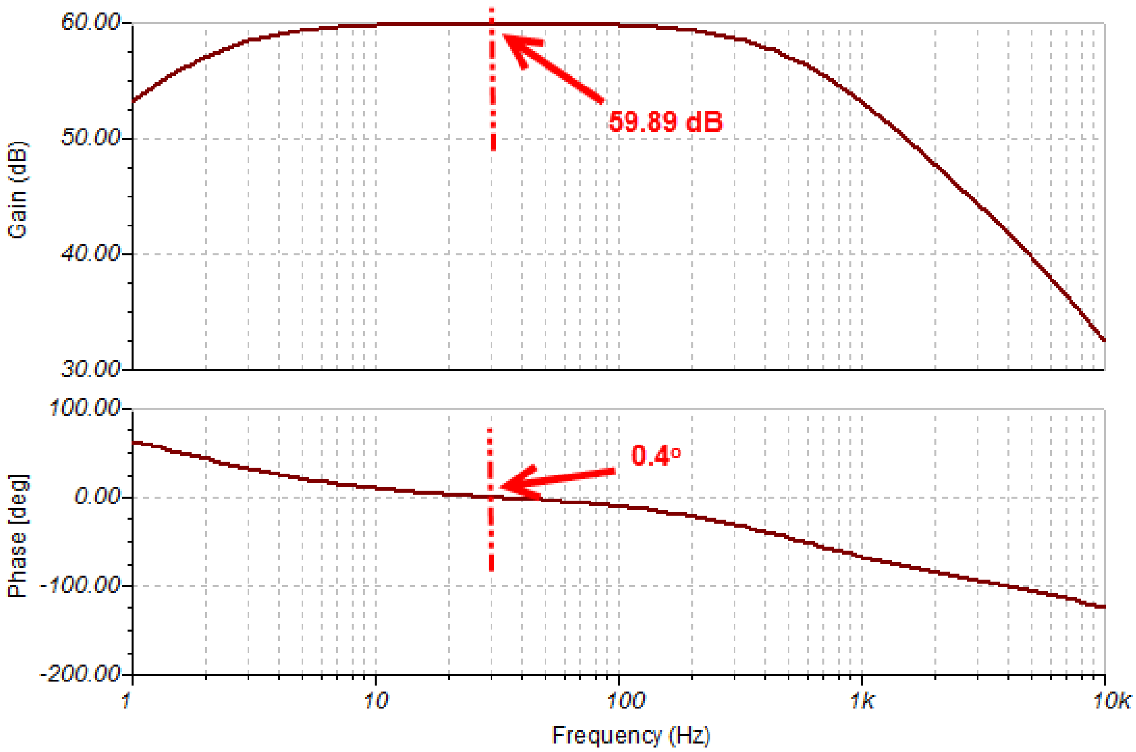

Figure 5.38: Frequency response of the AC signal conditioning circuit.

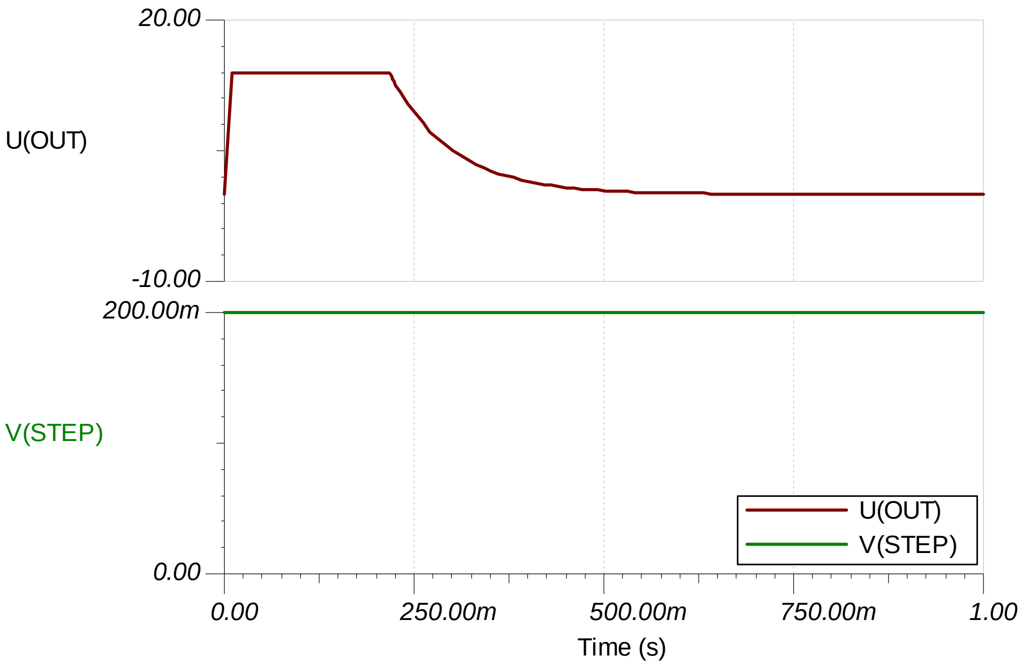

Figure 5.39: Transient response of the AC signal conditioning circuit to a step change in input voltage V(STEP) at t = 0

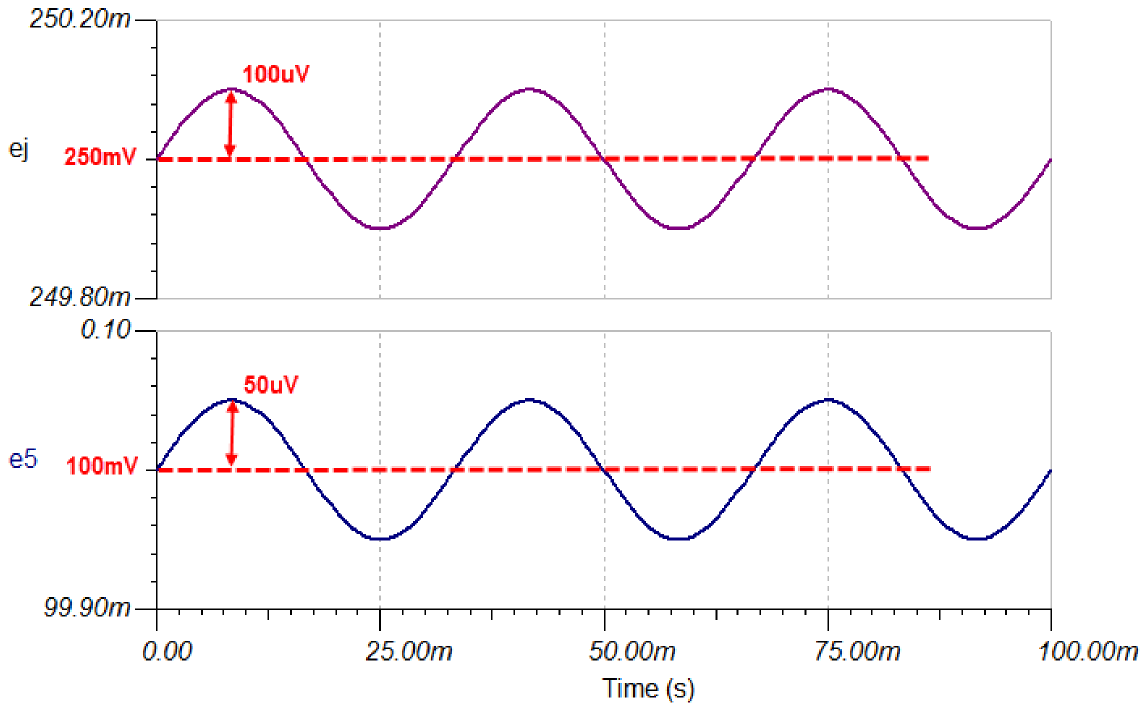

Figure 5.40: 100μV flow induced voltage with a DC offset of 250 mV at e_j and 50 μV flow induced voltage with a DC offset of 100 mV at e_5

The source (water) impedance was modelled as a resistor of 100 kΩ in parallel with a capacitor of 47 nF, i.e. impedance with some parasitic capacitance, and its impedance was imbalanced by 10%. The cable and RFI filter impedance was imbalanced by 1%. However, due to the high CMRR of the signal conditioning circuit due to the IA and the “right-leg drive” amplifier, this common-mode noise was significantly rejected. The output voltage of the circuit is given in Figure 5.42 which was around 49.45 mV at 30 Hz after amplification by 987. This was expected because the potential difference between electrodes e_j and e_5 was 50 μV. This example shows the great advantage of using the IA and the “right-leg drive” amplifier as they both greatly reduced the 50 Hz common-mode noise. The testing of the physical circuit is presented in Section 6.9 which also showed the same results approximately.

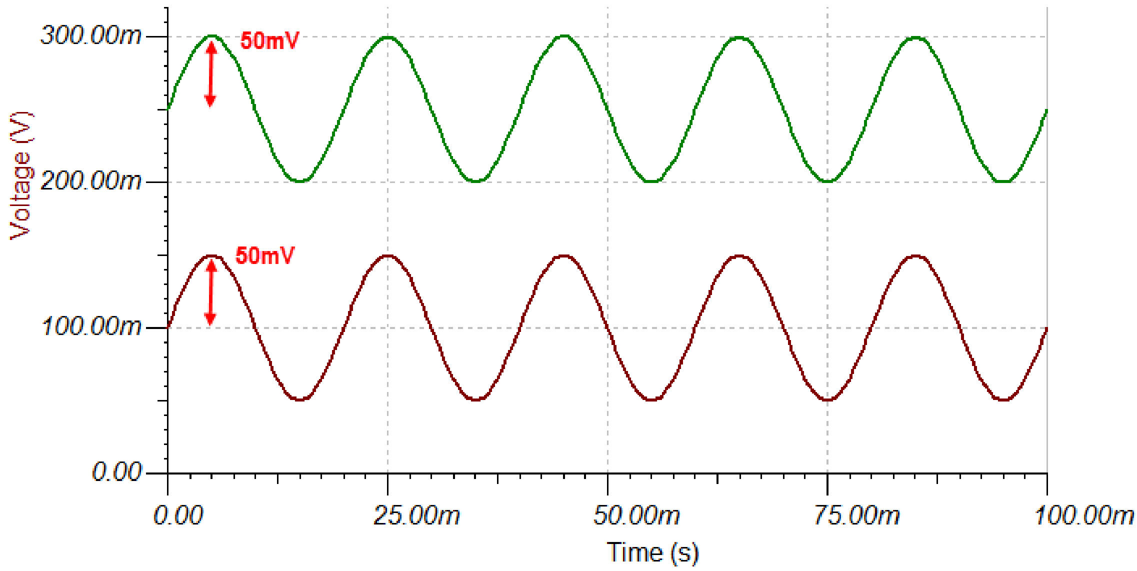

Figure 5.41: Common-mode 50 Hz noise is the dominant voltage signal on electrodes e_j and e_5

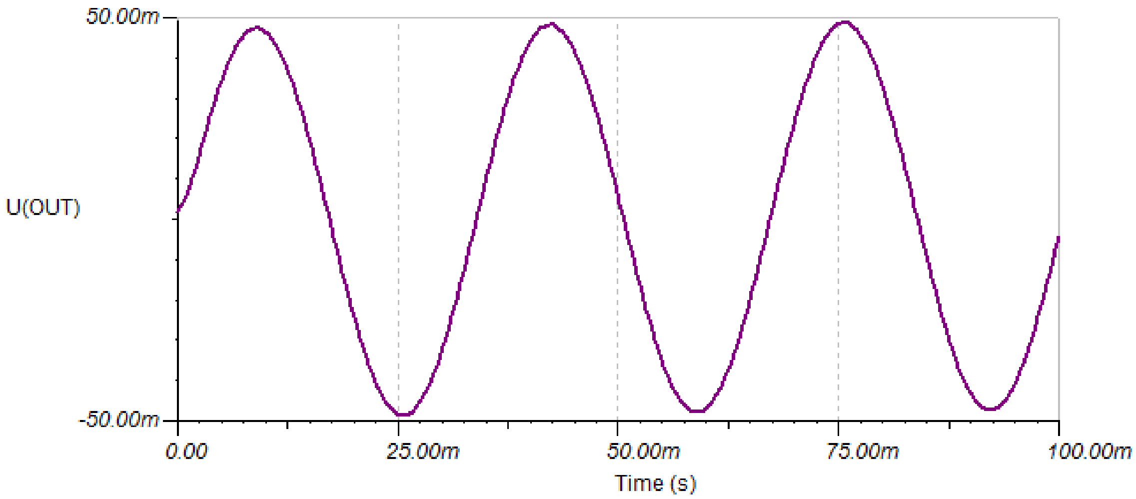

Figure 5.42: The output voltage of the circuit which was 49.45 mV after an amplification of 987.

5.8 16:1 Analogue Multiplexer Circuit

All 15 electrodes e_j (where *j* is 1 to 16 apart from 5) had to be measured with respect to the reference electrode e_5. The use of an analogue multiplexer circuit allowed all electrodes to be measured using one AC signal conditioning circuit instead of 15 circuits. Hence, the complexity of the measuring system was reduced. The analogue multiplexer used was a DG406 IC by Intersil [198]. It has 16 equally matched analogue switches, features very low on-resistance (<100 Ω) and handles voltage signals up to

30 $V_{pk\text{-}pk}$ when operated by a ±15 V power supply. Figure 5.43 illustrates the functional diagram of the analogue multiplexer. The switching of the inputs is performed via the 4-bit logic input of the IC; A_0, A_1, A_2 and A_3. The logic sequence is generated by MATLAB software and sent to the multiplexer via the NI PCI-6254 DAQ device.

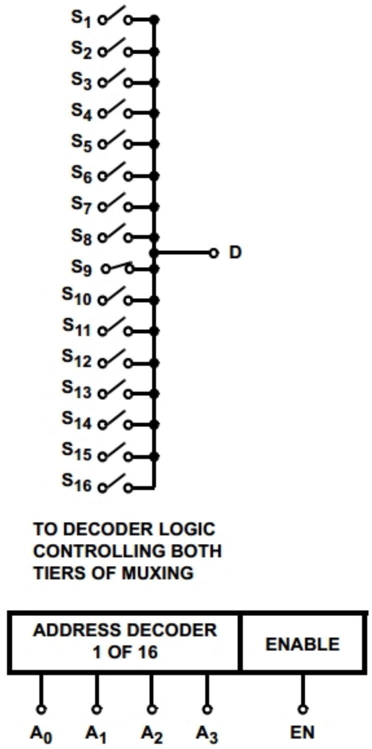

Figure 5.43: Functional diagram of the multiplexer circuit [198]

The transient response of the AC signal conditioning circuit (Figure 5.39) shows that the circuit reaches its steady-state value after 0.5 s. Hence, every time one switch of the multiplexer is selected, there must be a delay of 0.5 s before the voltage measurement is taken. For 15 measurements and for a sampling period of 1 s for each electrode, the total time for all voltage measurements is 22.5 s. This time can be reduced significantly by improving the transient response time of the AC circuit and increasing the sampling frequency (reducing the sampling time) of the DAQ device. However, the response time was satisfactory for the practical experimentation.

5.9 NI PCI-6254 Data Acquisition Device

The output of the AC signal conditioning circuit was digitised via the NI PCI-6254 DAQ device. This DAQ device features 16-bit resolution, 32 analogue inputs and 48 digital I/O lines. The A/D subsystem of the DAQ device can be set to a sampling frequency of 1 MHz for a multichannel scan or 1.25 MHz for a single channel scan. The input voltage range of the A/D subsystem is ± 10 V and can be configured as either bipolar (positive and negative voltages) or unipolar (positive only). The smallest voltage difference V_{min} that can be measured for a given input voltage range and resolution is given by

$$V_{min} = \frac{V_+ - V_-}{2^{n_{bits}}} \qquad \text{Eq. 5-34}$$

where V_+ and V_- are the limits of the input voltage range and n_{bits} is the resolution of the A/D. Thus, for an input range of ± 10V, the smallest voltage difference that the A/D sub-system can measure is 305 μV. The smallest flow induced voltage after amplification is around 10 mV which is 33 times larger than the smallest voltage difference V_{min}.

The sampling frequency f_s of the A/D sub-system was set to 1024 Hz which satisfies the Nyquist condition which states that the sampling frequency must be at least twice the frequency of interest (30 Hz) to avoid anti-aliasing [199]. The acquisition time was set to 1 second to obtain N = 1024 samples. For f_s = 1024 Hz and N = 1024, the Fast Fourier Transform of a sampled signal will have a frequency resolution (df) of 1 Hz. The df equation is given by

$$df = \frac{f_s}{N} \qquad \text{Eq. 5-35}$$

Fast Fourier Transform (FFT) was required to perform the DFT on the measured potential difference signals $U_{j,f}$ to obtain the real (Re) and imaginary (Im) parts. This was necessary for the implementation of the digital PSD technique in software which is described in Chapter 6.

Two analogue inputs (Channels 0-1) and five digital outputs (Channels 0-4) were used from the NI PCI-6254. Analogue inputs 0 and 1 were connected to the outputs of the AC signal conditioning circuit and the peak coil current measurement I_0 circuit, respectively. Digital outputs 0-4 were used to send the switching sequence to the logic control input (EN, A_0, A_1, A_2, A_4) of the analogue multiplexer circuit. The control of the NI PCI-6254 DAQ device was performed via MATLAB software using its Data Acquisition Toolbox.

5.10 MATLAB Program for NI PCI-6254

MATLAB 2013b was utilised for two tasks in this project. The first task was to configure the NI PCI-6254 card to sample the voltages picked up by the electrodes and the coil current I_0 of the electromagnet. It was also used to control the switching sequence of the logic input of the multiplexer circuit so that all electrodes would be sampled sequentially. The program flowchart of the first task is shown in Figure 5.44. The functions used to configure the NI PCI-6254 card are available in Data Acquisition Toolbox Documentation [200]. The second task was to implement the PSD method which is explained in Chapter 6.

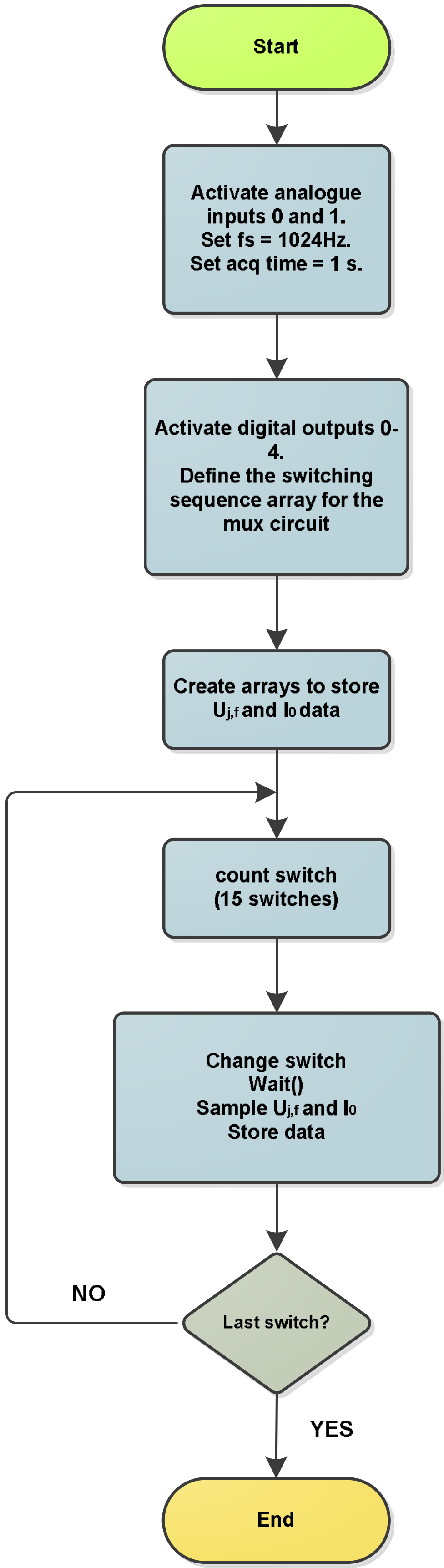

Figure 5.44: Task 1 MATLAB program source code.

5.11 The Complete Measurement System

Figure 5.45 shows the overall block diagram of the complete measurement system. The electrodes are interfaced to the AC signal conditioning circuit via the analogue multiplexer circuit. The AC signal conditioning circuit is represented by the RFI filter and amplifier block (inside the red rectangle). Note that the reference electrode e_5 bypassed the multiplexer circuit as each potential difference measurement is taken with respect to e_5. The output of the AC signal conditioning circuit is connected to the NI PCI-6254. The control of the NI PCI-6254 device and the signal processing is performed on the PC using MATLAB 2013b software. Refer to Appendix D for an image of the complete SVS flow test rig, and the AC signal conditioning circuit.

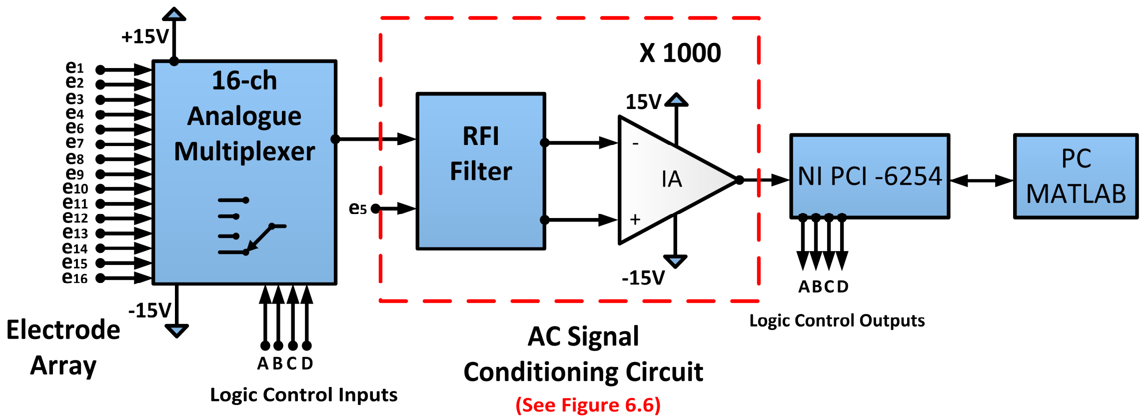

Figure 5.45: The overall voltage measurement system

5.12 Summary

The first task in completing the practical experiment setup for testing the proposed EM induction method was to construct the physical SVS model and the electromagnet for the generation of the magnetic field across the flow channels in the SVS. The mechanical design of the SVS consisted of a porous ceramic cylinder and plastic housing which had an embedded 16-electrode array. The ceramic cylinder, which was 40 mm in diameter, had two flow channels and each channel was 10 mm in diameter.

The porous material itself modelled a lump of conductive tissues such as muscles and fat when saturated sufficiently in water. The plastic housing – in which the porous ceramic was inserted – had a length of 240 mm and external and internal diameters of 75 mm and 50 mm, respectively. The 16-electrode array was embedded in the plastic housing and had a diameter equal to the internal diameter of the housing, i.e. 50 mm.

The electromagnet was comprised of a C-shaped silicon steel core - with an air-gap of 80 mm in length – and 320 turns of multi-stranded enamelled copper coil. It was designed to be powered by a 30 Hz AC power supply and could be operated at a peak current of up to 10 A. At the maximum peak current rating, the voltage is 200 V and the peak magnetic flux density was calculated to be 0.05 T. The electromagnet was tested independently and the results are provided in Chapter 6. In the next chapter, the design of the power supply for the electromagnet is presented. The signal conditioning system for measuring flow induced potential differences is also presented.

The 30 Hz AC power supply of the electromagnet consisted of a function generator, power amplifier, 1:5 transformer and PFC capacitor. The function generator was set to generate an output of ± 4 V at up to a 1 A at a frequency of 30 Hz. The power amplifier boosted the voltage and current to ± 40 V and 5 A. The 1:5 transformer stepped up the voltage by a factor of 5, i.e. ± 40 V and as a result, the maximum current that could be drawn from the power supply was 1 A. The PFC capacitor, which was placed in parallel with the electromagnet to reduce the current drawn from the power supply to minimum, had a value of 260 μF. It will be shown in the bench testing, explained in Chapter 6, that by using the PFC capacitor, only 475 mA was drawn from the power supply for the coil current of the electromagnet to reach a peak current of 10 A which is the value of current required to achieve a magnetic field density of 0.05 T.

The flow induced potentials generated in the fluid were very small in amplitude, had a large DC offset due to polarisation and were severely contaminated with EMI, i.e. mains and RF. A signal conditioning system was designed to overcome these problems which consisted of an RFI suppression filter, 1st-stage gain AC-coupled instrumentation amplifier, 2nd-stage gain inverting amplifier and the RLD inverting amplifier. The RFI suppression filter was designed to eliminate any relatively high amplitude RF signals that may cause the IA to malfunction. The AC-coupling of the IA reduced the large DC offset presented in the flow induced potential differences. The 1st-stage was also set to a low gain of 10 to ensure that the DC offset does not saturate the amplifier. The RLD amplifier performed common-mode noise cancellation by phase inverting the common-mode signal and then feeding back its output to the SVS ‘T’ metal connectors which were in contact with the water. A 2nd-stage amplifier provided additional gain of 100 to amplify the flow induced potentials to a voltage level that was suitable for the AD conversion in the DAQ device.

The 16-electrode array was interfaced to the signal conditioning system via a 16:1 analogue multiplexer which was digitally controlled to switch between the electrodes. This approach simplified the design of the signal conditioning system substantially. The multiplexer switching and the sampling and recording of the flow induced voltage signals were performed via the NI PCI-6254 DAQ device which was controlled by a program written in MATLAB software.

Chapter 6
Design of the Signal Processing System and Bench Testing

Contents

6.1 Introduction

The first part of this chapter addresses the design of the signal conditioning system – the last necessary part of the practical system – using a digital implementation of the PSD method. PSD is a technique by which the amplitude and the phase of a very small AC signal can be measured accurately in the presence of significant sources of noise [201]. This is achieved by exciting a system using a reference signal (the frequency and phase are known), and comparing the total measured output of the system to the reference signal. Then the signal that has the same frequency and the required phase, which is buried in the total measured signal, can be extracted using simple mathematical operations, i.e. multiplication and averaging.

The implementation of PSD can be found in lock-in amplifiers which are used to perform precise signal measurements in a wide range of applications including optical spectroscopy, magnetometry and electrical impedance tomography [173, 202-204]. Lock-in amplifiers are the main component in electronic instruments such as sub-milliohm digital ohmmeters, spectrum and network analysers and noise measurement units [205, 206]. PSD can be implemented using analogue or digital electronics which are discussed later on.

The PSD method was essential to separate the flow induced potential differences (in-phase component with the magnetic field) from the transformer induced voltages (quadrature component, i.e. 90° out of phase) which have the same frequency but differ in phase as was explained in Section 2.5.2. The PSD method had been suggested and used previously in EM flow metering and this was discussed in the literature review (Section 2.5.9). In these methods the coil current was measured using a shunt resistor and used as a reference signal to separate the flow induced potential differences from the transformer voltage signals. The coil current is in phase with the flow induced potentials, whereas it is 90^o out of phase with the transformer signal [127, 144-146, 148].

The last part of this chapter describes the tests that were carried out to verify the operation of the electromagnet and its power supply and the AC signal conditioning system. This was an important step in preventing any unexpected behaviour or results during the water flow tests. The magnetic field generated in the air gap was measured in terms of its magnitude and direction. For the proposed EM method, the magnetic field has to be essentially uniform with a constant value of magnetic flux density B_0 at the cross-section area where induced voltage measurements are taken (refer to Eq. 3-39).

For the signal conditioning circuitry, it was necessary to test the system for its responses in transient and normal operation. Moreover, the gain and the phase of the signal conditioning circuitry at the frequency of the flow induced potential difference, i.e. 30 Hz, had to be measured. The gain value was used to find the actual amplitude of the flow induced potential differences after amplification. Any phase shift between the input and the output of the signal conditioning had to be measured and compensated for in the digital PSD software to ensure accurate measurements of the flow induced potential differences as explained in Section 6.6.

Moreover, the additional noise detected by the electrodes was also investigated to determine the source of this noise and its frequencies. This was done by performing spectral analysis on the potential difference between electrodes e_1 and e_5. Since all electrodes are very close to one another, the noise is expected to be very similar on the other electrodes.

The layout of this chapter is as follows: the basic principle of operation of the digital and analogue PSD methods is introduced in **Section 6.2**. Then, **Section 6.3** describes mathematically the digital PSD technique used in the present study for detecting the flow induced voltages. The digital PSD was designed in software using MATLAB and this is explained in **Section 6.4**. The MATLAB program was tested using simulated in-phase, quadrature and noise signals which were generated in MATLAB and the results are presented and discussed in **Section 6.5**. The PSD method depends highly on the phase integrity of the measurement system and any errors in the phase will reduce the accuracy of the flow induced voltage measurements. The effect of the error in the phase is highlighted in **Section 6.6**. During the practical experimentation, it was observed that there was some in-phase noise which can lead to significant error in the flow induced voltage measurements. This problem had to be overcome to allow accurate flow rate measurement and this is explained in **Section 6.7**.

In **Section 6.8**, the test setup and results for the electromagnet and its AC power supply are presented. The test setup for the AC signal conditioning system and the results are presented in **Section 6.9**. Lastly, the electrical noise investigation is provided in **Section 6.10**. When all the systems were fully tested, they were connected together to be used to measure the flow induced potential differences that are generated in the SVS and these results are covered in Chapter 7.

6.2 Background Theory of Phase Sensitive Detection

6.2.1 Basic Principle of Analogue PSD.

A conventional lock-in amplifier consists of a PSD unit and a low-pass filter. A system under test is usually excited by a reference signal $r(t)$ with a frequency f_r as shown in Figure 6.1 [207].

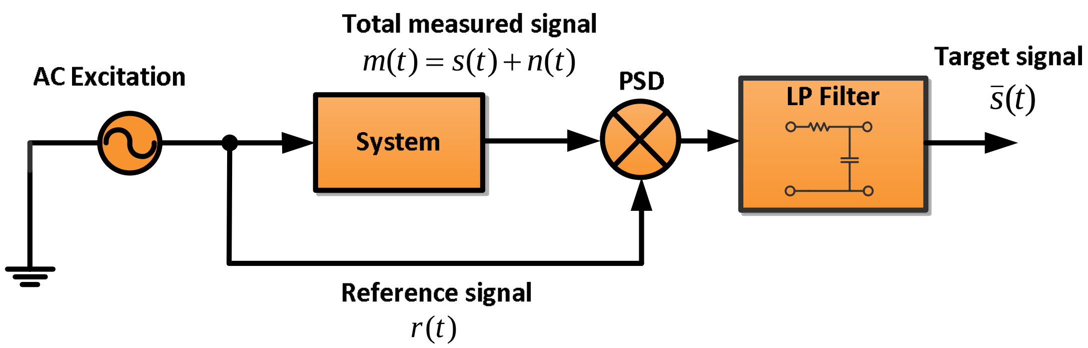

Figure 6.1: Block diagram of system arrangement to utilise a lock-in amplifier

The output response of the system $m(t)$ is the sum of the signal of interest $s(t)$ and sources of noise $n(t)$ such as ambient noise, RF interference and mains harmonics. The signal of interest $s(t)$ is a complex signal with real and imaginary components which has the same frequency as the frequency of the reference signal $r(t)$. The target signal $\bar{s}(t)$ is in phase with the reference signal $r(t)$. If the reference signal $r(t)$ is in phase with the real part of $s(t)$ then the output $\bar{s}(t)$ will be proportional to the real part of $s(t)$. However, if the reference signal $r(t)$ is in phase with the imaginary part of $s(t)$ then the output $\bar{s}(t)$ will be proportional to the imaginary part of $s(t)$

The total signal $m(t)$ is fed to the PSD unit which multiplies it by the reference signal $r(t)$. The output of the PSD is then low-pass filtered, i.e. averaged. When the portion of the measured signal $m(t)$ is in phase with the reference signal, the resultant output voltage of the low-pass filter is the mean value $(2/\pi)$ of the amplitude of the target signal $s(t)$. When the portion of the signal is out of phase (can be in quadrature), the output of the low-pass filter is close to zero. Mathematically, the output of the lock-in amplifier $y(t)$ is given by

$$y(t) = \frac{1}{T}\int_0^T m(t) \cdot r(t)\, dt \qquad \text{Eq. 6-1}$$

where T is the averaging time. The lock-in amplifier can be considered an extremely narrow band-pass filter with a centre frequency selected by the frequency of the reference signal. However, the amplifier will only pass the portion of the signal at its input that is in phase with the reference signal.

Square Wave Reference Signal

In an analogue design, the multiplication (or mixing) is achieved by using a switching multiplier [207] as shown in Figure 6.2. The reference voltage signal $r(t)$ is a square wave of ± 1 and has the same frequency as the target signal $s(t)$. The phase between the target signal $s(t)$ and the reference can either be in phase or in quadrature, depending on whether it is necessary to measure the real or imaginary component of $s(t)$. The switching multiplier is often called a ‘synchronous rectifier’.

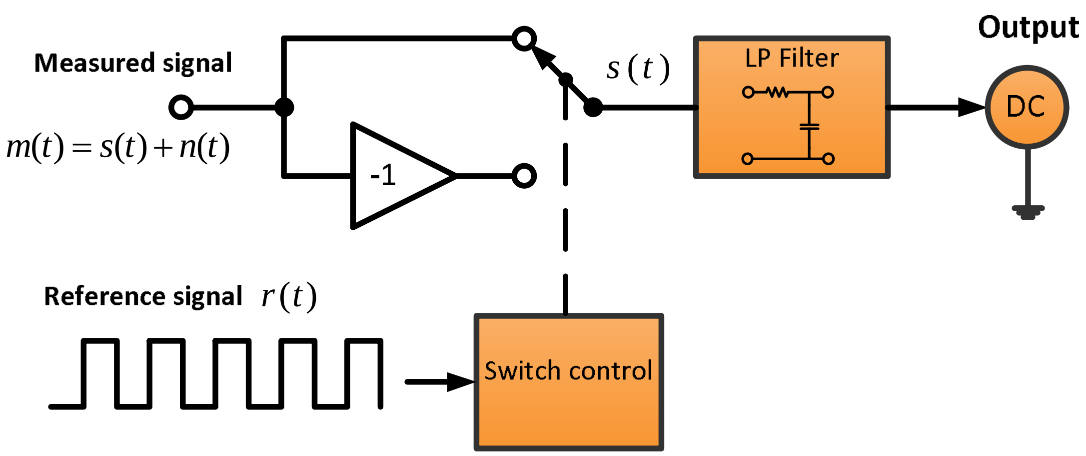

Figure 6.2: Analogue lock-in amplifier

When the target signal $s(t)$, buried in the measured signal $m(t)$, is positive (positive half cycle), it is multiplied by +1, and when it is negative (negative half cycle), it is multiplied by -1, resulting in a full wave rectified version of the target signal. This rectified signal is low-pass filtered to obtain the mean value of the target signal. Figure 6.3 illustrates the operation of the PSD when the target signal is in phase with the reference signal. The target signal is a sinusoidal signal with amplitude of 1 V and frequency of 1 Hz. The reference signal $r(t)$ is a unit square wave with the same phase and frequency as the target signal $s(t)$. The product of the target signal $s(t)$ and the reference signal $r(t)$ results in a rectified signal as shown in the 3rd plot in Figure 6.3. The mean value of the rectified signal is 0.637 V ($2/\pi$).

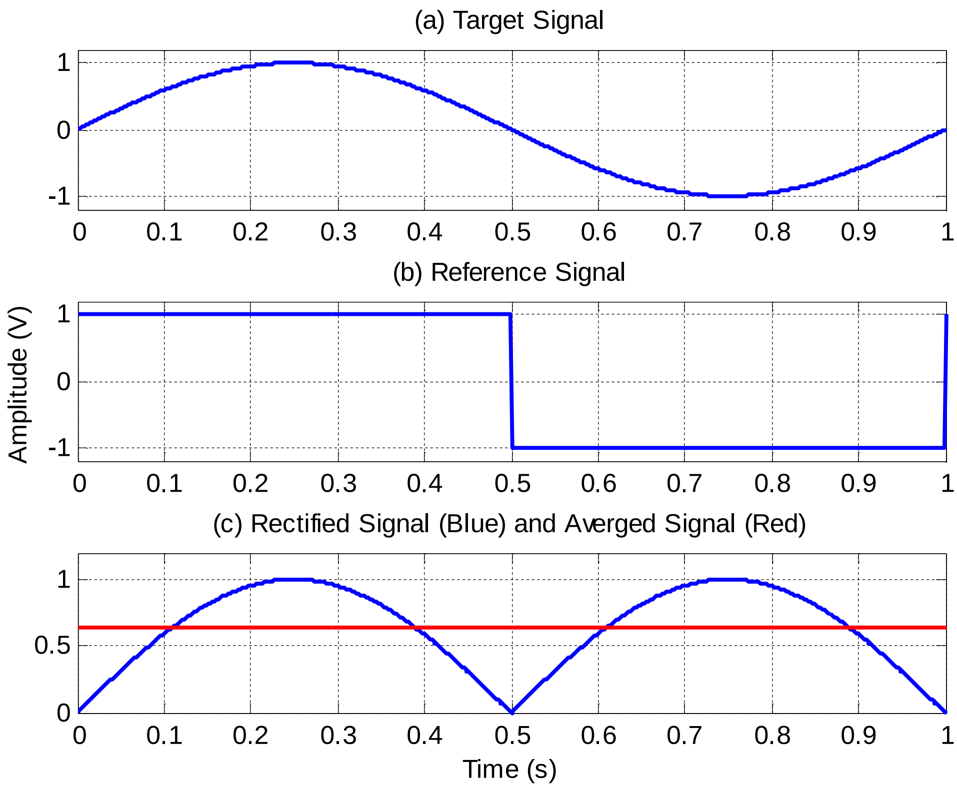

Figure 6.3: Operation of the PSD when the target signal is in phase with the reference signal

When the measured signal $m(t)$ has a different frequency or phase to the reference signal, the rectified output signal has a mean value close to zero. The unwanted signal in

Figure 6.4 has a frequency of 10 Hz. The reference signal is the same as in Figure 6.3. The product of both signals gives a rectified signal whose mean value is zero.

The cut-off frequency f_c of the low-pass filter in Figure 6.2 is given by,

$$f_c = \frac{1}{2\pi RC} \qquad \text{Eq. 6-2}$$

The time constant of the filter ($\tau_{LP} = RC$) is the averaging time T. The longer the averaging time, the more the unwanted frequencies are attenuated. Moreover, the higher the order of the low-pass filter is, the better the filtering of the unwanted frequencies becomes.

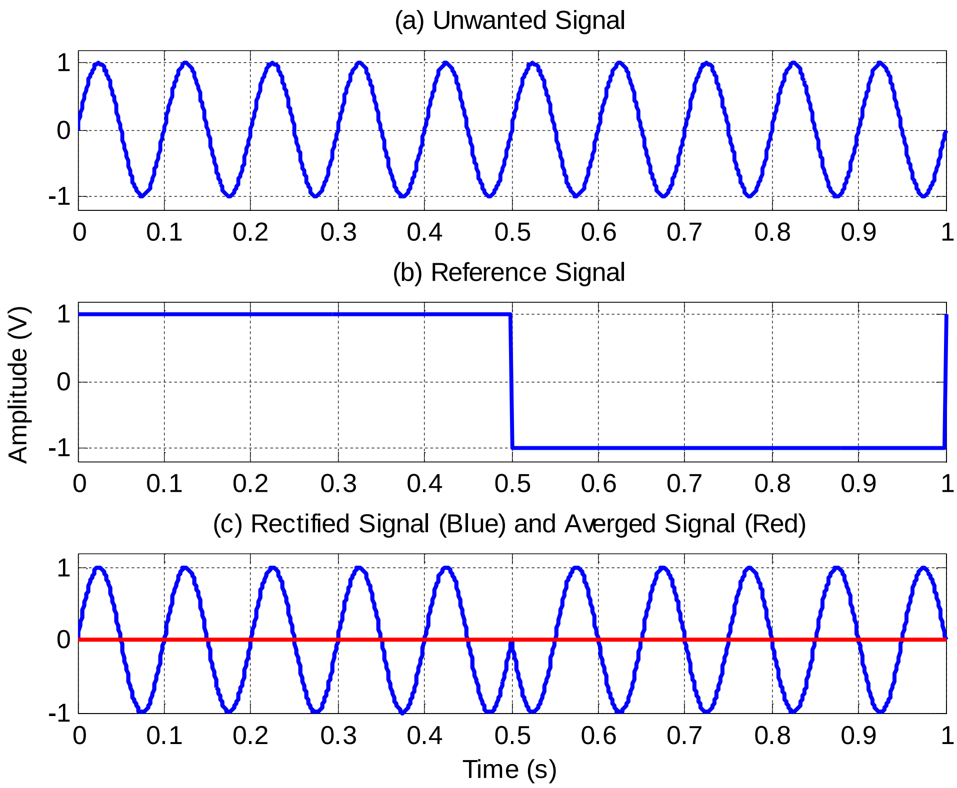

Figure 6.4: Operation of the PSD when the signal measured is out of phase with the reference signal

Both the real and imaginary components can be measured simultaneously by adding another PSD unit (multiplier) and low-pass filter as shown in Figure 6.5. The reference signal $r(t)$ has to be shifted by 90° before being multiplied by the measured signal

$m(t)$ to detect the quadrature component, which is 90° out of phase with the in-phase component.

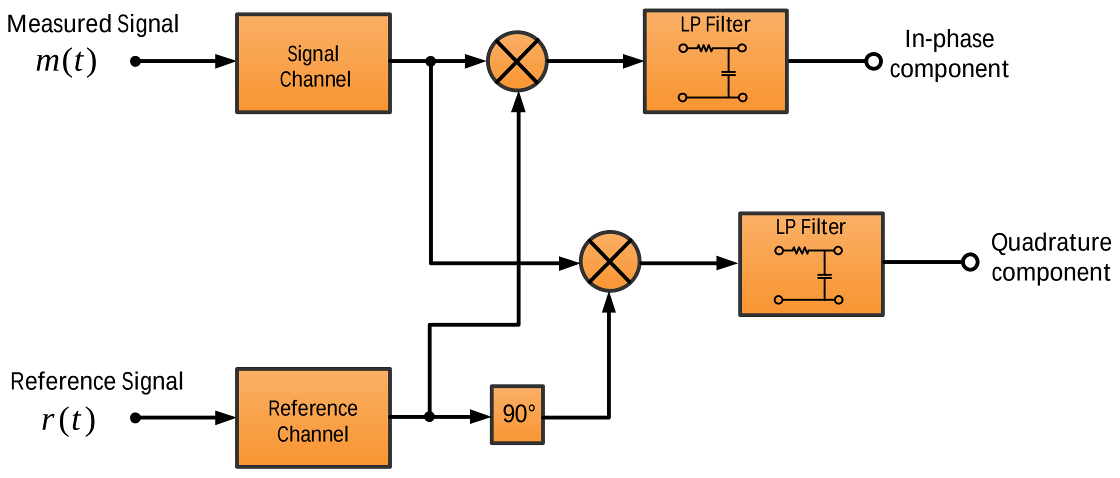

Figure 6.5: Analogue PSD to obtain real and imaginary part of the target signal

Sinusoidal Reference Signal

Using a square wave as a reference signal is common in analogue lock-in amplifiers as it is simple to design in practical terms. However, there is a disadvantage in using a square wave, which is its limited response to the odd harmonics [207]. The n^{th} odd harmonic is only attenuated by a factor of n when using a square wave. This causes an additional DC output voltage after filtering which is not related to the amplitude of the target signal. In Figure 6.6, the unwanted signal frequency was set to 3 Hz. It can be seen that when the amplitude of the square wave reference signal is +1, the average value of the sine wave is not zero (two peaks and one trough). Hence, the additional DC voltage corresponds to the area under the extra peak.

There are two solutions to this problem: (1) adding notch filters to attenuate mains harmonics, i.e. 50 Hz, 100 Hz and 150 Hz or (2) using a sinusoidal reference signal instead of a square wave. For a sinusoidal input signal $V(t)$ which is given by

$$V(t) = A\,sin(\omega t + \phi) \qquad \text{Eq. 6-3}$$

The reference signal is also sinusoidal and is given by

$$r(t) = sin(\omega_0 t) \qquad \text{Eq. 6-4}$$

When the frequency of the input signal ω is not equal to the reference frequency ω_0, the product of both signals is given by

$$V(t)r(t) = \frac{A}{2}(cos[(\omega - \omega_0)t + \phi] - cos[(\omega + \omega_0)t + \phi]) \qquad \text{Eq. 6-5}$$

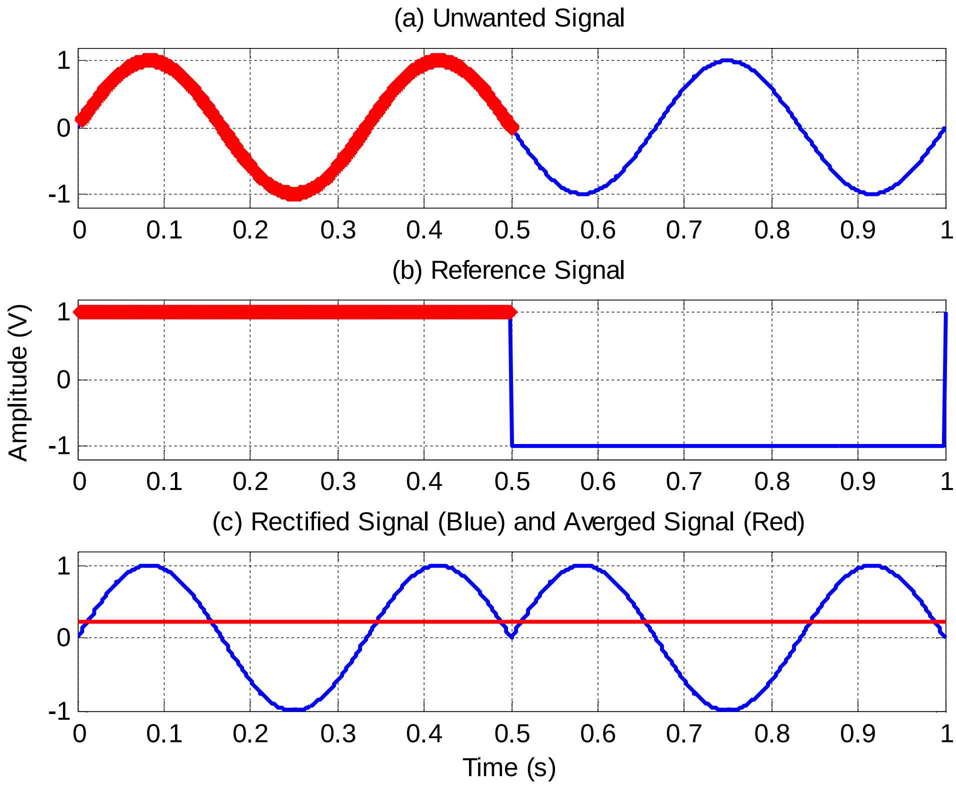

Figure 6.6: The unwanted signal is an odd harmonic of the reference signal, i.e. 3 Hz

The mean value of Eq. 6-5 is zero [208]. When the frequency of the input signal ω is equal to the reference frequency ω_0, the resultant product is given by

$$V(t)r(t) = \frac{A}{2}(cos[\phi] - cos[2\omega_0 t + \phi]) \qquad \text{Eq. 6-6}$$

When the signal in Eq. 6.6 is averaged, the only component left is $\frac{A}{2}$ which corresponds to half of the input signal amplitude. Any noise signal that oscillates at a different frequency from ω_0 is averaged to zero, and any noise signal that oscillates at the same frequency but with time-dependant phase is also averaged to zero. In Figure 7.7, the input and the reference signals have the same frequency, i.e. 1 Hz, and therefore the amplitude of the output after filtering is 0.5 V ($\frac{A}{2}$). In Figure 7.8, the input signal is the 3rd odd harmonic (3 Hz) of the reference signal (1 Hz). It can be seen that the mean value of the product of both signals is zero.

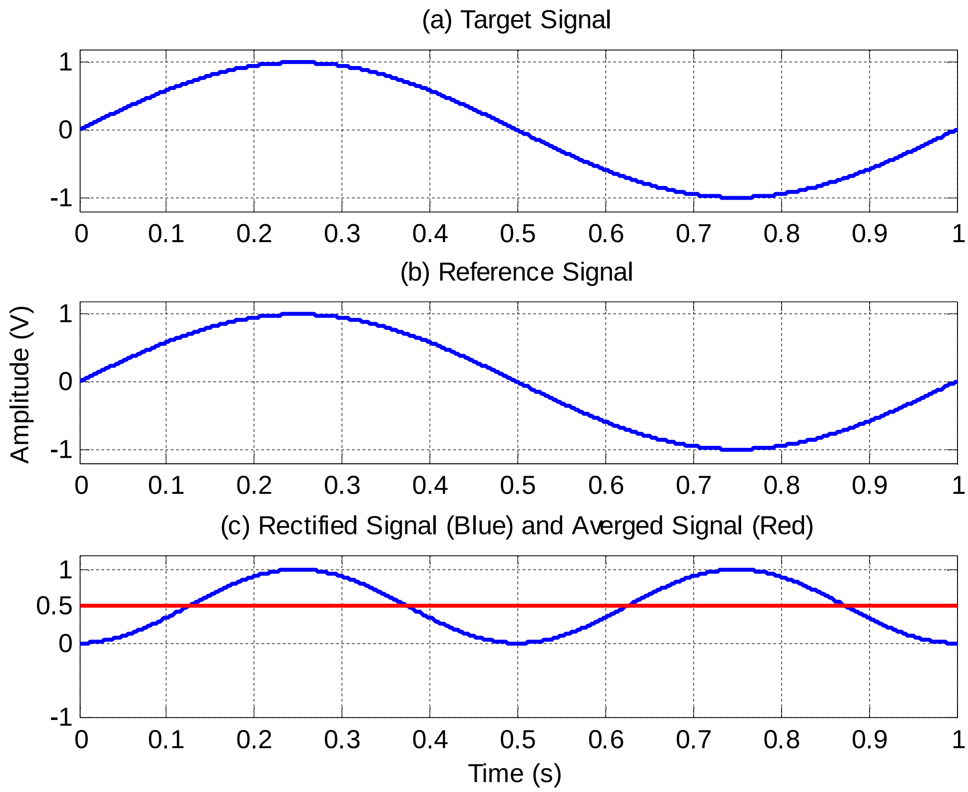

Figure 6.7: The input signal is in-phase with the sinusoidal reference signal and hence the output is 0.5 of the input signal.

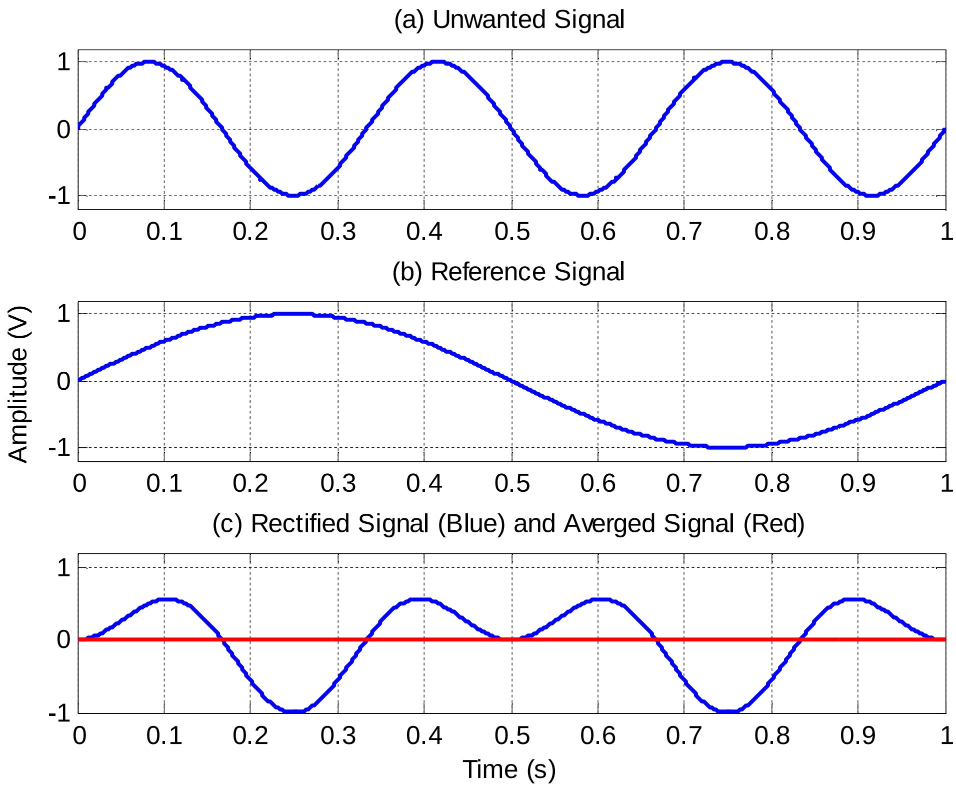

Figure 6.8: The input signal is the 3rd harmonic of the reference signal and therefore, the resultant output is zero.

6.2.2 Principles of Digital PSD

Analogue lock-in amplifiers suffer from: (1) component tolerances (2) temperature drift and (3) gain and phase non-linearity in op amps [209]. These problems can cause an error in the frequency or phase accuracy of the reference signal. As a result of such an error, an additional DC voltage appears at the output of the lock-in amplifier which is not related to the amplitude of the target signal. Therefore, complex and expensive design is required to achieve high accuracy. Digital lock-in amplifiers do not suffer from these problems. They can also operate at very low frequency, and do not suffer from $1/f$ noise [210].

There are two main schemes that are used for digital PSD [150]. The first method is based on the same principle as the analogue PSD described in Section 7.2.1. The measured signal is digitised and then, it is multiplied by internally generated in-phase and quadrature reference signals to obtain the real and imaginary parts of the signal of interest, respectively. In the second method, the DFT is used to obtain the amplitude and phase of the target signal $s(t)$ which is buried in the measured signal $m(t)$. Then, the reference signal $r(t)$ is used to determine the in-phase and quadrature components of the target signal $s(t)$. Note that multiplying the signal $m(t)$ by a sinusoidal reference signal $r(t)$ of a certain frequency f to obtain the amplitude and phase (real and imaginary parts) of the target signal $s(t)$, is similar to applying the DFT on the measured signal for that specific frequency.

The time-continuous signal $y(t)$ shown in Eq. 6-1, which is the average of the product of the two periodic signals, i.e. the output measured signal $m(t)$ [NB: the target signal $s(t)$ is buried in the signal $m(t)$] and the reference signal $r(t)$, in a digitised form, is given by

$$Y = \frac{1}{N}\sum_{n=0}^{N-1} m(nT) \cdot r(nT) \qquad \text{Eq. 6-7}$$

where N is the number of samples and T is the sampling period given by

$$T = dt\, N \qquad \text{Eq. 6-8}$$

In Eq. 6-8, dt is the sampling interval and is the reciprocal of the sampling frequency f_s, i.e.

$$f_s = \frac{1}{dt} \qquad \text{Eq. 6-9}$$

Eq. 6-7 can be simplified to the following equation,

$$Y = \frac{1}{N}\sum_{n=0}^{N-1} m(n) \cdot r(n) \qquad \text{Eq. 6-10}$$

If the in-phase and quadrature components (real and imaginary parts) of the target signal $s(n)$, which is buried in the measured signal $m(n)$, are to be found, then for the in-phase component, the reference signal $r_i(n)$ (real part component) is given by [202]

$$r_i(n) = cos\frac{2\pi fn}{f_s} \qquad \text{Eq. 6-11}$$

where f is the frequency of the target signal buried in the input signal $m(t)$. For the quadrature component (imaginary part) of the target signal $s(n)$, the reference signal $r_q(n)$ is given by

$$r_q(n) = sin\frac{2\pi fn}{f_s} \qquad \text{Eq. 6-12}$$

Euler's formula states that any complex number can be written in a discrete form as,

$$\begin{aligned} z = a + jb = |z|(cos\frac{2\pi fn}{f_s} + j\,sin\frac{2\pi fn}{f_s}) = re^{j\frac{2\pi fn}{f_s}} \\ z = a - jb = |z|(cos\frac{2\pi fn}{f_s} - j\,sin\frac{2\pi fn}{f_s}) = re^{-j\frac{2\pi fn}{f_s}} \end{aligned} \qquad \text{Eq. 6-13}$$

From Eq. 6-10 to Eq. 6-13, the discrete form of the complex number related to the sinusoidal target signal $s(n)$ (assuming $r = 1$) is given by

$$Y = \frac{1}{N}\sum_{n=0}^{N-1} m(n) \cdot e^{-j\frac{2\pi fn}{f_s}} \qquad \text{Eq. 6-14}$$

Now, the DFT of a time series x_h is a series of N complex numbers $X(k)$ (k = 0, 1, 2,…etc) which are defined by the following expression:

$$X(k) = \frac{1}{N}\sum_{h=0}^{N-1} x_h \cdot e^{-j\frac{2\pi kh}{N}} \qquad \text{Eq. 6-15}$$

where k = 0, 1, 2, …, N −1. Values for $X(k)$ exist only for frequencies f_k where f_k is defined as

$$f_k = \frac{k}{T}$$ Eq. 6-16

where k = 0, 1, 2, …, N. However, unique values for $X(k)$ only exist from 0 Hz to the Nyquist frequency, i.e. for

$$0 \leq f_k \leq \left(\frac{N}{2}\right)\frac{1}{T}$$ Eq. 6-17

that is for k = 0, 1, 2, …, $N/2$. It can be noted that Eq. 6-14 and Eq. 6-15 are almost identical. In Eq. 6-14, a complex number at the frequency of the signal of interest only is obtained whereas, in Eq. 6-15 complex numbers for all frequencies up to the Nyquist frequency are obtained.

The complex number $X(k)$ in Eq. 6-15 at the frequency f_k of interest consists of real and imaginary components, i.e. $X(k) = a_k + jb_k$. The amplitude r and the phase θ of the target signal are given by the following equations:

$$r = \sqrt{a_k^2 + b_k^2}$$ Eq. 6-18

$$\theta = tan^{-1}\frac{b_k}{a_k}$$ Eq. 6-19

where the phase θ is the angle between $X(k)$ and the positive real axis (Re) as illustrated in Figure 6.9 (i.e. it is the argument of $X(k)$). Physically, the phase angle θ also represents the phase angle between the sampled signal of interest x_h and a cosine wave at the same frequency. By taking the DFT of the sampled signal of interest x_h, (e.g. the potential difference between an electrode and the reference electrode), and by taking the DFT of a sampled reference signal B_h, (e.g. a voltage corresponding to the phase of the applied magnetic field), the phase of both x_h and B_h with respect to the same cosine wave can be determined. Hence, the phase relationship between x_h and B_h

is readily determined, enabling the "in-phase" and "quadrature" component of x_h with respect to B_h to be easily determined.

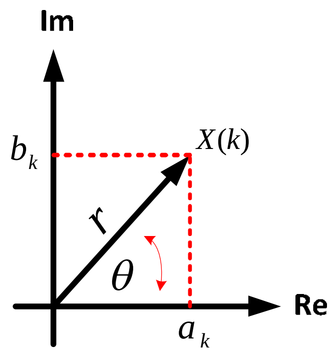

Figure 6.9: Complex number $X(k)$ presented on an Argand diagram

For this research, the second digital PSD method was used as the DFT provides in-phase and quadrature information for all frequencies, including the target frequency, up to the Nyquist frequency. The frequency components obtained by the DFT also included the main sources of noise superimposed on the measured signal. Additionally, it was more efficient to implement DFT in MATLAB 2013b using its Signal Processing Toolbox. However, in terms of processing power, memory and speed, using DFT requires more computational resources than using the standard PSD technique. This factor could be considered for future developments of this work.

6.3 Digital PSD Implementation in the Present Study

In Section 6.2.2, it was concluded that when the DFT is applied to a signal, the real and imaginary components of the signal can be obtained and therefore, the amplitude and the phase of the signal can be determined. The purpose of digital PSD using the DFT is to distinguish the flow induced potential difference from the transformer voltage as the flow induced potential difference is in phase with the magnetic field and the transformer voltage is 90° out of phase with the magnetic field (refer to Section 2.5.2). Moreover, applying the DFT shows all the frequency components, including the 30 Hz component, up to the Nyquist frequency. Hence, it provides information on what other frequencies are present in the measured signal and could help in eliminating them if found to be an issue.

Suppose that the electromagnet of the flow test rig, shown in Figure 5.18, is operated at 30 Hz and there is water flow in the SVS. Furthermore, suppose a voltage $U_{j,f}$ (j = 1 to 16 and where f represents the flow condition), between any of the electrodes e_j and the reference electrode e_5, and a voltage corresponding to the phase of the magnetic field density B_0 (the coil current I_0 is in phase with the magnetic field) are measured. When the DFT is applied to the voltage signals and the DFT components are extracted at 30 Hz, the phase angles $\phi_{j,f}$ and $\psi_{j,f}$ are determined using Eq. 6-19 where $\phi_{j,f}$ is the phase angle which the voltage signal $U_{j,f}$ makes with the positive real axis (Re) and $\psi_{j,f}$ is the phase angle which the magnetic field B_0 makes with the positive real axis, as illustrated in Figure 6.10.

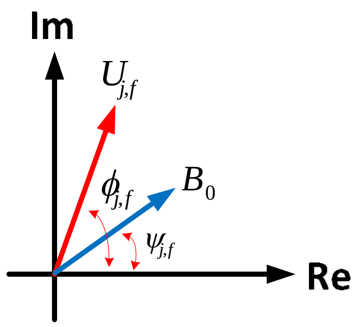

Figure 6.10: The induced voltage $U_{j,f}$ and the magnetic field density B_0 lead the positive real axis by $\phi_{j,f}$ and $\psi_{j,f}$, respectively

Thus, subtracting the phase angle $\psi_{j,f}$ from $\phi_{j,f}$ gives $\theta_{j,f}$, i.e.

$$\theta_{j,f} = \phi_{j,f} - \psi_{j,f} \qquad \text{Eq. 6-20}$$

where $\theta_{j,f}$ is the phase angle by which the voltage signal $U_{j,f}$ leads the magnetic field B_0 as depicted in Figure 6.11 (in Figure 6.11, the magnetic field density vector is assumed to coincide with the positive real axis).

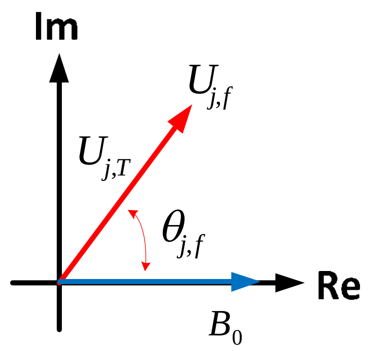

Figure 6.11: The voltage signal leads the magnetic field by θ_j

The amplitude of the voltage signal $U_{j,f}$, i.e. $U_{j,T}$ can also be obtained according to Eq. 6-18 (NB: $U_{j,T} = |U_{j,f}|$). The in-phase component $U_{j,f,in}$ of the voltage signal $U_{j,f}$ is given by

$$U_{j,f,in} = U_{j,T} \cos \theta_{j,f} \qquad \text{Eq. 6-21}$$

The quadrature component $U_{j,f,q}$ (90^{o} out of phase with the voltage signal $U_{j,f,in}$) is given by

$$U_{j,f,q} = U_{j,T} \sin \theta_{j,f} \qquad \text{Eq. 6-22}$$

The in-phase component $U_{j,f,in}$ is the flow induced potential difference component of $U_{j,f}$ that is in phase with the magnetic field and $U_{j,f,q}$ is the transformer voltage component of $U_{j,f}$ that is in quadrature with the magnetic field as shown in Figure 6.12. Note that using Eq. 6-21 and Eq. 6-22:

- If $U_{j,f,in}$ is positive, this component is in-phase with the magnetic field, as shown in Figure 6.12, and if it is negative, it is 180° out of phase with the magnetic field.

- If $U_{j,f,q}$ is positive, then it leads the magnetic field by 90°, as shown in Figure 6.12 and if it is negative, then it lags the magnetic field by 90°.
- The correct sign of the $U_{j,f,in}$ and $U_{j,f,q}$ components is automatically given by Eq. 6-21 and Eq. 6-22 so the quadrant in which the phasor $U_{j,f}$ lies relative to the magnetic field does not have to be considered.

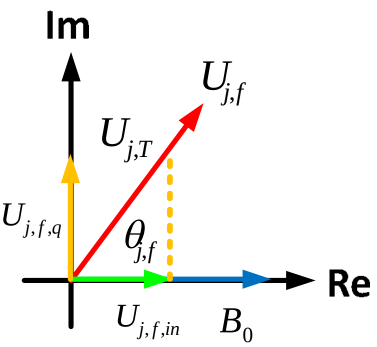

Figure 6.12: The in-phase and quadrature components of U_j

Figure 6.13 shows a block diagram of the implementation of the digital PSD. The voltage signal $U_{j,f}$ between electrode e_j and electrode e_5 (under flow condition f) and the voltage corresponding to the coil current I_0 are sampled simultaneously by the NI PCI-6254 DAQ device (two ADC channels). Both signals are sampled after being conditioned (the signal conditioning system is not shown). The DFT is then applied and the real and imaginary components $(a + jb)$ of the voltage $U_{j,f}$ and coil current I_0 signals are obtained at the operating frequency. After that, the real and imaginary terms are converted to a polar form $(a + jb \to r < \theta)$. Then, the phase angle $\theta_{j,f}$ is found which is the difference between the phase angle of the induced voltage signal $\phi_{j,f}$ and the phase angle of the coil current $\psi_{j,f}$ (which is also the phase angle of the magnetic field density B_0). Finally, Eq. 6-21 and 7-22 are applied to obtain the in-phase component $U_{j,f,in}$ and the quadrature component $U_{j,f,q}$. Only the in-phase component is of interest and this is recorded accordingly. The analogue multiplexer then switches to the next electrode and the same process is repeated.

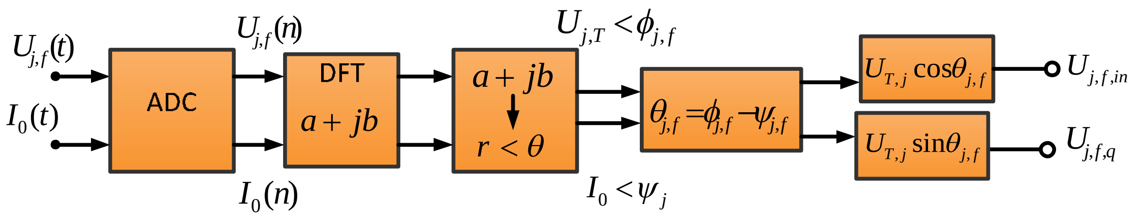

Figure 6.13: Block diagram of the digital PSD used

6.4 Implementation of the Digital PSD Method in MATLAB

The MATLAB program, explained in Section 5.10, records all 15 voltage measurements $U_{j,f}$ (j=1 to 16 apart from 5) from the electrode array via the NI PCI-6254 DAQ device and the multiplexed AC signal conditioning circuit. For each voltage measurement $U_{j,f}$, the coil current I_0 is also sampled to be used as a reference signal for the digital PSD method. The DFT is applied to both the measured voltage difference $U_{j,f}$ and the measured coil current I_0 to obtain their real and imaginary terms at the operating frequency. Then, the flow induced voltage $U_{j,f,in}$ for each electrode is found by finding the phase angle between the measured voltage $U_{j,f}$ and the coil current I_0, i.e. $\theta_{j,f}$, as described above. Figure 6.14 shows the flowchart of the MATLAB program.

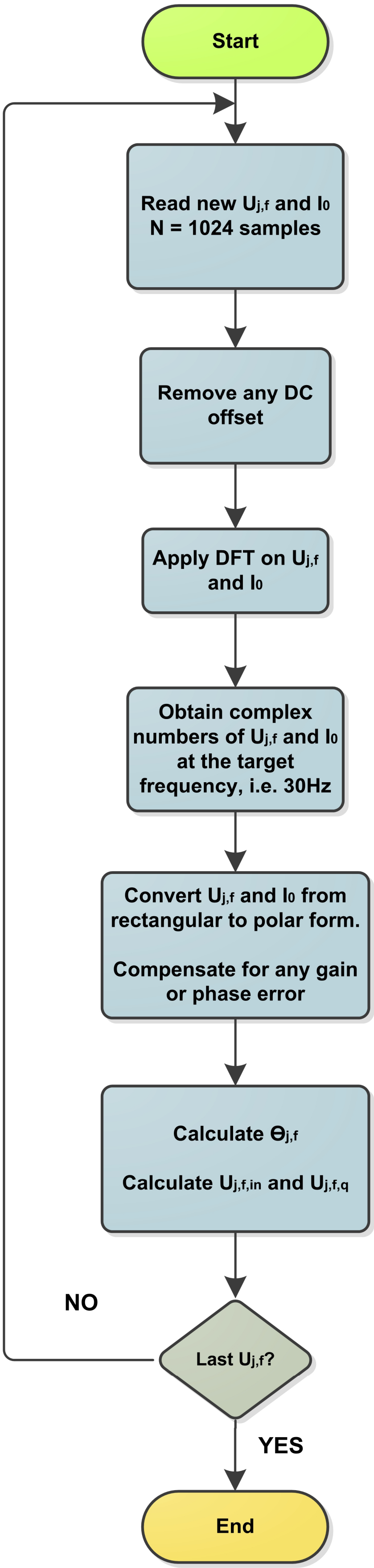

Figure 6.14: Flowchart of MATLAB program which explains the applied digital PSD

6.5 Results for Testing the Digital PSD & Discussion

The digital PSD implemented in MATLAB as described in the previous section was tested offline by generating a simulated voltage signal $U_{j,f}$ in MATALB that consisted of an in-phase voltage component $U_{j,f,in}$ (flow induced voltage), quadrature voltage component $U_{j,f,q}$ (transformer voltage) and random noise U_n. The in-phase flow induced voltage $U_{j,f,in}$ was set to a peak voltage of 100 mV, the transformer (or quadrature) voltage $U_{j,f,q}$ was set to a peak voltage of 5 V and the random noise U_n had a peak voltage of 300 mV. The frequency of the flow induced voltage and the transformer voltage was set to 30 Hz which is the same operating frequency as the one used in the practical experiment. Note that the quadrature voltage component is 50 times greater than the in-phase component. The random noise was created using the MATLAB built-in function **randn(n)**. The selected peak voltages of the signals were similar to the voltage levels observed in the practical experiment after amplification by the AC signal conditioning circuit. The flow induced voltage $U_{j,f,in}$ was given by

$$U_{j,f,in}(t) = 0.1\cos\left(2\pi(30)t + \left[(80°)\frac{\pi}{180°}\right]\right) \qquad \text{Eq. 6-23}$$

where the phase shift of 80° means that the in-phase component $U_{j,f,in}$ is leading the real positive axis (Re). The quadrature voltage component was given by

$$U_{j,f,q}(t) = 5\cos\left(2\pi(30)t + \left[(170°)\frac{\pi}{180°}\right]\right) \qquad \text{Eq. 6-24}$$

The quadrature voltage $U_{j,f,q}$ leads the real positive axis by 170° and leads the in-phase voltage component $U_{j,f,in}$ by 90° (170°−80°) which means that it is in quadrature with the in-phase component. The combined voltage signal $U_{j,f}$, which is the sum of the in-phase, quadrature and the random noise components, is given by

$$U_{j,f} = U_{j,in} + U_{j,q} + U_n \qquad \text{Eq. 6-25}$$

The coil current I_0, which was used as the reference signal (in-phase with the magnetic field B_0 and the flow induced voltage $U_{j,f,in}$) is assumed to be given by

$$I_0 = 2\cos\left(2\pi(30)t + \left[(80°)\frac{\pi}{180°}\right]\right) \qquad \text{Eq. 6-26}$$

This reference signal was used to determine the in-phase and quadrature voltage components as was described in Section 6.3.

To generate the signals given in Equations 7-23 to 7-26 in MATLAB, the number of samples of each signal N and the acquisition time T had to be set. These settings were chosen to have the same values as those used in the MATLAB data acquisition program which was used to control the analogue multiplexer – the front-end of the AC signal conditioning circuit – and the NI PCI-6264 device as described in Section 6.6. The number of samples N was 1024 and the sampling frequency was 1024 Hz. The reason behind the selection of these two values is explained in Section 5.9. Figure 6.15 presents the in-phase voltage component $U_{j,f,in}$ (blue trace), the quadrature voltage signal $U_{j,f,q}$ (red trace) and the noise voltage, separately. Figure 6.16 shows the combined signal of these three components, i.e. $U_{j,f}$ and also shows the reference coil current signal I_0. It can be seen that the in-phase component $U_{j,f,in}$ is buried completely in the total voltage signal $U_{j,f}$ and the PSD method is required to extract it. Using the approach explained in the previous section, the DFT was applied to the total voltage signal $U_{j,f}$ and the coil current signal I_0. It can be seen from Figure 6.17 and Figure 6.18 that there are real and imaginary components at 30 Hz corresponding to the total voltage $U_{j,f}$ and coil current I_0 signals. The amplitudes of the real and imaginary components of the DFT of the total voltage and coil current signals are shown in Figure 6.17 and Figure 6.18, respectively.

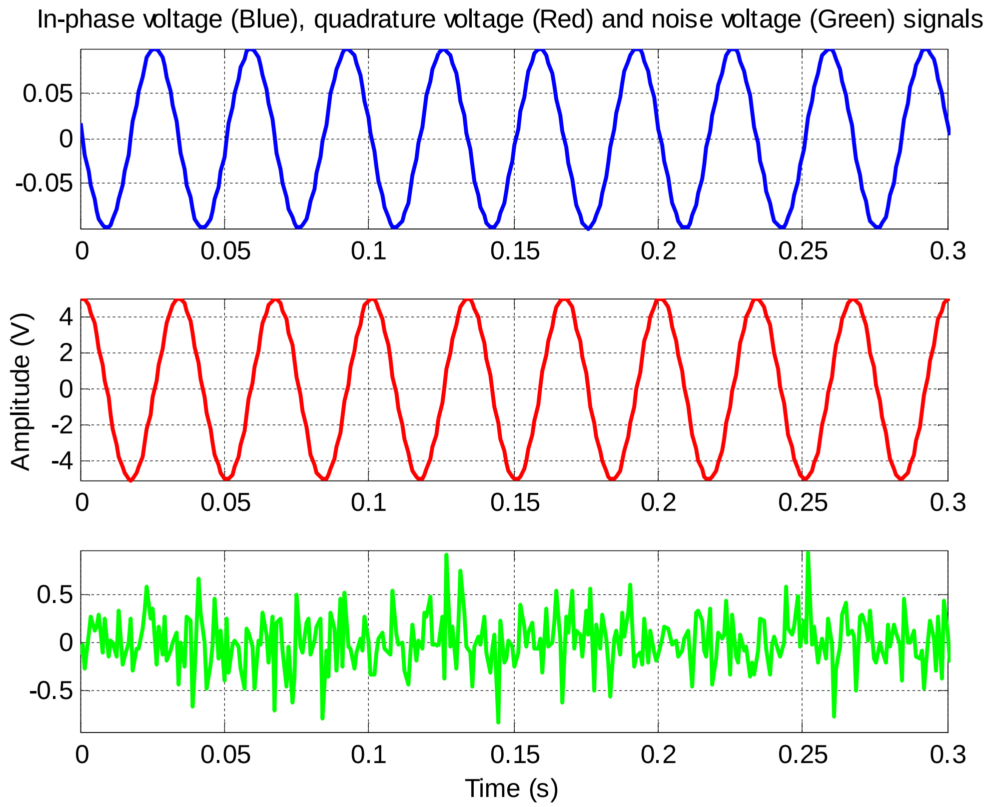

Figure 6.15: The simulated flow induced voltage, transformer voltage and noise signals

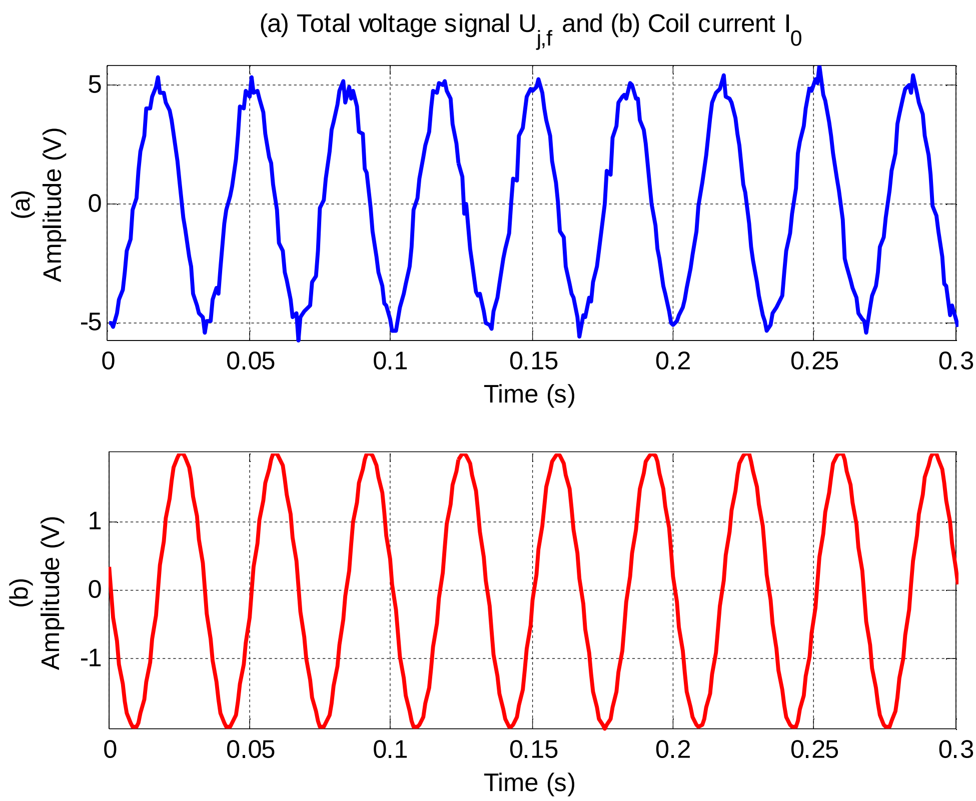

Figure 6.16: The combined total voltage $U_{j,f}$ and the coil current I_0

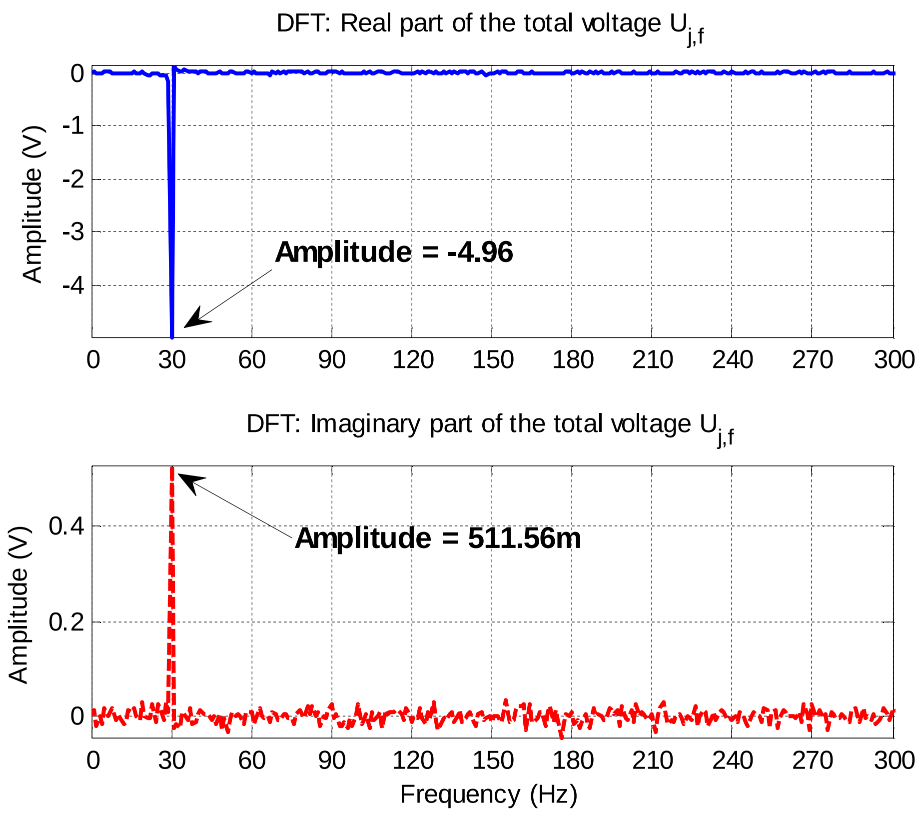

Figure 6.17: DFT result for $U_{j,f}$ at the target frequency 30 Hz

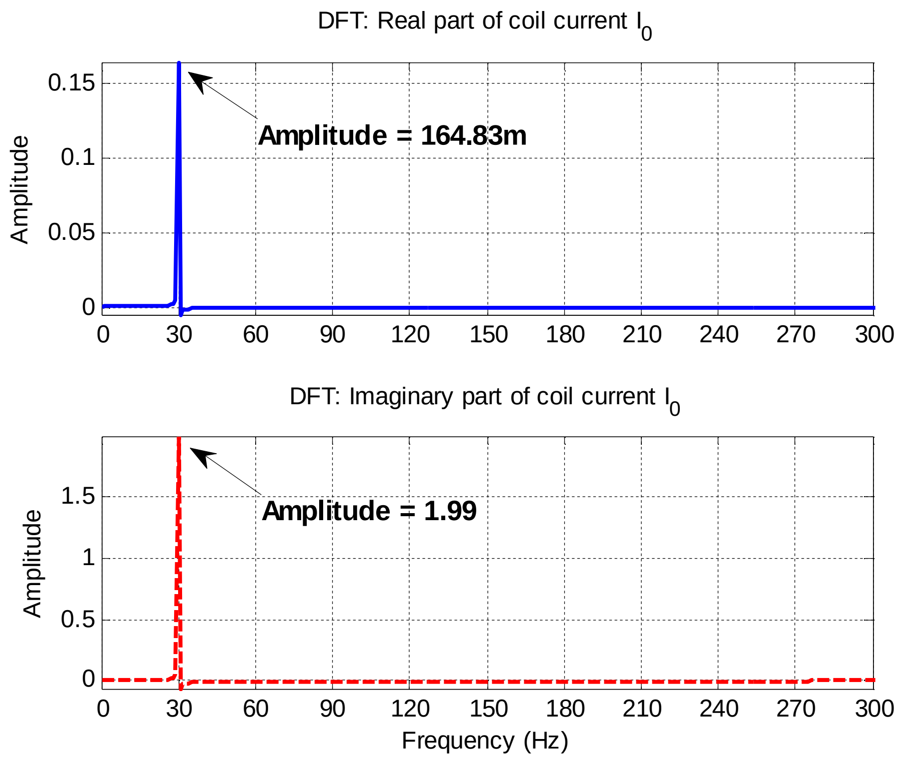

Figure 6.18: DFT results for I_0 at the target frequency 30 Hz

From the amplitude values obtained from Figure 6.17 and Figure 6.18, the total voltage and coil current signals in complex form are given by

$$U_{j,f} = -4.96 + j511.56\text{m} = 4.99 < 174.11° \quad \text{Eq. 6-27}$$

$$I_0 = 164.83\text{m} + j1.99 = 2.00 < 85.26° \quad \text{Eq. 6-28}$$

From Eq. 6-27, the total voltage signal $U_{j,f}$ has an amplitude of $U_{j,T} = 4.99$ V and leads the positive real axis by $\phi_{j,f} = 174.11°$ and from Eq. 6-28, the coil current I_0 leads the positive real axis by $\psi_{j,f} = 85.26°$ (the amplitude of the current is not important). Both signals are presented on an Argand diagram as illustrated in Figure 6.19.

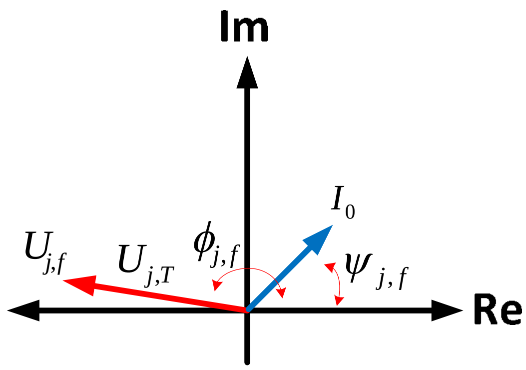

Figure 6.19: The total voltage signal and the coil current phasors

Hence, the phase angle $\theta_{j,f}$ between the total voltage signal $U_{j,f}$ and the coil current I_0 is 88.85° as shown in Figure 6.20.

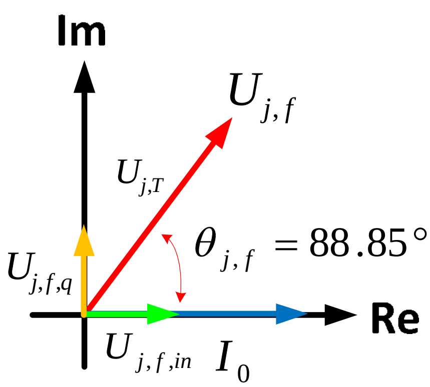

Figure 6.20: The phase angle $\theta_{j,f}$ between the total voltage and coil current signals

Using Eq. 6-21, the amplitude of the in-phase voltage signal can be determined as shown below.

$$U_{j,f,in} = 4.99\cos(88.85°) = 100.15\,\mathrm{m}V \qquad \text{Eq. 6-29}$$

Similarly, using Eq. 6-22, the amplitude of the quadrature voltage signal is equal to

$$U_{j,f,q} = 4.99\sin(88.85°) = 4.99\,V \qquad \text{Eq. 6-30}$$

From Eq. 6-29, it can be seen that the amplitude of the in-phase component is almost equal to the actual value which is 100 mV. There is only 0.002% error between the two values and that is considerably low. Similarly, the quadrature voltage obtained from the PSD was 4.99 V and the actual value is 5 V. The results showed that the digital PSD method is valid and accurate. If the noise level was higher, ensemble averaging may be required [211]. Note that in the practical experiment, only the in-phase voltage component was of interest which was the flow induced voltage; the quadrature voltage value was not taken into account.

6.6 Effect of Error in the Phase Angle Measurement of the PSD

It was stated in Section 5.7.1 that the output signal of the signal conditioning circuit leads the input signal by 2.4° and this phase lead must be compensated for in the PSD method. The effect of not considering this phase error is significant and can lead to a large error in the flow induced voltage measurement. Figure 6.21 shows the amplitude of the in-phase voltage component $U_{j,f,in}$ for values of $\theta_{j,f}$ between 84° and 90°. The correct value of $U_{j,f,in}$ is at $\theta_{j,f}$ = 88.85° and it can be seen that for a small change in the angle, a large error occurs in the measurement of $U_{j,f,in}$. For example, at $\theta_{j,f}$ = 86.55°, which is a decrease of 2.3°, the amplitude of $U_{j,f,in}$ is 300 mV and that is three times the value of the actual amplitude. Hence, the phase integrity of the system is highly important. The phase lead introduced by the signal conditioning system is compensated for by subtracting 2.4° (θ_{error}) from the value of $\theta_{j,f}$ once it is measured, i.e.

$$\theta_{j,f} - \theta_{error} \tag{Eq. 6-31}$$

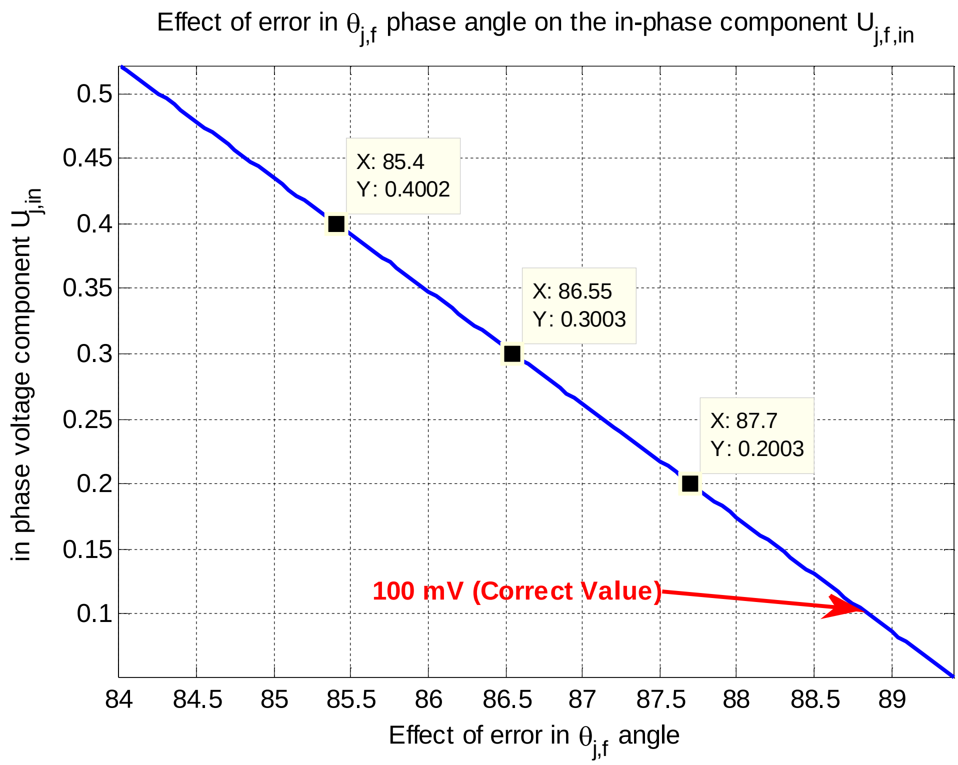

Figure 6.21: Effect of the variation in $\theta_{j,f}$ on the amplitude of the in-phase component $U_{j,f,in}$

6.7 In-phase Noise Voltage

During the flow induced measurements experiment (Chapter 7), it was observed that there was some in-phase noise, i.e. noise that was in-phase with the magnetic field when there was no flow. This in-phase noise sometimes had amplitude several orders of magnitude higher than the flow induced potential difference and the PSD technique was unable to eliminate it because it was in-phase with the magnetic field. Various sources can cause this problem and they were highlighted in the literature review, Section 2.5.9 and also discussed in Section 7.5. The solution was to make two consecutive sets of voltage measurements: one set during a "no flow" condition and one set during a period of water flow. During each set, all induced potential differences detected by the 16 electrodes were measured. Then, the digital PSD technique, described in Section 6.3, was applied to each set and the in-phase voltage component was determined. When there was no flow, the in-phase voltage component was due to noise only, i.e. $U_{j,nf,in}$ (nf: no flow) and during flow, the in-phase component $U_{j,in}$ was the sum of the flow induced voltage $U_{j,f,in}$ and the in-phase noise $U_{j,nf,in}$, which was assumed to have the same voltage as it did during the no-flow condition given that the two sets of measurements were made successively and within a short time of each other. Hence, the in-phase voltage component related to flow $U_{j,f,in}$ was found by subtracting the in-phase noise $U_{j,nf,in}$ from the in-phase voltage component during flow $U_{j,in}$, i.e.

$$U_{j,f,in} = U_{j,in} - U_{j,nf.in} \qquad \text{Eq. 6-32}$$

6.8 Bench Testing of the AC-excited Electromagnet

The aim of this experiment was to measure the magnetic flux density distribution (magnitude and direction) in the air gap of the electromagnet where the electrode array of the SVS is located. This is crucial as the magnetic field must be near uniform for the theoretical work described in Chapter 3 to be valid. When the magnetic field is near uniform it can be assumed that it has a constant value B_0 as given in Eq. 3-32 and Eq. 3-39. In addition to measuring the magnetic field density, the voltage across the electromagnet coil V_0, the transformer voltage, the coil current I_0 and the input real power were also monitored by using power analysers. According to the transformer circuit theory, the transformer voltage is 180° out of phase with the supply voltage (Lenz's law) – the transformer emf is equal to the rate of change of the magnetic field but opposes the source that caused it (Section 2.5.2). Moreover, the current in the coil lags the supply voltage by a phase angle very close to 90^{o} (inductive load with a small resistance).

6.8.1 Test Setup

The schematic diagram of the setup is illustrated in Figure 6.22. Equipment that were used are: (1) Two GPM-8212 power analysers, (2) 4-channel Agilent oscilloscope DSOX2014X and (3) GM07 Gauss meter. The supply voltage V_s across the electromagnet and the supply current I_s were monitored by the power analyser PA1. The coil current (between the capacitor and electromagnet) was monitored by the power analyser PA2. The transformer induced voltage was monitored by placing a search coil (made of several wire turns) on the electromagnet. The time-varying magnetic flux induces a voltage in the search coil which is proportional to the rate of change of flux with respect to time ($emf = N\frac{d\phi}{dt}$). As discussed in Section 5.6, the signal generator was set to a ±4 V, 30 Hz sinusoidal voltage signal and hence, the power amplifier output was ±40 V at the same frequency. The transformer stepped up the ±40 V signal to around ±200 V.

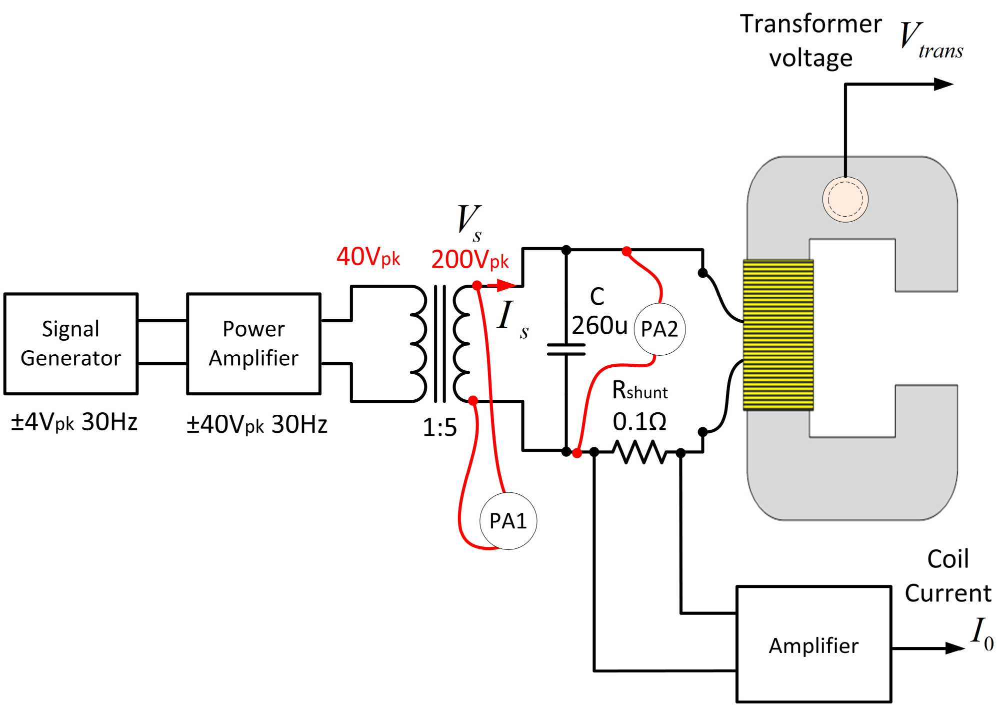

Figure 6.22: Electromagnet test setup

The Gauss meter, which had an axial probe, was used to sense the amplitude and direction of the magnetic flux density B. This enabled the measurement of the magnetic field which is applied to the cross section of the physical SVS. The magnetic field magnitude and direction were measured at x = 0, y = −40 to +40 mm and z = −40 to +40 mm as shown in the shaded square area in Figure 6.23. This YZ plane (x = 0) was the area of interest as it is orthogonal to the water flow in the SVS. Referring to Figure 6.24, at every intersection point (shown in red) between y and z, the magnitude and direction of the magnetic flux density was measured to confirm the uniformity of the magnetic field. It can be seen in Figure 6.24 that the flow channels of the SVS are located within the magnetic field generated in the air gap.

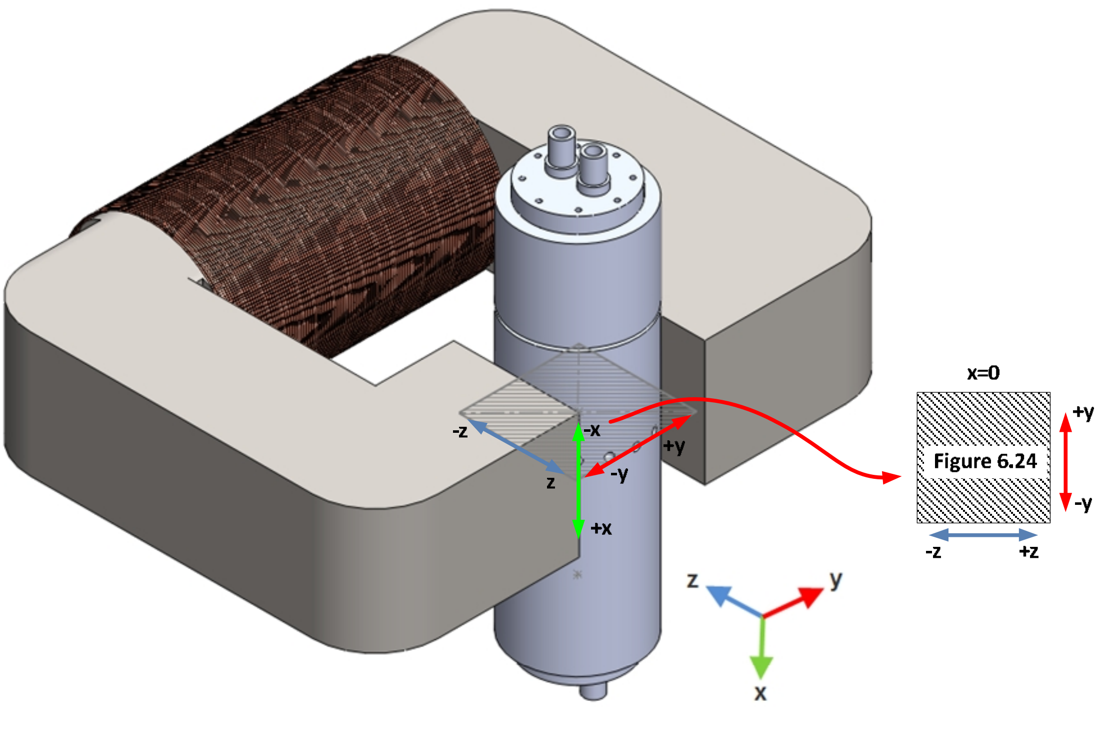

Figure 6.23: Measurement of the magnetic field distribution in the shaded area where the SVS channels are orthogonal to the magnetic field as shown in Figure 8.3

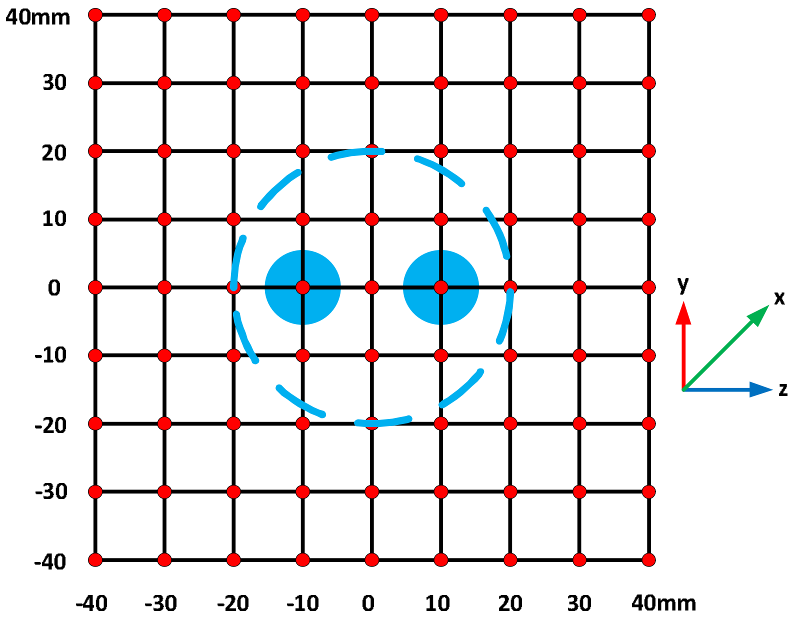

Figure 6.24: Measuring the magnitude and direction of the magnetic field at each intersection point. Note that x = 0, y = -40 to +40 mm and z = =40 to +40 mm.

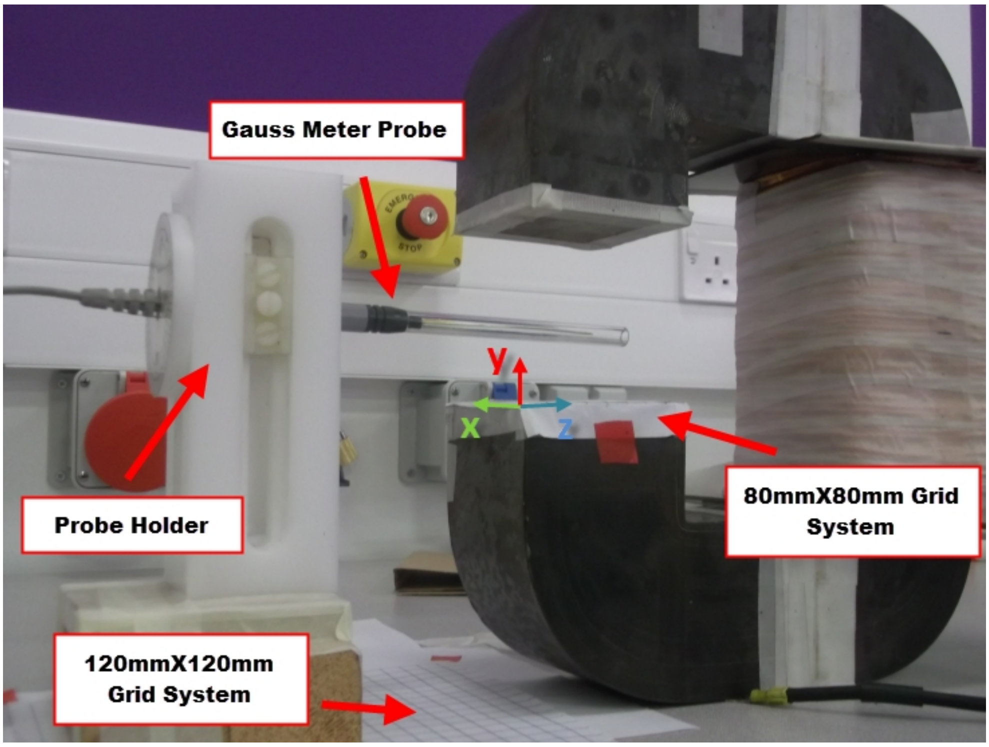

Figure 6.25: Test setup for measuring the magnitude and direction of the magnetic flux density

To perform the magnetic field magnitude and direction measurements, the electromagnet was placed upright on the bench for ease of access, as shown in Figure 6.25, and the following procedure was followed:

- Two grid systems were created using a plain sheet of A4 paper to be used as a reference guide for moving the Gauss meter probe correctly within the air gap. The first grid system was 80 mm×80 mm with an interval of 10 mm separating each grid line; the other grid system was a 120 mm×120 mm grid system, which also had an interval of 10 mm between the grid lines (refer to Figure 6.25)
- The 80 mm× 80 mm grid system was placed in the XZ plane of the bottom surface of the core air gap while the 120 mm×120 mm grid system was placed on the bench in front of the air gap of the electromagnet, and also in the XZ plane as shown in Figure 6.25.
- The probe holder allowed the probe to be rotated at a known angle and moved up or down at intervals of 10 mm in the y direction. Rotating the probe enables the direction of the magnetic field at the location of the probe to be determined because, as described below, when the probe's Hall Effect sensor was aligned with the local magnetic field, a maximum reading from the probe for the local magnetic flux density was obtained. The point representing the coordinates $x = 0$, $z = 0$ and $y = 0$ was marked as the centre of the air gap for both grid systems.
- For the measurements of the magnitude and direction of the magnetic field, the probe was moved in steps of 10 mm horizontally and vertically in the Y and Z directions at $x = 0$. At each step change, the probe was turned to the angle at which the highest magnetic flux density value was obtained, and then the measured magnetic flux magnitude and probe angle were recorded in a table together with the position of the measurement. The Hall-effect sensor of the probe had to be facing the flux lines to measure the magnitude of the magnetic flux density.

6.8.2 Results & Discussion

At the operating frequency of 30 Hz, the supply current I_s required for the coil current to reach a peak current I_0 of 10 A was 475 mA (rms value) and the peak voltage across the coil V_0 was 200 V. It can be seen that there is a significant advantage in using the power-factor correction capacitor. Instead of drawing a peak current of 10 A from the power supply, only 475 mA was required. However, the peak current I_0 between the capacitor and the coil was 10 A because they are at resonance at 30 Hz as described in Section 5.6. The total input power P_{in} recorded by PA1 was 62 W which means that the effective resistance R_{eff} of the electromagnet was 1.24 Ω ($R_{eff} = P_{in}/{I_{coil}}^2 = 62/7.07^2$). This is because varying voltages and currents introduce effects that are not present in DC circuits such as radiation losses, eddy currents and hysteresis losses as stated in Section 5.6 [153]. Note that the DC resistance of the coil was 0.9 Ω.

Figure 6.26 shows the waveform of the voltage across the coil, the quadrature voltage and the coil current. It can be seen that the quadrature voltage was 180° out of phase with the voltage across the coil, which was expected according to Lenz's law. Moreover, the coil current lags the voltage across the coil and this phase lag was measured to be 86° which was also expected as the electromagnet is not a pure inductive load and has some resistance, and therefore, the phase lag would not be 90°.

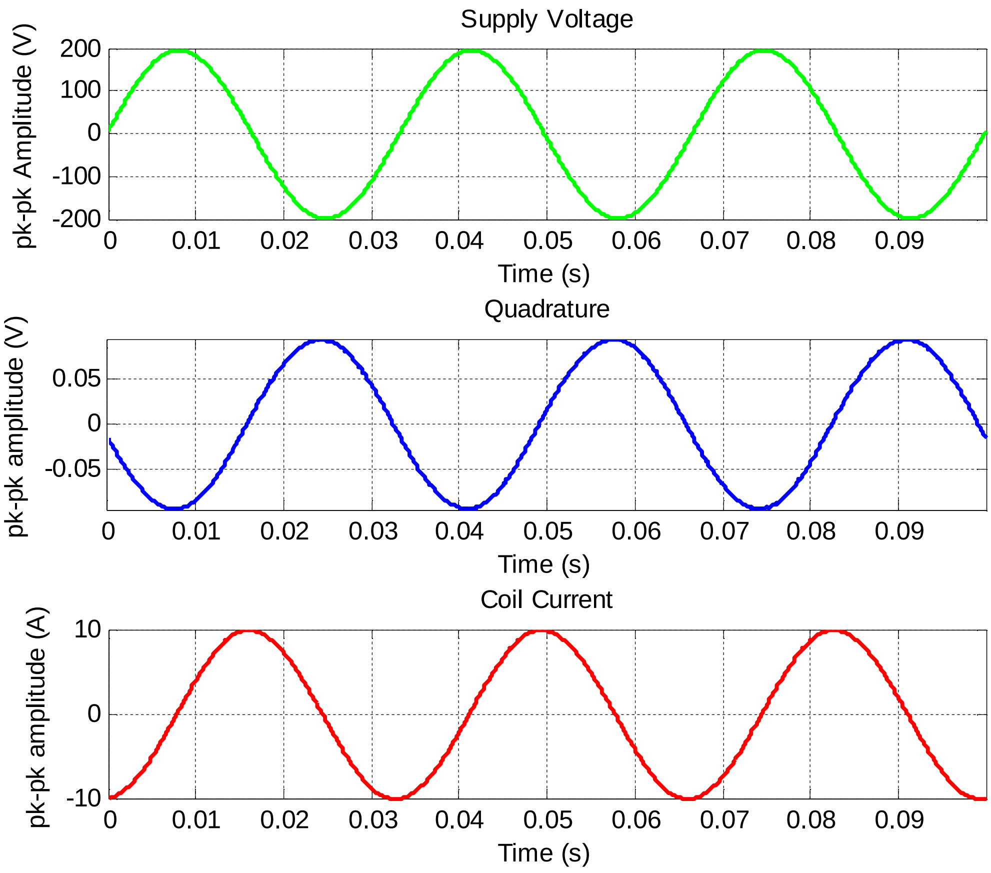

Figure 6.26: The supply voltage across the coil, the quadrature voltage and the coil current

The results of measuring the magnitude and direction of the flux lines of the magnetic field distribution in the YZ plane at x = 0, according to Figure 6.24, is presented in Figure 6.27. The flow channels of the SVS are also displayed on Figure 6.27 to give an indication of how uniform the magnetic field is across the channels. It can be seen that the magnitude and direction of the magnetic flux density is almost uniform. The average rms value of the magnetic flux density between $z = -20$ mm to $z = +20$ m, y = −20 to +20 and at x = 0 (where the porous ceramic is located) was 301 Gauss (rms value) and the standard deviation value was 4.3 Gauss. Hence, the magnetic field density B_0 across the flow channels is near uniform and can be assumed that it has a constant value B_0 as given in Eq. 3-32 and Eq. 3-39.

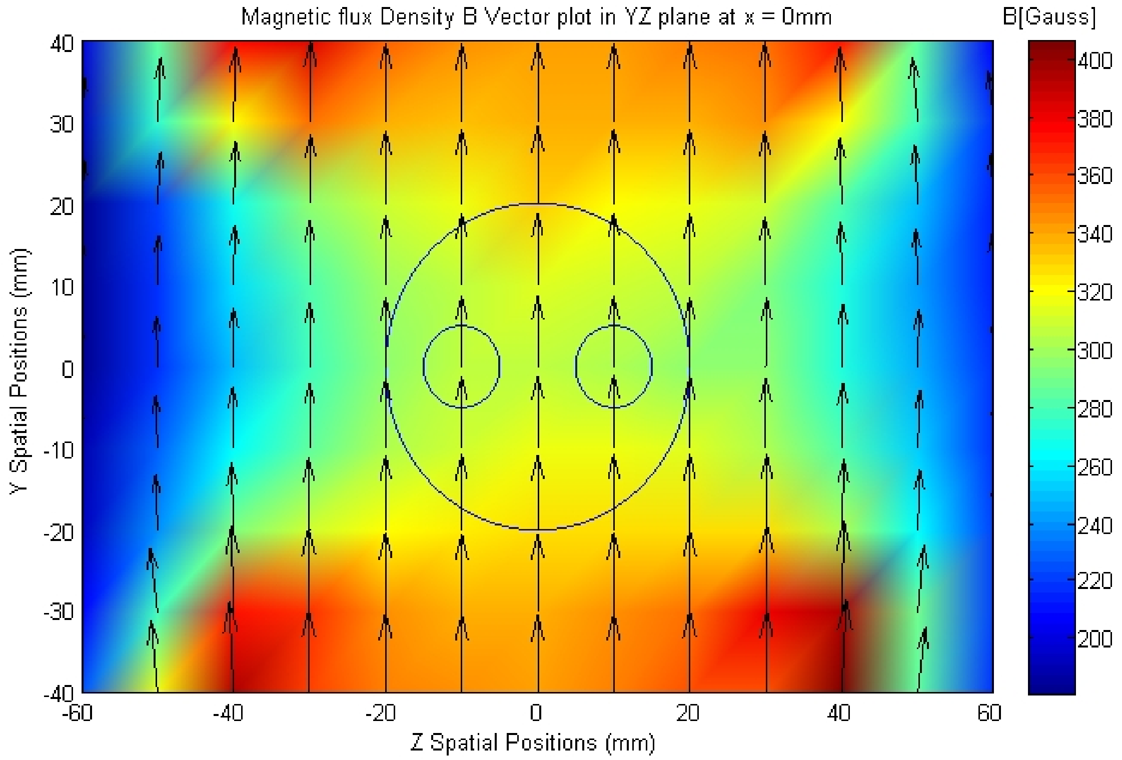

Figure 6.27: Vector plot of the magnetic flux density (RMS) in YZ plane at x = 0 mm

Theoretically (referring to Section 5.3.2), the rms magnetic flux was calculated to be 353 Gauss (500 Gauss peak). The reason for this decrease was due to the fringing effects as explained in Section 5.3.2 which increased the effective area of the air gap A_g. Theoretically, for the physical air gap area A_g = 6400 mm^2, peak current I_0 = 10 A and peak voltage V_0 = 201 V, the peak magnetic flux density B_0 value calculated was 500 gauss. However, in the practical electromagnet, the measured peak magnetic flux density value was 425 gauss (301 gauss rms), and by using the equations in Section 5.3, the calculated effective area of the air gap A_g is 7500 mm^2.

6.9 Bench Testing of the AC Signal Conditioning System

The AC signal conditioning circuit was tested for its transient and frequency responses and its normal operation. The transient response determines the time required for the output to reach its steady state value after power up. The frequency response shows the gain and phase information for a range of frequencies. It was important to measure the gain and the phase of the system (input voltage with respect to the output voltage) at the frequency of the flow induced potential differences which is 30 Hz. The gain value of the signal conditioning system had to be accurately measured in order to determine the actual value of the flow induced potential differences after amplification. Moreover, any phase error between the input and the output voltage signals introduced by the conditioning system had to be measured and then compensated for in the PSD MATLAB software. This would ensure that the PSD determines the flow induced voltage potential differences accurately as the PSD depends on the phase relationship between the total measured voltage and the coil current (the reference signal). If this error is not compensated for, the in-phase flow induced potential measurements would suffer from an error in amplitude, and that reduces the accuracy of the total flow rate measurement.

6.9.1 Test Setup

The only equipment needed for this test was the DSOX2014X oscilloscope. The built-in function generator of the oscilloscope was connected to the inputs of the AC signal conditioning circuit, i.e. U_j and U_5 (refer to Figure 6.28). The output (V_{out}) of the circuit was monitored on the oscilloscope. The test setup depicted in Figure 6.28 was used to perform the normal operation, the transient response and the frequency response tests.

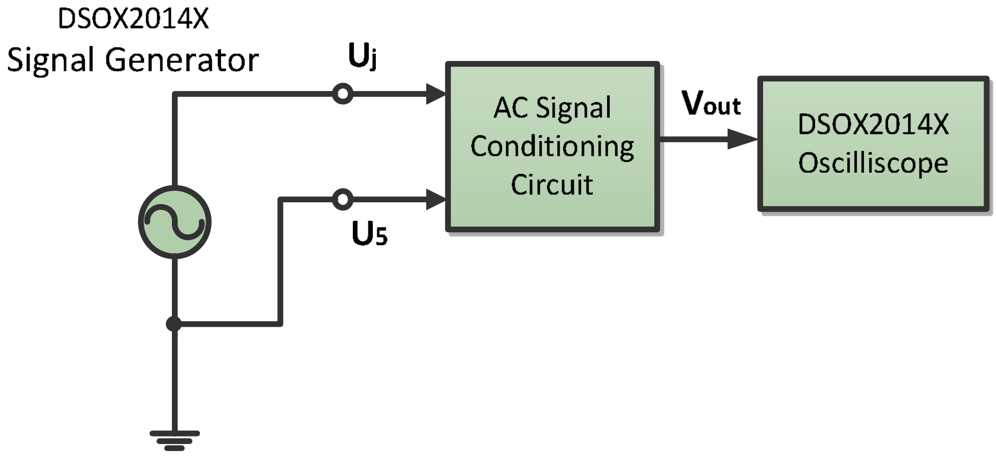

Figure 6.28: Test setup for the AC signal conditioning circuit

6.9.2 Results & Discussion

For the transient response, the circuit was tested at power-up condition with DC offsets of 0 V, 100 mV and 200 mV present in the voltage signal U_j. A step change of 100 mV or 200 mV simulated the case when the analogue multiplexer switches its input to connect to another electrode. All electrodes suffer from the DC offset in the range of 100 mV to 200 mV (observed in the practical experiment) due to polarisation which is explained in Section 2.5.9. It is important to determine the transient period of the signal conditioning system for different DC offset values (electrodes have different DC offsets) to find the longest possible period that can occur. Then, based on the longest period that could occur, a time delay can be introduced in the MATLAB program which controls the NI PCI-6254 DAQ device. This time delay ensures that the DAQ device samples the output of the signal conditioning system after the transient period of signal conditioning system has elapsed.

Figure 6.29 shows the transient response of the circuit at power-up condition with zero DC offset. Both voltage inputs of the circuit were grounded. It was found that the output takes about 0.4 s (4.35 s − 3.92 s) to reach the steady-state value which is 0 V. Figure 6.30 shows the transient response of the circuit when 100 mV DC and 200 mV DC offsets were applied, respectively. For the 100 mV DC offset, the circuit took about 0.6 s (2.39 s – 1.8 s) to reach the steady-state value and 0.7 s when the DC offset was changed to 200 mV.

In MATLAB program 1 (Section 6.6), a time delay of 1 s was added between the switching to another electrode (via the multiplexer) and the start of the data sampling process to avoid the transient period of the AC signal conditioning circuit, and this value was found to be appropriate for testing the SVS for the flow conditions as described in Chapter 7.

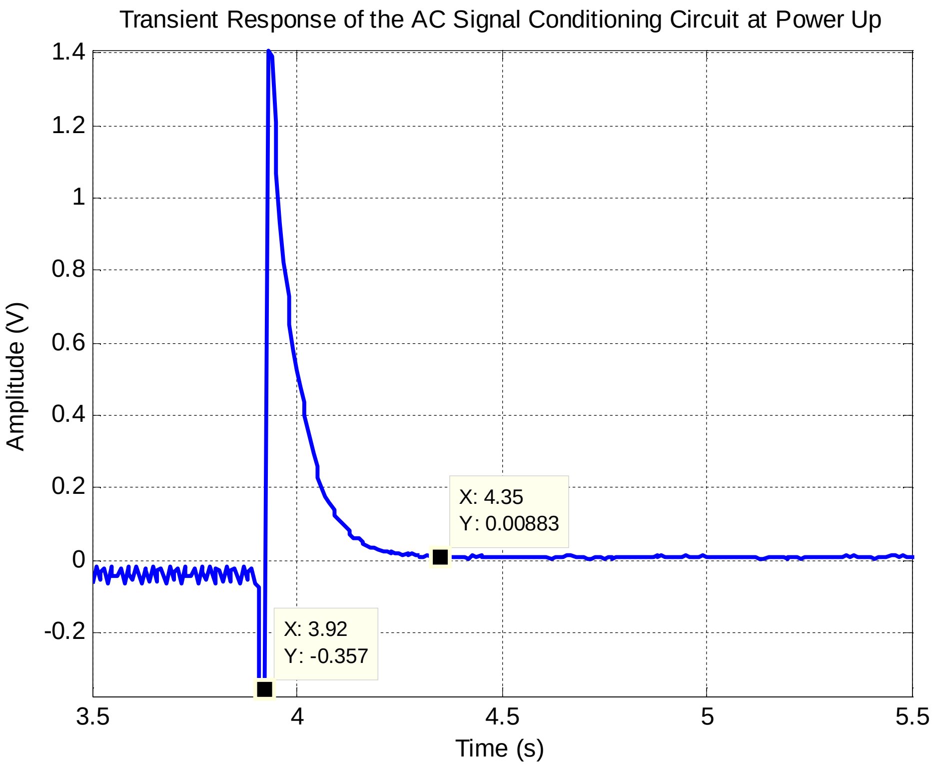

Figure 6.29: Transient response of the circuit at power-up state.

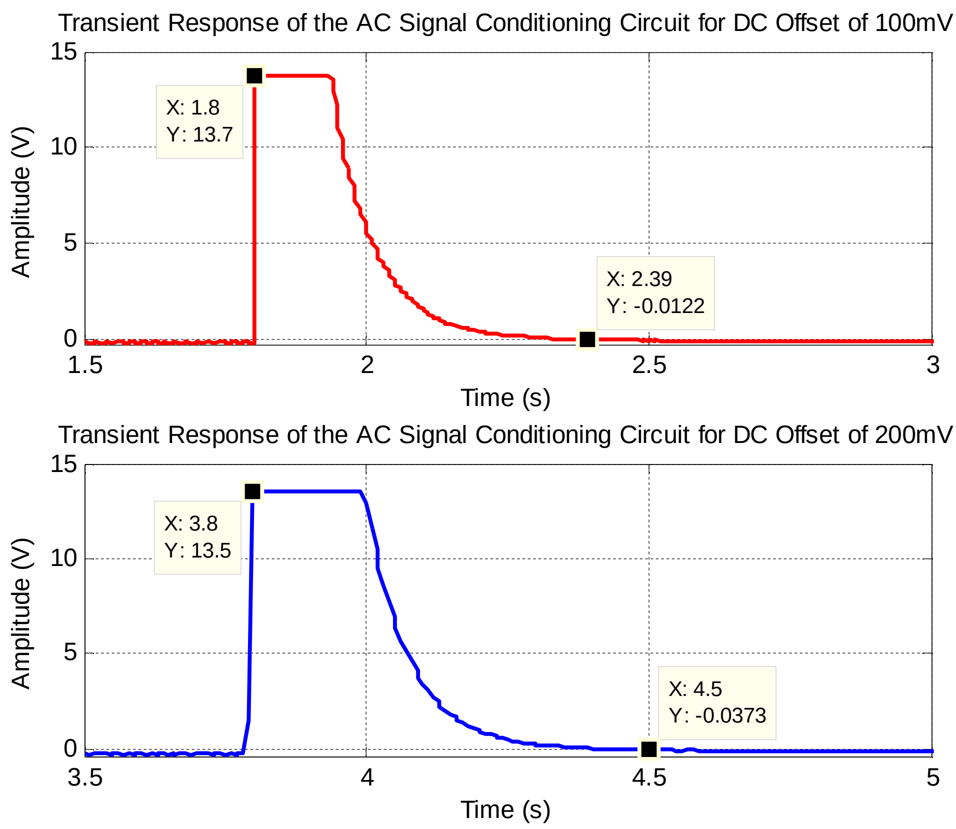

Figure 6.30: Transient response of the AC signal conditioning circuit for 100mV and 200 mV DC offsets

For the frequency response, the input signal U_j was set to a peak voltage of 10 mV and the output voltage was measured for a range of frequencies from 0.1 Hz to 12 kHz. The frequency response (gain and phase vs frequency) of the circuit is shown in Figure 6.31 and Figure 6.32. It was found that, at 30 Hz, the gain of the circuit is 59.81 dB, corresponding to an actual gain of 978, and the output voltage led the input voltage by 2.4°. Consequently, during the flow measurements described in Chapter 7, the flow induced voltages detected by the electrodes will be amplified by a factor of 978, and for the PSD method, the 2.4° phase error has to be compensated for to reduce the error in amplitude of the flow induced potential differences as explained in Section 6.6.

Finally, Figure 6.33 shows the input and output voltage waveforms of the circuit after the transient period (the normal operation). The input voltage U_j applied (blue trace) had an amplitude of 10 mV with a DC offset of 100 mV and frequency of 30 Hz. The output voltage (red trace) was amplified by a gain of 978, i.e. 9.78 V, and as stated earlier, there was a phase shift of 2.4° between the input and output voltages. Note that the DC offset did not appear on the output voltage as it was removed by the high-pass filter effect of the signal conditioning circuit, as described in Section 5.7.3.

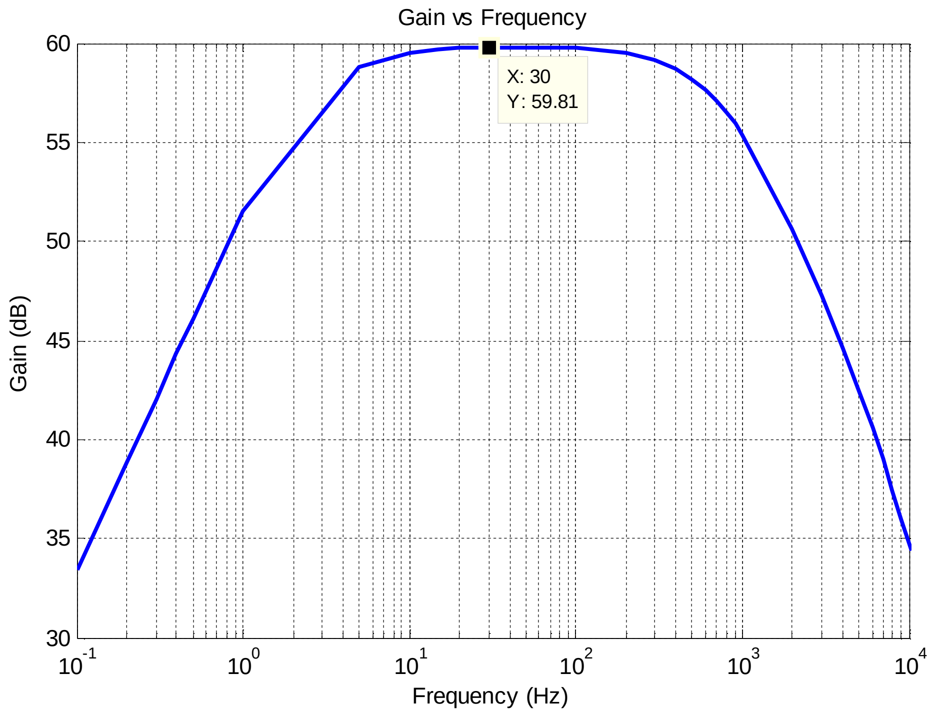

Figure 6.31: Gain vs frequency response of the AC signal conditioning circuit [X refers to frequency and Y refers to phase angle]

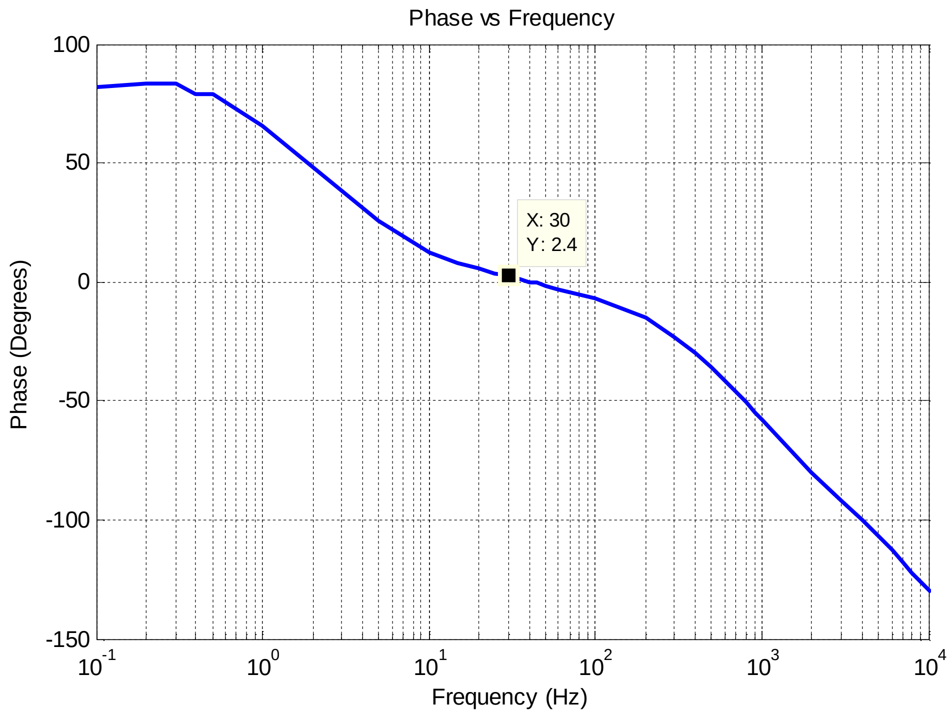

Figure 6.32: Phase vs frequency response of the AC signal conditioning circuit [x refers to frequency, y refers to phase angle]

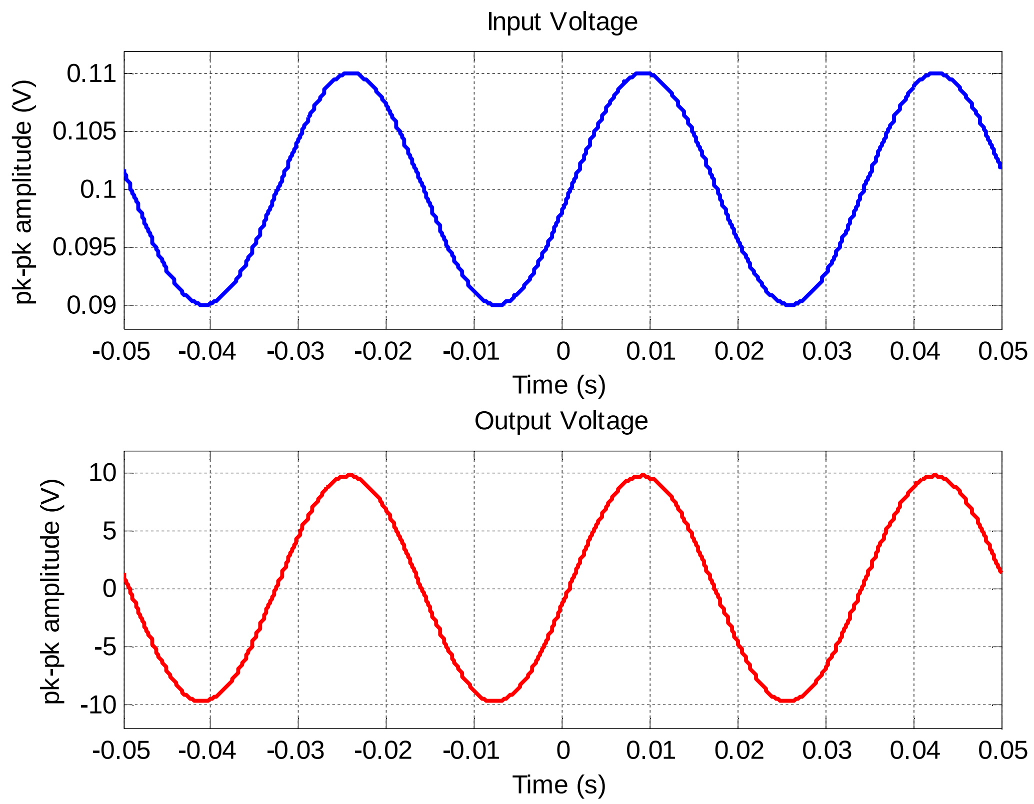

Figure 6.33: Normal operation of the AC signal conditioning circuit

6.10 Electrodes Electrical Noise Investigation

Before the flow induced potential difference measurements were obtained, the sources of voltage noise that were buried in the potential difference signals detected by the electrodes were examined. This helped in understanding the dominant source of voltage noise in the signals picked up by the electrodes. The noise analysis was done by performing a spectral analysis on the potential difference measured between electrodes e_1 and e_5. It could have been performed with any other electrode pair as they are all very close to each other and the noise between the other pairs would be very similar.

The potential difference between electrodes e_1 and e_5 was measured by the AC signal conditioning system and then sampled by the NI PCI-6254 DAQ. The potential difference measurement was then divided by the gain of the signal conditioning system which is 978. The spectral analysis was performed using NI Signal Express 2013 software. The sources of noise were first analysed while the electromagnet was switched off, and then it was switched on and any differences in the spectrum were observed. Figure 6.34 shows the spectrum of the potential difference measured between electrodes e_1 and e_5 when the electromagnet was off and the water valve was shut.

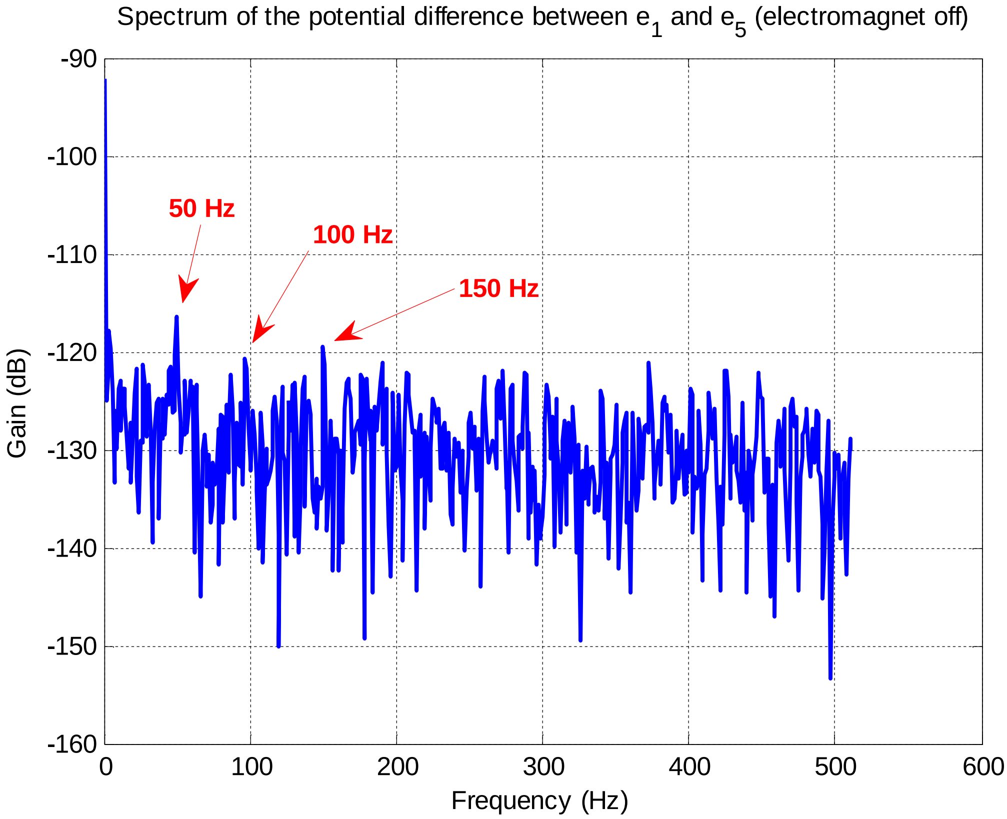

Figure 6.34: Spectral analysis of the potential measurement between electrodes e_1 and e_5 when the AC power supply of the electromagnet was off and the water supply was shut off.

It can be seen from Figure 6.34 that the mains frequency component and its harmonics were present in the voltage signal but were at a very minimal level. The 50 Hz component was -116 dB (refer to Figure 6.34) which meant that the amplitude of the 50 Hz component was 1.6 μV (measured with respect to the reference level of the spectrum analyser which is 1 V, i.e. 0 dB). The harmonics of the mains frequency were less than -116 dB and therefore, they were insignificant sources of noise. It can be concluded that the CMRR of the AC signal conditioning system was sufficient to reject mains common-mode signals, i.e. the 50 Hz component and its harmonics, for the purpose of the flow induced potential difference measurements.

Afterwards, the AC power supply of the electromagnet was switched on and the water supply valve remained closed. The potential difference between electrodes e_1 and e_5 was measured and the spectral analysis of the voltage signal was obtained as shown in Figure 6.35.

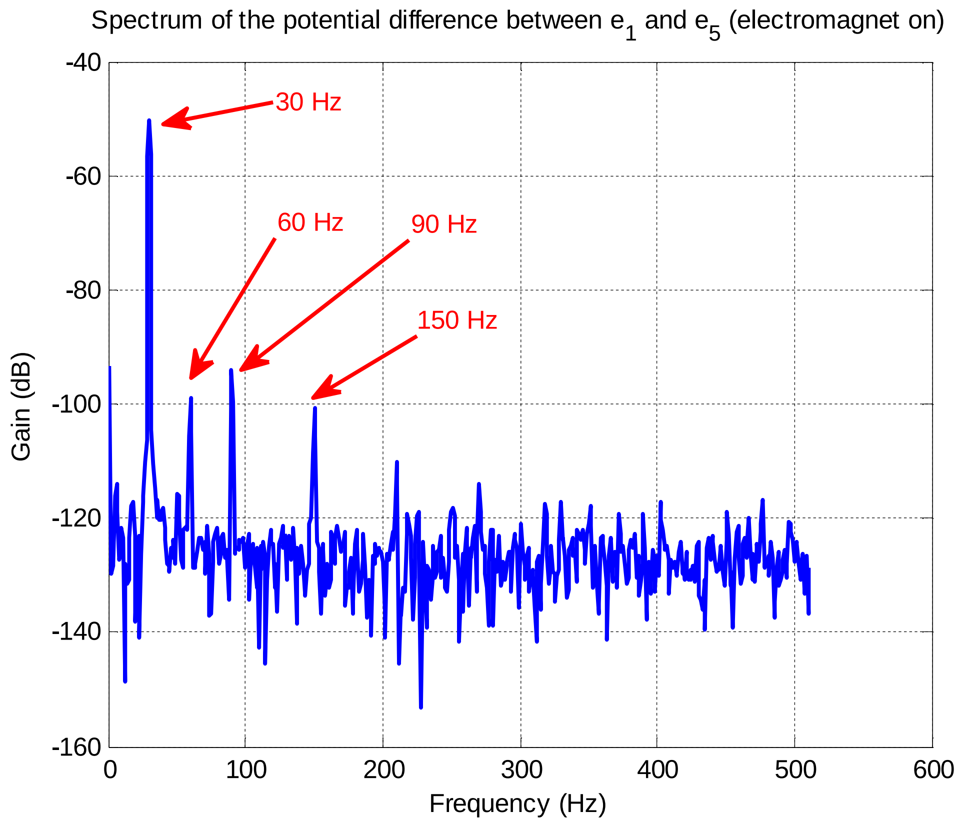

Figure 6.35: Spectrum analysis of the potential measurement between electrodes e_1 and e_5 when the AC power supply of the electromagnet was on.

It can be observed that there is a 30 Hz component as was expected along with its harmonics at 60 Hz and 90 Hz. This 30 Hz signal was due to the transformer emf induced in the electrode cables as there was no water flow in the SVS tubes. This component was mainly a differential-mode signal and the CMRR of the signal conditioning signal did not reject it. Referring to Figure 6.35, the gain of the 30 Hz component was about -50 dB which means that the amplitude of the transformer emf was 3.2 mV (measured with respect to the reference level of the spectrum analyser which is 1 V, i.e. 0 dB) and this is important because the voltage amplitude of the flow induced potential differences measured ranged between 10 μV and 185 μV. In other words, the amplitude of the transformer potentials in the voltage signals detected by the electrodes was in the mV range (voltage signals from other electrodes were also examined) whereas the flow induced potential differences were in the μV range. Hence, this demonstrate that the digital PSD method (see Section 6.3) was vital in order to be able to distinguish between the flow induced and transformer induced potential differences.

It can also be seen that the 150 Hz component increased from -120 dB (Figure 6.34) to -100 dB (Figure 6.35) which is a voltage gain increase of 10. This was due to the signal generator that is part of the power supply of the electromagnet. This signal generator has a transformer in its power supply and it runs from the mains. The 150 Hz noise is predominantly caused by the hysteresis of the transformer core and it couples magnetically to systems. It could have coupled to the electrode array, AC signal conditioning system or any cables in between. However, this 150 Hz component can be detected and removed when the digital PSD method is applied.

6.11 Summary

The voltage signals picked up by the electrodes after being conditioned by the AC signal conditioning circuit are the sum of two induced voltages: motional and transformer. The motional induced voltage is due to the fluid flow in the magnetic field and this is the desired voltage. The transformer induced voltage is the unwanted voltage which is caused by the cable loops in the presence of the sinusoidal (time-varying) magnetic field. The PSD technique was essential in order to distinguish the flow induced potential differences (in-phase component) from the transformer voltages (quadrature component). For accurately measuring a signal from a system using a PSD method, the system must be excited by a reference signal with a known frequency. One method of applying the PSD is to multiply the output of the system by the reference signal and then the resultant signal is passed to a low-pass filter function to obtain the mean value of the target signal. This method can be implemented using analogue or digital electronics as described in Section 6.2. Alternative implementation is to apply the DFT to the measured voltage signals, detected by the electrodes, and the reference signal to obtain their amplitude and phase. Then, once the phase difference between the total voltage and reference signals is found, the in-phase and quadrature components can be determined. This latter method was utilised for the practical SVS system and it was implemented in MATLAB. All electrode signals and the coil current were sampled by the data acquisition device and then the MATLAB-based PSD was applied. The program developed in MATLAB was also tested using simulated flow, transformer and noise signals to verify its function before usage in the practical experiment and the results obtained from the test were correct and as predicted. It was found that any small error in the phase angle between the measured voltage and the reference signal can cause a significant error in the amplitude of the in-phase component, as discussed in

Section 6.7, which is the component that is necessary to measure. The phase lead introduced by the signal conditioning circuit which is 2.4° is compensated for in the digital PSD MATLAB software by subtracting this value from the phase angle measured between the voltage signal and the coil current.

The AC-excited electromagnet and its power supply and the signal conditioning system were tested on the bench, to verify their operation before obtaining the flow induced potential differences. The electromagnet, described in Section 5.3, and its power supply (refer to Section 5.6.2) were tested to ensure that the magnetic field, generated in the air gap, was uniform across the SVS flow channels. The mean magnetic field density value was 301 Gauss (rms value) and the standard deviation was 4.3 Gauss. The flux lines of the magnetic field were also found to be in a constant direction as shown in Figure 6.27. Hence, fluctuations in the magnetic flux density were minimal and so, the magnetic field was near uniform. The peak voltage across the coil of the electromagnet was 200 V and the peak coil current was 10 A as was predicted. Note that, the current drawn from the power supply was 475 mA (rms) and the power consumption was 62 W. The reason for this power consumption was the effective resistance R_{eff} of the electromagnet which is caused by radiation losses, eddy currents and hysteresis losses.

The AC signal conditioning circuit was tested for its transient and frequency responses. The transient response test showed the time the circuit takes from power up to reach its steady-state value. The test also demonstrated that when the multiplexer switches to another electrode, a delay must be inserted before starting to sample the output of the circuit. This ensures that the output signal is sampled when the circuit has reached its steady-state value. This time delay was chosen to be 1 s which was found satisfactory for the operation of the circuit. The frequency response test provided the gain and phase values of the circuit at 30 Hz – the frequency of the flow induced voltages. The gain of the circuit at 30 Hz was 978 and the output signal of the circuit led the input by 2.4°. This phase was compensated for in the digital PSD method to prevent any phase error from affecting the accuracy of the flow induced potential difference measurements as explained in Section 6.6.

Lastly, the electrical noise detected by the electrodes was investigated and it was found that it is very crucial to have the signal processing system to be able to separate the flow induced potential difference from the transformer voltage as the latter has the same frequency and is few magnitudes larger than the flow induced potential difference.

Chapter 7
Flow Induced Potential Difference Measurements from the Practical SVS Model and their Analysis

Contents

7.1 Introduction

This chapter discusses the flow induced potential difference measurements obtained from the practical experiments. The SVS flow rig, shown in Section 5.5, was used to conduct several flow rate measurement tests. Each test had different settings, i.e. different numbers and locations of the flow channels and different flow rate values – similar to the FE simulations that were performed in Chapter 4. For each flow rate test, flow induced potential differences and other unwanted signal (noise and transformer induced voltages) were detected by the electrodes and then conditioned (using the AC signal conditioning system) and processed (using the digital PSD method) to obtain the required flow induced potential differences. Afterwards, these flow induced potential difference measurements were compared to the flow induced potential difference measurements obtained from the theoretical model given in Eq. 3-32 and Eq. 3-33 (refer to Section 3.4) for given number and location of, and the flow rate in, the flow channels and the peak magnetic flux density B_0. The aim was to compare the results of the flow induced potential difference measurements obtained from the practical experiment with the flow induced potential difference measurements obtained from the proposed theoretical model described in Eq. 3-32 and Eq. 3-33. This is very similar to the FE simulations carried out in Chapter 4 in which the flow induced potential difference measurements obtained from the FE model were compared with the flow induced potential measurements obtained from theoretical model.

The practical induced potential difference measurements were obtained from tests performed for different positions of the SVS tubes ‘a’ and ‘b’. For each position, two water flow rates were used, i.e. 117×10^{-6} m^3/s and 195×10^{-6} m^3/s (average values). These two flow rates were obtained when the valve of the water supply was either half or fully open. In these tests, water flow was imposed through either tube 'a' only, tube 'b' only or in both tubes. These tests showed the effects of: (i) the flow rate, and (ii) the number and location of the flow channels, within the area bounded by the electrode array, on the flow induced potential differences.

Next, the DFT was applied to the 16 flow induced potential difference measurements U_j (j =1 to 16 and U_5 = 0) obtained from each test. Note that when DFT is performed on 16 samples, only 8 DFT values are unique. The modulus of $X(1)$, i.e.$|X(1)|$ is proportional to the total flow rate Q_T and the peak magnetic flux density B_0 as was shown in Eq. 3-39. For convenience the relationship between the modulus of the fundamental component of the DFT $|X(1)|$, the total flow rate Q_T and the magnetic flux density B_0 is stated below.

$$|X(1)| \propto Q_T B_0 \qquad \text{Eq. 7-1}$$

Hence,

$$|X(1)| = k_1 Q_T B_0 \qquad \text{Eq. 7-2}$$

where k_1 is a calibration factor which was determined from the flow tests discussed in this chapter. Then, the practical calibration value k_1 was compared to the value obtained from the theoretical model which can be calculated using Eq. 3-33. The theoretical, practical and FE calibration factor k_1 values should be the same as the factor depends only on the radius of the electrode array which is 25 mm.

7.2 Test Setup

The SVS flow cross section (including the electrode array) is shown in Figure 7.1. All electrodes were connected to the multiplexer circuit which is the front-end of the AC signal conditioning circuit as shown in Figure 5.45. For each flow rate test, the potential difference $U_{j,f}$ between each electrode e_j and electrode e_5 was obtained via the AC signal conditioning circuit (refer to Figure 5.24). Each potential difference $U_{j,f}$ was sampled by the NI PCI-6254 DAQ device. The coil current I_0 was also sampled by the DAQ device during the measurement of $U_{j,f}$. It was necessary to use the coil current as the reference signal in the PSD software to extract the in-phase flow induced potential difference $U_{j,f,in}$[7] from the potential difference $U_{j,f}$ as described in Section 6.3. The PSD method was applied to all potential differences $U_{j,f}$ to obtain 16 flow induced potential differences, i.e. e_1-e_5, e_2-e_5, e_3-e_5, …, e_{16}-e_5. This process was performed for each flow rate measurement test. Note that, the 16 flow induced potential difference measurements, shown later in this chapter, were obtained by averaging 10 samples to provide more accurate results.

[7] The in-phase potential difference $U_{j,f,in}$ is equivalent to U_j in the mathematical modelling in Chapter 3

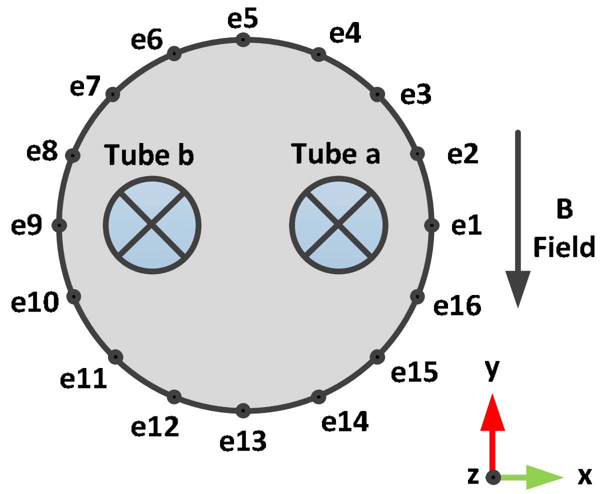

Figure 7.1: Cross section of the SVS and the electrode array

Three sets of flow tests were performed for: (i) tube ‘a’, (ii) tube ‘b’ and (iii) both tubes as follows:

(i) Flow induced potential distribution measurements were obtained from water flowing through tube ‘a’ only for low and high flow rates. For each flow rate, tube ‘a’ was positioned at 0°, 22.5° and 45° anti-clockwise with respect to electrode e_1 as depicted in Figure 7.2.

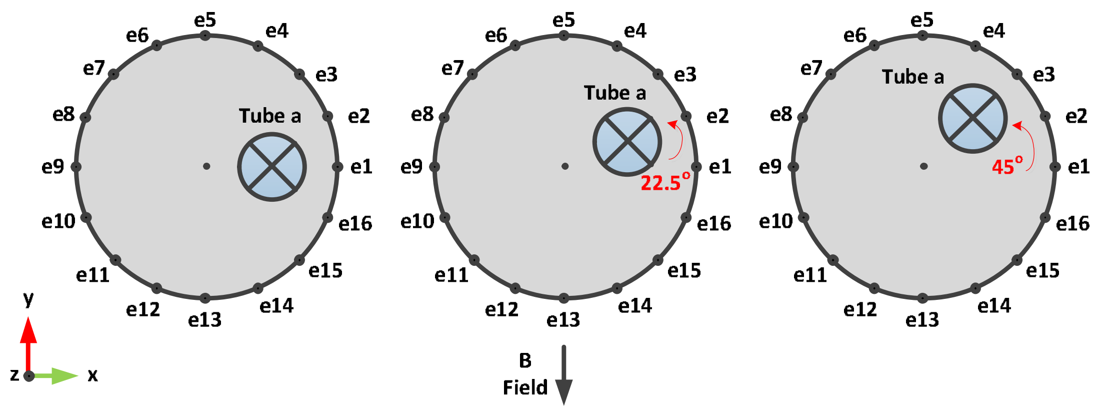

Figure 7.2: Three different test setups for tube 'a' at 0°, 22.5° and 45° with respect to electrode e_1

(ii) Next, flow induced potential distribution measurements were obtained from water flowing through tube ‘b’ only for low and high flow rates. For each flow rate, tube ‘b’ was positioned at 180°, 202.5° and 225° with respect to electrode e_1 as illustrated in Figure 7.3.

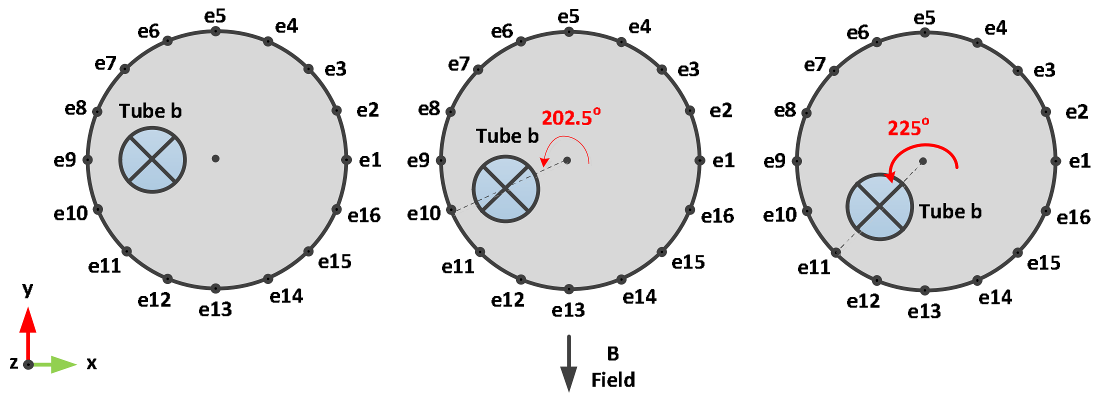

Figure 7.3: Three different test setups for tube 'b' at 180°, 202.5° and 225° with respect to electrode e_1

(iii) Finally, flow induced potential distribution measurements were obtained from water flowing through both tubes ‘a’ and ‘b’ simultaneously for low and high flow rates. For each flow rate, both tubes were positioned at 0°, 22.5° and 45° for tube ‘a’ and 180°, 202.5° and 225° for tube ‘b’ with respect to electrode e_1 as shown in Figure 7.4.

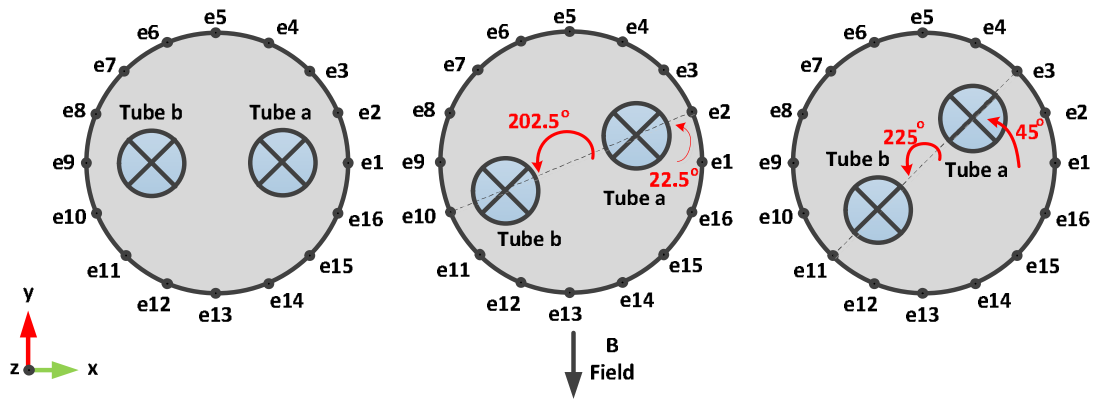

Figure 7.4: Three different test setups for tubes 'a' and ‘b’ at 0°-180°, 22.5°-202.5° and 45°-225° with respect to electrode e_1

The positions of the tubes in the three test cases shown above were chosen to be similar to the FE COMSOL test cases so that the results from both models could be compared. Moreover, it was easier to rotate the electromagnet at the angles specified above because the electrodes are 22.5° apart from each other and were used as a guide.

In the practical experiment, because it was necessary for the SVS pipe model to be firmly fixed to its base, the electromagnet was rotated around the SVS unit rather than rotating the SVS. Tubes ‘a’ and ‘b’ were rotated “virtually” without the need for physically moving the SVS pipe model. This operation was performed by rotating the electromagnet by an angle θ clockwise and that is equivalent to rotating tubes ‘a’ and ‘b’ by the same angle anti-clockwise. In other words, rotating the electromagnet by a number of steps n of a given angle θ where the angle θ is measured with respect to electrode e_1 (refer to Figure 7.5) is equal to rotating the tubes by the same angle in the opposite direction. However, this is only valid if the current index number of the electrodes j is changed according to the number of steps n, i.e. $j' = j + n$ where j' is the new indexing number of the electrodes. Note that, if the value $j + n$ is greater than 16 then the electrode number $j' = (j + n) - 16$.

The angle of rotation θ of the tubes was chosen to be 22.5° as the electrodes are placed at this angle apart, and it was easy to rotate the electromagnet in such steps. For example, suppose tubes ‘a’ and ‘b’ are needed to be rotated by 22.5° anti-clockwise, with respect to the electrode array and the magnetic field so that their position changes from that shown in Figure 7.1 to that shown in Figure 7.5(A). This can, in effect, be accomplished by rotating the magnetic field shown in Figure 7.5(B) one step ($n = 1$) of angle θ, i.e. $\theta = 1 \times 22.5°$, clockwise and by changing the electrode index to

$j' = j + 1$ as illustrated in red in Figure 7.5(B). The reference electrode is always electrode e_5 so the new reference potential is at $j' = 5$ which is electrode e_4 physically.

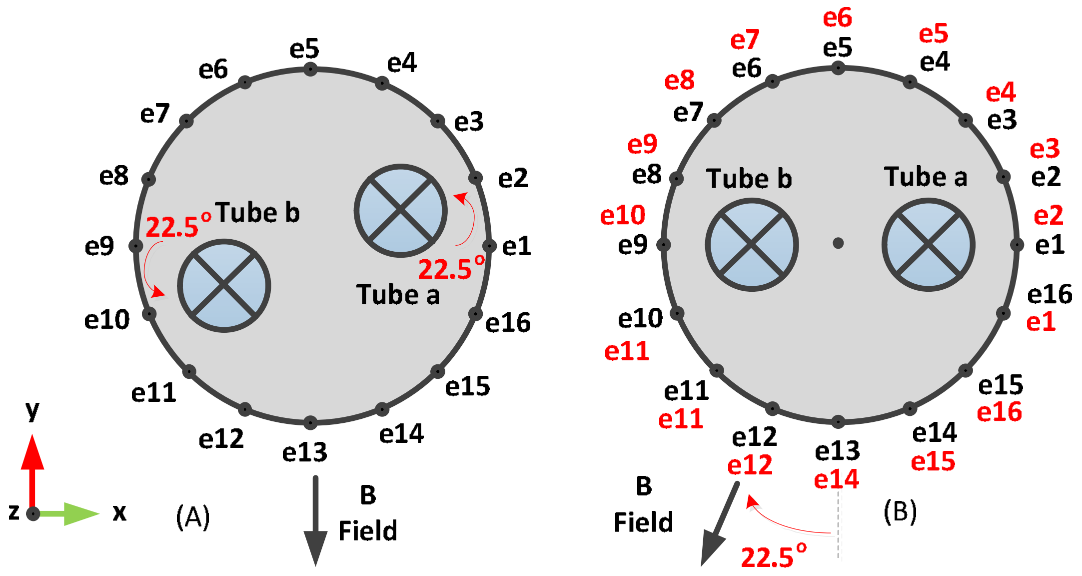

Figure 7.5: Rotating the electromagnet by 22.5° clockwise and changing the indexing j to j' as shown in B is equivalent to rotating both tubes by 22.5° anti-clockwise with respect to electrode e_1 as shown in A. The electrode numbers shown in black are j and the electrode numbers in red are j'

7.3 Flow Induced Boundary Potential Results

The flow induced potential differences obtained from the practical experiments (described in Section 7.3), were compared with the flow induced potential differences obtained from the mathematical model given in Eq. 3-32 and Eq. 3-33 for the same value of the magnetic field, the flow rate and the number, size and location of the flow channels. The procedure that was used to find the flow induced potential differences mathematically is explained in Section 4.7.2. The value of k_1, using Eq. 3-33, was always 6.37 m^{-1} when calculating the flow potential differences.

7.3.1 Test 1: Water Flow Imposed in Tube ‘a’

In these tests, tube ‘b’ was blocked and the water was flowed through tube ‘a’ only. Tube ‘a’ was virtually rotated by rotating the electromagnet by 22.5° then 45° with respect to electrode e_1. The indexing j of the electrode array was also changed accordingly when the electromagnet was rotated. The first position of tube ‘a’ was at 0° as shown in Figure 7.6. The water flow through tube ‘a’ only was measured to be on average 120×10^{-6} m^3/s for the low flow rate and 190×10^{-6} m^3/s for the high flow rate.

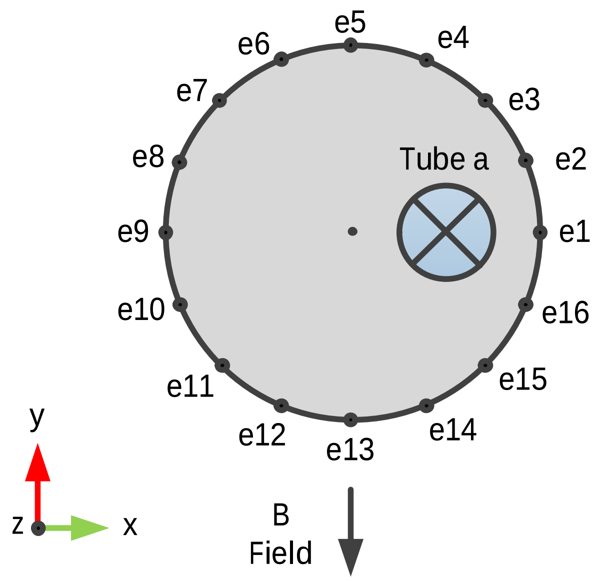

Figure 7.6: Tube 'a' positioned at 0° with respect to electrode e_1 (no change in indexing was required)

Figure 7.7 shows a comparison between the flow induced potential difference measurements obtained from the practical experiment and the flow induced potential differences obtained from the theoretical model (Eq. 3-32 and Eq. 3-33) for the low and high flow rates. It can be observed that for both low and high flow rates, the profile of the potential distribution is very similar. The only difference is that the amplitude of the potential difference measurements is higher for the greater flow rate and this is expected as the flow rate is directly proportional to the flow induced potential differences. There was a percentage difference in the amplitude of the potential differences obtained from the practical experiment and theoretical model. This difference was mainly due to noise that was in-phase with the flow induced potential differences and is discussed in

Section 7.4 (refer also to Section 6.7). The magnitude of the largest measured induced potential difference measurement was 116 μV between electrode e_1 and e_5 for the low flow rate, whereas for the high flow rate, the largest measured magnitude was 172 μV.

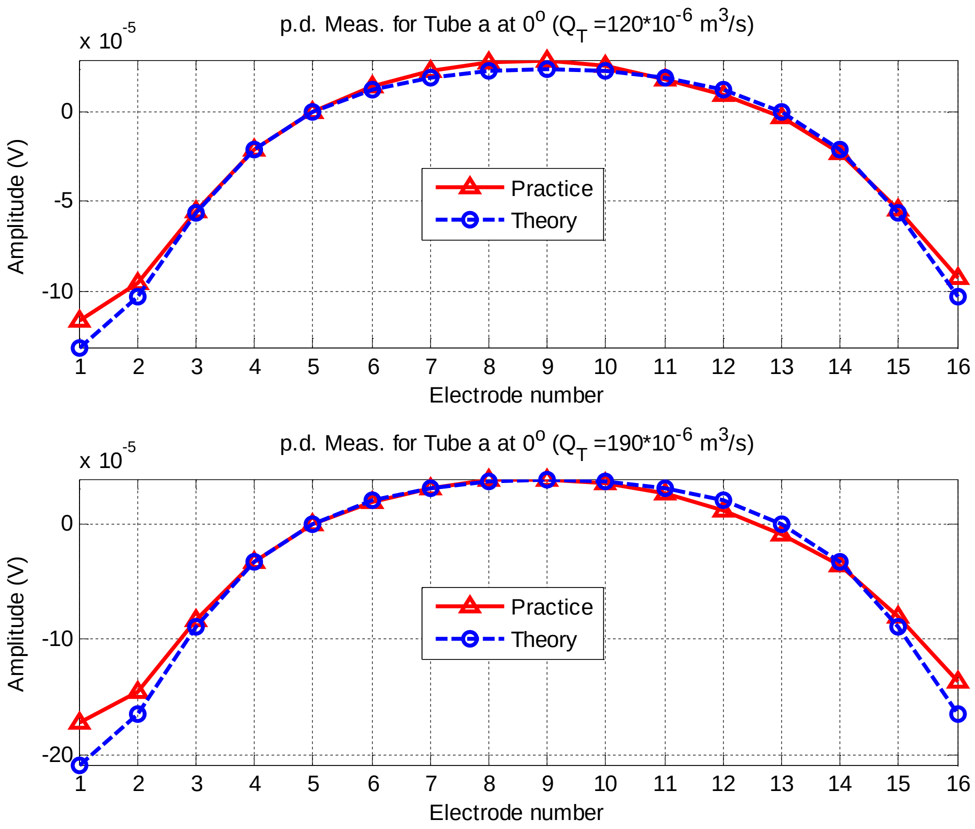

Figure 7.7: Practical and theoretical flow induced potential difference measurements for tube 'a' located at 0° with respect to electrode e_1 for flow rates of 120×10^{-6} m^3/s and 190×10^{-6} m^3/s

In the next test, the electromagnet was rotated by 22.5° clockwise, and the indexing of the electrode array j was changed to $j' = j + 1$ or $j' = (j + 1) - 16$, if $j + 1$ was greater than 16 as shown in Figure 7.8(B). This is equivalent to rotating tube 'a' by 22.5° as illustrated in Figure 7.8(A). The electrode numbers shown in black are j and the electrode numbers in red are j'. The low and high water flow rates were on average 118×10^{-6} m^3/s and 170×10^{-6} m^3/s, respectively. The practical and theoretical flow induced potential difference measurements for this test are presented in Figure 7.9. It can be noted that in Figure 7.9, the potential distribution was different to the results in

Figure 7.7 for relatively similar flow rate values. This was due to the change of position of tube ‘a’ by 22.5° with respect to electrode e_1.

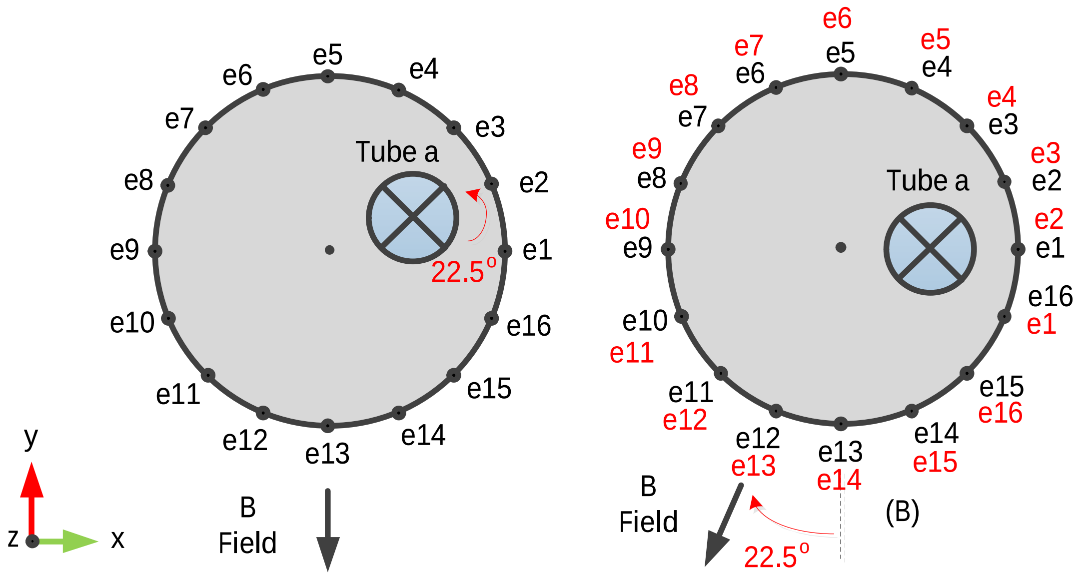

Figure 7.8: (A) Rotating tube ‘a’ by 22.5° anti-clockwise is equivalent to (B) rotating the electromagnet by 22.5° clockwise with respect to electrode e_1 and changing the electrode indexing number from j to j'. The electrode numbers shown in black are j and the electrode numbers in red are j'

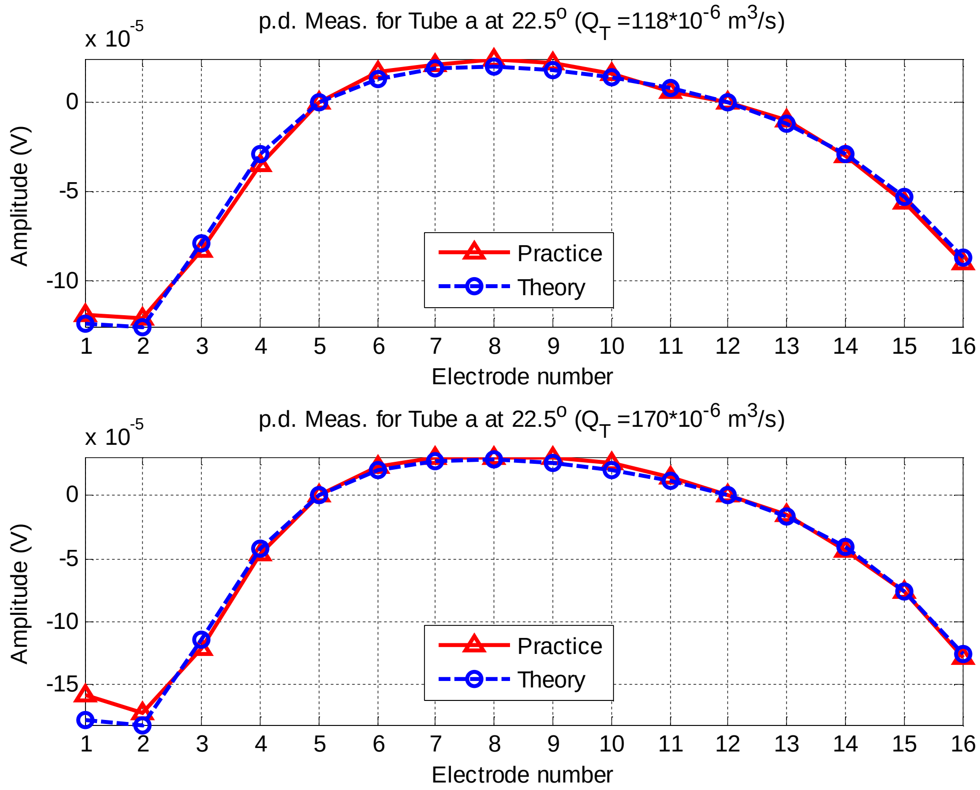

Figure 7.9: Practical and theoretical flow induced potential difference measurements for tube 'a' located at 22.5° with respect to electrode e_1 for flow rates of 118×10^{-6} m^3/s and 170×10^{-6} m^3/s

The next test involved changing the position of tube ‘a’ by 45° with respect to electrode e_1 as shown in Figure 7.10(A). The electromagnet was rotated by 45° clockwise and the indexing of the electrode array j was changed to $j' = j + 2$ or $j' = (j + 2) - 16$, if $j + 2$ was greater than 16 as shown in Figure 7.10(B). The reference electrode was physical electrode e_3 (virtual electrode e_5) and the low and high water flow rate values were 120×10^{-6} m^3/s and 190×10^{-6} m^3/s, respectively. The flow induced potential difference measurement results are presented in Figure 7.11. Again, the boundary potential distribution changed due to the position change of tube ‘a’.

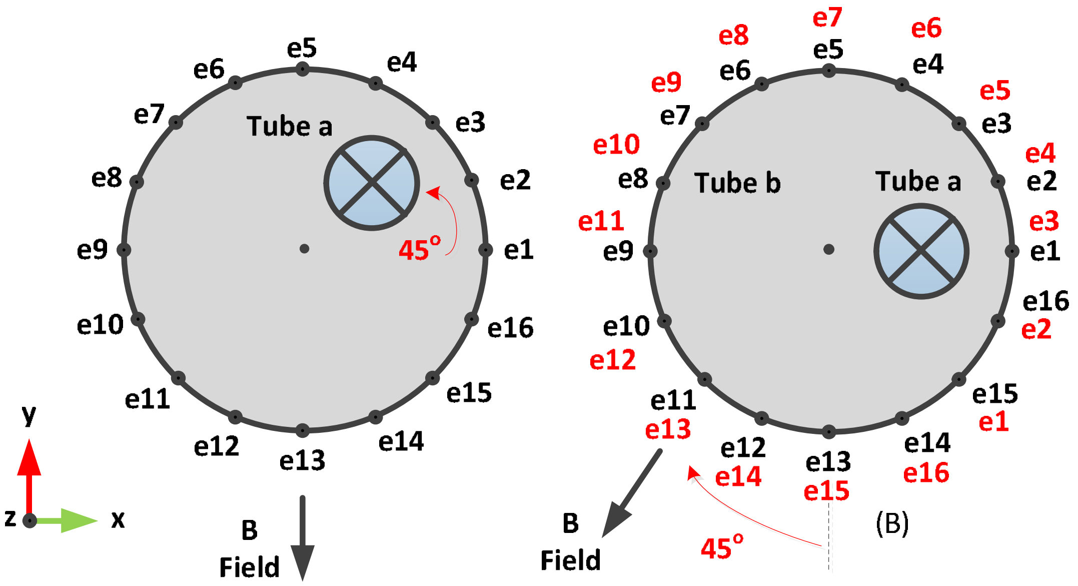

Figure 7.10: (A) Rotating tube 'a' by 45° anti-clockwise is equivalent to (B) rotating the electromagnet by 45° clockwise with respect to electrode e_1 and changing the electrode indexing number from j to j'. The electrode numbers shown in black are j and the electrode numbers in red are j'

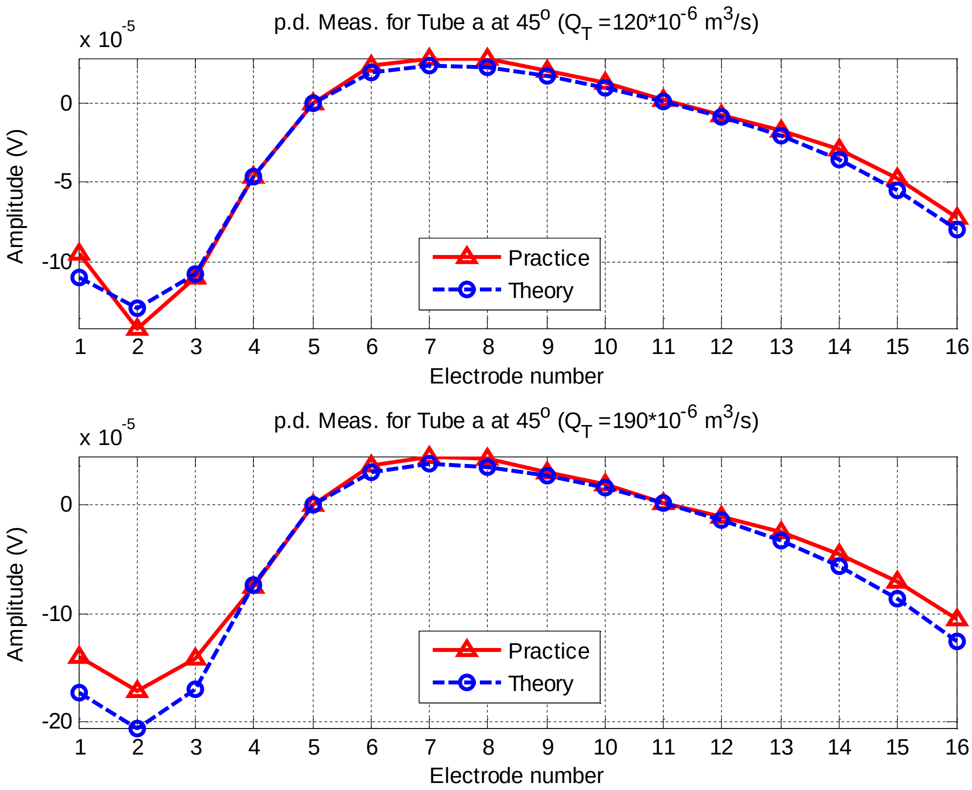

Figure 7.11: Practical and theoretical flow induced potential difference measurements for tube 'a' located at 45° with respect to electrode e_1 for flow rates of 120×10^{-6} m^3/s and 190×10^{-6} m^3/s

7.3.2 Test 2: Water Flow through Tube 'b'

In the following tests, tube 'a' was blocked and water flow was only imposed in tube 'b'. Tube 'b' was positioned at 180°, 202.5° and 225° with respect to electrode e_1. For each position, two flow rates were used, similar to the tests described in Section 4.7. In the first test, tube 'b' was at 180° with respect to electrode e_1 as illustrated in Figure 7.12. The magnetic field and the indexing of the electrode were not changed. The water low and high flow rates were, on average, 110×10^{-6} m^3/s and 210×10^{-6} m^3/s. The practical and theoretical results (using Eq. 3-32 and Eq. 3-33 in Section 3.4) for the flow induced potential difference measurements are shown in Figure 7.13.

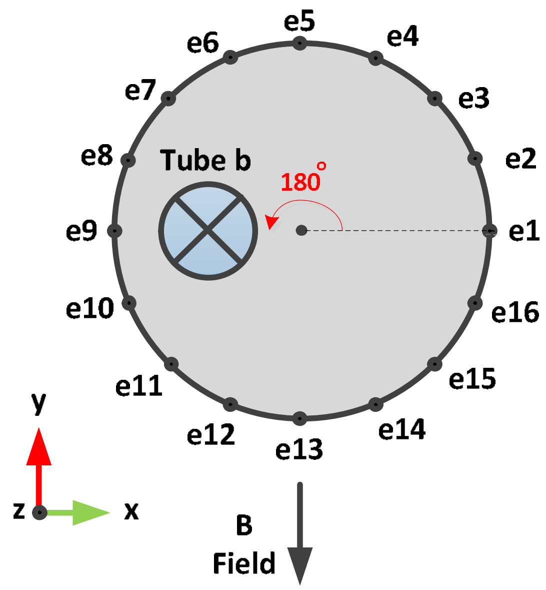

Figure 7.12: Tube 'b' at 180° with respect to electrode e_1

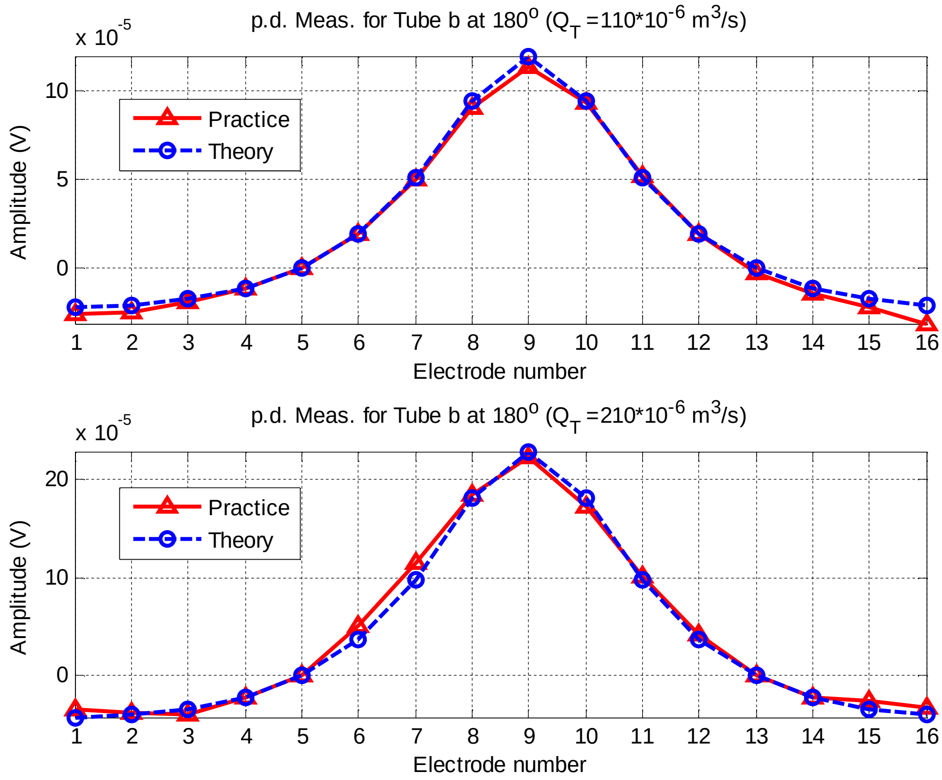

Figure 7.13: Practical and theoretical flow induced potential difference measurements for tube 'b' located at 180° with respect to electrode e_1 for flow rates of 110×10^{-6} m^3/s and 210×10^{-6} m^3/s

There is good agreement between the practical and theoretical flow induced potential difference measurements. However, the practical results were affected by noise which caused a slight difference between the practical and theoretical results. Similar to the tests performed for tube ‘a’, the flow rate value only changed the amplitude of the induced potential difference measurements. The position of tube ‘b’ had an effect on the boundary potential distribution and it was a different profile when compared to the tests for tube ‘a’ in Section 7.3.1.

Tube ‘b’ was then rotated virtually by 22.5° to be at 202.5° with respect to electrode e_1. Firstly, the electromagnet was rotated by 22.5° clockwise and the indexing of the electrode array was changed to $j' = j + 1$ or $j' = (j + 1) - 16$, if $j + 1$ is greater than

16 as illustrated in Figure 7.14. The water flow rates used were, on average, 118×10^{-6} m^3/s and 190×10^{-6} m^3/s.

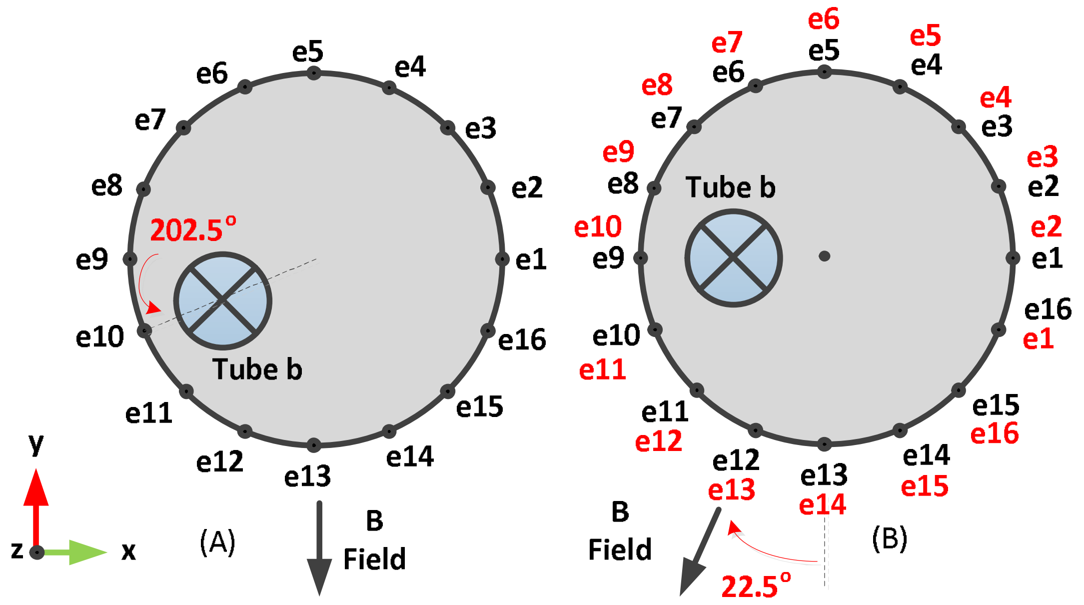

Figure 7.14: (A) Rotating tube 'b' by 22.5° anti-clockwise to position it at 202.5° with respect to electrode e_1 is equivalent to (B) rotating the electromagnet by 22.5° clockwise and changing the electrode indexing number from j to j'. The electrodes numbers shown in black are j and the electrode numbers in red are j'

The corresponding practical flow induced potential difference measurements in comparison with the measurements obtained from the theoretical model are shown in Figure 7.15. The new position of tube ‘b’ had an effect on the boundary potential distribution. It can be observed that for every new location, the profile of the induced potential difference measurements has a different distribution.

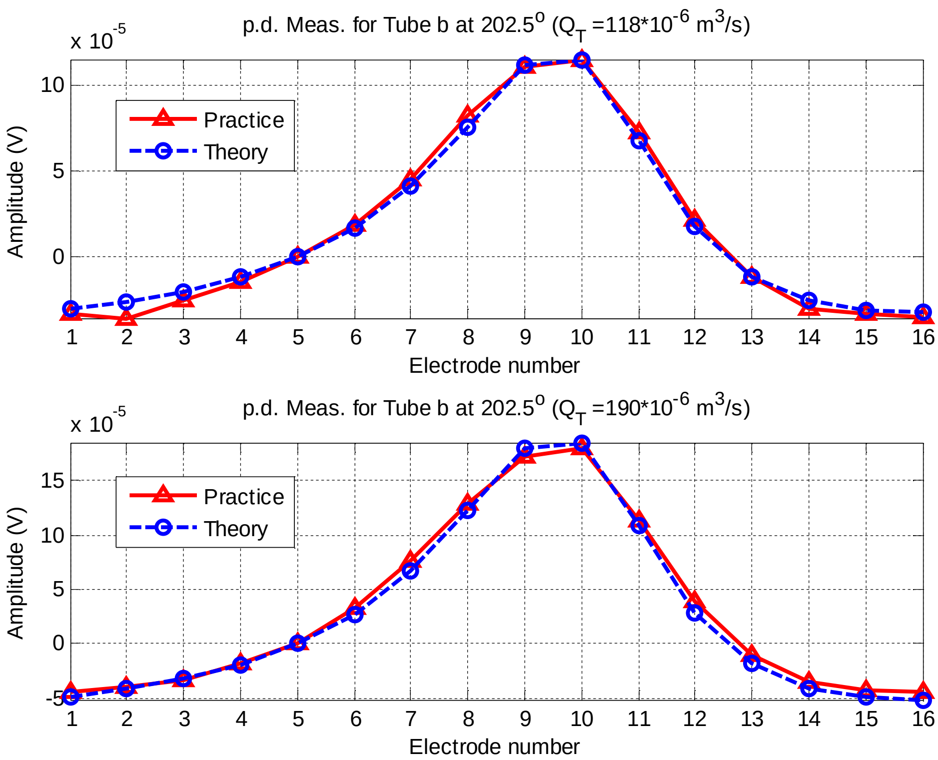

Figure 7.15: Practical and theoretical flow induced potential difference measurements for tube 'b' at 202.5^{o} with respect to electrode e_1 for flow rates of 118×10^{-6} m^3/s and 190×10^{-6} m^3/s

Lastly, the electromagnet was rotated by another 22.5° clockwise to give the virtual position of tube ‘b’ to be at 225° with respect to electrode e_1 as illustrated in Figure 7.16(A). The electromagnet was rotated by 45° clockwise, thus the indexing of the electrode array was changed to $j' = j + 2$ or $j' = (j + 2) - 16$, if $j + 2$ was greater than 16 as shown in Figure 7.16(B). The flow rates used were 110×10^{-6} m^3/s and 190×10^{-6} m^3/s. The corresponding practical and theoretical flow induced potential difference measurements are presented in Figure 7.17. There was good agreement between the practical and the theoretical results. The new position of tube 'b' changed the boundary potential distribution as expected. The amplitude of the induced potential difference measurements obtained from the low flow rate was smaller than the amplitude of the induced potential measurements obtained from the high flow rate test as predicted.

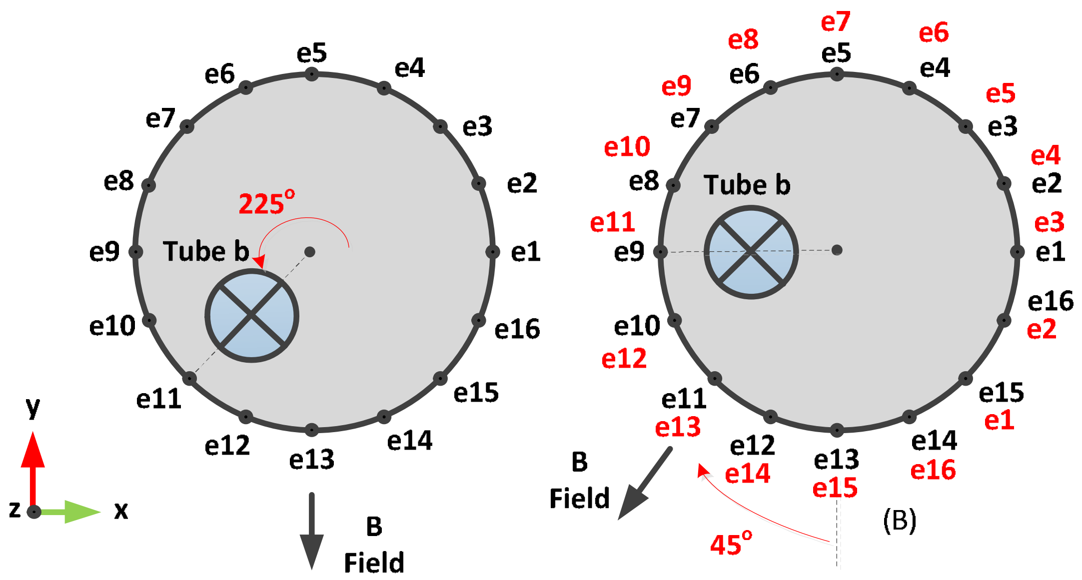

Figure 7.16: (A) Rotating tube 'b' by 45° clockwise to position it at 225° with respect to electrode e_1 is equivalent to (B) rotating the electromagnet by 45° anti-clockwise and changing the electrode indexing number from j to j'. The electrode numbers shown in black are j and the electrode numbers in red are j'

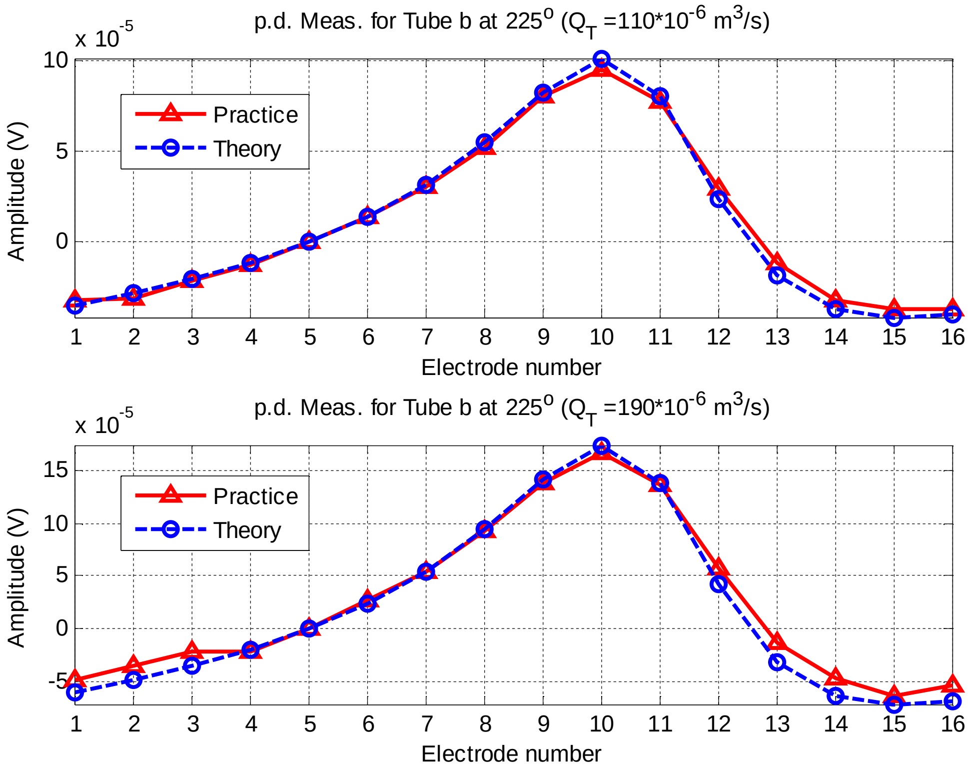

Figure 7.17: Practical and theoretical flow induced potential difference measurements for tube 'b' at 225° with respect to electrode e_1 for flow rates of 110×10^{-6} m^3/s and 190×10^{-6} m^3/s

7.3.3 Test 3: Water Flow through Tubes ‘a’ and ‘b’

In the final test setup, both tubes ‘a’ and ‘b’ were used. Firstly, tubes ‘a’ and ‘b’ were positioned at 0° and 180° with respect to electrode e_1 as shown in Figure 7.18. The low and high water flow rate values for the total flow in both tubes were 118×10^{-6} m^3/s and 200×10^{-6} m^3/s. The corresponding flow induced potential difference measurements obtained from the practical experiment and the theoretical model are presented in Figure 7.19. In Figure 7.19, the induced potential distribution is the result of the flow in the both tubes. The value of the total flow rate has no effect on the shape of the potential distribution as was observed in the previous tests (Sections 7.3.1 and 7.3.2). However, higher potential amplitudes were associated with greater flow rate.

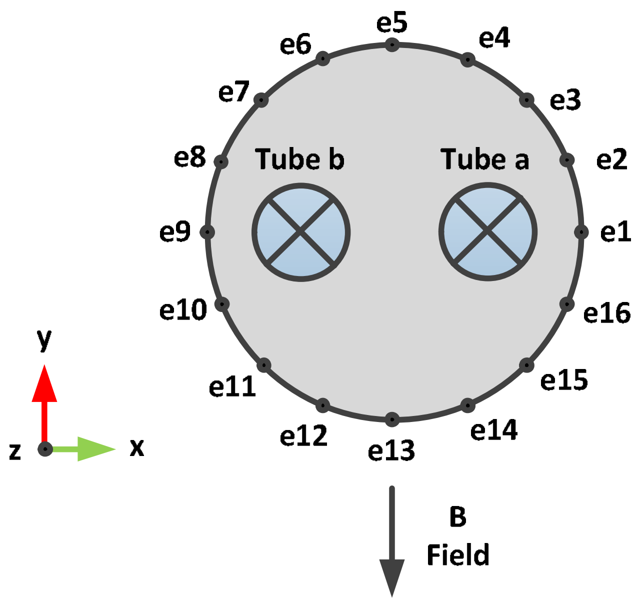

Figure 7.18: Tubes 'a' and 'b' at 0° and 180° with respect to electrode e_1

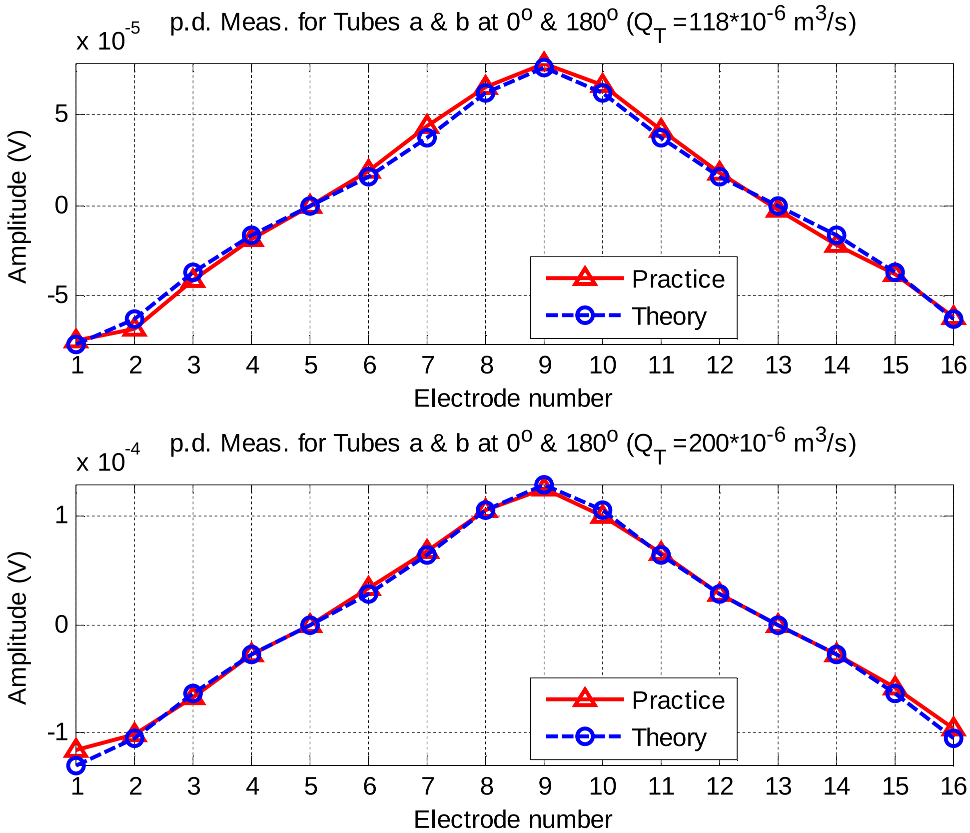

Figure 7.19: Practical and theoretical flow induced potential difference measurements for tubes 'a' and 'b' located at 0° and 180° with respect to electrode e_1 for flow rates of 118×10^{-6} m^3/s and 200×10^{-6} m^3/s

Tubes ‘a’ and ‘b’ were then positioned virtually at 22.5° and 202.5° with respect to electrode e_1 as illustrated in Figure 7.20(A). The position of the electromagnet and the indexing number of the electrode array were changed accordingly as illustrated in Figure 7.20(B). The recorded total water flow rate values were 112×10^{-6} m^3/s and 201×10^{-6} m^3/s for the low and high flow rates. The flow induced potential difference measurements for both flow rates obtained from the practical experiment and the theoretical model are shown in Figure 7.21.

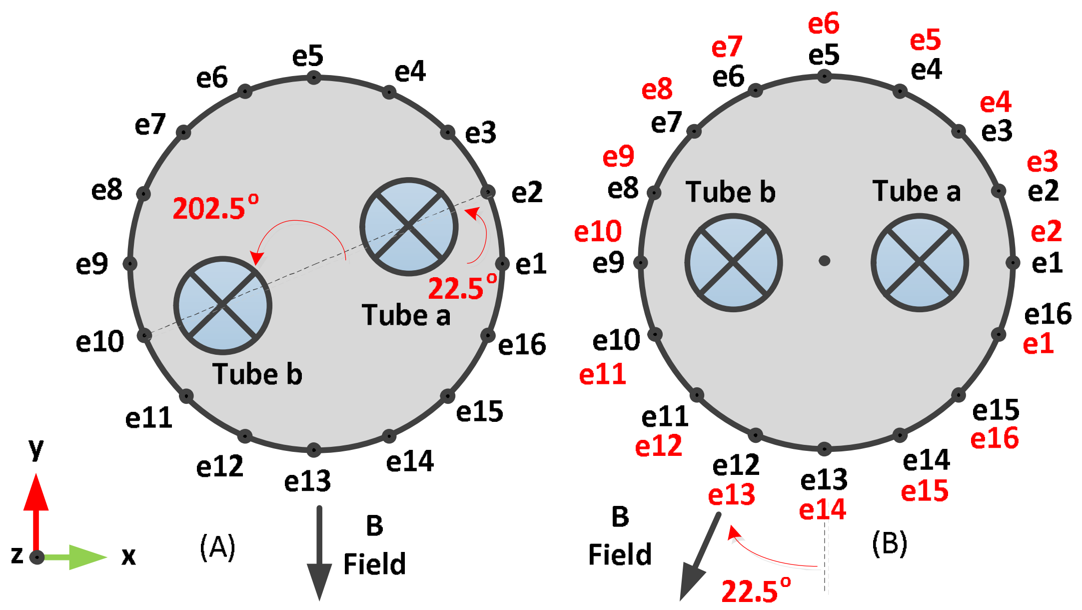

Figure 7.20: (A) Rotating tubes ‘a’ and ‘b’ by 22.5° clockwise is equivalent to (B) rotating the electromagnet by 22.5° anti-clockwise and changing the electrode indexing number from j to j'. The electrode numbers shown in black are j and the electrode numbers in red are j'. Tubes 'a' and 'b' are virtually at 22.5° and 202.5° with respect to electrode e_1.

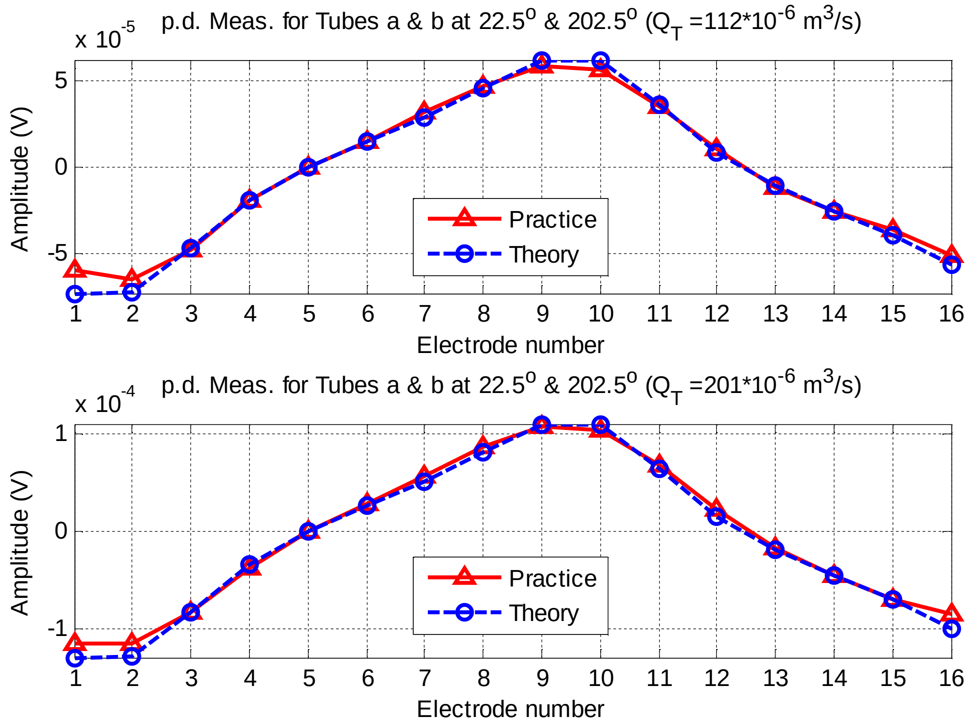

Figure 7.21: Practical and theoretical flow induced potential difference measurements for tubes 'a' and 'b' located at 22.5° and 202.5° with respect to electrode e_1 for flow rates of 112×10^{-6} m^3/s and 201×10^{-6} m^3/s

Finally, tubes ‘a’ and ‘b’ were positioned at 45° and 225° with respect to electrode e_1 as shown in Figure 7.22(A). The total flow rates recorded were 118×10^{-6} m^3/s and 201×10^{-6} m^3/s and the corresponding flow induced potential difference measurements for both flow rates are shown in Figure 7.23. It can be observed from the results obtained for tubes ‘a’ and ‘b’ at all three different positions that if only the flow rate values change then, the shape of the flow induced potential distribution stays the same. The only difference is that the amplitude of the flow induced potential differences for high flow rates is greater than the amplitude of the flow induced potential differences obtained for the low flow rates. However, changing the position of the tubes alters the shape of the flow induced potential distribution.

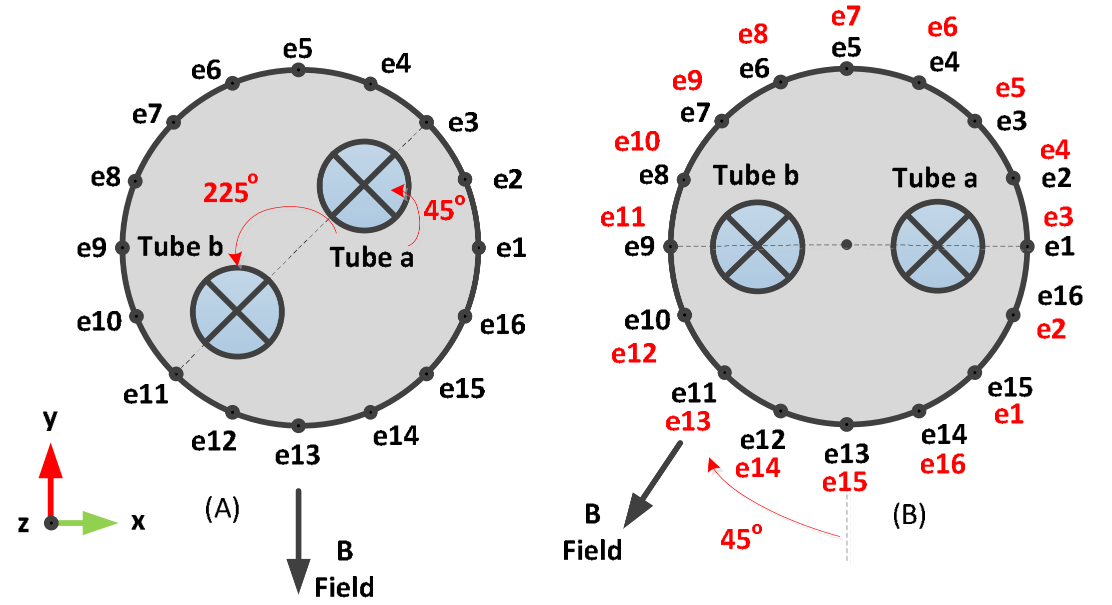

Figure 7.22: (A) Rotating tubes ‘a’ and ‘b’ by 45° clockwise is equivalent to (B) rotating the electromagnet by 45° anti-clockwise and changing the electrode indexing number from *j* to *j′*. The electrode numbers shown in black are *j* and the electrodes number in red are *j′*. Tubes 'a' and 'b' are virtually at 45° and 225° with respect to electrode e_1.

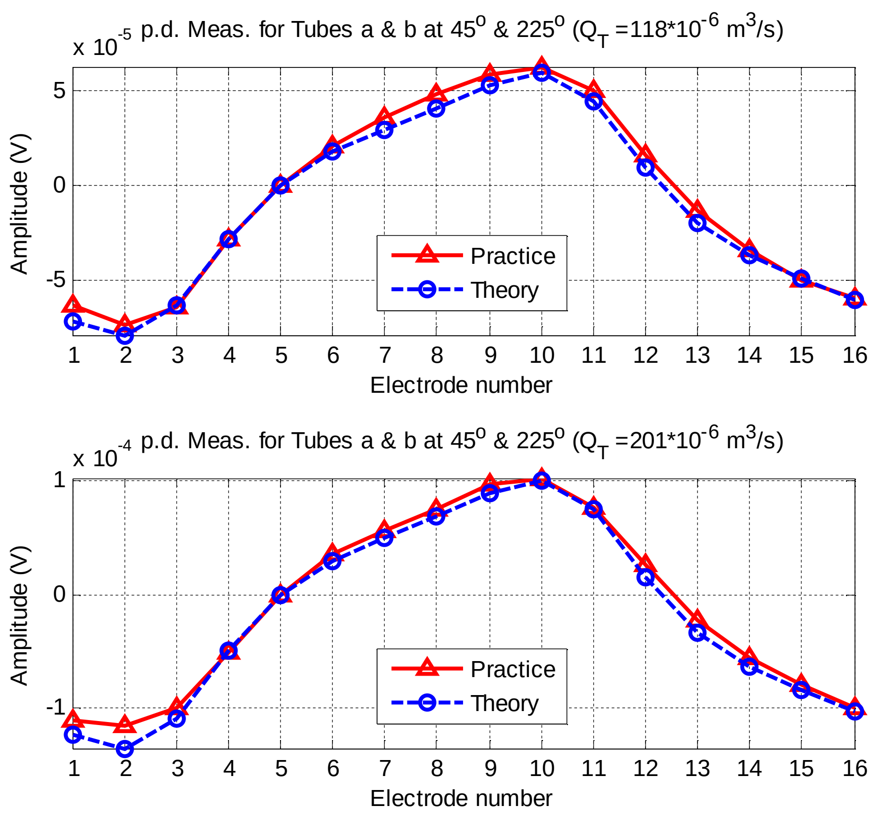

Figure 7.23: Practical and theoretical flow induced potential measurements for tubes 'a' and 'b' located at 45° and 225° with respect to electrode e_1 for flow rates of 118×10^{-6} m^3/s and 201×10^{-6} m^3/s

7.4 Analysis of the Flow Induced Potential Distributions

The DFT was applied to the flow induced potential distributions obtained from each test described in Section 7.3. As stated previously in Sections 4.8 and 7.1, only the DFT component at the fundamental frequency, i.e. $X(1)$, is of interest because the modulus of $X(1)$, i.e. $|X(1)|$, is predicted to be proportional to the total flow rate Q_T and the peak magnetic flux density B_0 regardless of the size, position and number of flow tubes present within the cross-sectional area bounded by the electrode array (Eq. 3-39 in Section 3.5).

For the tests performed in Section 7.3 (Tests 1, 2 and 3), the value of the total flow rate Q_T and the peak magnetic flux B_0 were known. The DFT was applied to the flow induced potential distributions obtained from the practical experiment for each test. The aim was to find the modulus $|X(1)|$ of the DFT harmonic component $X(1)$ from each practical test, and then divide it by $Q_T B_0$ to calculate the calibration factor of k_1 which should be a constant value. The theoretical k_1 value is 6.37 m^{-1}, calculated using Eq. 3-33. The two values of k_1 obtained from the theoretical and practical models should be equal, theoretically (for a given Q_T and B_0). Once k_1 is determined for the current geometry of the flow cross section of the SVS, any unknown total flow rate Q_T can be determined by measuring the flow induced potential distributions, obtaining its DFT and then applying Eq. 3-39.

Table 7-1 shows the theoretical and practical values for the modulus $|X(1)|$ of the DFT component $X(1)$ and the calibration factor k_1 for the low flow rate tests (the average value of the total flow rate for the low flow rate tests was 116×10^{-6} m^3/s). The peak magnetic flux density B_0 was 425 gauss (42.5 mT) for the tests for tubes ‘a’ and ‘b’.

The calibration factor k_1 value obtained from the practical experiments and theoretical k_1 value (Eq. 3-33) were plotted side by side in Figure 7.24.

It can be noted from the percentage difference graph in Figure 7.24 that the percentage difference between the practical and the theoretical k_1 values varied from one test to another. The percentage difference between the practical and the theoretical k_1 values for the low flow rate tests was 3.74% on average with a standard deviation of 2.10%. The highest percentage difference was 6.77% for test 8, which was for a water flow in both tubes 'a' and 'b' positioned at 22.5° and 202.5°, respectively. However, the mean value of k_1, obtained for the entire set of the practical tests, was 6.42 m^{-1}, whereas, the theoretical k_1 value, obtained from Eq. 3-33, was 6.37 m^{-1}. Hence, the percentage difference between both values was only 0.8%. The cause of the differences in the practical results was due to the in-phase electrical noise affecting the measurements of the flow induced potential differences which will be explained in detail in the next section.

Table 7-2 shows the practical and theoretical values for the modulus $|X(1)|$ of the DFT component $X(1)$ and the calibration factor k_1 for the high flow rate tests (the average total flow rate for the high flow rate tests was 194×10^{-6} m^3/s) and again, the peak magnetic flux density B_0 was 425 gauss. The percentage difference between the practical and theoretical k_1 values for the high flow rate tests was 4.71% on average with a standard deviation of 4.46%. The highest percentage difference between the theoretical and practical k_1 values was 12.43% (refer to Figure 7.25). This percentage difference was obtained from test 3 (refer to Table 7-2), which was for tube 'a' only positioned at 45° with respect to electrode e_1. Nevertheless, when the mean value of k_1, obtained from the practical tests, i.e. 6.08 m^{-1}, is compared with the theoretical k_1 value, i.e. 6.37 m^{-1}, the percentage difference is only 4.6%.

By inspecting the values for $|X(1)|$ in Table 7-1 and Table 7-2, it can be noted that the values of $|X(1)|$ for the high flow rate tests in Table 7-2 are greater than the values in Table 7-1 for the low flow rate which was predicted, since the value $|X(1)|$ is directly proportional to the total flow rate Q_T.

#Test	Position of tubes a and b	Practical $\lvert X(1)\rvert$ (μV)	Theoretical (Eq. 3-39) $\lvert X(1)\rvert$ (μV)	Q_T (m^3/s) ×10^{-6}	Practical k_1	Theoretical k_1
1	'a' at 0°	31.24	32.49	120	6.13	6.37
2	'a' at 22.5°	32.80	31.95	118	6.54	6.37
3	'a' at 45°	32.58	32.49	120	6.39	6.37
4	'b' at 180°	30.46	29.78	110	6.52	6.37
5	'b' at 202.5°	34.19	31.95	118	6.82	6.37
6	'b' at 225°	28.88	29.78	110	6.18	6.37
7	'a' and b' at 0° and 180°	33.76	31.95	118	6.73	6.37
8	'a' and b' at 22.5° and 202.5°	28.34	30.32	112	5.95	6.37
9	'a' and b' at 45° and 225°	32.72	31.95	118	6.53	6.37
Avg		31.66	31.40	116	6.42	6.37

Table 7-1: Values of $|X(1)|$ and k_1 obtained from practical and theoretical models for the low flow rate tests (average Q_T= 116×10^{-6} m^3/s)

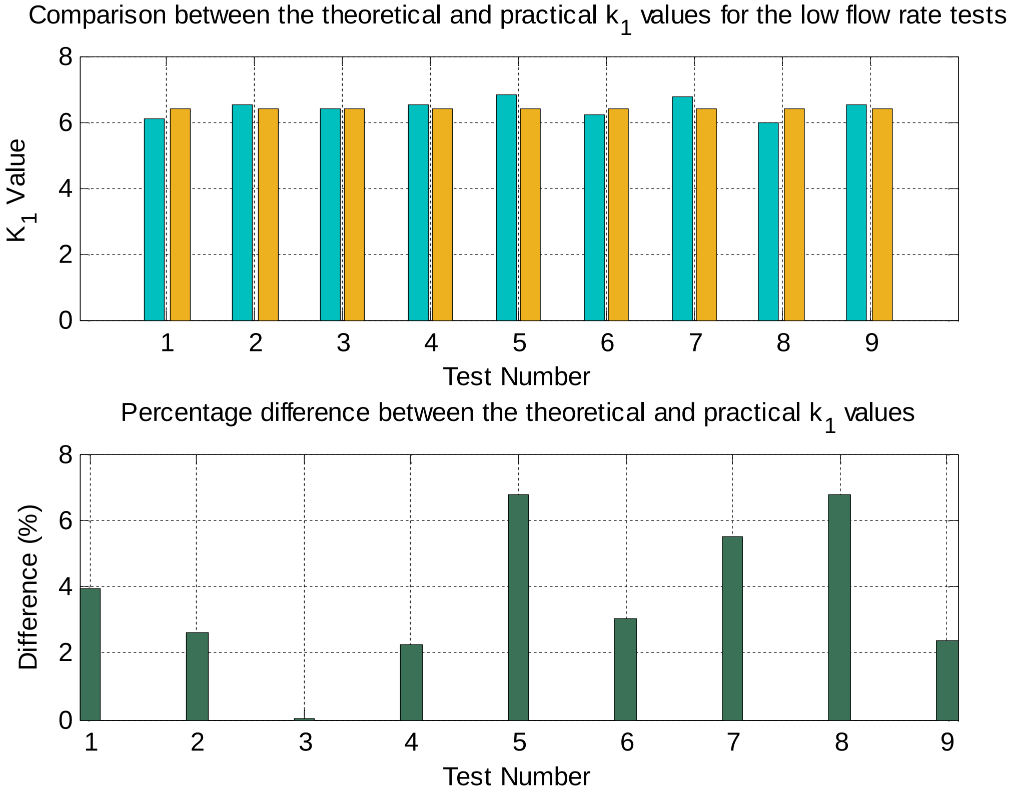

Figure 7.24: Comparison between values of k_1 obtained from the practical and theoretical models for the low flow rate tests (average Q_T= 116×10^{-6} m^3/s)

#Test	Position of tubes a and b	Practical $\|X(1)\|$ (μV)	Theoretical (Eq. 3-39) $\|X(1)\|$ (μV)	Q_T (m^3/s) ×10^{-6}	Practical k_1	Theoretical k_1
1	'a' at 0°	45.71	51.44	190	5.66	6.37
2	'a' at 22.5°	46.07	46.02	170	6.38	6.37
3	'a' at 45°	45.42	51.44	190	5.62	6.37
4	'b' at 180°	56.56	56.85	210	6.34	6.37
5	'b' at 202.5°	50.73	51.44	190	6.28	6.37
6	'b' at 225°	47.80	51.44	190	5.92	6.37
7	'a' and b' at 0° and 180°	52.46	54.15	200	6.17	6.37
8	'a' and b' at 22.5° and 202.5°	52.26	54.42	201	6.12	6.37
9	'a' and b' at 45° and 225°	53.54	54.42	201	6.27	6.37
Avg		50.06	52.40	194	6.08	6.37

Table 7-2: Values of $|X(1)|$ and k_1 obtained from the practical and theoretical models for the high flow rate tests (average Q_T= 194×10^{-6} m^3/s)

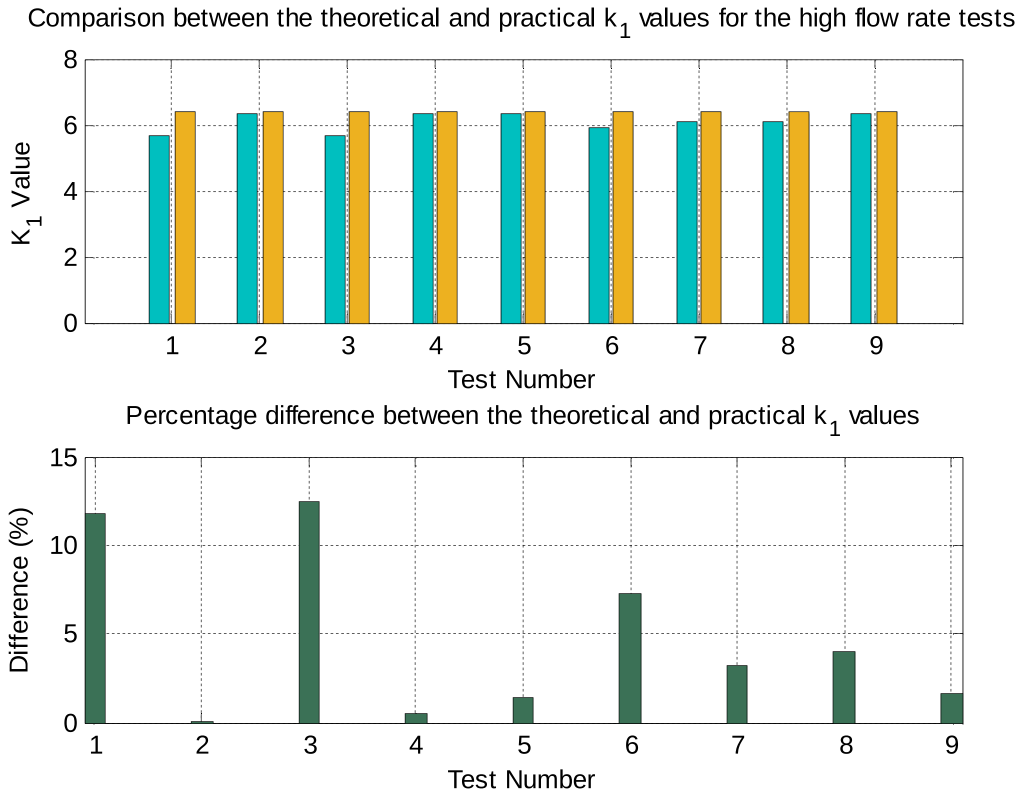

Figure 7.25: Comparison between values of k_1 obtained from the practical and theoretical models for the high flow rate tests (average Q_T= 194×10-6 m3/s)

7.5 Discussion

It can be concluded from tests (i), (ii) and (iii), given in Sections 7.3.1, 7.3.2 and 7.3.3, that the shape of the boundary induced potential distribution changes due to a change in the position and number of the flow tubes within the cross-sectional area bounded by the electrode array. However, the shape of the potential distribution does not change for a change in the flow rate value. For single or multiple tubes in a fixed position, the flow rate value only changes the amplitude of the flow induced potential difference measurements, the higher the flow rate value, the greater the amplitude of the flow induced potential differences. This is due to the linearity of the system, i.e. the amplitude of the flow induced potential differences is directly proportional to the flow rate. Moreover, the flow induced potential differences obtained from the theoretical model (Eq. 3-32 and Eq. 3-33) and the practical experiments, presented in Section 7.3, showed very good agreement. It can be seen that, when single or multiple tubes were in the same position, the induced potential differences from both the theoretical model and the practical experiment were similar. However, there was a difference in amplitude between the flow induced potential differences obtained from the practical experiment in comparison with the results obtained from the theoretical model. The main reason for this difference was voltage noise affecting the practical experiment which will be explained later in this section.

When comparing the flow induced potential difference measurements obtained from the COMSOL FE model (Section 4.7) with the practical results (Section 7.3), it can be noted that, for a tube or tubes in the same position, the shape of the distribution of the flow induced potential difference measurements is very similar and the only difference is the amplitude level of the potential difference because the flow rate and magnetic flux density values used in the COMSOL modelling and the practical experiment were different.

For example, the shape of the flow induced potential difference boundary distribution in Figure 4.17, obtained from the COMSOL FE model for tube 'a' positioned at 22.5^{o} with respect to electrode e_1, is similar to the shape of the distribution for the practical test shown in Figure 7.9 which gives the results for tube 'a' at the same position. The only difference was the amplitude of the flow potential differences between Figure 4.17 and Figure 7.9, and this was because the flow rate and magnetic flux density values were different. In the COMSOL FE model, the low and high flow rate values were 1.96×10^{-3} m^3/s and 3.93×10^{-3} m^3/s respectively, and the peak magnetic flux density B_0 = 1 mT. However, in the practical test, the low and high flow rates were 118×10^{-6} m^3/s and 170×10^{-6} m^3/s respectively, and the peak magnetic flux density B_0

was 42.5 mT. This also applies to the other results obtained from the COMSOL FE model (Section 4.7) and the practical experiments in this chapter. This confirms the agreement between the theoretical model, the COMSOL simulations and practical experiments for the same geometry and tube locations within the flow cross-section.

The sensitivity of the shape of the boundary potential distribution to the number and location of the flow channels shows the possibility for further improving this EM flow metering technique to determine the location of the flow tubes as well by using tomographic and iterative methods. The tomographic method could be applied using the velocity reconstruction techniques explained in the reference [121] and described in Section 2.5.6. This velocity reconstruction technique could be extended, as will be explained in Section 8.3.1, and used to give an estimate of the peak arterial blood flow rate Q_g in, and the radial and angular coordinates r_g and θ_g of, the g^{th} artery for each of the G arteries crossing the plane of the 16-electrode array using the 16 flow induced potential difference values obtained from the electrodes.

In the practical experiment, the potential difference measured between each electrode and the reference electrode consisted of various components and the main ones of which were: (1) DC offset due to polarisation, (2) flow induced potential difference, (3) transformer induced voltage and (4) mains and RF interference. The DC offset and mains and RF interference were reduced substantially when passed through the AC signal conditioning system. The signal conditioning system is a band-pass filter with cut-off frequencies of 1.94 Hz and 519 Hz. The high-pass filtering, provided by the AC-coupling of the IA, removed the DC offset and the RFI low-pass filter attenuated any RF signal above 23.4 kHz. The system also had high CMRR which was around 97 dB

(83 dB without the right-leg drive circuit) and that played an important role in eliminating the common-mode signals.

The electrode cables were also twisted and screened which prevented any magnetic flux passing through the cable loops resulting in induced voltage error. Additionally, the digital PSD required the DFT to be applied to the total measured voltage signals which are detected up by the electrodes, as explained in Section 6.4. Then, the 30 Hz frequency component was extracted which consisted of the flow induced and transformer potential difference components. This was effectively an additional method of filtering as all unwanted frequencies, including mains and RF signals, were eliminated. The digital PSD was then applied on the 30 Hz frequency component to separate its in-phase component, which is the flow induced potential difference (in-phase component with the coil current), from the quadrature component, which is the transformer potential difference.

However, the flow induced potential difference was still affected by an in-phase noise. This in-phase noise was sometimes of the amplitude of several hundreds of microvolts which is greater than the highest measured value of flow induced potential differences during all tests, i.e. 185 μV. An investigation was carried out to identify the source of this in-phase noise. It was found that the leads carrying current to the electromagnet coil were inductively coupling to the measurement system including the electronic circuit which measures the coil current to be used for the digital PSD. The coil current and the signal conditioning circuits were electrostatically shielded only. The induced voltage from this magnetic coupling was at the operating frequency of 30 Hz, but was not necessarily in quadrature with the coil current (voltage is induced in networks of different impedance) and therefore, the PSD technique (Section 6.3) could not distinguish it as a quadrature voltage, resulting in noise that was in-phase with the flow induced potential differences. This problem is highlighted in the EM flow metering literature and also reviewed in Section 2.5.9 [127, 144, 145]. Moreover, if this magnetically-coupled 30 Hz noise affects the coil current phase (noise induced in the coil current measurement circuit), this would increase the in-phase noise as explained in Section 6.6. This is due to the sensitivity of the PSD method to the phase error in the angle $\theta_{j,f}$ between the total measured voltage $U_{j,f}$ during flow and the reference coil current I_0.

This problem was overcome in the practical experiment by obtaining the total in-phase induced potential differences during flow and no-flow conditions as explained in Section 6.7. Then, the in-phase induced potential difference measurements obtained from the no-flow condition were subtracted from the potential difference measurements obtained during flow and the result was the in-phase flow induced potential difference measurements without the in-phase noise. The results from this problem were considerably worse for the low flow induced potential differences which were of the order of a few microvolts. This problem would ideally have been solved by magnetically shielding the induced voltage and coil current measurement systems, and also ensuring that the power supply for the electromagnet and its cables were at a reasonable distance from the measurement system. Magnetically shielding the electrodes' cables would also improve the magnetic shielding of the overall system. These optimisations were not implemented due to time constraints. The flow induced potential difference measurements and the calibration factor k_1 obtained from the practical experiments were nevertheless satisfactory overall.

By inspecting Table 7-1 and Table 7-2 in Section 7.4, it can be concluded that the value of the practical calibration factor k_1 for all the test scenarios was nearly constant – very close to the theoretical counterpart values – regardless of the number of flow tubes, their position and the flow rate values used. According to Eq. 3-33, the calibration factor value k_1 depends on the radius R of the cross-sectional area bounded by the electrode array. For the geometry of the flow cross section used in the theoretical modelling, COMSOL simulation and the practical experiment, the radius was 25 mm. Using Eq. 3-33, this gives a theoretical k_1 value of 6.37 m^{-1}. The average value of k_1 obtained from the practical experiment (averaging the mean values from the low flow and high flow tests in Table 7-1 and Table 7-2) was 6.25 m^{-1}; and from the COMSOL FE model, it was 6.14 m^{-1}. The percentage difference between the theoretical and FE k_1 values is 3.70%, whereas the difference between the theoretical and the practical k_1 values is 1.90%. Both percentages are small and demonstrate that there is a good agreement between the theoretical model, COMSOL FE model and the practical experiment.

The practical calibration k_1 value of 6.25 m^{-1} can be used to determine any flow rate once the flow induced potential differences are obtained and the modulus $|X(1)|$ of the fundamental DFT component $X(1)$ is found. For example, if the unknown flow rate through tube 'b' is 210×10^{-6} m^3/s (similar to Test 4 in Table 7-2), the modulus $|X(1)|$ of the DFT component $X(1)$ of the measured flow induced potential differences is 56.56 μV and the peak magnetic flux B_0 is 42.5 mT. By using the practical value for k_1, i.e. 6.25 m^{-1}, the predicted total flow rate is given by

$$Q_T = \frac{|X(1)|}{k_1 B_0} = \frac{56.56\ \mu\text{V}}{(6.25\ \text{m}^{-1})(42.5\ \text{mT})} = 212.93 \times 10^{-6}\ \text{m}^3/\text{s}$$

The difference between this flow rate value and the actual total flow rate is therefore 1.39%. If the actual flow rate is 190×10^{-6} m^3/s (test 5 in Table 9-2), the predicted total flow rate Q_T can be obtained using the practical k_1 equal to 6.25 m^{-1}

$$Q_T = \frac{|X(1)|}{k_1 B_P} = \frac{50.73\ \mu\text{V}}{(6.25\ \text{m}^{-1})(42.5\ \text{mT})} = 190.98 \times 10^{-6}\ \text{m}^3/\text{s}$$

The error in this case is only 0.51%. Both percentage differences 1.39% and 0.51% are small and acceptable for practical blood flow monitoring applications. If the practical calibration factor was not determined and only the theoretical k_1 value was available from the theoretical model, i.e. $k_1 = 6.37$ m^{-1}, then using this value for the above two conditions would predict flow rate values of 209×10^{-6} m^3/s and 187.40×10^{-6} m^3/s and these values correspond to errors of 0.50% and 1.38%, respectively, when compared to the actual flow rates. It can be concluded that using the theoretical calibration factor instead of the practical value also gives the flow rate values with high accuracy. This means that this proposed EM blood flow metering method can be calibrated offline if nothing more than the radius of the electrode array is known. This is a very important feature because human limbs vary in size and yet, by knowing only the radius of the electrode array that is fitted, the calibration factor k_1 can be calculated.

For the first prototype of this method to be tested in clinical trials, several sizes of electrode array can be made for different sizes of human limbs. The calibration value k_1 can be calculated for each electrode array. Then, one suitable electrode array will be fitted around a limb across which a uniform magnetic field is applied. Afterwards, the flow induced potential differences due to the arterial flow only are obtained (refer to Section 3.6). Lastly, the modulus $|X(1)|$ of the DFT component is determined and by using the calculated calibration factor k_1, the total arterial blood flow rate Q_T in the human limb can be calculated. Alternatively, instead of having different electrode arrays, the electrode array size can be adjusted and its diameter value can then be entered in the software for the flow rate calculations.

Based on the results obtained from the theoretical, COMSOL FE and practical models, it can be stated that the EM induction technique developed has been verified. This technique can measure the total volumetric flow rate for multiple tubes within the cross-sectional area bounded by the electrode array in the presence of a uniform magnetic field.

7.6 Summary

The practical experiment of the SVS flow test rig was executed to obtain flow induced potential difference measurements resulting from water flow in the SVS channels at various positions in the presence of the generated magnetic field. The aim was to compare these flow potential differences with the counterpart measurements obtained from the mathematical model given in Eq. 3-32 and Eq. 3-33. Furthermore, the modulus $|X(1)|$ of the DFT component $X(1)$, obtained from the flow induced potential differences, was found from the practical experiment and also the calibration factor k_1 value. These values were also compared with the counterparts obtained from the theoretical model (Eq. 3-39 and Eq. 3-33).

Three sets of tests were performed: water flow imposed in tube ‘a’ only, tube ‘b’ only and then both of the tubes. For each set of tests, the tube or tubes were rotated to three different positons: (i) tube ‘a’ was positioned at 0°, 22.5° and 45° with respect to electrode e_1 (Section 7.3.1), (ii) tube ‘b’ was positioned at 180°, 202.5° and 225° with respect to electrode e_1 (Section 7.3.2) and lastly, (iii) both tubes ‘a’ and ‘b’ were positioned at 0°-180°, 22.5°-202.5° and 45°-225° with respect to e_1 (Section 7.3.3). Two flow rate values were used for each positon of the tubes, which were, on average, 116×10^{-6} m^3/s and 194×10^{-6} m^3/s.

The voltage signals sensed by the 16 electrodes were passed to the signal conditioning system to amplify the signals so that they were suitable for AD conversion and also to remove any DC offset on the voltage signals, due to polarisation, and mains and RF interference. The voltage signals starting from electrode e_1 were then sampled by the DAQ device sequentially and during each signal measurement, the coil current was also sampled to be used as the reference signal in the MATLAB-based PSD software. Then, the PSD was applied for each voltage signal to determine the portion of the voltage signal that is in-phase with the coil current, which is the flow induced potential difference. The flow induced potential differences, obtained from the practical experiment, were affected by an in-phase voltage noise mainly caused by the magnetic coupling of the electromagnet cables of the coil current to the signal conditioning circuitry. To remove this in-phase noise, potential difference measurements were made during no-flow and flow conditions to determine the in-phase noise. This was a temporary solution; however, ideally, magnetic shielding should be in place to protect the measuring system from noise due to magnetic coupling.

It was found, from the flow induced potential difference results in Section 7.3, that the amplitude of the flow induced potential differences is directly proportional to the flow rate value. A higher flow rate value results in greater amplitude of the flow induced potential differences. The flow induced potential differences measured were observed to be from 10 μV to 90 μV for a flow rate of 116×10^{-6} m^3/s and from 10 μV to 185 μV for the flow rate value 194×10^{-6} m^3/s. It was noted that the shape of the boundary potential distribution is sensitive to the number and position of the of the flow channels within the cross-sectional area bounded by the electrodes.

The DFT was applied on all the flow potential differences obtained from the practical flow tests. The modulus $|X(1)|$ of the fundamental DFT component $X(1)$ and the calibration factor k_1 for all tests were tabulated in Table 7-1 for the low flow rate tests, 116×10^{-6} m^3/s on average, and Table 7-2, for the high flow rate tests, 194×10^{-6} m^3/s on average, as shown in Section 7.4. The counterpart theoretical values of the modulus $|X(1)|$ of the DFT component $X(1)$ and the calibration factor k_1, calculated using Eq. 3-39 and Eq. 3-33, were also included for comparison. It was noted from the results, that $|X(1)|$ values for the higher flow rate tests were greater and that was predicted, since the value $|X(1)|$ is directly proportional to the total flow rate. The practical calibration factor k_1 obtained was 6.25 m^{-1} on average and the theoretical value was 6.37 m^{-1} (using Eq. 3-33) and thus, the percentage difference was only 1.90%. Hence, the proposed EM method can be calibrated offline, and only the radius R of the electrode array is required to find the calibration factor k_1.

In conclusion, it was shown that the flow boundary potential distribution, for a number of flow channels within the cross-sectional area bounded by the electrodes, can be predicted using Eq. 3-32 and Eq. 3-33 – given that the radial and angular coordinates of, and flow rates in, the flow channels are known. The practical results in Section 7.3 confirmed that the theoretical model can predict the boundary potential distribution for any flow scenario. This is the first major outcome of the practical experiment.

Moreover, it was shown (Section 7.4) that when the DFT is applied to the flow potential differences, the modulus $|X(1)|$ of the fundamental DFT component $X(1)$, is directly proportional to the total volumetric flow rate Q_T. This confirmed the mathematical model given in Eq. 3-39 which shows that the total volumetric flow rate, within a cross sectional area bounded by the electrode array, can be estimated by only finding $|X(1)|$ and knowing the magnetic field density B_0 and the calibration factor k_1, irrespective of the number and location of the flow channels. This is the second and most important outcome of this research as it confirms the main research objective which is to find a method that can be used to estimate the total volumetric flow rate of a conductive fluid flowing in multiple flow channels. These flow channels are located within the cross-sectional area that is bounded by the electrode array. The method was found to give a flow rate measurement with high accuracy (see Section 7.4). The use of 16-electrode system makes it insensitive to velocity profiles, unlike previous attempts, and this was proven when water flow was imposed in a single channel (tube 'a' or 'b') only. The method also can be calibrated offline as the calibration factor k_1 is only required which can be calculated mathematically using Eq. 3-33. For the aforementioned outcomes, this method has a potential application in non-invasive blood flow metering. The Further Work (Section 8.3) includes the next phases required to take this research idea towards clinical applications.

Chapter 8
Conclusions & Recommendations for Further Work

Contents

8.1 Conclusions

Blood flow rate measurement has a variety of important applications in the areas of cardiology, diabetes and dermatology. It is an important measurement in the diagnosis of cardiovascular diseases such as peripheral vascular disease and deep vein thrombosis. Blood flow measurement can be performed using both invasive and non-invasive techniques. Invasive methods are the least favourable as they require surgical intervention. Advanced screening techniques such as MRI, arteriography and venography are not often used for routine or regular tests as they are expensive, bulky and require highly experienced operators. A common method for non-invasive blood flow diagnosis is duplex ultrasound. This method is widely accepted by health practitioners, and has proved its use in clinical applications. However, it has been shown in Section 2.4.6 that ultrasound suffers from several drawbacks including the appearance of artefacts and, in some cases, it is not possible to use. Primary health care providers are also not in favour of using the ABI test when staff availability is limited as it is a time-consuming process. It may also lead to false diagnosis of elderly and diabetic patients as discussed in Section 1.3.1.

The research work in this thesis has proposed an alternative novel non-invasive method based on EM induction for blood flow rate measurement. It comprises a ring of 16 electrodes into which a limb is inserted and across which a magnetic field is applied. It is shown in this thesis that this method can determine the total volumetric flow rate in a cross section regardless of the number of tubes (blood vessels) or their location within the cross-sectional area bounded by the electrodes. Generally the EM flow metering technique is attractive because it is linear, i.e. the amplitude of the flow induced potential differences is directly proportional to the flow rate, and insensitive to viscosity, density, temperature and pressure loss. Additionally, this proposed method, unlike conventional EM blood flow meters, is insensitive to spatial distribution of velocity and can be calibrated offline. It can potentially be implemented to create a non-invasive, portable and low cost blood flow monitor for use in clinical applications.

The research work undertaken in this thesis has included a mathematical model for this proposed method (Chapter 3) by extending the virtual current theory for multiple flow channels within a cross-sectional area bounded by multiple electrodes. Firstly, it was shown how, for a number of flow channels within the cross-sectional area bounded by the electrodes, the potential distribution can be calculated in terms of the radial r_g and angular θ_g coordinates of, and flow rates Q_g in, the flow channels and the peak magnetic flux density B_0. Then, it was shown that the modulus $|X(1)|$ of the DFT component $X(1)$ of the boundary flow induced potential distribution U_j is proportional to the total volumetric flow rate Q_T and the peak magnetic flux density B_0, irrespective of the number, size and location of the flow channels. It was also shown that the calibration factor k_1 relating $|X(1)|$ to Q_T depends only on the radius of the electrode array (surrounding the limb) which simplifies the calibration process significantly as it allows offline calibration.

An FE model of the SVS was developed using COMSOL Multiphysics (Chapter 4) software in order to validate the theoretical model (Eq. 3-32, Eq. 3-33 and Eq.3-39) of the proposed EM method. Minimal computational errors were encountered in the FE model due to the selected meshing size, chosen to save simulation time. The FE model consisted of a conductive cylindrical region with flow channels and a Helmholtz coil to generate a uniform magnetic field across the conductive cylindrical region. Flow induced potential difference measurements were obtained for a variety of test conditions, i.e. different numbers and locations of the flow channels and different flow rate values. The potential difference measurements obtained from the FE model and the theoretical model for the same test setup showed very good agreement with each other. It was concluded that the shape of the boundary potential distribution is sensitive to the number, size and location of the flow channels. However, it was demonstrated that the modulus $|X(1)|$ of the DFT component $X(1)$ of the boundary potential distribution is proportional to the total volumetric flow rate Q_T and the peak magnetic flux density B_0, regardless of the number, size and location of the flow channels.

Lastly, a physical model was designed and built to demonstrate the proposed EM method, and also to compare the measured potential differences with the potential differences obtained from the theoretical model described above. The physical model (known as the SVS) consisted of pipework with similar geometry to the FE model (i.e. two flow channels and a 16-electrode array). It also used an AC-powered electromagnet and signal conditioning and processing systems. This model simulated a human limb with two blood vessels. Water flow could be imposed in one or both flow channels. The magnetic field across the electrode array was generated by the AC-powered electromagnet at an operating frequency of 30 Hz. This frequency was selected to avoid the effects of mains interference and to improve accuracy in measuring the flow induced potential differences at 30 Hz. A PFC was utilised in the design of the power supply of the electromagnet to minimise the supply current requirement. The current required from the power supply was only 475 mA (rms value) to generate a peak current of 10 A in the coil of the electromagnet. With this coil current a spatially uniform AC magnetic field with a peak magnetic flux density of 42.5 mT was generated in the air gap of the electromagnet.

The 16-electrode system was interfaced to an AC signal conditioning system by an analogue multiplexer, which reduced the number of channels required for the signal conditioning system. Screened and twisted cables were used for connecting the electrodes to the multiplexer to minimise mains interference and RFI. The purpose of the AC signal conditioning system was to amplify the measured flow induced potential differences and to filter out unwanted noise components. All potentials sensed by the electrodes were measured with respect to electrode e_5 (the reference electrode). The signal conditioning system consisted of an RFI suppression filter, 2-stage gain amplifiers and a “right-leg” drive circuit. The overall gain of the system ($\approx$1000) was split over two amplification stages ($\times$10 and $\times$100) to prevent the DC offset present in the signals, due to electrode polarisation, from saturating the system. The “right-leg” drive circuit is a technique often used in medical devices such as ECG and EEG to minimise EM interference, especially mains harmonics, at the source. It is performed by sensing the common-mode noise at the input of the signal conditioning circuit, and then the phase of the noise was inverted and fed back to the source to reduce the noise. This improved the CMRR of the overall conditioning system. The output of the conditioning system was connected to a DAQ device for AD conversion and data storage. The control of the switching sequence of the multiplexer and the DAQ was performed on a PC via MATLAB software.

The last part of the practical system was a signal processing technique which applied digital PSD to the measured induced voltage signals from the electrodes to differentiate between the flow induced potential differences and the transformer emfs. The digital PSD method was implemented using a DFT approach rather than conventional PSD techniques. The measured voltage signal $U_{j,f}$ for each electrode and the coil current I_0 signal were sampled simultaneously. Then, the DFT was applied to extract the real and imaginary parts of the voltage signal $U_{j,f}$ and the coil current I_0 at the operating frequency. Next, the PSD method was applied using the coil current as a reference signal to determine the portion of the $U_{j,f}$ signal that is in phase with the coil current i.e. the flow induced potential difference. The PSD method was performed using a program written in MATLAB software.

The flow induced potential difference measurements obtained from the physical model for different test conditions were similar to the potential differences predicted using the theoretical model given in Eq. 3-32 and Eq. 3-33. As was found from the outcomes of the comparison between the theoretical and FE models, it was again found that the flow induced potential distribution for the practical model was sensitive to the number, size and location of the flow channels. However, the modulus of the $|X(1)|$ of the fundamental DFT component $X(1)$ of the boundary potential distribution was directly proportional to the total volumetric flow rate Q_T irrespective of number, size and location of the flow channels. Sources of error in the practical model were identified and explained. The main source of error was an in-phase induced voltage due to the magnetic coupling between the coil current-carrying cables and the measurement system. It was proposed that magnetic shielding could be used in the future to reduce the noise in the system and to improve the quality and phase integrity of the measured signals. The magnetic shield can of in the form of a foil that can be placed in the enclosure, surrounding the measurement circuit to direct magnetic flux away.

The research work in this thesis provides a solid foundation for the development of the first non-invasive multi-electrode EM blood flow meter for use in clinical applications. Future research and designs can be based on the theoretical, FE and practical work developed in this research. The theoretical work in this thesis has the flexibility to be further developed and improved and could also be used to predict or validate the operation of any prototype device. Further work is suggested below to take this research closer to clinical trials.

8.2 Contribution to Knowledge

This research has proposed a novel method based on EM induction for non-invasive blood flow measurement. In the proposed method, flow induced potentials are measured on the boundary of a region in which flow occurs in the presence of a magnetic field. These potentials are sensed by a ring of electrodes into which a limb is inserted and across which a magnetic field is applied. From these potentials, the total volumetric flow rate Q_T in the cross-sectional area bounded by the electrodes can be measured, irrespective of number, size and location of the blood vessels. The main areas of original contribution are:

- A mathematical model is developed based on the "virtual current" theory to find the flow induced potential distribution U_j, for single or multiple flow channels located within a cross-sectional area bounded by an electrode array, in terms of the radial and angular coordinates (r_g and θ_g) of, and the flow rates Q_g in, the flow channels and the peak magnetic flux density B_0 (Eq. 3-32 and Eq. 3-33). It was also shown that the appropriate calibration factor k_1 depends only on the radius of the electrode array (into which the limb is inserted) which simplifies the calibration process significantly.

- A mathematical relationship is provided (Eq. 3-39) and proven which shows that the modulus $|X(1)|$ of the DFT component $X(1)$ of the flow induced boundary potential distribution measured at the electrode array is directly proportional to the total volumetric flow rate Q_T in the flow channels and the peak magnetic flux density B_0, irrespective of the number, size and location of the flow channels within the cross-sectional area bounded by the electrode array. Provided the calibration factor k_1 is known, determination of $|X(1)|$ enables the total volumetric flow rate in the cross-sectional area bounded by the electrode array to be found.
- An FE model was developed in COMSOL software to validate and support the mathematical model. This model can predict the flow induced potential distribution at the boundary of a region across which a magnetic field is applied for a given flow distribution within the region. This model can also be used as a 'dry calibration' method for a device based on the proposed EM method. It can also be utilised for further research work including tomographic methods (See Section 8.3.1) and modelling of human skin and tissue surrounding the blood vessels.
- A practical physical system was designed and built to test and validate the proposed EM method. This system demonstrated the framework for building a device based on the EM method for clinical applications. It defines the major parts required for a fully working system, i.e. an electrode array, the AC-powered electromagnet, a

multiplexed AC signal conditioning system and a signal processing system. Each part was fully designed and tested. Issues such as large DC offsets due to polarisation, EM interference and transformer emf have been discussed, and methods have been suggested and implemented to overcome these issues. All these major contributory parts can also be further developed and optimised.

This research presented a novel EM induction method that can be applied to measure the total volumetric blood flow rate in a human limb, non-invasively. This method overcomes problems encountered in previous attempts for measuring blood flow such as sensitivity to velocity profile and the need for online calibration. It can be an alternative method in cases where the application of ultrasonic technology is incapable of making accurate measurements. A medical device built using this method can be portable and low in cost due to its simple design. Hence, it could be available in health centres and clinics to be used by GPs, nurses, physiotherapists and podiatrists in various applications including the diagnosis of PAD and DVT.

8.3 Recommendations for Further Work

There are number of areas which can be further developed and investigated in order to take this research a significant step closer to the first non-invasive EM blood flow meter for clinical trials. These areas can be divided into three categories, i.e. theoretical modelling, simulation and practical work.

8.3.1 Theoretical Modelling

- Tomographic methods

Currently, the EM method can only provide information on the total volumetric flow rate in the cross-sectional area bounded by the electrode array. Recent progress has been made in the area of inductive flow tomography (IFT) based on multi-electrode EM flow metering for use in industrial applications, i.e. single and multi-phase flow [121]. IFT enables the velocity profile in the cross-section of the pipe bounded by the electrodes to be reconstructed. In the IFT technique, the flow induced potential differences U_j obtained from the electrode array are associated with the local flow velocity distribution via variables referred to as 'weight values' which are found using finite element software such as COMSOL Multiphysics. Then, a matrix inversion method is applied using these weight values to reconstruct the velocity profile. The cross section bounded by the electrodes is considered as being divided into N sub-regions (or pixels) – for example, in Figure 8.1, the flow cross-section is divided into 30 pixels (30-pixel model) – and the matrix technique mentioned above is used to find the axial flow velocity in each sub-region [121, 212].

A similar approach could be used for blood flow monitoring applications. The values of the potential difference measurements could be used to determine the peak blood flow rate in each artery, and also the spatial location of each artery, by extending the IFT 'matrix inversion' velocity reconstruction method. Suppose that a sequence of P different 'magnetic field projections' is used, where each projection consists of a different magnetic flux density distribution in the region bounded by the electrode array. Suppose also that for the p^{th} projection and for 16 boundary electrodes, 15 independent potential difference measurements $U_{j,p}$ can be made. Due to the inherent linearity of the system [213], (and for moderate (≤ 5:1) change in the local conductivity) $U_{j,p}$ can be expressed as

$$U_{j,p} = \frac{2B_{0,p}}{\pi R}\sum_{i=1}^{N} w_{i,j,p}A_i v_i \qquad \text{Eq. 8-1}$$

where $B_{0,p}$ is the peak of magnetic flux density for the P^{th} projection, at a specific reference point in the magnetic field, R is the radius of the region bounded by the electrode array, A_i is the cross-sectional area of the i^{th} sub-region, v_i is the peak arterial blood flow velocity in the i^{th} sub-region, $w_{i,j,p}$ is the relevant weight value and $N = 15P$.

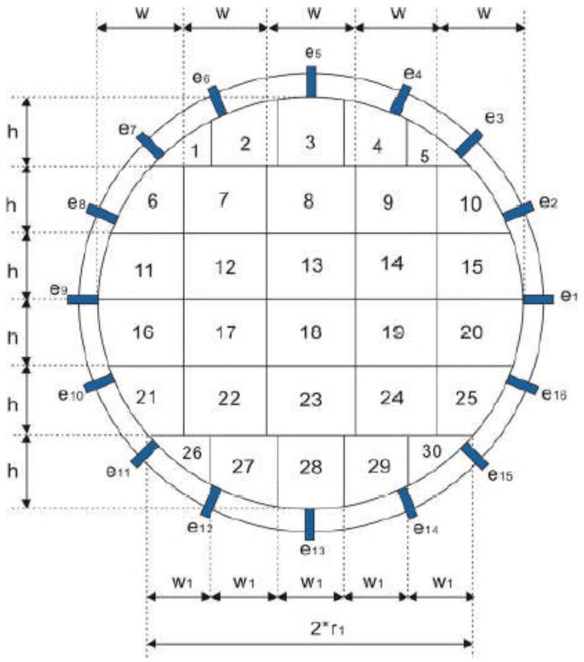

Figure 8.1: Flow cross-section divided into 30 regions (pixels)

It has previously been shown [121] that the weight values $w_{i,j,p}$ can be calculated using finite element software such as COMSOL Multiphysics. A solution to Eq. 8-1 for the velocities in the N sub-regions has been shown [121] to be given by the matrix equation

$$\boldsymbol{V} = \frac{\pi R}{2}[\boldsymbol{WA}]^{-1}[\boldsymbol{R_B U}] \qquad \text{Eq. 8-2}$$

where $\boldsymbol{V}$ is the matrix of velocities in the N sub-regions, $\boldsymbol{U}$ is the matrix of measured potential differences, $\boldsymbol{W}$ is the weight value matrix, $\boldsymbol{A}$ is the matrix of the sub-region areas and $\boldsymbol{R_B}$ is a matrix containing the values of $B_{0,p}$ for the different magnetic field projections. Note that v_i represents the 'area weighted' mean velocity in the i^{th} sub-region and so, provided all of the major arteries lie in different sub-regions, the peak blood volumetric flow rate Q_g for an artery lying in the i^{th} sub-region is given by $Q_g = A_i v_i$. The spatial position of each artery is given by the position of the sub-region in which that artery resides.

Other analytical methods have been developed which enable reconstruction of the velocity profile from the measured boundary potential distribution. One such method [212] assumes that the velocity profile is made up of polynomial velocity components, the properties of which are determined from the higher order components $X(2)$, $X(3)$, $X(4)$, …, etc, of the DFT of the flow induced boundary potential distribution measured at the electrode array. These polynomial velocity components can be combined to reveal the flow velocity distribution within the electrode array to a high level of spatial resolution.

8.3.2 Finite Element Analysis Modelling

- Validation of Tomographic methods

The current FE model described in this thesis can be used to implement and validate the tomographic methods proposed above. The FE model can also be used to calculate the weight values which are used to relate the contribution of local flow velocity in different parts of the cross-section of the region bounded by the electrode array to the measured flow induced potential differences.

- Simulation of Effect of Conductivity on Current EM Method

Despite the observation that for moderate (≤ 5:1) variations in local conductivity there is minimal effect on the performance of the EM flow meter as it is a linear device, it would be a useful investigation to model the effects of the conductivities of tissues in the vicinity of the major arteries (flow channels) such as the femoral or brachial arteries on the flow induced potential distribution. Such tissues include regions of skin, muscle and bone. Moreover, the variation of haematocrit level in the blood could also be investigated as discussed in Chapter 2 (Section 2.4.2). The typical conductivity value for dry skin is 0.0002 S/m (conductivity of wet skin is 0.1 S/m [214]), muscle is 0.5 S/m and bone is 0.06 S/m [215]. In the current FE model, the cylindrical region, which has two flow channels, has uniform conductivity of 0.013 S/m and is surrounded by a 5 mm annulus which represents a layer of static water of the same conductivity. The current FE model could be modified to account for different conductivities of tissues. Such modifications to the FE model are not complex as it is only the cross-sectional area bounded by the electrode array which is the area of interest. Modelling of the skin, muscle and bone can be in the form of simple geometries using conductivity values similar to those given above.

Haematocrit level can also alter the conductivity of the blood as discussed in Section 2.5.7. In the current model, the imposed water had conductivity of 0.013 S/m, and for normal haematocrit level, i.e. 47%, the blood conductivity is 0.7 S/m which is 47 times greater in value. It does not seem that the haematocrit level would affect the EM method as it was tested with a low value of conductivity. However, the effect of the haematocrit levels could be investigated.

8.3.3 Practical Work

- Development of human-like phantom limb

An independent investigation[8] was carried out to design and construct a phantom limb that has a similar electrical conductivity distribution as a real human limb. Marconite and Bentonite materials were studied and samples were made of different conductivities that are similar to those of human tissues such as muscle and bone. Both Marconite and Bentonite are commonly used in the concrete mixes for foundations (replacing sand) of power distribution towers and lighting and communication aerials to provide proper electrical earthing [216]. Bentonite and Marconite have resistivities 3 Ω/m and 0.1 Ω/m, respectively. Relationships were established between the volume sample and conductivity of Bentonite and Marconite. Hence, for a desired conductivity, the volumes required of Marconite/Bentonite, cement, sand and water can be determined.

Conductivities similar to that of bone (0.04 S/m) and muscle (0.07 S/m) were achieved. Figure 8.2 shows the top and side view of a phantom limb made using Marconite. The model consisted of bone, muscle and artery regions.

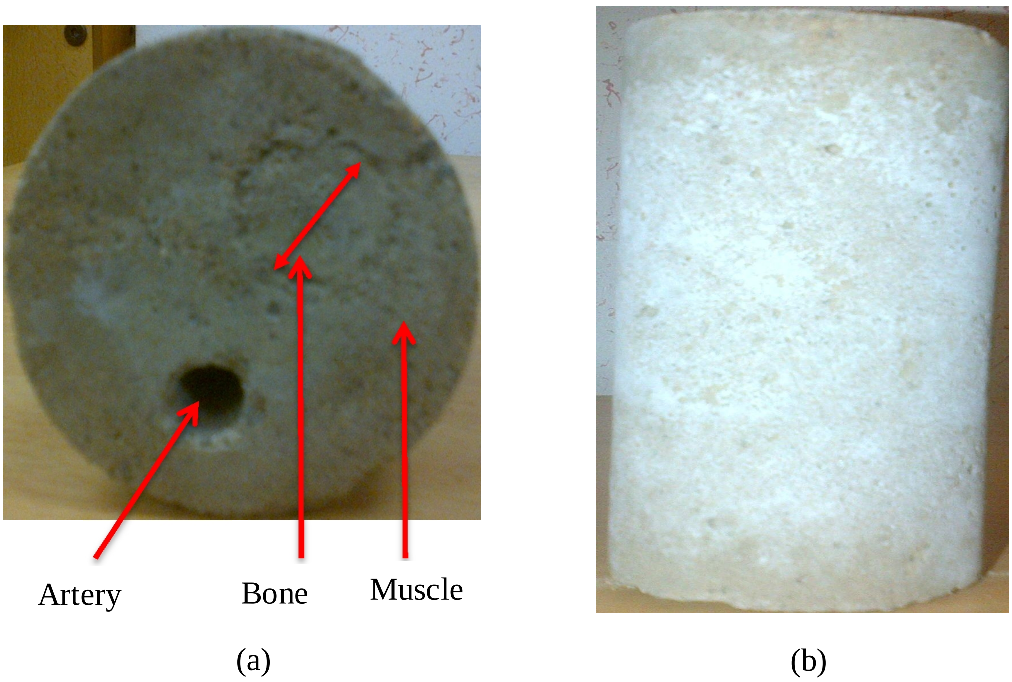

Figure 8.2: (a) Top-view of the phantom limb and (b) side-view of the model

[8] This was an MSc project – by Raymond Webilor – in which the author of this thesis was involved.

Other models with a different number of bones or blood vessels could also be constructed based on this work. Such models could be integrated in a flow loop to be tested with the EM method developed. It was also found in the literature that for *in vitro* (artificial) testing, phantom models can be constructed from C-Flex tubing, mimicking vessels, and surrounded by agar-based material, which models tissues [101]. The C-Flex tubing can model stenosed and unstenosed vessels. This could also be considered for future models of phantom limbs.

- Use of ultra-high input-impedance front-end amplifiers

In ECG and EMG systems, either wet or dry electrodes are used for potential difference measurements. In wet-electrode measurements, the skin requires preparation such as cleaning, shaving and applying electrolyte gel to reduce its impedance. Dry-electrodes are often used for long-term monitoring and therefore, they require ultra-high input impedance amplifiers to avoid any loss in signal amplitude. The design of an ultra-high input-impedance front-end amplifier could be considered for either dry or capacitive electrodes. Such an amplifier could utilise the bootstrapping technique, i.e. a small portion of the output of the amplifier is fed back to its non-inverting pin through (positive feedback) a filter network (high-pass filter), to increase its input impedance (Figure 8.3) [217].

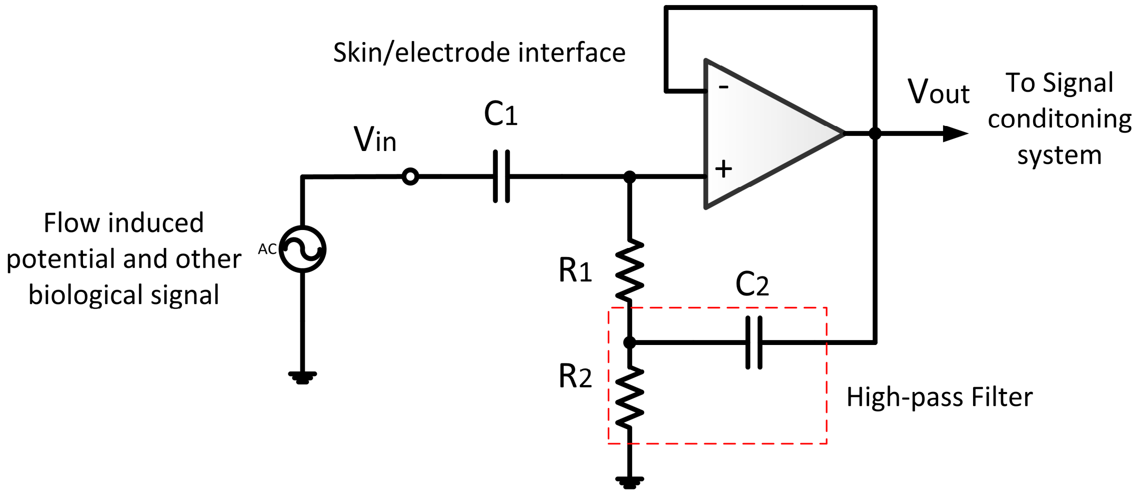

Figure 8.3: Bootstrapped voltage follower

- Development of pulsatile flow loop

Pulsatile flow can be created artificially using a pneumatic pump which can be electrically controlled to simulate arterial flow in the circulatory system.

- Other electrical and electronic improvements

The measurement system could also be magnetically shielded to minimise in-phase noise voltage to improve the phase integrity of the system. Other sources of the in-phase noise could also be investigated. The operating frequency could also be changed to 75 Hz which could have several benefits such as (1) faster response for electronic systems, (2) additional attenuation of low-frequency noise as the lower cut-off frequency of the measurement system could be increased and (3) less data acquisition time would be required for sampling the measured signals. Moreover, harmonics of a 75 Hz power supply would be the same as 50 Hz mains harmonics, and therefore, no additional noise components are introduced in the surrounding mains power lines. However, a change of operating frequency would require modifications for the current, voltage and PFC settings.

- Generation of different magnetic field projections

Using the tomographic methods suggested above would require additional magnetic field projections. Rotating the electromagnet manually might be inconvenient. Hence, one solution would be to rotate the magnetic field itself. This could be achieved using a design similar to that of a 3-phase AC stator. In an AC stator, a rotating magnetic field is generated by controlling the applied sinusoidal voltages with different phases, i.e. 120° apart. The stator can consist of 3 coil pairs. Each coil pair is controlled by an H-bridge power drive.

- Conceptual design of a non-invasive EM blood flow meter

A conceptual design of the first EM blood flow meter is provided in Figure 8.4. The stator-like electromagnet allows the magnetic field, applied at the electrode plane, to be either projected in one direction or rotated. The direction of the magnetic field is controlled by modifying the phase of the three-phase AC voltage supply which is applied to the stator pairs – similar in a way to the working principle of AC electrical motors [218]. The electrode-array is clamped around the limb and coupled electrically to the limb by using an electrolyte gel similar to the one used with ECG devices. Figure 8.5 depicts a cross-sectional view of the design, showing the stator poles.

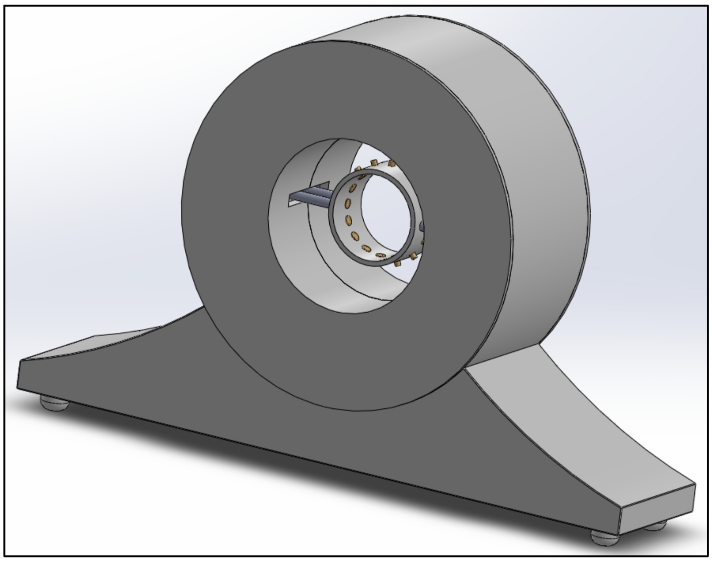

Figure 8.4: Conceptual design of the non-invasive EM blood flow meter

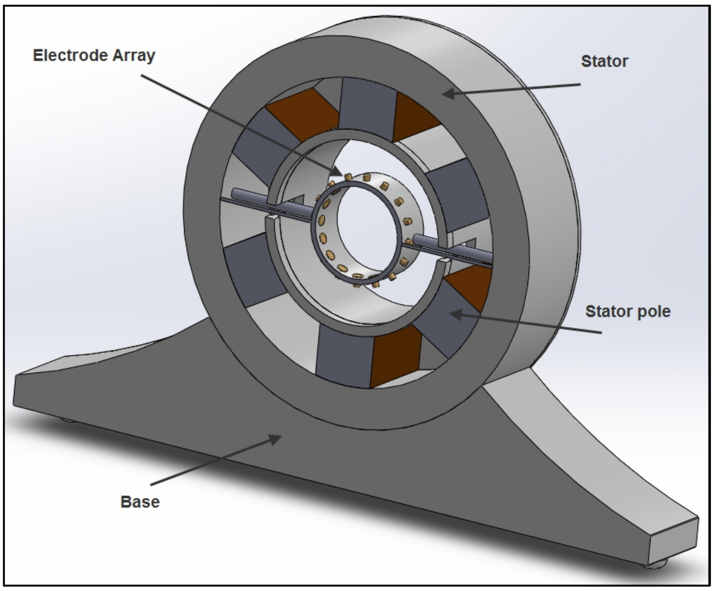

Figure 8.5: Cross-sectional view of the non-invasive blood flow meter

REFERENCES

[1] A. Kolin, "An electromagnetic flowmeter: principle of the method and its applications to blood measurements.," *Proc. Soc. Exp. Biol. Med.*, vol. 35, 1936.

[2] OpenStax. (2013). *Anatomay & Physiology*. Available: http://cnx.org/content/col11496/latest/ [Date Accessed: 06-08-2014]

[3] F. H. Martini, *Fundamentals of Anatomy and Physiology*. Englewood Cliffs, N. J.: Prentice Hall, 1995.

[4] G. A. Thibodeau and K. T. Patton, *Anatomy and Physiology*, 4th ed., 1999.

[5] Medical Anatomy. (2013). *Labeled Diagram Of The Circulatory System*. Available: http://medicalanatomy.net/wp-content/uploads/labeled-diagram-of-the-circulatory-system-186.jpg [Date Accessed: 27-08-2014]

[6] Openstax. (2014). *Dual System of the Human Blood Circulation*. Available: http://cnx.org/resources/768468e4045165d8d50e587887511b75/2003_Dual_System_of_Human_Circulation.jpg [Date Accessed: 27-08-2014]

[7] Openstax. (2014). *Relationship between the Cardiac Cycle and ECG*. Available: http://cnx.org/contents/14fb4ad7-39a1-4eee-ab6e-3ef2482e3e22@6.27:128 [Date Accessed: 28-08-2014]

[8] R. E. Klabunde. (2011). *Cardiac Cycle*. Available: http://www.cvphysiology.com/Heart%20Disease/HD002%20cardiac%20cycle%202007r1.gif [Date Accessed: 07/03/2015]

[9] W. W. Nichols, M. F. O'Rourke, and C. Vlachopoulos, *McDonald's Blood Flow in Arteries: Theoretical, Experimental and Clinical Principles*, 6th ed., 2011.

[10] B. Rubin. (2012). *Buffy Coats*. Available: http://bloodcenter.stanford.edu/blog/archives/2012/10/buffy-coats.html [Date Accessed: 18-09-2014]

[11] Openstax. (2014). *Composition of Blood*. Available: http://cnx.org/resources/c00848abae0dfc6541ca6c6547c167a6/1901_Composition_of_Blood.jpg [Date Accessed: 28-08-2014]

[12] K. S. Saladin, *Anatomy and Physiology: The Unity of Form and Function*, 2nd ed. New York: McGraw-Hill, 2001.

[13] A. C. Guyton and J. E. Hall, *Textbook of Medical Physiology*, 9th ed. Philadelphia: W. B. Saunders, 2001.

[14] Openstax. (2014). *Structure of Blood Vessels*. Available: http://cnx.org/resources/eb32c73d8a54eae9afcb591776047cec/2102_Comparison_of_Artery_and_Vein.jpg [Date Accessed: 28-08-2014]

[15] Openstax. (2014). *Types of Arteries and Arterioles*. Available: http://cnx.org/resources/40810c77aa97a13ee9b46170c52426a1/2103_Muscular_and_Elastic_Artery_Arteriole.jpg [Date Accessed: 28-08-2014]

[16] Openstax. (2014). *Comparison of Veins and Venules*. Available: http://cnx.org/resources/b2880fb332edc3769bcfae166a261342/2106_Large_Medium_Vein_Venule.jpg [Date Accessed: 28-08-2014]

[17] Openstax. (2014). *Systemic Arteries*. Available: http://cnx.org/resources/3a71bd56fff5472d26737c84a041bbb3/2120_Major_Systemic_Artery.jpg [Date Accessed: 28-08-2014]

[18] Openstax. (2014). *Major Arteries Serving the Thorax and Upper Limb*. Available: http://cnx.org/resources/b2a006d59fe6c13601282be32d2508e6/2127_Thoracic_Upper_Limb_Arteries.jpg [Date Accessed: 28-08-2014]

[19] Openstax. (2014). *Major Arteries Serving the Lower Limb*. Available: http://cnx.org/resources/73c88b0605a5d814974bab909892f885/2129ab_Lower_Limb_Arteries_Anterior_Posterior.jpg [Date Accessed: 28-08-2014]

[20] Openstax. (2014). *Major Systemic Veins of the Body*. Available: http://cnx.org/resources/aac8d0802718efdf0b2297aeda1db372/2131_Major_Systematic_Veins.jpg [Date Accessed: 28-08-2014]

[21] Openstax. (2014). *Veins of the Upper Limb*. Available: http://cnx.org/resources/4f0532020032835ece1042081c889217/2134_Thoracic_Upper_Limb_Veins.jpg [Date Accessed: 28-08-2014]

[22] Openstax. (2014). *Major Veins Serving the Lower Limbs*. Available: http://cnx.org/resources/7ededb92ca7b88f203d2698a3f3b3ac5/2136ab_Lower_Limb_Veins_Anterior_Posterior.jpg [Date Accessed: 28-08-2014]

[23] Openstax. (2014). *Systemic blood pressure*. Available: http://cnx.org/resources/926253e1c100ca64de271d56c1c97ab2/2109_Systemic_Blood_Pressure.jpg [Date Accessed: 28-08-2014]

[24] Openstax. (2013). *College Physics*. Available: http://cnx.org/content/col11406/latest/ [Date Accessed: 13-08-2014]

[25] Openstax. (2014). *Relationships among Vessels in the Systemic Circuit*. Available: http://cnx.org/resources/19611bf7ad7003a166bcea075987c6b6/2112_Vessel_Blood_Pressure_Relationships.jpg [Date Accessed: 28-08-2014]

[26] P. T. O'Gara, "Aortic Aneurysm," *Circulation*, vol. 107, pp. 43-45, 2003.

[27] L. Ferrara, M. Mancini, R. Lannuzzi, T. Marotta, I. Gaeta, F. Pasanisi, *et al.*, "Carotid Diameter and Blood Flow Velocities in Cerebral Circulation in Hypertensive Patients," *Circulation*, vol. 26, pp. 418-421, 1995.

[28] T. Sandgren, B. Sonesson, A. Ahlgren, and T. Lanne, "The diameter of the common femoral artery in healthy human: Influence of sex, age, and body size," *Journal of Vascular Surgery*, vol. 29, pp. 503-510, 1999.

[29] H. Chami, M. Keyes, J. Vita, M. G., M. Larson, S. Fan, *et al.*, "Brachial artery diameter, blood flow and flow-mediated dilation in sleep-disordered breathing," 2009.

[30] A. Augst, B. Ariff, S. Thom, X. Xu, and A. Hughes, "Analysis of complex flow and the relationship between blood pressure, wall shear stress, and intima-media thickness in the human carotid artery," *American Journal of Physiology*, vol. 293, 2007.

[31] A. Zambanini, S. Cunningham, K. Parker, A. Khir, S. Thom, and A. Hughes, "Wave-energy patterns in carotid, brachial, and radial arteries: a noninvasive approach using wave-intensity analysis," *American Journal of Physiology*, vol. 289, 2005.

[32] M. Hennerici and Neuerburg-Heusler, *Vascular Diagnosis with Ultrasound*: Thieme, 2005.

[33] National Institutes of Health. (2011). *What is Atherosclerosis?* Available: http://www.nhlbi.nih.gov/health/health-topics/topics/atherosclerosis/ [Date Accessed: 14-08-2014]

[34] NHS. (2014). *Atherosclerosis*. Available: http://www.nhs.uk/conditions/atherosclerosis/Pages/Introduction.aspx [Date Accessed: 14-08-2014]

[35] NHS. (2012). *Cardiovascular disease*. Available: http://www.nhs.uk/conditions/cardiovascular-disease/Pages/Introduction.aspx [Date Accessed: 14-8-2014]

[36] World Health Organization. (2013). *Cardiovascular diseases (CVDs)*. Available: http://www.who.int/mediacentre/factsheets/fs317/en/ [Date Accessed: 14-08-2014]

[37] Openstax. (2014). *Atherosclerosis*. Available: http://cnx.org/resources/18874f88b57fcf4f2fb8cf58f8ed4b16/2113ab_Atherosclerosis.jpg [Date Accessed: 28-08-2014]

[38] American Diabetes Association. (2013). *Foot Complications*. Available: http://www.diabetes.org/living-with-diabetes/complications/foot-complications/ [Date Accessed: 14-8-2014]

[39] H. L. Gornik and J. A. Beckman, "Peripheral Arterial Disease," *Circulation*, pp. e169-e172, 2005.

[40] Ash. (2014). ASH Research Report: Smoking and Peripheral Arterial Disease (PAD). Available: http://ash.org.uk/files/documents/ASH_190.pdf [Date Accessed: 15-08-2014]

[41] A. Halabi. (2009). *The Facts about Peripheral Arterial Disease*. Available: http://www.michiganmedicalreport.com/Portals/0/Templates/Images/PAD%20atherosclerosislegSJMO.jpg [Date Accessed: 28-08-2014]

[42] P. J. Skerrett. (2012). Difference blood pressure in right and left arms could signal trouble. Available: http://www.health.harvard.edu/blog/different-blood-pressure-in-right-and-left-arms-could-signal-trouble-201202014174 [Date Accessed: 18-08-2014]

[43] J. Roberts, C. Custalow, T. Thomsen, J. Hedges, A. Chanmugam, C. Chudnofsky*, et al.*, *Roberts and Hedges' Clinical Procedures in Emergency Medicine*, 6th ed.: Elsevier, 2014.

[44] BPJ Issue 60. (2014). *The ankle-brachial pressure index: An under-used tool in primary care?* Available: http://www.bpac.org.nz/BPJ/2014/April/img/systolic-pressure.jpg [Date Accessed: 28-08-2014]

[45] D. Xu, J. Li, L. Zou, Y. Xu, D. Hu, S. Pagoto*, et al.*, "Sensitivity and specificity of the ankle–brachial index to diagnose peripheral artery disease: a structured review," *Vascular Medicine*, vol. 15, pp. 361-369, 2010.

[46] E. S. H. KIM, K. WATTANAKIT, and H. L. GORNIK, "Using the ankle-brachial index to diagnose peripheral artery disease and assess cardiovascular risk," *Cleveland Clinic Journal of Medicine*, vol. 79, pp. 651-661, September 1, 2012 2012.

[47] G. A. Tew, M. Klonizakis, H. Crank, J. D. Briers, and G. J. Hodges, "Comparison of laser speckle contrast imaging with laser Doppler for assessing microvascular function," *Microvascular Research*, vol. 82, pp. 326-332, 2011.

[48] N. Benjamin, A. Calver, J. Collier, B. Robinson, P. Vallance, and D. Webb, "Measuring Forearm Blood Flow and Interpreting the Responses to Drugs and Mediators," *Hypertension*, vol. 25, pp. 918-923, 1995.

[49] C. Tidy. (2012). *Deep Vein Thrombosis*. Available: http://www.patient.co.uk/health/deep-vein-thrombosis-leaflet [Date Accessed: 05-09-2014]

[50] NHS. (2014). *Deep vein thrombosis*. Available: http://www.nhs.uk/conditions/deep-vein-thrombosis/Pages/Introduction.aspx [Date Accessed: 05-09-2014]

[51] CDC. (2012). *DVT/PE Data & Statistics*. Available: http://www.cdc.gov/ncbddd/dvt/data.html [Date Accessed: 05-09-2014]

[52] CDC. (2012). *DVT & PT Facts*. Available: http://www.cdc.gov/ncbddd/dvt/facts.html [Date Accessed: 05-09-2014]

[53] CDC. (2012). *DVT/PE Dianosis of DVT and PE*. Available: http://www.cdc.gov/ncbddd/dvt/diagnosis.html [Date Accessed: 05-09-2014]

[54] s. dynamics. (2012). *Deep vein thrombosis*. Available: https://www.flickr.com/photos/sportex/6634103129/ [Date Accessed: 05-09-2014]

[55] S. Miller. (2013). *End-stage kidney disease*. Available: http://www.nlm.nih.gov/medlineplus/ency/article/000500.htm [Date Accessed: 26-08-2014]

[56] NHS. (2013). *Dialysis*. Available: http://www.nhs.uk/conditions/Dialysis/Pages/Introduction.aspx [Date Accessed: 26-08-2014]

[57] T. Panetta. (No Date). *Dialysis Access Management*. Available: http://www.panettavascular.com/images/fistula-diagram.jpg [Date Accessed: 28-08-2014]

[58] S. Cheng, A. Vijayan, K. E. Henderson, and T. M. Defer, *The Washington Manual: Nephrology*, 3rd ed.: Lippincott Williams & Wilkins, 2012.

[59] L. Goldman and A. Schafer, *Goldman's Cecil Medicine*, 24th ed.: Elsevier, 2012.

[60] V. Mickley, "Stenosis and thrombosis in haemodialysis fistulae and grafts: the surgeon's point of view," *Nephrol Dial Transplant*, vol. 19, pp. 309-311, 2004.

[61] T. Ogawa, O. Matsumura, A. Matsuda, H. Hasegawa, and T. Mitarai, "Brachial artery blood flow measurement: A simple and noninvasive method to evaluate the need for arteriovenous fistula repair," *Dialysis and Transplantation*, vol. 40, pp. 206-210, 2011.

[62] T. Savage, A. L. Clarke, M. Giles, C. R. V. Tomson, and A. E. G. Raine, "Calcified plaque is common in the cartoid and femoral arteries of dialysis patients without clinical vascular disease," *Nephrol Dial Transplant*, vol. 13, pp. 2004-2012, 1998.

[63] B. Gleich, *Principles and Applications of Magnetic Particle Imaging*: Springer, 2014.

[64] W. L. Smith and T. A. Farrell, *Radiology 101: The Basics and Fundamentals of Imaging*, 4th ed.: Lippincott Williams & Wilkins, 2013.

[65] H. Singh and J. Neutze, Eds., *Radiology Fundamentals: Introduction to Imaging & Technology*. Springer, 2011, p.^pp. Pages.

[66] Cedars-Sinai. (2014). *Diagnostic Procedures: Angiography*. Available: http://www.cedars-sinai.edu/Patients/Programs-and-Services/Heart-Institute/Diagnostic-Procedures/Images/470787_DrugElutingStent-3.jpg [Date Accessed: 22-09-2014]

[67] M. Brady. (2004). Basics of MRI. Available: http://www.robots.ox.ac.uk/~jmb/lectures/medimanallecture1.pdf [Date Accessed: 21-09-2014]

[68] M. B. Srichai, R. P. Lim, S. Wong, and V. Lee, "Cardiovascular Applications of Phase-Contrast MRI," *American Journal of Roentgenology*, vol. 192, pp. 662-675, 2009.

[69] NHS. (2013). *Meglumine Gadopentetate*. Available: http://www.nhs.uk/medicine-guides/pages/MedicineSideEffects.aspx?condition=MRI&medicine=meglumine%20gadopentetate&preparation= [Date Accessed: 21-09-2014]

[70] Texas Instruments. (2013). TI HealthTech Imaging Guide. Available: http://www.ti.com/lit/sg/slyb155c/slyb155c.pdf [Date Accessed: 18-08-2014]

[71] C. G. Elliott. (2000). *The Diagnostic Approach to Deep Venous Thrombosis*. Available: http://www.medscape.com/viewarticle/410882_2 [Date Accessed: 05-09-2014]

[72] RadiologyInfo.org. (2013). CT Angiography (CTA). Available: http://www.radiologyinfo.org/en/pdf/angioct.pdf [Date Accessed: 22-09-2014]

[73] National Council on Radiation Protection & Measurements. (2009). *Medical Radiation Exposure Of The U.S. Population Greatly Increased Since The Early 1980s*. Available: www.sciencedaily.com/releases/2009/03/090303125809.htm [Date Accessed: 22-09-2014]

[74] D. J. Brenner and E. J. Hall, "Computed Tomography — An Increasing Source of Radiation Exposure," *N Engl J Med,* vol. 357, pp. 2277-2284, 2007.

[75] P. Mudgal and Y. Weerakkody. (2014). MRI artifacts. Available: http://radiopaedia.org/articles/mri-artifacts [Date Accessed: 18-08-2014]

[76] H. Knipe and D. Blackmore. (2014). CT arifacts. Available: http://radiopaedia.org/articles/ct-artifacts [Date Accessed: 18-08-2014]

[77] A. W. Hewlett and J. G. van Zwaluwenburg, "The rate of blood flow in the arm," *Heart,* vol. 1, pp. 631-646, 1909.

[78] J. Malmivuo and R. Plonsey, *Bioelectromagnetism - Principles and Applications of Bioelectric and Biomagnetic Fields*. New York: Oxford University Press, 1995.

[79] I. B. Wilkinson and D. J. Webb, "Venous occlusion plethysmography in cardiovascular research: methodology and clinical applications," *Br J Clin Pharmacol,* vol. 52, pp. 631-646, 2001.

[80] J. G. Webster, *Medical Instrumentation Application and Design*, 4th ed.: John Wiley & Sons Inc., 2009.

[81] J. C. Golden and D. S. Miles, "Assessment of Peripheral Hemodynamics Using Impedance Plethysmography," *Journal of the American Physical Therapy Association,* vol. 66, pp. 1544-1547, 1986.

[82] J. G. Webster and H. Eren, *Measurement, Instrumentation, and Sensors Handbook, Second Edition: Spatial, Mechanical, Thermal, and Radiation Measurement*, 2nd ed.: CRC Press, 2014.

[83] P. Wells, J. Hirsh, D. Anderson, A. Lensing, G. Foster, and C. Kearon, "Comparison of the accuracy of impedance plethysmography and compression ultrasonography in outpatients with clinically suspected deep vein thrombosis. A two centre paired-design prospective trial," *Thromb Haemost,* vol. 74, pp. 1423-1427, 1995.

[84] R. Patterson, R. Fowl, J. Keller, W. Schomaker, and R. Kempczinski, "The limitations of impedance plethysmography in the diagnosis of acute deep venous thrombosis," *journal of Vascular Surgery,* vol. 9, pp. 725-9, 1989.

[85] J. Moore and G. Zouridakis, Eds., *Biomedical Technology and Devices Handbook*. CRC Press, 2003, p.^pp. Pages.

[86] Panametrics-NDT. (2006). Ultrasonic Transducers Technical Notes. Available: https://www.olympus-ims.com/data/File/panametrics/UT-technotes.en.pdf [Date Accessed: 20-08-2014]

[87] J. T. Bushberg, J. A. Seibert, and J. M. Boone, *The Essential Physics of Medical Imaging*: Lippincott Williams & Wilkins, 2011.

[88] C. Hartley, "Ultrasonic Blood Flow and Velocity Measurement," ed: CRC Press LLC, 2004.

[89] P. R. Hoskins, "A review of the measurement of blood velocity and related quatities using Doppler ultrasound," *Proc. Ins. of Mech Eng, Part H: journal of Eng. in Med.,* vol. 213, pp. 391-400, 1999.

[90] V. Teodorescu, S. Gustavson, and H. Schanzer, "Duplex Ultrasound Evaluation of Hemodialysis Access: A Detailed Protocol," *International Journal of Nephrology*, vol. 2012, 2012.

[91] P. Cattin. (2013). *Ultrasound: Priciples of Medical Imaging*. Available: https://miac.unibas.ch/PMI/05-UltrasoundImaging.html#(43) [Date Accessed: 23-09-2014]

[92] A. Carovac, F. Smajlovic, and D. Junuzovic, "Application of Ultrasound in Medicine," *Acta Inform Med.*, vol. 19, pp. 168-171, 2011.

[93] UltrasoundSupply.com. (2014). *GE P6D Pencil Ultrasound Probe*. Available: http://www.ultrasoundsupply.com/wp-content/uploads/2014/04/Probe-Image-41.jpg [Date Accessed: 28-08-2014]

[94] Wikipedia. (2014). *Ultrasonic testing*. Available: http://upload.wikimedia.org/wikipedia/commons/thumb/a/ae/UT_principe.svg/750px-UT_principe.svg.png [Date Accessed: 28-08-2014]

[95] Ultrasound Image Gallery. (2013). *Ultrasound and Color Doppler imaging of vascular diseases*. Available: http://www.ultrasound-images.com/admin/uploads/carotid-plaque-2b.jpg [Date Accessed: 28-08-2014]

[96] ICU Sonography. (2009). *Tutorial 2 - Modes of Ultrasound*. Available: http://www.criticalecho.com/sites/default/files/images/2.2.png [Date Accessed: 28-08-2014]

[97] M. W. Mulholland, K. D. Lillemoe, G. M. Doherty, R. V. Maier, and G. R. Upchurch, *Greenfield's Surgery: Scientific Principles and Practice*: Lippincott Williams & Wilkins, 2010.

[98] NHS. (2012). *Coronary heart disease - Diagnosis* Available: http://www.nhs.uk/Conditions/Coronary-heart-disease/Pages/Diagnosis.aspx [Date Accessed: 23-09-2014]

[99] L. National Heart, and Blood Institue. (2014). *How Is Peripheral Arterial Disease Diagnosed?* Available: http://www.nhlbi.nih.gov/health/health-topics/topics/pad/diagnosis.html [Date Accessed: 23-09-2014]

[100] SonoNet. (2010). *Lower Extremity Arterial Exam*. Available: http://www.sononet.us/images/leart.jpg [Date Accessed: 28-08-2014]

[101] E. Y. L. Lui, A. H. Steinman, R. S. C. Cobbold, and K. W. Johnston, "Human factors as a source of error in peak Doppler velocity measurement," *Journal of Vascular Surgery*, vol. 42, pp. 972.e1-972.e10, 2005.

[102] C. Deane. (2002). *Doppler ultrasound: principles and practice*. Available: http://sonoworld.com/Client/Fetus/html/doppler/capitulos-html/chapter_01.htm# [Date Accessed: 23-09-2014]

[103] P. R. Hoskins, "Peak velocity estimation in artieral stenosis models using colour vector Doppler," *Ultrasound in Medicine & Biology*, vol. 23, pp. 889-897, 1997.

[104] C. Deane. (2002). *Doppler ultrasound: principles and practice*. Available: http://sonoworld.com/Client/Fetus/html/doppler/capitulos-html/imagens-cap-01/fig-06.jpg [Date Accessed: 28-08-2014]

[105] D. A. Christopher, P. N. Burns, J. W. Hunt, and F. S. Foster, "The effect of refraction and assumed speeds of sound in tissue and blood on doppler ultrasound blood velocity measurements," *Ultrasound in Medicine & Biology*, vol. 21, pp. 187-201, 1995.

[106] M. J. Lunt. (2000). Review of duplex and colour Doppler imaging of lower-limb arteries and veins. Available: http://www.worldwidewounds.com/2000/sept/Michael-Lunt/Doppler-Imaging.html [Date Accessed: 25-04-2014]

[107] J. A. Shercliff, *The Theory of Electromagnetic Flow-Measurement*: Cambridge University, 1962.

[108] J. Williams, "The Induction of Electromotive Forces in a Moving Liquid by Magnetic Field and its Application to an Investigation of the Flow of Liquids," *Proceedings of Physics Society,* vol. 42, pp. 466-478, 1930.

[109] B. Thürlemann, "Methode zur elektrischen Geschwindigkeitsmessung in Flüssigkeiten," *Helv. Phys. Acta,* vol. 14, pp. 383-419, 1941.

[110] R. Tabrizchi and N. Iida, *Electromagnetic Blood Flow Measurements*: CRC Press LLC, 2004.

[111] E. Joseph and D. Bronzino, *The Biomedical Engineering Handbook*: CRC Press LLC, 2000.

[112] D. G. Wyatt, "The electromagnetic blood flowmeter," *Journal of Scientific Instruments,* vol. 1, pp. 1146-1152, 1968.

[113] R. Serway, *Physics for Scientists and Engineers with Modern Physics*, 3rd ed., 1992.

[114] F. Ulaby, E. Michielssen, and U. Ravaioli, *Fundamentals of Applied Electromagnetics*, 5th ed., 2010.

[115] D. Fleisch, *A Student's Guide to Maxwell's Equations*. Cambridge: Cambridge University Press, 2008.

[116] D. Griffiths, *Introduction to Electrodynamics*, 4th ed.: Addison-Wesley, 2014.

[117] M. Tarabad and R. Baker, "Integrating electromagnetic flowmeter for high magnetic Reynolds numbers," *J. Phys. D: Appl. Phys.,* vol. 15, pp. 739-745, 1982.

[118] T. Togawa, T. Tamura, and P. Oberg, *Biomedical TRANSDUCERS and INSTRUMENTS*: CRC Press, 1997.

[119] B. Horner, F. Mesch, and A. Trachtler, "A multi-sensor induction flow meter reducing errors due to non-axisymmetric flow profiles," *Meas. Sci. Technol.,* vol. 7, pp. 354-360, 1996.

[120] L. J. Xu, X. M. Li, F. Dong, Y. Wang, and L. Xu, "Optimum estimation of the mean flow velocity for the multi-electrode inductance flowmeter," *meas. Sci. Technol.,* vol. 12, pp. 1139-1146, 2001.

[121] T. Leeungculsatien and G. P. Lucas, "Measurement of velocity profiles in multiphase flow using a multi-electrode electromagnetic flow meter," *Flow Measurement and Instrumentation,* vol. 31, pp. 86-95, 2013.

[122] M. Bevir, "The theory of induced voltage electromagnetic flowmeters," *Fluid Mech.*, vol. 43, pp. 577-590, 1970.

[123] T. Teshima, S. Honda, and Y. Tomita, "Electromagnetic flowmeter with multiple poles and electrodes," in *Instrumentation and Measurement Technology Conference, 1994. IMTC/94. Conference Proceedings. 10th Anniversary. Advanced Technologies in I & M., 1994 IEEE*, 1994, pp. 1221-1224 vol.3.

[124] D. G. Wyatt, "Electromagnetic blood-flow measurements," *IEE Medical Electronics Monograph I,* pp. 181-243, 1971.

[125] M. Bevir, "Theory of induced voltage electromagnetic flowmeasurement," *Magnetics, IEEE Transactions on,* vol. 6, pp. 315-320, 1970.

[126] M. K. Bevir, V. T. O'Sullivan, and D. G. Wyatt, "Computation of electromagnetic flowmeter characteritics from magnetic field data," *J Phys D: Appl Phys,* vol. 14, pp. 373-388, 1981.

[127] D. G. Wyatt, "Blood flow and blood velocity measurement in vivo by electromagnetic induction," *Transactions of the Institute of Measurement and Control,* vol. 4, pp. 61-78, 1982.

[128] J. Hemp, "Improved magnetic field for an electromangetic flowmeter with point electrodes," *J Phys D: Appl Phys,* vol. 8, pp. 983-1002, 1975.
[129] B. Horner and F. Mesch, "An induction flowmeter insensitive to asymmetric flow profiles," presented at the ECAPT'95—Process Tomography 1995: Implementation for Industrial Process, Bergen, 1995.
[130] W. Engl, "Der inductive Durchflussmesser mit inhomogenem magnetfeld," *Arch. Electrotechnik,* vol. 53, p. 344, 1970.
[131] G. Lucas and T. Leeungculsatien, "Measurement of velocity profiles in multiphase flow using a multi-electrode electromagnetic flow meter," *Flow Measurement and Instrumentation,* 2012.
[132] G. Lucas and T. Leeungculsatien, "Means and method of monitoring the flow of fluid," United Kingdom Patent, 2011.
[133] C. J. Mills, "A catheter tip electromagnetic velocity probe," *Phys Med Biol,* vol. 11, pp. 323-324, 1966.
[134] R. Tabrizchi and M. K. Pugsley, "Methods of blood flow measurement in the arterial circulatory system," *Journal of Pharmacological and Toxicological Methods,* vol. 44, pp. 375-384, 2000.
[135] H. Kanai, "The effects upon electromagnetic flowmeter sensitivity of non-uniform fields and velocity profiles," *Med & Biol Engng,* vol. 7, pp. 661-676, 1969.
[136] U. Gessner, "Effects of the Vessel Wall on Electromagnetic Flow Measurement," *Biophys J.,* pp. 627-637, 1961.
[137] V. T. O'Sullivan, "Effect of blood vessels on electromagnetic flowmeter sensitivity," *Phys Med Biol,* vol. 27, pp. 277-284, 1982.
[138] A. Mandal. (2013). *Catheter Uses*. Available: http://www.news-medical.net/health/Catheter-Uses.aspx [Date Accessed: 15-07-2014]
[139] H. J. Boccalon, B. Candelon, J. J. Tillie, A. Graulle, H. G. Doll, P. F. Puel, *et al.*, "New non-invasive device of pulsatile blood flow measurement," presented at the 11th International Conference on Medical and Biological Engineering, Ottawa, 1976.
[140] T. Togawa, O. Okai, and M. Oshima, "Observations of blood flow EMF in externally applied strong magnetic field by surface electrodes," *Med & Biol Engng,* vol. 5, pp. 169-170, 1967.
[141] H. J. Boccalon, A. Lozes, W. Newman, and H. G. Doll, "Noninvasive electromagnetic blood flowmeter: theoretical aspects and technical evaluation," *Med. Biol. Eng. Comput.,* vol. 20, p. 671, 1982.
[142] H. Kanai, E. Yamano, and K. Nakayama, "Transcutaneous blood flow measurement by electromagnetic induction," *IEEE Trans Biomed Eng,* vol. 21, pp. 144-151, 1974.
[143] T. Leeungculsatien and G. Lucas, "Measurement of velocity profiles in multiphase flow using a multi-electrode electromagnetic flow meter," *Flow Meas. Instrum,* vol. 31, pp. 86-95, 2013.
[144] J.-E. Cha, Y.-C. Ahn, and M.-H. Kim, "Flow measurement with an electromagnetic flowmeter in two-phase bubbly and slug flow regimes," *Flow Meas. Instrum,* vol. 12, pp. 329-339, 2002.
[145] T. J. Cox and D. G. Wyatt, "An electromagnetic flowmeter with insulated electrodes of large surface area," *J Phys E: Sci. Instru.,* vol. 17, pp. 487-503, 1984.
[146] V. J. Cushing, "Electromagnetic Fluid Flow Meter With Tolerance to Spurious Signals," 1979.

[147] T. Wray, "Phase Measurement in Measurement Device," United Kingdom Patent, 2006.
[148] F. Olmsted, "Phase Detection Electromagnetic Flowmeter-Design and Use," *Bio-Medical Electronics, IRE Transactions on*, vol. 9, pp. 88-92, 1962.
[149] H. S. Lew, Y. S. Lew, and Y. K. Lew, "Magnetic Flowmeter Determining Flow Rate from Phase Angle Difference," United States Patent, 1995.
[150] S. Zhang and A. Soukas, "Optimization of phase sensitive detectors using fast Fourier transform," *Meas. Sci. Technol.*, vol. 2, pp. 13-18, 1991.
[151] A. Westersten, G. Herrold, E. Abbott, and N. S. Assali, "Gated Sine-Wave Electromagnetic Flowmeter," *Medical Electronics, IRE Transactions on*, vol. ME-6, pp. 213-216, 1959.
[152] A. Westersten, "Flowmeter," United States Patent, 1969.
[153] R. Boylestad, *Introductory Circuit Analysis*, 11th ed.: Pearson International, 2007.
[154] A. Rich, "Understanding Interferance-Type Noise," *Analog Dialogue*, vol. 16, pp. 16-19, 1982.
[155] A. Rich, "Sheilding and Guarding," *Analog Dialogue*, vol. 17, pp. 8-13, 1983.
[156] Analog Devices. (2009). MT-095 Tutorial: EMI, RFI, and Shielding Concepts. Available: http://www.analog.com/static/imported-files/tutorials/MT-095.pdf [Date Accessed: 30-07-2014]
[157] D. Prutchi and M. Norris, *Design and Developement of Medical Electronic Instrumentation*: John Wiley and Sons Inc., 2005.
[158] Analog Devices. (2011). An-940 Low Noise Amplifier Selection Guide for Optimal Noise Performance. Available: http://www.analog.com/static/imported-files/application_notes/AN-940.pdf [Date Accessed: 30-07-2014]
[159] E. Kreyszig, *Advanced Engineering Mathematics*, 8th ed.: John Wiley & Sons, 1999.
[160] A. J. Hogg. (2001). Fluid Dynamics: Separable solutions to Laplace's equation. Available: http://www.maths.bris.ac.uk/~maajh/fluids/handout3.pdf [Date Accessed: 24-06-2014]
[161] D. DeTurck. (2012). Laplace equation in polar coordinates; consequences and properties. Available: http://www.math.upenn.edu/~deturck/m241/laplace_in_polar.pdf [Date Accessed: 24-06-2014]
[162] E. Kersale. (2004). Analytic Solutions of Partial Differential Equations. 49-68. Available: http://www1.maths.leeds.ac.uk/~kersale/Teach/M3414/Notes/m3414_1.pdf [Date Accessed: 24-06-2014]
[163] Yorkshire Water. (2013). Annual Water Quality Report. 3. Available: http://www.ywonline.co.uk/web/WQZ.nsf/0/3035CDC75110F89C802574FD0030D37D/$file/Holme%20Valley%20WSZ.pdf [Date Accessed: 23-04-2014]
[164] B. S. Guru and H. Hiziroglu, *Electromagnetic Field Theory Fundamentals (2nd Edition)*. West Nyack, NY, USA: Cambridge University Press, 2004.
[165] COMSOL. (2013). Introduction to COMSOL Multiphysics. Available: http://www.uk.comsol.com/shared/downloads/IntroductionToCOMSOLMultiphysics.pdf [Date Accessed: 20-04-2014]
[166] COMSOL. (2012). Introduction to AC/DC Module. Available: http://www.comsol.com/model/download/120723/IntroductionToACDCModule.pdf [Date Accessed: 20-04-2014]
[167] L. M. Millanta, A. Agostini, and S. Lazzerini, "Helmholtz coils: Static and frequency-dependent performance limitations," in *Electromagnetic*

Compatibility, 1993. Symposium Record., 1993 IEEE International Symposium on, 1993, pp. 377-378.
[168] E. R. Javor and T. Anderson, "Design of a Helmholtz coil for low frequency magnetic field susceptibility testing," in *Electromagnetic Compatibility, 1998. 1998 IEEE International Symposium on*, 1998, pp. 912-917 vol.2.
[169] COMSOL. (2008). AC/DC Module User's Guide. Available: https://extras.csc.fi/math/comsol/3.5a/doc/acdc/acdcmodlib.pdf [Date Accessed: 23-04-2014]
[170] Wikimedia, "Helmholtz coil," ed: Wikimedia Commons.
[171] COMSOL. (2008). Magnetic Field of a Helmholtz Coil solved with COMSOL Multiphysics 3.5a. [Date Accessed: 24-04-2014]
[172] R. H. Bishop, *The Mechatronics Handbook*: CRC Press, 2002.
[173] H. Chuanhong, Z. Li, L. Bin, X. Zheng, and Z. Zhanlong, "A digital phase-sensitive detector for electrical impedance tomography," in *Automation Congress, 2008. WAC 2008. World*, 2008, pp. 1-4.
[174] T. Bera and J. Nagaraju, "Switching of a Sixteen Electrode Array for Wireless EIT System Using a RF-Based 8-Bit Digital Data Transmission Technique," in *Global Trends in Computing and Communication Systems*. vol. 269, P. V. Krishna, M. R. Babu, and E. Ariwa, Eds., ed: Springer Berlin Heidelberg, 2012, pp. 202-211.
[175] National Instruments. NI PCI-6254. Available: http://sine.ni.com/nips/cds/view/p/lang/en/nid/14126 [Date Accessed: 18-01-2014]
[176] HP Technical Ceramics. [Online]. Available: http://www.tech-ceramics.co.uk/porous%20ceramics.htm
[177] Magnetic Metals. (2001). 3% Grain Oriented Silicon Steel. Available: http://www.magmet.com/nam/images/NAM_cat_combinedCh2.pdf [Date Accessed: 03-01-2014]
[178] Topward. Instruction Manual for Function Generator Model 8102/8105. Available: http://www.topward.com.tw/data/8102,8105.pdf [Date Accessed: 14-01-2014]
[179] Newtons4th Ltd. (2005). LPA05 User Guide. Available: http://newtons4th.com/wp-content/uploads/2014/05/LPA05-User-Guide.pdf [Date Accessed: 15-03-2015]
[180] Rosemount Inc Measurement Division. (1995). Magnetic Flowmeter Fundamentals. Available: http://www.automaatika.ee/pdf/Fundament.pdf [Date Accessed: 18-01-2014]
[181] B. G. Liptak, *Instrument Engineers' Handbook*, 4th ed. vol. 1: CRC Press, 2003.
[182] T. Kugelstadt, "Getting the Most out of your Instrumentation Amplifier Design

" *Analog Applications*, 2005.
[183] I. obeid, M. Nicolelis, and P. Wolf, "A low power multichannel analog front end for portable neural signal recordings," *Journal of neuroscience methods*, vol. 133, pp. 27-32, 2004.
[184] Analog Devices. (2012). A Flexible 4-Channel Analog Front End for Wide Dynamic Range Signal Conditioning. Available: http://www.analog.com/static/imported-files/circuit_notes/CN0251.pdf [Date Accessed: 18-01-2014]
[185] P. Szakacs-Simon, S. A. Moraru, and F. Neukart, "Signal conditioning techniques for health monitoring devices," in *Telecommunications and Signal Processing (TSP), 2012 35th International Conference on*, 2012, pp. 610-614.

[186] C. Kitchin and L. Counts. (2006). *A Designer's Guide to Instrumentation Amplifiers (3rd ed.)*. Available: http://www.analog.com/static/imported-files/design_handbooks/5812756674312778737Complete_In_Amp.pdf [Date Accessed: 19-01-2014]

[187] C. Kitchin, L. Counts, and M. Gerstenhaber. (2003). Reducing RFI Rectification Errors in In-Amp Circuits AN-671. Available: http://www.analog.com/static/imported-files/application_notes/AN-671.pdf [Date Accessed: 19-01-2014]

[188] Texas Instruments. (2015). *SPICE-Based Analog Simulation Program*. Available: http://www.ti.com/tool/tina-ti [Date Accessed: 15-02-2015]

[189] Texas Instruments. (2005). INA128/129 Instrumentation Amplifier Datasheet. Available: http://www.ti.com/lit/ds/sbos051b/sbos051b.pdf [Date Accessed: 22-01-2014]

[190] T. Instruments, "OPA2137 Low Cost FET-input Operational Amplifiers MicroAmplifier Series," 2013.

[191] K. Ogata, *Modern Control Engineering*, 5th ed.: Prentice Hall, 2010.

[192] M. Stitt. (1991). AC Coupling Instrumentation and Difference Amplifiers - SBOA003. [Date Accessed: 22-01-2014]

[193] C. Becchetti and A. Neri, *Medical Instrument Design and Development: From Requirements to Market Placements*, 2013.

[194] V. Acharya. (2011). Improving Common-mode Rejection Using the Right-leg Drive Amplifer. Available: http://www.ti.com/lit/an/sbaa188/sbaa188.pdf [Date Accessed: 20-07-2014]

[195] M. W. Hann. (2011). Signal Chain Basics #58: Analyze the RL Drive in an ECG Front End using SPICE. Available: http://www.planetanalog.com/document.asp?doc_id=528240 [Date Accessed: 23-01-2014]

[196] S. Wu, "Noise Cancelling Headphones," 2008.

[197] E. Process. (2013). Installation and Grounding of Magmeters in Typical and Special Applications. Available: http://www2.emersonprocess.com/siteadmincenter/PM%20Rosemount%20Documents/00840-2400-4727.pdf [Date Accessed: 13-09-2014]

[198] Intersil. (2013). Single 16-Channel/Differential 8-Channel, CMOS Analog Multiplexers. Available: http://www.intersil.com/content/dam/Intersil/documents/fn31/fn3116.pdf [Date Accessed: 08-01-2014]

[199] S. Smith, *The Scientist and Engineer's Guide to Digital Signal Processing*, 1st ed.: California Technical, 1998.

[200] MathWorks. (2013). Documentation Centre: Data Acquisition Toolbox. Available: http://www.mathworks.co.uk/help/daq/ [Date Accessed: 08-07-2015]

[201] D. P. Blair and P. H. Sydenham, "Phase sensitive detection as a means to recover signals buried in noise," *J. Phys. E: Sci. Instrum.*, vol. 8, pp. 621-627, 1975.

[202] J. M. Masciotti, J. M. Lasker, and A. H. Hielscher, "Digital Lock-In Detection for Discriminating Multiple Modulation Frequencies With High Accuracy and Computational Efficiency," *Instrumentation and Measurement, IEEE Transactions on*, vol. 57, pp. 182-189, 2008.

[203] R. Josephs, D. Crompton, and C. Krafft, "Application of digital signal processing to vibrating sample magnetometry," *Magnetics, IEEE Transactions on*, vol. 23, pp. 241-244, 1987.

[204] G. Machel and M. von Ortenberg, "A digital lock-in-technique for pulsed magnetic field experiments," *Physica B: Condensed Matter,* vol. 211, pp. 355-359, 1995.

[205] L. Bengtsson, "A microcontroller-based lock-in amplifier for sub-milliohm resistance measurements," *Review of scientific instruments, American Institue of Physics,* vol. 83, 2012.

[206] F. Heer and S. Hafizovic, "Apparatus for lock-in amplifying an input signal and method for generating a reference signal for lock-in amplifier," 2011.

[207] M. Meade, "Advances in lock-in amplifiers," *J. Phys. E: Sci. Instrum.,* vol. 15, pp. 395-403, 1982.

[208] A. Bradly. (2008). Phase sensitive detection: the lock-in amplifier. Available: http://www.phys.utk.edu/labs/modphys/lock-in%20amplifier%20experiment.pdf [Date Accessed: 15-13-2014]

[209] D. Wenn. (2007). AN1115 - Implementing digital lock-in amplifier using the dsPIC DSC. Available: http://ww1.microchip.com/downloads/en/AppNotes/01115A.pdf [Date Accessed: 20-02-2014]

[210] P. Probst and B. Collet, "Low-frequency digital lock-in amplifier," *Review of scientific instruments, American Institue of Physics,* vol. 56, pp. 466-470, 1984.

[211] D. E. Newland, *An Introduction to Random Vibrations, Spectral & Wavelet Analysis: Third Edition (Dover Civil and Mechanical Engineering)*, 3rd ed.: Dover Publications, 2005.

[212] L. E. Kollar and G. P. Lucas, "Proposed method for reconstructing velocity profiles using a multi-electrode electromagnetic flow meter," *Meas. Sci. Technol.,* vol. 25, 2014.

[213] J. Z. Wang, G. Y. Tian, and G. P. Lucas, "Relationship between velocity profile and distribution of induced potential for an electromagnetic flow meter," *Flow Measurement and Instrumentation,* vol. 18, pp. 99-105, 2007.

[214] C. Gabriel and S. Gabried. Compilation of the Dielectric Properties of Body Tissues at RF and Microwave Frequencies. Available: http://niremf.ifac.cnr.it/docs/DIELECTRIC/Report.html [Date Accessed: 20-02-2016]

[215] D. Miklavčič, N. Pavšelj, and F. X. Hart, "Electric Properties of Tissues," in *Wiley Encyclopedia of Biomedical Engineering*, ed, 2006.

[216] T&D. (2013). *Earthing Compound - Bentonite and Marconite*. Available: http://www.cablejoints.co.uk/sub-product-details/earthing-lightning-protection/bentonite-marconite-earthing-compounds [Date Accessed: 10-09-2014]

[217] R. Pallas-arnet and J. Colominas, "An Improved Buffer for Bioelectric Signals," *IEEE Trans Biomed Eng,* vol. 36, pp. 490-493, 1989.

[218] T. Wildi, *Electrical Machines, Drives and Power Systems*, 6th ed.: Prentice Hall, 2005.

APPENDICES

Appendix A

Derivation of the unit for k_1 in Equation 3-39

From Eq. 3-39, the factor k_1 is given by

$$k_1 = \frac{|X(1)|}{Q_T B_0} \qquad \text{Eq. A-1}$$

where the modulus $|X(1)|$ of the DFT component $X(1)$ unit is V, the total flow rate Q_T unit is m^3s^{-1} and the peak magnetic flux density B_0 unit is T. Hence the unit of k_1 is given by

$$k_1 = \frac{\mathrm{V}}{\mathrm{m^3 s^{-1} T}} = \mathrm{V\,s\,T^{-1}\,m^{-3}} \qquad \text{Eq. A-2}$$

The base units for V and T are kg m^2 A^{-1} s^{-3} and kg A^{-1} s^{-2}, respectively. Substituting these units in Eq. A-2 gives

$$k_1 = \frac{\mathrm{V}}{\mathrm{m^3 s^{-1} T}} = \frac{\mathrm{kg\,m^2}}{\mathrm{A\,s^3}}\,\mathrm{s}\,\frac{\mathrm{A\,s^2}}{\mathrm{kg}}\,\frac{1}{\mathrm{m^3}} = \frac{1}{\mathrm{m}} = \mathrm{m^{-1}} \qquad \text{Eq. A-3}$$

Hence the unit of k_1 is $\mathrm{m^{-1}}$ which is predicted as k_1 is given by Eq. 3-33 as

$$k_1 = \frac{1}{2\pi R} \qquad \text{Eq. A-4}$$

where R is the radius of the cross section area bounded by the electrodes.

Appendix B

Derivation of the Peak Magnetic Flux Density B_0 (Equation 5-7)

The electromagnet obeys ohm's law for a magnetic circuit which states that,

$$\mathcal{F} = \Phi\mathcal{R} \qquad \text{Eq. B-1}$$

where $\mathcal{F}$ is the magnetomotive force 'mmf' (unit: ampere-turns At), Φ is the magnetic flux (unit: Weber Wb) and $\mathcal{R}$ is the total reluctance of the circuit (unit: At/Wb). The magnetomotive force is the product of the number of turns N of, and current I through, the coil. It is defined by [153]

$$\mathcal{F} = NI \qquad \text{Eq. B-2}$$

From Eq. B-1 and Eq. B-2, the magnetic flux Φ can be given as

$$\Phi = \frac{NI}{\mathcal{R}} \qquad \text{Eq. B-3}$$

The magnetic flux lines Φ passing through an area A (unit: m^2) is called the magnetic flux density B (unit: Tesla or Wb/m) which is given by

$$B = \frac{\Phi}{A} \qquad \text{Eq. B-4}$$

Therefore, the peak magnetic flux density B_0, using Eq. B-3 and Eq. B-4, can be given as

$$B_0 = \frac{NI_0}{\mathcal{R}A} \qquad \text{Eq. B-5}$$

where I_0 is the peak current (unit: A) flowing through the coil of the electromagnet. For the electromagnet in consideration (Figure 5.13), the total reluctance of the magnetic circuit is the sum of the reluctance of the core $\mathcal{R}_c$ and the reluctance of the air gap of the core $\mathcal{R}_g$. However, the reluctance of the air gap is much greater than the reluctance of the core ($\mathcal{R}_g \gg \mathcal{R}_c$) therefore, the reluctance of the core is negligible. Hence, the peak magnetic flux density B_0 of this electromagnet is expressed as

$$B_0 = \frac{NI_0}{\mathcal{R}_g A_g} \qquad \text{Eq. B-6}$$

where A_g is the area of the air gap. The electromagnet is also an electrical AC circuit with a very small resistance and large inductance. The peak current I_0 of the circuit can be given by

$$I_0 = \frac{V_0}{Z_{total}} \qquad \text{Eq. B-7}$$

Assuming a pure inductive load as the small resistance of the electromagnet coil can be negligible, the total impedance of the circuit Z_{total} is equal to the reactive impedance Z_L where

$$Z_L = jX_L \qquad \text{Eq. B-8}$$

where j is the imaginary term which indicates that the current I_0 in a pure inductive load lags the supply voltage V_0 by 90° and X_L is the reactance of the inductor (electromagnet) and is given by

$$X_L = 2\pi f L \qquad \text{Eq. B-9}$$

The inductance of the electromagnet L can also be expressed in terms of the number of turns of the coil N and the reluctance of the air gap [153] (reluctance of the core is negligible) which is given by

$$L = \frac{N^2}{\mathcal{R}_g} \qquad \text{Eq. B-10}$$

Substituting Eq. B-10 and Eq. B-9 into Eq. B-8 gives,

$$Z_L = j2\pi f \frac{N^2}{\mathcal{R}_g} \qquad \text{Eq. B-11}$$

From Eq. B-7 and Eq. B-11 (ignoring the term j as phase information is not required)

$$N^2 = \frac{V_0 \mathcal{R}_g}{2\pi f I_0} \qquad \text{Eq. B-12}$$

By taking the square of Eq. B-6, the following equation is obtained,

$$B_0{}^2 = \frac{N^2 I_0{}^2}{\mathcal{R}_g{}^2 A_g{}^2} \qquad \text{Eq. B-13}$$

Substituting Eq. B-12 into Eq. B-13 gives

$$B_0{}^2 = \frac{V_0 I_0}{2\pi f \mathcal{R}_g A_g{}^2}$$

Or

Eq. B-14

$$B_0 = \frac{1}{A_g}\sqrt{\frac{V_0 I_0}{2\pi f \mathcal{R}_g}}$$

Appendix C

AC-coupled instrumentation amplifier: Frequency response Test Setup

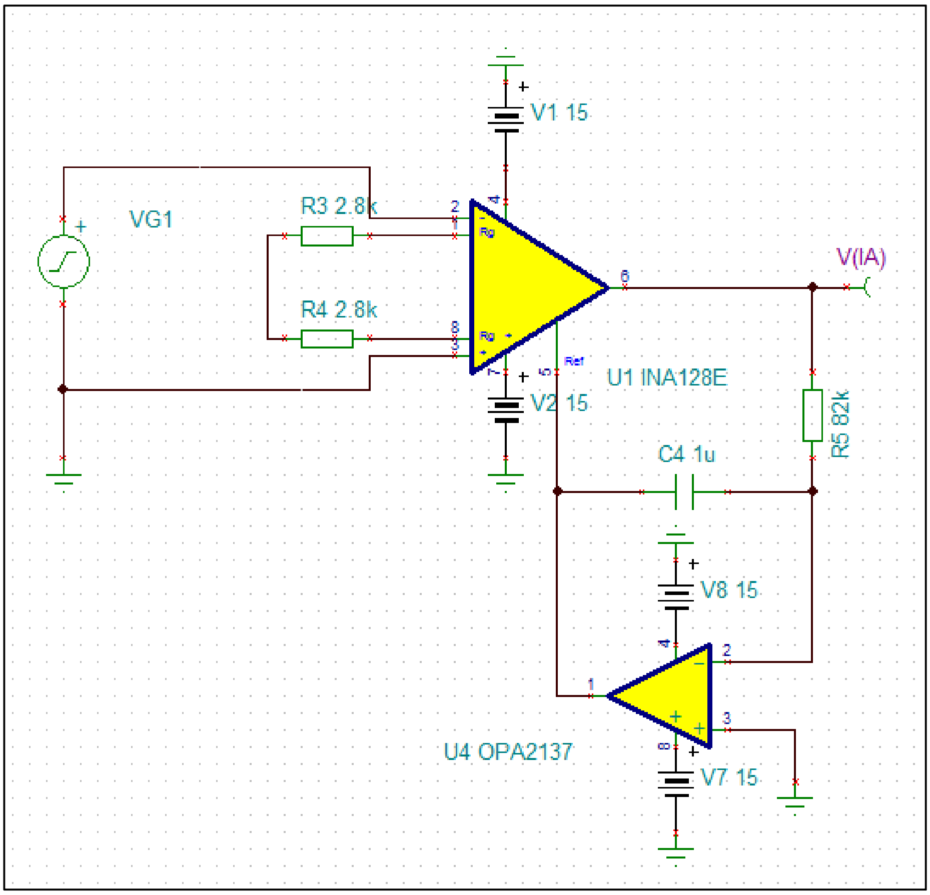

Figure C.1: Frequency response test setup for AC-coupled instrumentation amplifier

Tina 9 Software by DesignSoft was used to perform the AC analysis for this circuit.

RFI and ac-coupled instrumentation amplifier circuits: Frequency Response Test Setup

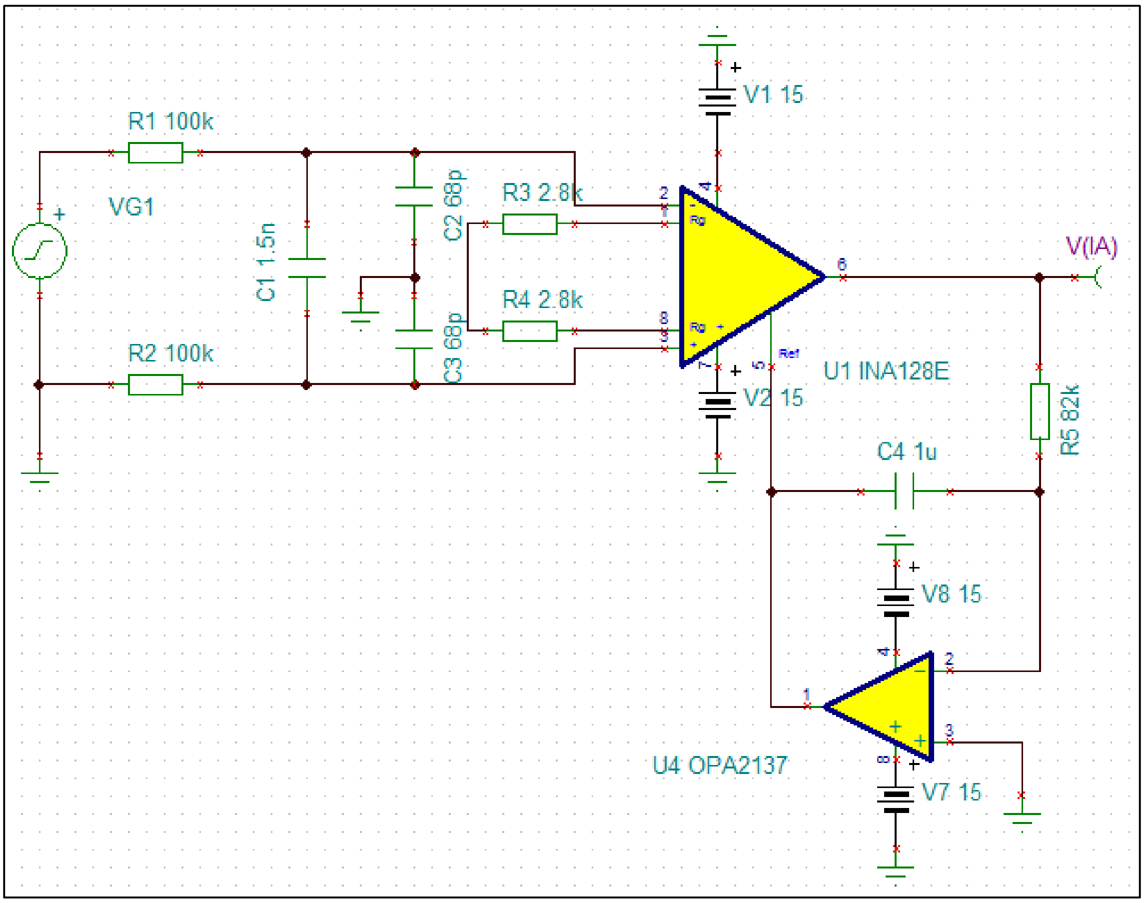

Figure C.2: Frequency response test setup for RFI and AC-coupled instrumentation amplifier

Both RFI filter and AC-coupled instrumentation amplifier are connected. AC analysis was performed in Tina 9 to obtain the frequency response of the circuit.

AC Signal Conditioning Circuit (Gain of 10): CMRR Test Setup

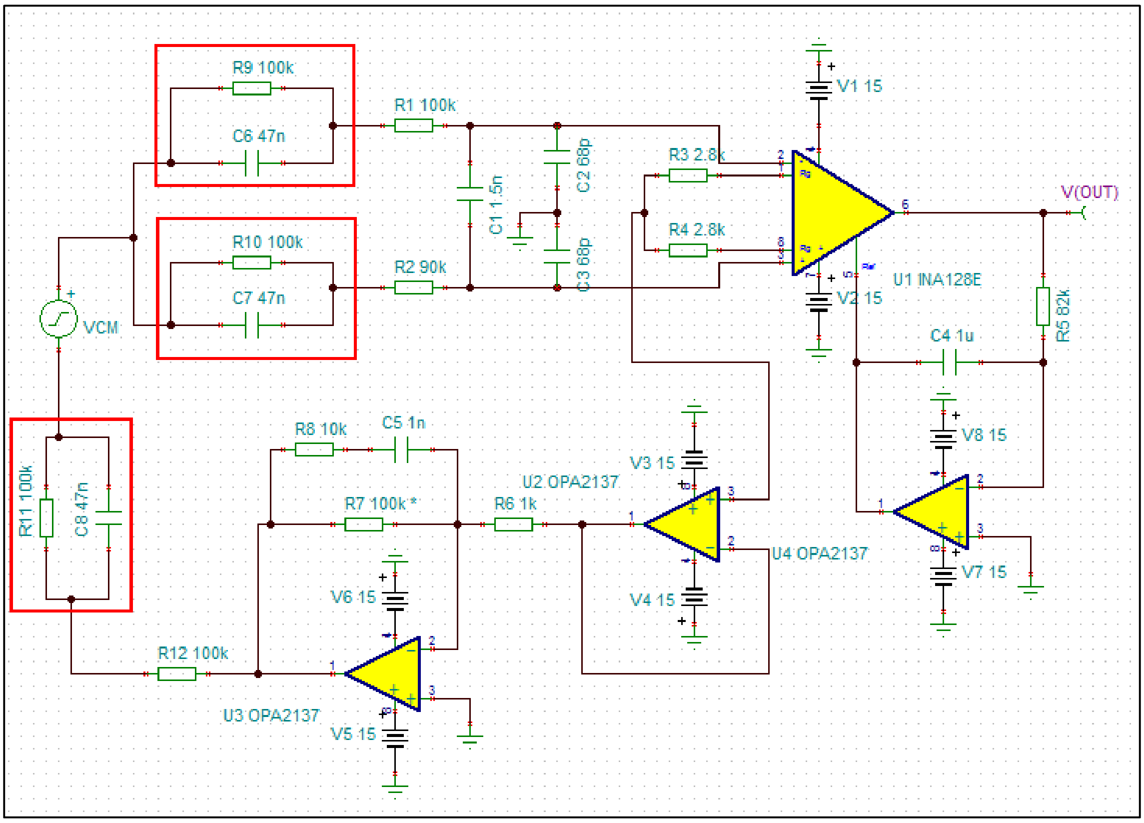

Figure C.3: CMRR test setup for AC signal conditioning circuit

In this setup, the signal source 'VCM' was connected to both input resistors R_1 and R_2 of the AC signal conditioning circuit via electrodes (R_9C_6 and $R_{10}C_7$ are basic electrode electrical models). The output of the RLD amplifier is connected to the negative terminal of the 'VCM' signal source via an electrode electric model ($R_{11}C_8$). AC analysis was performed to obtain CMRR vs frequency plot. The inverting amplifier circuit is not tested in this circuit as it only amplifies the output voltage by a gain of 100.

AC Signal Conditioning Circuit (Gain of 1000): Normal Operation Test Circuit

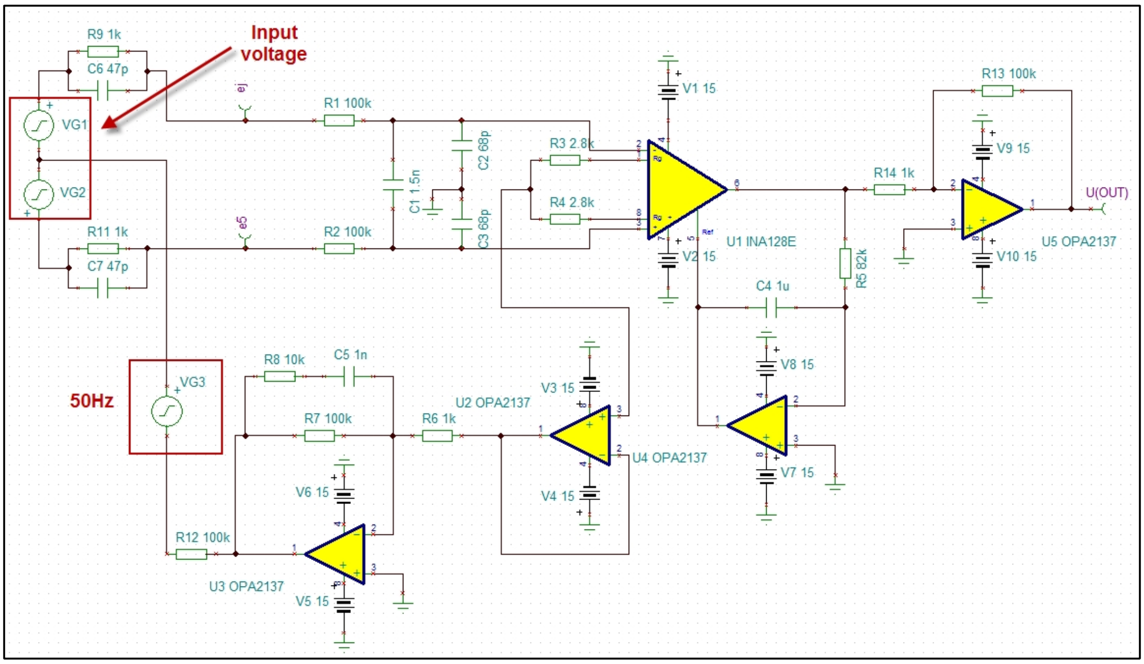

Figure C.4: Normal operation test setup for AC signal conditioning circuit

In this test, a small sinusoidal voltage (VG1 andVG2) is applied to the inputs of the AC signal conditioning circuit via electrode models. A 50 Hz noise (VG3) is also added to the input voltage to simulate mains interference. The inverting amplifier is connected in this circuit to amplify the signal by a further factor of 100.

AC Signal Conditioning Circuit: Transient and Frequency Responses Test Circuit

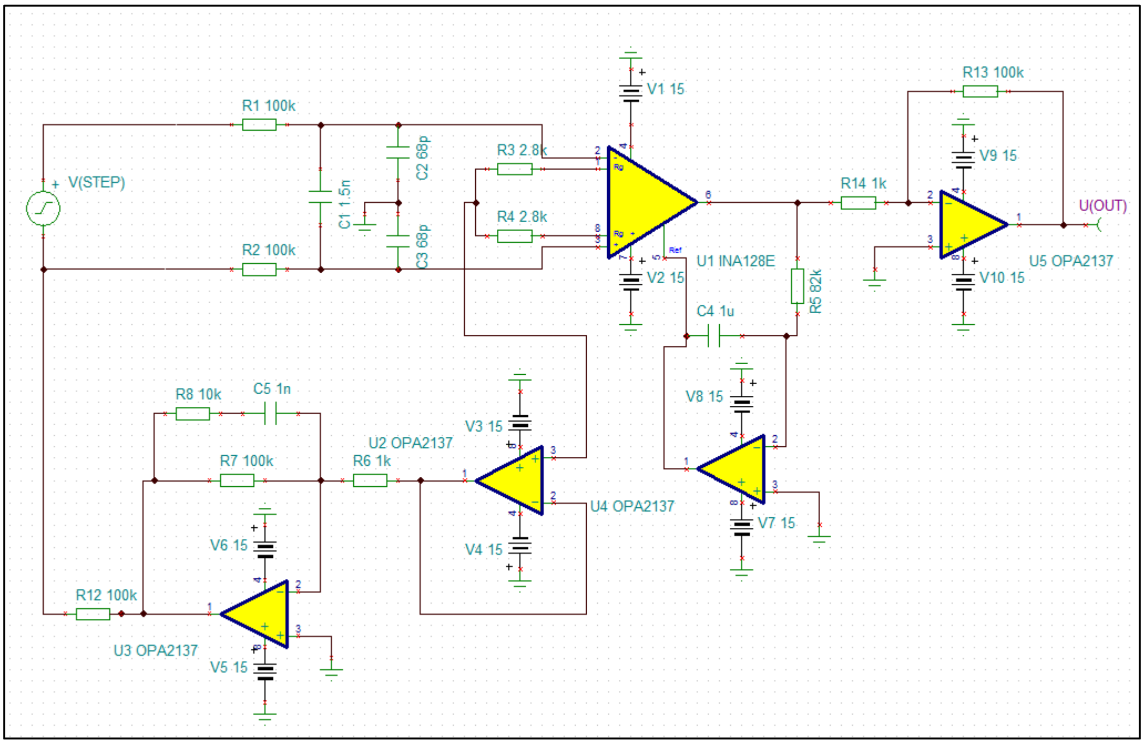

Figure C.5: Transient and frequency responses test setup for AC-coupled instrumentation amplifier

This test setup was used to test the AC signal conditioning circuit for its transient and frequency responses. Both tests were done using TINA 9 software.

Appendix D

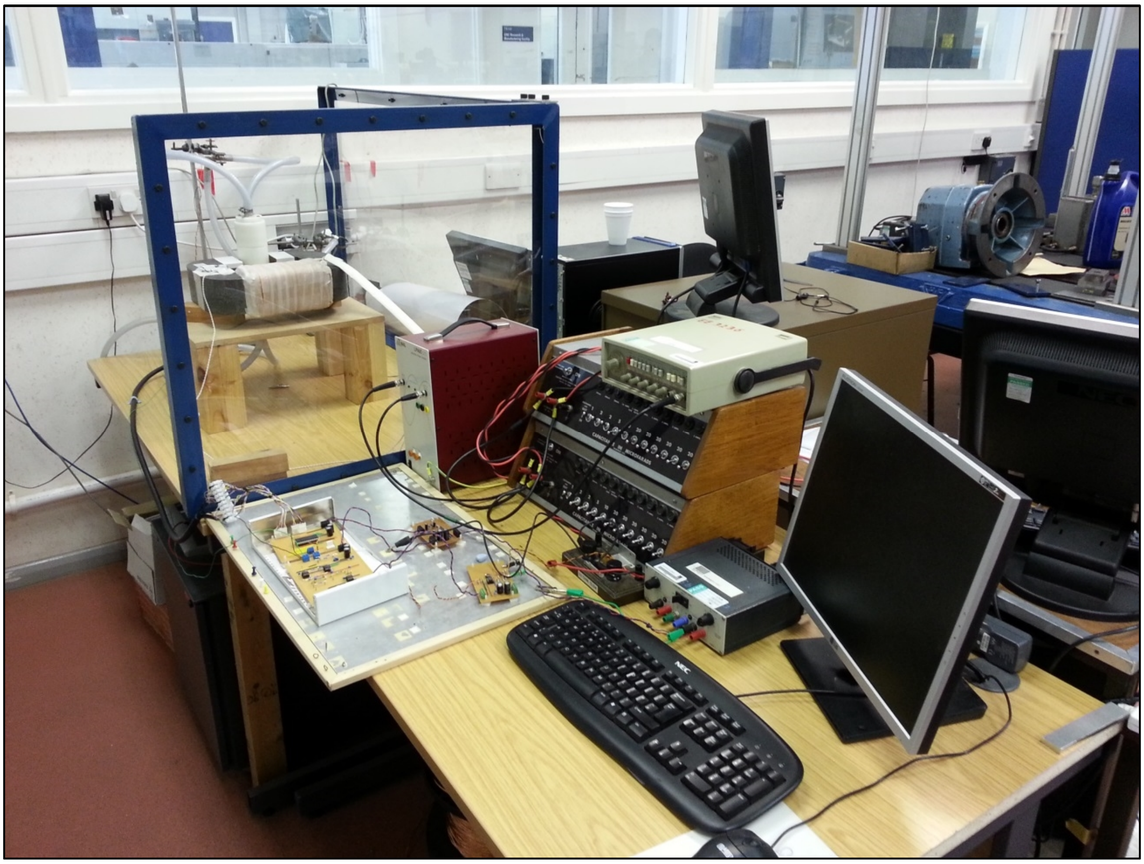

Figure C.6: The SVS flow test rig, the power supply and the measurement system